THE
PHYSICAL REVIEW

A journal of experimental and theoretical physics established by E. L. Nichols in 1893

SECOND SERIES, VOL. 79, NO. 4 AUGUST 15, 1950

Fine Structure of the Hydrogen Atom.* Part I

WILLIS E. LAMB, JR., AND ROBERT C. RETHERFORD†
Columbia Radiation Laboratory, Columbia University, New York, New York
(Received April 10, 1950)

The fine structure of the hydrogen atom is studied by a microwave method. A beam of atoms in the metastable $2^2S_{1/2}$ state is produced by bombarding atomic hydrogen. The metastable atoms are detected when they fall on a metal surface and eject electrons. If the metastable atoms are subjected to radiofrequency power of the proper frequency, they undergo transitions to the nonmetastable states $2^2P_{1/2}$ and $2^2P_{3/2}$ and decay to the ground state $1^2S_{1/2}$ in which they are not detected. In this way it is determined that contrary to the predictions of the Dirac theory, the $2^2S_{1/2}$ state does not have the same energy as the $2^2P_{1/2}$ state, but lies higher by an amount corresponding to a frequency of about 1000 Mc/sec. Within the accuracy of the measurements, the separation of the $2^2P_{1/2}$ and $2^2P_{3/2}$ levels is in agreement with the Dirac theory. No differences in either level shift or doublet separation were observed between hydrogen and deuterium. These results were obtained with the first working apparatus. Much more accurate measurements will be reported in subsequent papers as well as a detailed comparison with the quantum electrodynamic explanation of the level shift by Bethe.

Among the topics discussed in connection with this work are (1) spectroscopic observations of the H_α line, (2) early attempts to use microwaves to study the hydrogen fine structure, (3) existence of metastable hydrogen atoms, their properties and methods for their production and detection, (4) estimates of yield and r-f power requirements, (5) Zeeman and hyperfine structure effects, (6) quenching of metastable hydrogen atoms by electric and motional electric fields, (7) production of a polarized beam of metastable hydrogen atoms.

A. INTRODUCTION

IN August, 1947 a brief account[1] was given of the use of microwaves to solve the problem of the fine structure of atomic hydrogen. A deviation from the predictions of the Dirac theory amounting to about 1000 Mc/sec. in the position of the $2^2S_{1/2}$ level was definitely established. The accuracy of these first measurements amounted to perhaps 100 Mc/sec. It was planned at that time to follow quickly with a paper setting forth fully the method and theory of the experiment. The first apparatus was necessarily crude, and we were already working on a new and improved version. Our goal was first set to achieve an accuracy of 10 Mc/sec., but this has since been changed to 1 Mc./sec. The program was a large one and encountered unexpected difficulties which required much time to surmount. As a result, the paper promised two years ago was delayed.

We are at present engaged in making the final measurements on our new apparatus. Owing to the increased experimental accuracy, a large number of small experimental and theoretical effects must be taken into account in the analysis of the data. It is felt that if all of these matters were also incorporated into one paper, the result would be unwieldy, and not do justice to the simple basic ideas involved in the experiment.

Therefore, it is planned to write a series of papers, of which this is the first. This article will contain a brief history of the problem, an account of the considerations involved in the choice of method, estimates of effects to be expected, a description of the apparatus constructed prior to May, 1947, and the experimental results obtained with that apparatus. Since the numerical estimates of expected effects depend considerably on quantities which were unknown when such estimates were first made, it has been decided to make use of present knowledge where convenient in order to avoid lengthy discussions. As a result, some of the estimates are applicable to later forms of the apparatus, but it is thought that this will not cause undue confusion to the reader.

The theory of the hydrogen atom and the Zeeman effect of its fine structure and hyperfine structure has

* Work supported jointly by the Signal Corps and ONR.
† Submitted by Robert C. Retherford in partial fulfillment of the requirements for the degree of Doctor of Philosophy in the Faculty of Pure Science, Columbia University.
[1] W. E. Lamb, Jr. and R. C. Retherford, Phys. Rev. **72**, 241 (1947). A later value for the term shift of 1062±5 Mc/sec. was reported by R. C. Retherford and W. E. Lamb, Jr., Phys. Rev. **75**, 1325 (1949).

UNIVERSITY OF MICHIGAN LIBRARIES

been reviewed, since it is necessary for an understanding of the experimental results. In the present paper, we have taken into account effects of the order of 10 Mc/sec. or larger, leaving a more accurate description to a later paper where it is really needed. The effect of reduced mass has been largely ignored, and only slight attention given to the existence of the anomalous magnetic moment of the electron.

B. DISCUSSION OF THE PROBLEM

1. General Considerations

The hydrogen atom is the simplest one in nature, and the only one for which essentially exact calculations can be made on the basis of theory. The theoretical discussions now usually start with the Dirac equation for the motion of an electron in the pure Coulomb field of a fixed point charge. Corrections for the motion of the proton, its possible finite size, and the hyperfine structure due to its magnetic moment can be taken into account to a good approximation. The same is true of the effects due to interaction of the electron with the quantized electromagnetic field which were discovered by Bethe[2] subsequent to the establishment of departures from the Dirac theory.

According to the Bohr[3] theory of 1913, the energy levels of a hydrogen-like atom are given by the equation

$$W_n = -hcRZ^2/n^2, \tag{1}$$

where R is the Rydberg wave number, $h=2\pi\hbar$ is Planck's constant, and c is the velocity of light. For an infinitely heavy nucleus, $R=(109{,}737.3)$ cm^{-1}. The transition from state $n=3$ to $n=2$ gives the red H_α line. This was discovered by Michelson and Morley[4] in 1887 to be actually a doublet. An explanation of this fine structure was given by Sommerfeld[3] in 1916 in terms of the relativistic variation of electron mass with velocity. The two possible motions for principal quantum number $n=2$ differed in energy by

$$\Delta W_2 = (\alpha^2/16)hcR[1+0(\alpha^2)], \tag{2}$$

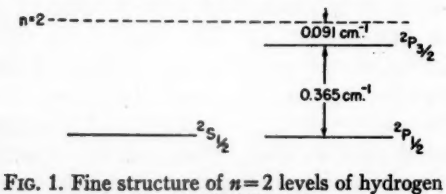

FIG. 1. Fine structure of $n=2$ levels of hydrogen according to the Dirac theory.

with $\alpha=1/(137.030)$ the fine structure constant (Birge, 1941).

When quantum mechanics was first introduced, it was found that, although the Bohr formula could be derived, the approximate inclusion of relativistic effects gave a separation of 8/3 times that of Eq. (2), which was at least in rough agreement with the observations of the time. Only when the Goudsmit-Uhlenbeck and Thomas model[3] of a spinning electron was incorporated into the theory did it again become possible to derive Eq. (2). Instead of two levels, there were now three, as shown in Fig. 1. This theory indicated that there should be an exact coincidence of the $2^2S_{1/2}$ and $2^2P_{1/2}$ levels, but the calculation was not entirely free of ambiguity, since the ratio 0/0 appeared in the derivation.

The Dirac theory of the electron of 1928 automatically endowed the electron with relativistic properties, spin and magnetic moment, and predicted the fine structure pattern of Fig. 1 without the above-mentioned ambiguity. The energy levels of a hydrogen-like atom are given by

$$W = mc^2\{[1+(\alpha Z)^2(n-|K| + (K^2-\alpha^2Z^2)^{\frac{1}{2}})^{-2}]^{-\frac{1}{2}}-1\}, \tag{3}$$

where $|K|=j+\frac{1}{2}$. In agreement with Fig. 1, the levels having the same principal quantum number n and inner quantum number j are degenerate. Expansion of Eq. (3) in powers of αZ gives

$$W_{nj} = -Z^2hcR/n^2 - (\alpha^2Z^4hcR/n^3)[(j+\tfrac{1}{2})^{-1}-(3/4n)]+\cdots. \tag{4}$$

According to this, the doublet separation for the $n=2$ state of hydrogen is

$$\Delta W_2 = (\alpha^2/16)hcR, \tag{5}$$

agreeing with the Sommerfeld result, since the next term in the expansion is entirely negligible for present purposes.

Although the treatment of the hydrogen atom given by the Dirac theory was beautiful and satisfying, the theory carried with it some strange consequences arising from the existence of the negative energy states. It was therefore considered highly desirable to subject the fine structure predictions to careful experimental tests. These were at first, naturally enough, observations on the spectrum of the hydrogen atom. Any departure from theory would be ascribed to one or more of the following causes: (1) error in the Dirac equation, (2) modification of the Coulomb law of attraction between electron and proton, possibly by a short-range non-electromagnetic interaction,[5] or positron theoretic vacuum polarization[6] effects, (3) some

[2] H. A. Bethe, Phys. Rev. **72**, 339 (1947). Relativistic calculations of the term shift have been made by N. M. Kroll and W. E. Lamb, Jr., Phys. Rev. **75**, 388 (1949) and J. B. French and V. F. Weisskopf, Phys. Rev. **75**, 1240 (1949). Different results have been obtained by A. D. Galinin, J. Exp. Theor. Phys. **19**, 521 (1949); Y. Nambu, Prog. Theor. Phys. **4**, 82 (1949); O. Hara and T. Tokano, Prog. Theor. Phys. 4, 103 (1949); Fukuda, Miyamoto, and Tomonaga, Prog. Theor. Phys. 4, 121 (1949).

[3] For a general discussion, see H. E. White, *Introduction to Atomic Spectra* (McGraw-Hill Book Company, Inc., New York, 1934).

[4] A. A. Michelson and E. W. Morley, Phil. Mag. **24**, 46 (1887).

[5] E. C. Kemble and R. D. Present, Phys. Rev. **44**, 1031 (1933); J. M. Jauch, Helv. Phys. Acta. **13**, 451 (1940); A. Sommerfeld, Naturwiss. **29**, 286 (1941), Zeits. f. Physik **118**, 295 (1941); P. Caldirola, Nuovo Cimento **5**, 207 (1948); E. David, Zeits. f. Physik **125**, 274 (1949).

[6] E. A. Uehling, Phys. Rev. **48**, 55 (1935).

finite and physically real remnant of the infinite radiative shift in the frequencies of all spectral lines predicted by the 1930 calculations of Oppenheimer,[7] or (4) unexplained effects. The work of Bechert and Meixner[8] showed that hyperfine structure and reduced mass effects could not be responsible for appreciable discrepancies.

2. Spectroscopic Observations of the H_α Line

The history of the spectroscopic work on the H_α doublet is a long one, starting with the first resolution of the doublet structure in 1887 and continuing today. The reader is referred to the 1938 paper by Williams[9] for an account of the earlier work. By 1940 the situation had become very unclear. On the one hand, the work of Houston[10] and Williams[9] indicated rather probable discrepancies between theory and experiment Pasternack[11] had shown that these could be explained if the $2^2S_{1/2}$ level were raised relative to the $2^2P_{1/2}$ level by about 0.03 cm^{-1}. In 1940 Drinkwater, Richardson, and Williams,[12] on the other hand, attributed any discrepancies to impurities in the source.

The theorists who attempted to account for Pasternack's shift in terms of a departure from the Coulomb law[5] were frustrated by the smallness of their predictions, or misled[13] by inadequacies in their theories. They rather eagerly hailed the results of Drinkwater, Richardson, and Williams[12] which confirmed the Dirac theory.

Postwar measurements by Giulotto[14] pointed again to a discrepancy, and recently Kuhn and Series,[15] using a liquid hydrogen cooled discharged tube, reported a shift of $2^2S_{1/2}$ of 0.043 ± 0.006 cm^{-1}.

The H_α complex of lines has two main peaks separated by about 0.317 cm^{-1}, and in the work of Williams with deuterium the lines had Doppler widths of 0.120 cm^{-1}. Under these circumstances, a really precise spectroscopic check of the theory is exceedingly difficult. It is made even more so by the fact that the intensities of the components often depart from the theoretically predicted values and vary with the discharge conditions.

Only the use of an atomic beam source to reduce the Doppler effect would seem to offer much hope for a real resolution of the H_α complex. The radiative width of the sharpest line would be only about 0.001 cm^{-1} (30 Mc/sec.), but according to estimates made by Mack,[16] the attainable width would be about ten times larger.

3. Possible Use of Radio Waves in Hydrogen Spectroscopy

It was pointed out as early as 1928 by Grotrian[16a] that the selection rules permitted optical transitions with zero change of the principal quantum number, n, and that it should be possible with radio waves to induce such transitions among the states $n=2$ corresponding to the doublet separation $\Delta\tilde{\nu}=0.365$ cm^{-1} or a wave-length $\lambda=2.74$ cm and frequency 10,950 Mc/sec.

There are some German papers[17,18] between 1932 and 1935 dealing with attempts to detect such a transition. At that time, only spark gap oscillators of exceedingly low power output were available for such wave-lengths. One had to work with a continuous spectrum of radiation, using the interference methods to select a reasonably monochromatic range of wave-lengths. The radiation was passed through an absorption vessel containing a hydrogen discharge of the Wood's[19] type, and the attentuation was determined as a function of wave-length. The first worker, Betz, claimed to have observed an absorption in the expected wave-length range of 3 cm. He also obtained selective absorptions at 9 and 27 cm corresponding to transitions between the fine structure states of the levels with $n=3$. Three years later, working in the same laboratory, Haase repeated the experiment more carefully and failed to find any absorption at 9 and 27 cm. He did not study the 3-cm region. Haase made estimates of the selective energy absorption to be expected from excited hydrogen atoms and concluded that it was too small to detect. This question will be discussed in Appendix I from a slightly more modern point of view. Strangely enough, Haase gave no specific reason for the positive results obtained by Betz.

4. Choice of Method

After reading of the Betz-Haase work, we inquired whether microwave techniques, which advanced so much during the war, would now permit a successful and clear-cut determination of the hydrogen fine structure by absorption of the appropriate radiation in a Wood's discharge. In the course of such considerations

[7] J. R. Oppenheimer, Phys. Rev. **35**, 461 (1930).
[8] K. Bechert and J. Meixner, Ann. d. Physik **22**, 525 (1935); G. Breit and G. E. Brown, Phys. Rev. **74**, 1278 (1948).
[9] R. C. Williams, Phys. Rev. **54**, 558 (1938), also F. K. Richtmeyer, *Introduction to Modern Physics* (McGraw-Hill Book Company, Inc., New York, 1934), second edition, p. 398.
[10] W. V. Houston, Phys. Rev. **51**, 446 (1937).
[11] S. Pasternack, Phys. Rev. **54**, 1113 (1938).
[12] Drinkwater, Richardson, and Williams, Proc. Roy. Soc. **A174**, 164 (1940).
[13] Fröhlich, Heitler and Kahn, Proc. Roy. Soc. **A171**, 269 (1939); Phys. Rev. **56**, 961 (1939); B. Kahn, Physica **8**, 58 (1941). See also the objections by W. E. Lamb, Jr., Phys. Rev. **56**, 384 (1939); **57**, 458 (1940) supported by calculations of J. M. Blatt, Phys. Rev. **67**, 205 (1945); and by M. Slotnick and W. Heitler, Phys. Rev. **75**, 1645 (1949).
[14] L. Giulotto, Ricerca Scient. **17**, Nos. 2–3 (1947); Phys. Rev. **71**, 562 (1947).
[15] H. Kuhn and G. W. Series, Nature **162**, 373 (1948). These workers have recently communicated an improved value of 0.0369 ±0.0016 cm^{-1}. Proc. Roy. Soc. **A202**, 127 (1950).
[16] J. E. Mack and E. C. Barkofsky, Rev. Mod. Phys. **14**, 82 (1942).
[16a] W. Grotrian, *Graphische Darstellung der Spektren von Atomen* (Verlag Julius Springer, Berlin, 1928).
[17] O. Betz, Ann. d. Physik **15**, 321 (1932).
[18] T. Haase, Ann. d. Physik **23**, 675 (1935).
[19] R. W. Wood, Phil. Mag. **42**, 729 (1921).

UNIVERSITY OF MICHIGAN LIBRARIES

FIG. 2. Schematic block diagram of apparatus.

we came upon the idea of a different method, which was actually used. While we did not reach a definite conclusion on the possibility of the use of a Wood's tube method, the indication was rather discouraging. An account of these deliberations, revised in the light of present knowledge, is given in Appendix I. In view of the extreme crudeness of our numerical estimates, it is by no means certain that one could not now detect transitions between the $n=2$ states of atomic hydrogen if the discharge conditions were properly chosen. From consideration of the perturbing effects of electric fields and ion collisions on the energy levels of the atom, however, it seems that even if the transitions could be detected, the results would be of greater value for an indication of the conditions within a Wood's discharge tube than for a determination of fundamental properties of an isolated hydrogen atom.

There are two main methods in radiofrequency spectroscopy. In one, some matter absorbs or otherwise affects the radiation passing through it. In the other, the radiation causes observable changes to take place in the matter. The former method is used in the conventional form of microwave spectroscopy[20] in which the radiation is transmitted through a long path of absorbing gas. The latter method is used in the molecular beam radiofrequency resonance[21] method when the particles absorbing radiation are deflected out of the beam by an inhomogeneous magnetic field. Since the first method did not seem to be too promising for the study of the hydrogen fine structure, we turned to an examination of the possibilities in the second method.

5. Atomic Beam Method

In the case of atomic hydrogen, the $2P$ states decay to the $1S$ state with the emission of a photon of wavelength 1216A in 1.595×10^{-9} sec., and the atom could move only about 1.3×10^{-3} cm in that time, assuming a speed of 8×10^{5} cm/sec. On the other hand, the possibility exists that the $2^2S_{1/2}$ state would be sufficiently metastable so that a beam of particles in this state could be used. If a transition were then induced by radiofrequency or otherwise to a $2P$ state, a decay to $1^2S_{1/2}$ would take place so quickly that the number of excited atoms in the beam would be reduced. If one could then find a detector which responded selectively to the excited hydrogen atoms, one would have the possibility of measuring the energy difference between the metastable $2^2S_{1/2}$ state and the various $2P$ states. The proposed experiment might then be represented in the block diagram in Fig. 2.

For this program to be carried out it was necessary to solve the following problems: (1) production of beam of atoms in the $2^2S_{1/2}$ state and (2) detection of such atoms. The program clearly depended on a knowledge of the properties of metastable hydrogen atoms. Such atoms had never been isolated in any clear-cut experiments, although they had been the subject of much speculation. The next section is devoted to the properties of metastable hydrogen atoms.

6. Metastable Hydrogen Atoms

In 1924, Compton and Russell[22] in trying to explain the large intensity of stellar Balmer lines pointed out that the lower of the two $n=2$ states obtained on the basis of Sommerfeld's theory should be metastable. In 1926, after the spinning electron theory was introduced, Sommerfeld and Unsöld[23] stated that the $2^2S_{1/2}$ state should still be metastable. On the other hand, Franck and Jordan[24] gave reasons for doubting that the $2^2S_{1/2}$ level would be metastable.

A certain amount of experimental work by Snoek, von Keussler and others[25] was carried out to test the Sommerfeld-Unsöld ideas on this point. They studied the relative intensities of the two main groups of components of the H_α line in absorption. If the $2^2S_{1/2}$ state in the absorbing discharge were appreciably metastable, the intensity ratio of the two peaks would be affected. From their results they concluded that the $2^2S_{1/2}$ level was not appreciably metastable.

Rojansky and Van Vleck[26] pointed out that the effect of an external electric field, however small, would mix the degenerate states $2^2S_{1/2}$ and $2^2P_{1/2}$ giving stationary state wave functions

$$\psi=2^{-\frac{1}{2}}[\psi(2^2S_{1/2})\pm\psi(2^2P_{1/2})], \qquad (6)$$

both of which would decay at the rate $(2\tau_p)^{-1}$, so that there could be no metastability. This conclusion, although correct in a sense, is not applicable to the experimentally realized situations where no stationary state exists. This was pointed out by Bethe[25] who gave a systematic theory of the effect of an electric field on the fine structure of hydrogen. In the complete absence of a perturbing electric field, an atom in the $2^2S_{1/2}$ state should have a very long life. (Bethe estimated that the life of an isolated atom would then be several months if relativistic effects were taken into

[20] W. Gordy, Rev. Mod. Phys. **20**, 668 (1948).
[21] J. M. B. Kellogg and S. Millman, Rev. Mod. Phys. **18**, 323 (1946).
[22] K. T. Compton and H. N. Russell, Nature **114**, 86 (1924).
[23] A. Sommerfeld and A. Unsöld, Zeits. f. Physik **36**, 259 (1926); **38**, 237 (1926).
[24] J. Franck and P. Jordan *Anregung von Quantensprüngen durch Stöese* (Verlag Julius Springer, Berlin, 1926), p. 117. W. de Groot and F. M. Penning, *Handbuch der Physik* (1933), second edition, Vol. 23/1, p. 78.
[25] H. A. Bethe *Handbuch der Physik* (1933), second edition, Vol. 24/1, pp. 452–462.
[26] V. Rojansky and J. H. Van Vleck, Phys. Rev. **32**, 327 (1928); V. Rojansky, Phys. Rev. **33**, 1 (1929).

account.) In the presence of a large perturbing electric field, the result would be that of Rojansky and Van Vleck. As the electric field is increased from zero, the lifetime would undergo a change from one limiting value to the other. Bethe showed that the results of von Keussler and Snoek were understandable in terms of the excitation cross sections of the various levels and the quenching of the metastability by the perturbing electric fields of the discharge. For an effective electric field of 10 volts/cm, he found that the life of the $2^2S_{1/2}$ state would be about five times the life τ_p. Over a large range of fields, the life varies inversely as the square of the field strength. Under typical Wood's tube conditions, Bethe estimated that the life would be about $2\tau_p$.

In 1940, Breit and Teller[27] refined some of Bethe's calculations, and discussed the metastability in connection with possible astrophysical applications. They showed that the decay mechanism of double quantum emission to the ground state was more important than the relativistic effects, and that the life of an isolated metastable atom on this basis would be $\frac{1}{7}$ sec.

It was clear to us from the foregoing that the $2^2S_{1/2}$ state would be markedly metastable only if the perturbing fields could be sufficiently reduced. For a beam length of 6 cm and a speed of 8×10^5 cm/sec., a life of the order 0.75×10^{-5} sec. would be necessary for 37 percent of the atoms to survive. According to Bethe's calculations, this would require a perturbing field of $\frac{1}{3}$ volt/cm or less. It would not be easy to keep the electrons and ions formed in the excitation process away from the detector with such fields unless an extremely long beam were used.

In actuality, of course, we now know that the $2^2S_{1/2}$ and $2^2P_{1/2}$ levels are not degenerate. This adds considerably to the stability of $2^2S_{1/2}$ against Stark effect quenching. According to a simple extension of Bethe's calculation given in Appendix II, the lifetime of $2^2S_{1/2}$ in moderate electric fields becomes

$$\tau_s=\tau_p\{\hbar^2(\omega^2+\tfrac{1}{4}\gamma^2)/V^2\}, \qquad (7)$$

where V is the matrix element of the perturbing electric energy and $\hbar\omega$ is the separation of the interacting levels $2^2S_{1/2}$ and $2^2P_{1/2}$. (Breit and Teller have discussed the stabilizing effect of the hyperfine structure splitting and found an increase in τ_s by a factor of four. Since the actual value of $\hbar\omega$ is much larger than the hyperfine structure splitting, the stability will not be much affected by the hyperfine structure, and we shall neglect it here.) According to Eq. (7), for $\omega/2\pi=1000$ Mc/sec., the life τ_s would be about 400 times longer than if there were no removal of the degeneracy.[28]

[27] G. Breit and E. Teller, Astrophys. J. **91**, 215 (1940). A correspondence theoretic analysis of double quantum emission has been given by J. A. Wheeler, J. Opt. Soc. Am. **37**, 813 (1947).

[28] This suggests the need for a reinterpretation of the experiments of Snoek, von Keussler and others. Some of the features which need consideration are indicated in Appendix I.

At the time, however, we did not take the possibility of a natural removal of the degeneracy by such a large amount very seriously, and planned to increase the stability of $2^2S_{1/2}$ by the application of a magnetic field to give a large Zeeman splitting of the states.

The presence of a magnetic field at right angles to the atomic beam would also serve to keep charged particles away from the detector. A third, and really the most important function of the magnetic field will be discussed in Section 14.

7. Production of a Beam of Metastable Hydrogen Atoms

A number of possible methods for the production of a beam of hydrogen atoms in the metastable $2^2S_{1/2}$ state were considered. The simplest source would be a hydrogen discharge tube with a small opening into a vacuum for the emergence of a beam. In the discharge, one would have a mixture of molecular and atomic hydrogen, electrons and ions, and a small proportion of excited atoms, together with a high intensity of Lyman and Balmer radiation. The population of $2^2S_{1/2}$ is estimated in Appendix I to be about 5×10^{10} atoms/cm^3. The question would be whether any appreciable number of these could escape through the hole before being quenched by the Holzmark fields due to ions and electrons simultaneously escaping. Even with the stabilizing effect of a magnetic field, this did not seem to be likely. It would also be possible for some of the normal atoms to be excited optically to the $3P$ level after leaving the discharge, and of these 12 percent[29] would decay to $2^2S_{1/2}$. The numerical estimate of the yield for this was discouraging. Furthermore, there would be a very high background intensity of ultraviolet radiation at the

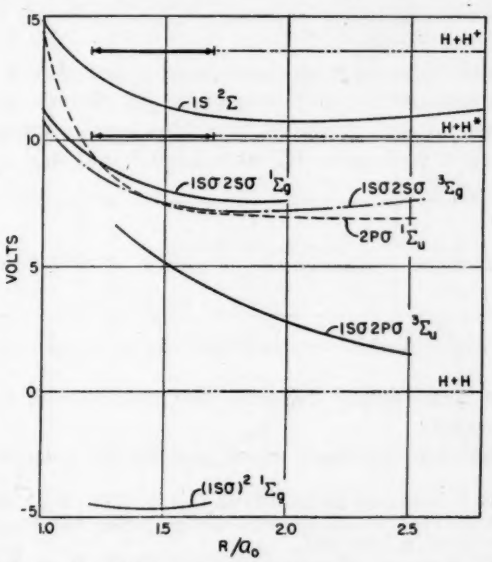

FIG. 3. Electronic energy levels of the hydrogen molecule as a function of internuclear distance.

[29] See reference 25, p. 444.

detector. This could cause trouble since most of the possible detectors of metastable atoms are also photosensitive. Subsequent to the success of the experiment by another method such a Wood's tube source was tried, but did not give positive results.

The second method which we considered was the bombardment of molecular hydrogen with electrons in a field-free region. A possible process is

$$H_2+e\rightarrow H+H^*+e', \tag{8}$$

where H* represents a metastable atom. The potential energy curves for the various excited electronic states of H_2 shown in Fig. 3 are based on calculations by Hylleraas, and by James, Coolidge, and Present.[30] The small segment of the ground state $^1\Sigma_g$ shown represents the limits of zero-point vibration in the lowest vibrational state. According to the Franck-Condon principle, electron bombardment should most strongly excite the $^3\Sigma_g$-state at energies below its dissociation limit into H+H*. One would, however, expect a small yield of metastable atoms for electrons of about 15 ev. Such a "violation" of the Franck-Condon principle would be analagous to the dissociation with ionization,

$$H_2+e\rightarrow H+H^++e'+e'', \tag{9}$$

observed by Bleakney[31] at 18 volts. Besides the $^3\Sigma_g$-curve shown, there are repulsive states leading to H+H*, and hence fast metastable atoms should be produced at higher bombarding energies.

One difficulty with this method of production is that the atomic fragments H+H* move off in directions oriented at random with respect to the electron beam, and hence the detector can conveniently intercept only a small fraction of them. The background effects due to the ultraviolet photons which are produced in molecular hydrogen beginning at 11.5 volts are likely to be troublesome.

In the first form of the apparatus described below, an unsuccessful search was made for metastable hydrogen atoms produced by the bombardment of molecular hydrogen. We now know[32] that had conditions been slightly different, this method would have succeeded.

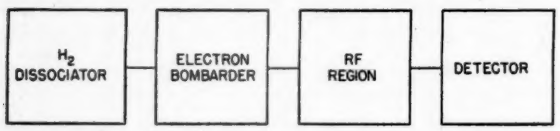

FIG. 4. Modified schematic block diagram of apparatus.

The third method, which was finally adopted, required the separate production of a beam of atomic hydrogen atoms in the ground state and the subsequent bombardment of the beam by electrons with an energy somewhat over the threshold of 10.2 volts for excitation to $2^2S_{1/2}$. The proposed experiment might now be represented by the block diagram shown in Fig. 4.

8. Dissociation of Molecular Hydrogen

A number of methods are available for the production of a beam of atomic hydrogen atoms: (1) Wood's tube, (2) microwave discharge, (3) thermal dissociation in a tungsten furnace. No very compelling reason can be given for the adoption of the last method. We were aware of the work in 1923 of Olmstead and Compton[33] who measured the critical potentials of atomic hydrogen formed in a tungsten oven, and we were greatly assisted by the advice of Dr. O. S. Duffendack[34] who pioneered in research with such ovens. On the other hand, the hydrogen atomic beam work[21] done before the war at Columbia made very successful use of a Wood's tube source. It was felt, however, that the ultraviolet background radiation would be troublesome in our case. The microwave discharge method[35] was ruled out because the leakage of a small amount of r-f power would complicate the spectroscopic observations.

Assuming thermal equilibrium, the extent of the dissociation of molecular hydrogen

$$H_2\rightarrow 2H \tag{10}$$

is given by

$$[P(H)]^2/P(H_2)=K(T), \tag{11}$$

where the equilibrium constant $K(T)$ is given in atmospheres as a function of the absolute temperature T by the equation

$$\log_{10}K=-21200/T+1.765\log_{10}T-9.85\times10^{-5}T-0.265, \tag{12}$$

as calculated by Bonhoeffer[36] from data of Langmuir. Writing

$$P(H)=XP, \tag{13}$$

where P is the total pressure,

$$P=P(H)+P(H_2), \tag{14}$$

we have the fractional dissociation, X, determined by the equation

$$X^2/(1-X)=K(T)/P. \tag{15}$$

In Fig. 5, X is shown as a function of T for several pressures.

[30] E. A. Hylleraas, Zeits. f. Physik **71**, 739 (1931); R. D. Present, J. Chem. Phys. **3**, 122 (1935); Coolidge, James, and Present, J. Chem. Phys. **6**, 730 (1938).

[31] W. Bleakney, Phys. Rev. **35**, 1180 (1930). H. F. Newhall, Phys. Rev. **62**, 11 (1942) has questioned this interpretation, but his apparatus may have discriminated against slow protons.

[32] W. E. Lamb, Jr. and R. C. Retherford, Phys. Rev. **75**, 1332 (1949).

[33] P. S. Olmstead and K. T. Compton, Phys. Rev. **22**, 559 (1923).

[34] O. S. Duffendack, Phys. Rev. **20**, 655 (1922); K. T. Compton, J. Opt. Soc. Am. **6**, 910 (1922).

[35] Davis, Feld, Zabel, and Zacharias, Phys. Rev. **76**, 1076 (1949).

[36] K. F. Bonhoeffer, Ergeb. d. exakt. Naturwiss. **6**, 201 (1927); also Wooley, Scott, and Brickwedde, J. Research Nat. Bur. Stand. **41**, 379 (1948).

No direct measurement of pressure in the tungsten oven could be conveniently made, but from the observed variation of yield with temperature when the experiment was successful, it seems reasonable that it was about 10^{-3} atmosphere in a typical case, and that the dissociation was 64 percent complete at $T=2500°K$. At this temperature, the most probable velocity in the beam is 8×10^5 cm/sec. for hydrogen atoms.

9. Excitation of Hydrogen Atoms by Electron Bombardment

The cross section for various electron excitation processes in hydrogen have been calculated by Bethe[37] according to the Born approximation, with neglect of electron exchange. Although this approximation is not expected to be very good for electron energies near the threshold, it was the only one available for our numerical estimates. The cross sections are given by

$$\sigma_{nl}=(8\pi hcR/mv^2)\,|(nl|x|10)|^2 \times[F_{nl}(y_{\max})-F_{nl}(y_{\min})] \quad (16)$$

where

$$y=1+(n/n+1)^2(Q/hcR)$$

$$F_{20}(y)=-(5y^5)^{-1}$$

$$F_{21}(y)=\log_e[(y-1)/y]+\sum_{s=1}^{5}(sy^s)^{-1}$$

$$F_{31}(y)=F_{21}(y)-(4/3y^6)+(4/7y^7)$$

$$Q_{\max}=(E^{\frac{1}{2}}+[E-E_{nl}+E_{10}]^{\frac{1}{2}})^2$$

$$Q_{\min}=(E^{\frac{1}{2}}-[E-E_{nl}+E_{10}]^{\frac{1}{2}})^2$$

E = electron energy,

E_{nl} = energy of atomic state.

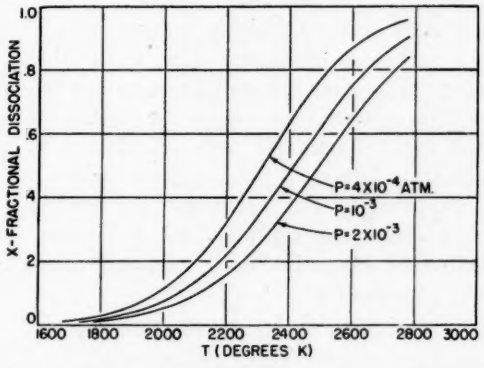

FIG. 5. Thermal dissociation of molecular hydrogen.

These cross sections are plotted as functions of electron energy in Fig. 6. The maximum cross section for $2s$ ($\sigma_{\max}=2.2\times10^{-17}$ cm^2) is about one-ninth that for $2p$, while that for $3p$ is smaller than that for $2s$ by a factor of 11. As a result, the yield of $2s$ by cascade from $3p$ may be neglected. The maximum yield for $2s$ comes at 14.8 volts, but does not fall below half the maximum value down to 11 volts.

Besides the errors inherent in the Born approximation, the neglect of electron exchange may be particularly serious for excitation of the optically inaccessible state $2s$, and one may hope to obtain a much larger cross section with a maximum nearer the threshold if exchange is included. Since no reliable calculations of exchange excitation, even with the Born approximation, seem to exist for hydrogen, we used the lower cross section $\sigma=10^{-17}$ cm^2, hoping to be on the save side.

If the detector is photo-sensitive there will also be a signal with the same threshold energy of 10.2 ev due to the Lyman photons from atoms excited to the $2p$ states. Any residual pressure of molecular hydrogen will also give photons. The threshold energy for the latter process is about 11.5 ev. Only a small fraction of these photons can reach the detector, but any background effects are undesirable.

10. Recoil Due to Bombardment

In the usual form of atomic beam experiment, one works with a very well-collimated beam. In the present case, it is necessary to bombard the hydrogen atoms after they leave the source, since Stark quenching must be minimized. One must then choose between bombardment at right angles to the beam, along it, or against it. The last two methods would not destroy the unidirectionality of the beam of atoms if the bombardment were at a voltage just above the threshold. Such a choice would be natural for other atoms, but not for metastable hydrogen atoms. In this case, one would be forced to have the magnetic field parallel to the electron beam. If the electrons were sent against the atomic beam, the metastable atoms would subsequently pass through an electric field which would quench them. If the electrons were sent along the beam, they could not easily be kept

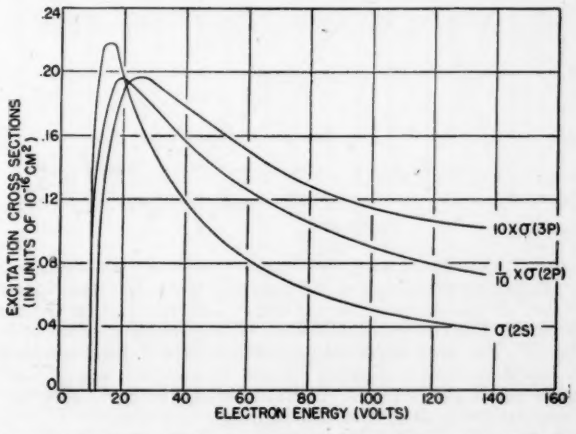

FIG. 6. Electronic excitation cross sections for states of atomic hydrogen calculated by Born approximation without exchange.

[37] See reference 25, p. 507.

UNIVERSITY OF MICHIGAN LIBRARIES

from the detector. Methods based on difference in time of flight were rejected on intensity grounds.

The first choice necessarily leads to a transverse recoil, and what is worse, an indefinite one, so that an originally well-collimated beam is diffused by the bombardment. This means that the use of slits of the order of 0.001 in. width as in the usual atomic beam work is ruled out. On the other hand, one does not have the problem met there of detecting the small deflections of the beam in inhomogeneous magnetic fields, since the effect of the radiofrequency is much more easily distinguished here by the removal of the excitation of the absorbing atom.

The distribution of recoil angles is calculated in Appendix III and the results for typical cases are shown in Fig. 7. Even at the threshold, there is a distribution in horizontal recoil angle ranging (with larger than half the maximum probability) from 4° to 8.7° because of the distribution of velocities in the atomic stream. At 13.6 ev, the distribution broadens to range from 3.6° to 10.8°, and there is a distribution of vertical recoil angles between ±3.4°.

11. Detection of Metastable Hydrogen Atoms

The atoms excited by the electron bombardment to the metastable $2^2S_{1/2}$ state are supposed to move off to a suitable detector. Several possible methods of detection were considered. Two of these had been used previously to detect metastable atoms other than hydrogen. It was discovered by Webb[38] in 1924 that metastable atoms of mercury could eject electrons from metals. Later work by Oliphant[39] showed that the same was true of helium metastable atoms. A theory of this process was given by Massey,[40] and by Cobas and Lamb.[41] If the excited atom comes close to the surface of a metal, it may be energetically possible for a collision of the second kind to occur in which the atom returns to the ground state and an electron is liberated from the system to take up the excess energy. One possibility for such a process is shown in Fig. 8. The energetic condition for this is that the excitation energy, I, of the atom should exceed the work function, ϕ, of the metal. In the case of helium, the excitation energy is about 20 ev and the condition should be satisfied for all metals. In the case of mercury, the excitation energy of the 2^3P_0 state is only 4.68 volts, and the condition becomes much more critically dependent on the work function of the surface. In fact, Sonkin[42] showed in 1933 that the efficiency of detection of mercury metastables was very sensitive, by a factor of 100 or more, to the presence of surface contaminations. On the other hand, Dorrestein[43] in 1942 found that the efficiency of detection of helium metastables on outgassed platinum was about 40 percent and was subject only to relatively small fluctuations over a day's run. No information was available on the detection of hydrogen metastables. In this case, however, the excitation energy, 10.2 volts, is well above the work functions of metals, and one would at first expect a high efficiency of detection as with helium.

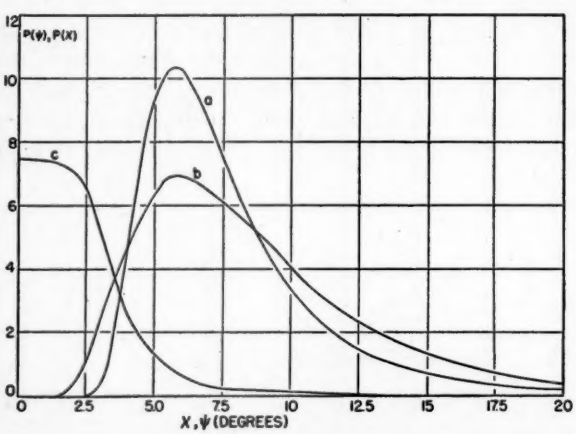

FIG. 7. Distributions in recoil angles. Curve (a): distribution in horizontal recoil angles ψ experienced by a hydrogen atom excited to the $2s$ state by electrons of energy just above the threshold. The temperature of the source of atoms is taken to be 2600°K. The total probability would be unity if the angle were measured in radians. Curves (b) and (c): distributions in horizontal recoil angles ψ and vertical recoil angles χ for hydrogen atoms excited to $2s$ by electrons of energy 13.6 ev.

According to rough calculations of the type mentioned above, metastable hydrogen atoms of thermal energy moving in toward a metal surface should, on the average, cause electron ejection before the atom reaches a distance of 2A. Since half of the electrons emitted probably go into the metal, one might expect an efficiency of the order of 50 percent.

Nevertheless, we were not very confident about the possibility of detecting hydrogen metastables by the above mechanism. These doubts arose in the following way: we were also considering another method based on the observation by Buehl[44] that metastable atoms of mercury falling on hot molybdenum are re-emitted as ions. This process is essentially the surface ionization detection method used for molecular beams in which an alkali atom falls on a hot tungsten surface, an electron is captured by the metal, and the resulting ion is evaporated from the surface. Such a process can be represented as shown in Fig. 9, and may take place if the energy inequality

$$\phi > I \qquad (17)$$

holds.

In the case of hydrogen atoms in the $2s$ state, the ionization potential $I = 3.4$ volts. Most surfaces which can be maintained under the conditions of the experi-

[38] H. W. Webb, Phys. Rev. **24**, 113 (1924).
[39] M. L. Oliphant, Proc. Roy. Soc. **A124**, 228 (1929).
[40] H. S. W. Massey, Proc. Camb. Phil. Soc. **26**, 386 (1930); **27**, 460 (1931).
[41] A. Cobas and W. E. Lamb, Jr., Phys. Rev. **65**, 327 (1944).
[42] S. Sonkin, Phys. Rev. **43**, 788 (1933).
[43] R. Dorrestein, Physica **9**, 433 and 447 (1942).
[44] A. Buehl, Helv. Phys. Acta **6**, 231 (1933).

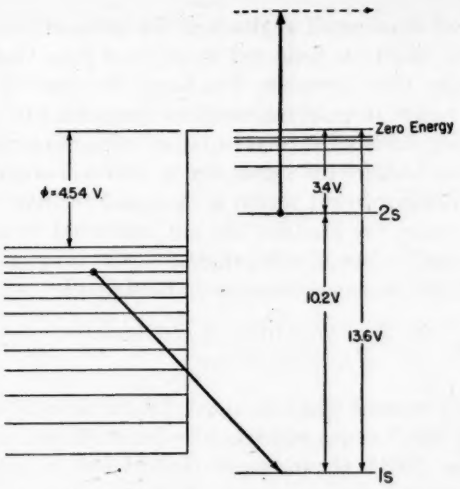

FIG. 8. A possible mechanism for ejection of electrons from tungsten by metastable hydrogen atoms due to the Coulomb interaction between the atomic and metallic electrons.

ment would probably have a work function $\phi > 3.4$ volts, and capture of the $2s$ electron by the surface is energetically possible. A rough estimate of the mean distance at which the process would occur gives 5A, i.e., a larger distance than that estimated for electron ejection. If the resulting proton could escape from the surface with appreciable probability, one would have a method for detecting metastable hydrogen atoms. If, however, the proton is neutralized in some way not involving electron emission, the process of electron capture might very well compete seriously with the desired process of electron ejection. When our experiment was successful, we found that electron ejection did occur, but probably not with the expected high efficiency. We have looked unsuccessfully for positive ion emission by metastable hydrogen atoms from cold and non-outgassed tungsten. Further investigation of the detection mechanism is clearly desirable.

We consider briefly, but did not attempt, methods involving the detection of the Lyman alpha 1216A radiation when a quenching field is applied to the beam or to the bombardment region.[45] Such a method would fit in well with the use of counters. Another possibility involving counters, which was not explored, would be to use secondary multiplication of the electrons ejected by the metastable atoms.

12. Estimate of Yield

We are now in a position to make a rough estimate of the yield of metastable hydrogen atoms and the resulting electron currents to be expected under typical experimental conditions. Consider the atoms emerging from the tungsten oven. According to ideal kinetic gas theory, the number of hydrogen atoms escaping

[45] This method was subsequently used by M. Skinner and W. E. Lamb, Jr., Phys. Rev. 75, 1325 (1949); 78, 539 (1950) for a determination of the fine structure anomaly in singly ionized helium.

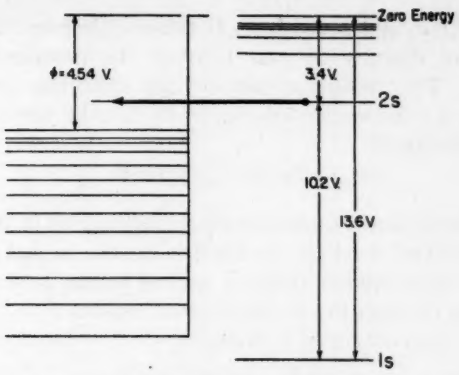

FIG. 9. Auto-ionization of a metastable hydrogen atom in the vicinity of a tungsten surface.

per second at an angle θ with the normal to the wall into a solid angle range Ω through a small opening of area a is

$$\text{rate of escape} = n_0 a v \Omega X \cos\theta / 4\pi, \tag{18}$$

where n_0 is the number of atoms and molecules per unit volume, X is the fractional dissociation, and v is an average velocity of the atoms in the oven.

Few of these atoms can reach the detector plate directly, because it is offset to allow for the small recoil angle. If, however, it were not so displaced, and no obstacles were in the way, a fraction of the atoms emerging from the oven slit would reach the detector of area A at a distance R from the slit. For this, $\Omega = A/R^2$ and $\cos\theta \sim 1$. Let f be the fraction of atoms which are excited to the $2s$ state as they pass through the electron gun region. The excited atoms experience a deflection approximately sufficient to allow them to strike the displaced detector target. As there is a spread of recoil angles, the metastable atoms may not necessarily all be able to reach the detector. Only if the solid angle Ω_1 subtended by the detector seen through the slit system from the center of the bombardment region is larger than the solid angle Ω_2 of the beam spread due to recoil will the metastable atoms clear the intervening slit system. Otherwise only a fraction δ of these, called the "recoil dilution" factor, may do so. One may then set

$$\delta = \begin{cases} \Omega_1/\Omega_2 & \Omega_1 < \Omega_2 \\ 1 & \Omega_1 \geqslant \Omega_2. \end{cases} \tag{19}$$

The number of electrons/sec. ejected from the target due to metastable atoms is then

$$S = n_0 a v X A f \delta \mu \eta / 4\pi R^2, \tag{20}$$

where the factor μ expresses the fraction of metastables surviving their passage through any quenching electric fields, and η is the efficiency of the electron ejection by a metastable hydrogen atom from the metal surface used in the target.

The bombardment efficiency f may be estimated as follows: Let the electron stream have I electrons/sec.,

a height h, and a width w. It takes a time w/v for an atom of speed v to pass through the bombardment region. The transition rate for an excitation process having a cross section σ is $I\sigma/wh$ so that the probability of excitation is

$$f=I\sigma/hv=2.3\times10^{-8} \tag{21}$$

with the typical values of bombarding current of 200 μa, $\sigma=10^{-17}$ cm^2, $h=1$ cm, $v=8\times10^5$ cm/sec., so that about one in forty million atoms is excited to the $2s$ state on passage through the bombardment region.

The detector signal is finally

$$S=n_0aXAI\sigma\delta\mu\eta/(4\pi R^2h) \text{ electrons/sec.} \tag{22}$$

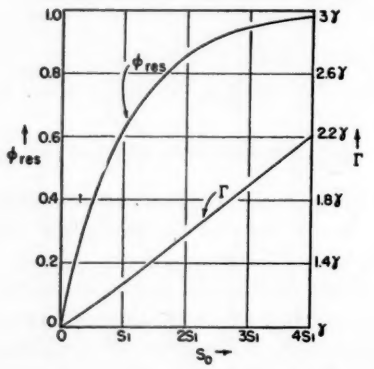

FIG. 10. Effects of r-f saturation. Resonance quenching and half-width as function of r-f power as given by Eqs. (28) and (25).

Unfortunately, many of the factors needed for the estimate of the yield were not known, and a certain degree of optimism was required in the assumption of relatively favorable values for then in order to predict a usable signal. Typical values were

$$\begin{aligned} &I=1.87\times10^{15} \text{ electrons/sec. (0.3 ma)}\\ &n_0=2.94\times10^{15} \text{ cm}^{-3} \text{ (10^{-3} atmos., 2500°K)}\\ &a=3.1\times10^{-3} \text{ cm}^2\\ &A=1.21 \text{ cm}^2\\ &R=6.35 \text{ cm}\\ &\sigma=10^{-17} \text{ cm}^2\\ &h=1 \text{ cm}\\ &X=0.64\\ &\delta=0.5\\ &\mu=0.5\\ &\eta=0.5. \end{aligned} \tag{23}$$

The values for a, A, R, h, I, n_0, and X were at least near the actual values used. As explained above, the value for σ was based on very inadequate theory. The value $\mu=\frac{1}{2}$ for the metastable survival factor was reasonable [Section 16] provided quenching effects were not present, including those which might be due to contact potential differences, or of electric fields due to charges trapped on insulating surface contaminations. The detector efficiency $\eta=0.50$ was taken most optimistically. The value of the recoil dilution factor $\delta=\frac{1}{2}$ was obtained by considering the width of the distribution of recoil angles and the areas of the holes through which the deflected beam must pass. One may not make these openings too large, for then the size of the region over which uniform magnetic and radio-frequency fields must be maintained becomes excessive. Also, the background signal due to photons originating in the bombardment region is increased relative to the signal, since the photons are not restricted to a relatively small range of solid angles.

With the above assumptions, the signal is

$$\begin{aligned} S&=3.26\times10^7 \quad \text{electrons/sec.}\\ &=5.2\times10^{-12} \quad \text{amp.} \end{aligned} \tag{24}$$

This is a current which is about 5×10^4 times the least current (10^{-16} amp.) which can be detected conveniently with an FP54 electrometer circuit and a sensitive galvanometer. Consequently, unless one or more of the estimates proved to be too optimistic, the signal should be large enough to detect, and even to use for accurate radiofrequency spectroscopy. As will be seen later, this estimate proved to be very optimistic.

13. Radiofrequency Power Required

The metastable atoms are to be subjected to radio-frequency waves somewhere between the source and detector. When the frequency is such that $\hbar\omega$ is equal or nearly equal to an energy difference between a Zeeman component of the $2^2S_{1/2}$ level and a Zeeman component of one of the 2^2P levels, the radiation may induce a transition to a non-metastable level and the detected signal will decrease. The amount of decrease will depend on the intensity of the radiation as well as its frequency, on the speed of the atoms, and the length of the radiofrequency field region. We will now estimate the amount of r-f power required for an appreciable quenching of the beam.

According to the quantum theory of radiation, the decay rate of state $2^2S_{1/2}$ to one of the $2p$ states due to r-f is[46]

$$1/\tau_s=(2\pi e^2\gamma S_0/c\hbar^2) \times|(|\hat{\mathbf{e}}\cdot\mathbf{r}|)|^2/[(\omega-\omega_0)^2+(\gamma/2)^2], \tag{25}$$

where S_0 is the incident energy flux density of the radiation having circular frequency ω and electric polarization parallel to the unit vector $\hat{\mathbf{e}}$, ω_0 is the resonance circular frequency and $(|\mathbf{r}|)$ is the matrix element of the coordinate vector $\mathbf{r}$ for the transition in question. As before, $\gamma=1/\tau_p$ is the radiative damping constant for $2p$ states. At resonance, $\omega=\omega_0$ and

$$1/\tau_s=(8\pi e^2S_0/c\hbar^2\gamma)|(|\hat{\mathbf{e}}\cdot\mathbf{r}|)|^2. \tag{26}$$

The matrix elements of $\hat{\mathbf{e}}\cdot\mathbf{r}$ can be calculated from equations[47] given by Bethe, and for a transition from $2^2S_{1/2}$ ($m=\frac{1}{2}$) to $2^2P_{1/2}$ ($m=-\frac{1}{2}$) with $\hat{\mathbf{e}}$ along x we find

$$|(|x|)|^2=3a_0^2. \tag{27}$$

[46] The validity of Eq. (25) will be discussed in a later paper.
[47] See reference 25, p. 447.

The fraction of atoms quenched by the r-f field is

$$\phi=1-\exp(-l/v\tau_s), \tag{28}$$

where l is the length of the r-f region, and v is the speed of the atoms. For $l=1$ cm and $v=8\times10^5$ cm/sec., the beam would be 63 percent quenched for

$$\tau_s=l/v=1.25\times10^{-6} \text{ sec.} \tag{29}$$

According to Eq. (26) this requires an energy flux density at resonance of $S_0=3.4$ mw/cm^2. Since this power density is easily obtained at any frequency up to 30,000 Mc/sec., we did not anticipate any difficulty with r-f power requirements.

It is clear from Eqs. (28) and (25) that when the r-f power is sufficient to give nearly complete quenching at resonance, the effective resonance curve will be appreciably broadened by r-f saturation. The dependence of quenching and effective half-width Γ on r-f power is shown in Fig. 10.

14. Breadth of Resonance Curves

According to Eq. (25), the decrease in the beam will take place when $\omega=\omega_0$ and also for a band of frequencies around $\omega_0/2\pi$ of half-width $\gamma/2\pi$ or 99.8 Mc/sec. This is just the uncertainty principle width ($\Delta E\Delta t\sim\hbar$) of the decaying 2^2P states and cannot be reduced. In addition, as we shall see later, hyperfine structure increases the width of the lines by as much as a factor of two in some cases. The large width of the resonance curves is a significant fraction of the frequencies of the transitions, and represents the greatest difficulty in the way of a really precise test of the Dirac theory. On the other hand, an opportunity is afforded for a quite accurate test of the Wigner-Weisskopf theory of radiation line shape, since the resonance curves have a natural width relative to the working frequency much greater than elsewhere in atomic physics.

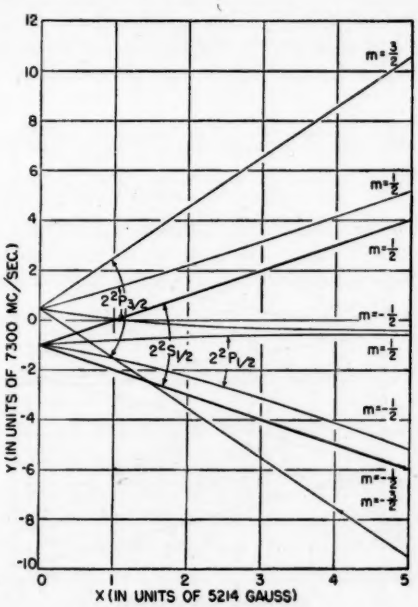

FIG. 11. Zeeman splitting of the fine structure of states $n=2$ of hydrogen according to the Dirac theory.

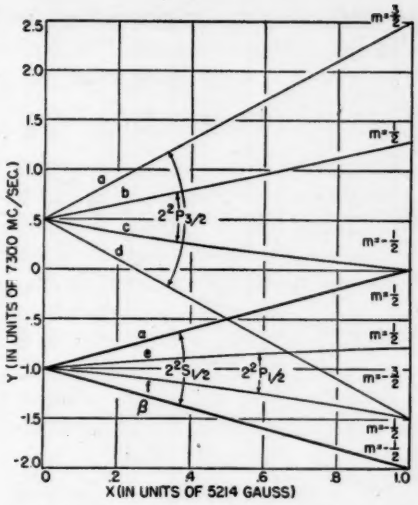

FIG. 12. Enlargement of Fig. 11 showing abbreviations used for the Zeeman component energy levels.

The most obvious way to determine the resonance frequencies $\omega_0/2\pi$ would be to measure the beam intensity as a function of radiofrequency, keeping the r-f power constant. Unfortunately, this is next to impossible to do. Microwave oscillators which can be tuned through hundreds of megacycles per second are available, but their output is frequency-dependent. Even if this were not the case, the transmission line or wave guide to the quenching region would be electrically long and unless the line were very well broad-banded, the standing wave ratio, and hence the r-f voltage seen by the atom would vary with frequency. One might hope to monitor the r-f power level with a crystal probe or bolometer mounted in the quenching region, but such devices are themselves frequency-sensitive.

Since a magnetic field was believed to be necessary anyway, we decided to take advantage of it to overcome the above difficulties. The frequency (and power level) of the oscillator is kept constant and the atomic energy levels are moved through resonance by varying the magnetic field. To a first approximation, the atomic energies, and therefore the frequencies, are linear functions of the magnetic field, so that a resonance curve taken in this way closely resembles in shape the usual sort. In order to interpret the result, however, it is necessary to know the values of the magnetic field and to have the theory of the Zeeman effect of the hydrogen fine structure levels for $n=2$. The results of this theory are summarized in the next section.

15. Zeeman Effect of the Fine Structure of Hydrogen

For the present, it will suffice to consider an approximate theory of the Zeeman effect of the hydrogen fine

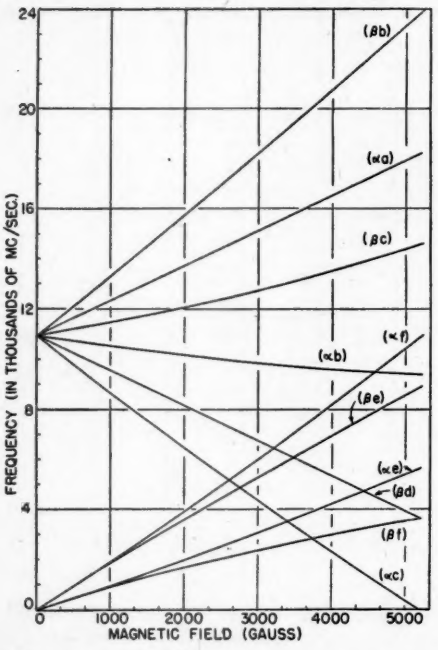

FIG. 13. Resonance frequencies to be expected as functions of magnetic field for all allowed transitions leading from the metastable states $\alpha(2^2S_{1/2},\ m=\frac{1}{2})$ and $\beta(2^2S_{1/2},\ m=-\frac{1}{2})$ to the nonmetastable states a, b, c, d $(2^2P_{3/2})$ and e, f $(2^2P_{1/2})$ according to the Dirac theory.

structure in which the interaction of the atom with an external magnetic field H is represented by the perturbing energy

$$\mathcal{H}'=\mu_0(\mathbf{L}\cdot\mathbf{H}+2\mathbf{S}\cdot\mathbf{H}), \tag{30}$$

where

$$\mu_0=e\hbar/2mc \tag{31}$$

is the Bohr magneton, $\mathbf{L}=(\mathbf{r}\times\mathbf{P})/\hbar$ the orbital angular momentum, and $\mathbf{S}$ the spin angular momentum of the electron, measured in units of $\hbar$. The splitting of the $2^2S_{1/2}$ levels may be considered independently of that of the 2^2P levels for $\mathcal{H}'$ has no matrix elements connecting s and p states. The solution of this problem is well known, and we simply take the results[48] from Bethe's article.

For $2^2S_{1/2},\ m_s=\pm\frac{1}{2}$

$$E(2^2S_{1/2},\ m_s;\ H)=E(2^2S_{1/2})+2\mu_0Hm_s. \tag{32}$$

For $2^2P_{3/2},\ m_j=\pm\frac{3}{2}$

$$E(2^2P_{3/2},\ m_j=\pm\tfrac{3}{2};\ H)=E(2^2P_{3/2})+(4/3)\mu_0Hm_j. \tag{33}$$

For the $m_j=\pm\frac{1}{2}$ levels of $2^2P_{1/2,\,3/2}$ the levels are given by the roots of a secular determinant as

$$E=\tfrac{1}{2}(E_++E_-)+\mu_0Hm_j \pm\tfrac{1}{2}[(E_+-E_-)^2+(4/3)\mu_0H(E_+-E_-)m_j+(\mu_0H)^2]^{\frac{1}{2}} \tag{34}$$

where E_+ and E_- are the zero field energies of $2^2P_{3/2}$ and $2^2P_{1/2}$ respectively.

[48] See reference 25, p. 396.

If we measure energy in units of

$$hf_1=2(E_+-E_-)/3\cong 7300 \text{ Mc/sec.} \tag{35}$$

from the center of gravity $\frac{1}{3}(2E_++E_-)$ and magnetic field in units

$$H_1=(2/3\mu_0)(E_+-E_-)\cong 5214 \text{ gauss} \tag{36}$$

by setting

$$\mu_0H=\tfrac{2}{3}(E_+-E_-)x \tag{37}$$

$$E=\tfrac{2}{3}(E_+-E_-)y+\tfrac{1}{3}(2E_++E_-), \tag{38}$$

we obtain

$$y=-\tfrac{1}{4}+m_jx\pm\tfrac{1}{2}(x^2+2m_jx+9/4)^{\frac{1}{2}}. \tag{39}$$

In the same notation, the energy levels for $2^2P_{1/2}$, $m=\pm\frac{3}{2}$ are given by

$$y=\tfrac{1}{2}\pm 2x \tag{40}$$

and for $2^2S_{1/2}$, $m_s=\pm\frac{1}{2}$

$$y=y_0-1\pm x \tag{41}$$

where y_0 measures any displacement upward of $2^2S_{1/2}$ compared to $2^2P_{1/2}$ in zero magnetic field. A plot of these energy levels is given in Fig. 11 showing the anomalous Zeeman, intermediate field, and Paschen-Back regions. Here $y_0=0$ as predicted by the Dirac theory. For the sake of brevity, these energy levels will be denoted by single letters. The two metastable levels $2^2S_{1/2}$, $m_s=\frac{1}{2}$ and $m_s=-\frac{1}{2}$ will be denoted by α and β, respectively (as suggested by the conventional symbols for Pauli spin wave functions). The 2^2P levels will be denoted by a, b, c, d, e, f as shown in Fig. 12 which enlarges the anomalous Zeeman and intermediate field regions of primary interest to us.

The selection rules for electric dipole radiation in the anomalous Zeeman region are $\Delta m_j=0$ for the electric vector of the radio waves parallel to the magnetic field, and $\Delta m_j=\pm 1$ for perpendicular polarization. Conse-

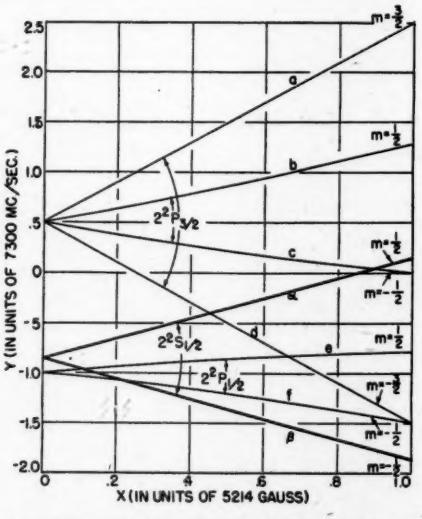

FIG. 14. Zeeman energy levels as in Fig. 11, but with the $2^2S_{1/2}$ pattern raised by 1000 Mc/sec.

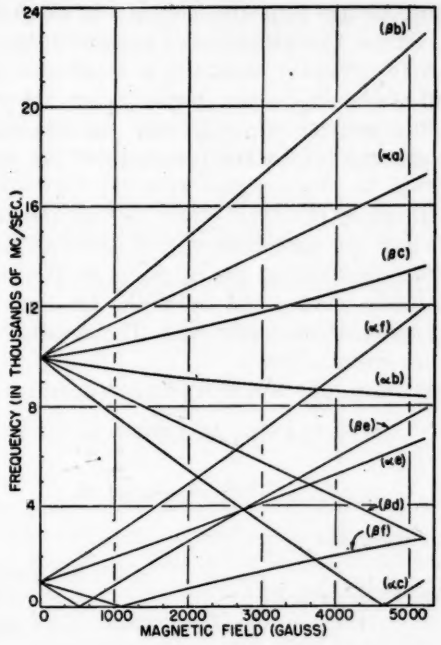

FIG. 15. Expected resonance frequencies as functions of magnetic field as in Fig. 13, but with the $2^2S_{1/2}$ state raised by 1000 Mc/sec.

quently, for parallel polarization the allowed transitions are αb, αe, βc, βf while for perpendicular polarization the allowed transitions are αa, αc, αf, βb, βd, βe. The frequencies to be expected for these ten transitions are plotted in Fig. 13 as a function of the magnetic field.

In actuality, taking the fine structure separation $\alpha^2 hcR/16$ as 10, 950 Mc/sec. and the s level shift Δ as 1000 Mc/sec., we now know that $y_0 \sim 0.137$ and not zero as predicted by the Dirac theory. On this basis the energy level curves are as shown in Fig. 14. The corresponding frequency *versus* field curves are shown in Fig. 15.

16. Production of a Polarized Beam of Atoms

It will be noted from a comparison of Figs. 12 and 14 that the existence of the $2^2S_{1/2}$ level shift gives rise to a marked difference in the stability of the two metastable states α and β in magnetic fields of around 540 gauss. For the quenching effect of an electric field $\mathbf{E}$ is given by

$$1/\tau_s = \gamma V^2/\hbar^2[\omega^2 + (\tfrac{1}{2}\gamma)^2], \tag{42}$$

where $V = (|e\mathbf{E}\cdot\mathbf{r}|)$ is the matrix element of the perturbation $e\mathbf{E}\cdot\mathbf{r}$ connecting the two interacting states, and $\hbar\omega$ is their energy difference. At 540 gauss, $\omega/2\pi$ is 2020 Mc/sec. for the separation between states αf and zero for the states βe. As a result, the quenching of the lower metastable state β will be more rapid than that of the upper state α by a factor of

$$1 + (4\omega^2/\gamma^2) \sim 1630. \tag{43}$$

The main known perturbing electric field is that due to the motion of the atoms at right angles to the magnetic field $\mathbf{H}$, and is given by

$$\mathbf{E} = (\mathbf{v}/c) \times \mathbf{H}. \tag{44}$$

Hence $\mathbf{E}$ is perpendicular to $\mathbf{H}$. If we introduce a right-handed Cartesian coordinate system with z along $\mathbf{H}$, x along $\mathbf{v}$, then $\mathbf{E}$ is along y. The perturbation energy $e\mathbf{E}\cdot\mathbf{r}$ has matrix elements connecting states β and e, but not states β and f. For $v = 8\times10^5$ cm/sec. and $H = 540$ gauss, $E = 4.3$ volts/cm.

The life of state β in a perturbing electric field of 4.3 volts/cm perpendicular to the magnetic field is given by Bethe's calculations as described in Section 6 to be 4.3×10^{-8} sec. while state α would have a life 1630 times greater, or 7×10^{-5} sec. This means that in the presence of the motional electric field, atoms in state α will nearly all be able to keep their excitation while they travel 6 cm to a detector, but practically none of the atoms originally in the lower metastable state β will be excited when they reach the detector. Hence, after moving a short distance along the beam from the electron bombarder, we will have a polarized beam of atoms, nearly all the excited atoms having electron spins oriented parallel to the magnetic field. The excited atoms with antiparallel spins have been filtered out by the quenching action of the motional electric field. This method of production of a highly polarized beam of matter is to be contrasted with the other known methods: the small spatial separations obtained in atomic beam deflection experiments, and the polarization of neutrons on passage through strongly magnetized absorbers.

The state of affairs described above is not confined to the critical field of $H = 540$ gauss for which the levels β and e cross, but extends over quite a range of field strengths. With the apparatus to be described in this paper, the transitions βb, βc, βd, βe, βf of Fig. 15 were not observed.

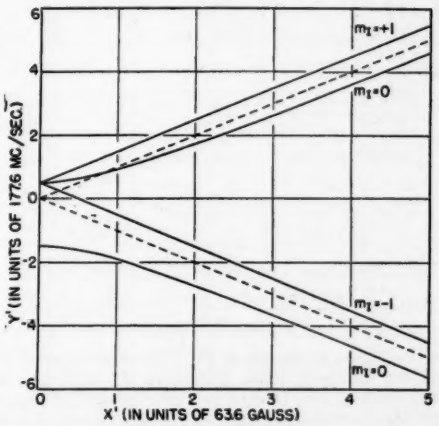

FIG. 16. Zeeman splitting of the hyperfine structure of $2^2S_{1/2}$. The zero-field separation is taken to be one-eighth that measured for the ground state by Nafe and Nelson. The dotted lines show the energy levels obtained if hyperfine structure is ignored.

Motional Stark quenching also occurs about the magnetic field where levels α and c cross, or $H=4700$ gauss. This region is much wider than for the βe crossing because the motional electric field is larger, and the beam of metastable atoms will be strongly quenched above 3000 gauss.

17. Effect of Hyperfine Structure of Energy Levels

The discussion of the energy levels of the $n=2$ states in Section 15 ignored the interaction of the magnetic moment of the nucleus (proton, deuteron, $\cdots$) with the electron. Fortunately, although the effects of this are not negligible by any means, they can be taken into account by perturbation theory for the purposes of the present discussion. The magnetic moment of the nucleus

$$\mathfrak{y}=g_I\mathbf{I}\mu_0 \tag{45}$$

produces a magnetic field derivable from the vector potential

$$\mathbf{A}=(\mathfrak{y}\times\mathbf{r})/r^3. \tag{46}$$

Here g_I is the Landé value for the nucleus (about 5.6/1836 for the proton and 1.7/1836 for the deuteron), μ_0 is the Bohr magneton (31) and $\mathbf{I}$ is the spin vector for the nucleus. According to Dirac's equation, the interaction energy with the electron is $e\boldsymbol{\alpha}\cdot\mathbf{A}$ where α_x, α_y, α_z are the Dirac matrices. The shift of the energy levels due to hyperfine structure is small and can be calculated using first-order perturbation theory by forming the average of $\boldsymbol{\alpha}\cdot\mathbf{A}$ over the unperturbed Dirac four-component wave function for the state of the electron. In forming this average, the two small component wave functions must be calculated with some care near the nucleus in order to avoid ambiguities due to the singularity at the origin in $\mathbf{A}$. The theory[49] is conveniently worked out by Bethe for the case of vanishing external magnetic field. The results for the energies are given below.

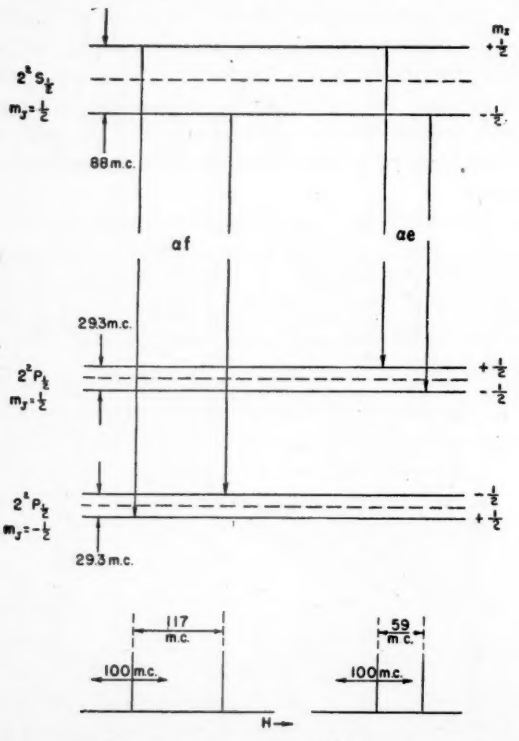

FIG. 17. Hyperfine structure of the $2^2S_{1/2}$ ($m=\frac{1}{2}$) and the $2^2P_{1/2}$ levels in strong magnetic field. The allowed transitions are indicated by the arrows. The resonance curve peaks are separated by 117 and 59 Mc/sec., respectively. This separation is to be compared with the radiative width of 100 Mc/sec. For simplicity, the hyperfine components have been taken to be equally separated from the dotted position corresponding to complete Back-Goudsmit decoupling.

For s states the effective perturbation operator is

$$w=(16\pi/3)g_I\mu_0^2|\psi(0)|^2\mathbf{I}\cdot\mathbf{S} \tag{47}$$

or

$$w=(8/3)g_I(Z^3/n^3)\alpha^2hcR\mathbf{I}\cdot\mathbf{S} \tag{48}$$

giving energy shifts

$$=(4/3)g_I(Z^3/n^3)\alpha^2hcR\begin{cases} I & \text{for } F=I+\frac{1}{2} \\ -(I+1) & \text{for } F=I-\frac{1}{2}. \end{cases} \tag{49}$$

The separation of the two states is

$$\Delta w_n=(8/3)g_I(I+\tfrac{1}{2})(Z^3/n^3)\alpha^2hcR. \tag{50}$$

For the ground state of hydrogen, this splitting amounts to 1416 Mc/sec., (increased to 1420 Mc/sec. by the anomalous magnetic moment of the electron as shown through the work of Nafe, Nelson, and Rabi[50]). For the case $n=2$, of interest to us, the splitting is one-eighth as much, or 177 Mc/sec.

The theory of the Zeeman effect of this hyperfine structure for all magnetic fields is given by the well-known Breit-Rabi[51] formula, and is illustrated in Fig. 16. For present purposes it suffices to consider only the strong field limit in which $\mathbf{I}$ and $\mathbf{S}$ are decoupled from each other and precess independently around H with projections m_I and m_s, respectively. Then $\mathbf{I}\cdot\mathbf{S}$ can be replaced by m_Im_s and we obtain for the hyperfine energy

$$w=(8/3)g_I(Z^3/n^3)\alpha^2hcRm_Im_s. \tag{51}$$

State α, for which $m_s=+\frac{1}{2}$ is therefore split into $2I+1$ states. For hydrogen, with $I=\frac{1}{2}$, there are two states separated by $(\frac{1}{2})\Delta w$ or 88 Mc/sec. State β, ($m_s=-\frac{1}{2}$) is similarly split, but with an inversion because of the sign change of m_s. In the interpretation of the more precise measurements to be described in a later paper, it will, of course, be necessary to question the validity of the strong field approximation. For the present purposes, the error is not large since the dimensionless parameter

$$x'=(g_J-g_I)\mu_0H/\Delta w \tag{52}$$

[49] See reference 25, p. 385.

[50] J. E. Nafe and E. B. Nelson, Phys. Rev. **73**, 718 (1948); P. Kusch and H. M. Foley, Phys. Rev. **74**, 250 (1948).

[51] G. Breit and I. I. Rabi, Phys. Rev. **38**, 2082 (1931).

reaches unity at a magnetic field of only 63.6 gauss, and nearly all of the data described here was taken at fields well above this.

For other than s states, Bethe assumed that the fine structure splitting was large compared to the hyperfine structure separation and derived the equation

$$w=2\mu_0^2 g_I\langle r^{-3}\rangle_{Av}[L(L+1)/J(J+1)]\mathbf{I}\cdot\mathbf{J}$$
$$=g_I(Z^3/n^3)(\alpha^2 hcR)(\mathbf{I}\cdot\mathbf{J})/[(L+\tfrac{1}{2})J(J+1)] \quad (53)$$

for the perturbation operator. In zero magnetic field,

$$\mathbf{I}\cdot\mathbf{J}=\tfrac{1}{2}[F(F+1)-I(I+1)-J(J+1)] \quad (54)$$

and

$$(\mathbf{I}\cdot\mathbf{J})_{F=|I-J|}-(\mathbf{I}\cdot\mathbf{J})_{F=I+J}=\begin{cases}I(2J+1) & J\geqslant I\\ J(2I+1) & J<I\end{cases}$$

so that for hydrogen the state $P_{1/2}$ splits into two states with resultant angular momentum quantum number $F=1$, 0 and $P_{3/2}$ splits into two states with $F=2$, 1. The separations are, respectively, 1/3 and 2/15 as much as for the corresponding $2S_{1/2}$ state.

In the presence of a magnetic field which is not large enough to break down the coupling between **L** and **S** to form a resultant **J**, one may continue to use Eq. (53). However, one must add to the Hamiltonian the energy of orientation of the vectors **I** and **J** in the magnetic field

$$\mu_0(g_J\mathbf{J}-g_I\mathbf{I})\cdot\mathbf{H}$$

and the problem becomes mathematically similar to that of the Zeeman effect of the hfs for S states so that the Breit-Rabi formula may be used, if either I or J is $\frac{1}{2}$.

We obtain a simplification if we consider magnetic fields which are strong enough to decouple **I** from the vector **J**, but not strong enough to decouple **L** and **S**. Then $\mathbf{I}\cdot\mathbf{J}$ may be replaced by $m_I m_J$ and the hyperfine energy becomes

$$w=(g_I Z^3\alpha^2 hcR/n^3 J(J+1)(L+\tfrac{1}{2}))m_I m_J$$
$$+\mu_0 H(g_J m_J-g_I m_I). \quad (55)$$

As a result of the hyperfine structure, again taking the case $I=\frac{1}{2}$ for simplicity, each state is in effect split into two states equally removed in energy from the unperturbed position. To the approximation considered here, the hyperfine splittings are dependent on magnetic field only because of the last term $-\mu_0 H g_I m_I$ of Eq. (55). The splittings are expected to be $(\frac{1}{2})\Delta w=88$ Mc for the $2^2S_{1/2}$ states, $(1/6)\Delta w=29$ Mc for the $2^2P_{1/2}$ states while it is $(1/30)\Delta w=6$ Mc for the $m_J=\pm\frac{1}{2}$ states of $2P_{3/2}$, and $(1/10)\Delta w=9$ Mc for the $m_J=\pm\frac{3}{2}$ states of $2P_{3/2}$. For the case of deuterium, when $I=1$ the patterns are more complicated but the splittings are very much small because of the smaller nuclear magnetic moment.

The splitting of the energy levels due to hyperfine structure gives rise to a complication of the observed

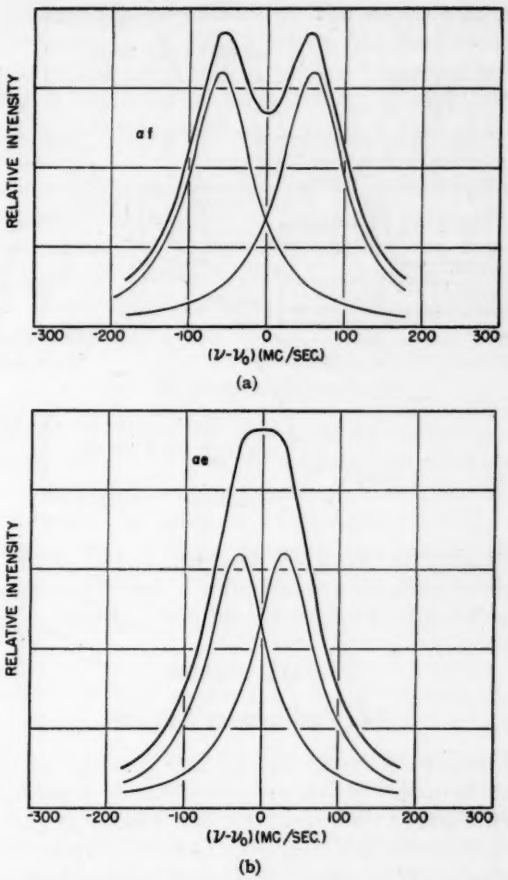

FIG. 18. Ideal theoretical resonance curves showing the effect of hyperfine structure for transitions αe and αf, respectively. When plotted as functions of magnetic field, the resonance curve for αf becomes the narrower of the two.

resonance curves. In most cases the natural width of the curves exceeds the splitting, and the result is a composite of two more or less imperfectly resolved resonance curves of the Wigner-Weisskopf type. The case of transitions from state $\alpha(2^2S_{1/2},\ m_s=\frac{1}{2})$ to states $e(2^2P_{1/2},\ m_j=\frac{1}{2})$ and $f(2^2P_{1/2},\ m_j=-\frac{1}{2})$ will serve to illustrate this. The observed transitions are electric dipole in type, and as the nuclear moment is decoupled from the other angular momentum vectors by the magnetic field, the selection rule $\Delta m_I=0$ obtains.

The allowed transitions are shown in Fig. 17. It will be noted that because of the reversal of sign of the product $m_I m_J$ the separation of the two peaks is $(4/3)\Delta w$ or 117 Mc/sec. for transition αf and only $(\frac{2}{3})\Delta w$ or 58 Mc/sec. for transition αf. The natural width of the separate transitions is 100 Mc/sec. When two such curves are superposed, the resulting complex has two peaks only if the component peaks are separated by half the natural width, or by 50 Mc/sec. The theoretical forms of such curves are shown in Fig. 18(a) and (b). Even in the case αf, where the separation is 117 Mc/sec., the result may be only a flattening of the top of the curve if there are other causes of

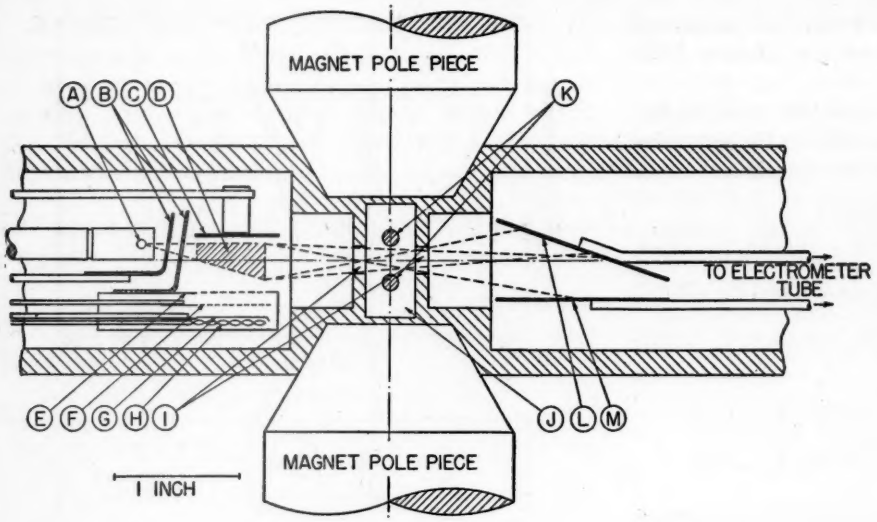

FIG. 19. Cross section of apparatus. A. Tungsten oven of hydrogen dissociator. B. Shields. C. Anode of electron bombarder. D. Bombardment region. E. Accellerator grid of electron bombarder. F. Control grid. G. Cathode of electron bombarder. H. Heater for cathode. I. Slits. J. Wave guide. K. Quenching wires and transmission lines. L. Metastable detector target. M. Electron collector.

broadening. In the work described in this paper, the observed peaks were considerably broader than expected above because of magnetic field inhomogeneity.

C. APPARATUS

18. Preliminary Efforts

Inasmuch as the production and detection of metastable hydrogen atoms were theoretically possible, but experimentally unproven, it was necessary at the outset to establish the occurrence of both processes simultaneously. The earliest apparatus was conceived as simply as possible consistent with this aim, as a source and detector of metastable atoms. These were enclosed in glass bulbs connected by a glass tube $\frac{1}{2}$ in. in diameter and 6 in. long. Magnetic fields could be applied to the source, detector, and intervening region. These were produced by permanent magnets of a type once used for K band magnetrons. It was thought that at a later time the connecting tube could be passed through the broad side of an X band wave guide (0.400×0.900 in. I.D.), so that the metastable atoms could be subjected to a radiation field having a frequency of about 10,000 Mc/sec.

The second method of Section 7, that of direct excitation by electron bombardment of the molecule, was selected as probably the easiest way to produce metastable hydrogen atoms. The electron bombarder consisted of an oxide-coated cathode, a grid and an anode. The latter two electrodes were held at the same positive potential with respect to the cathode to produce a relatively field-free region where metastable atoms could be formed. This arrangement was capable of supplying electrons with energies up to 50 ev.

For reasons discussed in Section 11, the electron ejection method of detection was adopted. The atoms were allowed to fall on a tungsten target and any electrons ejected passed to a positive collector electrode. This method has the disadvantage that electrons ejected from the surface by any other means, such as photoelectric effect, form a background which has to be held within reasonable bounds. However, the background photoelectric current made possible a study of the behavior of the electron bombarder by taking excitation curves for hydrogen and helium.

Hydrogen gas was admitted near the electron bombarder and if metastable atoms were formed, some would have passed through the connecting tube to the detector. Unfortunately, the bombardment of molecular hydrogen produced a variety of effects difficult to distinguish from those expected of metastable hydrogen. With the aid of the magnetic fields and an electric field produced by a pair of auxiliary electrodes introduced for that purpose into the connecting tube, it was shown that these phenomena could be attributed to photons, electrons, positive ions and charges accumulated on the glass walls. The last effect was particularly confusing.

The usual method of study at this stage was to take rough excitation curves as a function of the bombarding voltage, with proper allowance for the presence of extraneous ions, electrons and the effects of charges on the glass walls. Although at this time it was not possible to verify the presence of metastable atoms, it was

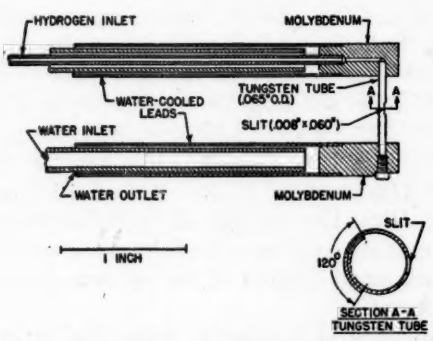

FIG. 20. Detail of hydrogen dissociator and tungsten oven.

evident from the size and low appearance potential of the photon background that the chosen excitation process was not as favorable as anticipated. It appeared that the two-step method of first dissociating the molecule and then exciting the atoms by electron bombardment would be less affected by this difficulty.

19. Working Model

Since it was clear that an extensive revision of the apparatus was necessary, a primarily all metal one was built incorporating all known improvements. Nevertheless, many modifications were made before meaningful results were obtained.

The general scheme of the apparatus is illustrated in Fig. 19 which is a horizontal cross section through the axis of the coaxial circular cylinders comprising the right- and left-hand chambers. The rectangular space, J, is the cross section of an X-band rectangular wave guide 0.400×0.900 in. I.D., which passes through the apparatus vertically. The magnetic field, neglecting fringing, is at right angles to both the wave guide and the right and left chambers. The magnet pole pieces fit into truncated conical indentations in the apparatus. Except for a certain amount of ferromagnetic material, such as steel and Kovar near the glass seals, the outer shell of the apparatus is principally composed of OFHC copper.

The right-hand chamber contains the detection electrodes and the left the hydrogen dissociator and the electron bombarder. The intervening chamber J is the r-f field region. Hydrogen atoms leave the hydrogen dissociator A and pass to the interaction space D where some of them are excited to the $2s$ state by electron bombardment. After experiencing a small recoil, they pass through the slits I and the r-f region to the detector target, L.

In agreement with the considerations discussed in Section 10 and in Appendix III, the recoil angle was taken into account in the choice of the relative positions of the hydrogen dissociator, the electron bombarder, and the slits I. The angle chosen was the average ψ for 13.6 ev. This is about 8° (see Appendix III).

20. Detector

The detection electrodes consist merely of two tungsten plates, L and M. In the manner described in Section 11 metastable atoms fall on L and eject electrons which are collected by M which is held 3 or 4 volts positive with respect to L. The electron current is measured by means of a standard FP54 electrometer circuit[52] with an input resistance of about 95,000 megohms. The current sensitivity was about 1.5×10^{-16} amp./mm. It was found that cleaning the target, which was at that time a tungsten ribbon 0.004 in. thick and $\frac{1}{4}$ in. wide, by heating to 1000°C or more had no lasting effect. Consequently, an unheated target was used with no apparent loss of sensitivity. The response to metastable atoms is not very sensitive to collector voltage so long as it is 2 or 4 volts but falls off rapidly when the potential difference is dropped toward zero, and becomes vanishingly small at negative values of a volt or so.

Inasmuch as the target surface was only superficially cleaned during assembly, it was very likely covered with a contaminating layer of some sort. In any case such layers frequently become visible after operation for a time, apparently without greatly affecting the detector efficiency.

21. Hydrogen Dissociator

Atomic hydrogen was produced by thermally dissociating molecular hydrogen as discussed in Section 8. The details of the arrangement are shown in Fig. 20. A thin-walled tungsten cylinder, 0.065 in. O.D., was fabricated from 0.004-in. tungsten sheet as indicated, and a slot 0.008×0.060 in. was cut near the center and parallel to the cylinder axis. The cylinder was then forced into the holes provided in the molybdenum ends of the water-cooled leads. Molecular hydrogen was introduced through a tube inside one of the water ducts. The tungsten tube could then be heated in its central portion to a temperature sufficient to produce a satisfactory degree of dissociation by the passage of electric current. The atoms so produced stream out of the small slot which serves as the source. Naturally, there is a fair amount of leakage of molecular hydrogen around the ends of the cylinder.

Operating temperatures in the central portion of the cylinder were usually about 2500°K. Higher temperatures, although possible and desirable, resulted in too high a mortality of the tungsten cylinders. No accurate data are available for the degree of dissociation so produced; however, on the basis of the estimate of Section 8, the degree of dissociation was about 64 percent. The disadvantage of working with this rather low degree of dissociation is outweighed by the general convenience of the method.

Alternating current was found to be satisfactory for heating the hydrogen dissociator. A current of 80 amp. and a voltage drop of 2 volts represent typical operating conditions. The transformer was stabilized by a Sola constant voltage transformer.

22. Electron Bombarder

The electron bombarder has proven to be the most troublesome part of the apparatus, and much effort was expended in determining how to make a good one. Inasmuch as considerably more work has been done on it in preparation for the more precise determination of the $2s$ level shift, this subject will be considered further in Part II.

From the discussions of Sections 6 to 10, it is quite possible to state the properties of an ideal electron gun

[52] L. A. duBridge and H. Brown, Rev. Sci. Inst. 4, 532 (1933).

for this experiment. The electric field in the bombarding region, including that due to space charge, should be as small as possible. The bombarding voltage should be kept near the threshold of 10.2 volts, (a) to reduce the spread of recoil angles and (b) to avoid background effects due to molecular hydrogen which enter at 11.5 volts. In practice, however, to obtain sufficient signal it is necessary to depart considerably from these principles.

The electron bombarder used consisted of a cathode, a control grid, an accelerator grid, and an anode as illustrated in Fig. 19. The cathode, *G*, was of the oxide-coated, indirectly heated type. The cathode and control grid, *F*, were completely enclosed by the accelerator grid electrode, *E*, which had grid wires only on the side facing the anode. This served to shield the interaction space, *D*, where excitation occurred, from the electric fields between the accelerator grid and the cathode. The shields *B* prevented radiation and evaporated matter from the hydrogen dissociator from reaching the electron bombarder and the detector. In the earlier models of this type of electron bombarder the anode *C* was absent, its purpose being served by the outer shell. With such an arrangement no metastable atoms were ever detected with certainty. This could have been ascribed to a lack of atomic hydrogen or to failure of the detection scheme. An independent proof of the presence of hydrogen atoms was made by allowing the hydrogen emerging from the dissociator to fall on a layer of yellow molybdenum oxide soot. The presence of hydrogen atoms was clearly indicated by the rapid reduction of the yellow oxide to the blue form. In the absence of a better check, the strong sensitivity of the detector to photons was taken as a fair indication that it would be sensitive to metastable hydrogen atoms as well. The electron bombarder was therefore indicated as a possible source of the difficulty. It was then established that the effects of space charge in the region between the accelerator grid and anode had been considerably underestimated. At the low electron energies used, 10 to 20 volts, the plate current of about 0.2 ma/cm^2 produced a large potential dip between the accelerator grid and the anode, which depended strongly on the distance separating the electrodes. The introduction of a separate anode reduced this clearance from 3 cm to about 1 cm or less. Thereafter, effects were immediately observed which were identified as being due to metastable hydrogen atoms.

It was found to be most advantageous to operate with an accelerator grid voltage of about 13.5 volts, and to bias the anode 3 volts positive with respect to the accelerator grid. The anode current was held at about 0.3 ma by adjusting the control grid voltage. These conditions were subject to considerable variation, the reasons for which will be discussed in Section 28. In general the operating conditions chosen represent a compromise between instability and signal strength.

The cathode base metal was nickel powder sintered to a molybdenum base and the coating was the usual triple mixture of barium, strontium, and calcium carbonates. The cathode area was approximately 1.5 cm^2. The control grid was formed of 0.002-in. diameter tungsten wires, 16 per in. and the accelerator grid of 0.002 in. diameter tungsten wires, 25 per in. The cathode-control grid and accelerator-control grid clearances were each about $\frac{1}{32}$ in. The accelerator grid-anode clearance was about $\frac{3}{8}$ in.

23. R-F and D.C. Quenching Fields

The metastable atoms are subjected to r-f or d.c. fields in the wave guide region *J*. The atoms enter and leave the region through the slits, *I* ($\frac{3}{16}$ in. wide by $\frac{5}{8}$ in. high). The wires, *K*, were installed long before any r-f fields were applied to aid in identifying the various electrons, ions, and photons that were at one time detected. Subsequently, they proved to be of great value in identifying metastable atoms, by virtue of the fact that an electric field applied between the wires will produce Stark effect mixing of the $2^2S_{1/2}$ and $2^2P_{1/2}$ states, thereby causing the metastable atoms to decay to the $1S$ state and cause a reduction in the electrometer current. In view of the difficulty encountered in maintaining a good supply of metastable atoms this feature of the apparatus was found to be indispensible, and not a temporary measure as originally intended. Furthermore, the transitions to the $2^2P_{1/2}$ levels occur at frequencies of 1500 to 6000 Mc/sec. at which the wave guide is beyond cut-off. For frequencies in that range the wires, *K*, were used as a two-wire transmission line.

The wires were positioned close to the line of edges of the slits, but without obscuring them. An electrostatic field produced by a voltage of 25 volts or more was sufficient to quench practically all of the metastable atoms. Since it is the electric field strength that determines the amount of quenching, the voltage required depends strongly on the configuration of the various electrodes and conductors.

Inasmuch as the r-f field configuration was rather complex and no attempt was made to terminate the line in a matched load, it would be difficult to estimate the r-f power required. It should naturally be in excess of the estimated value of Section 13. In practice, it was found that the signal generator used should deliver power in the neighborhood of 10 mw or more; the amount required depending on the frequency, presumably because of the frequency dependence of the load impedance.

Frequencies between 3000 and 10,000 Mc/sec. were obtained directly from 2*K*41, 2*K*44, or 2*K*39 klystrons. Those frequencies near 12,000 Mc/sec. were obtained by doubling the frequency from a 2*K*44 klystron in a 1*N*23 crystal multiplier. Frequencies from 1500 to 2600 Mc/sec. were obtained from a 2*C*40 lighthouse tube oscillator. The frequency stability resulting from

the use of ordinary regulated power supplies was found to be sufficient. The frequency, or rather the wavelength, of the radiation was measured by means of coaxial or cavity wave meters.

24. Magnetic Field

The magnetic field was produced by a small electromagnet used in this laboratory during the war for testing magnetrons. The pole pieces were 2 in. in diameter and tapered to 1 in. in diameter at the very ends. A 1-in. gap was used in this experiment. Magnetic fields of 3000 gauss or more were readily obtained. The magnet was supplied from a rectifier and filter, stabilized by a Sola constant voltage transformer.

The field was calibrated by moving the detector electrodes and inserting a small search coil into the center of the r-f region through the slit, I. The usual standard demagnetization procedure and magnetization curve method was followed in obtaining the calibration curve of magnetic field strength *H versus* magnet current, and throughout the measurements. The calibration was made to an accuracy of about 0.5 percent. This was more than sufficient accuracy, for it was found that the field in the r-f interaction space was non-uniform by some 33 gauss out of a total of 1000.

25. Gas Supply and Pumps

Hydrogen gas of commercial purity was used throughout. The Ohio Chemical Company claims that this gas is 99.7 percent, or better, of hydrogen, the balance being oxygen in the form of water vapor.

Gas was stored in a set of three one-liter glass bulbs and was admitted to the hydrogen dissociator through a fixed gas leak made by sealing an uncleaned piece of tungsten wire 0.020 in. diameter in a small bore Pyrex capillary tube. It was usually necessary to make three or four of these before obtaining one with the right degree of leakiness. The leak size was approximately 5×10^{-6} liter/sec. of air at one atmosphere. It was possible to control the rate of gas admission by adjusting the gas pressure in the storage bulbs below one atmosphere. The decay of the gas pressure in the storage bulbs during a run was undesirable, but its effect was small in comparison with fluctuations and changes due to other causes.

On account of the small size of the signals obtained, the gas admission rate was increased until the operating pressure in the apparatus was greater than 10^{-3} mm Hg. At somewhat higher pressures the diffusion pump would stop pumping. The pumping speed was evidently inadequate, but not so much so that the experiment could not be carried out.

The apparatus was evacuated through two one-inch pump leads (not shown in Fig. 19) by a three-stage fractionating pump. This was backed by a mechanical pump.

D. OBSERVATIONS

26. Size of the Signal

The detector current consisted of the signal, or current of electrons ejected by metastable atoms, and the background or current of photo-electrons arising primarily from excitation of molecular states in the background pressure of hydrogen molecules, and to some extent from excitation of atomic states other than the $2^2S_{1/2}$. At the electron energies used, the background was three or more times as large as the signal. A magnetic field of 100 gauss or more prevented the detection of ions and electrons from the electron bombarder.

The signal was observed as the galvanometer deflection obtained when a d.c. field large enough to quench practically all of the metastable atoms was applied to the wires K of Fig. 19 as described in Section 23. This deflection was usually some 20 to 50 cm and on occasion as much as 80 cm, or a current of 1.2×10^{-13} amp. This is smaller than the estimated value of Section 12 by a factor of about 40. An undetermined part of this discrepancy could be attributed to quenching by stray electric fields in the electron bombarder due to charges accumulated on insulating deposits on metal surfaces (Section 28). This has at times caused the signal to practically disappear. On the other hand, the maximum signal was obtained when the metal surfaces were cleared of all deposits. It seems unlikely that enough insulating material could remain to account for such a large amount of quenching.

In Eq. (20) all quantities but the detector efficiency have probably been underestimated so that S represents a lower bound of the expected signal. The discrepancy could be accounted for by taking η to be $1/80$ instead of $\frac{1}{2}$ as in Section 12. A possible reason for such a low detection efficiency was indicated in Section 11.

27. Dependence of the Signal on the Magnetic Field

The observations covered a range of magnetic field intensity of about 50 to 3000 gauss. At each value of the magnetic field a portion of the beam of metastable atoms is lost by quenching due to the motional electric field given by Eq. (44). The amount of this loss increases with the magnetic field intensity, as can be seen from the discussions of Sections 6 and 16. It was observed that the signal decreased in general throughout the range covered and was fairly small at the highest fields, in qualitative agreement with the theory. The mode of construction of the apparatus did not permit an accurate study of this phenomenon. In addition to bad geometry, interfering effects in the electron gun would have made the results difficult to interpret.

28. Stability of the Signal

It was mentioned in Section 26 that the signal was subject to considerable variation. Part of this was ex-

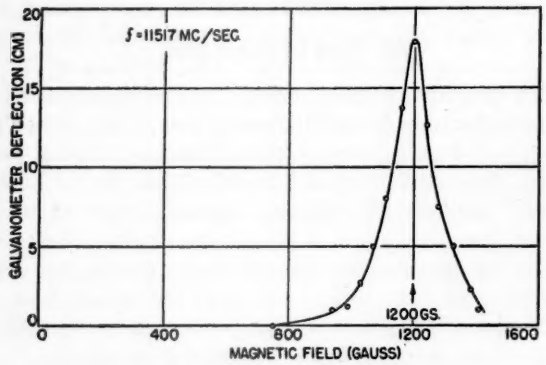

FIG. 21. Observed resonance curve.

plained in Section 27 as due to the magnetic field, but there was also an uncontrolled part principally caused by the electron bombarder. Some of this was due to the cathode which had to be replaced every three or four days because of emission poisoning. This was presumably caused by pump oil vapor or water vapor admitted with the hydrogen. As long as enough emission was available, the decay in the current could be corrected by adjustment of the control grid voltage.

In addition to emission poisoning, the optimum operating current and voltages of the electron bombarder kept changing as mentioned in Section 22. This was accompanied by a decrease in the signal which was appreciably less at the end of a run than at the beginning. The cause for this was not understood at the time, but is now known to be due to the formation of charged insulating layers on the grids and the anode. Thermal breakdown of pump oil vapor and perhaps wax is responsible for at least part of the material.‡ Dissociation under electron bombardment also occurs, and alkaline earth oxides evaporated from the cathode surface may also contribute. The charges accumulating on the layers add to the stray electric field quenching of the metastables, and thereby cause a decrease in the signal. They also have a large effect on the electronic behavior of the electron bombarder. This subject will be considered further in Part II.

In order to obtain a sufficiently large signal, it was necessary to increase the source pressure until the background pressure was just short of being sufficient to cause appreciable collision quenching. This condition was unfortunately accompanied by a large amount of short period fluctuation, largely in the background which, as indicated in Section 26, was already much larger than the signal. Fluctuations in the background were superposed on those in the beam of metastable atoms and placed a serious limitation on the accuracy of the measurements.

Changes in the detector efficiency could conceivably cause both long- and short-period variations; however, these have usually also been ascribable to other causes.

‡ Suggested to us by Dr. A. L. Samuel.

29. Procedure

It was shown in Section 14 that it would be very difficult to observe the shape of a resonance curve by holding the magnetic field fixed and varying the frequency. The reverse procedure was followed, wherein the oscillator frequency was held at a predetermined value and the magnetic field varied. The procedure was simply to demagnetize the magnet and to increase the magnetic field in steps, at each one observing the increase in the signal due to interruption of the power in the r-f line. Resonance curves obtained in this manner at various frequencies are plotted in Figs. 21 to 24. In these the galvanometer deflection obtained by interrupting the r-f power is plotted *versus* the magnetic field.

The variability of the electron bombarder, discussed in the previous section, made it necessary to seek a new optimum set of operating conditions before each run. This would usually suffice for two or three hours operation.

In view of the difficult experimental conditions, an excessive amount of r-f power was used throughout to enhance the size of the effect.

In principle, the effects of the long-period fluctuations and the variation of the signal with magnetic field could have been canceled by measuring the signal at each point by applying a d.c. quenching field, and expressing the r-f quenching as the ratio of r-f to d.c. quenching. This quantity when plotted *versus* H would have given more accurate resonance curves. On the whole, however, it was rather difficult to keep the apparatus in an operating condition long enough to take a resonance curve in the manner described above with only a few observations of the total signal. Thus it was not feasible to use the more accurate method. Nevertheless, the resonance curves were sufficiently sharp that they were not greatly in error due to variations of the signal with magnetic field strength.

E. ANALYSIS OF DATA AND RESULTS

30. Shape and Width of Resonance Curves

Some resonance curves typical of the better data are shown in Figs. 21 to 24 which represent examples of all

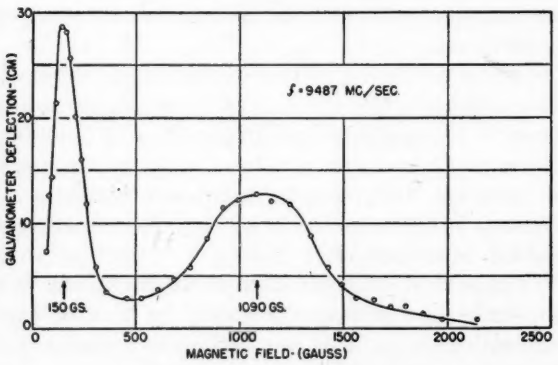

FIG. 22. Observed resonance curve.

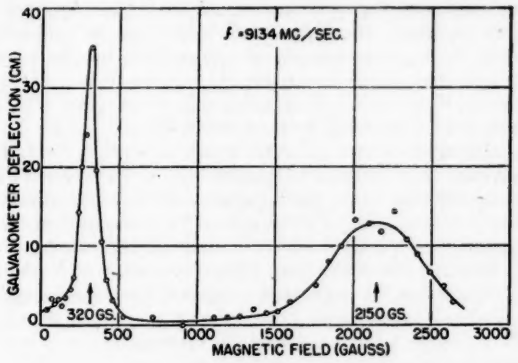

FIG. 23. Observed resonance curve.

observed transitions. It will be noted that these are just the transitions originating from the upper metastable level, α. In agreement with the considerations of Section 16, the other transitions were not observed.

Comparison of the resonance curves for hydrogen in Fig. 24, with the theoretical curves in Fig. 18(a) shows that the expected partially resolved hyperfine structure of the αf transition is completely obscured. Nor does the αe resonance exhibit the flat top shown in Fig. 18(b). Magnetic field inhomogeneity and r-f saturation could account for this discrepancy. The magnetic field inhomogeneity of 33 gauss per 1000 gauss in region J contributes to the smearing out of the hyperfine structure and adds to the expected theoretical width. As explained in Section 13, r-f saturation also adds to the half-width and thereby impairs the resolution of hyperfine structure. An additional cause of broadening may be due to the leakage of r-f through the rather large opening into the bombardment region. The atoms quenched there are in a magnetic field somewhat weaker than that found in the wave guide. Consequently, it would be expected that the half-widths of the peaks would considerably exceed the calculated values. This is shown in Table I. These calculated values take into account only the radiation width of 100 Mc/sec. and the unresolved hyperfine structure of the S and P levels. Doppler broadening may be neglected. The expected difference between hydrogen and deuterium is obscured, possibly because of greater saturation effects in the case of the latter.

31. Results

The resonance magnetic fields were located simply by taking the apparent peak in the case of sharp peaks, and by averaging the fields at half-amplitude for broad peaks. No corrections were made for overlap or other factors. The resonance magnetic fields so obtained at the various frequencies are plotted in Fig. 25. The theoretically calculated curves for the Zeeman effect, assuming validity of Dirac's theory, are plotted as solid lines, while for comparison with observed points, the calculated curves have been shifted down by 1000 Mc/sec. in the case of transitions to the $2^2P_{3/2}$ levels and up by 1000 Mc/sec. for those to the $2^2P_{1/2}$ levels. In view of the uncertainty introduced by inhomogeneity of the magnetic field and distortion of the peaks due to the falling off of the signal, no attempt was made to obtain a "best fit."

TABLE I. Half-widths of the peaks.

Substance	Transition	Obs. (Mc/sec.)	Calc. (Mc/sec.)
H	αf	410	219
H	αe	320	159
D	αf	400	128
D	αe	320	114

The results clearly indicate that contrary to the Dirac theory, but in essential agreement with Pasternack's hypothesis, the $2^2S_{1/2}$ level is higher than the $2^2P_{1/2}$ by about 1000 Mc/sec. (0.033 cm^{-1}) or about 9 percent of the spin relativity doublet separation. Within the precision of these results, there is no discrepancy between the Dirac theory and the doublet separation of the P levels.

The coincidence of the hydrogen and deuterium resonances indicates that with this precision, the $2^2S_{1/2}-2^2P_{1/2}$ shift for deuterium is the same as for hydrogen.

The authors have benefited greatly from the continuous cooperation and assistance of Dr. M. Phillips and Messrs. Bernstein, Costello, Dechert, and Richter, and other members of the Columbia Radiation Laboratory staff. The calculations referred to in Section 11 were made by Mr. D. Sternberg.

APPENDIX I. CONDITIONS IN A WOOD'S DISCHARGE

The absorption of radio waves by excited hydrogen atoms in a Wood's discharge tube depends on the populations of the various states. These in turn depend on the rates of production and decay of the excited atoms. It would involve a lengthy program of research to make quantitative calculations of these, and we shall be content here with the roughest sort of estimate. Only the $n=1$ and $n=2$ states of atomic hydrogen will be considered.

We shall assume that the $2p$ states decay to $1s$ at a rate corresponding to the natural lifetime $\tau_p=1.6\times10^{-9}$ sec., and that the excitation of $2p$ is due primarily to two causes: (1) electron bom-

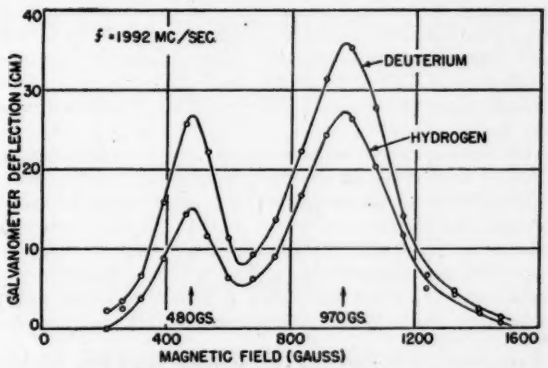

FIG. 24. Observed resonance curve showing similar curves obtained for hydrogen and deuterium.

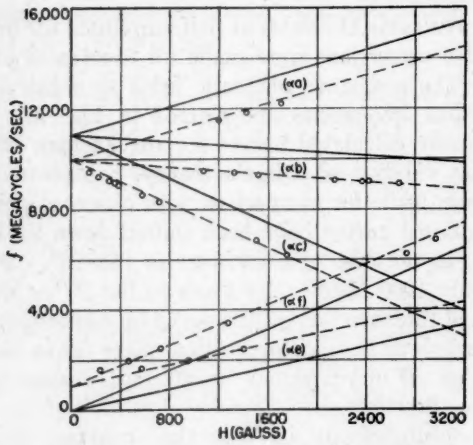

FIG. 25. Summary of data on resonance peaks. The solid curves correspond to the Dirac theory as in Fig. 13 while the dotted curves correspond to the modified curves of Fig. 15 with the $2^2S_{1/2}$ level raised by 1000 Mc/sec. The fit with the observed points clearly indicates the reality of such a shift.

bardment and (2) absorption of the Lyman resonance radiation emitted by other atoms. Since the absorption coefficient for this radiation is very large, a resonance radiation quantum can, on the average, only escape from the tube after a large number of absorptions and re-emissions. This number has been estimated[53] to be 500 to 1000 for typical discharge conditions. As a result, the effective decay rate of the $2p$ states is much smaller than that given by the natural lifetime, and the population of states $2p$ is correspondingly increased.

The situation is markedly different for the $2^2S_{1/2}$ state. As indicated in Section 9, excitation from $1^2S_{1/2}$ by electron bombardment is about one-tenth as likely as for $2p$ excitation. The imprisonment of resonance radiation plays no role here, for the $2^2S_{1/2}$ state cannot combine optically with the ground state. As a result, however, the $2^2S_{1/2}$ state under certain circumstances may be metastable, and despite the low rate of production, the population increased. As shown in Section 6, the decay rate of $2^2S_{1/2}$ increases with the electric field acting on the atom, and decreases with increasing separation of the states $2^2S_{1/2}$ and $2^2P_{1/2}$. If this separation is zero as given by the Dirac theory, the life of $2^2S_{1/2}$ in a typical Wood's discharge is a few times the natural life, but if the separation corresponds to 1000 Mc/sec., the life is increased to about 900 τ_p, and the population of $2^2S_{1/2}$ is correspondingly increased.

Let us consider the transitions between $2^2S_{1/2}$ and $2^2P_{3/2}$ induced by radio waves. If these states are populated in accordance with their statistical weights (equipartition), there will be no appreciable net absorption of r-f since the induced emission exactly cancels the induced absorption. (Spontaneous transitions between $2^2P_{3/2}$ and $2^2S_{1/2}$ occur at a negligible rate.) If the population of $2^2S_{1/2}$ is increased relative to $2^2P_{3/2}$, there will be a net absorption of r-f. If, on the other hand, $2^2P_{3/2}$ is more highly populated, there will be a net induced emission (negative absorption!).

On the basis of the preceding discussion alone, one would expect that the $2p$ levels would be about five to ten times more populated than the $2s$ levels. In that case, one would expect to find a negative absorption, and as estimated below, a large one. Admittedly the population estimates are rough. Still it would seem to require an accident for exact equipartition, unless there is some mechanism efficiently coupling $2^2S_{1/2}$ and $2^2P_{1/2}$. As indicated above, and as described quantitatively in Section 6, there is Stark effect coupling between these two states. If it were not for the entrappment of resonance radiation, the $2^2P_{1/2}$ state would not be sufficiently populated for the establishment of equipartition by this mechanism, but on the basis of the numerical estimates given above, and in Appendix II, it seems quite possible that it can occur, and that the absorption of r-f would be markedly reduced.

If equipartition is not achieved, a net absorption or induced emission can occur. In order to form an idea of the expected magnitude, we shall calculate the unbalanced rate of transitions induced by r-f from $2^2S_{1/2}$ to $2^2P_{3/2}$ ignoring the reverse transitions which might nearly cancel out or reverse the sign of the whole effect. Although the result may be an overestimate of the expected "absorption," it provides a convenient basis for discussion.

We proceed to estimate this absorption rate. In a typical Wood's discharge tube, there might be a pressure of 0.15 mm of mercury corresponding to a density of

$$n_{\mathrm{H}}=(0.15\times 2.687\times 10^{19})/(760)=5.3\times 10^{15} \tag{56}$$

hydrogen atoms per cubic centimeter. The number of atoms excited to $2^2S_{1/2}$ per unit volume per second is given by

$$J\sigma n_{\mathrm{H}}$$

where eJ is the electron current density, and σ is the excitation cross section. If we equate this to the assumed rate of density decay

$$n^*/(900\tau_p)$$

we obtain

$$n^*=900J\sigma\tau_p n_{\mathrm{H}}. \tag{57}$$

Taking an electron current density corresponding to 0.1 amp./cm^2

$$J=(0.1)/(1.602\times 10^{-19})=6.24\times 10^{-17}\ \text{electron/cm}^2\text{/sec.}$$

and

$$\sigma=10^{-17}\ \text{cm}^2$$

(Section 9), we find

$$n^*=4.7\times 10^{10}\ \text{cm}^{-3} \tag{58}$$

in state $2^2S_{1/2}$.

We now consider the absorption of radio waves by these excited hydrogen atoms, taking as explained above, only the transitions to $2^2P_{3/2}$ into account. As in Section 13, the transition probability for absorption of radiation is

$$1/\tau_{\text{induced}}=(2\pi e^2S_0\gamma/c\hbar^2)|(|\hat{\mathbf{e}}\cdot\mathbf{r}|)|^2/[(\omega-\omega_0)^2+(\gamma/2)^2], \tag{59}$$

where S_0 is the incident energy flux density of the radiation having circular frequency ω and electric polarization vector parallel to the unit vector $\hat{\mathbf{e}}$, ω_0 is the circular resonance frequency, $(|\mathbf{r}|)$ is the matrix element of the coordinate vector $\mathbf{r}$ of the atomic electron for the transitions from $2^2S_{1/2}$ to $2^2P_{3/2}$, $\gamma=1/\tau_p$ is the reciprocal lifetime of the $2^2P_{3/2}$ state. For some estimates it is useful to use instead of a transition probability a cross section σ_{induced} for the absorption of a microwave photon. This is given by the equation

$$J_p\sigma_{\text{induced}}=1/\tau_{\text{induced}} \tag{60}$$

where J_p is the flux density of such photons. Now $J_p=S_0/\hbar\omega_0$ and hence

$$\sigma_{\text{induced}}=\hbar\omega_0/S_0\tau$$

or

$$\sigma_{\text{induced}}=2\pi(e^2/\hbar c)|(|\hat{\mathbf{e}}\cdot\mathbf{r}|)|^2\omega_0\gamma/[(\omega-\omega_0)^2+(\gamma/2)^2]. \tag{61}$$

For the sum of all transistions to the sub-levels of $2^2P_{3/2}$ one has $|(|\hat{\mathbf{e}}\cdot\mathbf{r}|)|^2$ equal to two-thirds of the value in which the sum is taken over all sub-levels of $2^2P_{1/2}$ and $2^2P_{3/2}$. This sum is just the value which would be calculated for the transitions from $2s$ to $2p$ ignoring electron spin. Hence[54]

$$|(|\hat{\mathbf{e}}\cdot\mathbf{r}|)|^2\rightarrow(\tfrac{2}{3})(27a_0^2/3)=6a_0^2. \tag{62}$$

At resonance

$$\omega=\omega_0=2\pi(10{,}950)\times 10^6\ \text{sec.}^{-1} \tag{63}$$

[53] Based on equations given by T. Holstein, Phys. Rev. 72, 1212 (1947). See also L. M. Bieberman, J. Exp. Theor. Phys. 17, 416 (1947).

[54] See reference 25, pp. 432 and 442.

and using

$$\gamma=1/(1.595\times10^{-9})=6.25\times10^{8}\ \text{sec.}^{-1} \tag{64}$$

we find

$$\sigma_{\text{induced}}=3.4\times10^{-15}\ \text{cm}^2. \tag{65}$$

For $n^*=4.7\times10^{10}$ atoms/cm^3 in state $2^2S_{1/2}$, the absorption coefficient would be $\mu=1.6\times10^{-4}$ cm^{-1}. This is a large absorption coefficient by modern microwave spectroscopic standards, but the breadth of the resonance $\gamma/2\pi\sim100$ Mc/sec. is many times the widths usually met in that field. As explained above, it is possible that this absorption is nearly all canceled out by the inverse transitions. In view, however, of the extreme crudeness of the numerical estimates, it is possible that some appreciable departure from equipartition may exist, and that an absorption or induced emission could be detected. It is therefore highly desirable that a search for such effects should be made, especially under discharge conditions which do not favor equipartition.

As a complicating factor, there will be a large and frequency dependent background absorption of microwaves in the discharge due to the electrons. Haase[18] found good agreement with an equation derived by Stewart[55]

$$\mu_{\text{electrons}}=(2e^2z\lambda^2N_e)/(\pi mc^3) \tag{66}$$

for the absorption coefficient of radiation with wave-length λ. Here z is the number of collisions with gas molecules per second experienced by an electron, and N_e is the number of free electrons per cubic centimeter. For the typical figures

$$\begin{aligned} z&=0.95\times10^{9}\ \text{sec.}^{-1}\\ N_e&=2\times10^{9}\ \text{cm}^{-3}\\ \lambda&=3\ \text{cm}\\ \mu_{\text{electrons}}&=1.03\times10^{-4}\ \text{cm}^{-1}. \end{aligned} \tag{67}$$

APPENDIX II. QUENCHING OF METASTABLE HYDROGEN ATOMS BY ELECTRIC FIELDS[56]

Our purpose here is to generalize the theory given by Bethe[25] for the effect of a uniform electric field on the lifetime of the $2^2S_{1/2}$ level, whose derivation did not take into account the removal of the degeneracy of $2^2S_{1/2}$ and $2^2P_{1/2}$.

We consider two excited levels with probability amplitudes a and b. The state a is metastable in the absence of an external electric field and has a small decay constant γ_a (double quantum emission to the ground state with life of $\frac{1}{7}$ sec.). Level b lies higher in energy by $E_b-E_a=\hbar\omega$ (ω may be negative), and decays to the ground state c with emission of resonance radiation at the rate $\gamma_b=1/\tau_p$. The equations of time dependent perturbation theory are then

$$\begin{aligned} i\hbar\dot{a}&=V^*e^{-i\omega t}b-\tfrac{1}{2}i\hbar\gamma_a a\\ i\hbar\dot{b}&=Ve^{i\omega t}a-\tfrac{1}{2}i\hbar\gamma_b b \end{aligned} \tag{68}$$

where $V=(b|e\mathbf{E}\cdot\mathbf{r}|a)$ is the matrix element of the perturbing electric field energy for the transition $a\to b$. The decay is treated phenomenologically by introduction of damping terms, but it is possible to justify this by writing out equations of the Wigner-Weisskopf[57] type.

The general solutions of Eqs. (68) are

$$\begin{aligned} a&=A_1\exp(\mu_1t)+A_2\exp(\mu_2t)\\ b&=-(\hbar/iV^*)[(\mu_1+\tfrac{1}{2}\gamma_a)A_1\exp((\mu_1+i\omega)t)\\ &\qquad+(\mu_2+\tfrac{1}{2}\gamma_a)A_2\exp((\mu_2+i\omega)t)] \end{aligned} \tag{69}$$

where μ_1 and μ_2 are the roots of the quadratic equation

$$(\mu+\tfrac{1}{2}\gamma_a)(\mu+i\omega+\tfrac{1}{2}\gamma_b)+|V|^2/\hbar^2=0. \tag{70}$$

[55] J. Q. Stewart, Phys. Rev. **22**, 324 (1923).

[56] P. Caldirola, Nuovo Cimento **5**, 399 (1948) considered the effect of the level shift on the Stark quenching of $2^2S_{1/2}$, but his calculation is subject to the error made in reference 26 mentioned in Section 6.

[57] See, for example, G. Wentzel, *Handbuch der Physik* (1933), second edition, Vol. 24/1, p. 752.

In most applications, the γ_a-terms may be dropped. Then for small electric fields

$$\begin{aligned} \mu_1&\sim-i\omega-\tfrac{1}{2}\gamma_b\\ \mu_2&\sim-|V|^2/[\hbar^2(i\omega+\tfrac{1}{2}\gamma_b)]. \end{aligned} \tag{71}$$

We represent the excitation of the metastable state by the initial conditions

$$a=1,\quad b=0\quad\text{at}\quad t=0. \tag{72}$$

This gives

$$\begin{aligned} A_1+A_2&=1\\ \mu_1A_1+\mu_2A_2&=0, \end{aligned} \tag{73}$$

whence

$$A_1=\mu_2/(\mu_2-\mu_1),\quad A_2=-\mu_1/(\mu_2-\mu_1). \tag{74}$$

The probability that level a is occupied after passage of time t is

$$|a|^2=|A_1\exp(\mu_1t)+A_2\exp(\mu_2t)|^2. \tag{75}$$

The first term has a small coefficient and is strongly damped. Since $|A_2|\sim1$, the effective decay rate is

$$\gamma_{\text{Stark}}=\mu_2+\mu_2^*=\gamma_b|V|^2/[\hbar^2(\omega^2+\tfrac{1}{4}\gamma^2)]. \tag{76}$$

For $\omega=0$, this reduces to Bethe's result. In case there are several well separated levels, b, none of which is too strongly coupled to a, the decay rates are simply additive.

In the limit $|V|^2\to0$, the exact solutions give $\mu_2+\mu_2^*=\gamma_a$ while for $|V|^2/\hbar^2[\omega^2+\frac{1}{4}\gamma_b^2]\to\infty$,

$$\mu_i+\mu_i^*=\gamma_b/2$$

for $i=1, 2$, giving the expected results. The approximate expression (76) suffices for most purposes.

In the discussion of Appendix I, a problem arose concerning the mechanism whereby equipartition could be established between the $2^2P_{1/2}$ and $2^2S_{1/2}$ states. Without any such mechanism, it was estimated that the population of $2^2P_{1/2}$ might be as much as 12 times that of $2^2S_{1/2}$. Consider now an atom excited by resonance radiation to $2^2P_{1/2}$. It decays rapidly to $1^2S_{1/2}$ by reemission of resonance radiation, but because of the Stark coupling, there is a small probability that a transition to the long lived $2^2S_{1/2}$ state take place. This probability may be calculated by solving Eqs. (68) subject to the initial conditions

$$b=1,\quad a=0\quad\text{at}\quad t=0. \tag{77}$$

The terms in μ_1 are rapidly damped, and the probability for reaching the metastable state is

$$\begin{aligned} |a|^2=|A_2'|^2&=|\mu_2/(\mu_2-\mu_1)|^2\simeq|V|^2/\hbar^2[\omega^2+\tfrac{1}{4}\gamma_b^2]\\ &=(\gamma_{\text{Stark}}/\gamma_b)\sim1/800. \end{aligned} \tag{78}$$

Since the resonance radiation on the average requires 400 to 1000 absorptions and re-emissions before escaping, there is a high probability that a long-lived $2^2S_{1/2}$ state will be populated before the escape can occur. Consequently there would seem to be at least one plausible mechanism for establishment of equipartition between $2^2P_{1/2}$ and $2^2S_{1/2}$.

APPENDIX III. DISTRIBUTION IN RECOIL ANGLES

As indicated in Section 10, the hydrogen atoms which are excited to the metastable state experience a recoil measured by an angle Θ giving the change in their direction of motion. Our task here is to compute the distribution in recoil angles. Let M be the mass of the atom, $\mathbf{V}_0$ its initial velocity, $\mathbf{V}_1$ its final velocity, and let the velocity of the bombarding electron of mass m be $\mathbf{v}_0$, that of the outgoing electron be $\mathbf{v}_1$. The momentum balance for the collision is then

$$M\mathbf{V}_0+m\mathbf{v}_0=M\mathbf{V}_1+m\mathbf{v}_1. \tag{79}$$

The energy balance is approximately

$$\tfrac{1}{2}mv_0^2-\tfrac{1}{2}mv_1^2=(\tfrac{2}{4})hcR \tag{80}$$

neglecting the kinetic energy change for the atom.

The momentum conservation may be represented as shown in Fig. 26 where ϵ is the angle of the inelastically scattered electron.

The circle is intended to represent the spherical locus of the vector $m\mathbf{v}_1$ and it must be remembered that $\mathbf{V}_1$ may therefore lie out of the plane of $\mathbf{V}_0$ and $\mathbf{v}_0$. For definite values of V_0 and v_0 the angle Θ will have a range of values because of the distribution in ϵ. To simplify matters, we shall assume this distribution to be spherically symmetrical. This assumption should not be too bad near the threshold where v_1 is relatively small and the outgoing wave function is mostly one of zero orbital angular momentum.

From an experimental standpoint, we are interested in horizontal and vertical recoil angles ψ and χ separately. We may approximately set

$$\tan\psi=(mv_0-mv_1')/(MV_0) \tag{81}$$

where v_1' is the magnitude of the projection of $\mathbf{v}_1$ along $\mathbf{v}_0$. Likewise

$$\tan\chi=(mv_1'')/(MV_0), \tag{82}$$

where v_1'' is the magnitude of the projection of $\mathbf{v}_1$ perpendicular to the horizontal plane. Since the angles ψ and χ are fairly small, the tangents may be replaced by the angles in radians. Under the assumption of a spherical distribution in $\mathbf{v}_1$, the probability distribution in v_1' is uniform between the limits v_1 and $-v_1$ and likewise[58] for v_1''. Hence the probability distribution in ψ is uniform for $\psi_1\leqslant\psi\leqslant\psi_2$ where

$$\psi_1=(mv_0-mv_1)/(MV_0) \quad \text{and} \quad \psi_2=(mv_0+mv_1)/(MV_0) \tag{83}$$

and it may be written as

$$P(V_0;\psi)d\psi=\begin{cases}(MV_0/2mv_1)d\psi & \psi_1\leqslant\psi\leqslant\psi_2\\ 0 & \text{otherwise}\end{cases} \tag{84}$$

satisfying the normalization condition

$$\int_{\psi_1}^{\psi_2}P(V_0;\psi)d\psi=1. \tag{85}$$

Likewise

$$P(V_0;\chi)d\chi=\begin{cases}(MV_0/2mv_1)d\chi & -\chi_1\leqslant\chi\leqslant+\chi_1\\ 0 & \text{otherwise}\end{cases} \tag{86}$$

where

$$\chi_1=mv_1/MV_0. \tag{87}$$

Expressions (84) and (86) are valid for definite initial velocities $\mathbf{v}_0$ and $\mathbf{V}_0$ of bombarding electrons and hydrogen atoms. The bombarding electrons may be assumed to be monoenergetic. The distribution of velocities of the atoms will give rise to an additional spread of recoil angles. Assuming thermal equilibrium in the oven at temperature T, the probability distribution of velocities in the beam is given by

$$N(V_0)dV_0=AV_0^3\exp(-V_0^2/U^2) \tag{88}$$

[58] The correlation of ψ and χ is neglected.

FIG. 26. Diagram showing momentum and energy relations for the recoil deflection experienced by a hydrogen atom excited to the $2^2S_{1/2}$ state by electron bombardment at 13.6 ev.

where A is determined from the normalization condition to be $A=2U^{-4}$, and the parameter U from $\frac{1}{2}mU^2=kT$. The most probable velocity contained in the beam is given by $(3/2)^{\frac{1}{2}}U$.

The combined distribution in ψ is given by

$$P(\psi)=\int_0^\infty N(V_0)P(V_0;\psi)dV_0=(M/2mv_1)\int_{V_a}^{V_b}N(V_0)V_0dV_0 \tag{89}$$

where

$$V_a=(mv_0-mv_1)/(M\psi) \quad \text{and} \quad V_b=(mv_0+mv_1)/(M\psi). \tag{90}$$

With the substitution $y=V_0/U$ this becomes

$$P(\psi)=(MU/mv_1)\int_{y_1}^{y_2}y^4\exp(-y^2)dy, \tag{91}$$

where

$$y_1=V_a/U \quad \text{and} \quad y_2=V_b/U. \tag{92}$$

Likewise

$$P(\chi)=(MU/mv_1)\int_0^{y_3}y^4\exp(-y^2)dy, \tag{93}$$

where

$$y_3=(mv_1/M\chi). \tag{94}$$

Bombardment at the Threshold

These expressions considerably simplify at the threshold where $v_1\to 0$. There is no vertical recoil and the horizontal distribution reduces to

$$P(\psi)=2(mv_0/MU)^4\psi^{-5}\exp[-(mv_0/MU\psi)^2]. \tag{95}$$

This is plotted in Fig. 7 for an oven temperature of $T=2600°\text{K}$ where $U=6.55\times10^5$ cm/sec. and $(3/2)^{\frac{1}{2}}U=8.03\times10^5$ cm/sec. gives the most probable atom velocity.

Bombardment at 13.6 e.v.

At this energy, $v_0=\alpha c$ and

$$v_1=\tfrac{1}{2}v_0=\tfrac{1}{2}\alpha c,$$

where α is the fine structure constant, so that

$$y_1=\tfrac{1}{3}y_2=(m\alpha c/2MU\psi), \quad y_3=(m\alpha c/2MU\chi).$$

The integrals (91) and (93) were calculated numerically and plots of $P(\psi)$ and $P(\chi)$ are shown in Fig. 7.

Bremsstrahlung in High Energy Nucleon-Nucleon Collisions*

ALBERT SIMON
University of Rochester, Rochester, New York
(Received March 3, 1950)

Field-theoretic calculations are made of the electromagnetic radiation accompanying a proton-neutron collision. The nucleons are treated non-relativistically, and it is assumed that their scattering is produced either by a scalar meson field with scalar coupling or a pseudoscalar field with pseudoscalar coupling. The resulting energy spectrum for the photons has the form $(\frac{1}{2}E_0-ck)^{\frac{1}{2}}dk/k$ for the scalar field and $(\frac{1}{2}E_0-ck)^{\frac{1}{2}}kdk$ for the pseudoscalar field. The ratio of the intensity at 90° to 0° (in the CM system) is about 100 for the scalar theory and about 1 for the pseudoscalar case for incident energies of about 200 Mev. Integrated cross sections are obtained for both theories. The yield decreases with energy for the scalar field and increases for the pseudoscalar field.

I. INTRODUCTION

RECENT experiments on radiation accompanying high energy nucleon-nucleon collisions[1] have made necessary the study of a possible bremsstrahlung origin of these rays. This process has been calculated by Ashkin and Marshak[2] using a phenomenological treatment in analogy with Coulombic bremsstrahlung. Specifically, they used an empirical potential derived from Berkeley data to accomplish the scattering. Such an approach necessarily omits the "exchange" terms which would be present in a third-order field theoretic treatment. Furthermore, this method cannot be used to study the effects of pseudoscalar mesons since these bring in negative energy states, even in a non-relativistic treatment.

We report in this paper the results of a calculation on the bremsstrahlung as a third-order effect. We shall investigate the contributions of the exchange terms to the total cross section, as well as the difference between the scalar and pseudoscalar theories. Calculations have been performed for both the charged and symmetric meson theories. The nucleons are assumed to obey the Dirac equation and are treated non-relativistically, making the same approximations as were made in reference 2. The nucleon energy will be restricted to values below the threshold for production of π-mesons. We shall treat the case of a scalar field with scalar coupling, and a pseudoscalar field with pseudoscalar coupling. These results will hold as well for scalar mesons with vector coupling, and pseudoscalar mesons with pseudovector coupling.[3]

II. THEORY

The interaction Hamiltonians are:

$$H_{NR}=-(4\pi)^{\frac{1}{2}}\boldsymbol{\alpha}\cdot\mathbf{A},$$
$$H_{MR}=[i(4\pi)^{\frac{1}{2}}e/hc](\phi^*\nabla\phi-\phi\nabla\phi^*)\cdot\mathbf{A}. \quad (1)$$

Here H_{NR} represents the interaction Hamiltonian of the nucleons with the electromagnetic field, and H_{MR} that of the mesons with the electromagnetic field. $\mathbf{A}$ is the vector potential, ϕ the meson field and $\boldsymbol{\alpha}$ is the Dirac operator. A term involving A^2 coupling has been omitted in H_{MR} as this is not important for this lowest order calculation. $\mathbf{A}$, and ϕ are expanded in the usual fashion (normalization is to unit volume).

$$\mathbf{A}=\sum_k \hbar c\boldsymbol{\varepsilon}/(2\omega_k)^{\frac{1}{2}}(a_k+a_{-k}^*)\exp(i\mathbf{k}\cdot\mathbf{r}/\hbar),$$
$$\phi=\sum_l \hbar c/(2E_l)^{\frac{1}{2}}(b_l^*+c_{-l})\exp(-i\mathbf{l}\cdot\mathbf{r}/\hbar),$$

where $\mathbf{k}$ is the momentum of a photon, ω_k its energy, $\boldsymbol{\varepsilon}$ is its polarization and a^* and a are creation and destruction operators for the photon. The meson momentum is $\mathbf{l}$ and $E_l^2=c^2(l^2+\mu^2c^2)$. For the scalar theory

$$H_{NM}=(4\pi)^{\frac{1}{2}}g\psi^*\beta\tau_i\psi\phi^i$$
$$=(4\pi)^{\frac{1}{2}}g(\psi^*\beta\tau_+\psi\phi+\text{c.c.}), \quad (2)$$

where the couplings for both the symmetric and charged theories are listed respectively.

The symbol ψ represents 8-component wave functions for the nucleons, since the nucleon can be either a proton or a neutron. We choose the representation so that:

$$\tau_+=\begin{pmatrix}00\\10\end{pmatrix},\quad \tau_-=\begin{pmatrix}01\\00\end{pmatrix},$$
$$\tau_+=\tfrac{1}{2}(\tau_1+i\tau_2),\quad \tau_-=\tfrac{1}{2}(\tau_1-i\tau_2).$$

If we use the notation of reference 2, the proton and neutron have initial momenta $\mathbf{p}_0$ and $-\mathbf{p}_0$, respectively, in the center-of-mass system, and final momenta $\mathbf{p}-\frac{1}{2}\mathbf{k}$ and $-\mathbf{p}-\frac{1}{2}\mathbf{k}$. The differential cross section is

$$d\sigma=(M^2/128\pi^5\hbar^7)(p/p_0)\langle|H'|^2\rangle k^2dkd\Omega_kd\Omega_p, \quad (3)$$

where the angular brackets around $|H'|^2$ denote the average over the initial spins of the nucleons and the summation over the polarization of the γ-ray and the final spins of the nucleons.

In our non-relativistic treatment we can omit transitions to negative energy states for the case of scalar

* This work was partially supported by the joint program of the ONR and the AEC.

[1] Bjorklund, Crandall, Moyer, and York, Phys. Rev. **77**, 213 (1950).
[2] J. Ashkin and R. E. Marshak, Phys. Rev. **76**, 58 (1949).
[3] K. M. Case, Phys. Rev. **76**, 14 (1949).

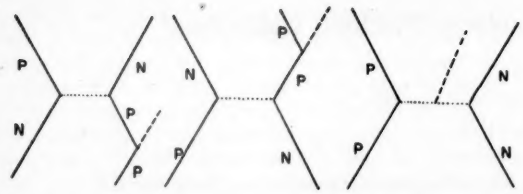

FIG. 1. Feynman diagrams for lowest order bremsstrahlung. Solid lines are nucleons, dotted lines mesons, and dashed lines are photons. Neutral meson exchanges are similar but are not indicated above.

coupling. Furthermore, we neglect $\mathbf{k}/2$ compared to $\mathbf{p}_0 \pm \mathbf{p}$ and also ω_k compared to $E_\pm = [(\mathbf{p}_0 \pm \mathbf{p})^2 + \mu^2]^{\frac{1}{2}}$, where μ is the mass of the meson. Magnetic emission gives no contribution in this approximation. This is to be expected for a spin independent potential. (Compare with reference 2.) Radiation in $p-p$ and $n-n$ collisions is negligible in this approximation since the dipole moment of the system remains constant.

There are three Feynman diagrams for this process. These are given in Fig. 1. Here the dashed line represents the emitted photon, and the dotted line is a virtual meson exchange.

We have not included exchanges of neutral mesons but these diagrams (omitting the third) are similar. The third diagram is clearly an exchange term since it represents radiation by a meson, which is not included in the phenomenological treatment. It is interesting to note that the first two diagrams also contain exchange terms as well as ordinary terms. Thus (in the first) if the neutron emits a π^- before the proton radiates, we have an exchange contribution. The Feynman method combines several possibilities into one diagram. However, since we wish to evaluate the relative contribution of the exchange terms, we must use the standard perturbation treatment.

Using this approach, the ordinary charged transitions are given schematically as:

$$\begin{array}{l}
\nearrow(-\mathbf{p}-\frac{1}{2}\mathbf{k},\ -\mathbf{p}_0,\ \mathbf{p}_0+\mathbf{p}+\frac{1}{2}\mathbf{k})\searrow \\
\longrightarrow(\mathbf{p}_0,\ \mathbf{p}+\frac{1}{2}\mathbf{k},\ -\mathbf{p}_0-\mathbf{p}-\frac{1}{2}\mathbf{k})\longrightarrow(-\mathbf{p}-\frac{1}{2}\mathbf{k},\ \mathbf{p}+\frac{1}{2}\mathbf{k}) \\
\qquad\qquad\qquad\qquad\qquad\qquad\qquad\qquad\qquad\qquad\qquad\qquad\searrow \\
\searrow \qquad\qquad\qquad\qquad\qquad\qquad\qquad\qquad\qquad\qquad\qquad\qquad\

for the charged theory are given by the first two terms, divided by 4.

In the pseudoscalar case we have the new interaction term

$$H_{NM}=(4\pi)^{\frac{1}{2}}g\psi^*\gamma_4\gamma_5\tau_i\psi\phi^i \\ =(4\pi)^{\frac{1}{2}}g(\psi^*\gamma_4\gamma_5\tau_+\psi\phi^*+\text{c.c.}) \tag{6}$$

for the symmetric and charged cases respectively.

The contribution of transitions to negative energy states can no longer be ignored since γ_5 is an odd operator, and we must use spur techniques to obtain our result. For example, the proton may radiate and go into a negative intermediate state. It then emits a positive virtual meson and becomes the final neutron. This may also occur through an intermediate state of positive energy. The energy denominators make both matrix elements of the same order in v/c.

If we write down the ordinary terms in the symmetric theory following the methods of Casimir, and sum over the intermediate states we obtain:

$$H_{\text{ord}}=C[(\mu_p{}^F|\gamma_4\gamma_5|\mu_N')(\mu_N{}^F|\gamma_4\gamma_5K'|\mu_p') \\ -(\mu_N{}^F|\gamma_4\gamma_5|\mu_p')(\mu_p{}^F|M'\gamma_4\gamma_5|\mu_N')] \\ +2C'(\mu_N{}^F|\gamma_4\gamma_5|\mu_N')(\mu_p{}^F|\gamma_4\gamma_5|\mu_p'), \tag{7}$$

where $K'=-ck(\boldsymbol{\alpha}\cdot\boldsymbol{\varepsilon})-4c(\mathbf{p}_0\cdot\boldsymbol{\varepsilon})$, $M'=ck(\boldsymbol{\alpha}\cdot\boldsymbol{\varepsilon})-4c(\mathbf{p}\cdot\boldsymbol{\varepsilon})$ and μ_N' represents the initial neutron state, etc. $C=(eg^2\hbar^3/ME_+^2)\cdot(2\pi/\omega_k)^{\frac{1}{2}}$ and C' is C with p replaced by $-p$. The first terms in both K' and M' are due to negative energy state transitions. The exchange terms now give a nucleon radiation contribution (unlike the scalar case; and due to negative energy transitions only) as well as the radiation by the meson. These terms are:

$$H_{\text{exc}}=-ckC[(\mu_N{}^F|\gamma_4\gamma_5|\mu_p')(\mu_p{}^F|(\boldsymbol{\alpha}\cdot\boldsymbol{\varepsilon})\gamma_4\gamma_5|\mu_N') \\ +(\mu_p{}^F|\gamma_4\gamma_5|\mu_N')(\mu_N{}^F|\gamma_4\gamma_5(\boldsymbol{\alpha}\cdot\boldsymbol{\varepsilon})|\mu_p') \\ -(2\text{Mc}^2(\mathbf{p}_0+\mathbf{p})\cdot\boldsymbol{\varepsilon}/E_+^2)\cdot(\mu_p{}^F|\gamma_4\gamma_5|\mu_N') \\ \times(\mu_N{}^F|\gamma_4\gamma_5|\mu_p')]. \tag{8}$$

Squaring the total matrix element and inserting projection operators we obtain our result. If we sum over the polarizations of the emitted quantum and its direction of emission, we have:

$$|H_{\text{tot}}|^2=4D^2\Big[(ck)^2(\text{Mc}^2)^2(\mathbf{p}_0+\mathbf{p})^2+(\mathbf{p}_0+\mathbf{p})^4(\mathbf{p}_0-\mathbf{p})^2 \\ +\frac{4(ck^2)(\text{Mc}^2)^2}{E_+{}^2}(\mathbf{p}_0+\mathbf{p})^4+\frac{4(ck)^2(\text{Mc}^2)^2}{E_+{}^4}(\mathbf{p}_0+\mathbf{p})^6\Big] \\ +2DD'\Big[(\mathbf{p}_0-\mathbf{p})^4(\mathbf{p}_0+\mathbf{p})^2+\frac{2(ck)^2(\text{Mc}^2)^2}{E_+{}^2} \\ \times\{2(ck)^2(\text{Mc}^2)^2-(\mathbf{p}_0+\mathbf{p})^2(\mathbf{p}_0-\mathbf{p})^2\}\Big]+D'^2(\mathbf{p}_0-\mathbf{p})^6. \tag{9}$$

Here $D=(2\pi/3)^{\frac{1}{2}}\cdot(C/M^2c^4)$. If we now integrate this over all directions of recoil of the proton we have:

$$d\sigma_{\text{P.S.}}=\tfrac{1}{6}(e^2/\hbar c)(g/\text{Mc}^2)^4(cp_0)^2F(p)dp,$$

where

$$F(p)=(2p/1-p^2)G(p)+8p(1-p^2)H(p) \\ +[p/2(1-p^2)]J(p),$$
$$G(p)=4p(1+p^2+2\lambda) \\ -4p\lambda U[(1-p^2)^2-2\lambda(1+p^2)+\lambda^2] \\ +L[(1-p^2)^2-4\lambda(1+p^2)+3\lambda^2],$$
$$H(p)=2L-20p\lambda U+12p\lambda^2U^2(1+p^2+\lambda) \\ -\tfrac{1}{3}p\lambda^3U^3[3(1+p^2+\lambda)^2+4p^2],$$
$$J(p)=12p(1+p^2)-8p\lambda-4p\lambda^3U \\ -\left[\frac{2\lambda(1+p^2)(2+2p^2+\lambda)}{1+p^2+\lambda}-3\lambda^2\right]L \\ +\frac{8p(1-p^2)^2}{1+p^2+\lambda}[2(1-p^2)^2+2(1+p^2)\lambda-\lambda^2]U \\ +4(1-p^2)^2\left[\frac{2(1-p^2)^2+2(1+p^2)\lambda-\lambda^2}{2(1+p^2+\lambda)^2}-1\right]L. \tag{10}$$

The charged theory is given by the first two terms in $F(p)$, divided by 4.

III. NUMERICAL RESULTS

The total cross section has been integrated numerically over all energies of the photon from $E_0/2$ to $E_0/4$

TABLE I. Total cross sections (in cm²) for bremsstrahlung in neutron-proton collisions. The relative contribution of the exchange terms is given by R. The incident energy is E_0 (in Mev).

	$\sigma/(g^2/hc)^2$	R	E_0
Charged theory:			
Scalar	1.50×10^{-28}	2.9	180
	1.47×10^{-28}	3.2	250
P.S.	0.47×10^{-31}		180
	1.30×10^{-31}	5.1	250
Symmetric theory:			
Scalar	5.1×10^{-28}	3.2	250
P.S.	3.9×10^{-31}	3.3	250

TABLE II. Differential cross section at 0° (in the laboratory) for bremsstrahlung in neutron-proton collisions. The ratio of the radiation at the two angles in the laboratory system corresponding to 0° and 90° in the CM system is given by I. The incident energy is E_0 (in Mev).

	Integrated cross section in the forward direction	I	E_0
Charged theory:			
Scalar	$\sigma/(g^2/hc)^2=2.4\times10^{-31}$	70.8	180
	3.7×10^{-31}	65.4	250
P.S.	0.48×10^{-32}	0.46	180
	0.76×10^{-32}	1.54	250
Symmetric theory:			
Scalar	2.0×10^{-30}	40.8	250
P.S.	3.2×10^{-32}	0.73	250
Phenomenological:			
$V=1V_0$		2.8	250
$V=P_MV_0$		9.2	250
$V=(1+P_M)V_0/2$		5.4	250

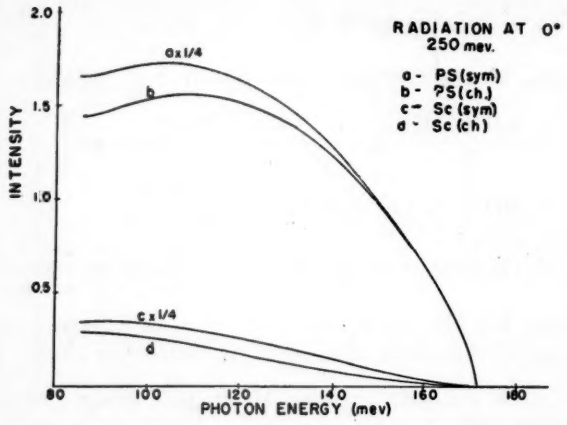

FIG. 2. Relative energy spectrum of proton-neutron bremsstrahlung in forward direction in the lab. system. Relative height based on assuming $g^4_{\text{scalar}}=40g_{\text{P.S.}}{}^4$. Incident energy is 250 Mev in the lab.

in the CM system. (E_0 is the incident energy in the lab. and $\sigma/(g^2/hc)^2$ is given in the first column of Table I.) The calculation was performed for both $E_0=180$ and 250 Mev and this choice is indicated in the last column of Table I. R is a measure of the relative contribution of the exchange terms; i.e., $R=\sigma_{\text{tot}}/\sigma_{\text{ord}}$.

Equation (5) leads to a $(\frac{1}{2}E_0-ck)^{\frac{1}{2}}dk/k$ spectrum in the scalar case and Eq. (10) leads to a $(\frac{1}{2}E_0-ck)^{\frac{1}{2}}kdk$ spectrum in the pseudoscalar case.

The total cross section decreases slowly with energy in the scalar case and increases approximately quadratically with energy in the pseudoscalar case.

The angular distribution of the emitted radiation is also of interest. The expressions for the radiation in the forward direction have been worked out. This result combined with the knowledge of the total cross section allows the radiation at 90° to be computed immediately. This is because the cross section at 90° turns out to be the difference between the total cross section (divided by $8\pi/3$) and the cross section at 0°. An extra term must be added, however, in the pseudoscalar case. The resulting expressions are even more complicated than for the total cross section and are not given. If we denote by I the ratio between intensities at the two angles in the laboratory system corresponding to 90° and 0° in the CM system (these angles are 0° and 72°10′ at $E_0=250$, or 74°12′ at $E_0=180$), we may combine this with the integrated cross section per unit solid angle in the forward direction in the laboratory system, in Table II. Note the striking difference in angular distribution between the scalar and pseudoscalar theories. This may offer an opportunity for experimental differentiation. For purposes of comparison, we have included the intensity ratios obtained by using a potential as in reference 2, where V_0 is a Yukawa well. The photon spectrum in the forward direction in the lab. is shown in Fig. 2 ($d\sigma(0°)=d\sigma(180°)$ in the c.g. system) for the various cases listed in Table II and for $E_0=250$.

We can obtain an estimate of the coupling constant by equating the total cross section given by the ordinary terms to the cross section obtained by Ashkin and Marshak[2] using a phenomenological treatment. This gives:

Scalar	$(g^2/hc)_{SYM}=0.13$,	$(g^2/hc)_{CH}=0.24$;
Pseudoscalar	$=4.8$,	$=10.7$.

These results are not too different from the constants obtained from nuclear forces.

IV. DISCUSSION

Most of our results can be anticipated by qualitative considerations. An exchange force (not to be confused with exchange terms) will give much more radiation than does an ordinary force because of the greater charge acceleration.[4] This is the reason for the small difference (other than a constant factor) between the charged and symmetric theories. The contribution of the meson radiation element is also small because it is proportional to $(\mathbf{p}_0+\mathbf{p})\cdot\boldsymbol{\varepsilon}$ which is small for the predominant backward scattering.

The fact that the pseudoscalar spectrum is of the form kdk rather than dk/k is due to the $1/r^3$ nature of the nuclear potential in the non-relativistic region. The other differences between the scalar and pseudoscalar theories are directly attributable to the intermediate transitions to negative energy states. These terms do not include a dipole effect, which fact leads to the much smaller 90° to 0° ratio in this case. They also bring in added exchange terms leading to a larger R for the pseudoscalar theory. The angular asymmetry in the scalar case is even larger than expected because of a partial cancellation due to the meson radiation element. This accounts for the comparatively smaller value of I in the phenomenological approach, which in many ways corresponds more closely to the scalar than to the pseudoscalar theory.

The results of Watson and Lepore[5] cast some doubt on the usefulness of the pseudoscalar predictions. As anticipated by Bethe,[6] the fourth-order corrections to nuclear scattering in the pseudoscalar case should be large compared to the second order, since this latter order contains $\gamma_5(\sim v/c)$ whereas the fourth-order terms contain $\gamma_5{}^2\sim 1$. However, the corrections in our calculation should not be as serious as in reference 5. One reason is that our process can be thought of as a scattering and a radiation. The average scattering energy is higher than that in reference 5. Thus the $(v/c)^4$ effect is lowered (by a factor of 3 at 250. See Fig. 2 of reference 5.). Furthermore, the fourth-order potential is also of a $1/r^3$ type, and we should expect the same spectral shape as in the second order. Finally, the fourth-order potential term is an ordinary one. This should reduce its effect since it results in forward scattering which gives little radiation. (See reference 4.)

I am greatly indebted to Dr. R. E. Marshak for many valuable discussions, and to Dr. L. L. Foldy for pointing out an error in the original manuscript.

[4] Pomeranchuk and Schmushkevich, Guide to Russ. Sci. Lit. **2**, 159 (1949) and Acad. of Sci. U.S.S.R. **64**, No. 4 (1949).
[5] Watson and Lepore, Phys. Rev. **76**, 1157 (1949).
[6] H. A. Bethe, Phys. Rev. **76**, 191 (1949).

Results of 12.4-Mev Proton-Proton Scattering at 90° *

F. E. Faris† and Byron T. Wright
University of California, Los Angeles, California

(Received February 27, 1950)

The differential cross section in the center-of-mass system for 12.4-Mev proton-proton scattering has been determined in the neighborhood of a scattering angle of 90°. A photographic technique was used with a camera having cylindrical symmetry. The function $f(E)$ as defined by Bethe has been calculated for each of the three cross-section runs which were made. The average value of $f(E)$ as determined by the experiment agrees closely with the value predicted by a linear extrapolation from the results below 4 Mev.

I. INTRODUCTION

NUMEROUS proton-proton scattering experiments showing an appreciable contribution from the nuclear interaction have been performed in the energy range from 0.176 to 14.5 Mev. Jackson[1] lists the experiments and summarizes the results. He points out that the results are not inconsistent with those to be expected from a purely S-state interaction for the nuclear part of the force.

Recently a simplified method for analyzing the results of S-wave scattering has been developed.[2–4] A certain function of phase shift and energy is defined and is predicted to be practically linear with energy until relatively high energies are reached. Below 6 Mev the experimental points can be fitted quite well by a straight line, but with the exception of the 14.5 Mev result the points calculated from experiments above 6 Mev fall quite far above the line.

In the experiment now being reported the differential cross section in the center-of-mass (CM) system near 90° was determined for protons having an energy of 12.4 Mev. The function mentioned in the previous paragraph has been calculated, and only a small deviation from the line extrapolated from the low energy experiments is found.

II. APPARATUS

Measurements of the cross section were made using a photographic technique. The information accumulated by Dearnley, Oxley, and Perry[5] from their experiment using photographic plates was found quite useful. The chief advantage of the photographic method when only weak beam currents are available lies in the relatively large solid angle which can be made available to scattered protons.

The details of the scattering camera are shown schematically in Fig. 1. The camera was designed so the plane of the film is perpendicular to the direction of the proton beam. The film used for the detection of scattered tracks consisted of a 30μ-thickness of Kodak NTB nuclear track emulsion mounted on ordinary film base. The first collimating hole was located at the cyclotron exit port and was $\frac{1}{4}$ in. in diameter. The second hole, which was $17\frac{1}{8}$ in. from the first, had a diameter of $\frac{1}{8}$ in. The geometry was such that neither the edge of the hole in the antiscattering baffle nor the edges of the collimating holes could be "seen" by the photographic film; thus a proton scattered from the edge of the second collimating hole also had to be scattered by the edge of the antiscattering baffle and then by one of the defining slit edges in order to reach the film.

Figure 2 shows the construction of the film holder and the slit edges. The film was held against the back face of the holder by two clamps. The slit opening was large in order to give reasonable times for the runs. The resulting poor angular definition was not serious because of the relatively constant value of the cross section near 90° in the CM reference system.

Prior to its installation in the holder the film was exposed beneath an optical mask[5a] to obtain latent reference lines. The reference lines so obtained defined areas within which tracks were counted after the film had been developed. One side of the mask was covered with a thin coating of metal. Circular reference lines 200μ apart were engraved on the metallic side, and four radial lines divided the circles into quadrants. When

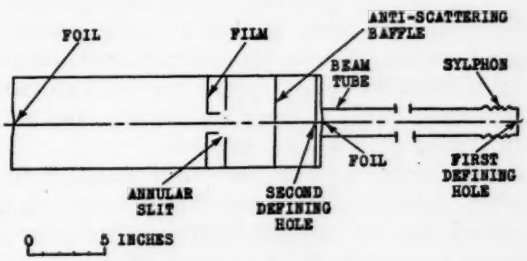

FIG. 1. Diagram of the scattering camera.

* Part of the work reported here was submitted as a thesis by one of us (F.E.F.) in partial fulfillment of the requirements for the Ph.D. degree at the University of California at Los Angeles. The work was supported in part by the joint program of the ONR and AEC.

† Now with North American Aviation, Inc.

[1] J. D. Jackson, "Theoretical interpretation of proton-proton scattering," ONR Technical Report No. 29, p. 38.

[2] L. Landau and J. Smorodinski, J. Phys. U.S.S.R. **8**, 154 (1944).

[3] J. Schwinger, Hectographed Harvard Lecture Notes.

[4] H. A. Bethe, Phys. Rev. **76**, 38 (1949).

[5] Dearnley, Oxley, and Perry, Phys. Rev. **73**, 1290 (1948).

[5a] The masks were manufactured by W. F. Koehler of Van Nuys, California.

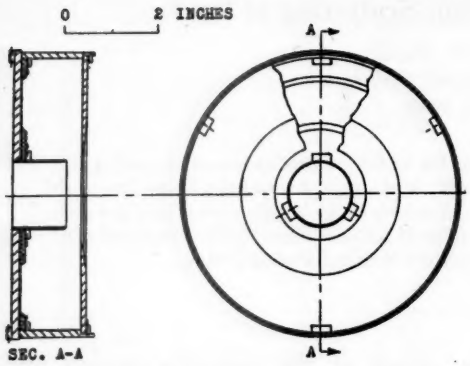

FIG. 2. Details of the film holder and the slit system.

examined under a microscope the lines were found to be sharply defined and to have a width of one or two microns. Lines obtained on the film resulted from the development of surface grains, and therefore it was possible to observe proton tracks beneath them.

Hydrogen was admitted to the camera through a heated palladium valve after the camera had been evacuated by an oil diffusion pump. The pressure of the hydrogen gas was measured by a manometer containing Apiezon oil.

The integrated beam current was obtained by using a Faraday cup which was mounted in an evacuated chamber. The entrance to the cup was in a magnetic field having an average value of about 800 gauss. Tests under similar circumstances by Herb *et al.*[6] indicated that the ionization current and any effect from secondaries would be negligible. The charge collected on the cup was measured by allowing it to build up on a 0.1-μf Fast polystyrene condenser and then discharging the condenser through a ballistic galvanometer. Calibration was accomplished by the use of a General Radio variable air condenser. Repeated tests of the integrating circuit showed that soakage and leakage were negligible.

III. EXPERIMENTAL PROCEDURE

In the course of the experiment seven runs were made. Of these there were three for the cross-section determination, three for a check of background scattering, and one for a determination of slit-edge penetration. The slit-edge penetration run differed from the cross-section runs only in that a much smaller slit opening was used. The background runs were performed under vacuum conditions, in one case with a dynamic system using liquid nitrogen and in two cases with a static system and no liquid nitrogen.

The scattering runs were made under static conditions with no liquid nitrogen in the trap after it had been estimated that background scattering would be negligible in the angular range involved. Such a procedure avoided many difficulties because preliminary tests had indicated that it would not be easy to determine the temperature accurately for other than a static situation with no liquid nitrogen in the trap. That the scattering from background gases was indeed negligible is demonstrated by the results of background measurements given in Section IV.

A 22-mil aluminum absorber was attached to one of the clamps in such a way that it covered a small portion of the film area. The purpose was to provide a check on background scattering during each run. The thickness was great enough so that no protons scattered by protons could get through the absorber and that of the protons scattered by background gases more than half could get through.

During a run the magnetic field current for the cyclotron was monitored by a potentiometer and maintained constant. The voltmeter for the deflector was held as close to 90 kv as possible during the cross-section runs. In the case of some of the background runs made when the cyclotron operation was somewhat unsteady, it was found necessary to change the potential by as much as 2.5 kv in order to maintain a reasonable beam current. A measurement of the effect of deflector voltage on beam energy (Section V) showed that such a variation corresponded to a 0.1-Mev change in energy. This was not serious particularly when it is considered that the background corrections were of the order of one percent. In the case of the hydrogen runs the pressure and the temperature were observed at 15-min. intervals. Runs lasted for about $1\frac{1}{4}$ hr. Average beam currents during the runs were of the order of 5×10^{-12} to 10^{-11} amp.

IV. CROSS-SECTION MEASUREMENTS

The quantities required for the cross-section calculation are the number of scattered tracks, the number of target nuclei per unit volume, and the geometrical parameters related to the solid angle and the scattering length. The pertinent values together with their probable errors are given in Table I.

The tracks were counted using a Spencer research microscope with a magnification of 450×. Two of the circular reference lines were visible in the field of view, and the stage was arranged so that the film could be

TABLE I. Basic data with probable errors.

	Run 1	Run 2	Run 3
Total number of tracks	10269 ±92	10365 ±93	9366 ±86
Background correction	81 ±6	94 ±7	86 ±6
Net number of tracks	10188 ±92	10271 ±93	9280 ±86
Number of incident particles $\times10^{-11}$	1.527 ±0.0039	3.164 ±0.0081	2.405 ±0.0062
Number of target nuclei per cm^3 ($\times10^{-18}$)	3.288 ±0.0050	2.823 ±0.0043	2.816 ±0.0042
Outside diameter of film reference area (cm)	9.8322 ±0.0017	9.8322 ±0.0017	9.8322 ±0.0017
Radial distance from O.D. of ref. area to I.D. (cm)	0.18045 ±0.00025	0.09987 ±0.00017	0.12006 ±0.00018

[6] Herb, Kerst, Parkinson, and Plain, Phys. Rev. **55**, 998 (1939).

rotated about its center while the tracks were being counted.

The background correction, which amounted to about 0.9 percent, was determined from the results of the two runs made with a static system and with no hydrogen present. A given area of the films from both runs was scanned, and the number of tracks which would have been mistaken for proton-scattered tracks was counted.

An area of the film which had been under the absorber (Section III) during the cross-section runs was scanned in each case. The area involved corresponded to about 6.4 percent of the uncovered area in which tracks were counted. In the entire area scanned for background, only one track which resulted from a proton scattered by background gas was found. It was hence concluded that the effect of scattering from background gases was negligible. This conclusion was confirmed by the fact that the number of scattered tracks observed in the case of the high vacuum background run (pressure $=2\times10^{-5}$ mm of mercury) did not differ, within the experimental error, from the number observed for the two static system background runs.

The probable error quoted for the number of scattered tracks includes the statistical error in the number observed, the error arising from the background correction, and the error arising from the fact that counting could not be reproduced exactly. It was found that a count of 2000 tracks by independent observers differed by 0.6 percent.

The circuit used to measure the number of incident particles has already been described in Section II. Immediate calibration at practically the same galvanometer deflection as that obtained for each run eliminated errors which might have resulted from nonlinearity or time-dependent changes in galvanometer sensitivity.

The determination of the number of target nuclei per unit volume required a knowledge of the density and the head of the manometer oil and the temperature of the gas. The density of the oil was found to be 0.8592 $\pm1.1\times10^{-4}$ g/cm^3 at 25.5°C with a temperature coefficient of -6.3×10^{-4} g/cm^3 per °C. The head of the oil was measured with a cathetometer, and the temperatures of the oil and the hydrogen were read from thermometers waxed to the manometer and to the camera. The values for the number of target nuclei per unit volume represent averages for each run with the probable error calculated from all the values obtained during the run.

The geometrical quantities necessary for the cross-section calculation are shown in Figs. 3 and 5. Measurements of geometry were made both before and after the experiment. The diameters of two of the reference circles were measured on one of the films after processing. One diameter was found to be smaller than the corresponding diameter on the optical mask by 0.02 percent, and the other was found to be smaller by 0.13 percent. A length of film was measured before and after drying in the vacuum chamber, and no change was found. It therefore seems reasonable to assume that changes in the dimensions of the reference circles resulted from shifts in the emulsion during processing. For this reason dimensions taken from the optical mask rather than from the film were used in the cross-section calculation. During the experiment it was noted that the film bowed slightly. The amount of the bowing was determined quantitatively by placing the holder containing the film in a vacuum drying chamber and measuring the distance from the slit system to the film upon removal. The distance Z in Fig. 3 ranged from 1.1961 in. for the case in which the least bowing was observed to 1.1886 in. for that in which the most was observed. The probable error in Z was determined from fifty such measurements.

The beam spread at the exit window of the camera was determined by photographing the beam for a short length of time and counting the number of tracks per unit area as a function of radius using the microscope. The distribution of beam particles per unit area had the general form of a Gaussian distribution, and the maximum radius at which particles were found was 1.4 cm. It was found that the presence of hydrogen at a pressure of 80 cm of oil did not change this distribution.

V. THE ENERGY MEASUREMENT

An integral range curve (Fig. 4) was determined by obtaining the ratio of the number of particles that went through a given thickness of aluminum absorber to the number incident. The number of incident protons was determined by observing the activity induced in a copper foil. The number of particles through the absorber was obtained using the Faraday cup and the integrating system described in Section II.

The abscissa of the range curve gives the total

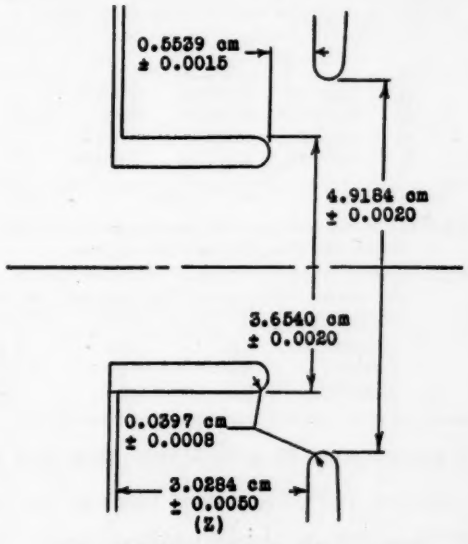

FIG. 3. Dimensions of the slit system.

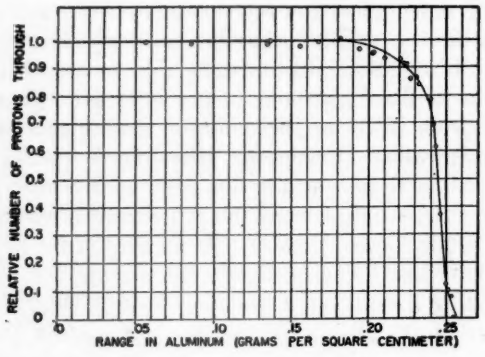

FIG. 4. The integral range curve.

equivalent aluminum thickness between the scattering center and the Faraday cup. The equivalence for the air gap between the camera and the Faraday chamber was obtained from the atomic stopping power given by Bethe and Livingston.[7] The equivalence for the copper was determined using the relative stopping power of 0.81 found by Teasdale.[8] The energy loss in the hydrogen gas was negligible.

The range curve was obtained with the deflector maintained at the same voltage as that used for the scattering runs. The mean range is observed to be 0.2445 g/cm² of aluminum which corresponds to an energy of 12.4 Mev.[9] In view of fluctuations in the deflector voltage and the accuracy to which the range curve could be drawn and the Princeton curve read, the energy is estimated to have an error of one percent. It is apparent from the curve that some relatively low energy protons were present, presumably as a result of penetration into the edges of the collimating holes. The low energy component is accounted for by correcting the cross section as is indicated in Section VI.

Several points were obtained with a different deflector voltage. It was found that increasing the deflector potential from 90 to 95 kv decreased the energy from 12.4 to 12.2 Mev.

TABLE II. Angles as shown in Fig. 5 (radians).

	Run 1	Run 2	Run 3
θ_1	0.89950	0.89950	0.89950
θ_2	0.87013	0.88349	0.88021
θ_3	0.67745	0.67745	0.67745
θ_4	0.64036	0.65719	0.65300

TABLE III. Cross sections with percentages by which corrections changed the final results.

Run No.	Cross section (barns)	Low energy component	Background tracks	Slit-edge penetration
1	0.0392	0.6	0.79	1.06
2	0.0409	0.6	0.91	1.05
3	0.0405	0.6	0.92	1.04

[7] M. S. Livingston and H. A. Bethe, Rev. Mod. Phys. 9, 272 (1937).
[8] John Teasdale, thesis, University of California, Los Angeles (1950).
[9] E. P. Gross, "Range, energy ionization curves," Palmer Physics Laboratory, Princeton University (1947).

VI. THE CROSS-SECTION CALCULATION

In order to obtain a formula for the cross section it is necessary to integrate over the scattering volume and over the area on the film within which protons were detected. Figure 5 gives the geometry, and Table II gives the values of the angles in randians. The result of an approximate integration is

$$N=12.168n_in_t(d\sigma/d\Omega)$$
$$\times[(b_0-h)\theta_1-(b_i-h)\theta_2-(b_0-c)\theta_3+(b_i-c)\theta_4].$$

In the formula N is the number of scattered protons, n_i is the number of protons incident during the run, n_t is the number of target nuclei per cubic centimeter,

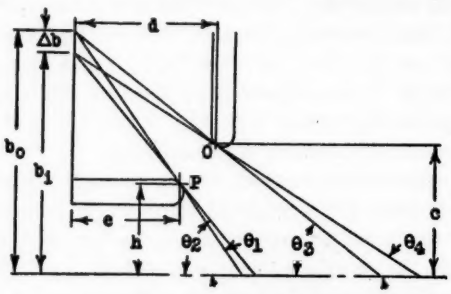

FIG. 5. Geometrical parameters. 0 and P are the average points of tangency.

$(d\sigma/d\Omega)$ is the differential cross section in the CM system, and the quantities in the brackets are geometrical parameters shown in Fig. 5. The finite area of the beam was considered in the integration, and it was found that the dependence on the beam radius was quite negligible for the geometry involved. For this reason the radius of the beam does not appear in the formula for the cross section. The constant is 12.168 instead of 4π because of the presence of the aluminum absorber for the background check. The absorber removed an area in the shape of a sector from the film region valid for counting.

A correction for the presence of low energy protons is made by introducing a quantity q on the right side of the cross-section formula; q is calculated from Fig. 4. The portion of the curve with abscissae greater than 0.18 g/cm² is divided into intervals of 0.01 g/cm². The energy corresponding to the mean range for each interval is obtained from the Princeton range-energy

TABLE IV. Probable errors contributing to the error in the cross section (percent).

Counting	0.97
Incident protons	0.4
Target nuclei	0.2
Geometry	0.3
Energy correction	0.1
Approximations	0.2

TABLE V. Calculated phase shifts and $f(E)$ values. $\bar{\theta}$ is the average angle used to compute the phase shifts.

Run No.	θ	Phase shfit	$f(E)$
1	41.3°	52°25′	21.0
2	41.5°	53°50′	20.3
3	41.5°	53°30′	20.5

curves,[9] and the differential cross section associated with each energy is computed from the usual S-wave formula using the phase shift given by Hatcher, Arfken, and Breit[10] for the Gauss error potential designated by $A'=51.44$ and $\alpha'=21.59$. The value of q is then computed from the formula

$$q=\frac{\sum_e n_e(d\sigma/d\Omega)_e}{(d\sigma/d\Omega)_m}.$$

Here n_e is the fractional number of particles which stopped in the interval e, $(d\sigma/d\Omega)_e$ is the corresponding cross section, and $(d\sigma/d\Omega)_m$ is the cross section for the energy associated with the mean range of the entire curve. $(d\sigma/d\Omega)_m$ is of course also computed using the phase shift for the error potential. The numerical value of q is found to be 1.006.

The number of scattered tracks N must be corrected for the number of protons which penetrated the slit edges. The correction is made by first using the N values from Table I to calculate a preliminary cross section. The cross section so calculated is then used to determine the number of tracks to be expected for the closed slit run. The difference between the number observed and the number calculated then represents the number assignable to slit-edge penetration. The correction amounts to 109 particles for the first run, 107 for the second, and 97 for the third.

Table III gives the corrected cross-section values for the three runs together with the percent by which the values were changed by the corrections which have been applied. All corrections reduced the value of the cross section. The probable error for the cross-section values is 1.2 percent based upon the probable errors in the quantities used for the calculation. The various probable errors are given in Table IV. The error for counting is larger than that given by Table I because the error from the slit-edge correction has been included.

VII. COMPARISON WITH THEORY

The phase shifts are calculated in the usual way from the observed cross section and the energy. In order to obtain some idea of the effect of the large angular range within which protons were scattered, two values of the phase shift are calculated for the first run. The value corresponding to a scattering angle of 45° in the laboratory system is found to be 52°20′. The smallest angle through which protons were scattered is 36°41′, and the phase shift calculated using this angle is 52°30′. As was indicated earlier, the poor angular definition is not serious. Since the result is nearly independent of the scattering angle used for the calculation, it is sufficient to calculate the phase shift from an average angle of scattering for each run. The values for each run together with the average scattering angles for which they were calculated are given in Table V. The probable error is one percent.

The function $f(E)$ as defined by Bethe[4] is calculated from the phase shift and the energy for each run, and the results are included in Table V. The probable error is 1.3 percent. The average value of $f(E)$ obtained from the experiment is plotted on the diagram taken from Bethe's paper, and the result is shown in Fig. 6. The average experimental value of 20.6 is to be compared with a value of 20.3 predicted by the line for 12.4 Mev. Although the small deviation may possibly indicate that the region of non-linearity has been reached, its magnitude should not be taken too seriously in view of the uncertainty in the present experiment and in the position of the line as extrapolated from the lower energy experiments. Bethe gives the accuracy of the line's slope as "five percent or better." The present point together with the one at 14.5 Mev does indicate that any deviation from linearity is small at energies of the order of 12 or 15 Mev and that the values of $f(E)$ for the other experiments above 6 Mev are apparently too high.

It should be noted that the discussion has proceeded under the assumption that the contribution from states other than the S-state is negligible at 12.4 Mev. Such a viewpoint appears entirely justified in the light of

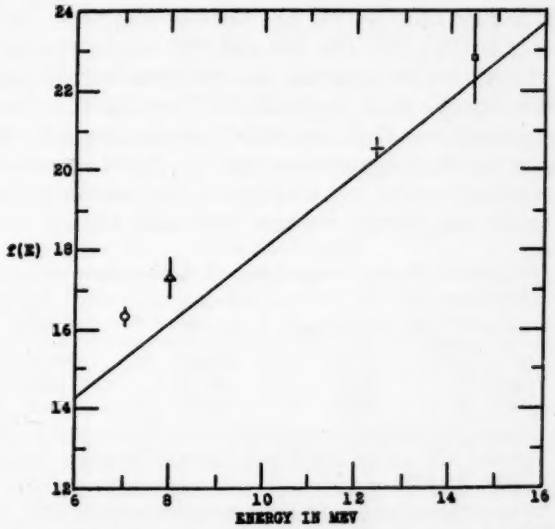

FIG. 6. Bethe's line with the new point added. ○ Dearnley, Oxley, and Perry; △ Wilson and Creutz; □ Wilson, Lofgren, Richardson, Wright and Shankland; · Present experiment.

[10] Hatcher, Arfken, and Breit, Phys. Rev. 75, 1389 (1949).

present information, particularly when it is considered that the scattering was in the neighborhood of 90° in the CM system.

The authors wish to express their gratitude to Professor J. R. Richardson for his suggestions and to thank Mr. S. Plunkett and Mr. G. Jones of the Cyclotron Laboratory and Mr. E. Griffiths and his staff in the Physics Department Shop for their aid in building and setting up the apparatus. The Eastman Kodak Company very kindly supplied the special film required.

PHYSICAL REVIEW VOLUME 79, NUMBER 4 AUGUST 15, 1950

New Radioactive Isotopes of Iridium*

T. C. Chu†
Radiation Laboratory and Department of Chemistry, University of California, Berkeley, California
(Received April 24, 1950)

Four new isotopes of iridium have been prepared by bombarding isotope-enriched rhenium as well as natural rhenium with alpha-particles, and osmium with deuterons. Three of them have been identified as follows:

Isotope	Half-life	Type of radiation	Energy of radiation (Mev) Particle	γ-rays	Produced by
Ir^{187}	11.8 hr.	$K\beta^+\epsilon^-\gamma$	β^+ 2.2 ϵ^- 0.28, 1.2	*L*, *K* x-rays 1.3	Re(α, 2*n*) Re^{185}(α, 2*n*) Os(*d*, 3*n*)
Ir^{188}	41.5 hr.	$K\beta^+\epsilon^-\gamma$	β^+ 2.0 ϵ^- 0.16, 0.85	*L*, *K* x-rays 1.8	Re(α, *n*), (α, 3*n*) Re^{187}(α, 3*n*) Os(*d*, 2*n*), (*d*, 3*n*)
Ir^{190}	3.2 hr.	$K(?)\beta^+\epsilon^-\gamma$	β^+ 1.7 ϵ^- 0.2, 0.8	—	Re(α, *n*) Re^{187}(α, *n*) Os(*d*, *n*), (*d*, 2*n*)

The 3.2-hr. period is an isomer of the 12.6-day Ir^{190}.
Another weak activity, possibly Ir^{189}, of more than 100-day half-life has been observed.
Four daughter activities of iridium (9.5-min., 6-hr., 35-hr. and *ca.* 50-day radio osmium) have been found, and their possible genetic relations discussed.
A rhenium activity of *ca.* 1-hr. half-life has been noticed in the Os+19-Mev deuteron experiment.

I. INTRODUCTION

THE previous work on this element, iridium, has resulted in the observation of a number of radioactive isotopes.[1] However, on the neutron deficient side of the stable isotopes only one period has been reported.[2] The isotope chart shows that the following mass numbers of Ir (186, 187, 188, 189 and 190) can be produced by (α, *n*), (α, 2*n*), and (α, 3*n*) reactions on rhenium, which has two stable isotopes, Re^{185} and Re^{187}, of relative abundance 37.07 and 62.93 percent respectively. Using the 60-in. cyclotron at the Crocker Laboratory, this attractive field was investigated. Enriched rhenium isotopes and spongy osmium were also used in confirmatory work concerning the reactions and the mass assignments of the products. (See Table I.)

TABLE I. Isotopic compositions of rhenium samples.

Isotope	Natural rhenium	"Re 185"*	"Re 187"*
	percent	percent	percent
185	37.07	85.38	1.78
187	62.93	14.62	98.22

* Obtained from Carbide and Carbon Company, Chemistry Division, Oak Ridge, Tennessee.

II. EXPERIMENTAL

Bombardments of rhenium with 38-Mev helium ions and of osmium with 19-Mev deuterons were made in the 60-in. cyclotron. Metallic rhenium powder (100 mg) was mounted on a copper target plate and covered with 0.2-mil tantalum foil. In the case of osmium, samples of the spongy metal were bombarded on a water-cooled platinum interceptor, also using 0.2-mil Ta foil to protect the powder. Experiments with low energy α-particles were made by placing a suitable thickness of Ta foil over the target to act as an absorber. (Calculated from the range-energy chart for α's drawn from the data of Aron, Hoffman and Williams.)

After bombardment, the rhenium target was dissolved in dilute nitric acid, and the osmium in aqua regia, in an all-glass distilling flask. Chemical separations were made after the addition of the proper inactive carriers. Osmium was separated by distillation of the volatile tetroxide followed by precipitation of the sulfide with sodium thiosulfate. The mother liquor was evaporated to dryness and then taken up with water. Iridium was reduced to the metal by formic acid in hot solution. After removal of these elements, rhenium was

* This work was performed under the auspices of the AEC.
† On leave from Institute of Chemistry, Academia Sinica, China.
[1] G. T. Seaborg and I. Perlman, Rev. Mod. Phys. **20**, 585 (1948).
[2] L. J. Goodman and M. L. Pool, Phys. Rev. **70**, 112 (1946); **71**, 288 (1947).

finally precipitated as the sulfide with sodium thiosulfate.

"End on" type argon-ethanol filled Geiger counters with approximately 3 mg/cm² mica windows were used throughout the experiment. Coincidence and geometrical corrections have been applied to all the counts. Variations in counter efficiency were checked by a UX_2 standard. A beta-ray spectrometer of low resolving power was used to differentiate the positrons and the beta-particles.

Radiation characteristics were studied by using beryllium, aluminum and lead absorbers. Electron and soft electromagnetic radiations were distinguished by their differential absorption in aluminum and beryllium.[3] The average energy of L x-rays in this region is of the order of 9 kev with an absorption half-thickness in beryllium of 700 mg/cm². For the lead absorption, lead screens were used with beryllium absorbers, placed below and above the lead, of sufficient thickness to remove all the electrons from the sample and the secondary electrons emitted from the lead, respectively.

The ratios of electrons and the electromagnetic radiations were determined with due corrections for counter window and air gap absorptions of electrons as well as for counting efficiencies of quantum radiations. Thus, for the L x-rays a counting efficiency of 5 percent was assumed, for γ-rays from 20 kev to less than 500 kev, 0.5 percent, from 500 kev to 1 Mev, one percent, etc. Cross sections were calculated for thin samples. The total beam current to the target was integrated by the cyclotron instruments. In these calculations the relative values should be more correct than the absolute values.

III. RESULTS

Four half-lives, 3.2±0.2 hr., 11.8±0.3 hr., 41.5±0.5 hr. and 12.6±0.3 day were observed in the iridium fraction separated from rhenium bombarded with 30-Mev helium ions. The first three isotopes emitted positive electrons (Fig. 1). A 19-Mev deuteron bombardment on osmium gave the above-mentioned activities and the well-known 75-day Ir^{192} as the major product.

One additional weak period of more than 100 days was observed in the iridium fraction from rhenium bombarded with approximately 40-Mev α-particles in the 184-in. cyclotron, but it was not studied in detail.

The relative yields of the activities obtained by varying the energy of the impinging alpha-particles are shown in Table II and Fig. 2.

11.8-Hr. Ir^{187}

In Fig. 2 it is seen that the yield of this activity increases with increasing alpha-energy in the bombardment of natural rhenium. From this and the results of the experiments with enriched rhenium isotopes, this period was assigned to Ir^{187} with confidence. The increasing trend of the yield curve might be explained by assuming the possible contribution of an $(\alpha, 4n)$ reaction in the 38- to 40-Mev alpha-range, where it is usually acknowledged that the $(\alpha, 3n)$ reaction should play the principal role.

From gross and differential decay its half-life was found to be 11.8±0.3 hr. Magnetic counter readings both from Re+α and Os+d sources indicated the presence of positrons (Fig. 1).

A satisfactory characterization of the radiations by absorption measurements was not obtained, since its measured activity was too close to that of the 41.5-hr. period. However, a group of harder electrons with a maximum energy of 1.2 Mev and a softer group of 0.28 Mev were found both from absorption measurements and from beta-ray spectrometer readings of the iridium

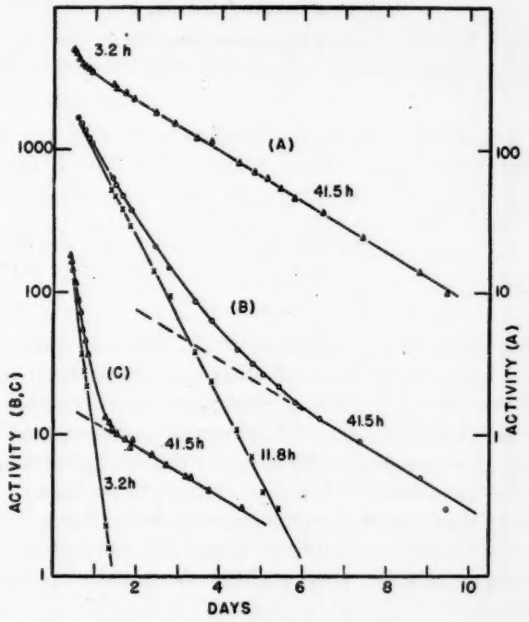

FIG. 1. Decay of positrons of radioactive iridium. (A) 41.5-hr. Ir^{188} from enriched "Re 187"+32-Mev α-particles. (B) 11.8-hr. Ir^{187} and 41.5-hr. Ir^{188} from "Re 185"+32-Mev α. (C) 3.2-hr. Ir^{190} and 41.5-hr. Ir^{188} from "Re 187"+22-Mev α.

TABLE II. Relative yields of the radioiridium at various α-energies.

Sample	Impinging α-energy	3.2 hr.	11.8 hr.	41.5 hr.	12.6 day
Natural Rhenium	21 Mev	14.8	5.9	36.2	43.0
	25	9.0	27.0	22.8	41.3
	~30	11.0	27.9	25.2	35.9
	38	3.0	38.2	42.5	16.2
	~40	2.5	41.5	43.7	12.2
Enriched "Re 187"	22 Mev	9.8	3.1	25.8	61.2
	32	2.2	—	78.7	19.0
"Re 185"	32 Mev	—	84.4	13.7	1.8

[3] G. Wilkinson, Phys. Rev. **75**, 1019 (1949).

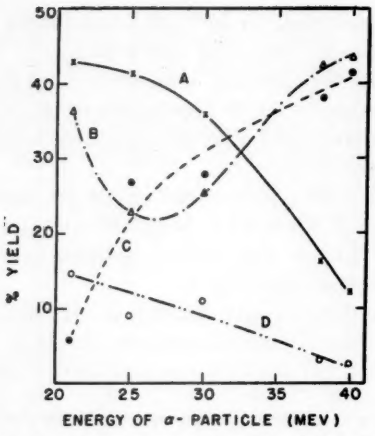

FIG. 2. Relative yields of the radioactive iridium from Re+α particles. (A) 12.6-day Ir^{190}. (B) 41.5-hr. Ir^{188}. (C) 11.8-hr. Ir^{187}. (D) 3.2-hr. Ir^{190}.

fraction isolated from the bombardments of the enriched Re^{185} target (Figs. 3 and 4(I)). The beta-ray spectrometer record was taken at an early stage when this activity was present predominantly. It shows that the positrons (curve A) had a maximum energy of 2.2 Mev and a mean energy of approximately 0.7 Mev. Since the β^+/electron capture branching ratio is small, their maximum energy was not determined by aluminum absorption. Any such contribution from β^+ would be buried in the strong electromagnetic background, which showed components with half-thicknesses in lead of 150 mg/cm², corresponding to 63 kev, and 12.5 g/cm², approximately 1.3 Mev. The former corresponds well with the osmium K x-rays. The L x-rays of half-thickness 24 mg/cm² aluminum, corresponded to about 9 kev.

An approximate ratio of positive and negative electrons and electromagnetic radiations was obtained from absorption measurements, the usual corrections for counter window, counting efficiencies, etc., being considered.

0.28 Mev e_1	1.2 Mev e_2	2.2 Mev β^+	L x-rays	K x-rays	1.3 Mev γ=
0.22	0.025	0.002	0.62	1	0.75

The ratio of L x-radiation to K x-rays is comparatively higher than those of other periods studied; this, and also the high yield of electrons seemed to suggest the possibility of some L electron captures, and of course, the possibility of a γ-ray of this energy accounting for the excess of L x-rays cannot be excluded. Assuming that one K x-ray represents one disintegration by orbital electron capture, about 0.2 percent of the disintegrations of this activity occurs by positron emission.

41.5-Hr. Ir^{188}

This isotope was produced both from α-bombardment on rhenium and from deuteron bombardment on osmium. A study of its yield from natural rhenium targets justifies postulating its formation by an (α, n) reaction on Re^{185} and an $(\alpha, 3n)$ reaction on Re^{187}.

Gross and differential decay measurements give 41.5 hr. as its half-life. The aluminum absorption curve (Fig. 5) which has been corrected for the contributions of the 12.6-day Ir^{190} and the 41.5-hr. L x-rays, 9 kev, shows at least three components. A hard one has an end point at 300 mg/cm² corresponding to a maximum energy of 0.85 Mev according to Feather's formula, a soft one has a range of 25 mg/cm² or an energy of 0.16 Mev, and a still harder particle of an approximate range of 900 mg/cm², approximately 2 Mev.

Beta-ray spectrometric examination showed also the existence of positrons. The momentum distribution curve (Fig. 4(II)) shows the end point corresponding to 2 Mev and a mean energy of approximately 0.5 Mev. Curve B of Fig. 4(II) stands for the negative electron distribution, with end point of the harder group corresponding to a maximum energy of 0.85 Mev and an average of 0.3 Mev, and the lower energy peak corresponded to 0.16 Mev for its softer group. All check very well with the aluminum absorption measurements.

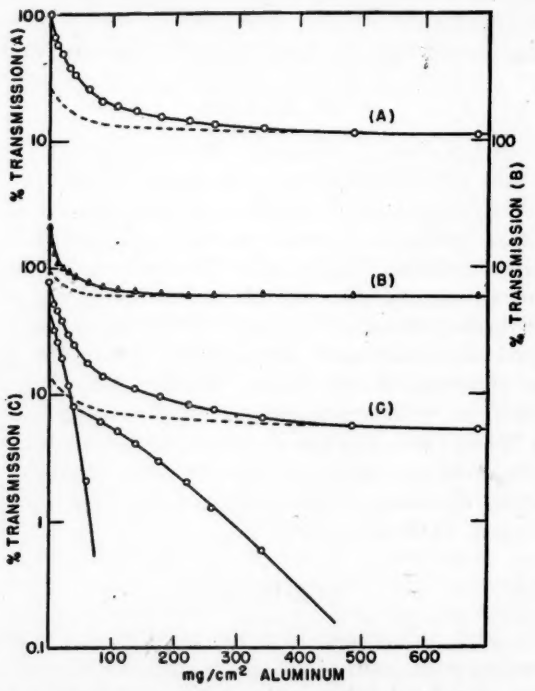

FIG. 3. Aluminum absorption of 11.8-hr. Ir^{187} and 41.5-hr. Ir^{188} from "Re 185"+α. (A) Measured curve for mixed activities. (B) Contribution of the 41.5-hr. activity at the time when (A) was taken. (C) Resolved absorption of 11.8-hr. Ir^{187}.

The soft part probably represents a single conversion electron, while the broader one may be a mixture of several conversion electrons.

In Fig. 5 is also shown the lead absorption of the electromagnetic radiations. The soft component has a half-thickness of 145 mg/cm² corresponding to 62 kev, which is quite an acceptable value for osmium K x-rays. The gamma-ray has a half-thickness of 15 g/cm² corresponding to 1.8 Mev.

The ratios of the various radiations were obtained from aluminum and lead absorption measurements as follows:

0.16 Mev e_1	0.85 Mev e_2	2 Mev β^+	L x-rays	K x-rays	1.8 Mev γ=
0.08	0.007	0.003	0.21	1	0.55

Assuming that some of the K x-rays arise from production of the conversion electrons, then from the above ratio, approximately 90 percent of the K x-rays must arise from orbital electron capture, and hence it is assumed that 0.90 K x-ray represents one disintegration. The branching ratio for the positron disintegration is approximately 0.3 percent.

3.2-Hr. Ir^{190}

In the course of this work the 3.2±0.2 hr. positron emitter was always found in small quantities both in the Re+α and Os+d reactions. The possibility of its being an impurity received first attention. Spectroscopic analysis of one of the natural rhenium samples showed only a trace of silicon present (0.01 to 0.1 percent), and any other impurities would not exceed this amount. Chemical separation proved it to be an iridium activity, and in several later experiments including those with enriched Re^{187}, it was present in amount greater than 10 percent of the total iridium activity.

From the results of the magnetic counter measurements (Fig. 4(III)), the positive electron has a maximum energy of 1.7 Mev and a mean value of approximately 0.6 Mev. The spectrum of the negative electron is complex and consists of at least two groups. A line of conversion electron appeared at $H\rho$=1570 gauss-cm corresponding to 0.2 Mev. The harder group has a maximum energy of 0.8 Mev and a mean value of 0.25 Mev. On account of the relatively strong intensities of both the 11.8-hr. and 41.5-hr. isotopes which occurred with this activity, the aluminum absorption curve (Fig. 6) is not resolved, but suggests that the mixed positive and negative electrons have a maximum range of energy of 1.8 Mev and a softer group of approximately 0.2 Mev. Even more trouble was encountered with the γ's.

Of these three positron emitting activities of iridium, this one must have the largest β^+ to electron capture branching ratio.

12.6-Day Ir^{190}

Goodman and Pool[2] have already assigned to Ir^{190} a 10.7-day activity obtained from deuteron bombardment of Os and from an (n, $2n$) reaction on Ir. In this experiment it was also produced by an (α, n) reaction on Re. Enriched Re^{187} produced more than 10 times the amount of this activity as the enriched Re^{185} when both were subjected to 32-Mev α-bombardment. The assignment of this period to Ir^{190} is therefore well-confirmed. The best value for its half-life, followed through nine half-lives, is 12.6±0.3 days.

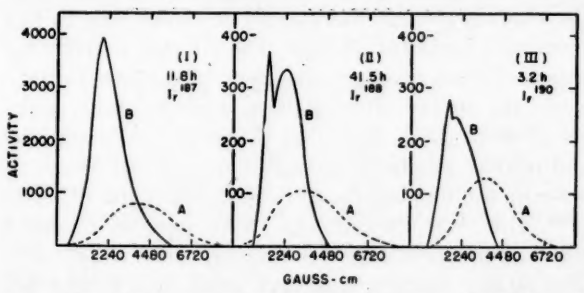

FIG. 4. The beta-spectra of the iridium isotopes. (A) Positrons. (B) Electrons. (I) 11.8-hr. Ir^{187}; (II) 41.5-hr. Ir^{188}; (III) 3.2-hr. Ir^{190}.

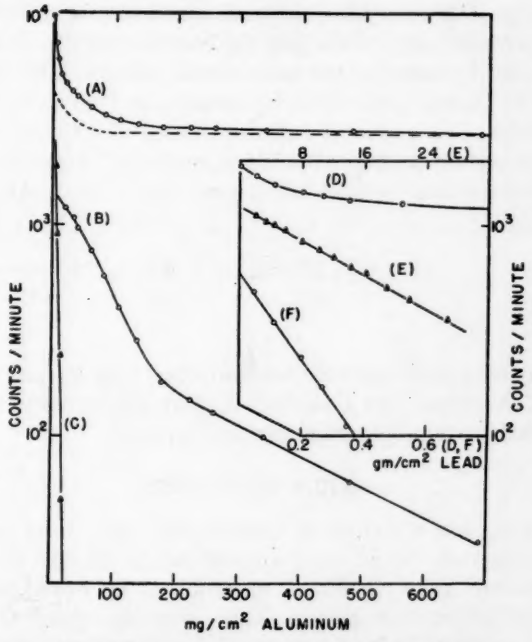

FIG. 5. Absorption curves for 41.5-hr. Ir^{188}. (A) Measured curve in aluminum, with L x-ray, K x-ray, and γ-ray background. (B) Positrons and hard electrons. (C) Soft electrons. (D) and (E) The first and second halves of the measured curve in lead, drawn in different scale, showing hard γ-ray of 15 gm/cm² half-thickness. (F) K x-ray, half-thickness 145 mg/cm².

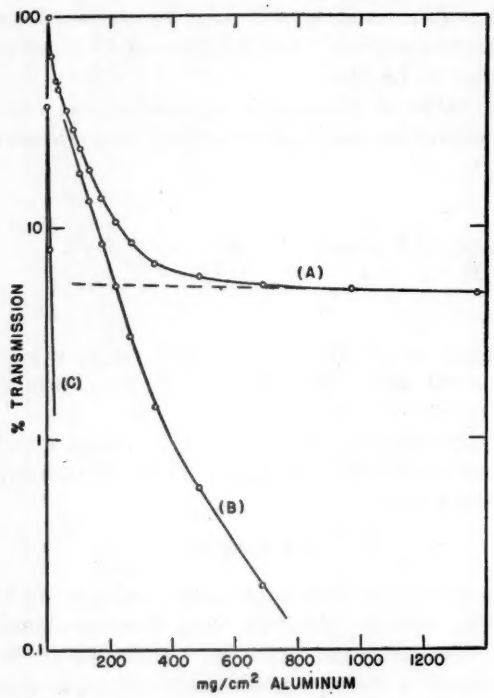

FIG. 6. Aluminum absorption of 3.2-hr. Ir^{190} and 41.5-hr. Ir^{188}. (A) Measured at 2 hr. after bombardment. (B) Positrons and hard electrons. (C) Soft electrons.

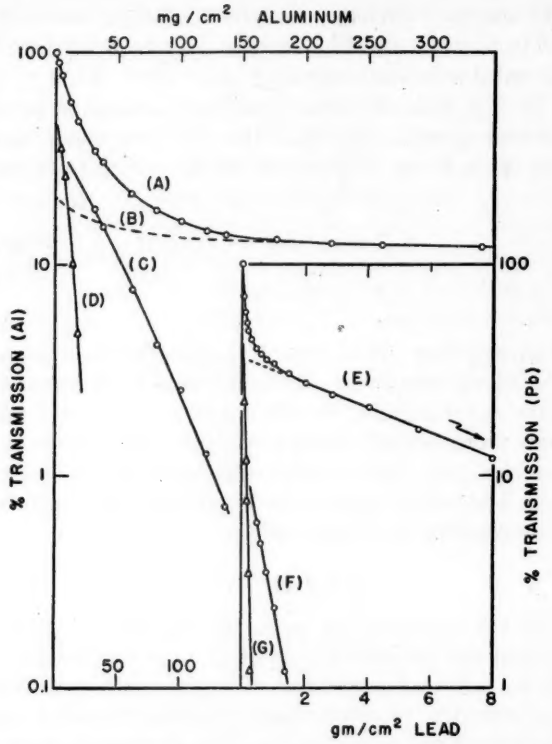

FIG. 7. Absorption curves of 12.6-day Ir^{190}. (A) Aluminum absorption curve. (B) L x-ray. (C) Hard electrons. (D) Soft electrons. (E) Lead absorption curve and the hard γ-ray. (F) Soft γ-ray. (G) K x-ray.

The aluminum absorption curve in Fig. 7, shows for the soft and hard groups of electrons, after correction for L x-rays, energies of 0.17 Mev and 0.5 Mev respectively. The absorption curve obtained from the Os+d experiment, after deducting the contributions from the 75-day Ir, revealed the same characteristics. This is a little different from what Goodman and Pool have observed. The γ-rays of half-thicknesses of 400 mg/cm² lead, corresponding to 0.17 Mev, and of 5.2 g/cm² lead, corresponding to 0.55 Mev, were clearly disclosed by lead absorbers (Fig. 7). The K x-rays were not definitely observed, the radiation resolved from soft and hard γ-quanta showing a half-thickness of only 80 mg/cm² lead. A stronger sample would probably give better results.

However, an estimate of the approximate ratios of radiations, with proper allowances for various assumptions, was made as follows:

0.17 Mev e_1	0.5 Mev e_2	L x-rays	K x-rays	0.17 Mev γ_1	0.55 Mev γ_2
0.07	0.04	0.15	1	0.45	0.42

Assuming that K x-radiation also arises from the process of conversion, then about 0.85 K x-ray will represent one disintegration by orbital electron capture.

OSMIUM DAUGHTERS

Four low activities of osmium, 9.5 min., 6 hr., approximately 35 hr. and approximately 50 day, were obtained from "milking" experiments on mixed artificial radioactive iridium. They were also observed in the osmium fraction separated directly from rhenium targets. In some instances the well-known 95-day osmium was found to be present in the direct separations.

The 9.5-min. period was present in every direct separation, but appeared only in the early milkings. In one sample from an Os+deuteron bombardment, the milking process was carried out from time to time covering a period of 35 days. The 9.5-min. activity disappeared after one day, the 35-hr. disappeared after a week, the 50-day after 17 days, while the 6-hr. period lasted throughout. Based on the interval of separation and relative number of atoms of growth and decay, the 9.5-min. osmium was found to be the daughter of 3.2-hr. Ir^{190}. The 35-hr. Os and 6-hr. Os are possibly related to the 11.8-hr. Ir^{187} and the 12.6-day Ir^{190} respectively. The 50-day osmium was very weak, but it was definitely distinguishable from the 95-day Os. In the first place, the Ir activities used for milking were reduced

after the mother liquor had been evaporated to dryness, expelling osmium activity which might remain in the mother liquor. Secondly, the gross decay curve of one of the direct separations has revealed the co-existence of the approximately 50-day and the 95-day periods.

The radiations of these activities have not been successfully studied. For the 9.5-min. period, the aluminum absorption curve give a maximum energy of 0.5 Mev, indicating the mixed energy of soft electromagnetic radiation and electrons (factor of decay being corrected) (Fig. 8). An aluminum absorption curve for the 6-hr. Os is also shown in Fig. 8.

No positrons were detected from one comparatively strong sample of these osmium activities.

OTHER ACTIVITIES

(1) 75-Day Ir^{192}

In the bombardment of osmium with deuterons there was a very good yield of the well-known Ir^{192}. The best value for its half-life is 74.7 days. The electron range in aluminum has a maximum value of 0.68 Mev according to Feather's method, and the gamma-energy from lead absorption is 0.42 Mev.

(2) 95-Day Os^{185}

The irradiation of rhenium with deuterons led to the production of the 95-day Os. It was also observed in minute quantities in the rhenium+α, and osmium+d bombardments. Its radiation characteristics were found to agree with those given by Katzin and Pobereskin.[4]

(3) 16-Day Os^{191}; 30.6-Hr. Os^{193}

These isotopes were observed as the products of (d, p) reactions on osmium. The best half-life for Os^{191}, after subtracting the contributions from the long-lived 95-day isotope is 16.0±0.3 days, and that for Os^{193} is 30.6±0.4 hr. The absorption curve of the 16-day Os with correction for L x-rays, showed a weak conversion electron of 0.15 Mev in aluminum, and the gamma in lead corresponded to 0.14 Mev. These data are consistent with Katzin and Pobereskin's[4] and Saxon's[5] measurements. The aluminum absorption curve of the 30.6-hr β-emitter showed an end point of 440 mg/cm² corresponding to 1.15 Mev as was found by Mandeville *et al.*[6]

(4) 90-Hr. Re^{186}; 17-Hr. Re^{188}

These well-established isotopes were formed by (d, p) reactions on rhenium in proportion very close to the natural abundance ratio of Re^{185} and Re^{187}. The β-particles of Re^{186} showed a range in aluminum corresponding to 0.96 Mev, and that of Re^{188} corresponded to 2.2 Mev.

They were also observed in the Re fraction from Re+α-bombardment, especially when the α-energy was below the threshold of (α, n) reaction. This is another instance of the large neutron cross section of rhenium.[7]

(5) 1-Hr. Re

In the experiment with Os+d (19 Mev), an activity of approximately 1-hr. half-life was noticed in the rhenium fraction. If it is not due to an impurity, it may probably be the product of a (d, α) reaction.

IV. DISCUSSION

From the curves of relative yields shown in Fig. 2, it seems quite probable to assign the 41.5-hr. period to Ir^{188}, the 11.8-hr. period either to Ir^{187} or to Ir^{189}, and the 3.2-hr. period as an isomer of the 12.6-day Ir^{190}.

The assignment of the 41.5 hr. to Ir^{188} was rather obvious considering its yield from natural rhenium which has two stable isotopes, 185 and 187, of relative abundance 37.07 and 62.93 percent, respectively. The predominance at lower energy α-bombardments of the (α, n) reaction on the 185 isotope, and at higher energies of the $(\alpha, 3n)$ reaction on the 187 isotope affords a ready explanation of the shape of the yield curve. Further evidence was obtained from experiment with enriched rhenium isotopes. In Table II, it is seen that a very much greater yield of this activity was obtained from "Re 187," which was subjected under the same

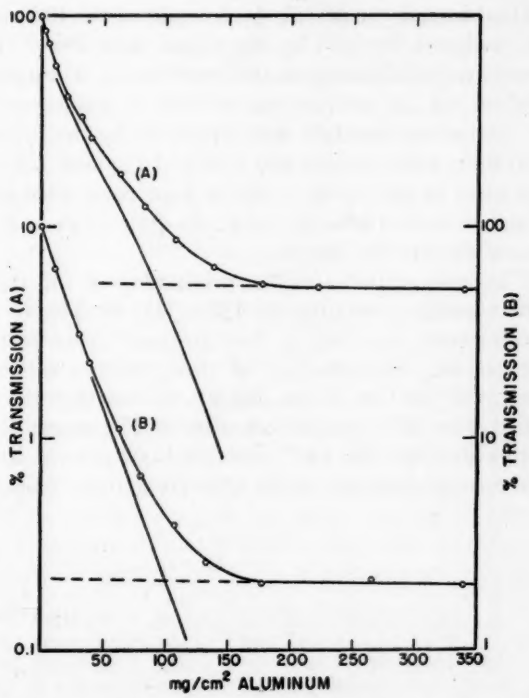

FIG. 8. Aluminum absorption curves for the 9.5-min. Os (A), and 6-hr. Os (B).

[4] L. I. Katzin and M. Pobereskin, Phys. Rev. **74**, 264 (1948).
[5] D. Saxon, Phys. Rev. **74**, 1264 (1948).
[6] Mandeville, Scherb, and Keighton, Phys. Rev. **74**, 888 (1948).
[7] Cork, Shreffler, and Fowler, Phys. Rev. **74**, 1657 (1948).

TABLE III. Cross sections in barns for α-particle reactions on enriched Re.

Sample	α-energy (Mev)	11.8-hr. Ir^{187}	41.5-hr. Ir^{188}	3.2-hr. Ir^{190}	12.6-day Ir^{190}
"Re 187"	22	0.009	0.13	0.01	0.24
"Re 187"	32	—	0.81	0.006	0.15
"Re 185"	32	1.2	0.21	—	0.022

experimental condition as "Re 185" (both being kept side by side at the center of the 32-Mev α-beam). Since an $(\alpha, 3n)$ reaction should predominate over (α, n) at 32 Mev, the above assignment is confirmed.

The allocation of the 11.8-hr. activity to Ir^{187} was strongly suggested by the joint bombardment of the enriched rhenium isotopes. With 32 Mev α's the "Re 185," which has been enriched to 85.38 percent Re^{185} (Table I), gave a corresponding ratio of yield of the 11.8-hr. Ir activity (84.4 percent), and none of this activity was obtained from the "Re 187" (98.22 percent Re^{187}) target. Additional support was obtained from the 19-Mev deuteron bombardment on osmium; wherein (d, n), $(d, 2n)$, and $(d, 3n)$ all were possible reactions. The relative yield of the 11.8-hr. Ir was about half as much as that of the 41.5-hr. Ir, which agreed with the ratio of the sum of the relative abundances of Os^{186} 1.59 percent+Os^{187} 1.64 percent+Os^{188} 13.3 percent (total 16.53 percent available for Ir^{187}) and that of Os^{187} 1.64 percent+Os^{188} 13.3 percent+Os^{189} 16.1 percent (31.04 percent available for Ir^{188}).

The 12.6-day period has been reported (as 10.7 day) and assigned to Ir^{190} by Goodman and Pool.[2] The present work substantiates their conclusion. The assignment of the 3.2-hr. positron emitter as an isomer of Ir^{190} rather than to Ir^{188} was supported by the ratio of yield both from natural and enriched rhenium targets. The yield of the 3.2-hr. activity kept reasonable pace with that of the 12.6-day, but it was quite different from that of the 41.5-hr. period.

The cross sections for the production of the radioactive isotopes are given in Table III. In spite of the uncertainties involved in the absolute cross section calculations, the reliability of their relative values is worthy of mention. From Table I we see that the enriched "Re 187" sample contains 98.22 percent Re^{187} isotope and the "Re 185" contains 14.62 percent Re^{187}. The rate of formation of the 12.6-day activity from the two enriched rhenium samples, $\sigma(Re^{187})/\sigma(Re^{185}) = 0.15/0.022 = 6.8$, corresponds very well to the ratio of the Re^{187} percentage compositions, $98.22/14.62 = 6.7$. Meanwhile by considering the relative cross sections of the production of the 3.2-hr. and 12.6-day activities from 22-Mev α- and 32-Mev α-bombardments, the ratio of the two members of Ir^{190} isomer may be estimated as about 1:20.

We should expect Ir^{186} and Ir^{189} to appear in this experiment as results of $(\alpha, 2n)$ and $(\alpha, 3n)$ reactions on Re. But since no other activity was apparent from 21-Mev α- up to 38-Mev α-bombardments (from 1 μah to 15 μah), we must presume that their half-lives are long or fairly short. In the latter case any radioactivity with a half-life less than 5 min. would have been difficult to observe, since there was necessarily a delay of $\frac{3}{4}$ hr. to one hr. between the end of bombardment and the first count. Whether the above-mentioned weak period of more than 100 days can be assigned to either of these, will require further study, but it could feasibly be Ir^{189}, which can be expected to have a comparatively long half-life.

The relative yields of osmium activities, found growing in the iridium fraction, and also found in the osmium fraction from Re+α-bombardment, were very small. They were probably formed as daughters of the Ir activities. The initial samples were all very weak, one could only relate the 9.5-min. Os to the 3.2-hr. Ir with certainty. The results of milking experiments suggested, in addition, a possible relationship between the 6-hr. Os and the 12.6-day Ir, and between the 35-hr. Os and the 11.8-hr. Ir. Since osmium isotopes of masses 186 through 190 exist in nature, any radioactivity due to them must be associated with the existence of excited states of the stable isotopes.

The author takes pleasure in expressing his gratitude to Professors G. T. Seaborg and W. M. Latimer for the opportunity of working at the Radiation Laboratory and the Department of Chemistry of the University of California. Special acknowledgment is made to Professor G. T. Seaborg who suggested the problem and offered many helpful suggestions and to Dr. E. K. Hyde, Dr. B. Jones, Dr. G. Wilkinson and other members of the laboratory for valuable discussions and assistance. He is also very grateful to Mr. T. M. Putnam, Jr., Mr. G. B. Rossi, Mr. J. T. Vale, and the crew members of the 60-inch and the 184-inch cyclotrons for their cooperation and assistance in making bombardments.

Non-Equilibrium Phenomena in a Bose-Einstein Gas. Part II. Heat Transfer*

WILLIAM BAND
Department of Physics, State College of Washington, Pullman, Washington
(Received December 19, 1949)

The model Bose-Einstein gas introduced in Part I is shown to yield superconductivity for heat transfer. The temperature dependence and order of magnitude of the thermal conductivity are shown to be the same as in liquid helium below the lambda-point.

I. INTRODUCTION

PART I of this paper[1] discussed the two basic modes of wave propagation in a quasi-ideal Bose-Einstein gas in which it was assumed that the relaxation time, τ, for readjustment of equilibrium in the numerical distribution of atoms among the lowest energy and the higher energy states was very long compared with the relaxation time for asymmetrical perturbations of the velocity distribution within any one energy state.

Such a gas might be described as a binary mixture of two semiphases, the low energy semiphase and the high energy semiphase. The two basic modes of wave propagation roughly correspond, respectively, (a) to density waves and (b) to waves of concentration of one semiphase in the mixture. Both modes of propagation can exist only at frequencies large compared with $1/\tau$, while at lower frequencies than this both variations can propagate only by diffusion, below the lambda-temperature.

This general situation, with regard to concentration waves, is essentially the same as that found in liquid helium below the lambda-temperature, where heat waves of sufficiently high frequency can propagate without appreciable attenuation as second sound. In both the Bose-Einstein gas and liquid helium the essential characteristic of the second mode of wave propagation is a disturbance of the relative numerical equilibrium between the populations of the two semiphases. Relaxation of this disturbance causes attenuation of second sound in both cases simply because such relaxation consists of population readjustments that must exchange momentum between the semiphases due to their relative motion, simulating mutual friction.

Meyer and Band first suggested[2,3] in 1947 that second sound in He II involves a lack of thermal equilibrium between the two semiphases: transitions from one semiphase to the other must take place within a certain time of relaxation to adjust populations as well as energy content to a new thermal equilibrium. Both in second sound and in a heat current the two semiphases move in opposite directions. Transitions, therefore, cause exchange of momentum; i.e., dissipation of momentum.[4–6] A steady heat current was, therefore, regarded as damped second sound. The times of relaxation derived from steady heat flow experiments on this theory are identical with those derived from the measured attenuation of second sound within the accuracy of available data.

Gorter and Mellink[7] later presented a theory of heat conduction in He II using a hypothetical mutual friction between the two component fluids (here called semiphases), but in which no account is taken of the non-equilibrium conditions existing. The momentum dissipation derived in reference 4 is formally identical with Gorter's "friction" only for the special case of zero frequency and no net mass flow;[8] but otherwise the theories are not equivalent.

In the present picture it is not the relative motion between the two semiphases that calls the momentum exchange into being, as would be the case if a true friction existed. Momentum exchange occurs only when the relative motion of the two fluids is such as to carry each of them into a situation where thermal equilibrium would demand a different population distribution: for example, steady motion down a temperature gradient. It is only this type of transition which can produce momentum exchange. Steady flow under isothermal conditions is in fact characterized by superfluidity of the low energy semiphase: there is no departure from equilibrium, no transitions are needed and therefore no momentum exchange occurs. Mutual friction as such does not in fact exist, and the term is liable to be misleading.

In the present paper the heat transfer in the Bose-Einstein model due to propagation of concentration oscillations is discussed, and it becomes apparent that, except just at T_λ and at 0°K both basic modes of wave propagation transfer heat with their respective phase velocities. This is because both modes include a proportion of concentration variations. When the frequency is reduced sufficiently below $1/\tau$ the wave equations both

* This work was begun at the Institute for the Study of Metals, the University of Chicago. It was completed at the State College of Washington as part of project NR 010-603 with support from the ONR.

[1] W. Band, Phys. Rev. **76**, 558 (1949).
[2] L. Meyer and W. Band, Phys. Rev. **71**, 828 (1947).
[3] W. Band and L. Meyer, Phys. Rev. **73**, 229 (1948).
[4] W. Band and L. Meyer, Phys. Rev. **74**, 386 (1948).
[5] L. Meyer and W. Band, Phys. Rev. **74**, 394 (1948).
[6] W. Band and L. Meyer, Phys. Rev. **76**, 417 (1949).
[7] C. J. Gorter, Phys. Rev. **74**, 1544 (1948). C. J. Gorter and J. H. Mellink, Physica **15**, 285 (1949). C. J. Gorter, Physica **15**, 523 (1949).
[8] L. Meyer, Abstracts of Meeting on Low Temperatures, M.I.T. Reports (September, 1949).

degenerate into diffusion equations. The density oscillations become a diffusion of mass down a density gradient, corresponding to the well-known fact that an ideal Bose-Einstein gas loses its bulk elasticity below the lambda-point. The present model would reduce to the ideal gas if τ were put zero. Provided τ is not zero, however, there exists a least frequency only below which ordinary sound fails to propagate. This minimum frequency increases from zero at T_λ to a maximum somewhat greater than $1/\tau$ and drops back toward zero again as T approaches 0°K. The model transmits ordinary audiofrequency sound waves, but static measurements of compressibility would yield zero bulk

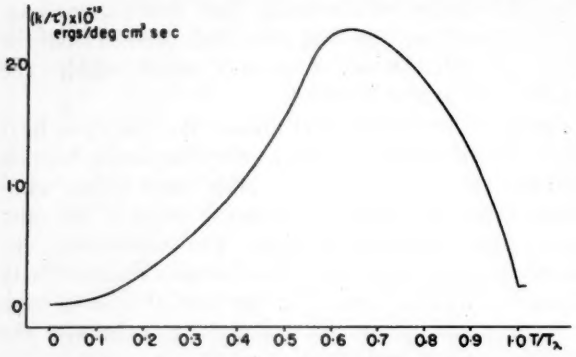

FIG. 1. Thermal conductivity as a function of temperature.

modulus, and there is strong dispersion of sound at very low frequencies.

Thermal conductivity as determined by thermal diffusion is proportional to the population relaxation time. The ratio of conductivity to relaxation time is calculated and found to have a similar form, as function of temperature, to the conductivity of He II: starting from a low value at T_λ it rises rather sharply to a maximum at about $T=0.65T_\lambda$ and drops again toward zero with a simple power law as T approaches zero. (See Fig. 1.) If the gas is arbitrarily given a density that sets the lambda-temperature at 2°K, the mass of the atom being equated to that of the helium atom, and the relaxation time assumed to be 2×10^{-3} sec. as found for liquid He II, the peak thermal current is identical with that found in He II under a temperature gradient of about 0.001° per cm. The cube root law dependence of the thermal current on temperature gradient observed in He II[9] does not follow for this Bose-Einstein model without special assumptions about the dependence of τ on thermal current.

II. THE WAVE EQUATIONS WITH ATTENUATION

Adopting the same notation as was used in reference 1, the displacement of the mass center of the mixture is $\mathbf{Y}$ and the displacement of the high energy semiphase relative to the mass center is proportional to $\mathbf{Z}$. The normal coordinates that diagonalize the Lagrangian are

$$\left.\begin{aligned}\mathbf{Y}^*&=\mathbf{Y}\cos\theta+\mathbf{Z}\sin\theta\\ \mathbf{Z}^*&=\mathbf{Z}\cos\theta-\mathbf{Y}\sin\theta\end{aligned}\right\}, \tag{1}$$

where θ is a given function of T [reference 1, Eqs. (3.20) and (3.18)]. The wave equations for the two basic modes of vibration, neglecting all damping terms, are

$$\left.\begin{aligned}V_1^2\nabla^2\mathbf{Y}^*&=\partial^2\mathbf{Y}^*/\partial t^2\\ V_2^2\nabla^2\mathbf{Z}^*&=\partial^2\mathbf{Z}^*/\partial t^2\end{aligned}\right\}, \tag{2}$$

where V_1 and V_2 are given functions of T [reference 1, Eqs. (4.1), (4.2), and (4.4)].

Under conditions in which viscous forces on the walls of the enclosure can be completely neglected, the only appreciable damping is due to momentum exchanges between the two semiphases occuring during their relative motion due to transitions tending to restore the population equilibrium. The momentum corresponding to the coordinate $\mathbf{Z}$ is $\dot{\mathbf{Z}}$, and the rate of exchange of this is $\dot{\mathbf{Z}}/\tau$. Changing to normal coordinates this yields

$$\dot{\mathbf{Z}}/\tau=\dot{\mathbf{Z}}^*(\cos\theta)/\tau+\dot{\mathbf{Y}}^*(\sin\theta)/\tau, \tag{3}$$

so that the wave equations may be written as

$$\left.\begin{aligned}V_1^2\nabla^2\mathbf{Y}^*&=\partial^2\mathbf{Y}^*/\partial t^2+(\partial\mathbf{Y}^*/\partial t)(\sin\theta)/\tau\\ V_2^2\nabla^2\mathbf{Z}^*&=\partial^2\mathbf{Z}^*/\partial t^2+(\partial\mathbf{Z}^*/\partial t)(\cos\theta)/\tau\end{aligned}\right\}. \tag{4}$$

From (1) it is apparent that the first mode carries heat (concentration of high energy phase) proportional to $\sin\theta$, while the second mode carries heat proportional to $\cos\theta$, each with its respective phase velocity. Writing $\Delta\rho_n$ for the amplitude of the variations of the concentration of the high energy semiphase, the total heat transported by the two modes of propagation into which these variations will divide is then equal to

$$\epsilon(\Delta\rho_n\cos\theta V_2+\Delta\rho_n\sin\theta V_1) \tag{5}$$

where ϵ is the mean energy density of the high energy semiphase.

The density waves transmitted in first sound suffer attenuation and dispersion for all frequencies less than

$$\nu_1=\sin\theta/2\pi\tau. \tag{6}$$

Density waves are also transmitted in second sound proportional to $\sin\theta$ and suffer attenuation and dispersion for all frequencies less than

$$\nu_2=\cos\theta/2\pi\tau. \tag{7}$$

If it is supposed that $\tau=2\times10^{-3}$ sec., as is required to make the model agree as closely as possible with liquid helium in its thermal conductivity, the frequencies ν_1 and ν_2 have values ranging between zero and about 80 cycles per sec. Their dependence on temperature, supposing that τ does not vary (which of course is entirely

[9] Keesom, Saris, and Meyer, Physica 7, 817 (1940).

unlikely!), would be identical with the curves for $\sin\theta$ and $\cos\theta$ given in reference 1.

III. THERMAL TRANSFER BY DIFFUSION

In the limit of zero frequency both of Eqs. (4) become diffusion equations:

$$\left.\begin{aligned} V_1^2\nabla^2\mathbf{Y}^* &= (\sin\theta)\dot{\mathbf{Y}}^*/\tau \\ V_2^2\nabla^2\mathbf{Z}^* &= (\cos\theta)\dot{\mathbf{Z}}^*/\tau \end{aligned}\right\}. \tag{8}$$

Consider a pure heat excitation such that $\mathbf{Z}$ alone oscillates, while $\mathbf{Y}$ remains zero. We then have from (1)

$$\left.\begin{aligned} &\mathbf{Y}^* = \mathbf{Z}\sin\theta \quad \text{and} \quad \mathbf{Z}^* = \mathbf{Z}\cos\theta \\ &\mathbf{Z} = \mathbf{Z}^*\cos\theta + \mathbf{Y}^*\sin\theta \\ &\mathbf{Y} = \mathbf{Y}^*\cos\theta - \mathbf{Z}^*\sin\theta = 0 \end{aligned}\right\}. \tag{9}$$

The two diffusion equations can now be written formally as

$$\left.\begin{aligned} V_1^2\nabla^2(\mathbf{Z}\sin\theta) &= (\sin^2\theta)\dot{\mathbf{Z}}/\tau \\ V_2^2\nabla^2(\mathbf{Z}\cos\theta) &= (\cos^2\theta)\dot{\mathbf{Z}}/\tau \end{aligned}\right\} \tag{10}$$

This separation into two normal modes in the diffusion limit (zero frequency) is of course highly artificial, but the diffusive process certainly goes over gradually from the second form in (10) at $\theta=0$ and T_λ to the first form in (10) at $\theta=\frac{1}{2}\pi$ at 0°K. The two forms can be combined into one equation which will at least formally take care of the situation between the above two extremes: thus multiplying the first Eq. (10) by $\sin\theta/V_1^2$, and the second by $\cos\theta/V_2^2$, and adding the two results we find

$$\nabla^2\mathbf{Z} = \{(\sin^3\theta)/\tau V_1^2 + (\cos^3\theta)/\tau V_2^2\}\dot{\mathbf{Z}} \tag{11}$$

This equation will be accepted here as a reasonable description of the diffusion process resulting from a combination of the two basic modes of transport.

Recalling that $\nabla\cdot\mathbf{Z}=\Delta\rho_n/\rho_n$, and taking the divergence of (11), we derive the equation for thermal diffusion as before[4-6]

$$\mathbf{W} = -\rho CD\nabla T, \tag{12}$$

where C is the specific heat and

$$D = \tau\{(\sin^3\theta)/V_1^2 + (\cos^3\theta)/V_2^2\}^{-1}. \tag{13}$$

Near T_λ where $\theta=0$, $D\to\tau V_2^2$, and the second mode alone is responsible for thermal transport. At the temperature T_1 where $\theta=\frac{1}{4}\pi$ concentration oscillations divide equally between the two basic modes, and D has its maximum:

$$T=T_1, \quad D_{\max} = 8\tau\{V_1^2V_2^2/(V_1^2+V_2^2)\}. \tag{14}$$

Near 0°K where $\theta=\frac{1}{2}\pi$, D approaches the value τV_1^2 and almost all the heat is transported by the first mode.

IV. MASS TRANSFER BY DIFFUSION

Consider a pure density oscillation with $\mathbf{Z}=0$ and

$$\left.\begin{aligned} &\mathbf{Y}^* = \mathbf{Y}\cos\theta, \quad \mathbf{Z}^* = -\mathbf{Y}\sin\theta \\ &\mathbf{Y} = \dot{\mathbf{Y}}^*\cos\theta - \mathbf{Z}^*\sin\theta \end{aligned}\right\}. \tag{15}$$

In the diffusion limit the wave equations (4) now become

$$\left.\begin{aligned} V_1^2\nabla^2(\mathbf{Y}\cos\theta) &= (1/\tau)\sin\theta\cos\theta\dot{\mathbf{Y}} \\ V_2^2\nabla^2(\mathbf{Y}\sin\theta) &= (1/\tau)\cos\theta\sin\theta\dot{\mathbf{Y}} \end{aligned}\right\}, \tag{16}$$

which again can be combined formally to give

$$\nabla^2\mathbf{Y} = (1/\tau)\sin\theta\cos\theta\{(\cos\theta)/V_1^2 + (\sin\theta)/V_2^2\}\dot{\mathbf{Y}}. \tag{17}$$

Writing $\nabla\cdot\mathbf{Y}=(\Delta\rho/\rho)$ Eq. (15) can be written as a diffusion equation for mass:

$$\nabla(\Delta\rho/\rho) = \eta\dot{\mathbf{Y}}, \tag{18}$$

where

$$\eta = (1/\tau)\sin\theta\cos\theta\{(\cos\theta)/V_1^2 + (\sin\theta)/V_2^2\} \tag{19}$$

can be regarded as a "bulk viscosity." In this zero frequency limit there is no pressure gradient possible under isothermal conditions, and it is not correct to recast (16) into the form of a viscous flow under a pressure gradient. The so-called "bulk viscosity" vanishes at T_λ and again at 0°K, having a maximum at T_1 where $\theta=\frac{1}{4}\pi$. The physical reason for the existence of this "bulk viscosity" is that, except at the two extremes of temperature just mentioned, density waves split into two components—the two normal modes—in each of which there exists relative motion between the two semiphases and a momentum exchange between them that causes attenuation. Although the concentration variations thus present in each mode cancel each other initially, they get transmitted with different speeds, and the two attenuation processes exist independently.

V. SUPERCONDUCTIVITY FOR HEAT

The anomalously high conductivity for heat follows from a comparison between the result (12) and (13) of the present paper, with the expression derived for thermal current on the formal first-order perturbation theory that neglected the presence of non-equilibrium conditions.[10] Equation (2.13) of reference 10 gave for the thermal conductivity below T_λ approximately

$$K_{\text{pert}} = (35/4)(\tau_n/m)(N_n/V)k^2T\zeta(7/2)/\zeta(3/2), \tag{20}$$

where τ_n is the time of relaxation for asymmetrical perturbations of the velocity distribution in the high energy semiphase. To compare this with (12) above we note that as $T\to T_\lambda$ Eq. (4.5) of reference 1 leads to the

[10] W. Band, Phys. Rev. **75**, 1937 (1949).

result

$$V_2^2 \rightarrow (5/4)(\rho_s/\rho)(P/\rho) = (5/4)(\rho_s/\rho)(kT/\rho)(N_n/V)\zeta(5/2)/\zeta(3/2),$$

while

$$\rho C = (15/4)(\rho_n k/m)\zeta(5/2)/\zeta(3/2),$$

so that the conductivity given by (12) is

$$K_{\text{non-eq}} \rightarrow \rho C V_2^2 = (75/16)(\tau/m)(N_n/V) \times (\rho_n\rho_s/\rho^2)k^2T\{\zeta(5/2)/\zeta(3/2)\}^2. \quad (21)$$

The order of magnitude of the ratio between the two expressions for conductivity is essentially the same as the ratio between the two relaxation times

$$K_{\text{non-eq}} : K_{\text{pert}} \sim (\tau/\tau_n)(\rho_n\rho_s/\rho^2). \quad (22)$$

On the present model $\tau \gg \tau_n$, so that as soon as T is appreciably below T_λ, Eq. (22) yields an anomalously large value for $K_{\text{non-eq}}$. If τ_n is assumed to be of the order 10^{-8} sec. and τ as above is of the order 10^{-3} sec., the jump in conductivity is of the order 10^5 times the normal conductivity.

To obtain the complete temperature dependence of thermal conductivity below the lambda-point, we use Eq. (4.4) of reference 1 for V_1^2 and V_2^2 in (13), and write

$$\left.\begin{aligned} C &= (15/4)(T/T_\lambda)^{\frac{1}{2}}(k/m)\zeta(5/2)/\zeta(3/2) \\ P/\rho_n &= (kT/m)\zeta(5/2)/\zeta(3/2) \end{aligned}\right\}. \quad (23)$$

This yields

$$K_{\text{non-eq}}/\tau = (25/4)(T/T_\lambda)^{5/2}(\rho k^2/m^2) \times \{\zeta(5/2)/\zeta(3/2)\}^2[(\sin^3\theta)/\{1+[1-3x(1-x)]^{\frac{1}{2}}\} + (\cos^3\theta)/\{1-[1-3x(1-x)]^{\frac{1}{2}}\}], \quad (24)$$

where

$$x = \rho_n/\rho = (T/T_\lambda)^{\frac{1}{2}} \text{ and } \tan 2\theta = [x(1-x)]^{\frac{1}{2}}/(2x-1).$$

Choosing $\rho = 0.095$ and m equal to the mass of the helium atom, so that (see reference 10) the lambda-transition occurs at 2°K, we calculate the curve given by (24) and find the result shown in Fig. 1. The similarity of this curve with the observed curve for thermal currents in liquid helium as a function of T,[9] is very remarkable. In particular, if the same τ-value is assumed as for liquid helium, namely 2×10^{-3} sec., the value of K given by (24) coincides with the observed conductivity in liquid helium when the temperature gradient is about 0.001° per cm. As mentioned in Section I, however, the dependence of the heat current on the cube root of the temperature gradient observed in liquid helium is not given on the present model without similar special considerations regarding the dependence of τ on the current to those already proposed in connection with liquid helium.[3]

VI. CONCLUSIONS

The Bose-Einstein model here discussed evidently succeeds in reproducing qualitatively the second sound and thermal characteristics of liquid helium, but at the same time reduces first sound to a similar behavior with second sound. In fact, first sound exists in the Bose-Einstein model below T_λ only as an effect of the "elasticity" associated with concentration variations. This can be seen in the following way. From reference 1 it is evident that the velocity of transmission, V_1, depends on the volume elasticity only through the expression

$$f = -\tfrac{1}{2}\rho^2(\partial^2E/\partial\rho^2)_x - \rho(\partial E/\partial\rho)_x - \tfrac{1}{2}x^2(\partial^2E/\partial x^2)_\rho.$$

In the Bose-Einstein model $E \propto x^{5/3}/\rho$ is exactly proportional to the volume so the expression for the isothermal bulk elasticity

$$\tfrac{1}{2}\rho^2(\partial^2E/\partial\rho^2)_x + \rho(\partial E/\partial\rho)_x$$

vanishes identically. The expression for f thus remains finite only because of the term in $(\partial^2E/\partial x^2)_\rho$.

Nevertheless, as was shown in reference 1, the velocity of propagation of first sound below T_λ as derived from this surviving term has the expected value $(5P/3\rho)^{\frac{1}{2}}$ just below T_λ and $(5P/3\rho_n)^{\frac{1}{2}}$ at low T.

This result is not a peculiarity of the particular relation[11] assumed between ρ_n/ρ and temperature; it remains valid even for the model in which $(\rho_n/\rho) \propto (T/T_\lambda)^k$ where k is any number, so long as $E \propto (1/\rho)$.

It must, therefore, be admitted that while the Bose-Einstein model reproduces with very remarkable fidelity the second-sound and thermal characteristics of liquid helium, it fails completely in its isothermal elastic properties. This failure is not very surprising, however, and may fairly be regarded as a natural consequence of the fact that helium is liquid while the Bose-Einstein model is a gas.

[11] G. E. Uhlenbeck and E. A. Uehling, Phys. Rev. **39**, 1014 (1931).

Investigation of Nuclear Energy Levels in Sulfur*

R. E. PETERSON, H. H. BARSCHALL, AND C. K. BOCKELMAN
University of Wisconsin, Madison, Wisconsin
(Received May 5, 1950)

The total cross section of sulfur has been measured for neutrons of energies from 15 to 1450 kev with energy spreads between 1.5 and 9 kev. Below 750 kev, nine well-defined maxima are observed, three of which are interpreted as caused by *s*-neutrons; the others are believed to be produced by *p*- or *d*-neutrons. The *s*-resonances have natural widths of about 15 kev, while one of the other resonances which was studied in detail has a width of 1.5 kev. In the case of the latter resonance, the compound nucleus appears to be formed with spin of $\frac{3}{2}$. Above 750 kev neutron energy the density of observed levels increases, and no interpretation of the resonances was attempted.

I. INTRODUCTION

IN order to study individual nuclear energy levels by investigating the variation of the total neutron cross section with neutron energy, it is necessary to use neutrons which have an energy spread small compared to the spacing of the energy levels, and comparable to the widths of the levels. For light nuclei, which have large level spacings and level widths, this requirement is easily met. In general, however, as the nuclear mass increases, the level widths and spacings decrease and it is difficult to obtain neutrons with sufficiently well-defined energies. In the present paper a description of measurements on the levels in sulfur will be given. Sulfur was chosen because preliminary experiments had indicated that its energy levels might be fully resolved with a neutron energy spread of the order of 1 kev, in contrast to aluminum, for example.

II. EXPERIMENTAL PROCEDURE

As in previous experiments,[1] total neutron cross sections were determined from transmission measurements. Neutrons were obtained from the $Li^7(p, n)Be^7$ reaction using the electrostatic generator to accelerate the protons. It has recently been found[2] that a second neutron group from this reaction is present if the energy of the main group is greater than 650 kev. The number of neutrons of lower energy appears to be so small, however, that this group did not produce observable resonance effects in the present experiment.

$B^{10}F_3$ proportional counters served as neutron detectors. One of the counters employed has been described previously;[1] a second counter, shown in Fig. 1, was used for some of the work carried out with high resolution and consequent low neutron intensity. The efficiency of the counter shown in Fig. 1 was 2×10^{-3} for neutrons from a Ra—Be source, or about five times that of the first counter.

In order to produce neutrons with a small energy spread, the protons striking the lithium target must be well defined in energy, the target must be thin, and the angle subtended by the detector at the target must be small.[1] As the neutron energy spread is reduced, the neutron flux decreases rapidly. Therefore, high resolution was used only in energy regions where structure had previously been located with a larger energy spread.

The energy of the protons was defined by passing them through the one-meter radius electrostatic analyzer.[3] The resolution function, or the distribution in energy of the protons, for this analyzer is triangular, and the effective proton energy spread is taken as the full width, at half-maximum, of the resolution function. This energy spread will be expressed in percent of the proton energy. With analyzer slit settings corresponding to a proton energy spread of 0.1 percent, about 2 μa of beam current were available, while with an energy resolution of 0.033 percent, 0.3 μa of proton current could be maintained.

In order to estimate the neutron energy spread used, it is necessary to know the thickness of the Li target.

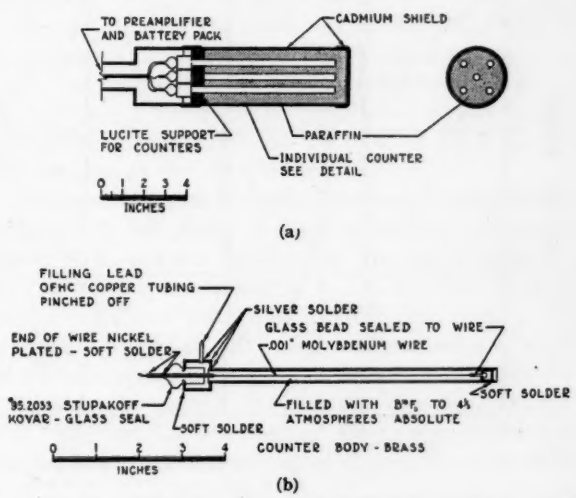

FIG. 1. Neutron detector. (a) Counter assembly. (b) Detail of single counter.

* This work was supported in part by the AEC and in part by the Wisconsin Alumni Research Foundation.

[1] Barschall, Bockelman, Peterson, and Adair, Phys. Rev. **76**, 1146 (1949).

[2] Johnson, Wilson-Laubenstein, and Richards, Phys. Rev. **77**, 413 (1950).

[3] Warren, Powell, and Herb, Rev. Sci. Inst. **18**, 559 (1947).

TABLE I. Estimated effective neutron energy spreads used in the study of nuclear energy levels in sulfur.

Target thickness (kev)	Analyzer resolution (percent)	Effective neutron energy spread (kev)
8	0.1	9
5.5	0.1	6.5
4	0.1	5.5
2.5	0.1	4
1.3	0.1	3
	0.05	2.5
	0.07	3.2
0.6	0.033	1.5

The previously described rise method[1,4] for determining target thickness may not be reliable for very thin targets, since it is not known how the cross section for the Li(p, n) reaction varies just above the threshold energy. Target thicknesses were therefore estimated on the basis of the neutron yields. A target thick enough to be measured by the rise method (about 8 kev) was prepared, and its neutron yield at a proton energy of 1.93 Mev was determined relative to a Ra—Be source. Thinner targets were then measured against this standard, assuming that the thickness of the target is proportional to its yield. This assumption is not valid if there is appreciable oxidation of the targets.

In order to help prevent the deposition of oil from the vacuum system onto the target, the oil-sealed rotating target previously used was replaced by a stationary target assembly. A jet of heated air was directed at the tantalum backing of the lithium target to reduce the rate of oil deposition. To prevent local heating of the target, the proton beam was swept in a small circle on the target by passing it between two pairs of plates placed about a meter from the target; two transformers, phased 90° apart, were connected to the plates. With these precautions, it was possible to use a target less than 1 kev thick for several hours with no loss of lithium, and with very little oil deposition.

During the course of the experiment, targets ranging in thickness from 0.6 to 8 kev were used. The analyzer resolution was adjusted to keep the energy spread of the incident proton beam comparable to or less than the target thickness. For all but the thinnest target, the detector was placed 25 cm from the target; the angle subtended by the counter at the target then introduced maximum neutron energy spreads of 2, 3.5, and 6 kev at neutron energies of 200, 700, and 1400 kev, respectively. With the 0.6-kev target, the counter was placed 33 cm from the target, and the maximum neutron energy spread introduced by the finite size of the detector was 2 kev at 600 kev neutron energy. The effective energy spread introduced by the variation of the neutron energy with angle was taken as 0.6 of these maximum values. This factor was obtained by assuming that all the incident neutrons were detected with equal

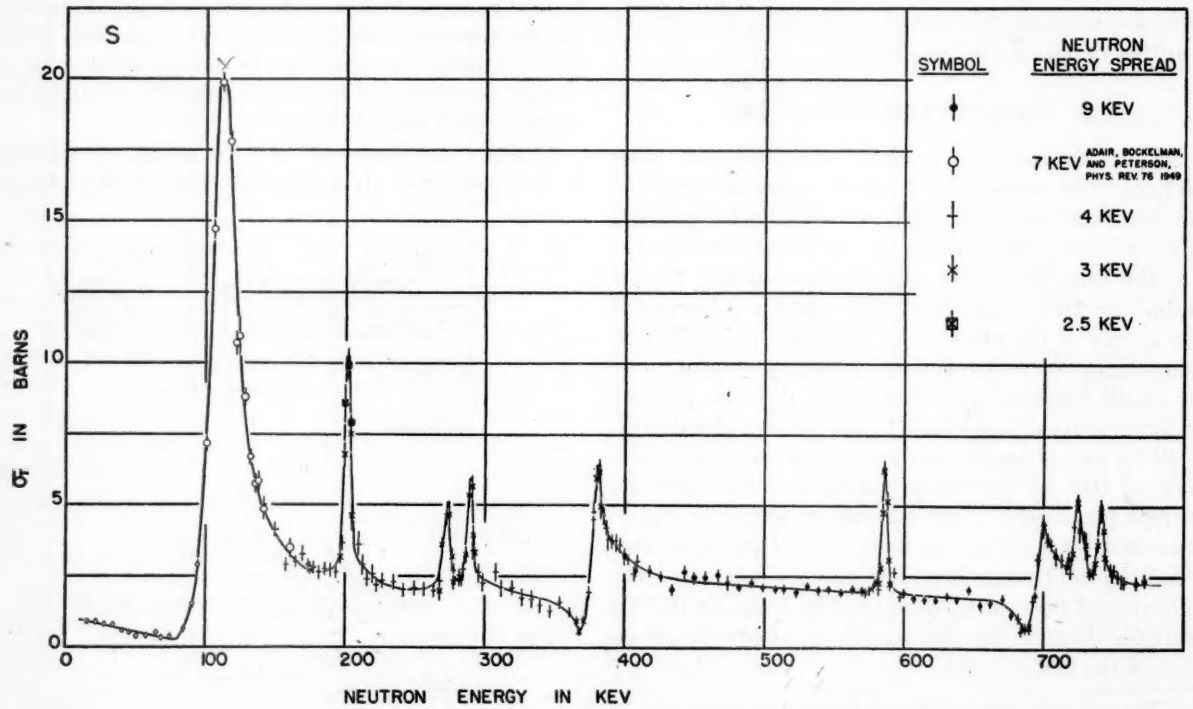

FIG. 2. The total neutron cross section of sulfur as a function of neutron energy. The heights of the symbols are equal to the standard statistical errors in the cross section. Different symbols represent the different neutron energy spreads used in determining the cross section.

[4] R. F. Taschek and A. Hemmendinger, Phys. Rev. 74, 373 (1948).

efficiency and by taking as the effective energy spread that energy interval which would include three-fourths of all the counted neutrons. The actual variation of sensitivity across the face of the counter is probably such that this estimate of the energy spread associated with the detector is too large. Therefore, the estimated over-all effective neutron energy spreads listed in Table I will probably be too large also, particularly for the cases of the thinner targets.

The resolution obtained with a given target and a particular analyzer setting is nearly independent of neutron energy. The Doppler effect contribution to the neutron energy spread is negligible.

III. MEASUREMENTS BELOW 750-KEV NEUTRON ENERGY

Results

Figure 2 shows the total neutron cross section of sulfur as a function of neutron energy for energies up to 750 kev. The energy spreads of the neutrons used are indicated in the legend of the graph. Maxima in the cross section were observed at 111, 203, 274, 290, 375, 585, 700, 725, and 742 kev neutron energy. There are pronounced minima preceding the 111-, 375-, and 700-kev maxima. At energies near maxima and minima, preliminary data obtained with the larger neutron energy spreads are not shown on the graph. It was found, however, that the observed heights of the maxima increased as the energy resolution was improved; this effect was less pronounced in the case of the broader maxima. The cross sections at the minima did not decrease as the neutron energy spread was reduced.

Figure 3 shows the results obtained by studying the 585-kev peak (Fig. 2) in greater detail, using an estimated neutron energy spread of 1.5 kev.

All the data presented on the graphs were corrected for neutron background and for the effect of neutrons scattered into the detector by the sulfur cylinders; the latter correction was based on the assumption of isotropic scattering from the sulfur. The thicknesses of the sulfur samples were adjusted to make the transmission approximately 60 percent at all energies.

Discussion

S^{32} is the main constituent (95 percent) of normal sulfur. The observed maxima in the total cross section should therefore be caused by levels of the compound nucleus S^{33}. For sulfur, the contribution of inelastic scattering to the total cross section should be small, since the lowest reported level in S^{32} occurs[5] at about 2.3 Mev, and so cannot be excited in the present measurements. The cross section for absorption of neutrons is small even at thermal energies and would not be expected to contribute appreciably to the total cross section at higher energies; the exothermic reaction $S^{32}(n, \alpha)Si^{29}$ has a cross section of only 0.07 barn at a neutron energy[6] of 2.8 Mev so that this process should be unimportant. The predominant interaction is therefore elastic scattering. In view of the shapes and separation of the cross-section maxima found for neutrons with energies up to 750 kev, it is assumed that these maxima show the effect of individual levels in S^{33}. It should therefore be possible to assign angular momenta to these levels on the basis of the heights of the maxima in the cross section.[7]

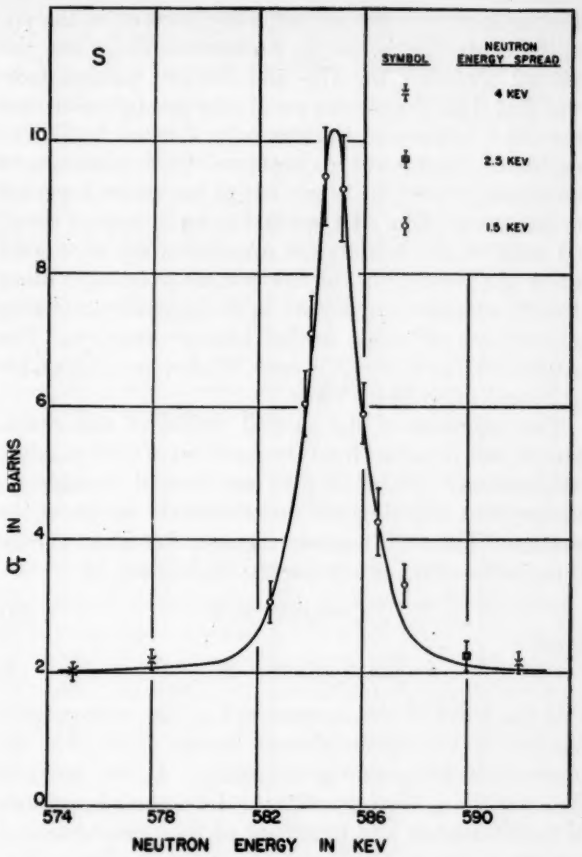

FIG. 3. The total neutron cross section of sulfur near the 585-kev resonance. The statistical errors in the cross section are given by the heights of the symbols.

The resonance at 111 kev has been discussed previously.[8] It was shown to be produced by neutrons of zero orbital angular momentum forming a compound nucleus with spin J equal to $\frac{1}{2}$, and the natural width of the level was estimated to be about 18 kev. The minimum preceding the peak was interpreted in terms of interference between resonance and potential scattering. At neutron energies of a few hundred kev, such interference is expected only near resonances caused by neutrons of zero orbital angular momentum,

[5] Beghian, Grace, Preston, and Halban, Phys. Rev. **77**, 286 (1950).

[6] P. Huber, Helv. Phys. Acta **14**, 163 (1941).

[7] Adair, Barschall, Bockelman, and Sala, Phys. Rev. **75**, 1124 (1949).

[8] Adair, Bockelman, and Peterson, Phys. Rev. **76**, 308 (1949).

since at such energies all but a few percent of the potential scattering is due to s-neutrons. Therefore, the minima preceding the 375- and 700-kev maxima indicate that these resonances are also caused by s-neutrons forming a compound nucleus with J equal to $\frac{1}{2}$. The heights of these peaks, as measured from minimum to maximum, are within 10 percent of the values expected on this assumption. The residual cross sections of about 0.5 barn at the minima are approximately accounted for by the presence of the five percent of isotopes other than S^{32} and the contribution to the potential scattering by neutrons of higher orbital angular momenta. The natural widths of the 375- and 700-kev resonances are estimated to be 12 ± 1.5 kev.

The estimates of the natural widths of the s-resonances were obtained from the positions of their maxima and minima;[9] the result does not depend strongly on assumptions regarding the distribution in energy of the neutrons. The total neutron cross section at an energy E near an s-resonance at energy E_r, is given by

$$\sigma_t=4\pi k^{-2}\sin^2\delta \tag{1}$$

where

$$\delta=\tan^{-1}[\tfrac{1}{2}\Gamma/(E_r-E)]+\varphi. \tag{2}$$

Γ is the width of the resonance, k is the neutron wave number in the center-of-mass system, and φ is the phase shift for potential scattering. At the energies $E_{\max}$ and $E_{\min}$, corresponding to the observed positions of the maximum and minimum of the cross section, δ has the values $\pi/2$ and zero, respectively. The substitution of these values of δ and of the associated values of E into Eq. (2) yields two relations from which E_r may be eliminated, with the result that

$$\Gamma=(E_{\min}-E_{\max})\sin 2\varphi. \tag{3}$$

The phase shift φ is obtained from the relation

$$\sigma_{\text{pot}}=4\pi k^{-2}\sin^2\varphi \tag{4}$$

by setting σ_{pot}, the cross section for potential scattering, equal to the depth of the dip in the cross-section curve.

The maxima at 203, 274, 290, 725, and 742 kev show no interference effects and are therefore caused by neutrons of greater than zero orbital angular momentum. Since at the lower energies the widths of d-resonances should be about 30 times less than those of p-resonances,[10] d-neutrons might not be expected to produce experimental cross sections as high as those found. Consequently, it is believed that the 203-, 274-, and 290-kev resonances are caused by p-neutrons. P-neutrons may form a compound nucleus of spin $\frac{1}{2}$ or $\frac{3}{2}$. While none of the maxima have observed heights larger than those expected for J equal to $\frac{1}{2}$, it is still possible that the levels might be associated with a higher spin of the compound nucleus, if their natural widths are appreciably less than the neutron energy spread.

At the 585-kev resonance, shown in Fig. 3, the cross section rises to about 7 barns above the off-resonance value. The height expected if the compound nucleus were formed with J equal to $\frac{3}{2}$ is 8.8 barns at this energy. Either p- or d-neutrons could therefore be responsible for the resonance. The experimental width of this resonance is 2 kev.

From the observed height and width of the resonance, and the expected theoretical height, it is possible to obtain both the natural width of the level and the width of the neutron energy distribution. This calculation will depend only in an insensitive way on the shape of the function describing the distribution in energy of the neutrons. If this function is taken to be Gaussian, the natural width of the 585-kev resonance is found to be 1.5 kev, and the neutron energy spread 1.1 kev. This value of the energy resolution should be compared with the energy spread of 1.5 kev listed in Table I. As was previously mentioned, the energy spread introduced by the finite size of the detector may have been overestimated, and the widths given in Table I may be too large.

For purposes of comparison, the widths of the resonances may be expressed in terms of their reduced widths,[11] which are independent of energy and the effects of centrifugal barriers. The reduced width of a resonance with a natural width Γ is

$$\gamma^2=\Gamma/2kT. \tag{5}$$

In Eq. (5), k is the neutron wave number at the resonance energy and T is a barrier penetration factor. T has the value unity for a resonance due to s-neutrons; for a p-resonance, it is[10]

$$k^2a^2/(1+k^2a^2) \tag{6}$$

where a is the nuclear radius, taken to be equal to $1.5A^{\frac{1}{3}}\cdot10^{-13}$ cm. The reduced widths of the 111-, 375-, and 700-kev s-resonances are found to be approximately 125, 45, and 30×10^{-13} kev-cm, respectively. Under the assumption that the 585-kev resonance is produced by p-neutrons, its reduced width is 12×10^{-13} kev-cm, while its reduced width is 145×10^{-13} kev-cm if it were produced by d-neutrons.

If Fig. 2 shows all the s- and p-resonances which occur in the energy interval from 15 to 750 kev, the level spacing in S^{33}, for an excitation energy between 9 and 10 Mev, is of the order of 100 kev. This spacing is appreciably closer than that found for S^{33} at excitation energies of approximately 6 Mev in studies[12] of the $S^{32}(d,p)S^{33}$ reaction. While it is possible that with the poorer energy resolution used in the latter experiment some levels may not have been observed, the higher excitation energy of the S^{33} nucleus in the present experiment may be responsible for the closer level spacing.

[9] M. R. MacPhail, Phys. Rev. **57**, 669 (1940).
[10] Feshbach, Peaslee, and Weisskopf, Phys. Rev. **71**, 145 (1947). See Section 5, Eq. (45a).
[11] E. P. Wigner, Am. J. Phys. **17**, 99 (1949).
[12] P. W. Davison, Phys. Rev. **75**, 757 (1949).

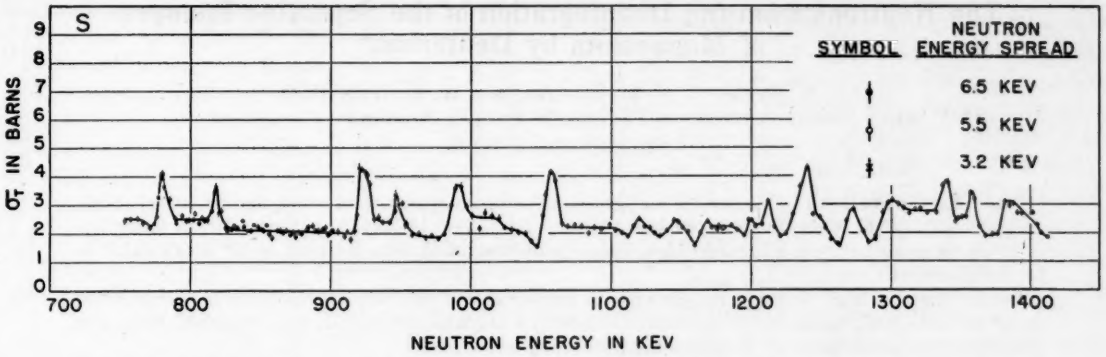

FIG. 4. The total neutron cross section of sulfur in the region of 750- to 1450-kev neutron energy. The statistical errors in the cross section are equal to the heights of the symbols.

IV. MEASUREMENTS ABOVE 750-KEV NEUTRON ENERGY

The total cross section of sulfur for neutrons of energies in the range from 750 to 1450 kev is shown in Fig. 4. A detailed comparison of these data with the earlier measurements of Freier *et al.*[13] is made difficult by the different energy resolutions used in the two experiments; there is, however, qualitative agreement between the two sets of measurements.

For neutron energies above about 1 Mev, several factors make it difficult to identify the energy levels responsible for the observed maxima. The theoretical heights of the resonances decrease with increasing neutron energy, so that the assignment of spins to resonances on the basis of their amplitudes becomes less reliable. Also, competition from the $S^{32}(n, p)P^{32}$ reaction, which has a threshold at a neutron energy of approximately 1 Mev, will reduce the expected height of the maxima, although this effect may not be important in view of the low cross section reported for this reaction by Klema and Hanson.[14] The distinction between *s*- and *p*-resonances will become less clear at higher neutron energies, since the contribution of neutrons of one unit of orbital angular momentum to the potential scattering will increase, and interference effects between resonance and potential scattering will be expected near both *s*- and *p*-resonances. An example of such interference for a *p*-resonance occurs below the 1055-kev maximum; the depth of the dip observed is consistent with the estimated 15 percent contribution of *p*-neutrons to the potential scattering cross section at this energy. Furthermore, at neutron energies in the region above 1 Mev, the widths of levels excited by *p*- and *d*-neutrons should differ only by a factor of the order of five, so that the effect of *p*- and *d*-neutrons can no longer be distinguished by considering level widths. As might be expected, the increased excitation energy of the compound nucleus and the greater widths expected for *d*-resonances increase the number of observable levels so that they are no longer well separated. It therefore does not seem possible to analyze most of the levels shown in Fig. 4.

[13] Freier, Fulk, Lampi, and Williams, Phys. Rev. **78**, 508 (1950).

[14] E. D. Klema and A. O. Hanson, Phys. Rev. **73**, 106 (1948).

The Neutrons from the Disintegration of the Separated Isotopes of Magnesium by Deuterons*

C. P. SWANN, C. E. MANDEVILLE, AND W. D. WHITEHEAD
Bartol Research Foundation of The Franklin Institute, Swarthmore, Pennsylvania

(Received May 8, 1950)

When Mg^{25} is irradiated by deuterons, four groups of neutrons appear from which nuclear energy levels are deduced in Al^{26} at 2.00±0.18 Mev, 3.63±0.18 Mev, and 5.13±0.18 Mev. The Q-value for the formation of Al^{26} in the ground state is 5.58±0.10 Mev. From the disintegration data, the mass of Al^{26} is calculated to be $25.9935\pm9\times10^{-4}$ mu.

Bombardment of Mg^{26} by deuterons gives rise to eight groups of neutrons corresponding to energy levels in Al^{27} at 0.88±0.07, 1.92±0.07, 2.75±0.07, 3.65±0.07, 4.33±0.07, 5.32±0.07, and 5.81±0.07 Mev. The Q-value for the formation of Al^{27} in the ground state is 5.68±0.05 Mev.

No quantitative analysis was made of the reaction $Mg^{24}(D, n)Al^{25}$. However, since Mg^{24} was the principal isotopic impurity, it was necessary to show that its presence made no contribution to the spectra of the two preceding reactions.

I. INTRODUCTION

THE separation of stable isotopes under the program of the United States AEC has made several elements available for study which have not been previously investigated. Among these are the three isotopes of magnesium, Mg^{24}, Mg^{25}, and Mg^{26}. Seventy-five percent of naturally occurring magnesium is Mg^{24}, the remaining percentage being about evenly divided between the two isotopes of higher mass numbers. The isotopic percentages in the various samples of separated materials are summarized in Table I.

The separated isotopes, in the form of MgO, were supplied together with the isotopic analyses, by the Y-12 plant, Carbide and Carbon Chemicals Division, Union Carbide and Carbon Corporation, Oak Ridge, Tennessee.

The experimental data to be described were obtained by irradiating thick targets of MgO by deuterons of energy 1.47 Mev, supplied by the Bartol Van de Graaff statitron. Ilford C_2 emulsions, making angles of 0° and 90° with the bombarding beam in the laboratory system of coordinate axes, were employed as detectors of the emergent neutrons. The track lengths of recoil protons making angles as great as 12° with the forward direction were accepted. From the track lengths, the neutron energies were deduced.

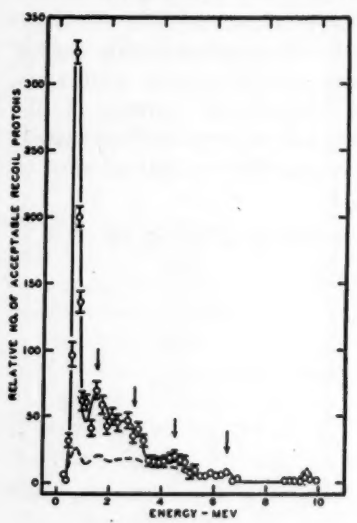

FIG. 1. Recoil protons of the neutrons from the disintegration of Mg^{25} by deuterons. Angle of observation 90°.

TABLE I. Isotopic composition of samples.

Mg^{24}		Mg^{25}		Mg^{26}	
Isotope	Percent	Isotope	Percent	Isotope	Percent
24	99.5	24	10.7	24	2.53
25	0.3	25	86.8	25	1.56
26	0.2	26	2.5	26	95.91

II. MAGNESIUM (25)

Among the several nuclear reactions occurring when Mg^{25} is bombarded by deuterons is the one concerned with neutron emission,

$$Mg^{25}+D\rightarrow Al^{26}+n^1+Q_1. \quad (1)$$

The energy spectrum of the neutrons emitted at 90° in this reaction is shown in Fig. 1. The intense group of particles in the vicinity of 1 Mev is the group of

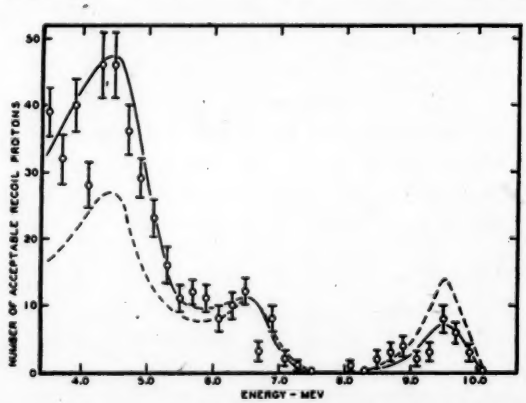

FIG. 2. High energy recoil protons of the neutrons from the disintegration of Mg^{25} by deuterons. Angle of observation 90°. The group of neutrons at 9.5 Mev is ascribed to the first excited state of the reaction $B^{11}(D, n)^*C^{12}$.

* Assisted by the joint program of the ONR and AEC.

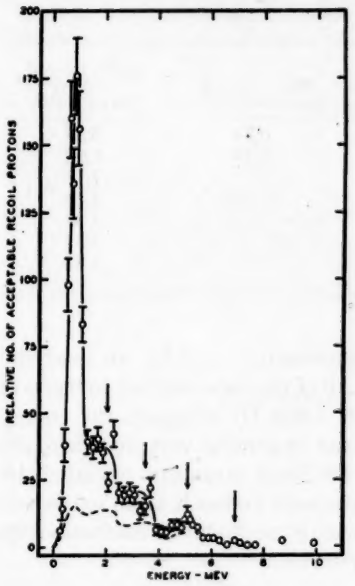

FIG. 3. Recoil protons of the neutrons from the disintegration of Mg^{25} by deuterons. Angle of observation 0°.

neutrons from the reaction

$$C^{12}+D\rightarrow N^{13}+n^1+Q_2. \quad (2)$$

The remaining four groups of higher energy are attributed to reaction (1). In order to obtain greater statistical accuracy in the region of higher energy, measurements accepting only neutrons of energy greater than 3.5 Mev were carried out. The tracks of Fig. 1 beyond 3.5 Mev were combined with these newly obtained tracks to give Fig. 2. The Q-value for formation of Al^{26} in its ground state is 6.22 Mev, as calculated from known mass values.[1] The appearance of the neutron group at 9.5 Mev could not therefore be explained by reaction (1). A spectrographic analysis had shown boron to be present to the extent of 0.01 percent as a chemical impurity. From the length of bombardment, the area of the photographic plate surveyed, and the intensity of the group, it was concluded that the group could be assigned to the first excited state of C^{12} in the reaction

$$B^{11}+D\rightarrow {}^*C^{12}+n^1+Q_3. \quad (3)$$

By a consideration of relative intensities, it can be shown that the remaining groups of the spectrum cannot be attributed to the presence of any contaminating boron.[2]

The neutrons of reaction (1) were also recorded in the forward direction as shown in Fig. 3, where the four groups from Mg^{25} are again present along with the neutrons from $C^{12}(D, n)N^{13}$. There was difficulty in locating precisely the peaks of the various groups owing to their breadths. It is probable that the two lower Q-values of reaction (1) may be mean values for several closely spaced overlapping groups in each case. The average Q-values for reaction (1), calculated from the data of Figs. 1 and 3, are 0.45±0.15, 1.95±0.15, 3.58±0.15 and 5.58±0.10 Mev, corresponding to energy levels in the residual nucleus, Al^{26}, at 2.00±0.18 Mev, 3.63±0.18 Mev, and 5.13±0.18 Mev. The mass of Al^{26} is calculated to be $[25.9935\pm9\times10^{-4}]$ mu, using the Q-value for the ground state of Al^{26} found in the present experiment and the mass values of reference 1.

The broken lines of Figs. 1, 2, and 3 represent the energy distribution of the neutrons from reaction (1), corrected for the variation with energy of the neutron-proton scattering cross section and the acceptance probability. The areas under the dotted lines are a measure of the intensities of the various groups.

III. MAGNESIUM (26)

When Mg^{26} is irradiated by deuterons, the monoisotopic Al^{27} is formed in the reaction

$$Mg^{26}+D\rightarrow Al^{27}+n^1+Q_4. \quad (4)$$

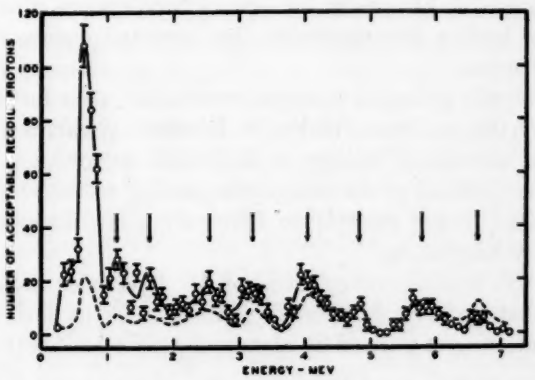

FIG. 4. Recoil protons of the neutrons from the disintegration of Mg^{26} by deuterons. Angle of observation 90°.

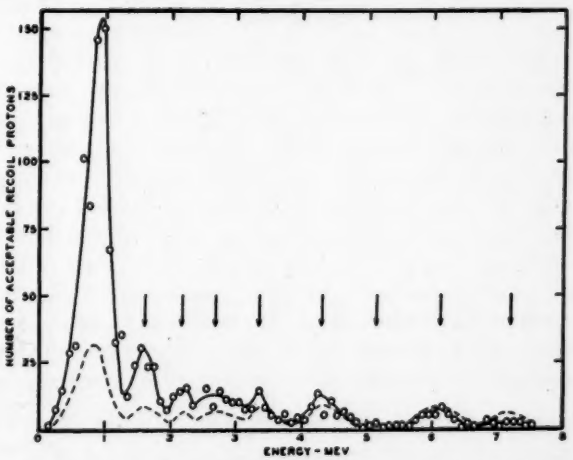

FIG. 5. Recoil protons of the neutrons from the disintegration of Mg^{26} by deuterons. Angle of observation 0°.

[1] H. A. Bethe, *Elementary Nuclear Theory* (John Wiley and Sons, Inc., New York).

[2] The relative intensities of the neutron groups from $B^{11}(D, n)C^{12}$ are known from a bombardment at 1.4 Mev in this laboratory. The data are unpublished.

TABLE II. Nuclear energy levels in Al^{27}.

Proton scattering Rochester (1941)	Proton scattering Princeton (1948)	Proton scattering Cambridge (1949)	Deuteron scattering Cambridge (1949)	Deuteron scattering Liverpool (1949)	$Mg^{27} \rightarrow Al^{27} + \beta^-$ Stockholm (1948)	$Mg^{26} + D \rightarrow Al^{27} + n^1 + Q$ Bartol (1950)
0.87	0.9	0.80, 0.97	0.88	0.99	0.84	0.88
2.03		2.15	2.15	2.17	1.85	1.92
2.70	2.9					2.75
3.5						3.65
						4.33
						5.32
						5.81

The Q-value for formation of Al^{27} in the ground state is 5.31 Mev when calculated from known mass values.[1] The neutron groups observed at 90° are shown in Fig. 4. In addition to the intense group of low energy neutrons from $C^{12}(D, n)N^{13}$, there are eight other groups corresponding to the formation of Al^{27} in the ground state and various excited states. The Q-values calculated from the neutron energies are (-0.13), 0.256, 1.35, 2.03, 2.93, 3.76, 4.80, and 5.68 Mev, giving energy levels at 0.88 ± 0.07, 1.92 ± 0.07, 2.75 ± 0.07, 3.65 ± 0.07, 4.33 ± 0.07, 5.32 ± 0.07, and 5.81 ± 0.07 Mev in the nucleus of Al^{27}. As in the case of the previous figures, the broken line represents the corrected energy distribution.

Similar groups of neutrons were found in the forward direction as shown in Fig. 5. However, Q-values were not calculated because of difficulties in locating the exact position of the group corresponding to the ground state. It was possible to find only a few acceptable very long tracks.

The nuclear energy levels of Al^{27} have been investigated by several different methods such as inelastic scattering of protons by aluminum,[3-5] inelastic scattering of deuterons by aluminum[6,7] and by an analysis[8] of beta-decay of Mg^{27}. All of the data relating to levels of Al^{27} are summarized in Table II. Although the energy values of Table II are not in general very accurate, the striking similarity of the level structure revealed by the various different methods makes it seem extremely probable that the several methods of excitation do excite the same energy levels.

IV. MAGNESIUM (24)

A short bombardment at 1.47 Mev with the photographic plates close to the target of $Mg^{24}O$ gave evidence of no tracks having a range in excess of that of the neutrons from $C^{12}(D, n)N^{13}$. This was to be expected since mass values[1] indicate a Q-value of only 0.17 Mev. These data also show that the neutrons from $Mg^{24}(D, n)Al^{25}$ made no appreciable contribution to the observed spectra of $Mg^{25}(D, n)Al^{26}$ or $Mg^{26}(D, n)Al^{27}$. Mg^{24} was the largest isotopic impurity in the samples of $Mg^{25}O$ and $Mg^{26}O$.

The writers wish to acknowledge the continued interest of Dr. W. F. G. Swann, Director of the Bartol Research Foundation.

[3] R. H. Dicke and J. Marshall, Jr., Phys. Rev. **63**, 86 (1943).
[4] H. W. Fulbright and R. R. Bush, Phys. Rev. **74**, 1323 (1948).
[5] E. H. Rhoderick, Nature **163**, 848 (1949).
[6] Greenlees, Kempton, and Rhoderick, Nature **164**, 663 (1949).
[7] J. R. Holt and C. T. Young, Nature **164**, 1000 (1949).
[8] Benes, Hedgran, and Hole, Arkiv. f. Mat. Astr. o. Fys. **35A**, No. 12 (1948).

Diffusion Coefficient of C in α-Iron*

C. A. WERT
Institute for the Study of Metals, University of Chicago, Chicago, Illinois
(Received March 7, 1950)

An equation of the form $D=D_0e^{-\Delta H/RT}$ is developed for interstitial diffusion in cubic lattices. This development uses a classical statistical mechanical treatment. Measurements of D for C in α-iron were made from $-35°$ to 200°C. Combined with earlier data they extend the knowledge of D in this system from $D=10^{-20}$ to $D=10^{-6}$ cm²/sec. The values of D_0 and ΔH obtained by fitting the above equation to the experimental points give $D_0=0.02$ cm²/sec. and $\Delta H=20{,}100$ cal./mole.

I. INTRODUCTION

NUMEROUS attempts have been made in the past to find an equation which describes adequately the process of diffusion in solids. These investigations have in general resulted in equations expressing the diffusion coefficient, D, in terms of such parameters as lattice geometry, temperature, and energy.[1] Experimental measurements which would test these theories have not been highly successful. There are two reasons for this: (1) some of the theories have resulted in relations containing parameters not easily measurable, and (2) the value of D has not been measured accurately enough, nor over a sufficient range, to permit adequate testing of the different expressions. The present investigation was a further attempt to solve this problem in a carefully selected alloy system using experimental techniques only recently developed. The investigation had two formal purposes: (1) to find an expression for D for diffusion of interstitial solute atoms in terms of measurable quantities, and (2) to test this expression by making measurements covering as wide as range in D as possible.

In Section II an expression for D will be developed; in Section III the experimental techniques used in the various temperature ranges will be discussed; and in Section IV the results of the experimental work will be presented.

II. ANALYSIS

Diffusion of the solute atoms in an interstitial solid solution is more easily analyzed than is diffusion in substitutional alloys. For an interstitial atom the diffusion mechanism is simply the jumping of the diffusing atom from one interstitial site to another. For a substitutional atom the mechanism has not yet been established by experiment. The following discussion is a classical, statistical mechanical, derivation of an equation for D which applies to the interstitial diffusion of dilute solid solutions. It is a simple problem in random walk to show that for interstitial diffusion in a cubic lattice the diffusion coefficient D is given by the expression[2]

$$D=\alpha(a^2/\tau), \tag{1}$$

where α is a constant depending on crystal geometry, a is the lattice parameter, and τ is the mean-time-of-stay of an atom at a given lattice site. The coefficient α is easily computed; it is found to be 1/12 for f.c.c. and 1/24 for b.c.c. lattices. The lattice parameter is, of course, well known for most common materials. To determine D it is only necessary to measure τ directly or to evaluate it from other known measurements. It is the purpose of the remainder of this section to find an expression for τ.

There have been developed a number of expressions for τ.[1] One group of these expressions has depended on a general investigation of the statistical theory of reaction rates by Eyring.[3] Though this rate theory is immediately applicable to the problem of diffusion, it is the opinion of the present author that it has not been applied in its most useful form. In the discussion which follows there will be presented a short derivation of τ which parallels the Eyring investigation to a certain point but which finally leads to a similar expression which is capable of much more direct physical interpretation. Though Eyring's development followed a quantum-mechanical treatment, it is sufficient to consider this interstitial diffusion problem from the point of view of classical statistics.

It is clear that in passing from one lattice site to another, the solute atom must have sufficient energy to pass over a potential barrier; the rate of jumping is then determined by the fraction of the time that an atom has this requisite energy. This is strictly true, of course, only if the interstitial site to which the atom would like to move is unoccupied; it is assumed that this is the case for the dilute solid solution considered here. In the discussion to follow, I will use the following nomenclature. x is the coordinate along a line connecting the interstitial sites. The coordinate of one interstitial site is $x_0=0$ and that of an adjacent site is $x=x_1$.

* This work was supported by the ONR.

[1] For a recent summary of this work see B. Chalmers, *Progress in Metal Physics* (Interscience Publishers, Inc., New York, 1949), Chapter 7.

[2] See for example C. Wert and C. Zener, Phys. Rev. **76**, 1169 (1949).

[3] H. Eyring, J. Chem. Phys. **3**, 107 (1935). Glasstone, Laidler, and Eyring, *The Theory of Rate Processes* (McGraw-Hill Book Company, Inc., New York, 1941).

x' is the position of the top of the potential barrier over which the particle must pass to go from x_0 to x_1. Let N be the number of particles in the site about x_0 and n the linear density of particles at x'. If $\bar{v}$ is the average velocity of all particles at x' crossing the barrier from the site at x_0 to x_1, then the rate at which particles pass the position x' is given by $n\bar{v}/N$. This flux of particles is proportional to the reciprocal of the mean-time-of-stay, τ, of the particles in the potential hole about x_0. It is assumed that the transmission coefficient of the barrier is unity. This assumption will be shown in Section IV to be consistent with the analysis of the experimental data. Thus

$$1/\tau = n'n\bar{v}/N, \tag{2}$$

where n' is the number of equivalent paths of diffusion from a given lattice site.

One must now evaluate the right member of this equation. To do this properly, one must first consider the number of coordinates of motion involved. To be sure, the "path of reaction" lies along x, but the diffusing atom may also oscillate in the y and z directions. In addition it is evident that some motion of the solvent atoms themselves may be involved. It is not clear how many of these atoms may be involved nor in detail how the atoms may move, but their motion may be formally introduced into the expression for $1/\tau$. The analysis of the data in Section IV will indicate that this is consistent with the experimental facts. In the light of these considerations Eq. (2) becomes

$$\frac{1}{\tau} = n' \frac{\int_{-\infty}^{\infty} \cdots \int \exp[-\phi(x', y, z, q_i)/kT] dydz \prod_i dq_i}{\int_{-\infty}^{\infty} \cdots \int \exp[-\phi(x, y, z, q_i)/kT] dxdydz \prod_i dq_i} \cdot \frac{\int_0^{\infty} \frac{P_x}{M} \exp[-P_x^2/2MkT] dp_x}{\int_{-\infty}^{\infty} \frac{P_x}{M} \exp[-P_x^2/2MkT] dp_x} \tag{3}$$

In this expression the first fraction represents the ratio n/N, the second, $\bar{v}$. The function $\phi(x', y, z, q_i)$ is the potential energy of the system (diffusing atom plus adjacent solute atoms) when the diffusing atom is at the position x'. The function $\phi(x, y, z, q_i)$ is the general potential energy of the system. The momentum of the diffusing atom is p_x, its mass, M. The q_i represent the coordinates of the unknown number of solute atoms which participate in the jumping. Since ϕ is unknown away from x_0, this expression cannot be evaluated in general. However, if the height of the barrier is large compared with kT, not much error is introduced by replacing in the denominator of Eq. (3) the function ϕ by $[\phi(x_0, y, z, q_i) + \frac{1}{2}Kx^2]$, where K is the force constant for a small region about $x_0 = 0$. With this approximation Eq. (3) becomes

$$\frac{1}{\tau} = n' \frac{\int_{-\infty}^{\infty} \cdots \int \exp[-\phi(x', y, z, q_i)/kT] dydz \prod_i dq_i}{\int_{-\infty}^{\infty} \cdots \int \exp[-\phi(x_0, y, z, q_i)/kT] dydz \prod_i dq_i} \cdot \frac{\int_0^{\infty} \frac{P_x}{M} \exp[-P_x^2/2MkT] dp_x}{\int\int_{-\infty}^{\infty} \frac{P_x}{M} \exp\left[-P_x^2/2MkT - \frac{kx^2}{2kT}\right] dp_x dx} \tag{4}$$

The second factor can be evaluated to yield $(1/2\pi)(K/M)^{\frac{1}{2}}$; this is just the frequency, ν, of small oscillations about x_0. The first fraction represents the ratio of two partition functions, the numerator that for the system with the particle moving in the yz plane at x', the denominator that for the system with the particle moving in the yz plane at x_0. Thus

$$1/\tau = n'\nu P'/P_0. \tag{5}$$

For comparison one would write a corresponding equation from the work of Eyring[3] and others

$$1/\tau = n'kTP'/hP_0^*. \tag{6}$$

Here kT/h represents the quantum-mechanical "frequency factor" and P' the same function as in Eq. (5). P_0^* on the other hand is different from P_0 since P_0^* still contains integration over the coordinate x; such integration has been carried out explicitly in Eq. (5). We will see at once that it is on precisely this point that the present work deviates from that of Eyring.

In terms of thermodynamical functions Eq. (5) can be written

$$1/\tau = n'\nu \exp[-\Delta G/RT]. \tag{7}$$

Here ΔG is the work done when a mole of solute atoms is moved isothermally from x_0 to x' at constant pressure. Since

$$\Delta G = \Delta H - T\Delta S,$$

Eq. (7) finally becomes

$$1/\tau = n'\nu \exp[\Delta S/R] \exp[-\Delta H/RT]. \tag{8}$$

Equation (1) can now be written

$$D = \alpha a^2 n'\nu \exp[\Delta S/R] \exp[-\Delta H/RT]. \tag{9}$$

ΔS and ΔH are termed the entropy and entalpy of activation; since there is at present no way to calculate these quantities, they must be determined by experiment. Such a determination is made in Section IV.

Eyring's analog to Eq. (7) is[3]

$$1/\tau = n'(kT/h) \exp[-\Delta F^*/RT], \tag{10}$$

where ΔF^* is again termed the "free energy of activation." From this expression it follows that

$$1/\tau = n'(kT/h)\exp[\Delta S^*/R]\exp[-\Delta H^*/RT], \quad (11)$$

where ΔS^* and ΔH^* are corresponding entropy and heat of activation. Since Eqs. (8) and (10) have been derived using the same general method and with the same initial assumptions, they ought to be equivalent and formally they are. Any apparent difference must be one of interpretation; this difference may be expressed in this way. We have seen in Eq. (7) that ΔG represents the work necessary to move isothermally from x_0 to x' one mole of solute atoms which are oscillating in the yz plane—both the initial and final states represents the same number of degrees of freedom for the solute atom. In Eq. (10), ΔF^* represents the work necessary to move isothermally from x_0 to x' a mole of atoms which have one more degree of freedom at x_0 than they do at x'—namely, the coordinate x. This is a direct result of the fact that in Eq. (6) P_0^* contains one more degree of freedom than P'. It seems to the present writer that ΔG as defined above thus has a much more reasonable physical interpretation than does ΔF^*. Hence, Eq. (7) is preferred at least in this simple case to Eq. (10).[4]

III. METHOD OF EXPERIMENT

The experimental values of D to be reported in Section IV are for the diffusion of C in α-iron. Those values of D determined in this laboratory were made by direct use of Eq. (1). Since α and a are well known for the b.c.c. α-iron, the only further measurement needed was the value of τ as a function of temperature. This was found by measuring, at selected temperatures, the relaxation time, τ_r, which will be shown to be related simply to τ. The relaxation time can be described in the following way: At equilibrium under no stress the atoms of carbon arrange themselves in equal numbers among the three types of lattice positions, the x, y, z sites. This can be expressed by writing $N_x^0 = N_y^0 = N_z^0 = N/3$. Let this equilibrium be disturbed by the transfer of an equal number of atoms from the y and z positions to the x position. (A carbon atom which migrates to, say, an x position has an equal chance of coming from a y or a z position; it cannot come directly from another x position.) The state of affairs is then expressed by the relations

$$N_x = N_x^0 + \Delta n',$$
$$N_y = N_z = \tfrac{1}{3}N - \tfrac{1}{2}\Delta n'.$$

The rate at which equilibrium is approached is given by the well-known exponential decay law

$$d(\Delta n)/dt = -\Delta n/\tau_r, \quad (12)$$

where Δn is the net number of atoms which must yet migrate for the equilibrium to be established, and τ_r is the relaxation time.

The relationship between τ and τ_r for a b.c.c. lattice is given by the equation

$$\tau = \tfrac{3}{2}\tau_r. \quad (13)$$

That this is true can be seen from the following argument. The probability for an atom which is at a given lattice site at time $t=0$ of remaining in that site is given by

$$P(t) = e^{-t/\tau}.$$

If N_x, N_y, and N_z be the number of atoms in positions x, y, and z then change in the number of atoms in, say, the x position in a time Δt short compared to τ is

$$\frac{dN_x}{dt}\Delta t = -\frac{N_x}{\tau}\Delta t + \frac{N_y}{2\tau}\Delta t + \frac{N_z}{2\tau}\Delta t. \quad (14)$$

Since $N_x + N_y + N_z = N$, Eq. (14) can be written as

$$dN_x/dt = -(N_x/\tau) + (N - N_x)/2\tau$$

which is equivalent to

$$d(N_x - \tfrac{1}{3}N)/dt = -3(N_x - \tfrac{1}{3}N)/2\tau.$$

In terms of quantities used in the preceding paragraph, this equation becomes

$$d\Delta n/dt = -3\Delta n/2\tau. \quad (15)$$

Equation (13) follows at once from a comparison of

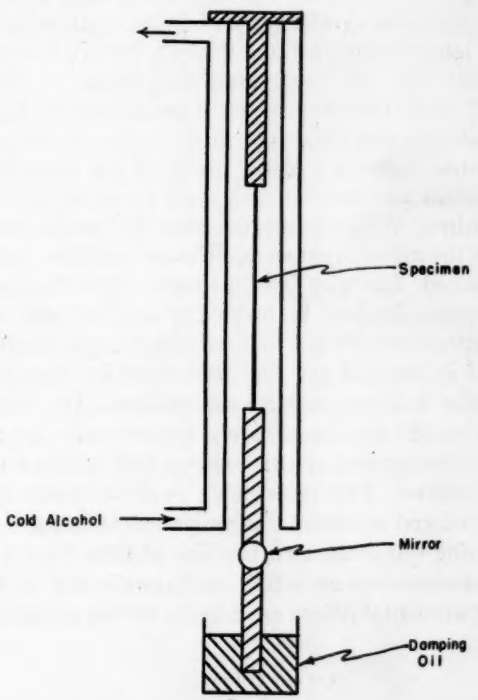

FIG. 1. Schematic diagram of apparatus used to measure elastic aftereffect.

[4] It has been shown by Wert and Zener (reference 2) that by appropriate treatment of Eq. (6) one can arrive also at Eq. (7).

Eqs. (12) and (15). It follows from Eqs. (1) and (13) that D can be computed once τ_r is known.

The relaxation times at different temperatures were measured by different experimental methods; use of a given method depended upon the magnitude of τ_r at a given temperature. At temperatures in the neighborhood of 0°C and less, the elastic aftereffect was used. At somewhat higher temperatures τ_r was measured by the internal friction method; at temperatures of about 40°C a torsional pendulum was used at approximately 1 c.p.s.; at 90° and 125°C a magnetic drive method was used at 100 and 1000 c.p.s., respectively. At still higher temperatures, a precipitation method was used. A brief description of these various methods follows.

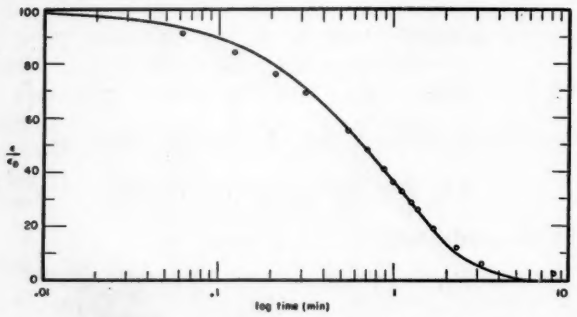

FIG. 2. Elastic aftereffect of C in α-iron at −10°C. $\epsilon=\epsilon_0 e^{-t/.98}$.

The elastic aftereffect has previously been employed to measure relaxation phenomena.[5] In the present case the experiment was performed in the following way:

The specimen (a wire of iron 0.03 in. in diameter and 1 foot long containing about 0.02 wt. percent C in solid solution) was mounted vertically inside a double-walled round chamber shown schematically in Fig. 1. Cold alcohol was circulated in the region between the concentric walls to cool the inside of the chamber. A light beam was focused on a scale three meters away by a mirror. With this arrangement the angular deflection of the mirror from an equilibrium position could be determined. The wire is held rigidly at the top by its supporting member. In making a measurement of τ_r the bottom support was first twisted through about 10° around its vertical axis and held there for some time. Then the bottom support was released. The angular deflection did not immediately become zero; approximately five percent of the previous strain (about 0.5°) still remained. This recoverable anelastic strain gradually reduced to zero; the measurement consisted in measuring this strain as a function of time.

A measurement at −10°C is shown in Fig. 2. Here the experimental points are fitted with the exponential form

$$\epsilon=\epsilon_0 \exp(-t/\tau_r) \qquad (16)$$

where t is the time after release of the bottom supporting member. It is seen that the experimental points do not fit the exponential exactly; the reason for this is not known. However, an average can be determined to an accuracy of at least 15 percent, which is adequate for our purposes.

The internal friction measurements with the torsional pendulum[2] and with the magnetic drive apparatus[5,6] are adequately described. The observation consists in a measurement of the temperature at which the maximum occurs in the internal friction for a given frequency, ω. Then τ_r is determined from the relation $\tau_r=1/\omega$. For the torsional pendulum, the specimens were wires 0.03 in. in diameter and 1 foot long. For the magnetic-drive method the specimens were two light bars of iron. One of these was about 1 foot long and about 0.1 in. in diameter; this gave resonance in flexural oscillations at about 100 c.p.s. The other was about 6 in. long and about 0.15 in. in diameter; it was resonant at about 1000 c.p.s.

It was at first thought to be reasonable to carry the internal friction type of measurements to higher temperatures by going to higher frequencies. This was prevented by the occurrence of rapid precipitation into Fe_3C of the supersaturated solid solution of C; such a process made good data difficult to obtain. However, by making use of the phenomenon of precipitation itself, two additional points at higher temperatures were obtained. The method is explained in this way. Let a highly supersaturated solution of carbon in α-Fe be prepared. Precipitate this carbon at some temperature T_1 and measure the amount of precipitate as a function of time. Find the time t_1 at which say half of the carbon has precipitated. Redissolve the precipitate at high temperature, quench, and reprecipitate say 10 percent of the carbon at T_1. Let the time required for this be t_0. Complete the precipitation at some higher temperature T_2. Let the time required for 50 percent of the transformation be t_2. These times are shown schematically

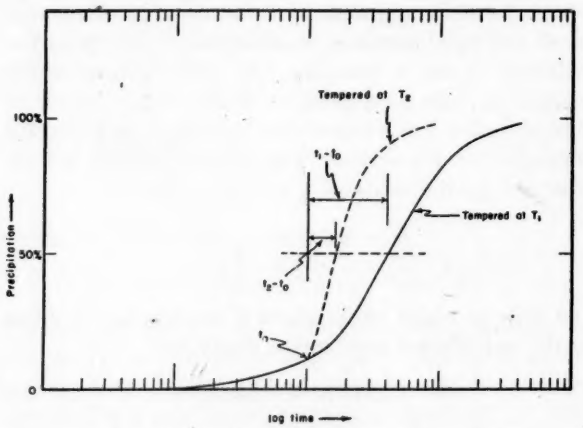

FIG. 3. Precipitation at temperatures T_1 and T_2 following nucleation at T_1.

[5] C. Zener, *Elasticity and Anelasticity of Metals* (University of Chicago Press, 1948).

[6] T. S. Kê, J. Metals (to be published).

in Fig. 3. It can be shown readily from earlier results from this laboratory[7] that under the conditions of the experiment the diffusion coefficients D_1 and D_2 at T_1 and T_2 are related by the equation

$$D_2=D_1(t_1-t_0)/(t_2-t_0).$$

If D_1 is known, D_2 can be computed.

IV. EXPERIMENTAL RESULTS

The results of all the measurements are shown in Fig. 4 in which log$D$ is plotted as a function of $1/T$. Four measurements were made by the elastic aftereffect technique, five with the torsional pendulum, two by the higher frequency internal friction method, and two more using the precipitation method. These last two points were made in two stages. One step was from 125° (where D had previously been measured) to 150°C; the next step going from 150° to 200°C. It seemed unwise to go any further than this since the measurements are not independent and errors are cumulative. These last two points are for this reason probably the least reliable.

The very high temperature data are from work reported by Stanley,[8] and were made by chemical analysis following bulk diffusion of C from a high (0.02 wt. percent) to a low carbon alloy. The remaining three points are computed from some carefully done work of Richter who in 1938 reported an aftereffect in carbonyl iron.[9] Though he did not know the cause of the effect which he observed, it appears from the agreement of his results with the present data that he, too, was measuring the relaxation effect of C in his material.

The solid line in Fig. 4 was drawn according to the equation

$$D=D_0e^{-\Delta H/RT} \tag{17}$$

where D_0, according to Eq. (9), is

$$D_0=\alpha a^2\nu n' e^{\Delta S/R}. \tag{18}$$

The parameters D_0 and ΔH in Eq. (17) were adjusted to give the best fit to the data (excluding that of Richter); these values are $D_0=0.02$ cm²/sec. and $\Delta H=20{,}100$ cal./mole. In Fig. 4 it is seen that the fit of Eq. (17) to the data is good. Using Eq. (18) it is possible to compute ΔS; such a computation gives $\Delta S\approx 5$ cal./mole °C. This value of ΔS is in good agreement with earlier work of Wert and Zener[2] concerning the theoretical range of ΔS. According to them ΔS may have the range zero to 5 cal./mole °C. Since the value of

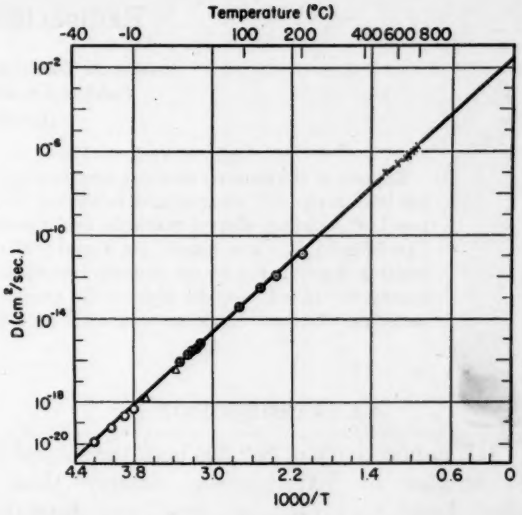

FIG. 4. Diffusion coefficient of C in α-iron as a function of $1/T$. The experimental data are identified in the following way: Elastic aftereffect—○; internal friction—⊕; precipitation measurements—⊙; elastic aftereffect (Richter)—△; bulk diffusion measurements (Stanley)—×. The straight line is drawn according to the relation $D=D_0\exp(-\Delta H/RT)$.

ΔS computed above, namely about 5 cal./mole °C, is near the top of the predicted range, a large part of the energy of activation must go into lattice strain energy. In passing it might be well to note that this calculation indicates that the transmission coefficient mentioned earlier is of the order unity. If it were considerably less than 1, the factor $e^{\Delta S/R}$ in Eq. (18) would have to be larger so that D_0 could keep its experimentally determined value. A very large increase in ΔS would be difficult to explain; hence, the conclusion must be that for the present case, the transmission coefficient is of order 1.

Because of the thermodynamic properties of ΔG, ΔS, and ΔH, it can be shown that

$$d(\ln D)/d(1/T)=\Delta H/R.$$

This means that at any temperature the slope of the curve in Fig. 4 gives the value of ΔH at that temperature. This is true regardless of how ΔH and ΔS might vary with temperature. That the experimental points in Fig. 4 can be fitted with a straight line means that over this temperature range ΔH is constant. This fact is perhaps the most surprising result of the analysis of the experimental work.

The author would like to express his gratitude to Mr. Robert Heikes and Mr. Ronald Sladek for assistance in making the measurements, and to Dr. Zener for numerous suggestions and discussions.

[7] C. Wert, J. App. Phys. **20**, 943 (1949). C. Zener, J. App. Phys. **20**, 950 (1949).
[8] J. K. Stanley, J. Metals **1**, 752 (1949).
[9] G. Richter, Ann. d. Physik **32**, 683 (1938).

Radioactivity of Scandium[44]*

JOSEPH A. BRUNER† AND LAWRENCE M. LANGER
Indiana University, Bloomington, Indiana
(Received May 8, 1950)

Because of the unusual beta-ray spectrum previously reported by Smith, a study of the Sc^{44} radioactivity has been made. Sc^{44} was prepared according to the reaction $K^{41}(\alpha, n)Sc^{44}$, and the activity was examined in two 180° focusing, shaped magnetic field spectrometers. A single positron group ($E_0=1.463\pm0.005$ Mev; $T_{\frac{1}{2}}=4.0\pm0.1$ hr.) was found; the Fermi plot of its momentum distribution has the allowed shape. The positron decay is fed by an isomeric transition ($E=271.3\pm0.7$ kev; $T_{\frac{1}{2}}=57\pm2$ hr.) and is followed by a gamma-ray ($E=1.16\pm0.01$ Mev) to the ground state of Ca^{44}. No positron transition directly to the ground state was observed. Evidence was found for a high proportion of K-capture to the excited state of Ca^{44}.

I. INTRODUCTION

THE radioactivity of Sc^{44} has been the subject of a number of investigations, notably those of Walke,[1] Smith,[2] and Hibdon, Pool, and Kurbatov.[3] The measurements, except those of Smith, were made using absorption techniques. Walke reported the presence of a 250-kev internally converted gamma-ray having a 52-hr. period, and positrons having 4.1-hr. and 52-hr. periods. Since the positron groups were found to have the same end-point energy, *viz.*, 1.50 Mev, Walke proposed a decay scheme (see Fig. 1 and Table I) according to which the gamma-ray emission represents an isomeric transition from a metastable state in Sc^{44} to the state from which the positron is emitted.

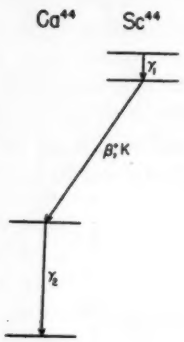

FIG. 1. Decay scheme for Sc^{44} (see Table I).

Hibdon, Pool, and Kurbatov obtained results in rough agreement with the above (see Table I), but found in addition a 1.33-Mev gamma-ray having the same composite period as that of the positrons, and evidence that the decay to Ca^{44} proceeded by means of K-capture about 50 to 75 percent of the time.

Smith, meanwhile, had made spectrometric measurements of the positron momentum distribution and of the internal conversion electrons from the long-lived gamma-ray, and arrived at approximately the same energy values (Table I). The most noteworthy of his results, however, was the unusual positron momentum spectrum obtained.[2] The shape of the Fermi plot of the momentum distribution shows a marked deviation from the straight line expected for an allowed transition. This suggests that either (1) the spectrum is complex, (2) the transition is forbidden, or (3) more than one isotope is present.

The first of these explanations is in disagreement with the findings of Walke and of Hibdon *et al.* The second seems very unlikely, because, even if the decay is 75 percent K-capture, the ft value for the positron transition is still less than 10^6. Smith considered the third possibility, but on the basis of several tests performed he concluded that not more than one isotope was present. Actually these tests, as described in

TABLE I. Summary of experimental results.[a]

Experimenter	Walke	Smith	Hibdon, Pool, and Kurbatov	Bruner and Langer
Method of production	$K^{41}(\alpha, n)Sc^{44}$	$Ca^{43}(d, n)Sc^{44}$	$K^{41}(\alpha, n)Sc^{44}$; $Sc^{45}(n, 2n)Sc^{44}$	$K^{41}(\alpha, n)Sc^{44}$
Method of measurement	Absorption	Spectrometer	Absorption	Spectrometer
γ_1 Period (hr.)	52±2	52±2	58.6±0.7	57±2
γ_1 Energy (kev)	250	269.3±1	280	271.3±0.7
β^+ Period (hr.)	4.1±0.1	4.1±0.1	3.92±0.03	4.0±0.1
β^+ Energy (Mev)	1.50±0.05	1.47±0.2	1.33	1.463±0.005
γ_2 Energy (Mev)	—	—	1.33	1.16±0.01
Coincidence measurements (absorption)	—	—	—	$\beta-\gamma$'s—1 group

[a] See also the decay scheme of Fig. 1.

* Assisted by ONR and AEC.
† AEC predoctoral fellow.
[1] H. Walke, Phys. Rev. **57**, 163 (1940).
[2] G. P. Smith, Phys. Rev. **61**, 578 (1942).
[3] Hibdon, Pool, and Kurbatov, Phys. Rev. **67**, 289 (1945).

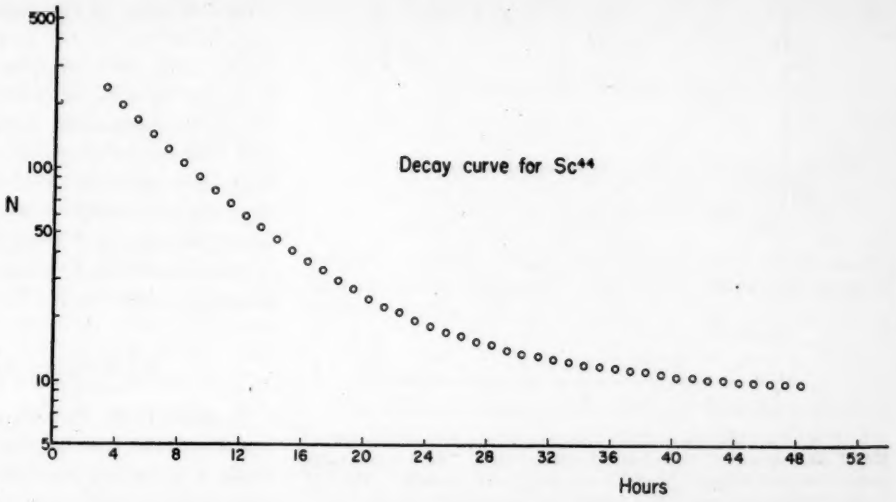

FIG. 2. Typical decay curve for Sc^{44}. To determine the periods of the activity, the decay was followed in this manner for five days.

detail,[4] appear to be inconclusive; this will be discussed later. In view of these facts it was considered worthwhile to reinvestigate the disintegration of Sc^{44}, with particular attention being paid to the positron spectrum.

II. EXPERIMENTAL APPARATUS AND METHODS

Sc^{44} was prepared according to the reaction $K^{41}(\alpha, n)Sc^{44}$. An enriched sample[4a] (92 percent K^{41}, 8 percent K^{39}) of K^{41} in the form of K_2SO_4 was bombarded with 17-Mev alpha-particles in the cyclotron, the bombardments ranging from 40 to 100 microampere hours. 0.5 mg carrier was added; the scandium was separated as $Sc(OH)_3$ and then redissolved in hot HCl.

Sources used for positron spectrum and conversion electron measurements were prepared by depositing the radioactive solution on a backing of 0.025 mg/cm² LC600 and drying it. The source thickness was about 0.4 mg/cm². Sources were electrically grounded at each end with 0.18 mg/cm² aluminum leaf.

The gamma-radiation was also studied by means of Compton and photo-electrons ejected from a 23-mg/cm² uranium radiator. The radiator was cemented to a small copper "box" inside of which the source solution was deposited and evaporated. The walls of the copper box were constructed $\frac{1}{32}$-in. thick in order to absorb all the positrons.

Two 180° focusing, shaped magnetic field spectrometers were employed in these studies, one[5] having a 15-cm radius of curvature, and the other[6] having a 40-cm radius of curvature (hereafter referred to as the "small" and "large" spectrometers, respectively). Sources for the small spectrometer measured 2 cm×0.3 cm, and those for the large spectrometer 2.7 cm×0.6 cm.

Simultaneously with each spectrometer run, the decay of the source material was followed automatically by means of a scaler feeding into a tape recorder. In this way decay corrections could be applied directly to the data. A typical decay curve is shown in Fig. 2.

In addition to the spectrometric studies, beta-gamma-coincidences were measured as a function of positron energy by varying the thickness of aluminum absorber between the source and positron counter.

III. RESULTS

A. Positron Spectrum

The positron spectrum was first measured in the small spectrometer. About 160 mg K_2SO_4 were bombarded in the cyclotron for $2\frac{1}{2}$ hours with a total of 45 microampere-hours of alpha-particles. Spectrometric measurements were begun 3 hours after the end of bombardment. The resulting Fermi plot is shown in Fig. 3. A number of points over the entire spectrum were remeasured several hours later, and these points, when corrected for decay by means of a curve such as in

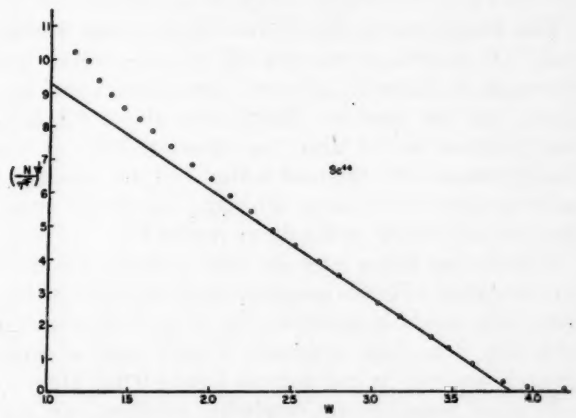

FIG. 3. Fermi plot of positron momentum distribution as measured soon after end of bombardment. The deviation from a straight line is caused by an impurity, probably Sc^{43}.

[4] G. P. Smith, Thesis, University of Michigan.

[4a] Supplied by the Y-12 Plant, Carbide and Carbon Chemicals Corporation, on allocation by the Isotopes Division of the United States AEC.

[5] J. A. Bruner and F. R. Scott, Rev. Sci. Inst. **21**, 545 (1950).

[6] L. M. Langer and C. S. Cook, Rev. Sci. Inst. **19**, 257 (1948).

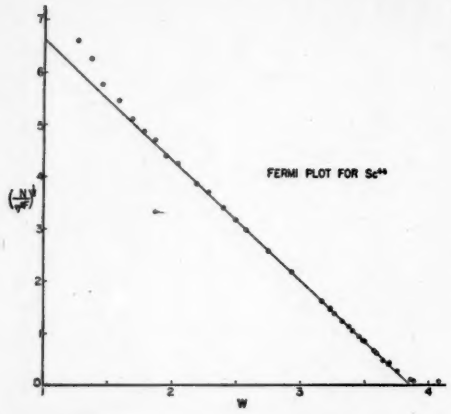

FIG. 4. Fermi plot of positron momentum distribution measured about 30 hours after the end of bombardment. The lower energy group does not appear, hence is not associated with Sc^{44}. The Sc^{44} positron spectrum end point energy is 1.463±0.005 Mev.

Fig. 2, appeared to be in good agreement with those taken earlier. This fact, together with the obvious curvature of the Fermi plot, was at first taken as evidence that two groups of positrons were present in the Sc^{44} activity[7] (the group of lower energy constituting only about 10 percent of the total).

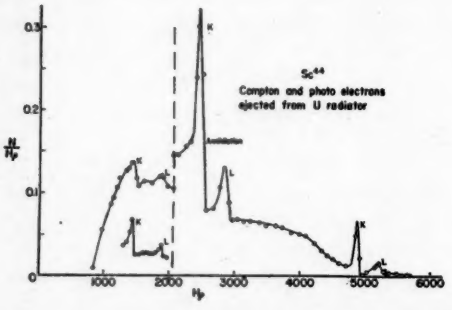

FIG. 5. Compton and photo-electrons from the 271.3-kev and 1.16-Mev gamma-rays. Points to the left of the dashed line have not been corrected for decay. The set of points at lower left was taken a day later than the rest.

The Fermi plot in Fig. 3 also shows a high energy "tail." To determine whether this tail was real or was the result of scattering, a more intense source was prepared, and the positron distribution above 1.3 Mev was examined in the large spectrometer. The tail was found to extend out to about 4 Mev, but the source was unfortunately too weak to determine accurately either the spectrum shape or the decay period.

Twenty-four hours later the main positron spectrum was measured with the same source in the large instrument. The result is shown in Fig. 4, and the contrast with Fig. 3 is quite apparent. Clearly only a single group is present; its end point is 1.463±0.005 Mev.

It then remained to determine whether the discrepancy was due to instrumental effects or to the different lapse of time after bombardment. The latter was found to be the case. A new bombardment was made, and two sources were prepared, differing in intensity by a factor of ten. The spectrum of the weaker source was measured immediately after bombardment, and that of the stronger source a day later, both in the large spectrometer. A comparison of the results showed that the low energy group, present soon after bombardment, disappeared after a day's decay. The indication is therefore that Sc^{44} has no positron group of energy less than 1.463 Mev.

[7] J. A. Bruner and L. M. Langer, Phys. Rev. **79**, 236 (1950).

B. Gamma-Ray Measurements

A search for gamma-rays was made in the small spectrometer, making use of the photo-electrons ejected from a uranium radiator. In addition to the intense annihilation radiation, two gamma-rays were found (see Fig. 5). Points to the left of the dashed line in Fig. 5 consist of photo-electrons from the 57-hour gamma-ray plus Compton electrons from all the gamma-radiation; hence in this region no attempt was made to correct the data for decay. Points to the right of the line have been corrected from a decay curve similar to that in Fig. 2. The lower set of points on the left was taken a day later.

Internal conversion electrons from these gamma-rays were sought and found in the large spectrometer. The results are shown in Fig. 6 and Table I. In Fig. 6 the 1.16-Mev line has been magnified 100 times.

C. Beta-Gamma-Coincidence Measurements

The beta-gamma-coincidence counting rate (see Fig. 7) was found to be constant up to 1.25 Mev, thus supporting the assertion that Sc^{44} has no positron group of less than that energy.

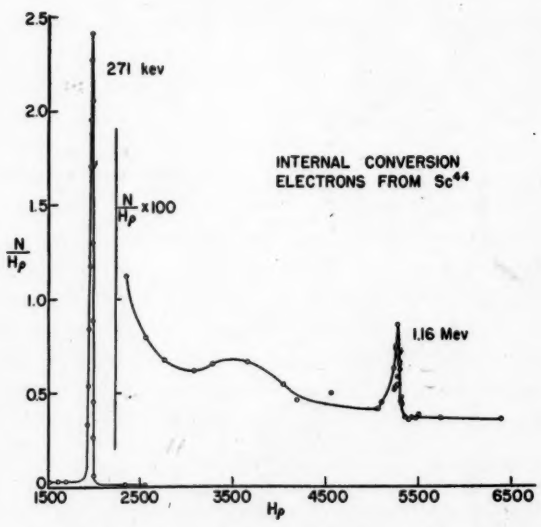

FIG. 6. Internal conversion electrons from the 271.3-kev and 1.16-Mev gamma-rays.

D. Conclusions

The activity of Sc^{44} can be represented by a decay scheme as in Fig. 1. The metastable state has a half-life of 57±2 hours and emits a gamma-ray of 271.3 ±0.7 kev. This is followed by a 1.463±0.005-Mev positron group having a period of 4.0±0.1 hr. A 1.16 ±0.01-Mev gamma-ray then completes the decay to the ground state of Ca^{44}. A comparison of the intensities of the annihilation radiation and the 1.16-Mev gamma-ray indicates that the 1.16-Mev gamma-ray is roughly twice as intense as is the positron disintegration. This argues in favor of a large proportion of *K*-capture, in agreement with Hibdon *et al.* Since, however, the amount of *K*-capture is not known accurately, the internal conversion coefficients cannot be calculated.

The positron transition directly to the ground state was not observed, possibly because its spectrum was masked by the high energy tail. On the basis of the nuclear shell model[8] one would expect the ground states of both Sc^{44} and Ca^{44} to have even parity; this indicates that the transition between these states is at least twice forbidden. If, as the *ft* value suggests, the positron transition to the excited state of Ca^{44} is allowed, then this excited state must also have even parity. Therefore the 1.16-Mev gamma-ray is probably either electric quadrupole or magnetic dipole radiation.[9]

It seems likely that the low energy positron group observed soon after bombardment is associated with the decay of Sc^{43}, which has a 1.1-Mev positron group[3] with a 3.92-hr. period. The Sc^{43} would be produced by the reaction $K^{41}(\alpha, 2n)Sc^{43}$. The high energy positron tail is most probably from either Sc^{42} [by $K^{39}(\alpha, n)Sc^{42}$] or Sc^{41} [by $K^{39}(\alpha, 2n)Sc^{41*}$], the long period in the latter case[10] resulting from a metastable state. An investigation of this question is planned for the near future.

[8] M. G. Mayer, Phys. Rev. **75**, 1969 (1949).
[9] S. M. Dancoff and P. Morrison, Phys. Rev. **55**, 128 (1939).
[10] L. D. P. King and D. R. Elliot, Phys. Rev. **60**, 489 (1941).

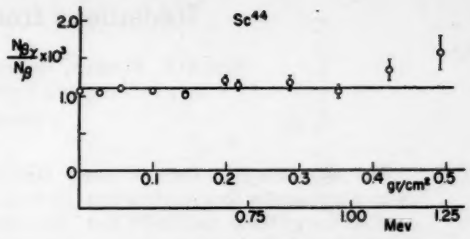

FIG. 7. Results of beta-gamma-coincidence measurements. The constant coincidence counting rate indicates a single group of positrons.

IV. DISCUSSION

The different results of Smith can now be explained in the following manner. In his experiment Sc^{44} was produced by $Ca^{43}(d, n)Sc^{44}$; but since Ca^{42} is almost 5 times as abundant naturally as Ca^{43}, it is to be expected that a large portion of Sc^{43} would be produced by the same type of reaction. The tests made by Smith to determine if more than one isotope were present were (1) comparison of spectral shapes, using bombarding deuterons of different energies, (2) observation of the decay at different values of $H\rho$, and (3) observation of the upper end point as a function of time. These tests would not serve to detect the presence of Sc^{43}, however, because *all of the test measurements*[4] *were made at or above 1.1 Mev;* i.e., near or beyond the Sc^{43} positron end point. Furthermore, Smith's curve can be resolved into two straight lines. On this basis, the end point of the lower group would be about 1.15 Mev. These facts indicate that a large fraction of Sc^{43} was present in his sources.

The authors wish to express their gratitude to Dr. Milo B. Sampson and the cyclotron crew for making the alpha-particle bombardment.

This work has been supported by a grant from the Frederick Gardner Cottrell Fund of the Research Corporation and by the joint program of the ONR and AEC.

Radiations from Os^{185}, Os^{191}, and Os^{193}*

MERLE E. BUNKER, ROBERT CANADA, AND ALLAN C. G. MITCHELL
Indiana University, Bloomington, Indiana

(Received May 10, 1950)

The radiations from Os^{185} (97 days), Os^{191} (32 hr.) and Os^{193} (15 days) have been investigated with the help of a magnetic lens spectrometer. Os^{185} decays by orbital electron capture accompanied by two gamma-rays of energy 0.648 and 0.878 Mev. The number of gamma-ray quanta of 0.648 Mev is six times that of 0.878 Mev. Os^{191} decays by the emission of beta-rays of maximum energy 1.10 Mev and does not appear to be accompanied by any gamma-rays. Os^{193} decays by beta-particle emission accompanied by two gamma-rays of energy 0.128 and 0.041 Mev. The beta-ray spectrum is obscured by internal conversion and Auger lines. The end point is approximately 0.135 Mev.

I. INTRODUCTION

WHEN osmium is bombarded with slow neutrons, three activities result with respective half-lives of approximately 32 hr., 15 days, and 97 days. The 15-day activity has been associated with Os^{193}. Early measurements[1] indicated that the half-life was 17 days, but by correcting for the presence of the 97-day activity, Katzin and Pobereskin[2] have shown it to be nearer 15 days. They report the decay to take place by emission of a beta-ray of energy not more than 0.165 Mev, followed by a highly converted 0.13-Mev gamma-ray and abundant x-rays. More recently, the spectrometer measurements of Saxon[3] have revealed a beta-ray end point of 0.142 Mev and two gamma-rays, one of 0.127 Mev and the other 0.039 Mev.

The 97-day activity is attributed to Os^{185} and was first observed by Goodman and Pool,[4] who produced it by a deuteron bombardment of rhenium. Katzin and Pobereskin[2] have also produced the activity with slow neutrons, and their absorption measurements indicated the presence of a 0.75-Mev gamma-ray and K and L x-rays. They found a relatively high ratio of soft quantum to hard quantum counts, and concluded that Os^{185} must decay predominantly by orbital electron capture.

Seaborg and Friedlander[1] assigned the 32-hr. activity to Os^{191} and reported that the radiation consists of a 1.5-Mev beta-ray and at least one gamma-ray. Goodman and Pool[4] have produced this activity by the action of deuterons on osmium and, using absorption methods, found a beta-ray end point of 0.95 Mev and a 1.17-Mev gamma-ray. Later Mandeville, Scherb, and Keighton,[5] using an osmium source which had been exposed to neutrons in a pile for one-half hour, measured

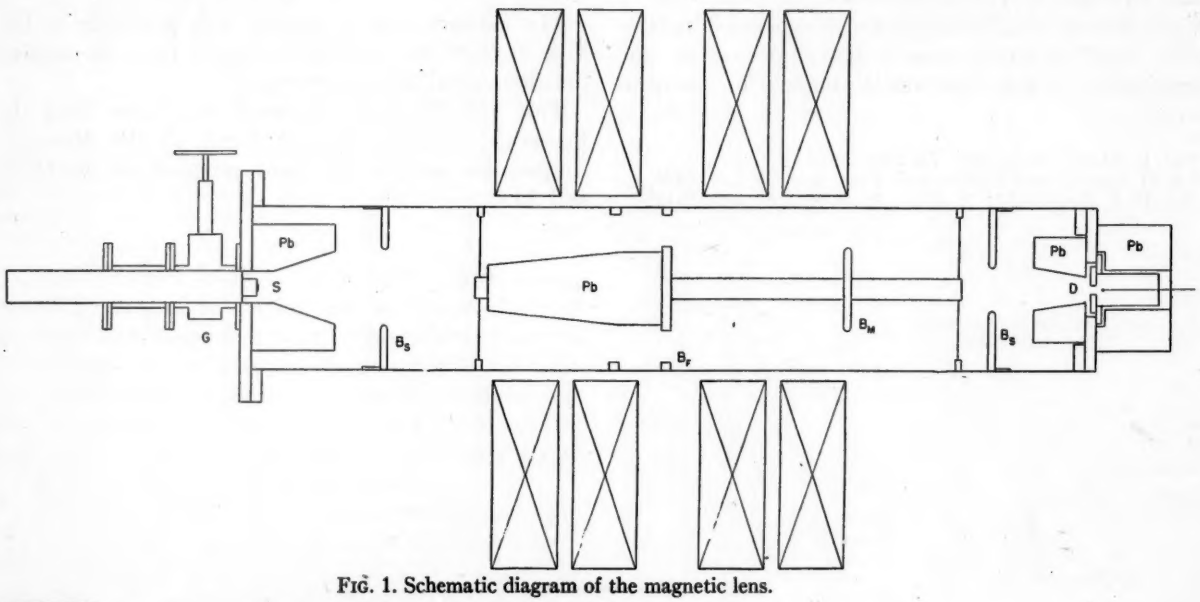

FIG. 1. Schematic diagram of the magnetic lens.

* This research was assisted by the joint program of the ONR and AEC.

[1] G. T. Seaborg and G. Friedlander, Phys. Rev. **59**, 400 (1941).
[2] L. I. Katzin and M. Pobereskin, Phys. Rev. **74**, 264 (1948).
[3] D. Saxon, Phys. Rev. **74**, 1264 (1948).
[4] L. J. Goodman and M. L. Pool, Phys. Rev. **71**, 288 (1947).
[5] Mandeville, Scherb, and Keighton, Phys. Rev. **71**, 288 (1947).

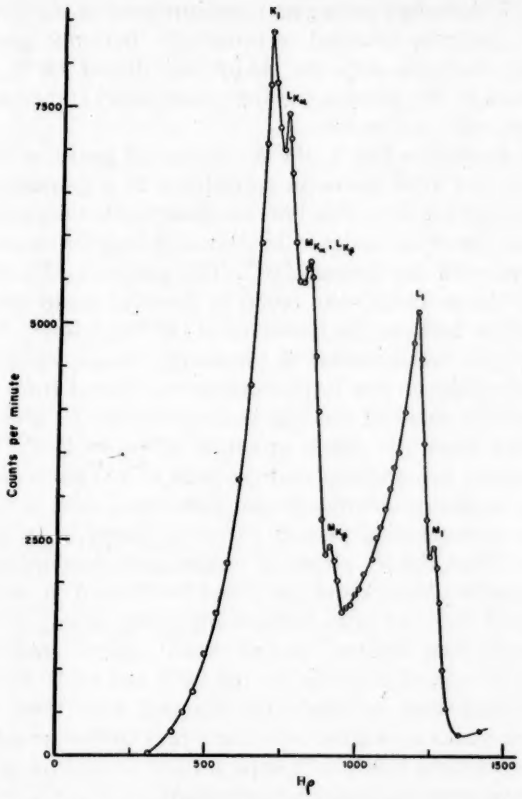

FIG. 2. Photo-electrons ejected from lead by gamma- and x-rays of Os^{193} and Os^{185}. (K_1—0.128-Mev Os^{193}); ($L\kappa_\alpha$ and $L\kappa_\beta$—x-rays of Ir^{193} and Re^{185}).

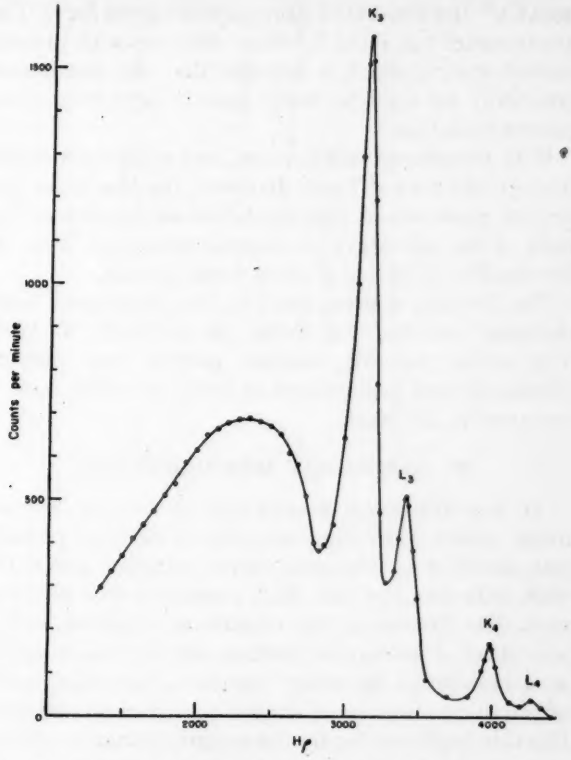

FIG. 3. Secondary electrons ejected from lead by gamma-rays of Os^{185}. (K_3—0.648 Mev); (K_4—0.878 Mev).

the beta-ray end point by absorption techniques and found a value of 1.15 Mev. In addition they found gamma-rays of energy 0.22 and 1.58 Mev. A small number of beta-gamma- and gamma-gamma-coincidences were observed.

In an effort to clarify some of the above-mentioned discrepancies, the radiations from the three osmium activities have been investigated with the aid of a magnetic lens spectrometer. No previous investigators have made a spectral analysis of both the beta- and gamma-radiations from these isotopes with an instrument of comparable resolving power.

II. APPARATUS

The magnetic lens spectrometer used in this work is of conventional design, similar to the instrument described by Deutsch, Elliott, and Evans.[6] The magnetic field used for focusing electrons is produced by four water-cooled coils which can be moved in pairs. Each coil measures $3\frac{5}{32}$ in. in thickness, $8\frac{1}{2}$ in. I.D., 28 in. O.D., and is wound with 1356 turns of 0.136 in. sq. copper wire covered with glass fiber insulation. Inner or outer coil sections may be used separately. In this experiment the coil pairs were $3\frac{1}{8}$ in. apart, placed symmetrically with respect to the center of the system, and all coil sections were used.

The vacuum chamber (Fig. 1) is a seamless brass tube 8 in. in diameter and 39 in. long containing suitable baffles and shielding. The fixed ring, B_F, and the movable disk, B_M, define the annular opening of the spectrometer. The size of the annulus through which the electrons are accepted is adjusted by moving the inner defining disk. This adjustment is made by means of a rod which passes through a Wilson seal at the end of the tube. Antiscattering baffles, B_S, and the lead shielding reduce the scattered and direct background radiation. The source ring, S, is placed in a Lucite holder mounted on the end of a brass tube which is passed into position through a gate valve and Wilson seal. The counter and its lead shield are fastened to the cover plate at the other end of the chamber and connections are made to a ballast tank so the counter can be evacuated and filled in position. This permits the use of thin zapon and Formvar films for counter windows.

The earth's magnetic field is neutralized in the region of the spectrometer chamber by a pair of rectangular coils, placed above and below the vacuum chamber with their axes parallel to the earth's field.

Since the instrument contains no iron, the focusing field is proportional to the current. The instrument has been calibrated by measuring the annihilation radiation

[6] Deutsch, Elliott, and Evans, Rev. Sci. Inst. 15, 178 (1944).

from Cu^{64} and the 0.4112-Mev gamma-ray of Au^{198}. The spectrometer can focus 8.5-Mev electrons with present current sources and it is intended that this instrument eventually be used to study prompt and short-lived gamma-radiation.

With the present coil location, and using sources and counter windows of 7-mm diameter, the lens gives two percent resolution at high resolution adjustment on the basis of the half-width of internal conversion lines. At low resolution setting it gives three percent.

The osmium sources used in the experiment were obtained from the Oak Ridge pile of the U. S. AEC. The active metallic osmium powder was purified chemically and precipitated as Os_2S_3, in which form it was used in this work.

III. GAMMA-RAY MEASUREMENTS

To investigate the gamma-rays of osmium, the osmium sulfide, exhibiting activities of all three periods, was placed in a cylindrical copper capsule 9 mm O.D., with walls and end just thick enough to stop all beta-rays. The flat end of the capsule was covered with a lead sheet of 16-mg/cm^2 surface density, which served as a radiator of secondary electrons. The distribution of photo-electrons and Compton electrons ejected from this thin lead radiator by the osmium gamma-radiation was examined in the lens a few hours after the source was received from Oak Ridge. The secondary electron spectrum obtained is shown in two parts, the low energy spectrum in Fig. 2 and the higher energy spectrum in Fig. 3. Although subsequent measurement of the beta-ray spectrum revealed a prominent beta-ray group which decayed with the 32-hr. half-life of Os^{191}, no portion of the gamma-spectrum was found to be associated with this period.

Referring to Fig. 2, the K, L, and M peaks at 695, 1193, and 1264 gauss-cm correspond to a gamma-ray of energy 128 kev. This line was observed to decay with a half-life of the order of 15 days and therefore is associated with the isotope Os^{193}. The peaks at 753, 831, and 916 gauss-cm were found to decay at a rate intermediate between the half-lives of Os^{193} and Os^{185}. This fact, plus consideration of the energy values, identifies these peaks as due to photoelectrons ejected from the L and M shells of the lead radiator by the K_α and K_β x-rays from the decay products Ir^{193} and Re^{185}. For example, by assuming that the peak at 753 gauss-cm is due to photo-electrons ejected from the L shell of lead, the corresponding photon energy is found to be 63.6 kev. Since the K_α x-rays of iridium and rhenium have respective energies of 64.1 and 60.6 kev,[7] it would appear that the peak in question is due mainly to the x-rays from iridium, as one would expect from the initial ratio of activities of the Os^{193} and Os^{185}. It was observed that as this ratio changed with time, the three peaks associated with the x-rays shifted nearer to the positions one would expect them to occupy if the x-rays were due entirely to rhenium.

In Fig. 2, the prominent K and L photo-electron peaks at 3128 and 3408 gauss-cm correspond to a

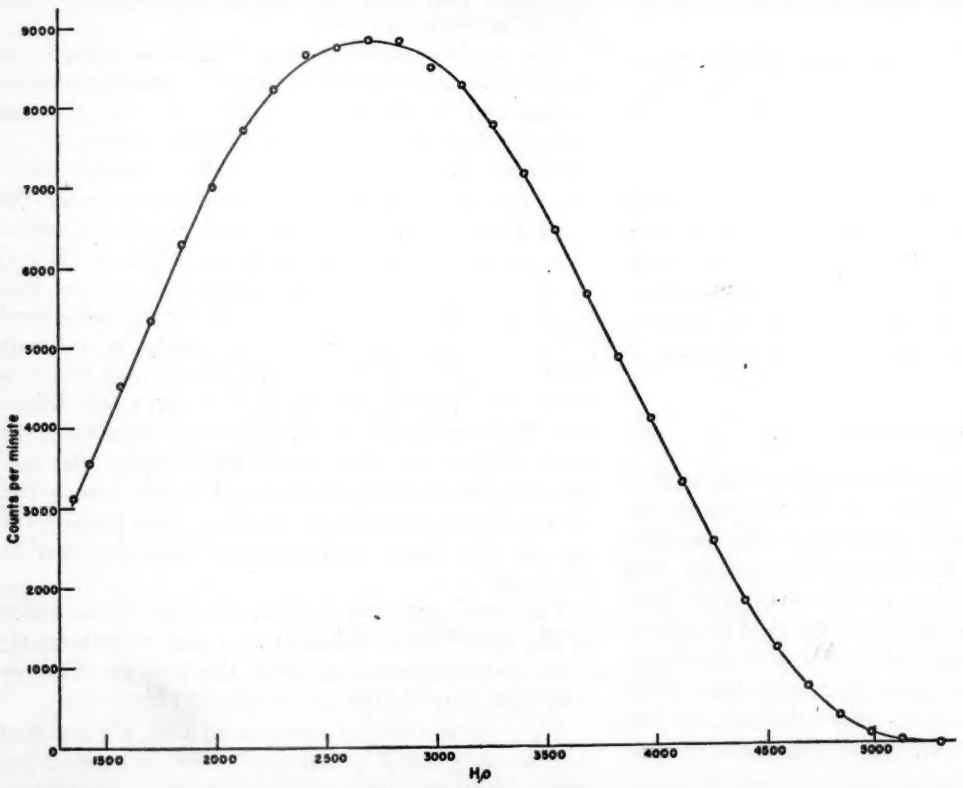

FIG. 4. Beta-ray spectrum of Os^{191}.

[7] A. H. Compton and S. K. Allison, *X-Rays in Theory and Experiment* (D. Van Nostrand Company, Inc., New York, 1935).

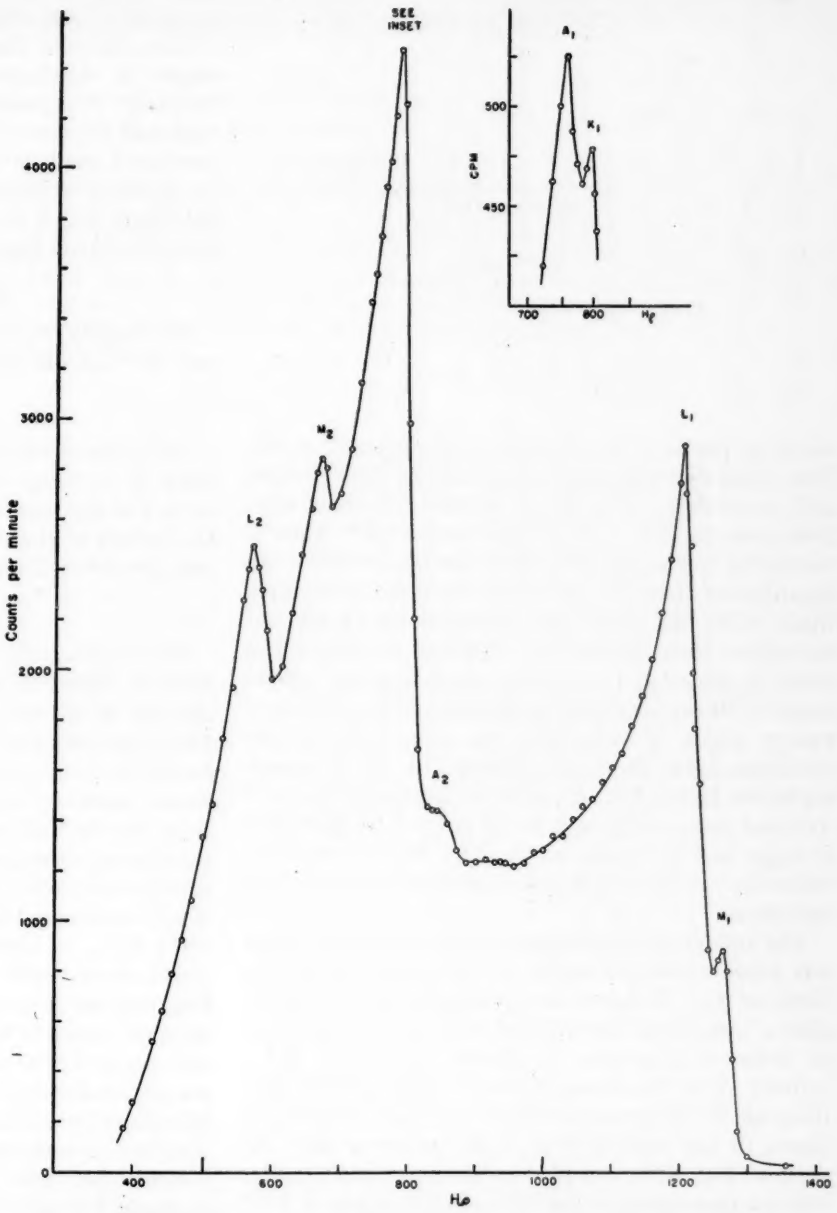

FIG. 5. Low energy beta-ray spectrum of Os^{193} and Os^{185}. (K_1 —0.128-Mev Os^{193}); (L_2—0.041-Mev Os^{193}); (A_1 and A_2—Auger lines from Ir^{193} and Re^{185}).

gamma-ray of 648-kev energy, and the two smaller peaks farther out on the curve correspond to the K and L peaks of a gamma-ray of 878-kev energy. Intensity measurements taken over a period of months indicate that the half-life of both lines is in the neighborhood of 95 days. Consequently, these two gamma-rays undoubtedly arise from the isotope Os^{185}. The areas under the 648- and 878-kev lines have been integrated graphically (on an $N/H\rho$ plot) and their ratio taken after properly correcting for the variation of the photoelectric absorption coefficient as a function of the energy by use of Gray's[8] empirical data. This gives a value of 6:1 for the ratio of the number of quanta of 648-kev energy to the number of quanta of 878-kev energy.

[8] L. H. Gray, Proc. Camb. Phil. Soc. **27**, 103 (1931).

IV. BETA-RAY MEASUREMENTS

In order to have a beta-ray source of sufficient activity that the spectrum could be studied over a period of months so that the various activities could be separated, it was necessary to use a source of about 10-mg/cm² surface density. The source material was mounted on a paper backing of surface density 0.67 mg/cm² and covered with a thin layer of zapon. An examination of the beta-ray spectrum approximately half a day after the source was received from Oak Ridge revealed the presence of a high energy beta-group and a relatively much stronger group of peaks below 1350 $H\rho$. Measurement of the decay of the higher energy group gave a half-life of about 32 hr., and consequently this group was identified as the hard beta-ray of Os^{191}

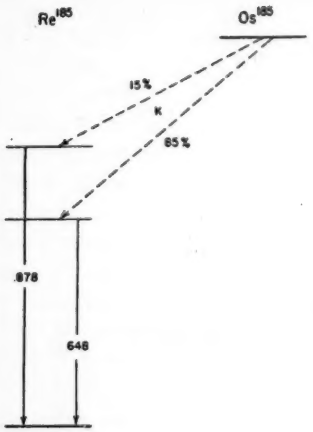

FIG. 6. Proposed disintegration scheme for Os^{185}.

found by previous investigators. Superimposed on this beta-group were small peaks identified by their energies and rate of decay to be due to internal conversion electrons from the 648- and 878-kev lines of Os^{185}. Thus to obtain the true shape of the beta-spectrum of Os^{191}, the contribution from the Os^{185} was measured some three weeks after the initial run, corrected for decay, and subtracted from the original composite spectrum. The result is shown in Fig. 4. The curve does not extend below 1350 gauss-cm due to interference from the low energy group. A Fermi plot has been made of this spectrum, using the approximation for the Coulomb correction factor, $F(Z, E)$, given by Bethe and Bacher.[9] The end-point energy was found to be 1.10 Mev. The ft value was calculated to be 2.1×10^7 and thus the transition would be expected to be either first or second forbidden.

The prominent low energy group mentioned above was found to be due mainly to the 15-day Os^{193}. The curve of Fig. 5 shows the appearance of this group after a three-week interval had been allowed to elapse in order to eliminate interference from the 32-hr. activity. After the elapse of several additional months, the peak at 782 gauss-cm was found to be complex, as shown in the inset of Fig. 5. By assuming that the peaks at 792, 1203, and 1264 gauss-cm are produced by internal conversion in the K, L, and M shells of Ir^{193}, one obtains a value of 128 kev for the energy of the gamma-ray, which agrees with the value obtained from the gamma-spectrum. The peaks at 570 and 670 gauss-cm, which were also found to decay with the 15-day period, correspond to electron energies of 28 and 38 kev. Since the L and M binding energies of iridium also differ by 10 kev, it is concluded that these peaks are due to internal conversion electrons produced by a 41-kev gamma-ray from Os^{193}. The peaks at 760 and 835 gauss-cm are identified as composite Auger electron lines resulting from the internal conversion process in Ir^{193} and the K-capture process of Os^{185}.

It is readily seen, by further examination of the curve of Fig. 5, that in addition to the peaks discussed above, there is some sort of underlying electron distribution. This distribution can reasonably be assumed to be the beta-ray spectrum of Os^{193}. However, this beta-ray group is so completely obscured by the internal conversion electrons that little can be said with certainty about its maximum energy, its complexity, or its intensity. It is possible, but not definite, that the flat region of the curve in the vicinity of 925 gauss-cm is a portion of the beta-ray spectrum. At least this portion of the curve establishes a maximum height for the beta-spectrum. Also it is evident that the beta-ray spectrum does not extend beyond about 1300 gauss-cm (135 kev).

V. DISCUSSION

The results which have been obtained on Os^{185}, Os^{191}, and Os^{193} are discussed below.

(a) Os^{191}

Os^{191}, whose half-life is 32 hr., appears to decay entirely by beta-ray emission unaccompanied by gamma-rays. The maximum energy of the beta-rays determined as a result of the present measurements is 1.10 Mev, and the comparative half-life is 2.1×10^7 sec.

(b) Os^{185}

Os^{185} appears to decay entirely by orbital electron capture. After all other osmium activities had been allowed to die out, the source was investigated in a 180°-type beta-ray spectrograph. No positrons were found in this investigation. As has been mentioned above, there are two gamma-rays associated with the decay of Os^{185} of energies 0.878 and 0.648 Mev. No gamma-ray corresponding to the difference of these two energies was found. The number of quanta of 0.648 Mev is approximately six times the number of quanta of 0.878 Mev, so there is no possibility that these two gamma-rays can be in cascade. It would appear, therefore, that in the process of orbital electron capture, two separate levels of Re^{185} are excited, one at 0.648 Mev and one at 0.878 Mev. In order to be sure that there are no gamma-rays in cascade, Mr. W. H. Cuffey of this laboratory investigated a source of Os^{185} in a coincidence counting apparatus and found no gamma-gamma-coincidences. The disintegration scheme of Os^{185} is shown in Fig. 6.

(c) Os^{193}

The measurement of the spectrum of Os^{193} is complicated by the presence of x-rays which are of the same order of magnitude in energy as that of the lower energy gamma-ray. In addition, the measurement of the beta-ray spectrum is complicated by the presence of strong internal conversion lines and Auger lines. The end point of the beta-ray spectrum is certainly not greater than 135 ± 5 kev and it is impossible to tell whether the spectrum is simple or complex. There are two gamma-ray lines of energies 128 and 41 kev. Owing to the presence of Auger electrons it is impossible to say much about the relative intensities of these lines. Both lines are highly internally converted.

The authors are indebted to Miss Elma Lanterman for making the chemical separations and to Mr. W. H. Cuffey for making the coincidence measurements.

[9] H. A. Bethe and R. F. Bacher, Rev. Mod. Phys. 8, 194 (1936).

PHYSICAL REVIEW VOLUME 79, NUMBER 4 AUGUST 15, 1950

High Energy Elastic Scattering of Electrons on Protons

M. N. ROSENBLUTH
Stanford University, Stanford, California

(Received March 28, 1950)

The theory of the elastic scattering of electrons on protons at very high energies is discussed in detail. A formula is given for the cross section. This formula contains certain parameters which depend on the action of the virtual photon and meson fields. In particular, curves have been calculated on the assumption of scalar and pseudoscalar meson theory. While these perturbation theory calculations are not very trustworthy, and the results depend on the choice of coupling constants, it is felt that qualitative features can be checked with experiment. It is concluded that at low relativistic energies ($E<50$ Mev) the experiment provides a valuable check on quantum electrodynamics. At higher energies it should yield data on the nature of the meson cloud of the proton.

I. INTRODUCTION

THE Stanford linear electron accelerator program is expected to make available large currents of relativistic electrons with various energies ranging from 6 to 1000 Mev. Among the experiments of considerable interest which may then be performed is the elastic scattering of electrons on protons. This may be done on a hydrogen gas or liquid target. Despite the smallness of the cross section at high energies, the expected large intensity of the beam should render the experiments possible.

It is the purpose of this paper to show that, at appropriate energies and angles, the experiment should give considerable information both about the validity of the "quantum electrodynamical radiative corrections" to scattering, and about the structure of the meson cloud associated with the proton.

Processes competing with electron-proton elastic scattering can be grouped into two classes: (a) those arising from electron-electron interactions; (b) other electron-proton processes. The electron-electron interactions have a much larger cross section at high energies than the electron-proton interactions. Background from the electron-electron interactions may be eliminated by (1) angular coincidences between the scattered particles, (2) energy selection of the scattered electron at a given angle [or a combination of (1) and (2)], or (3) direct observation of the recoil protons by photographic plates.

The competing electron-proton processes are bremsstrahlung and meson production. They will have cross sections comparable to the corrections to the elastic scattering which are discussed below. Methods (1) and (2), discussed above, would also eliminate background from these processes. If the proton is observed directly a determination of its energy by grain counting and a correlation of energy and angle could be used to eliminate these processes. At very high energies it may prove experimentally impossible to separate the different electron-proton processes, in which case the bremsstrahlung and meson production must be added to the elastic scattering which is calculated in this paper.

II. ELASTIC SCATTERING OF AN ELECTRON AND PROTON

The elastic scattering of an electron and a proton can be represented schematically on a Feynman[1] diagram as in Fig. 1.

Figure 1 shows a proton of 4-momentum $\mathbf{p}_1$ and an electron of 4-momentum $\mathbf{p}_2$ exchanging a virtual quantum of 4-momentum $\mathbf{q}=\mathbf{p}_3-\mathbf{p}_1=\mathbf{p}_2-\mathbf{p}_4$ and being scattered to momenta $\mathbf{p}_3$ and $\mathbf{p}_4$, respectively. Here M is the proton rest-mass, e'' is the effective charge of the electron, e' the effective charge of the proton, and $\kappa' e'/2M$ its effective anomalous magnetic moment. The effective

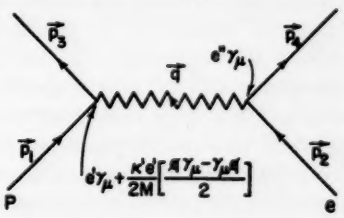

FIG. 1. Diagram for the elastic scattering of a physical proton and a physical electron. (The letter "q" with the bar through it in this figure is the same as the German letter, $\mathfrak{q}$, used in the text.)

charges and magnetic moments are functions of $q^2=q_4^2-q_3^2-q_2-q_1^2$ as discussed below. The notation of a German letter, $\mathfrak{q}$, means $q_4\gamma_4-q_3\gamma_3-q_2\gamma_2-q_1\gamma_1$, where the γ's are given in terms of the usual Dirac matrices by $(\boldsymbol{\gamma}, \gamma_4)=(\beta\boldsymbol{\alpha}, \beta)$.

The cross section for this process is computed by standard spur techniques to be

$$\sigma d\Omega=\left(\frac{e'e''}{2E}\right)^2 \operatorname{ctn}^2\frac{\theta}{2}\csc^2\frac{\theta}{2}\left\{\frac{1+2(E/M)\sin^2(\theta/2)+(E^2/M^2)[2(1+\kappa')^2\tan^2(\theta/2)\sin^2(\theta/2)+\kappa'^2\sin^2(\theta/2)]}{[1+(2E/M)\sin^2(\theta/2)]^2}\right\}d\Omega. \quad (1)$$

[1] R. P. Feynman, Phys. Rev. **76**, 749 and 769 (1949). The methods of calculation and the notation used in this paper are just those of Feynman unless otherwise indicated. We also use natural units, $\hbar=c=1$.

Here E is the energy of the incident electron and θ the angle through which it is scattered, both as measured in the system where the proton is initially at rest. The rest-mass of the electron has been neglected compared to its energy. We also introduce the useful parameter

$$q^2=\frac{-4E^2\sin^2(\theta/2)}{1+2(E/M)\sin^2(\theta/2)}. \quad (2)$$

For electron energies small compared to the proton rest-mass Eq. (1) reduces just to the usual Mott-Rutherford formula for scattering of an electron by a fixed electrostatic potential. Since κ', the effective anomalous proton magnetic moment, may be larger than 1 (for $\mathbf{q}=0$, $\kappa'=\kappa_0=1.79$) the magnetic moment

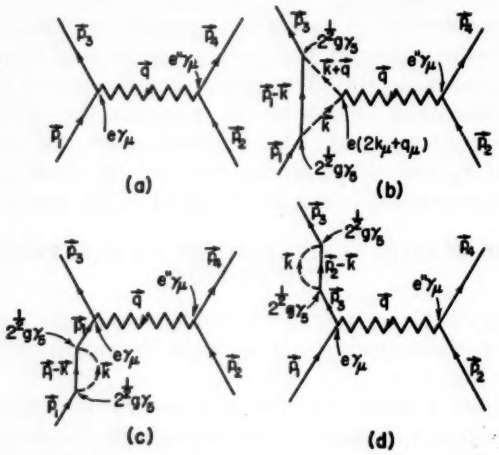

FIG. 2. Diagram showing the effect of a virtual charged pseudoscalar meson on electron-proton scattering.

will play an important role in the very high energy region.

That the effective electron charge e'' differs from its "natural" value e is due to the so-called radiative correction to scattering,[2] i.e., to the possibility that the electron may emit and reabsorb a virtual quantum, or emit a low energy real quantum, during the scattering process. This modification has been treated extensively by Schwinger.[3] His formula is valid under the assumption that the proton acts as a fixed electrostatic potential. This is the case in the low energy region in which this is the most important correction term. At higher electron energies, the more exact expression could be derived by a modification of the radiative correction to Møller scattering, which has been calculated at Cornell.[4] Here we restrict ourselves to the remark that the Schwinger correction is a slowly varying function of angle and energy and corresponds to a decrease of the order of magnitude of five percent in the effective electron charge for the region of interest.

[2] Strictly speaking, we should also give the electron an anomalous magnetic moment, but this is quite small and decreases rapidly at high energy.

[3] J. Schwinger, Phys. Rev. 76, 813 (1949). In our notation $(e''/e)^2=e^{-\delta}$ where δ is given by Schwinger in his Eq. (2.105).

[4] R. P. Feynman (private communication).

III. MESON FIELD CORRECTIONS TO ELECTRON-PROTON SCATTERING

The modification of the proton charge and anomalous magnetic moment is here assumed to be caused by the action of a virtual meson field. At electron energies small compared with the meson rest-mass these modifications will be small. Thus, at low energies the scattering will give us information concerning chiefly the radiative corrections to scattering; at higher energies we may expect to learn something of the nature of the meson cloud which surrounds the proton.

The action of a scalar meson field in modifying the effective proton charge and magnetic moment can be understood qualitatively by assuming that during a fraction R of the time the proton exists as a neutron and a positive meson. Its charge and anomalous moment then will be spread out like $e^{-2\mu}/r^2$ (the square of the meson wave function) where μ is the mass of the meson. Thus a high energy electron is able to penetrate the meson cloud and hence see a smaller effective charge and magnetic moment. Under these assumptions Schiff[5] has given the effective charge and magnetic moment to be

$$(e'/e)=[(1-R)+R2\mu/(-q^2)^{\frac{1}{2}}\tan(-q^2)^{\frac{1}{2}}/2\mu], \quad (3)$$
$$(\kappa' e'/\kappa_0 e)=2\mu/(-q^2)^{\frac{1}{2}}\tan^{-1}(-q^2)^{\frac{1}{2}}/2\mu,$$

where q^2 is given by Eq. (2).

We will here calculate in the covariant manner of Feynman the effective charge and magnetic moment of the proton as given by four theories: Neutral and charged scalar mesons with scalar-coupling, neutral and charged pseudoscalar mesons with pseudoscalar coupling. The results for symmetrical theories may be obtained simply by adding the results for charged and neutral theories. Other meson theories lead to divergent results.

To illustrate the method, we will discuss briefly the case of charged pseudoscalar theory. The effect of the virtual mesons on the scattering is shown in Fig. 2.

Figure 2(a) shows the usual electromagnetic interaction between two Dirac-type particles of charge e and e''. Figure 2(b) shows the proton emitting a positive meson which absorbs the virtual photon and is then reabsorbed by the neutron. Figure 2(c) shows the meson being emitted and reabsorbed before the scattering takes place. Figure 2(d) shows the virtual emission and reabsorption taking place after the scattering. Here g is the meso-nuclear coupling constant; $\gamma_5=i\gamma_1\gamma_2\gamma_3\gamma_4$; the factor 2 is inserted for simplicity in later discussing symmetrical theory; and the $2k_\mu+q_\mu$ at the meson-quantum vertex reflects the fact that a Klein-Gordon particle interacts with the electromagnetic field through the terms $i\partial(A_\mu\psi)/\partial x_\mu+iA_\mu\partial\psi/\partial x_\mu$ where ψ is the meson wave function, and A_μ the electromagnetic potential.

We endeavor to show that adding the diagrams 2(a) to 2(d) produces a situation like that in Fig. 1, and to

[5] L. I. Schiff, Stanford Microwave Laboratory Report No. 102, p. 8 (1949).

deduce the values of e' and κ'. For the case of $\mathbf{q}$, the photon momentum, equal to zero, diagrams (b), (c), and (d) are found to add to zero as might be expected, since there is then no scattering process. (There are non-essential mass renormalization terms but they do not concern us.) Moreover, the value of $\mathbf{q}$ does not affect the proton-meson parts of diagrams (c) and (d). Therefore we can obtain the final proton-meson portion of the amplitude by adding the proton-meson parts of diagrams (a) and (b) and subtracting off the value of diagram (b) for $\mathbf{q}=0$.

The proton-meson amplitude matrix from diagram (a) is simply $e\gamma_\mu$, that from diagram (b) can be written:[6]

$$e\frac{2g^2}{\pi i}\int d^4\mathbf{k}\frac{\gamma_5(\mathbf{p}_1-\mathbf{l}+M)\gamma_5(2k_\mu+q_\mu)}{[(\mathbf{p}_1+\mathbf{k})^2-M^2][k^2-\mu^2][(\mathbf{k}+\mathbf{q})^2-\mu^2]}.$$

Here μ is the meson rest-mass; the integration is to be performed over all virtual mesons; and we are interested in the element between initial and final proton states of this matrix.

After the integral over the virtual mesons is performed, and the amplitudes from diagrams (a) and (b) added, with the $\mathbf{q}=0$ value of diagram (b) subtracted, we obtain as final amplitude:

$$e\gamma_\mu\left\{1-\frac{g^2}{2\pi}\int_0^1 dx\int_0^1 dy\left[\frac{1}{2}\ln\left(1+\frac{u}{a}\right)-\frac{u[3y^3-(5-(a/2))y^4+2y^5]}{[(1-y)^2+uy^2+ay][(1-y)^2+ay]}\right]\right\} \tag{4}$$
$$+\frac{e}{2M}\left[\frac{q\gamma_\mu-\gamma_\mu q}{2}\right]\frac{g^2}{\pi}\int_0^1 dx\int_0^1 dy\left(\frac{y(1-y)^2}{(1-y)^2+uy^2+ay}\right).$$

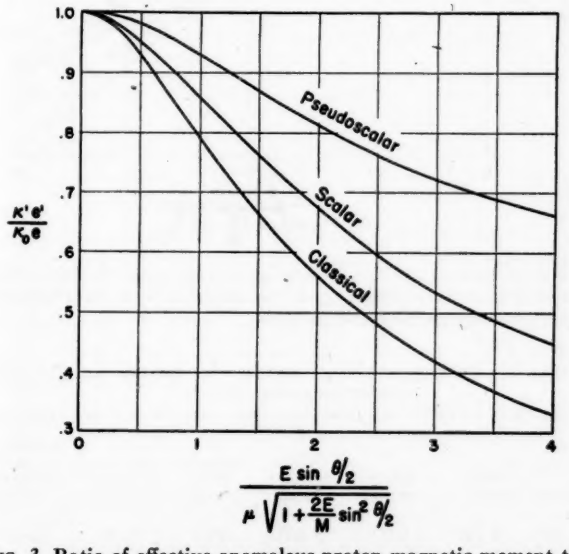

FIG. 3. Ratio of effective anomalous proton magnetic moment to its zero-energy value for charged meson theories.

[6] See Feynman, reference 1, for a full discussion of the method notation, and calculation techniques. In particular, the Appendix, p. 785, gives a full discussion of the evaluation of the radiative correction to scattering integral which is very analogous to our case.

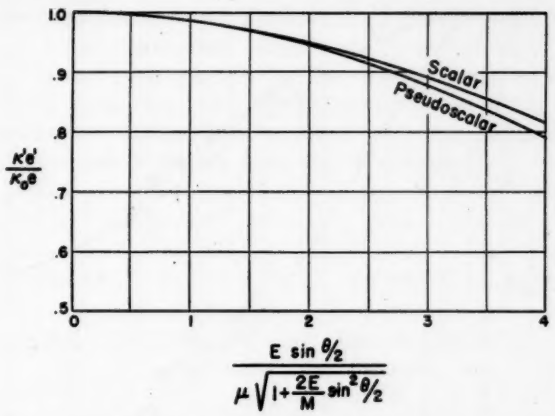

FIG. 4. Ratio of effective anomalous proton magnetic moment to its zero-energy value for neutral meson theories.

Here x and y are integration parameters, $a=\mu^2/M^2$; $u=q^2(x^2-x)/M^2$. The first term here represents the effective charge of the proton, the second its anomalous magnetic moment. For $u=0$ this term gives just the value for the anomalous moment previously derived by Case.[7]

For the case $u\neq 0$ the integrals are very complicated. The integral on y can be performed analytically. The remaining integral on x then depends on the parameters q^2/μ^2 and q^2/M^2. If q^2 is of comparable order of magnitude to μ^2, but much smaller than M^2, a region of considerable interest, the integral may be expanded to first order in the parameter q^2/M^2 and then performed analytically. For larger values of q^2 it must be carried out numerically. The other meson theories require the same type of calculation.

Figures 3, 4, 5, and 6 give the results of these integrations.

Figures 3 and 4 are graphs of $\kappa'e'/\kappa_0 e$, the ratio of the effective anomalous magnetic moment to the zero-energy anomalous moment. On Fig. 3 we have also plotted the "classical" formula (3). We have assumed in all calculations that μ, the meson mass, is 276 electron masses, consistent with experimental values for the π-meson. These ratios are independent of the coupling constant, which will determine only the magnitude of the zero-energy moment. It should be noted, however, that the scalar charged and pseudoscalar neutral theories predict the wrong sign for the proton moment.

Figures 5 and 6 are graphs of the effective proton charge. For reasons discussed below, we have plotted $e'/e=e^{-\delta}$, rather than $e'/e=1-\delta$ as obtained directly from (4). As can be seen from (4), δ is directly proportional to g^2. We have plotted $e^{-\delta}$ for those values of g^2 necessary to predict the correct value for the magnitude of the zero-energy proton moment. These values are given in Table I.

To illustrate the use of the graphs, and to show how they may be adapted to symmetrical theory, let us

[7] K. Case, Phys. Rev. 76, 6 (1949).

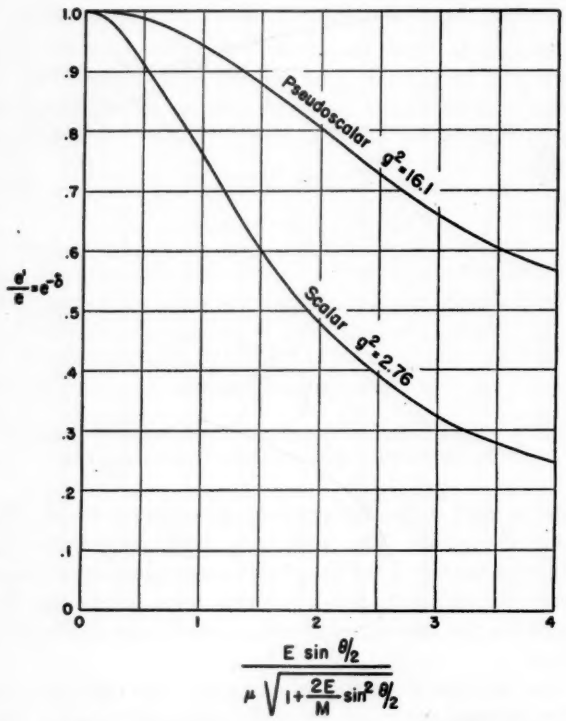

FIG. 5. Effective proton charge for charged meson theories with coupling constants chosen to fit the magnitude of the observed proton anomalous magnetic moment.

calculate the effective charge and magnetic moment for a 500-Mev electron scattered through 90° on the basis of symmetrical pseudoscalar theory with coupling constant 57.2. The abscissa

$$\left(E\sin\frac{\theta}{2}\right)\Big/\mu\left(1+\frac{2E}{M}\sin^2\frac{\theta}{2}\right)^{\frac{1}{2}}=(-q^2)^{\frac{1}{2}}/2\mu$$

in this case is equal to 2.03. Since the neutral and charged theories give opposite signs for the magnetic moment:

$$(\kappa' e')_s=(\kappa' e')_c-(\kappa' e')_n.$$

Using Table I and Figs. 3 and 4,

$$(\kappa' e'/\kappa_0 e)_s=0.81(57.2/16.1)-0.94(57.2/22.4)=0.48.$$

To obtain the effective charge:

$$\delta_s=\delta_c+\delta_n=0.22(57.2/16.1)+0.15(57.2/22.4)=1.16,$$
$$(e'/e)_s=\exp(-\delta_s)=0.31.$$

To obtain the final cross section these values for e' and κ', and Schwinger's[3] value for e'' are substituted in (1).

It will be noted that symmetrical theory predicts a rapid dropping off of magnetic moment and charge due to the large coupling constant.

IV. CONCLUSIONS

It will be noted at once that the values of g^2 listed in Table I are so large as to throw grave doubts on the use of second-order perturbation theory. This is especially true for the pseudoscalar case where we expect second-order terms to be small compared to higher order terms. In this connection it may be noted that the values of g^2 listed in Table I do not give the correct neutron moment. Some justification for the perturbation theory procedure may be found in the fact that experimental results on photo-meson production do seem to agree with the qualitative predictions of second-order pseudoscalar perturbation theory.[8] (There has been no effort to measure the absolute cross section so that no experimental value of g^2 is obtained.) It is because of doubt of the adequacy of the second-order theory that we have plotted $e'/e=\exp(-\delta)$, thus considering at least some of the higher order terms.

It will be noted that even though the meson clouds are more tightly bound than a naive picture would predict (see Fig. 3), there is nonetheless a very sizeable decrease in proton charge and magnetic moment to be expected at high energies. This is especially true if we assume the large values of coupling constant necessary to predict the proper proton moment. Even if only the qualitative features of these curves are dependable the experimental results should at least indicate (1) if the proton magnetic moment is really due to the π-meson

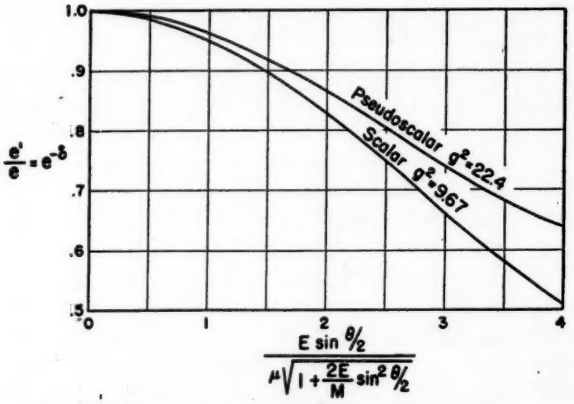

FIG. 6. Effective proton charge for neutral meson theories with coupling constants chosen to fit the magnitude of the observed proton anomalous magnetic moment.

TABLE I. Coupling constants necessary for correct magnitude of proton magnetic moment.

Theory	Scalar charged	Scalar neutral	Scalar symmetrical	Pseudoscalar charged	Pseudoscalar neutral	Pseudoscalar symmetrical
g^2	2.76*	9.67	3.86*	16.1	22.4*	57.2

* Indicates wrong sign for magnetic moment.

[8] J. Steinberger, experiments performed at Berkeley and not yet published.

field, (2) whether a loose-bound scalar type theory or a tight-bound pseudoscalar-type theory is preferable, and (3) how much faith can be placed in the "quantum electrodynamical radiative corrections" to scattering and in the far more dubious second-order meson corrections to scattering.

I would like to thank Professor L. I. Schiff for many helpful discussions and suggestions. I would like to express my gratitude also to Dr. Ross Thompson of Cornell University who has performed most of these calculations independently, and who very kindly checked, and improved upon one of, my results.

PHYSICAL REVIEW VOLUME 79, NUMBER 4 AUGUST 15, 1950

Anomalous Molecular Rotation and the Temperature of the Upper Atmosphere*

LEWIS M. BRANSCOMB**
Lyman Laboratory of Physics, Harvard University, Cambridge, Massachusetts
(Received May 12, 1950)

This experiment verifies the prediction of Oldenberg that the spectroscopically measured rotational temperature of a diatomic gas will be lower than the translational temperature when (1) the pressure is low, (2) the gas is excited by electron impact, and (3) the excited electronic state from which the measured bands are radiated has an equilibrium nuclear separation greater than the internuclear distance in the ground state. For gas temperatures from 400 to 670°K rotational temperatures from the second negative bands of O_2^+ were found in qualitative agreement with the predicted relation $T_{rot}=T_{trans}\,B'/B''$. Upper atmosphere temperatures derived from band profiles in night sky spectra are consistently lower than temperatures estimated from other data. The possible occurrence of anomalous rotation of the night sky molecules casts some doubt on the meaningfulness of the night sky temperature measurements. A partial rotational analysis in the course of this experiment suggests revisions of the B_0 and α-values for the O_2^+ molecule in the $^2\Pi_u$- and $^2\Pi_g$-states.

I. INTRODUCTION

A KNOWLEDGE of the molecular density and temperature at high altitudes is fundamental to an understanding of the processes occurring in the earth's upper atmosphere. For the region above 80 km the atmospheric temperature is deduced from indirect evidence from various sources. Unfortunately most of the data is only qualitative and, to make matters worse, much of it is contradictory. Evidence for a steadily increasing temperature above 80 km (a gradient of perhaps 4°/km) is found in the relative widths of the ionosphere layers, the apparent scarcity of helium at high altitudes, and the slow decrease in density at very great heights (as is indicated by high altitude auroral rays).[1] On the other hand, the more direct spectroscopic measurements on bands in the spectra of the aurora and the night sky luminescence are interpreted by some authors as conclusive evidence for a constant temperature of about 250°K above 90 km, a result which seems quite incompatible with the other temperature estimates.

These spectroscopic temperature measurements are based on the relationship between the equilibrium temperature of a radiating diatomic gas and the relative intensities of the lines in the rotational fine structure of an emission spectrum. The relative intensities of the rotational lines depend on two quantities: the relative transition probabilities of the lines, and the population of the initial rotational levels. If the temperature dependence of the populations of the initial rotational states is known, one can calculate the transition probabilities from quantum theory and can then calculate the gas temperature from the experimental relative intensities of the lines in a band.

In the measurements on upper atmospheric spectra it was assumed that the excited molecules in the aurora and night sky are in a Boltzmann distribution with respect to rotational energy, at an equilibrium temperature T. The significance of the spectroscopic temperature measurements depends on the validity of this assumption. Laboratory investigations of bands excited by electron impact in a glow discharge have afforded many examples of cases in which the excited radiating molecules are indeed in a Boltzmann rotational energy distribution, for the spectroscopically determined temperatures were quite close to the directly measured gas temperatures.

In 1934 Oldenberg[2] pointed out that although the molecules in a low pressure glow discharge are initially in thermal equilibrium, the assumption of thermal equilibrium in the *excited* rotational states is justified only for molecules whose nuclear separation is the same in the excited and ground states. Although this is usually the case, there are certain molecules in which the excited state has a much larger nuclear separation

* This work is described in detail in the author's Ph.D. thesis, Harvard University (1949).

** Now a member of the Society of Fellows, Harvard University.

[1] S. K. Mitra, *The Upper Atmosphere* (the Royal Society of Bengal, Calcutta, 1947); G. P. Kuiper, *The Atmosphere of the Earth and Planets* (University of Chicago Press, Chicago, 1947). See especially chapters by P. Swings and L. Spitzer, Jr.

[2] O. Oldenberg, Phys. Rev. 46, 210 (1934).

than in the ground state. By coincidence all of the night sky bands used for temperature measurements arise from just such states. Taking into account this change in internuclear distance in the upper atmosphere spectra yields values of the temperature almost twice as high as those found by assuming an equilibrium distribution in the excited states (as was done in the original experiments). Although it is not at all clear that the correct excitation conditions prevail in the upper atmosphere for the production of this abnormal rotation effect, any type of excitation other than electron impact renders the assumption of thermal equilibrium in the excited states equally doubtful. The purpose of this research was to demonstrate this anomalously low rotation in the laboratory, using one of the atmospheric gases, and then to discuss the spectroscopic temperature measurements in the upper atmosphere in light of the results.

II. LOW ROTATION AFTER ELECTRONIC EXCITATION AND INCREASED INERTIA

Consider a diatomic gas in thermal equilibrium at a low pressure and excited by a weak electric current in a glow discharge. The relative population of the rotational states of the unexcited molecules is given by

$$N''(j) \propto j(j+1)\exp(-E''/kT) \propto j(j+1)\exp(-E_r''/kT) \quad (1)$$

where the double prime refers to the ground state, E is the total energy, and E_r is the rotational energy. The vibrational and electronic components of the energy may be neglected since they lead to exponential factors independent of j. The rotational energy of a diatomic molecule is, to a good approximation,

$$E_r=(h/4\pi cI_v)j(j+1)=B_v j(j+1)\ \text{cm}^{-1}, \quad (2)$$

so that[3]

$$N''(j) \propto j(j+1)\exp[-B_v''j''(j''+1)/kT]. \quad (3)$$

Owing to the large disparity between the masses of the molecule and of the exciting electron, the electron does not impart an appreciable angular momentum to the molecule. Since the total angular momentum of the molecule is $[j(j+1)]^{\frac{1}{2}}h$, such an excitation process requires that the rotational quantum number j remain constant. If the value of B_v' (in the upper electronic state) is smaller than B_v'', the rotational energy levels of the excited state are more closely spaced than in the ground state, and the rotational *energy* of the molecules in the state j is decreased after excitation by the ratio of B_v' to B_v''. Thus the population of the jth rotational state remains constant during excitation, and the compression of the energy levels yields a new energy distribution which no longer corresponds to equilibrium at the original temperature. Quantitatively,

$$N'(j)=N''(j) \propto j(j+1)\exp[-B''j(j+1)/kT] \propto j(j+1)\exp[-B'j(j+1)/kT_{\text{eff}}]$$

where

$$T_{\text{eff}} \equiv TB_v'/B_v''. \quad (4)$$

The new population distribution is indeed of the Boltzmann form, but corresponds to equilibrium at a smaller value of the temperature, T_{eff}. In order for the band spectrum to indicate this low temperature distribution, the pressure must be sufficiently low that collisions during the life of the excited molecule do not partially restore thermal equilibrium before radiation can occur. This condition is fulfilled in the upper atmosphere for allowed transitions and may also be achieved in low pressure laboratory discharges. Under such conditions it should be possible to measure the gas temperature fairly accurately by multiplying the result obtained assuming thermal equilibrium in the excited state (T_{eff}) by the ratio B''/B'.

Although there are many well-known experimental examples of excessively high rotational temperatures in band spectra (resulting from other mechanisms), abnormally low rotation is relatively rare because of the very special conditions which must be met. We have found only two reports of observation of this effect. The first case is the discovery by Schüler and others[4] of remarkably deficient rotation in the spectrum of CuH in a very low pressure hollow cathode discharge. At 0.03 mm pressure of helium with a trace of hydrogen, they found the P_1 line to be the only rotational line with appreciable strength, indicating that only the zeroth rotational level was populated before radiation. The molecular free path was of the order of the cathode diameter, making gas collisions quite rare, so that Schüler was doubtless observing CuH molecules in the rotational state in which they left the cathode. This absence of rotation is probably due to the mechanism of formation and ejection of the CuH from the cathode surface. Plans are underway to investigate this phenomenon further in this laboratory. It is quite certain that the small increase in the inertia of the CuH molecule which does occur upon electronic excitation is quite inadequate to account for the extraordinary absence of rotation observed by Schüler.

The second observation of deficient rotation is probably explained by Oldenberg's prediction. In 1941 Ginsburg and Dieke[5] found an effective temperature of only 237° in the Fulcher bands of hydrogen excited in an a.c. discharge at 0.06 mm pressure. In this case $B''/B' \sim 2$. No direct temperature measurements of the discharge were made; one can only say that the molecular

[3] This is strictly true only for $^1\Sigma$-states, with additional terms appearing in the energy formula for states of higher multiplicity and orbital angular momentum. The terms which are constant for a particular sub-band may be factored out with the vibrational energy. Other terms involve B_v as a factor and do not affect the following argument.

[4] H. Schüler and H. Gollnow, Zeits. f. Physik **108**, 714 (1938); **109**, 432 (1938); **111**, 484 (1939). H. Schüler and H. Haber, Zeits. f. Physik **112**, 614 (1939).

[5] N. Ginsburg and G. H. Dieke, Phys. Rev. **59**, 632 (1941).

kinetic temperature must have been above room temperature. It was our purpose to demonstrate the existence of this low rotation effect conclusively using one of the atmospheric gases with more carefully controlled temperature conditions, so that the results might be less ambiguously applicable to the upper atmosphere.

III. SELECTION OF BAND SYSTEM

A. Schumann-Runge Bands of O_2

We would like to have studied in this experiment the same bands which are observed to give very low effective temperatures in night sky spectra. Unfortunately these bands (the Herzberg system of O_2 and the Vegard-Kaplan bands of N_2) are forbidden transitions which cannot be excited with sufficient intensity by electron impact in the laboratory. The Schumann-Runge bands of O_2 would have been ideal, for they involve states for which B_0''/B_0' is 1.76 and have a conveniently simple rotational structure. Although usually excited in an arc through oxygen at atmospheric pressure, intense production of these bands in the r-f electrodeless discharge has been reported by Lal in India.[6] We made a thorough search for the Schumann bands in glow discharges at pressures below 1 mm from 1800 to 7000A using electrodeless, condensed and uncondensed a.c. and d.c. discharges through spectroscopically pure oxygen. No trace of the Schumann bands was found, even when the gas was heated to 1000°K in an electric furnace. The failure to excite these bands (which arise from a completely allowed transition) is easily understood on the basis of the Frank-Condon principle. The desirable property of large inertial change after excitation is the very factor which causes the molecules to dissociate, so great is the vibrational potential energy produced. This result was also found by Feast[7] and must be kept in mind when discussing the identification of the Schumann bands in emission in night sky spectra. These experiments and theoretical considerations throw grave doubt on the results of Lal.

B. Second Negative Bands of O_2^+

The beta-bands of NO were considered but rejected to avoid possible excitation by chemical reaction or polyatomic dissociation. The O_2^+ second negative system was finally used, in spite of the difficulties resulting from the complex structure. The transition is from a $^2\Pi_u$-state intermediate between Hund's case (a) and case (b) to a $^2\Pi_g$-state in case (a). The ground states of both the ion and the neutral molecule have roughly equal internuclear distances. Hence, the anticipated temperature effect would be almost the same, whether the oxygen molecule is first ionized and later excited, or is ionized and excited in a single step.

[6] Lalji Lal, Nature **161**, 477 (1948).

[7] M. W. Feast, Nature **162**, 215 (1948); Proc. Phys. Soc. (A) **62**, part 2, 114 (1949).

IV. APPARATUS

The discharge tube was a cylindrical Vycor tube, 1 in. O.D. and 24 in. long, with a fused quartz window melted directly to one end of the tube. An electric furnace was constructed about the tube so that the walls of the discharge tube could be maintained at any temperature from room temperature up to 1000°K.

The electrodeless discharge was excited by a self-excited oscillator which could deliver up to 50 watts at 23.9 Mc to the discharge. The oscillator was capacitively coupled to the discharge tube by connecting the tank circuit in parallel with strips of copper wrapped around the discharge tube just outside each end of the furnace.

The oxygen was prepared electrolytically from distilled water. Hydrogen was removed by passing the gas through heated platinized asbestos and over phosphorus pentoxide. Carbon dioxide was removed in a liquid air trap, which also served to condense any traces of water vapor and the mercury vapor from the diffusion pump.

Because of the complexity of the rotational structure of the bands, high resolving power was required. A discharge sufficiently intense to allow use of a large grating would have prevented controlled temperature conditions in the gas. As a compromise the Hilger *E*-1 Littrow-type quartz spectrograph was used. It was found that the ultimate resolving power of the instrument could only be achieved if the room temperature was held constant to about 0.1°C because of the thermal coefficient of the prism refractive index and the very large f ratio of the instrument. A change in room temperature of two degrees between two exposures to an iron arc produced doubled spectrum lines.

V. PROCEDURE

To measure the relative intensities of the rotational lines in the O_2^+ bands we calibrated our plates by a method described by Barbier.[8] There are two great advantages in this method of plate calibration. First, each spectrum is its own calibration, eliminating errors due to non-uniform emulsion or development. Second, a fairly non-uniform slit illumination can be tolerated since only two adjacent parts of each line require photometry.

For comparison with the effective temperatures calculated from rotational profiles, it was necessary to measure the molecular translational temperatures by some direct and independent method. Metal thermocouples cannot be trusted in an oxygen discharge because of the reassociation of oxygen atoms which occurs very readily at metal surfaces. By operating the discharge at 10 microns pressure, the mean free path is slightly larger than the tube radius, and collisions with the walls are more numerous than collisions with excited molecules. Then if the discharge current is kept

[8] D. Barbier, Ann. d'Astrophys. **10**, No. 2 (1947).

weak, the temperature of the walls should determine the molecular translational temperature.[9] In any event, the average wall temperature is a lower bound to the average gas temperature, after the small cooling effect of diffusion into the cooler part of the system is taken into account. The effect of any radial temperature inhomogeneity was minimized by restricting the power drawn by the discharge to about 10 watts and then heating the discharge tube with the furnace to several hundred degrees C.

So many vibrational transitions are allowed with appreciable intensity in the first negative bands of O_2^+ (a direct result of the desired large difference in the internuclear distance of the two electronic states involved) that many of the bands are confused by the overlapping of weaker bands of the same system. If all of the rotational lines are not resolved, this precludes accurate intensity measurements in the overlapped bands. The (8, 1) band at 2343.3A and the (1, 6) band at 3494.2A were found to be most free from overlapping and of sufficient intensity. The complete rotational analysis of the (0, 6), (0, 7), (1, 6), and (1, 7) bands near 3500A has been carried out by Stevens[10] so that

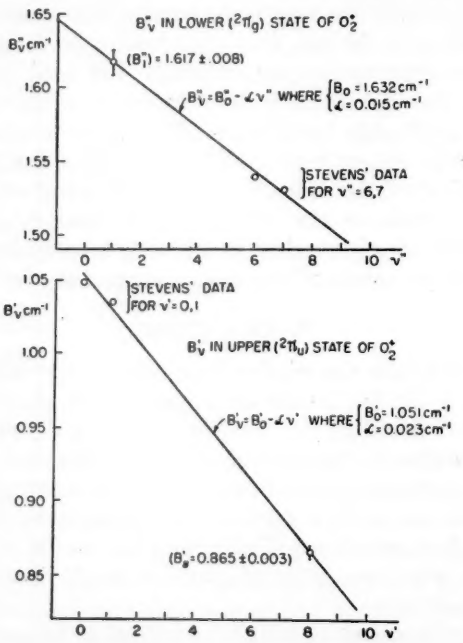
B''_v IN LOWER ($^2\Pi_g$) STATE OF O_2^+
B''_v cm^{-1}
$(B''_1) = 1.617 \pm .008$
$B''_v = B''_0 - \alpha v''$ WHERE $B_0 = 1.632$ cm^{-1}, $\alpha = 0.015$ cm^{-1}
STEVENS' DATA FOR v" = 6,7
STEVENS' DATA FOR v' = 0,1
B'_v cm^{-1}
B'_v IN UPPER ($^2\Pi_u$) STATE OF O_2^+
$B'_v = B'_0 - \alpha v'$ WHERE $B'_0 = 1.051$ cm^{-1}, $\alpha = 0.023$ cm^{-1}
$(B'_0 = 0.865 \pm 0.003)$
v"
v'

FIG. 1. This plot of B_v against vibrational quantum number for the upper and lower $^2\pi$-states of O_2^+ shows the data of Stevens and the two new points from our partial rotational analysis. New values of B_0 and α are found.

[9] The extent of dissociation in the discharge is unknown. Oxygen atoms produced with considerable kinetic energy may be sufficiently numerous to exert an appreciable heating effect in the volume of the discharge.

[10] D. S. Stevens, Phys. Rev. 38, 1292 (1931). Note that Stevens assigns v'' values which are two units larger than those used in this paper. The smaller v'' values are now generally accepted. Stevens' values of α must also be corrected in light of this change in Stevens' vibrational numbering. See R. S. Mulliken and D. S. Stevens, Phys. Rev. 44, 720 (1933).

the line identifications and molecular constants are known for these bands. However, the rotational lines in the (1, 6) band could not be completely resolved, while those in the (8, 1) band could, since the dispersion increases fourfold from 3500 to 2350A. The advantage gained by the greater dispersion at 2350A is partially offset by the necessity for making a rotational analysis of the (8, 1) band, for an extrapolation of the empirical constants describing the vibration-rotation interaction from $v'=0$ and 1 to $v'=8$ proved to be in serious error. As a mutual check and as an investigation of method, effective temperatures were measured from both the (1, 6) and the (8, 1) bands, using quite different techniques.

VI. ROTATIONAL TEMPERATURES FROM THE RESOLVED (8, 1) BAND

In addition to intensity measurements, calculation of the rotational temperature from a band requires accurate knowledge of both line identifications and the molecular constants from which the transition probabilities are calculated. The bands are double headed, and we confine our measurements to the first sub-band, in which the lines are not so closely spaced. B_8' and $B_1^{*\prime\prime}$, as well as the assignment of rotational quantum numbers to the branches, were determined graphically, principally from the frequency difference relations

$$\Delta\nu_R = \nu_{R(k)} - \nu_{R(k+1)} = 2(B^{*\prime\prime} - B')k + B^{*\prime\prime} - 2B' + (-1)^{k+1}(2k+1)(0.018)$$

$$\Delta\nu_P = \nu_{P(k)} - \nu_{P(k+1)} = 2(B^{*\prime\prime} - B')k + 5B^{*\prime\prime} - 2B' + (-1)^{k+1}(2k+1)(0.018)$$

from which

$$d(\Delta\nu_R)/dk = d(\Delta\nu_P)/dk \simeq 2(B^{*\prime\prime} - B')$$
$$\Delta\nu_P - \Delta\nu_R = 4B^{*\prime\prime} + 0.076 \text{ cm}^{-1}.$$

The last term in the first two equations gives the Λ-type doubling. By standard spectroscopic notation, $B_v^* = B_v(1 - B_v/A)$, and the rotational quantum number k is used instead of j for convenience. These equations can be derived from the selection rules, the Λ-doubling results of Stevens,[10] and the Hill-Van Vleck[11] formula for the rotational terms of a $^2\Pi$-molecule. In the graphical method used, one need only know at the outset which lines belong to main branches, as can be determined from inspection. Identification of the main branches as P and R comes out of the analysis. The method actually yields several possible values of B^* (0.8, 1.6, and 2.5 cm^{-1}), from which we must pick the only reasonable one (1.6), since the extrapolation of Stevens' data is certainly *roughly* correct and yields[12] 1.56 cm^{-1} for B_1^*. Using the line and branch identifications so obtained, the accuracy of B' and $B^{*\prime\prime}$ was improved by plotting 11 other combination difference

[11] E. L. Hill and J. H. Van Vleck, Phys. Rev. 32, 250 (1928).

[12] For a detailed description of this method of line identification the reader is referred to the author's thesis.

relations between lines in the P, R, and ${}^{S}R$ branches. (The ${}^{Q}P$ branch was badly masked by the P branch.) The final results obtained are

$$B_8' = 0.865 \pm 0.003 \text{ cm}^{-1}, \quad B_1^{*\prime\prime} = 1.604 \pm 0.008 \text{ cm}^{-1}.$$

From the definition of B^* and using $A = 195$ cm^{-1},

$$B_1'' = 1.617 \pm 0.008 \text{ cm}^{-1}.$$

To obtain B_0 and α for the upper and lower electronic states we combine these results graphically with Stevens' measurements in Fig. 1. These results suggest revision of the constants of the O_2^+ molecule as given below, although a complete rotational analysis with a large grating should be carried out before final adoption of these values, for more accurate values could be obtained.

Upper $^2\Pi$-state: $B_0' = 1.051$ cm^{-1}; $\alpha' = 0.023$ cm^{-1}.
Lower $^2\Pi$-state: $B_0'' = 1.623$ cm^{-1}; $\alpha'' = 0.015$ cm^{-1}; $r_e'' = 1.132$A.

The rotational transition probabilities were calculated for $v' = 8$ and 1, applying the theory of Hill and Van Vleck[11] to the lines in the first sub-band. Their general theory was applied to this special case of a $^2\Pi - {}^2\Pi$-transition from a state of intermediate coupling to a case (a) state. Algebraic manipulation yields the following simple formulas for the relative transition probabilities, $i(j)$, of the lines in the first sub-band of such a transition:

$$\begin{aligned} i_P(j) &= A(j+1)(1+B) & i_R(j) &= A(j)(1+B) \\ iQ_P(j) &= A(j+1)(1-B) & iS_R(j) &= A(j)(1-B) \end{aligned} \quad (5)$$

where

$$A(j) = (4j^2-1)/8j \qquad C = A/B'(A/4B'-1)$$
$$B(j) = \tfrac{1}{2}(\lambda-2)[(j-\tfrac{1}{2})^2+C]^{-\frac{1}{2}} \qquad \lambda = A/B'.$$

Figure 2 shows a microphotometer trace of the (8, 1) band at 2343A, showing the two-headed structure and the prominence of the main P and R branches.

The intensity of the jth line in a branch is

$$I(j) \propto i(j) \exp[-(B'/kT_{\text{eff}})\{j(j+1) \pm [(j+\tfrac{1}{2})^2+C]^{\frac{1}{2}}\}].$$

The terms in the braces are the parts of the rotational energy dependent on j from the Hill-Van Vleck formula.[3] If one plots

$$\ln I(j)/i(j) = \text{const.} - (B'/kT_{\text{eff}}) \times \{j(j+1) \pm [(j+\tfrac{1}{2})^2-C]^{\frac{1}{2}}\}, \quad (7)$$

T_{eff} is found from the slope of the resulting straight line. (In these formulas the plus sign is used with the satellite branches, the minus with the main branches.) Figure 3 shows a typical result; for an average gas temperature of about 512°K the effective temperature is 285±70°K, yielding $T/T_{\text{eff}} = 1.80 \pm 0.45$. The points on the plot are very badly scattered. The vertical lines drawn through the points indicate only the uncertainty in the position of the points due to grain in the plate. This is a considerably smaller effect than the scatter in the points due to the overlapping of weak bands in the background. The intensity available did not permit the increased dispersion which might have eliminated this scatter.

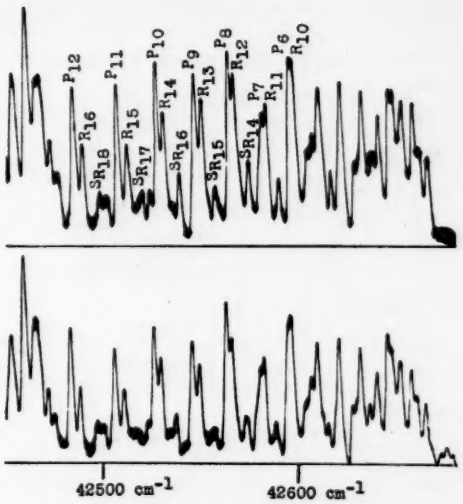

FIG. 2. Microphotometer traces of the first sub-band of the (8, 1) band at 2343.3A showing strong main branches, weak satellite branches, and the beginning of the second band on the left. The lower trace is of that part of the spectral lines which were attentated by an aluminized disk to provide an intensity calibration.

These results show conclusively that the effective temperature lies well below the lower bound of the gas temperature, as was anticipated. The experimental error in the determination of the slope of the straight line in Fig. 3 makes it impossible to determine whether there is accurate experimental agreement with Eq. (4). The ratio of the B values of the vibrationless ground states of the *neutral* O_2 and the excited *ionized* molecule with $v' = 8$ is $1.422/0.865 = 1.644$. If the $v' = 0$ level of the ground state of the *ionized* molecule is the initial state of the excitation, the ratio is $1.583/0.865 = 1.829$. Since the molecules are originally close to thermal equilibrium and the pressure is sufficiently low, T/T_{eff} should lie between 1.64 and 1.83, probably closer to the first value. The mean of results from three spectra of the (8, 1) band yields $T/T_{\text{eff}} = 2.1 \pm 0.5$, which does not contradict the prediction of Eq. (4).

VII. ROTATIONAL TEMPERATURES FROM THE UNRESOLVED (1,6) BAND

In the case of the (1, 6) band at 3494.2A it was necessary to open the spectrograph slit and intentionally smear out the rotational structure because the maximum resolution was not sufficient. Since this is the method which must perforce be applied to night sky bands, it is instructive to investigate its limitations. Spectra were obtained with the slit widened so that the lines were rectangular and of width 30 cm^{-1}. A typical

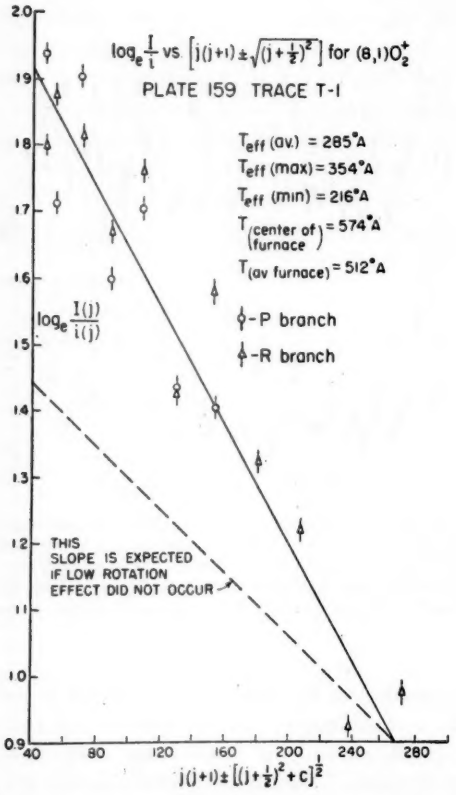
$\log_e \frac{I}{i}$ vs $\left[j(j+1)\pm\sqrt{(j+\frac{1}{2})^2}\right]$ for $(8,1)O_2^+$
PLATE 159 TRACE T-1
T_{eff} (av.) = 285°A
T_{eff} (max) = 354°A
T_{eff} (min) = 216°A
$T_{(center\ of\ furnace)}$ = 574°A
$T_{(av\ furnace)}$ = 512°A
$\log_e \frac{I(j)}{i(j)}$
-P branch
-R branch
THIS SLOPE IS EXPECTED IF LOW ROTATION EFFECT DID NOT OCCUR
$j(j+1)\pm[(j+\frac{1}{2})^2+c]^{\frac{1}{2}}$

FIG. 3. Typical measurement of effective rotational temperatures from the (8, 1) band of O_2^+. Vertical lines through points indicate grain errors only and not the large scatter produced by overlapping weak lines.

trace is shown in Fig. 4. Virtually all of the rotational structure has been removed, the first sub-band having a smooth shape (except for an annoying faint overlapping near the tail). Using Stevens' analysis of this band, artificial band shapes were computed for six effective temperatures ranging from 200 to 600°K. The experimental band shapes were compared graphically with the family of theoretical shapes predicted for various temperatures. The results for three plates are shown in Fig. 5.

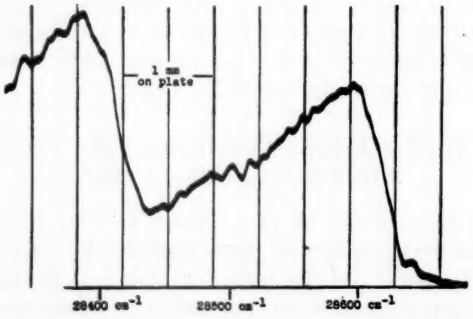

FIG. 4. Microphotometer trace of the (1, 6) band of O_2^+ at 3494A. The slit was opened to produce a line width of 30 cm^{-1}. Both first and second band heads are shown. After intensity calibration this band shape is related to rotational temperature in Fig. 5.

Again the increase in moment of inertia after excitation acts indirectly to reduce the sensitivity of the band profile to changes in temperature. The band branches are so strongly degraded that the line spacing changes rapidly from head to tail. As a result, the crowding of the lines near the head is more effective in determining the position of the intensity maximum than are the relative intensities of the individual lines. The slope of the tail of such an unresolved band is the only useful temperature indication, and it is rather insensitive to temperature changes.

Table I shows a summary of seven runs on the (1, 6) band for furnace temperatures ranging from about 400 to 670°K. The mean value of T/T_{eff} is 1.50±0.25, where the assigned error is a necessarily subjective estimate. In this case we expect T/T_{eff} to lie between 1.37 and 1.59, depending on whether the initial state of the excitation process is the neutral molecule or the ion. Again the experimental result is in qualitative agreement with the theory.

Since experimental difficulties prohibited precise quantitative results, no detailed discussion of sources of error will be included here. Suffice it to say that we have observed an effect characteristic of abnormally low rotation in the excited state of the O_2^+ molecule, and the magnitude of the abnormality is in general agreement with the prediction of Oldenberg.

VIII. THE UPPER ATMOSPHERE

A. Schumann-Runge Bands of O_2

As regards the Schumann-Runge bands of O_2, tentatively identified in night sky spectra,[1] we conclude that their presence requires an excitation mechanism producing a molecule with low vibration or removing the excess vibrational energy after the O_2 molecule is excited. Three-body reassociation of oxygen atoms in the presence of an oxygen or nitrogen molecule has been postulated as the mechanism for producing the Schumann bands in the upper atmosphere. Such a process has a density cubed dependance and becomes most improbable at auroral densities. Whether the low specific probability of three-body collisions at auroral densities

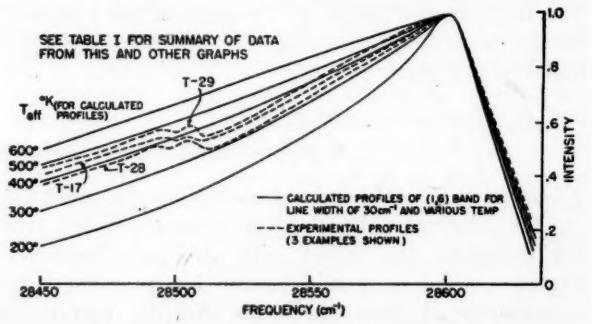

FIG. 5. Graphical method of deducing rotational temperatures from the (1, 6) band of O_2^+. This method is much less sensitive than that of Fig. 3, but must be used in the unresolved night sky bands.

is compensated for by the large volume without walls which the upper atmosphere represents remains to be seen. Consideration of the oxygen potential curves and the Frank-Condon principle shows that any excitation of the Schumann bands which does result from electron impact at low pressure will lead to radiation in the vacuum ultraviolet and perhaps in the infra-red, but not in the near ultraviolet. For if the oxygen molecule is excited by electron impact, the Frank-Condon rule tells us that the excited state will be strongly vibrating. Radiation is most probable at the turning points of the vibrational motion; the quantum jumps to the ground state are quite large when the nuclei are closest and small when swinging farthest apart. The well-known near ultraviolet bands of the Schumann-Runge system result from the population of the lowest vibrational levels of the upper state. Hence the positive identification of the near ultraviolet Schumann-Runge bands in the night sky would require the existence of an excitation process other than electron impact.

B. Upper Atmosphere Temperature

For discussions of the diverse evidence regarding the kinetic temperature of the atmosphere above 80 km the reader is referred to the detailed reviews on the subject.[1] In general most of the evidence, except that derived from spectroscopic band profiles, suggests an increasing temperature above 80 km. At 100 km the N.A.C.A. "most probable" temperature[13] is about 310°K. In night sky spectra, Cabannes and Dufay[14] found $T_{eff}=230$°K for the Vegard-Kaplan bands of N_2. Barbier[15] found values ranging from 170 to 220°K for the Herzberg bands of O_2. Swings[16] roughly estimated the rotational temperature in the Herzberg bands to be about 150°K. The altitude of emission of these bands is not established, although the most recent evidence[17] favors a layer at 100 km. If the altitude of emission of the night sky bands is equal to or greater than 100 km, the disparity between the spectroscopic temperature data and the N.A.C.A. value is 70° or greater for the N_2 bands, and over 100° for the O_2 data. If the night sky radiation originates as low as 80 km, there is no obvious discrepancy between the spectroscopic temperature measurements and the N.A.C.A. curve. Also, as D. R. Bates has pointed out, there is a possibility that the rotational temperature measurements in the particular case of the Vegard-Kaplan bands are reliable. For if the lifetime of the excited state is sufficiently long, collisions may restore equilibrium even at auroral densities. The evidence for the existence of these collisions is the small intensity of the Vegard-Kaplan bands compared to the first positive bands, suggesting strong collisional depopulation of the metastable level[18] in N_2.

TABLE I. Comparison of measured gas temperatures and effective rotation temperatures in the (1, 6) O_2^+ (2nd neg.) band.

Trace No.	T_f[a]	T_{eff}	T_f/T_{eff}
16	447±20°K	330°K	1.35
17	573±30	350	1.64
19	462±20	340	1.36
24	400±20	320	1.25
25	432±20	330	1.31
28	542±20	310	1.75
29	667±40	370	1.80
		Average	1.50

[a] T_f is the average temperature of the walls of the discharge and is approximately the translational gas temperature.

The most widely favored night sky excitation theories are based on: (a) three-body recombination processes (which are well known to produce abnormally high, not low rotation[19]) and (b) two-body charge transfer processes involving positive and negative ions (whose effect on rotation is unknown). With such types of excitation, spectroscopic temperatures are quite unreliable, providing collisions do not restore equilibrium in the excited state.

On the other hand, if the excitation is by electron impact (as seems improbable) and the pressure is sufficiently low, we must correct the spectroscopic data for the effect of the changes in inertia during excitation of the Vegard-Kaplan and Herzberg bands. If we multiply these spectroscopic effective temperatures by the respective values of B''/B' (1.5 and 1.4) we get temperatures of 260 to 340°K for the Herzberg bands and 320°K for the Vegard-Kaplan bands. This brings the O_2 and the N_2 data into harmony with each other and with the N.A.C.A. conclusions (at an emission altitude of 100 km).

In any case, we may conclude that the rotational temperatures found from night sky bands should not be relied on as an indication of the kinetic molecular temperature in the emitting layer until we know the lifetimes of the excited states. For if the excitation is by electron impact (or any other method conserving molecular angular momentum) the temperatures must be revised upward by a factor B''/B', and if the excitation is by any other method we can only conclude that this method is totally unreliable, inasmuch as there is no experimental or theoretical basis for predicting the amount of angular momentum gained or lost by the excited molecule.

This discussion cannot be complete without reference

[13] E. F. Cox, Am. J. Phys. **16**, 472 (1948).
[14] J. Cabannes and J. Dufay, Ann. d. Geophys. **2**, 290 (1946).
[15] D. Barbier, Comptes Rendus **224**, 635 (1947); Ann. d'Astrophys. **10**, No. 2 (1947).
[16] P. Swings, Astrophys. J. **97**, 72 (1943).
[17] Lecture by C. T. Elvey concerning the unpublished results of Elvey, Swings, and Barbier.
[18] This statement may require revision if Elvey is proved correct in suggesting that the strong radiation at about 10,400A may be OH and not the (O, O) band of the N_2 first positive system.
[19] Feast (reference 7) found rotational temperatures of 2000 to 3000°K in an investigation of the Schumann-Runge bands of O_2, apparently excited by three-body reassociation.

to the rotational temperatures measured by Vegard[20] and his collaborators[21] from the intensity distribution in the R branch of the 4278A (0, 1) band of N_2^+ in the *aurora* at Trömso, Norway. Vegard and Tönsberg found $T_{eff}=219\pm25°K$ for the auroral region from 90 to 140 km. Although most of their spectra are of auroras at this altitude, studies of rays extending to 600 to 800 km show no increase in rotational temperature. In this band system the moments of inertia of the molecule are almost identical in the excited N_2^+ state and in the ground states of both N_2^+ and N_2, so that B''/B' is unity. In addition, the intensities of the auroras permit the use of a much greater resolving power than in the case of night sky spectra. A third factor increasing the reliability of these measurements is that the N_2^+ band involves no inertial change upon radiation, so that the shape of the unresolved band profile is much more sensitive to the temperature than are the shapes of the Herzberg and Vegard-Kaplan bands. Penndorf[22] calls attention to the fact that Vegard's measurements are all made in the arctic winter, while the night sky experiments and radio sounding data have been primarily low latitude experiments. However, Penndorf's criticism does not explain the extension of auroral rays to 1000 km which is occasionally observed in the arctic winter and is one of the best evidences of a high mean temperature at high altitudes. Comparison of measurements made in widely different latitudes using different techniques should perhaps be interpreted with caution.

It would be very desirable to obtain independent confirmation of Vegard's results, particularly in low latitudes. In addition, a systematic investigation of the latitude dependence of the temperature at 100 km is called for using the same experimental method at all latitudes.

I am greatly indebted to Professor Otto Oldenberg who suggested this problem and assisted with many stimulating discussions. I also wish to acknowledge the generous support of a Predoctoral Research Fellowship from the National Institute of Health.

[20] L. Vegard, Geofys. Publ. **9**, No. 11 (1932); Terr. Mag. **37**, 389 (1932); Phil. Mag. **24**, 588 (1937); Naturwiss. **26**, 639 (1938).
[21] L. Vegard and E. Tönsberg, Geofys. Publ. **11**, No. 2 (1935); **12**, No. 3 (1938); **13**, No. 1 (1940) and No. 5 (1941). Nature **145**, 588, 623 (1940).
[22] R. Penndorf, Bull. Am. Met. Soc. **27**, 331 (1946).

PHYSICAL REVIEW VOLUME 79, NUMBER 4 AUGUST 15, 1950

The Liquid-Solid Transformation in Helium near Absolute Zero

C. A. SWENSON*
The Clarendon Laboratory, Oxford University, England
(Received March 13, 1950)

Although helium is normally a liquid to absolute zero, it can be solidified by the application of moderately high pressures. This transformation is of particular interest, since by the third law of thermodynamics the entropy difference between the liquid and the solid must disappear as the absolute zero is approached. This can most easily be shown by the disappearance of the heat of melting. Measurements from 1.0° to 1.8° of the slope of the melting pressure curve and the change in the molar volume of helium on melting are described, from which the heat of melting and the change in internal energy on melting were calculated. These results verify the predictions made by the third law. The measurements are also combined with those due to earlier workers to show the discontinuities in the various thermodynamic functions at the intersection of the λ-point-pressure curve with the melting pressure curve.

I. INTRODUCTION

SOLID helium, in contrast with liquid helium, is a relatively normal substance, although it exists only under relatively high pressures (Fig. 1). W. H. Keesom and his collaborators were the first investigators to observe solid helium,[1] and they have performed many fundamental experiments with it, all of which point to the fact that a transformation of the λ-type does not take place.

The fact that helium can be solidified by the application of pressure, although under its saturated vapor pressure it remains a liquid to absolute zero, makes the liquid-solid transformation very interesting from the thermodynamic point of view. This has been pointed out in another paper,[2] and it is worth noting that, by the third law of thermodynamics, the entropies of liquid and solid helium must become the same at very low temperatures. This means that both the heat of melting and dP/dT must approach zero as a limit. The fact that the melting pressure curve as first determined by Keesom (Fig. 1)[3] did seem to approach a positive pressure with $dP/dT=0$ at absolute zero was taken as a direct confirmation of the validity of the third law.

Probably the most interesting point on the melting pressure curve, with the exception of the point at the absolute zero, is the intersection of the melting pressure and λ-point pressure curves[3,4] at 1.8°. This is a form of

* Now at Harvard University, Cambridge, Massachusetts.
[1] W. H. Keesom, *Helium* (Elsevier, Amsterdam, 1942), p. 180.
[2] F. Simon and C. A. Swenson, Nature **165**, 829 (1950).
[3] W. H. Keesom, reference 1, p. 202.
[4] W. H. Keesom, reference 1, p. 226.

"triple point" between liquid He I, liquid He II, and solid helium, and since it is at this point that dP/dT begins to decrease rapidly, it would seem that the other thermodynamic quantities characteristic of the transformation—$\Delta V = V_L - V_s$, the change in molar volume, ρ, the heat of melting, and $\Delta U = U_L - U_s$, the change in internal energy—would also tend to change rapidly below this temperature. All previous determinations of these quantities have been confined to temperatures above 2°.

Because of this expected very rapid decrease in the heat of melting below the λ-point, it is obvious that thermal measurements would soon become so inaccurate as to be impracticable as the temperature was lowered. Therefore, the most logical solution seemed to be to determine ΔV and dP/dT from the λ-point to as low temperatures as possible, and to calculate ρ and ΔU from them using the Clausius-Clapeyron equation. A general discussion of these results was published in another paper,[2] and it is the purpose of this paper to show how the results were obtained and to give some further data.

II. DESCRIPTION OF THE APPARATUS

The liquid helium was produced by means of a Simon expansion liquefier[5] of about 65 cc capacity. The actual cryostats (one for the melting pressure determinations and one for the ΔV measurements) were suspended alternately from the bottom of the liquefier expansion vessel in the vacuum jacket by thin-walled German silver tubes. The required accuracy and reproducibility in the melting pressure measurement (0.01 atmos. in 25 atmos.) were obtained using a simple piston-in-cylinder pressure balance which has been described elsewhere.[6]

A separate phosphor-bronze resistance thermometer was used for each experiment, and the thermometers were calibrated against the vapor pressure of helium (Bleaney and Simon scale) using mercury and oil manometers. The resistance wires were permanently attached to the cryostats by well-baked Bakelite varnish, and under these conditions the calibrations remained constant in spite of repeated warmings up to room temperature. Resistance measurements of sufficient accuracy were obtained by using a Tinsley vernier potentiometer, and current variations were kept to a minimum.

III. THE MELTING PRESSURE MEASUREMENTS

The melting pressure measurements were made by the conventional blocked capillary technique.[1] The cryostat (shown schematically in Fig. 2) consisted of a 15 cc copper vessel, A, with a fine (0.5 mm) capillary attached to the inside of its base. The temperature of the liquid helium in A was lowered by pumping through the 3 mm German silver tube, C, and the vapor pressure was measured through the 2 mm tube, D. The phosphor-bronze wire was wound about A.

By means of other fine capillaries, the two ends of the cryostat capillary were attached at room temperature to opposite sides of a sensitive bellows manometer, E, one side of which was connected to the pressure balance. In practice the temperature of A was kept constant by throttling the pump, and by adding 10 g weights to the pressure balance piston, the pressure on the helium in the capillary was slowly raised in 0.01 atmos. steps until the capillary blocked; whereupon further increase in pressure resulted in a depression of the bellows and an electrical contact, F, was broken. The bellows sensitivity was roughly 0.01 atmos.; that is, an increase of pressure of 0.01 atmos. with the capillary blocked was enough to close the contact.

The apparatus worked very well for temperatures below 1.5° and these results are given in Fig. 3. It can be seen that the points (representing several different days' work) are reproducible to ±0.01 atmos. Points for higher temperatures were much more difficult to obtain accurately, since dP/dT is so large that a temperature shift of only 0.001° produces a very appreciable change in P. In this region the data were only good enough to show that the P *vs.* T curve is continuous through the λ-point. The rapid change in dP/dT at the λ-point (to be discussed later) was shown nicely in a semiquantitative sort of way.

Fortunately, the melting points obtained above 1.4° agreed within experimental error with previous results given by Keesom and Miss Keesom.[7] These data were

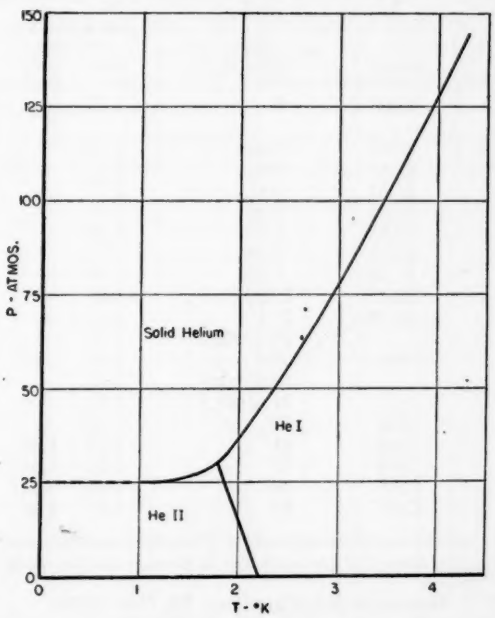

FIG. 1. The melting pressure and λ-point-pressure curves for helium.

[5] W. H. Keesom, reference 1, p. 160.
[6] C. A. Swenson, Rev. Sci. Inst. 21, 22 (1950).
[7] W. H. Keesom and A. P. Keesom, Leiden Comm. 224e (1933).

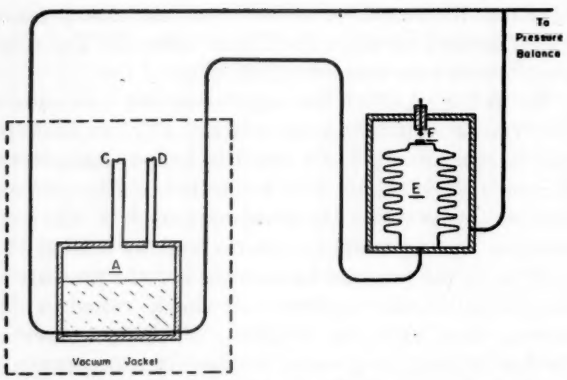

FIG. 2. The blocked capillary melting pressure cryostat.

analyzed by Haggenmacher[8] to fit an interpolation formula, and from this formula, he obtained the following expresion for dP/dT:

$$dP/dT=100[(T-1.14)/(32-P)] \text{ atmos./deg.} \quad (1.5^\circ \text{ to } 1.75^\circ \text{ K}). \quad (1)$$

This formula is only useful as far as interpolation is concerned, since the expression for the pressure has no physical significance at absolute zero.

Below 1.5°, the curve given here is slightly below the data given by Keesom and Keesom, with a maximum deviation of about 0.1 atmos. at 1.2°. Since their curve (with the temperature corrected to the Bleaney and Simon scale) extends only to approximately this temperature, and was obtained as a supplementary part of another experiment, the data in Fig. 1 were accepted as correct and were fitted to an extrapolation curve which was used to calculate dP/dT from 1.4° to 1.0°.[8a] The experimental points in Fig. 1 can be represented by the following equation in this range within experimental accuracy:

$$P=0.053T^8+25.00 \text{ atmos.} \quad (1.0^\circ \text{ to } 1.5^\circ \text{ K}). \quad (2)$$

Therefore, dP/dT is given by:

$$dP/dT=0.425T^7 \text{ atmos./deg.} \quad (1.0^\circ \text{ to } 1.4^\circ \text{ K}). \quad (3)$$

Finally, to obtain values for dP/dT above the λ-point, the earlier data due to Keesom[3] were fitted to the following curve, and dP/dT was calculated from it; giving the formula

$$P=15.45T^{1.57}-8 \text{ atmos.} \quad (2.0^\circ \text{ to } 4.0^\circ \text{ K}). \quad (4)$$

These data are summarized in Table I, column 3, and are plotted in Fig. 4. The rapid drop in dP/dT by a factor of 100 from the λ-point (1.77°) to the lowest temperature reached (1.0°) shows the expected effect due to the decrease in the entropy difference between liquid and solid helium. The values for dP/dT are accurate to about 2 percent below the λ-point, and to roughly 5 percent between 2° and 4°.

Equation (2) enables us to extrapolate the melting curve to absolute zero, yielding a value

$$P_0=25.00(\pm 0.05) \text{ atmos.} \quad (T=0^\circ \text{ K}).$$

TABLE I. Thermodynamic data for the liquid-solid trans. in helium below 4°K.*

1	2	3	4	5	6	7	8	9	10	11
Temp. °K	P atmos.	dP/dT atmos./deg.	$\Delta V=V_L-V_s$ cm³/mole meas.	calc.	V_L cm³/mole	V_s cm³/mole	ρ (cal./mole) calc.	meas.	$P\Delta V$ calc./mole	$\Delta U=U_L-U_s$ cal./mole
0°	25.00	0	2.07	—	23.25	21.18	0	—	1.22	−1.22
1.00	25.05	0.425	2.07	—	23.24	21.17	0.021		1.23	−1.21
1.10	25.11	0.82	2.07	—	23.23	21.16	0.045		1.24	−1.20
1.20	25.22	1.51	2.07	—	23.22	21.15	0.090		1.24	−1.15
1.30	25.43	2.66	2.07	—	23.18	21.11	0.170		1.25	−1.08
1.40	25.81	4.50	2.06	—	23.11	21.05	0.310		1.27	−0.96
1.50	26.37	6.36	2.00	—	23.02	21.02	0.456		1.25	−0.79
1.60	27.16	9.43	1.89	—	22.84	20.95	0.684		1.23	−0.55
1.70	28.4	15.20	1.65	—	22.50	20.85	1.00		1.10	−0.10
1.75	29.25	21.1	1.52	—	22.30	20.78	1.34		1.06	+0.28
1.77	—	29.8(calc.)	1.48	—	22.22	20.75	—	1.89	—	—
1.78	30.0	30.5	1.47	—	—	—	1.91	—	1.06	+0.85
1.80[5]	—	30.8(calc.)	1.47	—	—	—		1.98	—	—
1.83[5]	—	31.6(calc.)	1.47	—	—	—		2.07	—	—
2.0	37.0	35	1.43	—	21.6[6]	20.2[2]		2.33	1.27	+1.06
2.5	57.0	41	1.33	1.36	20.6[0]	19.2[7]		3.34	1.82	+1.52
3.0	79.0	45[5]	1.25	1.31	19.7[2]	18.4[7]		4.35	2.38	+1.97
3.5	103.[5]	49[5]	1.15	1.31	19.0[0]	17.8[5]		5.45	2.97	+2.48
4.0	129.[0]	53	1.0	1.26	18.4[0]	17.2[5]		6.50	3.55	+3.05

* The data above 2.0° are mostly due to Keesom, as is the whole of column 6 (see text).

[8] J. E. Haggenmacher, Phys. Rev. 74, 1539 (1948).

[8a] A possible source of error in melting pressure determinations by the blocked capillary technique has been pointed out by Bridgman [Rev. Mod. Phys. 18, 28 (1946)], who noted that the shearing stress exerted on the solid by the pressure difference across it can very easily lead to a lower than normal melting point. However, in these experiments, the pressure was increased in 0.01 atmos. increments, and the pressure difference across the solid helium in the capillary was never greater than 0.02 to 0.03 atmos. Thus, this effect should be negligible.

The error here arises not so much in the extrapolation as in the absolute calibration of the pressure balance. The temperature and pressure of the intersection of the λ-point-pressure curve with the melting curve (called the "λ-point" in this paper) can also be determined from these data and from the ΔV data as

$$P_\lambda = 30.0(\pm 0.1) \text{ atmos.}, \quad T_\lambda = 1.77°(\pm 0.005).$$

These figures agree quite well with data given by Keesom.[4]

IV. THE MEASUREMENT OF ΔV

The cryostat shown in Fig. 5 was used to determine the volume change of solid helium on melting. Liquid helium was condensed into the upper compartment, *A*, and low temperatures were obtained by pumping this helium through the thin-walled German silver tube, *C*. As in the previous experiments, the resistance thermometer was calibrated with vapor pressures measured through the 2 mm tube, *D*. The resistance thermometer was wound directly on the lower or high pressure compartment, *B*, which contained either liquid helium or solid helium under pressure, and which was connected directly to the pressure balance. As the solid helium melted, liquid helium was pushed out through the capillary, and, if all external conditions were kept constant, this was shown directly by the rise of the pressure balance piston in its cylinder as it rose to keep the pressure of the system constant by increasing its volume.

In practice, the cryostat was cooled to approximately 1° by pumping the helium in *A*. The excess liquid helium was then evaporated away by an auxiliary heater wound on *A*. When it had all disappeared, the normal heating curve of the cryostat (temperature *vs.* time, with no heat applied) was taken. This was essentially governed by the natural heat influx and the specific heat of the solid helium in *B*. A simultaneous curve of pressure balance piston height *vs.* time was also taken. At the melting point, the change in volume of the solid helium as it melted resulted in a rather rapid rise of the pressure balance piston, while the heat of melting caused a plateau in the heating up curve. Thus, the melting temperature and the change in volume of the solid helium on melting could be determined at the pressure given by the weights on the pressure balance. Actually, while these determinations of temperature were accurate enough for the measurements, of ΔV, they were not good enough for really accurate melting pressure measurements, and thus the first set of experiments was performed.

Thermal measurements were difficult because, due to the high thermal conductivity[9] of He II, most of the heat influx came down the capillary. This correction is very temperature sensitive, and is also complicated by the flow of "cold" liquid helium out of the cryostat. Thus, it was only around the λ-point, where the natural heat influxes were relatively small, that direct determinations of the heat of melting could be made. Three of these are given in column 9 of Table I, and can be seen to check within experimental error (roughly 3 percent) the dP/dT and ΔV values that were determined in the same set of experiments.

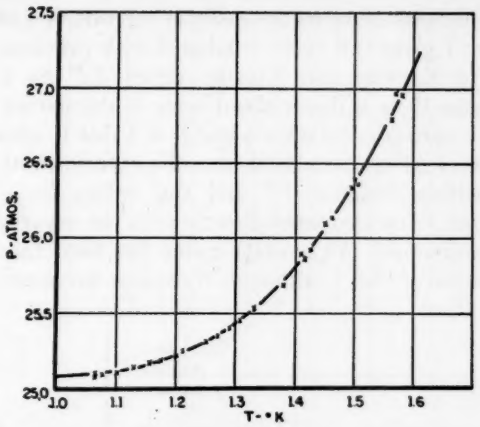

FIG. 3. The experimental points for the melting pressure curve of helium below 1.6°.

It might be added that this high heat influx down the capillary performed one useful function in that it made certain that the helium in the capillary melted first, and made less likely any form of superheating effects.

The values of ΔV were calculated from the volume of *B* (2.50 cc at 1° K) and the mass of helium pushed out of the cryostat (obtained from the pressure balance rise). The densities of liquid helium along the melting curve were also needed and were deduced from the isopyncnal data given by Keesom and Keesom.[8] These (or, rather, the molar volumes, $V_L = 4.003/d_L$) are tabulated in column 6 of Table I, and are plotted in the upper curve of Fig. 8.

The actual experimental points for ΔV are plotted in Fig. 6. The estimated experimental error is 3 percent,

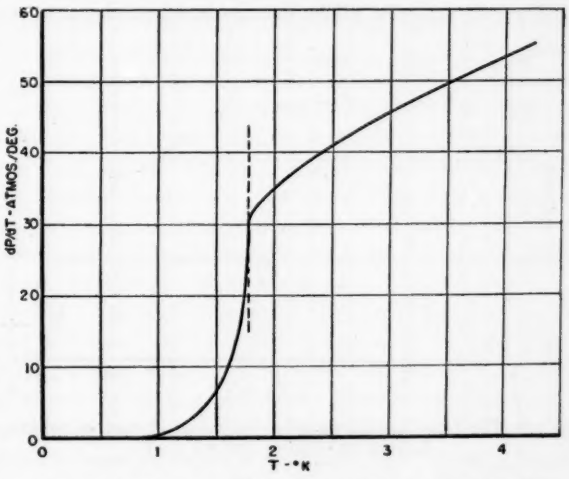

FIG. 4. dP/dT for the liquid-solid transformation in helium.

[9] W. H. Keesom, reference 1, p. 282.

and the measurements are easily as reproducible as this. Figure 7 gives this curve combined with previous data due to Keesom and Keesom (from 2.2° to 4.0°),[10] although there is doubt about some of this earlier data. This is shown in columns 4 and 5 of Table I, where the values of ΔV as calculated from the experimental heats of melting (column 9)[11] and the values for dP/dT (column 3) are compared directly with the experimental determinations. An average value has been taken for the curve of Fig. 7, although there is some uncertainty near 4°.

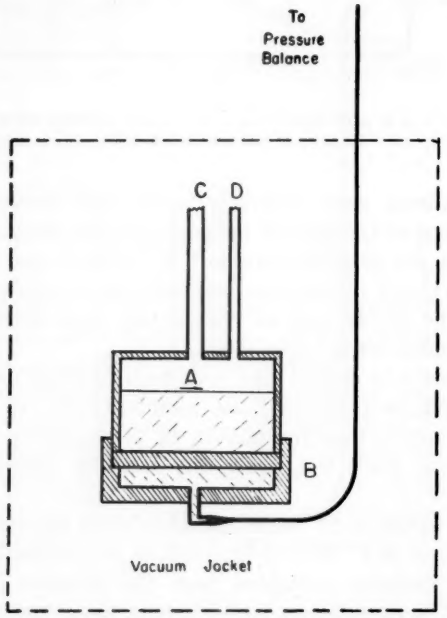

FIG. 5. The cryostat for measurement of ΔV.

By use of the curves of V_L and ΔV, the densities of solid helium on melting (V_s) were calculated. These are tabulated in column 7 of Table I, and are plotted in the lower curve of Fig. 8. The accuracy of these figures depends very much on the accuracy of the data for V_L, and can only be estimated at roughly 0.5 percent.

These figures can all be extrapolated to absolute zero quite easily. From Fig. 6, it can be seen that ΔV is constant from about 1.45° to 1.2°, so it is possible to say that at absolute zero:

$$\Delta V = 2.07(\pm 0.06) \text{ cm}^3/\text{mole} \quad (T = 0° \text{ K}).$$

The extrapolation of V_L and V_s from Fig. 8 is more difficult, but fortunately the melting pressure also varies very slightly with temperature in this region. If instead of plotting the molar volumes as functions of temperature, they are plotted as functions of the melting pressure, the extrapolation to 25.00 atmos. is quite simple and the following values are obtained:

$$V_{L0} = 23.25(\pm 0.05) \text{ cm}^3/\text{mole},$$
$$V_{s0} = 21.18(\pm 0.1) \text{ cm}^3/\text{mole}.$$

V. CALCULATIONS

The heats of melting, ρ, were calculated from the Clausius-Clapeyron equation,

$$\rho = T\Delta V dP/dT. \tag{4}$$

They are tabulated in column 8, Table I, and are plotted as the upper curve in Fig. 9. Below 1.4°, ΔV is practically constant, and dP/dT is given by Eq. (3), so that a simple analytical expression can be given for the heat of melting:

$$\rho = 0.021T^8 \text{ cal./mole} \quad (1.4° \text{ to } 1.0° \text{ K}). \tag{5}$$

The figures for the heats of melting in column 9, Table I, are experimental values due to Keesom and Keesom[11] and Kaischew and Simon.[12] They extend only down to about 2.2°, but extrapolate to the heats of melting determined directly in these experiments.

From these data and the relation

$$\Delta U = \rho - P\Delta V \tag{6}$$

the change in the internal energy of liquid helium on solidification is easily calculated. This is also shown in Fig. 9 and in Table I. The interesting effect here is that, while ρ approaches zero very rapidly, ΔU approaches a negative value at absolute zero. This is a direct consequence of the fact that the liquid-solid transformation exists with a definite ΔV at absolute zero, as has been pointed out previously.[2]

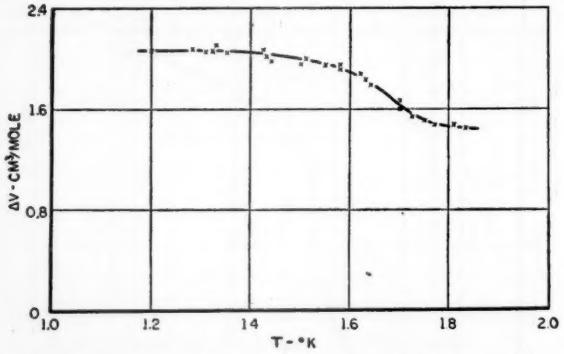

FIG. 6. The experimental data for the molar change in volume of helium on melting, $\Delta V = V_L - V_s$.

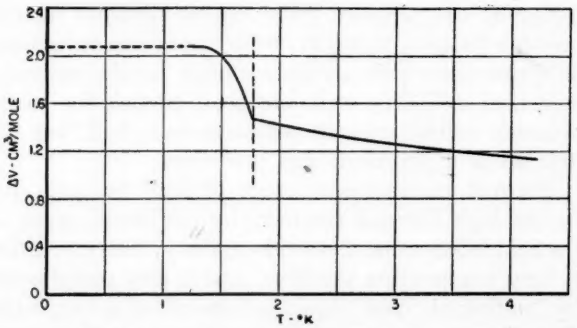

FIG. 7. The change in molar volume of helium on melting, $\Delta V = V_L - V_s$.

[10] W. H. Keesom, reference 1, p. 210.
[11] W. H. Keesom and A. P. Keesom, Leiden Comm. 240b (1936).
[12] R. Kaischew and F. Simon, Nature 133, 460 (1934).

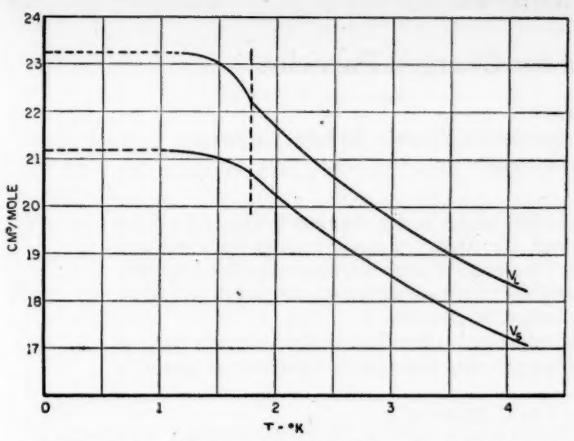

FIG. 8. The molar volumes of liquid (V_L) and solid helium (V_s) along the melting curve.

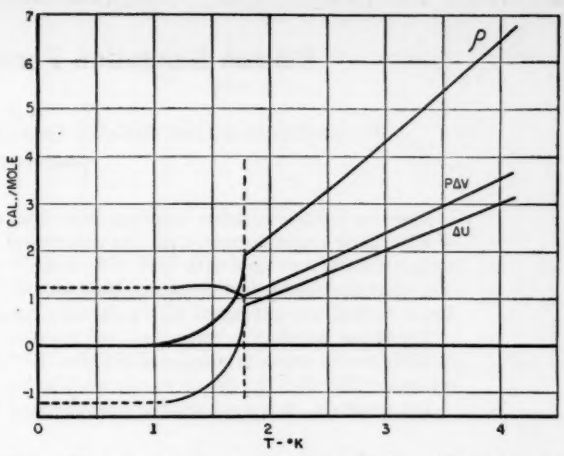

FIG. 9. The molar heat of melting, ρ, $P\Delta V$, and the change in internal energy, $\Delta U=\rho-P\Delta V$, for helium on solidification.

The actual internal energy of solid helium at absolute zero can also be calculated. From the work of Bleaney and Simon[13] on the vapor pressure of helium below 1.6°, the latent heat of vaporization of liquid helium at absolute zero can be calculated to be 14.3 cal./mole; therefore the internal energy of liquid helium at zero temperature and pressure is -14.3 cal./mole. The increase in internal energy of liquid helium upon the application of 25 atmos. pressure can be calculated from the integral $\int PdV$, which gives -1.1 cal./mole, using data due to Keesom and Keesom.[14] Finally, from Fig. 9, the internal energy difference between the liquid and solid under 25 atmos. pressure and at absolute zero can be determined as -1.25 cal./mole. These data are summarized in Table II, together with the other constants for liquid and solid helium at absolute zero.

One other calculation can be made, concerning the specific heat of liquid helium near 1° K and under a pressure of 25 atmos. Using the thermodynamic formula,

$$C_{PL}-C_{PS}=\frac{d\rho}{dT}-\frac{\rho}{T}+\frac{\rho}{\Delta V}\left(\frac{\partial(V_L-V_S)}{\partial T}\right)_P, \quad (7)$$

and the experimental results summarized in Eq. (5), the following relation is obtained for temperatures slightly above 1°, where the melting pressure is practically constant (the last term in Eq. (7) being negligible):

$$C_{PL}-C_{ps}=0.15T^7 \text{ cal./mole deg.} \quad (8)$$

In this region, C_{vs} (which differs very little from C_{ps}) can be extrapolated roughly to[15]

$$C_{vs}=0.03T^4 \text{ cal./mole deg.} \quad (9)$$

This gives the specific heat of liquid helium under 25 atmos. pressure, near 1°, as:

$$C_{PL}=0.15T^4(T^3+\tfrac{1}{5}) \text{ cal./mole deg.} \quad (8a)$$

As a rough check, the specific heat of liquid helium as calculated from the specific heat of the liquid at 1° and zero pressure and

$$(\partial C_P/\partial P)_T=-T(\partial^2 V/\partial T^2)_P$$

agrees in order of magnitude with this equation quite nicely. Of course, $(\partial V/\partial T)_P$, much less, $(\partial^2 V/\partial T^2)_P$, is not very well known.

TABLE II. The molar volumes and internal energies of liquid and solid helium at absolute zero.

	P (atmos.)	U (cal./mole)	V (cm³/mole)
Liquid, 0° K	0	−14.3	27.4
Liquid, 0° K	25	−13.2	23.25
Solid, 0° K	25	−11.9	21.2

The following conclusion can be drawn. The specific heat of liquid helium near 1° and under 25 atmos. pressure varies as some power of the temperature closer to T^7 than to T^4 (probably T^6). This is in good, although probably coincidental, agreement with the Leiden data[16] for the specific heat of liquid helium under its saturated vapor pressure in this same region.

The effect of the λ-transformation in liquid helium is shown quite markedly in the thermodynamic functions for the liquid-solid transformation. For a normal substance, the curves of Fig. 9 would terminate at a triple point which would occur at approximately the same temperature as does the λ-transformation. Helium, however, instead of losing its entropy by becoming a solid, becomes some form of degenerate liquid, and as such loses its entropy in a complicated manner. Thus, near absolute zero, the curves in Fig. 9 represent a curious type of mechanical transformation from a crystal of high spatial order to a liquid with a high degree of order of a different type.

I wish to thank Professor F. E. Simon for suggesting this problem, and for his continuous interest and advice. I also wish to thank Dr. R. Berman for his assistance in taking the data. This work was made possible in part by a Parker Travelling Fellowship in Physics from Harvard University, and in part by a grant from the Carnegie Fund for Overseas Students.

[13] B. Bleaney and F. Simon, Trans. Faraday Soc. **35**, 1205 (1939).
[14] W. H. Keesom, reference 1, p. 240.
[15] W. H. Keesom, reference 1, p. 227.
[16] W. H. Keesom, reference 1, p. 220.

Fission Excitation Functions for Charged Particles

J. JUNGERMAN*
Physics Department and Radiation Laboratory, University of California, Berkeley, California
(Received March 9, 1950)

Absolute fission excitation functions have been measured with an ionization chamber to detect the pulse of a recoiling single fragment. In the experiment performed, the 60-in. Crocker cyclotron deuterons and alpha-particles were used with Th^{232}, U^{235}, and U^{238} targets. Thresholds of these reactions were also observed. The maximum alpha-particle energy used was 33.5 Mev and the maximum deuteron energy was 17.5 Mev. Beam current was integrated with a Faraday cup and an ionization chamber.

The 184-in. synchrocyclotron was used to extend the fission excitation functions to alpha-particle energies of 390 Mev and deuteron energies of 193 Mev. Bi^{209} and Au^{197} targets were also added. Preliminary results with protons of 340 Mev maximum energy are also reported.

The results of the experiments are summarized in Figs. 3 to 17 inclusive.

I. INTRODUCTION

THE production of fission by means of bombardment with charged particles has been observed by various investigators.[1–5] All of the investigations have utilized the beta-activity of the fission fragments as the indicator of the number of fissions. In particular, in the excitation function measurements of S. C. Wright and the author[5] it was necessary to make an assumption concerning the beta-activity of the fission fragments in order to obtain an absolute cross-section scale. The assumption was made that the beta-activity of the complex of fission fragments was the same, for a given time after a short bombardment, for fission produced by charged particles or by thermal neutrons.

In recognition of the possibly unwarranted assumptions made in the above work concerning the beta-activity of the fragments from the charged particle fission, it was decided to repeat the experiment by a more direct method. This method consisted in counting the pulses of ionization produced by the fission fragments in an ionization chamber. The detection of a fission pulse in the presence of the ionization produced by the beam itself is made possible by use of a cancellation principle due to Baldwin and Klaiber,[6] and independently suggested by C. Wiegand. This principle was used to measure fission excitation functions on the 60-in. Crocker cyclotron and the 184-in. synchrocyclotron.

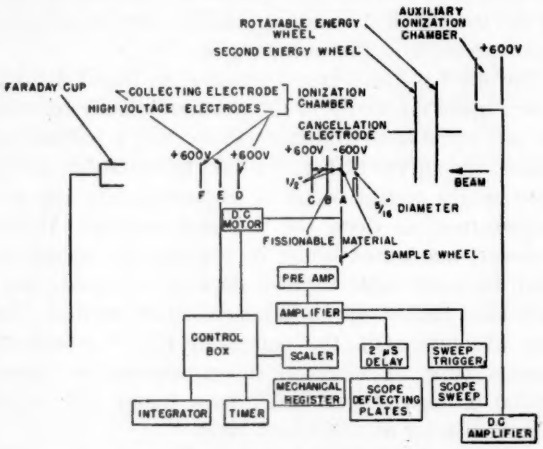

FIG. 1. Experimental arrangement.

II. 60-IN. CYCLOTRON EXPERIMENTS

A. Apparatus

(1) *Beam Collimation and Energy Reducing Equipment*

Figure 1 shows a schematic drawing of the experimental arrangement.

The beam collimation was similar to that of Kelly and Segrè[7] except that the exit slit of the collimator was widened to $\frac{1}{4}$ in. The beam emerging from the defining slit was found to be quite homogeneous in energy by Kelly and Segrè because the fringing field of the cyclotron magnet causes the collimating tube to act as a velocity selector. The energy of this homogeneous beam could be varied by means of aluminum foils placed in the two wheels shown in Fig. 1. The arrangement was similar to that described by Kelly[8] except that a window of 0.001 in. dural was substituted for the Faraday cup. One of the wheels could be rotated while the cyclotron was in operation. This wheel had aluminum foils ranging in thickness from 1.5 mg/cm² to 30 mg/cm² and one slot had 339 mg/cm² of aluminum, which was greater than the range of either the deuteron or the alpha-particle beams. The second wheel was provided with aluminum foils whose thickness increased about 30 mg/cm² from slot to slot. In this way it was possible to vary the energy of the beam particles over the entire energy range of the excitation function in steps corresponding to the energy loss in 1.5 mg/cm² of aluminum.

* Present address: Floyd Newman Laboratory of Nuclear Studies, Cornell University, Ithaca, New York.
[1] D. H. T. Gant, Nature 144, 707 (1939).
[2] I. C. Jacobsen and N. O. Lassen, Phys. Rev. 58, 867 (1940).
[3] G. Dessauer and E. M. Haffner, Phys. Rev. 59, 840 (1941).
[4] E. Fermi and E. Segrè, Phys. Rev. 59, 680 (1941).
[5] J. Jungerman and S. C. Wright, Phys. Rev. 74, 150 (1948).
[6] G. C. Baldwin and G. S. Klaiber, Phys. Rev. 71, 3 (1947).
[7] E. L. Kelly and E. Segrè, Phys. Rev. 75, 999 (1949).
[8] E. L. Kelly, Phys. Rev. 75, 1006 (1949).

(2) *Fission Ionization Chamber and Beam Current Collecting Equipment*

After leaving the wheels the beam passed through a 0.001 in. dural window, then through about 1 cm of air, and then entered the fission chamber through another 0.001 in. dural window. The beam encountered the fissionable material after passing through 3.4 cm of argon and another 0.001 in. of aluminum upon which the fissionable material was deposited. Any of six different samples could be selected while the cyclotron was in operation by means of a remote-controlled sample changer.

Each sample was provided with a mask which covered all but a circular area of $\frac{3}{8}$ in. diameter. Before striking the sample the beam was collimated by passing through a hole $\frac{5}{16}$ in. in diameter in aluminum of 0.0625 in. thickness. The hole was accurately positioned with respect to the sample mask. It was thus assured that all of the beam particles passing through the ionization chamber had actually traversed the fissionable substance.

The distance from the sample wheel to plate B was $\frac{1}{2}$ in. This was equal to the range of the fission fragments at the pressures used (about 150 cm Hg). Plate B was connected to the grid of the first tube of the preamplifier. It was constructed of aluminum leaf (0.17 mg/cm^2) which was held in position by a brass ring. Plate C was constructed similarly and served as a cancellation electrode. It was placed such that plate B was equidistant from A and C. The potentials were as indicated on Fig. 1.

Plates D, E, and F constituted an ionization chamber used to measure the beam current. The center collecting electrode, E, was surrounded by plates at high potential (600 v) so that the charges would not be collected that were not formed in the region between the ionization chamber plates.

After traversing the ion chamber, the beam passed through a 0.001 in. dural window. It then passed through 2 cm of air and entered a Faraday cup through a similar window. Being near the cyclotron, the apparatus was operated in a magnetic field of 2000 gauss; in this magnetic field the geometry of the cup was such that secondary electrons ejected from the cup by the beam would have to exceed 4 Mev in order to escape striking the entrance walls of the cup.

(3) *Electronics*

A block diagram of the electronic arrangement is also shown in Fig. 1. The pulses from the fission ionization chamber were preamplified before the signal was sent through the thrity feet of cable that was necessary to reach the amplifier outside the cyclotron shielding. The preamplifier was equipped with magnetic shields around each tube so that the effect of the magnetic field on the tube gain would be minimized. The preamplifier was so oriented that the path of the electrons in the tubes was parallel to the magnetic lines of force. A test showed that the electron collection in the fission ionization chamber was unaffected by the magnetic field.

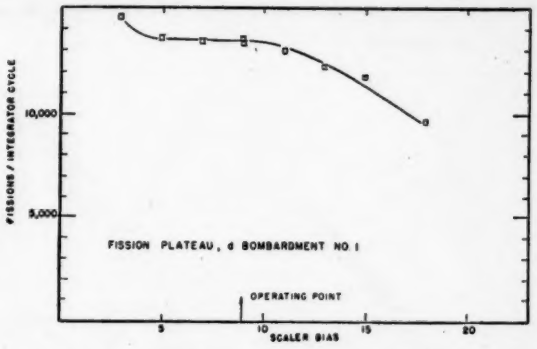

FIG. 2. A typical fission count *versus* discriminator bias curve.

The output of the amplifier was connected to a scale of 64 and mechanical register. By using an oscilloscope with 5 microsecond sweep speed the form of the ionization pulse was observed. A delay in the arrival of the pulse on the deflection plates provided time for the sweep to start. The shape of a typical fission pulse can be obtained by observing the pulse form when fission is induced by slow neutrons.

The pulses recorded as fissions in this experiment were observed to have the same form and magnitude as the slow neutron fission pulses. (Slow neutrons were generated with paraffin and a Ra-Be source.) The amplifier RC was adjusted so that the pulse decayed to $1/e$ in 5 microseconds.

(4) *Beam Current Integrator*

The beam current was integrated by measuring the voltage attained by a known capacitor. The capacitor could be charged directly by the beam current caught in the Faraday cup, or it could be charged with the beam current magnified by the order of ten thousand times by measuring the charge collected by the ionization chamber. Polystyrene coaxial cables conducted the currents to the voltage measuring equipment. The voltage measurement was done electronically using a circuit of Vance.[9] The circuit is characterized by a high input resistance and therefore makes it possible to measure the voltage of the condenser without changing the value of the voltage. This instrument was calibrated using a potentiometer. It was found that no appreciable change in calibration occurred during the course of the experiment.

For the integration of the current from the ionization chamber a capacity of about 10 μf was needed. The condensers made by the John Fast Company of Chicago with a polystyrene dielectric were found to be satisfactory.

Since "fast" condensers of greater than 0.1 μf were not available, the range of the instrument was extended

[9] A. W. Vance, Rev. Sci. Inst. 7, 489 (1936).

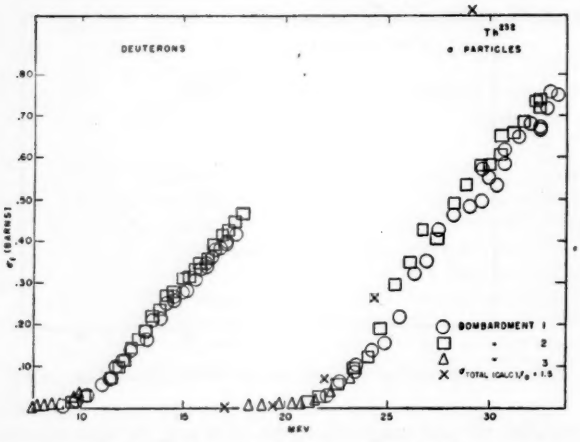

FIG. 3. Fission excitation functions for Th^{232}.

by using a potential dividing arrangement of these capacitors. All capacity elements were measured with a capacity bridge which was in turn calibrated with a standard capacitor.

A control box contained a master gang switch which simultaneously actuated a sweep-second timer, the scaling circuit, and the current integrator. It had two "on" positions; one position allowed voltage on the ionization chamber to be measured by the integrator, while the other connected the Faraday cup to the integrator.

(5) *Targets*

The samples of fissionable material were prepared as described in reference 5. The amount of fissionable material was determined by alpha-counting and weighing. The alpha-counting was done with the ionization chamber and the electronic equipment used for the experiment. In addition the samples were removed and counted in the laboratory alpha-counter. The thicknesses agreed within experimental error (three percent).

The homogeneity of the Th^{232} and U^{238} samples was tested by alpha-counting portions of the large foil from which the bombarded sample was cut. These portions were of the same area as the sample and the alpha-activities differed by a maximum of three percent from the mean. In the case of U^{235} the inhomogeneity would be expected to be greater since it was made in 21 coats and bakings whereas the other samples were made in 130. The thickness of the targets were as follows: U^{238}, 0.85_0 mg/cm²; Th^{232}, 0.68_3 mg/cm²; and U^{235}, 0.19_2 mg/cm². The U^{235} sample contained greater than 95 percent U^{235}. Since the ranges of fission fragments and alpha-particles are of the same order of magnitude the determination of sample thickness by alpha-count cancels to some degree the error made in the fission count due to the finite thickness of the sample. The error in the fission cross section is estimated to be less than 10 percent from this source.

B. Method

(1) *Excitation Functions*

In the excitation function measurements, operation was as follows: a value of the beam energy was selected by rotating the wheel containing the fine steps of aluminum thickness to the appropriate position. A target was selected with the sample changer. Then the master switch was turned to the ionization chamber position. When the integrator showed that the capacity had reached the appropriate potential, the master switch was returned to the "off" position and the number of fissions and the time was recorded. At full beam energy this process would take about two minutes and several thousand fissions would be obtained. The target was then changed and the process repeated. After all three targets had been bombarded, the energy was again changed by a small amount. In this manner three excitation functions were obtained simultaneously.

At the beginning of each bombardment the number of fissions per unit beam current *versus* the discriminator setting of the scaler was measured. After a certain value of the bias is reached, practically all the fissions are counted and therefore one obtains a fission plateau. Figure 2 shows a typical fission count *versus* discriminator bias curve. At very low values of the bias setting a point is reached where the pulses due to the beam ionization are counted and the plateau ends. In order to minimize the number of spurious counts from the uncanceled beam ionization, the operating point was chosen near the end of the plateau on the high bias side. Fallacious counts could also arise from sparking of the deflector or of the high voltage on the dees of the cyclotron. These were of greater height than the fission pulses and hence could not be removed by discrimination. It was therefore necessary to have the cyclotron in a very steady condition if reliable results were to be obtained. This was found to be the case if the cyclotron had been running previously for several days so that it was well baked in.

One of the samples consisted of an aluminum blank of the same thickness (0.001 in.) as that upon which the fissionable materials were deposited. By selecting this sample while the cyclotron continued to operate at the same level, it was possible to discover how many spurious counts were being recorded as fissions for a given discriminator setting. If operating conditions of the cyclotron were satisfactory, it was always possible to reduce the number of spurious counts from the aluminum blank target to zero.

A second condition on the method of operating the cyclotron was that it produce as few neutrons as possible. To minimize the effect of the neutrons the sample area was made as nearly the same as the beam area as was practicable, and the entire fission ionization chamber was covered with $\frac{1}{32}$ in. of cadmium. An upper limit for the neutron fission background could be obtained

for any fissionable sample selected by rotating the energy wheel to the slot which had sufficient aluminum thickness to stop the cyclotron beam. The background obtained by counting the number of neutron fissions for the same time as the charged particle bombardment. The auxiliary ionization chamber, discussed below, monitored the cyclotron radiation level during the measurement.

It was found that the lowest neutron background was reached when the arc current and voltage of the cyclotron were as low as possible. This is reasonable since then the amount of beam that is circulating between (and some of it striking) the dees is as small as possible. In practice the auxiliary ionization chamber shown in Fig. 1 was found useful for estimating the neutron background. It was merely a large (108 in.^{3}) air-filled chamber with 600 v positive potential and a collecting electrode. It was placed near the target chamber of the cyclotron. The collected current was delivered to a direct current amplifier which read 10^{-9} amp. full scale. It was discovered that there was a definite positive correlation between the neutron background and the reading of the d.c. amplifier. This is plausible since it means that the general density of radiation in the target area increased when the neutron density increased. In this manner a continuous check on the quality of the beam was obtained. When optimum conditions were reached the current from this ionization chamber was of the order of 10^{-11} amp. The neutron background was especially important in the case of U^{235}. In this case, although it was only about one percent at the full beam energy, it became the limiting factor at threshold energies.

(2) *Measurement of the Average Energy Required to Form an Ion Pair*

In each excitation function bombardment, data were also taken to find the number of ion pairs produced by one of the beam particles in passing through the ionization chamber. This was done by turning the master switch to the Faraday cup position so that the integrator measured the voltage on the Faraday cup. In the meantime the ionization chamber was charging its circuit. After the Faraday cup had reached an appropriate potential, the energy wheel was turned so as to stop the beam. After grounding the Faraday cup and integrator, the master switch was turned to the ionization chamber position and the potential of its condenser was determined. Photographs of the beam were taken at the entrance to the Faraday cup to check the alignment of the apparatus. The multiplication (number of ions produced by one beam particle) produced in the ionization chamber is then:

$$M=C_{I.C.}V_{I.C.}v/C_{F.C.}V_{F.C.}, \quad (1)$$

where v is the number of electronic charges of the beam particle C and V refer to the capacities and voltages

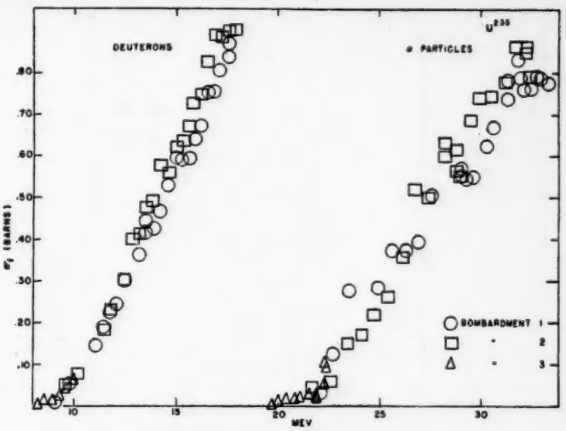

FIG. 4. Fission excitation functions of U^{235}.

of the Faraday cup and ionization chamber circuits. If the energy lost by one of the beam particles in the ionization chamber is known, the average number of electron volts, w, necessary to form an ion pair in argon can be determined for the energy region involved

$$w=\Delta E/M. \quad (2)$$

ΔE is the energy loss in the ionization chamber in electron volts and M is the quantity referred to above. In this experiment ΔE was calculated from the usual expression for the rate of energy loss by ionization:

$$dE/dx=(4\pi Nz^2Ze^4/mv^2)[\ln(2mv^2/I(1-\beta^2))-\beta^2]. \quad (3)$$

This calculation was made by Aron *et al.*,[10] who used the value $11.5Z$ for I. This value was determined by Wilson[11] for protons of 4 Mev. The number of argon atoms per cm^3, N, can be determined from the gas laws if the pressure and temperature of the gas are known. The temperature was measured for each bombardment and the pressure was measured on a mechanical pressure gauge which in turn was calibrated against a mercury column.

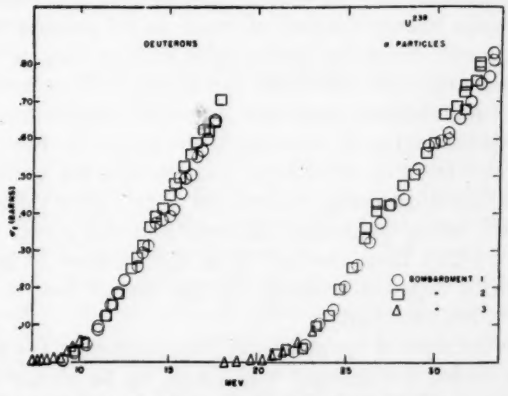

FIG. 5. Fission excitation functions for U^{238}.

[10] W. A. Aron, B. G. Hoffman, and F. C. Williams (private communication).
[11] R. R. Wilson, Phys. Rev. **60**, 749 (1941).

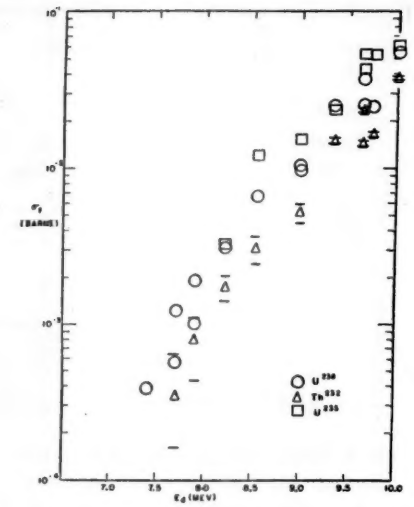

FIG. 6. Fission excitation functions for threshold energies of deuterons.

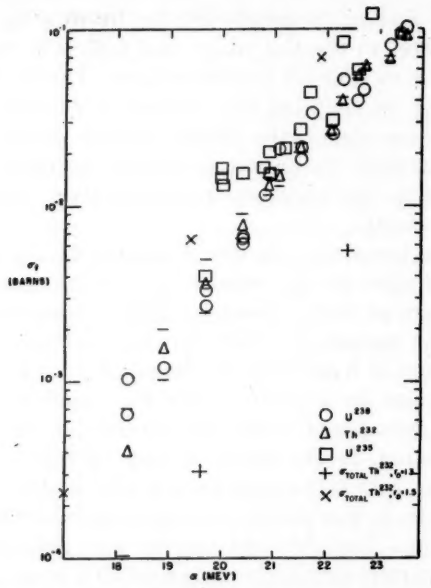

FIG. 7. Fission excitation functions for threshold energies of α-particles.

(3) *Beam Energy Determination*

In each bombardment the energy of the beam particles was determined. This was done by measuring the current collected by the ionization chamber as a function of the amount of aluminum placed in the beam by rotating the energy wheels. When the mean range was determined, the beam energy was obtained from the range-energy relation calculated from the expression for dE/dx given above.

C. Results

(1) *Excitation Functions*

Figures 3 to 5 show the excitation functions for the three substances investigated. In the case of deuterons the number of fissions observed for a point at full beam energy was about 13,000 for U^{238}, 7500 for Th^{232}, and 4300 for U^{235}. In the case of alpha-particle bombardment the corresponding number of fissions was 7300 for U^{238}, 5400 for Th^{232}, and 1800 in the case of U^{235}. The value of the beam energy differed as much as 2.5 percent from run to run. Since the fission cross section rises rapidly with energy, this difference is important if agreement is to be obtained between different bombardments. Besides changing the abscissa of the excitation function plot, an error in the energy also changes the ordinate such that if the energy is assumed to be higher than the correct value, the ordinate is lower and vice versa. This effect arises from the fact that the number of beam particles depends inversely on the energy loss in the ionization chamber.

In the case of the deuteron bombardments the neutron fission background was found to be about two counts for U^{238}, zero for Th^{232}, and about 20 for U^{235}. These background figures are given relative to the number of beam particles giving the number of charged particle fissions quoted above for full energy. For the alpha-particle bombardments the neutron fission background was about one count for U^{238}, zero for Th^{232}, and about 15 in the case of U^{235}. For the latter substance it was necessary to find the neutron background for each point since the numbers given could vary considerably at different times during a bombardment. The sensitivity of the neutron background to beam conditions is illustrated by the fact that during one of the alpha-particle bombardments a change of filament in the ion source raised the neutron background by a factor of four above the figures given.

Figures 6 and 7 show the fission excitation functions near the threshold in greater detail. A logarithmic ordinate was used since in this energy region the cross section is limited by penetration of the Coulomb potential barrier. The results shown include the ends of bombardments 1 and 2 as well as the special threshold bombardment, 3. The lowest points on these curves represent the observation of less than 10 fissions and are therefore unreliable. In the case of U^{235} the excitation function was not carried below the energy at which the neutron background became one-half of the total

TABLE I. Experimental values for w.

Particle	Energy (Mev)	w (ev)
d	16.9	27.1
d	17.0	28.4
d	17.0	29.7
d	16.0	33.2
d	9.6	31.8
α	30.1	31.6
α	28.8	28.7
α	30.4	30.5
α	29.6	31.0
α	22.4	31.4

fission count. Probable errors are shown on the Th^{232} points, which are the most reliable because of low neutron fission background.

(2) *Value of w*

The value of w, the average number of electron volts necessary to form an ion pair, was determined in several preliminary bombardments as well as bombardments that proved unsatisfactory for the determination of the fission excitation functions. The results are tabulated in Table I. Each value given represents the average of several observations for the given bombardment. The results for lower energy seem to show that the value of w is constant over the energy range of the experiment within the experimental error.

The average value of w for deuterons of about 17 Mev is then 29.6 ev, and for alpha-particles of about 30 Mev it is 30.5 ev. These values were used to find the multiplication factor, M, introduced by the ionization chamber when the computation of the fission cross sections was made. The results reported here for w in argon are higher than those given by other investigators. Nicodemus[12] gives 26.9 for 17.4-Mev electrons[12a] and

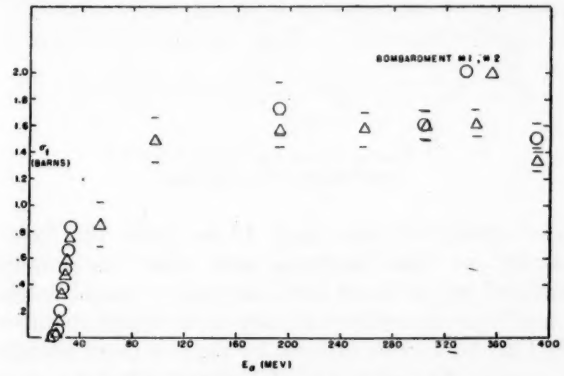

FIG. 8. Fission excitation function for U^{238} bombarded with alpha-particles.

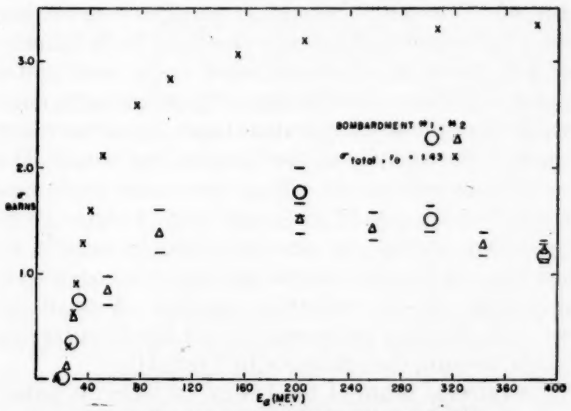

FIG. 9. Fission excitation function for Th^{232} bombarded with alpha-particles.

[12] D. B. Nicodemus, thesis, Stanford University (1946).
[12a] Quoted from Rossi and Staub, *Ionization Chambers* (McGraw-Hill Book Company, Inc., New York, 1949), p. 227.

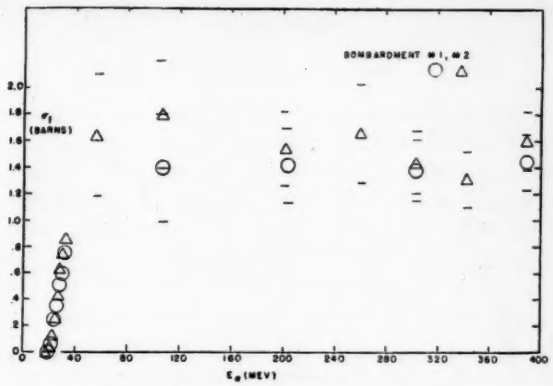

FIG. 10. Fission excitation function for U^{235} bombarded with alpha-particles.

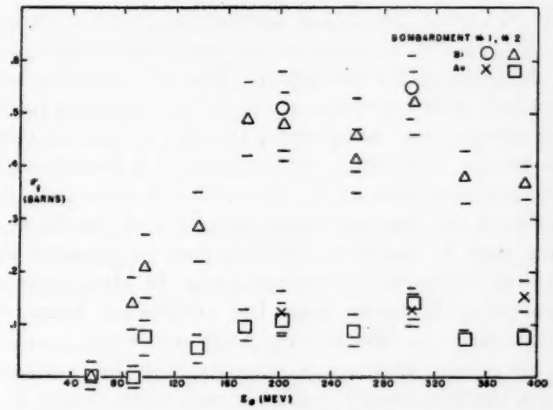

FIG. 11. Fission excitation functions for Bi^{209} and Au^{197} bombarded with alpha-particles.

Stetter[13] reports 28.4 ev for the alpha-particles of polonium. Fano[14] has given an approximate calculation of w which makes it plausible that w should be fairly insensitive to the energy or type of projectile. Recently experiments of Jesse *et al.*[15] have shown w to be constant for α-particles in the range one to nine Mev. If this constancy prevails at higher energies, then Stetter's value for w would give more accurate values for the fission cross sections.

D. Discussion

(1) *Comparison with Beta-Activity Experiment*

Comparison of the present results with those found in the previous experiment[5] indicates that the assumption made concerning the beta-activity of the complex of fission fragments is incorrect by a factor of about 1.5 to 1.7. In each case the charged particle fission seems to give more beta-activity in the fragments for the times after bombardment investigated. Newton[16] has investigated the fission yield *versus* mass spectrum for fission induced in throium by alpha-particles. He finds

[13] G. Stetter, Zeits. f. Physik **120**, 643 (1943).
[14] U. Fano, Phys. Rev. **70**, 44 (1946).
[15] Jesse, Forstat and Sadauskis, Phys. Rev. **77**, 782 (1950).
[16] A. S. Newton, Phys. Rev. **75**, 17 (1949).

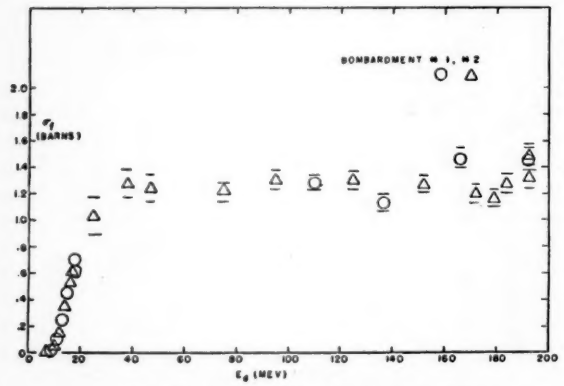

FIG. 12. Fission excitation function for U^{238} bombarded with deuterons.

that the usual dip in the distribution found with low energy projectiles (neutrons) has risen from 1/600 to 1/2 of the peaks of the distribution. The corresponding new beta-activities appearing in the fission fragments might well account for the apparent increase in beta-activity per fission. Newton finds the value 0.6 barn for the fission cross section at 27.5 Mev. This is lower than the results of the present experiment. Part of the discrepancy may be found in the fact that he assumes the incident alpha-particle energy to be 39 Mev, whereas measurements made with the collimated beam by Jungerman and Wright,[5] by Kelly and Segrè,[7] and in in the present experiment, indicate that the maximum alpha-particle energy available was more nearly 37.5 Mev. This would also account for the discrepancy in the fission threshold reported by Newton. He finds 23 to 24 Mev for the threshold, whereas the results of the beta-activity experiment and the present one indicate a value of around 21 Mev.

(2) *Comparison of Fission Cross Sections and Calculated Total Reaction Cross Sections*

Weisskopf[17] has calculated the total reaction cross section for alpha-particles on a thorium target. He assumes 1.48×10^{-13} cm for the radius of the alpha-particle so that the interaction radius between the alpha-particle and the target nucleus has the form $R=(r_0A^{\frac{1}{3}}+1.48)\times10^{-13}$, where A is the mass number of the target nucleus. Weisskopf gives points for $r_0=1.3$ and $r_0=1.5$. These points are plotted on the threshold excitation function for alpha-particles. It is seen that $r_0=1.3$ is excluded since it gives a fission cross section greater than the reaction cross section.

By continuing the total reaction cross-section curve above the threshold an estimate of the competition existing with fission can be obtained. This is shown for the choice $r_0=1.5$ on the *Th* (α, fission) excitation function. Since all target nuclei will have about the same total reaction cross section for a given projectile and projectile energy, the conclusion is reached that competition is greatest in the case of thorium, and least for U^{235}.

[17] V. P. Weisskopf, MDDC-1175 (1947), Lecture Series in Nuclear Physics.

III. 184-IN. SYNCHROCYCLOTRON EXPERIMENT

A. Apparatus and Method

The fission chamber and samples used were the same as those used for the 60-in. cyclotron experiment. The sample areas were increased to $\frac{1}{2}$ in. diameter and the beam was again collimated to $\frac{5}{16}$ in. Collimation was done after the absorber used to reduce the beam energy so that beam particles scattered in the absorber at large angles would not be able to traverse the fission chamber. However, it was not practicable to have a collimator for each sample as in the 60-in. cyclotron experiment. The

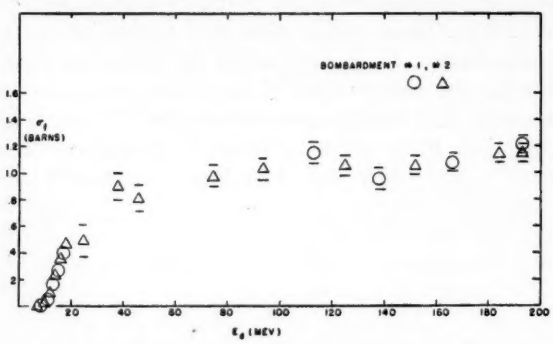

FIG. 13. Fission excitation function for Th^{232} bombarded with deuterons.

major collimation was done 12 in. from the fission chamber so that neutrons and other background generated by the beam arresting process would not be formed in the immediate vicinity of the fission chamber. The Faraday cup was altered for the new beam energies by making the collector a solid copper cylinder 3 in. in diameter and $4\frac{1}{2}$ in. in length. This geometry is sufficient to trap the proton beam (340 Mev) according to the data of V. Petersen.[17a] Secondary particles were trapped with a hollow two inch copper cylinder $1\frac{1}{8}$ in. in diameter and $\frac{1}{8}$ in. thick, which was attached to the beam end of the large cylinder. Since the beam intensities were much smaller than the 60-in. cyclotron beam, it was necessary to reduce the capacity of the Faraday cup circuit. This was done by placing the voltage measuring equipment for the Faraday cup in the target area. A meter giving the voltage on the cup was then brought outside the shielding. An identical circuit also simultaneously gave the voltage on the ionization chamber. A small air-cooled oil diffusion pump maintained the Faraday cup at high vacuum (less than 5×10^{-4} mm Hg).

The external beam of the 184-in. cyclotron is pulsed so that all beam particles in a given pulse arrive within the resolving time of the apparatus. This circumstance makes the counting of fission pulses more difficult than

[17a] V. Petersen (private communication).

in the relatively continuous beam of the 60-in. cyclotron, even though the energy loss by ionization of the beam particle in the fission chamber has decreased due to the high energies involved. Thus it is essential that the cancellation be as complete as possible. A suggestion of O. Chamberlain made it possible to vary the cancellation electrically. This was done by connecting a variable capacity in series with each of the plates A and C shown in Fig. 1. The value of one of these variable capacities could be changed during bombardment by rotating it with an electric motor. Thus while the cyclotron beam was kept constant, the amount of uncanceled beam pulse could be observed in the oscilloscope and minimized with the electric motor.

It was found possible to operate with no spurious beam pulses counting as fissions, provided the beam strength was such that, for example, about 150 fissions per minute were observed with deuterons of 190 Mev incident on the U^{238} sample. If the beam strength were proper, reasonable fission plateaus were again obtained. As in the 60-in. cyclotron experiment the pulse form was observed during operation as a check that the pulses observed were really fissions.

It was also possible to get an estimate of the background fission rate by inserting an absorber into the beam whose thickness was greater than the beam range. This could be done by remote control so that the cyclotron beam was not changed. Twelve different absorbers could be placed in the beam by this remote control device. Aluminum absorbers were used for alpha-particles and deuterons, and copper absorbers were used for protons. This allowed various energies to be selected without shutting off the cyclotron and also provided a method of beam range determination. It was necessary to measure the beam range in each bombardment in order to determine accurately the residual range of the beam in the region where the high energy curves join the curves obtained at the 60-in. cyclotron in the case of alpha-particle and deuteron bombardments.

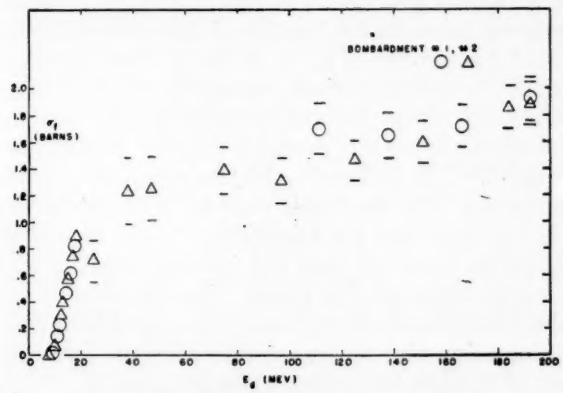

FIG. 14. Fission excitation function for U^{235} bombarded with deuterons.

B. Results

(1) *Excitation Functions*

Figures 8 to 15 inclusive show the excitation functions observed for alpha-particle and deuteron bombardments. The probable errors in the deuteron bombardments are in general less than for alpha-particles because the energy loss in the fission chamber by a beam particle is less for the former and also because the maximum intensity of the alpha-particle beam was much less than the deuteron beam. The alpha-particle beam was always used at full intensity. The points shown without probable error are from the 60-in. cyclotron experiment. The probable errors of the points that have zero cross section are computed on the assumption of one observed fission. The neutron fission background was about two percent of the charged beam fission rate when deuterons were used on a target of U^{238}. In the case of alpha-particles this background was less than one percent.

Figures 16 and 17 show the present status of the proton excitation functions. These data are quite preliminary since only one bombardment has been made. The low value of the cross section observed as compared with the results of the alpha-particle and deuteron bombardments is rather surprising. Because of this, a check on the equipment was made by changing the cyclotron beam to alpha-particles at the end of a proton bombardment. The alpha-particle cross sections so obtained for U238 and U235 checked within statistics with previous bombardments. The neutron fission background was about two percent for U^{238} for the proton case.

(2) *Faraday Cup Measurements*

In the case of deuterons the dE/dx curve as calculated from formula (3) was verified within ten percent in the range from 38 Mev to 192 Mev. The best fit was obtained for $w=29.5$ ev/ion pair. In the case of alpha-particles, the measurements were more difficult due to the smaller beam strength, but verification was

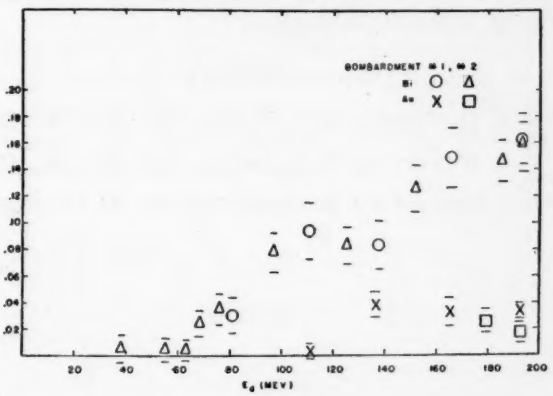

FIG. 15. Fission excitation functions for Bi^{209} and Au^{197} bombarded with deuterons. The ordinate scale should read σ_f (barns).

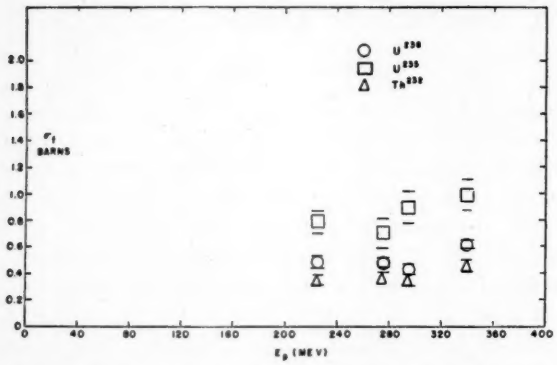

FIG. 16. Fission excitation functions for U^{238}, U^{235}, and Th^{232} bombarded by protons.

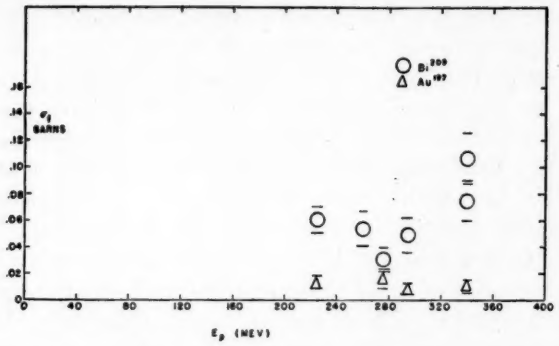

FIG. 17. Fission excitation functions for Bi^{209} and Au^{197} bombarded by protons.

again obtained to about twenty percent in the range 100 Mev to 390 Mev using 30 ev/ion pair. In the case of the proton bombardments, agreement to about twenty percent was obtained in the energy region above 200 Mev with 30 ev/ion pair.

C. Discussion

The fission cross section for full deuteron energy was investigated by Goeckermann and Perlman[18] using chemical techniques. They found a value of 0.2 barn, which is in agreement with the present experiment within the experimental errors. O'Connor and Seaborg[19] have investigated the spallation products and fission products of U^{238} bombarded by 390-Mev alpha-particles. They estimate the value of the fission cross section to be about two barns. This is seen to be somewhat higher than the results of the present experiment.

It is interesting to compare the calculated reaction cross section and the observed fission cross section in the high energy region. For the case of alpha-particles on a thorium target, the threshold data from the 60-in. cyclotron show that for $r_0=1.43$ the fission cross section observed would equal the calculated reaction cross section. Taking this value of r_0 the total reaction cross section can be calculated in the region above the Coulomb barrier by an approximate formula given by Bethe and Konopinski[20]

$$\sigma_{\text{reaction}}=\pi\lambda^2 P_0 l_c^2,$$

where

$$l_c^2=g^2(x-1)+0.744g^{4/3}(2x-1)^{2/3} \quad \text{for} \quad x>1.$$

P_0 is the penertration probability of the Coulomb barrier and λ is the projectile wave-length divided by 2π; x is the ratio of the energy to the effective barrier height, and g is a constant which depends on the nuclear radius. Since Bethe and Konopinski did not use a finite radius for the alpha-particle their r_0 should be 1.67 in order to correspond to Weisskopf's choice of 1.43. This value of r_0 gives the effective barrier height as 25.6 Mev, and a value of g of 23.0. The results of this calculation appear on the excitation function of thorium bombarded with alpha-particles (Fig. 9). It should be emphasized that the compound nucleus concept is not valid when the velocity of the projectile is much greater than the velocity of the nuclear particles (i.e., for $E_\alpha>$approx. 200 Mev).[21] This choice of r_0 gives the minimum possible competition with the fission process. With this choice of r_0 it is seen that the competition begins to become appreciable above 30 Mev and increases steadily with increasing alpha-particle energy. There is some chamical evidence obtained by James[16] that appreciable competition exists with the fission process for the bombardment of thorium by 37-Mev alpha-particles.

The author is especially grateful for the stimulating interest of Professor E. Segrè throughout this investigation and also wishes to thank Professor G. C. Wick and Professor V. Weisskopf for helpful discussions of the theoretical problems. Thanks are also due C. Wiegand and Dr. O. Chamberlain for many valuable suggestions. The cooperation of the personnel of the Crocker cyclotron and of the 184-in. cyclotron is gratefully acknowledged.

[18] R. H. Goeckermann and I. Perlman, Phys. Rev. **73**, 1127 (1948).
[19] P. R. O'Connor and G. T. Seaborg, Phys. Rev. **74**, 1189 (1948).
[20] H. A. Bethe and E. J. Konopinski, Phys. Rev. **54**, 130 (1938).
[21] R. Serber, Phys. Rev. **72**, 1114 (1947).

The Production of Mesons by Photons*

K. A. BRUECKNER
Radiation Laboratory, University of California, Berkeley, California
(Received February 27, 1950)

The general features of the process of photo-meson production are discussed on a semiclassical basis and also on the basis of perturbation theory in the weak coupling approximation applied to scalar, pseudoscalar, vector, and pseudovector meson theory. These calculations are carried out with the Feynman-Dyson methods to give covariant expressions for the cross sections. The corrections of next higher order in the meson-nucleon coupling are calculated for pseudoscalar mesons and are shown to give large contributions. Comparison of the conclusions of the theory with the experimental results seems to indicate that the meson is of spin zero and is closely bound to the nucleons as is characteristic of pseudoscalar theory.

I. INTRODUCTION

THE production of mesons by photons has recently been accomplished experimentally,[1] and extensive experimental work is now being done on the problem.[2] It has been found that the present experimental techniques permit the study of the production of mesons by photons with greater accuracy and detail than is possible for production by nucleon-nucleon collision. The theoretical analysis of this information is also considerably simplified by the nature of the interaction. It will be shown that the results depend very markedly on the nature of the coupling of the mesons to the electromagnetic field. Since processes involving this coupling can be handled readily for non-relativistic energies by treating the interactions as weak, the usual methods of perturbation theory can be applied with some confidence to this aspect of the production process. The uncertainties concerning the nature of the coupling of mesons to nucleons, which, as is well known, lead to incorrect predictions of scattering phenomena, do not strongly affect this process. In fact, the characteristic differences between the behavior of the photon-ejected spin zero and spin one mesons will be shown to be due almost entirely to the nature of the meson coupling to the electromagnetic field.

The theory of the production of photo-mesons has been studied by a number of people,[3] the most complete work being the recent contribution of Feshbach and Lax. The methods used have been those of perturbation theory in the weak coupling approximation. Effects of the recoil of the nucleons have been neglected. The results obtained differ markedly for the various theories. It is not immediately apparent how the characteristic differences are related to the detailed features of the theories. It is therefore of interest to attempt to understand by classical arguments, without reference to perturbation theory, some details of the process. It has further been thought worth while to carry out the calculations using the new covariant formalism, eliminating unnecessary approximations and exhibiting the simplicity of the methods. Finally, the higher order corrections in the meson-nucleon interaction have been calculated for the pseudoscalar theory, using the new subtraction techniques, and found to give finite and unambiguous results.

II. GENERAL DESCRIPTION

A. Ratio of Cross Section for Production of Negative and Positive Mesons

One of the most striking of the early experimental observations on the production of mesons by photons was the excess of negative over positive mesons.[1] At present this is still the best established experimental fact. It was pointed out by Brueckner and Goldberger[4] that very simple classical arguments could give an explanation of this result. These arguments simply pointed out that there is an essential asymmetry in the production of negative and positive mesons. When the former are produced from neutrons, the charge-carrying nucleon is the final proton with large recoil velocity. When positive mesons are produced, the proton is initially at rest and does not interact through its charge. Using the interaction

$$e\mathbf{v}\cdot\mathbf{A}/(1-v/c\cos\theta) \tag{1}$$

which differs from the non-relativistic expression $e\mathbf{v}\cdot\mathbf{A}$ because of retardation effects in the interaction of the charge with the electromagnetic field, one obtains for the ratio of the interactions leading to the production of positive and negative mesons

$$\frac{I(\text{positives})}{I(\text{negatives})}=\frac{e\mathbf{v}\cdot\mathbf{A}/(1-v/c\cos\theta)(\text{meson})}{-e\dfrac{\mathbf{v}\cdot\mathbf{A}}{1-v/c\cos\theta}(\text{meson})+e\dfrac{\mathbf{v}\cdot\mathbf{A}}{1-v/c\cos\theta}(\text{recoil proton})}. \tag{2}$$

* This work was performed under the auspices of the AEC.
[1] McMillan, Peterson, and White, Science **110**, 579 (1949).
[2] Cook, Steinberger, McMillan, Peterson, and White (private communications).
[3] W. Heitler, Proc. Roy. Soc. **166**, 529 (1938); M. Kobayashi and T. Okayama, Proc. Phys. Math. Soc. Japan **21**, 1 (1939); H. S. W. Massey and H. C. Corben, Proc. Camb. Soc. **35**, 84 (1939) and **35**, 463 (1939); L. Nordheim and G. Nordheim, Phys. Rev. **54**, 254 (1938); H. Feshbach and M. Lax, Phys. Rev. **76**, 134 (1949); L. Foldy, Phys. Rev. **76**, 372 (1949).
[4] K. Brueckner and M. Goldberger, Phys. Rev. **76**, 1725 (1949).

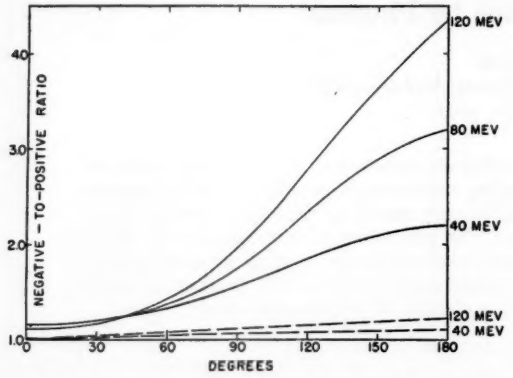

FIG. 1. The ratio of the cross sections for the production of negative and positive mesons. The solid curves are calculated with the assumption that the neutron does not interact with the electromagnetic field (Eq. (3)), the dotted curves with the assumption that the neutron interacts with the anomalous moment observed in a static field (Eq. (5)). The energies indicated in this and the following figures are the meson energies, which are related to the photon energy as shown in Fig. 6.

The ratio of the cross sections then is the square of the ratio of the interactions. Using over-all energy and momentum conservation, this ratio can be written

$$\frac{\sigma(\text{positives})}{\sigma(\text{negatives})}=[1-(q_0/Mc^2)(1-v/c\cos\theta)]^2, \quad (3)$$

where q_0 = meson energy including rest energy, M = nucleon mass, v = meson velocity, θ = angle between meson and photon velocity vectors. The dependence on meson energy and angle of this function is given explicitly in Fig. 1 (solid curves).

In this very simple argument the effects of the magnetic moments of the particles have been ignored. However, in Section V a generalization of the argument given here shows, for theories in which the electric dipole interactions are predominant, that the negative-to-positive ratio is changed by only a few percent. If, as can happen in some theories, the electric dipole moment is suppressed, and the magnetic moment interactions predominate, the ratio is given by

$$\sigma(+)/\sigma(-)=[1-(\gamma_p-\gamma_n/\gamma_p+\gamma_n)q_0/Mc^2(1-v/c\cos\theta)]^2, \quad (4)$$

where γ_n and γ_p are the magnitudes of the magnetic moments of the neutron and proton. It is interesting to observe that, if the magnetic moment of the nucleon is ignored, the ratio would be the same as that given by Eq. (3). If the numerical values of the static magnetic moments are substituted in this expression, we obtain

$$\sigma(+)/\sigma(-)=[1-0.20q_0/Mc^2(1-v/c\cos\theta)]^2. \quad (5)$$

This function is given graphically in Fig. 1 (dashed curves). It is apparent that, if nucleon moment interactions are important, the introduction of a magnetic moment for the neutron removes much of the asymmetry in the process leading to the production of positive and negative mesons and leads to a plus-to-minus ratio which is nearly unity.

We remark here that we have assumed that, with photons at energies of about the meson rest energy, the nucleons interact with the anomalous moments observed in a static field. This will be true only if the circulating currents which give rise to the anomalous moments are confined to a region small compared with the wavelength of the radiation. If this is not true, the anomalous moments will show energy dependence and the values of the static moments cannot be used.

We have ignored the interaction of the meson magnetic moments. These could contribute only if the meson were a vector particle, i.e., with spin one. It is apparent that such interactions are symmetrical for the production of either negative or positive mesons. Therefore strong meson-moment interactions would give a negative-to-positive ratio close to one.

One can conclude that a verification of the results of Eq. (3) would indicate that the meson does not interact strongly through a magnetic moment and that the neutron anomalous magnetic moment does not play an important part in the process. We have seen that these conclusions do not depend on the nature of the coupling of the mesons to the nucleons.

B. Angular Distribution

If the photon is absorbed by the ejected meson at photon energies for example of 200 to 300 Mev, $\beta=v/c$

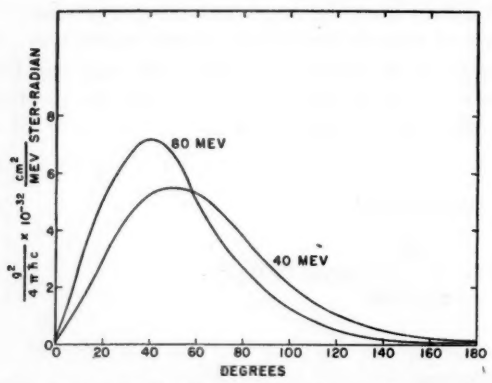

FIG. 2. Angular distribution of positive scalar mesons from dK/K photon spectrum.

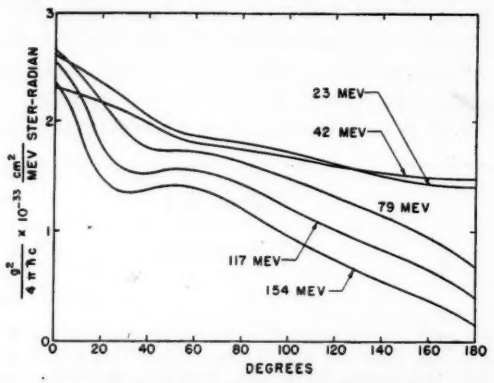

FIG. 3. Angular distribution of positive pseudoscalar mesons from dK/K photon spectrum.

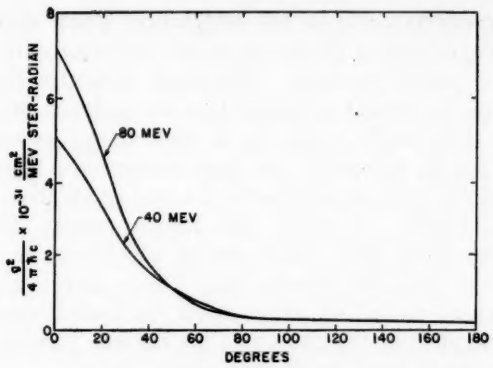

FIG. 4. Angular distribution of positive vector mesons from dK/K photon spectrum.

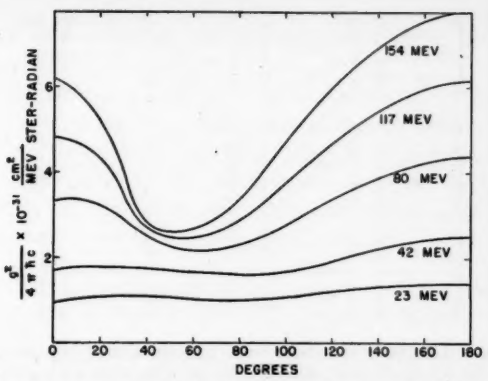

FIG. 5. Angular distribution of positive pseudovector meson from dK/K photon spectrum.

for the meson will not be small compared with unity. The angular distribution will show a large asymmetry about 90 degrees due to the presence in the differential cross section of the denominator

$$(1-\beta\cos\theta)^{-2} \tag{6}$$

which appears because of the retardation effects in the interaction of charge with the electromagnetic field. However, if the absorption of the photon is through its coupling with the nucleon, $v/c \ll 1$ for the nucleon and the angular distribution will be nearly symmetric about 90 degrees. One would therefore expect that the degree of symmetry would indicate which particle interacts most strongly with the photon.

If the interactions are primarily of the form $e\boldsymbol{v}\cdot\mathbf{A}$ then, since the photon field is transverse, the angular spectra must fall off to zero at 0 or 180 degrees. Spectra which do not exhibit this behavior must be due to magnetic moment-like interactions.

III. THE PRINCIPAL FEATURES OF THE VARIOUS THEORETICAL RESULTS

The calculations, unless otherwise specified, are for the first non-vanishing order in which the process can take place. The nucleons are treated as Dirac particles and the effects of their recoil are fully taken into account. The scalar, pseudoscalar, vector, and pseudovector theories are considered, using the couplings with the nucleon field which do not involve derivatives of the meson field.

The spectra shown in Figs. 2 to 5 are for positive mesons produced by a dK/K photon spectrum. This approximates the bremsstrahlung energy distribution at high energies which is used in the laboratory to produce mesons. The relation between the meson and the photon energy, as a function of angle, is given in Fig. 6.

A. Scalar Meson

The scalar meson characteristically shows a dipole angular distribution (Fig. 2) at low energies which is strongly distorted in the forward direction at energies above a few Mev by the factor of Eq. (6). This is due to the predominance of the photon-meson interaction and the absence of a magnetic moment for the meson. This simple result is quite analogous to the low energy photoelectric effect in an atom, since the mesons are spherically symmetric in distribution about the nucleon, and the photon interacts relatively weakly with the nucleon. This is in agreement with the fact that the meson cloud about the nucleon extends to distances of the order $\hbar/\mu c$, while the circulating currents associated with the magnetic moment of the nucleon are distributed over a region of order $\hbar/Mc$ and therefore give contributions which are smaller in the ratio $(\mu/M)^2$. The plus-to-minus ratio from the lowest order calculations is the same as that obtained by the classical argument, as would be expected since the nucleons are treated as Dirac particles and the meson has no magnetic moment interaction.

B. Pseudoscalar Meson

The pseudoscalar theory shows a roughly isotropic angular distribution (Fig. 3) indicating the predominance of the coupling of the photon to the magnetic moment of the nucleon. The unimportance of the electric-dipole terms in the interaction, i.e., the coupling to the linear motion of charge, is due to the close binding of the meson cloud to the nucleon. The probability of

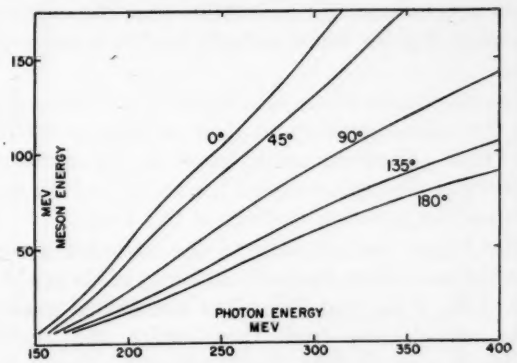

FIG. 6. Relation between meson and photon energy as a function of the angle of the meson with the photon beam direction.

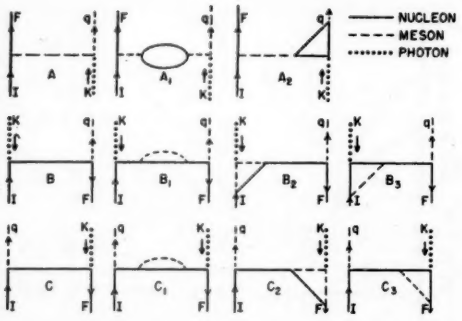

FIG. 7. Diagrams for photo-meson production. Diagrams A, B, C are for production in lowest order ge; diagrams with subscripts are for production in order g^3e.

finding a meson at a distance $\hbar/\mu c$, which is the wavelength of the photon, is relatively small. However, the direct coupling of the photon to the magnetic moment of the nucleon, preceded or followed by the emission of the final meson, is relatively probable. Examination of the matrix elements involved in these transitions indicates that this behavior is due to the existence of intermediate states in which the nucleon undergoes transitions to negative energy states. For such processes the matrix elements of the couplings to the electromagnetic and meson fields are of the order unity instead of v/c for the nucleons. The ratio of negative to positive mesons given by the lowest order calculation is the same as that for the scalar theory.

Preliminary experimental results indicate that the spectrum of mesons observed is roughly isotropic in angular distribution as predicted by the pseudoscalar theory. Therefore this theory was selected for examination of the corrections of higher order in the nucleon-meson coupling constant g. This involves another emission and reabsorption of a virtual meson, as indicated in Fig. 7. It was hoped that the investigation of the corrections would answer questions concerning the contribution of the anomalous magnetic moments of the nucleons and the possible large effects of corrections to processes in which the photon is coupled directly to the meson or its associated Dirac vacuum field. Examination of the effects of higher order processes would also indicate the probability that the expansion in powers of $g^2/4\pi$ would actually lead to a convergent series.

The calculation of the next higher order terms shows that they give contributions about as large as the first-order terms, therefore casting grave doubts on the convergence of the expansion and the validity of the application of perturbation methods of this kind.

The largest contribution to the corrections comes from the anomalous magnetic moments of the nucleons, Figs. 7-B_1, 7-B_2, and 7-B_3. The anomalous moments differ considerably from those which the nucleons exhibit in a static field, as calculated by Case.[5] Non-static effects occur in the interaction which decrease the magnitudes of the moments and also change the sign of the proton moment. This result indicates that it may not be correct to assume that the nucleons interact, with their static moments, in high energy processes. The actual magnitude of these corrections, however, probably can be believed only in a very qualitative way.

Corrections in which the meson creates virtual nucleon pairs (Fig. 7-A_1), one of which may interact directly with the photon (Fig. 7-A_2), give negligible contributions and so do not affect the predominance of the coupling of the photon to the nucleon through the Dirac and anomalous moments.

C. Vector and Pseudovector

The vector theory shows a strongly asymmetric angular distribution (Fig. 4), indicating the predominance of the photon-meson interaction. This distribution is also peaked markedly forward showing that the interaction is due at least in part to the magnetic moment of the meson. The pseudovector theory shows a nearly isotropic angular spectrum (Fig. 5). This, however, is not due to the largeness of the nucleon photon coupling but to the large magnetic moment interaction of the meson. The negative to positive ratio (Fig. 8) also reflects the large effects of the magnetic moment of the spin-one mesons, differing considerably from the result obtained by ignoring the meson moment. Also very characteristic of vector and pseudovector meson is the rapid increase of the cross section with energy (Figs. 4 and 5). This is due both to the strong energy dependence of the electromagnetic field coupling with longitudinally polarized mesons and to the magnetic moment interactions.

Higher order corrections probably would not particularly affect these results, since processes involving production of virtual nucleon pairs by the mesons seem to give negligible contributions. Higher order processes involving the coupling of the photon to the nucleon and its associated meson field would give corrections to terms which are already relatively unimportant in the process.

IV. CONCLUSIONS

We have seen that certain features of the process of production of mesons by photons are nearly independent of the nature of the coupling of mesons to nucleons. In particular, one can expect through the measurement of the distribution in energy and angle of photo-mesons at energies above a few Mev: (1) to determine with some confidence the spin of the meson, through the characteristic behavior of particles with a magnetic moment in the electromagnetic field. The strong energy dependence of the coupling of spin-one mesons to photons has been used previously by Christy and Kusaka[6] to demonstrate that cosmic-ray mesons cannot be of this

[5] K. M. Case, Phys. Rev. 76, 1 (1949).

[6] R. F. Christy and S. Kusaka, Phys. Rev. 59, 414 (1941).

type; (2) to examine the distribution of mesons about the nucleon, since if the distribution extends to distances of the order $\hbar/\mu c$, one would expect that the electric-dipole terms would be predominant in the coupling to the electromagnetic field. Only if the meson distribution is singular, i.e., closely bound to the nucleons, can one expect the interaction with the circulating currents of the magnetic moments to become relatively important; (3) through a measurement of the plus-to-minus ratio to determine the effects of a meson magnetic moment and the nature of the anomalous moments for the nucleons. The anomalous moments will be nearly independent of the frequency of the electromagnetic field only if they are confined to regions small compared with the wave-length of the radiation.

The further details of the calculation made with perturbation theory can probably not be accepted quantiatively since higher order corrections are not negligible. For example, explicit calculation of the higher effects for the pseudoscalar theory predicts large anomalous magnetic moment interactions for the nucleons including corrections, as large as the lowest order terms, corresponding to polarization of the vacuum by the nucleons. The anomalous moments are considerably smaller than those which the nucleons exhibit in a static field and different in sign for the proton. The importance of the corrections for the pseudoscalar theory appears to be the result of the close binding of the mesons to the nucleons, which in turn leads to the characteristic predominance of the nucleon magnetic moment interactions in the production process. Higher order effects, however, do not change the general features of the lowest order results. There, therefore, seems to be ground for hope that the lowest order calculations for all of the theories may give qualitatively correct results.

The experimental results obtained by the Berkeley workers,[2] although still preliminary, indicate that mesons of 40 to 100 Mev produced by photons on hydrogen are nearly isotropic in angular distribution from 45 to 135 degrees in the laboratory system. The cross section for mesons produced in this energy and angular range from hydrogen appears to decrease slowly with increasing meson energy. The magnitude of the total cross section, about 10^{-28} cm^2, can be fitted for the theories giving roughly isotropic angular spectra at low energies (Figs. 3 and 5) with a value of the coupling constant $g^2/4\pi\hbar c$ of about 40 for pseudoscalar mesons and 0.4 for pseudovector mesons. The mesons produced from carbon show an excess of negative over positive mesons in the ratio of 1.7 ± 0.2 in the energy range of 30 to 100 Mev observed at 90 degrees to the photon beam direction. This is in agreement with the ratio given in Fig. 1, with the assumption that the neutron does not interact with the electromagnetic field. However, it is not clear that the complications of the binding of the nucleons in the carbon nucleus are unimportant. A more detailed study of the dependence on energy and angle of the negative-to-positive ratio is being carried on at present.

These results all seem to indicate that the general features of the pseudoscalar meson theory are correct, i.e., the zero spin of the meson and the close binding of the meson cloud to the nucleons. It is hoped that the degree of validity of these conclusions will be indicated as the experimental work is completed.

V. EFFECTS OF MAGNETIC MOMENT INTERACTIONS ON THE NEGATIVE TO POSITIVE RATIO

The elementary argument given in Section II must be generalized considerably before it can be applied to magnetic moment interactions. One can formulate the argument in the following manner: The interaction with the electromagnetic field leading to the ejection of mesons is of the form

$$I=A_\mu\int j_\mu(\mathbf{r}',t)\exp[i(\mathbf{K}\cdot\mathbf{r}'-K_0t)]d\tau'dt, \qquad (7)$$

where j_μ is the total current carried by the interacting particles. The current can be separated into curl-free and divergence-free parts; the former corresponds to a linear motion of the charge and the latter to circulating currents. Thus

$$j_\mu=qv_\mu+\partial M_{\mu\nu}/\partial x_\nu, \qquad (8)$$

where v_μ is the relativistic velocity with spacial components $\mathbf{v}/(1-\beta^2)^{\frac{1}{2}}$, q the charge, and $M_{\mu\nu}$ is an antisymmetric tensor. The interaction then is

$$I=A_\mu\int(qv_\mu+\partial M_{\mu\nu}/\partial x_\nu)\exp[i(\mathbf{K}\cdot\mathbf{r}'-K_0t)]d\tau'dt$$

$$=A_\mu\int(qv_\mu-iM_{\mu\nu}K_\nu)\exp[i(\mathbf{K}\cdot\mathbf{r}'-K_0t)]d\tau'dt. \qquad (9)$$

We can easily evaluate this integral, considering each interacting particle separately. If the wave-length of the radiation is large compared with the region over which the charges and currents are distributed, or if one assumes a delta-function of position for the spacial

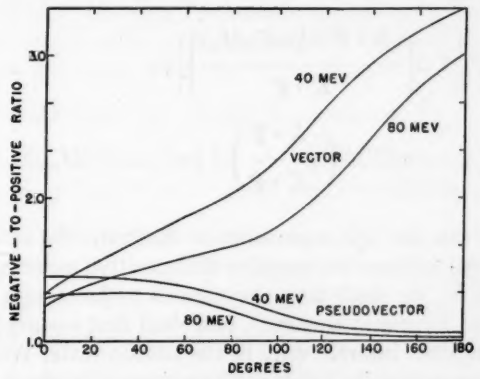

FIG. 8. Ratio of cross sections for production of positive and negative mesons, vector, and pseudovector theory.

distribution, the dependence on $\mathbf{r}'$ can be given by

$$\begin{aligned} v_\mu(\mathbf{r}', t) &= v(t)\delta[\mathbf{r}'-\mathbf{r}(t)] \\ &= v_\mu(t)\delta[\mathbf{r}'-\mathbf{r}(t)](1-\beta^2)^{\frac{1}{2}}, \\ M_{\mu\nu}(\mathbf{r}', t) &= M_{\mu\nu}(t)\delta[\mathbf{r}'-\mathbf{r}(t)](1-\beta^2)^{\frac{1}{2}}. \end{aligned} \quad (10)$$

The integral for each particle then is

$$I=A_\mu\int[qv_\mu(t)-iM_{\mu\nu}(t)K_\nu](1-\beta^2)^{\frac{1}{2}} \times\exp i[\mathbf{K}\cdot\mathbf{r}(t)-K_0t]dt. \quad (11)$$

A change of variable and a partial integration gives

$$I=A_\mu\int\frac{d}{ds}\left[\frac{v_\mu(s)-iM_{\mu\nu}(s)K_\nu}{K_0(1-\beta\cos\theta)}\right]e^{is}(1-\beta^2)^{\frac{1}{2}}. \quad (12)$$

If the interaction takes place over a time much shorter than the period of the radiation, the variation of the exponential term can be ignored. This gives

$$I=-\Delta\left[\frac{A_\mu P_\mu+\frac{1}{2}mM_{\mu\nu}F_{\mu\nu}}{K\cdot P}\right], \quad (13)$$

where the four-vector product is

$$K\cdot P=-K_0P_0+\mathbf{K}\cdot\mathbf{P},$$

and $\Delta[\ ]$ denotes the change during the interaction.

In this expression for the interaction of the electromagnetic field with the charges and currents of the meson-nucleon system, we have not included the dependence of the meson emission on such factors as the strength of the coupling of the mesons to the nucleons and the spins of the nucleons. We shall assume that a simple multiplicative factor, U, gives the spin dependence of the forces and the strength of the coupling. When we consider the application of field theory to this process, we shall see that this actually is the case for spin-zero mesons. The quantum nature of the process also has not been considered. We actually need the matrix element between the initial and final nucleon states of the operator which we have derived. The interaction therefore can be written for each particle as

$$\begin{aligned} I&=\psi_F^+\left\{U\Delta\left[\frac{q\mathbf{A}\cdot\mathbf{P}+\frac{1}{2}mF_{\mu\nu}M_{\mu\nu}}{K\cdot P}\right]\right\}\psi_I \\ &\equiv\langle U\rangle\Delta\left(q\frac{\mathbf{A}\cdot\mathbf{P}}{K\cdot P}\right)+\tfrac{1}{2}mF_{\mu\nu}\Delta(\langle UM_{\mu\nu}\rangle). \end{aligned} \quad (14)$$

We can use this expression to evaluate the ratio of the cross sections for negative and positive mesons. For simplicity we shall take the mesons to have spin zero (i.e., no magnetic moment), and shall first assume that the nucleons interact only in the proton state. When a positive meson is produced the proton is the initial nucleon at rest, and so interacts only through its magnetic moment with the transverse photon.

$$I(+)=-e\frac{(\mathbf{A}\cdot\mathbf{q})\langle U\rangle}{K\cdot q}+\tfrac{1}{2}m\frac{\langle UM_{\mu\nu}\rangle}{K\cdot I}F_{\mu\nu}, \quad (15)$$

where q is the meson 4-momentum, and I is the initial nucleon 4-momentum. When a negative meson is produced, the proton is the final recoil nucleon carrying current $e\mathbf{F}/m$

$$I(-)=e\left(\frac{\mathbf{A}\cdot\mathbf{q}}{K\cdot q}-\frac{\mathbf{A}\cdot\mathbf{F}}{K\cdot F}\right)\langle U\rangle-\tfrac{1}{2}m\frac{\langle UM_{\mu\nu}\rangle}{K\cdot F}F_{\mu\nu}, \quad (16)$$

where F is the final nucleon 4-momentum. If we now use over-all 4-momentum conservation, we find that

$$\mathbf{A}\cdot\left(\frac{\mathbf{q}}{K\cdot q}-\frac{\mathbf{F}}{K\cdot F}\right)=\frac{\mathbf{A}\cdot\mathbf{q}}{K\cdot q}\frac{K\cdot I}{K\cdot F}$$

and

$$\begin{aligned} I(-)&=-\frac{K\cdot I}{K\cdot F}\left[e\frac{\mathbf{A}\cdot\mathbf{q}}{K\cdot q}\langle U\rangle+\tfrac{1}{2}m\frac{\langle UM_{\mu\nu}\rangle}{K\cdot I}F_{\mu\nu}\right] \\ &=-[K\cdot I/K\cdot F]I(+). \end{aligned} \quad (17)$$

Therefore, under these assumptions, the plus-to-minus ratio would be

$$\begin{aligned} \sigma(+)/\sigma(-)&=(K\cdot F/K\cdot I)^2 \\ &=[1-(q_0/Mc^2)(1-v/c\cos\theta)]^2. \end{aligned} \quad (18)$$

This is the same result as was obtained in Eq. (3) when magnetic moment terms were ignored. It is interesting to observe that the ratio of the linear current interactions is the same as the ratio of the magnetic moment interactions, so that the plus-to-minus ratio is independent of the values of

$$\langle U\rangle=\psi_F^+U\psi_I, \quad \langle UM_{\mu\nu}\rangle=\psi_F^+UM_{\mu\nu}\psi_I.$$

If the nucleons interact not only in the proton state, but also with anomalous moments, we can write

$$\begin{aligned} M_{\mu\nu}(\text{proton})&=\gamma_PM_{\mu\nu}, \\ M_{\mu\nu}(\text{neutron})&=-\gamma_NM_{\mu\nu}, \end{aligned} \quad (19)$$

where γ is the magnitude of the magnetic moment of the nucleon in Bohr magnetons, with

$$\gamma_P=2.87, \quad \gamma_N=1.91. \quad (20)$$

This gives for the ratio of the interactions

$$\frac{I(+)}{I(-)}=\frac{-e\dfrac{\mathbf{A}\cdot\mathbf{q}}{K\cdot q}\langle U\rangle-\tfrac{1}{2}mF_{\mu\nu}\left(\dfrac{\gamma_P}{K\cdot I}+\dfrac{\gamma_N}{K\cdot F}\right)\langle M_{\mu\nu}U\rangle}{e\dfrac{\mathbf{A}\cdot\mathbf{q}}{K\cdot q}\dfrac{K\cdot I}{K\cdot F}\langle U\rangle+\tfrac{1}{2}mF_{\mu\nu}\left(\dfrac{\gamma_P}{K\cdot F}+\dfrac{\gamma_N}{K\cdot I}\right)\langle M_{\mu\nu}U\rangle}. \quad (21)$$

If $\langle M_{\mu\nu}U\rangle=\langle M_{\mu\nu}\rangle\langle U\rangle$ then the factor U cancels. The ratio of the cross section averaged over photon polariza-

tion and over nucleon-moment orientation gives

$$\sigma(+)/\sigma(-)=(\boldsymbol{K}\cdot\boldsymbol{F}/\boldsymbol{K}\cdot\boldsymbol{I})^2[1+0(\mu^2/M^2)].$$

Therefore, if the interaction is of this type, the ratio of the cross sections is nearly unchanged by the anomalous moments, since $\mu^2/M^2\approx 2$ percent. This is a result of the predominance of the coupling of the electromagnetic field to the linear motion of charge; i.e., to the electric dipole formed by the meson-nucleon charges.

If $\langle M_{\mu\nu}U\rangle\gg\langle M_{\mu\nu}\rangle\langle U\rangle$, or what is equivalent, if the magnetic moment terms are predominant in the interaction, then

$$\frac{\sigma(-)}{\sigma(+)}=\left[1-\frac{\gamma_P-\gamma_N}{\gamma_P+\gamma_N}(q_0/Mc^2)(1-v/c\cos\theta)\right]^{-2}. \quad (22)$$

These results are discussed in Section II.

VI. METHOD OF CALCULATION (LOWEST ORDER)

The calculation of matrix elements can be simplified greatly by use of the Feynman-Dyson methods.[7] The necessary operators can be derived by a technique due to Feynman, the correctness of which can be demonstrated by Dyson's methods. The calculations can also be carried out by the older methods of perturbation theory to give exactly the results derived here. The meson couplings to the nucleon field that are used are those which do not involve derivatives of the meson field, since these introduce non-renormalizable singularities in the higher order processes.

In the following, the notation used is such that $h=c=M=1$, where M is the nucleon mass. Therefore, all energies and momenta will be measured in units of the nucleon mass. All products of the form $\boldsymbol{A}\cdot\boldsymbol{B}$ will be understood to be 4-vector products, with $\boldsymbol{A}\cdot\boldsymbol{B}=-A_0B_0+\mathbf{A}\cdot\mathbf{B}$. We also use the notation $\boldsymbol{U}\equiv U_\mu\gamma_\mu$ with the Dirac matrixes $\gamma_i=ia_i\beta(i=1,2,3)$, $\gamma_4=\beta$. The adjoint operator ψ^+ is related to the complex conjugate by the condition $\psi^+=i\psi^*\gamma_4$.

The equations of motion for the fields are

(*A*) *Free particles*

$$(\boldsymbol{P}-i)\psi=0, \quad \text{(Dirac)} \quad (23)$$

$$(\Box-\kappa^2)\phi=0, \quad \text{(spin zero)} \quad (24)$$

$$\frac{\partial}{\partial x_\mu}\left(\frac{\partial\phi_\nu}{\partial x_\mu}-\frac{\partial\phi_\mu}{\partial x_\nu}\right)-\kappa^2\phi_\nu=0. \quad \text{(spin one)} \quad (25)$$

The last equation can also be written as

$$(\Box-\kappa^2)\phi_\nu=0, \quad \text{(spin one)}$$

with the divergence condition

$$\partial\phi_\mu/\partial x_\mu=0. \quad (26)$$

[7] R. P. Feynman, Phys. Rev. **76**, 769 (1949); F. J. Dyson, Phys. Rev. **75**, 1736 (1949).

(*B*) *Interaction of mesons with Dirac field*

$$(\Box-\kappa^2)\phi=g\psi^+U\psi, \quad U=(-1)^{\frac{1}{2}} \quad \text{(scalar)} \quad (27)$$
$$=\gamma_5 \quad \text{(pseudoscalar)}$$

$$\frac{\partial}{\partial x_\mu}\left(\frac{\partial\phi_\nu}{\partial x_\mu}-\frac{\partial\phi_\mu}{\partial x_\nu}\right)-\kappa^2\phi=g\psi^+U_\nu\psi, \quad (28)$$

$$U_\nu=\gamma_\nu \quad \text{(vector)}$$
$$=\gamma_5\gamma_\nu. \quad \text{(pseudovector)}$$

The last equation can be written

$$(\Box-\kappa^2)\phi_\nu=\left(\delta_{\mu\nu}-\kappa^{-2}\frac{\partial^2}{\partial x_\mu\partial x_\nu}\right)g\psi^+U_\mu\psi, \quad (28')$$

$$(\boldsymbol{P}-i)\psi=g\phi U\psi \quad \text{(spin zero)} \quad (29)$$
$$=g\phi_\nu U_\nu\psi. \quad \text{(spin one)}$$

(*C*) *Interaction with electromagnetic field*

$$(\boldsymbol{P}+e\boldsymbol{A}-i)\psi=0, \quad \text{(Dirac)} \quad (30)$$

$$\left[\left(\frac{\partial}{\partial x_\mu}+ieA_\mu\right)\left(\frac{\partial}{\partial x_\mu}+ieA_\mu\right)-\kappa^2\right]\phi=0, \quad \text{(spin zero)} \quad (31)$$

$$\left(\frac{\partial}{\partial x_\mu}+ieA_\mu\right)\left[\left(\frac{\partial}{\partial x_\mu}+ieA_\mu\right)-\left(\frac{\partial}{\partial x_\nu}+ieA_\nu\right)\phi_\mu\right]-\kappa^2\phi_\nu=0. \quad \text{(spin one)} \quad (32)$$

To order e, these can be written

$$(\boldsymbol{P}-i)=-e\boldsymbol{A}\psi, \quad \text{(Dirac)} \quad (30')$$

$$(\Box-\kappa^2)\phi=-2ceA_\mu\partial\phi/\partial x_\mu, \quad \text{(spin zero)} \quad (31')$$

$$(\Box-\kappa^2)\phi_\nu=-ie\left(2A_\lambda\frac{\partial}{\partial x_\lambda}\delta_{\mu\nu}-A_\nu\frac{\partial}{\partial x_\mu}-\frac{\partial A_\nu}{\partial x_\mu}-A_\mu\frac{\partial}{\partial x_\nu}\right)\phi_\mu. \quad \text{(spin one)} \quad (32')$$

If we consider the direct solution of these equations of motion, following Feynman's general arguments, we find the following expressions to be inserted into the Feynman-Dyson diagram:

(*B'*) *Emission of a meson of momentum* P_μ

$$gU \quad \text{(spin zero)} \quad (33)$$
$$g(\delta_{\mu\nu}+P_\mu P_\nu/\kappa^2)U_\mu. \quad \text{(spin one, polarization } \nu)$$

(*C'*) *Absorption of a photon*

$$-e\boldsymbol{A} \quad \text{(Dirac)}$$
$$2e\boldsymbol{A}\cdot\boldsymbol{P}' \quad \text{(spin zero, momentum } P_\mu') \quad (34)$$
$$e[2\boldsymbol{A}\cdot\boldsymbol{P}'\delta_{\mu\nu}-A_\nu P_\mu'-K_\mu A_\nu-A_\mu q_\nu].$$

(spin one, momentum P_μ', initial polarization μ, final polarization ν).

(*D*) *Propagation of an intermediate particle with momentum* P_μ'.

$$1/(P'-i) \quad \text{(Dirac)} \quad (35)$$
$$-1/(P'^2+\kappa^2) \quad \text{(boson, mass } \kappa\text{)}.$$

Exponential factors of the form $\exp[i(\boldsymbol{P}\cdot\boldsymbol{x})]$ have been omitted, since after spacial integrations have been carried out, they simply give 4-momentum conservation at each point of the diagram and for the over-all process.

Using these expressions we can now write down matrix elements directly. A virtual meson emitted by a nucleon can absorb a photon and go into a free meson. This is represented by diagram *A* of Fig. 7, and gives the matrix elements

$$ge\psi_F^+\left[2\boldsymbol{A}\cdot\boldsymbol{q}\frac{-1}{(\boldsymbol{q}-\boldsymbol{K})^2+\kappa^2}U\right]\psi_I\phi, \quad \text{(spin zero)} \quad (36)$$

$$ge\psi_F^+(\delta_{\mu\nu}+\kappa^{-2}q_\mu'q_\nu')U_\mu$$
$$\times\left(\frac{-2\boldsymbol{A}\cdot\boldsymbol{q}\delta_{\lambda\nu}+A_\lambda q_\nu'+K_\nu A_\lambda+A_\nu q_\lambda'}{(\boldsymbol{q}-\boldsymbol{K})^2+\kappa^2}\right)\psi_I\phi_\lambda.$$

(spin one) (37)

The nucleon can emit a real meson, going into a virtual intermediate state, and then absorb the photon. The photon absorption can also come first, followed by the meson emission. These processes are represented by diagrams *B* and *C* of Fig. 7, giving the matrix elements

$$-ge\psi_F^+\left(A\frac{1}{\boldsymbol{F}-\boldsymbol{K}-i}U\right)\psi_I\phi, \quad \text{(spin zero)} \quad (38)$$

$$-ge\psi_F^+\left[A\frac{1}{\boldsymbol{F}-\boldsymbol{K}-i}(\delta_{\mu\nu}+\kappa^{-2}/q_\mu q_\nu)U_\mu\right]\psi_I\phi_\nu$$

(spin one). (39)

If the nucleons are treated as Dirac particles, the photon can be absorbed only by a proton. Therefore, this diagram represents the production of a negative meson. For production of a positive meson, simply replace *I* by *F* and invert the order of the operators.

Combining these two contributions from diagram *A* and *B*, we obtain for the lowest order matrix element for the transition

$$M_2=ge\psi_F^+U\left(\frac{\boldsymbol{A}\cdot\boldsymbol{q}}{\boldsymbol{K}\cdot\boldsymbol{q}}-\frac{\boldsymbol{A}\cdot\boldsymbol{I}}{\boldsymbol{K}\cdot\boldsymbol{I}}-\frac{\boldsymbol{K}\boldsymbol{A}}{2\boldsymbol{I}\cdot\boldsymbol{K}}\right)\psi_I\phi.$$

(spin zero) (40)

For negative mesons replace *I* by *F* in the bracket. This is of the form (Eq. (11)) derived above, with the moment tensor for the Dirac field

$$M_u=-\tfrac{1}{4}ie(\gamma_\mu\gamma_\nu-\gamma_\nu\gamma_\mu)=\tfrac{1}{2}e\sigma_{\mu\nu},$$

$$M_2=ge\psi_F U_\nu\left[\frac{2\boldsymbol{A}\cdot\boldsymbol{q}\phi_\nu+A_\nu\boldsymbol{\phi}\cdot\boldsymbol{K}-K_\nu\boldsymbol{\phi}\cdot\boldsymbol{A}}{2\boldsymbol{q}\cdot\boldsymbol{K}}-\phi_\nu\frac{\boldsymbol{A}\cdot\boldsymbol{I}}{\boldsymbol{K}\cdot\boldsymbol{I}}\right.$$
$$\left.-\phi_\nu\frac{\boldsymbol{K}\boldsymbol{A}}{2\boldsymbol{I}\cdot\boldsymbol{K}}-\frac{F_\nu-I_\nu}{\kappa^2}\left(\frac{\boldsymbol{q}\cdot\boldsymbol{K}\,\boldsymbol{\phi}\cdot\boldsymbol{A}-\boldsymbol{A}\cdot\boldsymbol{q}\,\boldsymbol{\phi}\cdot\boldsymbol{K}}{2\boldsymbol{q}\cdot\boldsymbol{K}}\right)\right]\psi_I.$$

(spin one) (41)

For negative mesons replace $\boldsymbol{I}$ by $\boldsymbol{F}$ in the bracket and

$$U_\nu\boldsymbol{K}\boldsymbol{A} \text{ by } -\boldsymbol{A}\boldsymbol{K}U_\nu. \quad (42)$$

In these expressions we can demonstrate gauge-invariance by substituting

$$A_\mu=A_\mu'+\partial\Lambda/\partial x_\mu=A_\mu'+iK_\mu\Lambda \quad (43)$$

which should leave the matrix element for the transition M_2 unchanged. This is equivalent to showing that replacing A_μ by K_μ reduces M_2 to zero. That this is so can be seen by inspection, using the condition

$$\boldsymbol{K}\boldsymbol{K}=K_\mu K_\mu=0.$$

If we now specialize to the transverse vector potential, $A\cdot I$ is zero since the momentum I_μ is along the direction of the photon momentum. We then have for the spin-zero mesons

$$M_2(\text{positive})=ge\psi_F^+\phi U\frac{\mathbf{A}\cdot\mathbf{q}}{\boldsymbol{K}\cdot\boldsymbol{q}}-\frac{\boldsymbol{K}\boldsymbol{A}}{2\boldsymbol{I}\cdot\boldsymbol{K}}\psi_I, \quad (44)$$

$$M_2(\text{negative})=-ge\psi_F^+\phi U\left[\mathbf{A}\cdot\left(\frac{\mathbf{q}}{\boldsymbol{K}\cdot\boldsymbol{q}}-\frac{\mathbf{F}}{\boldsymbol{F}\cdot\boldsymbol{K}}\right)\right.$$
$$\left.-\frac{\boldsymbol{K}\boldsymbol{A}}{2\boldsymbol{F}\cdot\boldsymbol{K}}\right]\psi_I$$
$$=\frac{\boldsymbol{K}\cdot\boldsymbol{I}}{\boldsymbol{K}\cdot\boldsymbol{F}}M_2(\text{positives}).$$

This is the same result as that obtained above (Eq. (18)).

The differential cross section in the laboratory system then can be obtained from the formula

$$d\sigma=2\pi|M_2|^2\rho_F, \quad (45)$$

where M_2 is to be summed over meson and final nucleon spins and averaged over initial nucleon spin and photon polarization. The sum over the meson spin can be performed easily. If ϵ_μ is the 4-vector representing the direction of polarization of the meson which satisfies

$$\epsilon_\mu q_\mu=0, \quad \text{(divergence condition)} \quad (46)$$
$$\epsilon_i^2+\epsilon_4^2=1/2q_0 \quad \text{(normalization condition)} \quad (47)$$

then

$$\sum_{\text{spin}}\boldsymbol{\varepsilon}\cdot\boldsymbol{A}\,\boldsymbol{\varepsilon}\cdot\boldsymbol{B}=(1/2q_0)\left[\boldsymbol{A}\cdot\boldsymbol{B}-\frac{\boldsymbol{A}\cdot\boldsymbol{q}\,\boldsymbol{B}\cdot\boldsymbol{q}}{\boldsymbol{q}\cdot\boldsymbol{q}}\right]. \quad (48)$$

Carrying out the indicated sums and averages gives, after simplification of the resulting expressions in the laboratory system, for positive mesons

$$\left[\frac{g^2}{4\pi}\frac{e^2}{4\pi}\frac{\pi}{2}\frac{1}{K_0^2}\right]^{-1}\frac{d\sigma}{dq_0}$$

$$=\frac{q^2\sin^2\theta(2-\frac{1}{2}\kappa^2)}{(\boldsymbol{q}\cdot\boldsymbol{K})^2}+1-\frac{\boldsymbol{q}\cdot\boldsymbol{K}}{\boldsymbol{I}\cdot\boldsymbol{K}} \quad \text{(scalar) (49)}$$

$$=-\tfrac{1}{2}\kappa^2\frac{q^2\sin^2\theta}{(\boldsymbol{q}\cdot\boldsymbol{K})^2}+1-\frac{\boldsymbol{q}\cdot\boldsymbol{K}}{\boldsymbol{I}\cdot\boldsymbol{K}} \quad \text{(pseudoscalar) (50)}$$

$$=\frac{1}{(\boldsymbol{q}\cdot\boldsymbol{K})^2}\Big[(\boldsymbol{I}\cdot\boldsymbol{K})^2-3\boldsymbol{I}\cdot\boldsymbol{K}\,\boldsymbol{q}\cdot\boldsymbol{K}+15/4(\boldsymbol{q}\cdot\boldsymbol{K})^2$$

$$+1/2(\boldsymbol{q}\cdot\boldsymbol{K})^3\left(\frac{-4}{\boldsymbol{K}\cdot\boldsymbol{I}}\frac{-1}{\kappa^2}\right)$$

$$+\frac{q^2\sin^2\theta}{2\kappa^2}[(\boldsymbol{I}\cdot\boldsymbol{K})^2-2\kappa^4-4\kappa^2]\Big]. \quad \text{(vector) (51)}$$

The cross section for pseudovector mesons can be obtained from the result for vector mesons by the addition of the expression

$$\frac{1}{(\boldsymbol{q}\cdot\boldsymbol{K})^2}\left[-\frac{2(\boldsymbol{q}\cdot\boldsymbol{K})^2}{\kappa^2}-\frac{2(\boldsymbol{q}\cdot\boldsymbol{K})^3}{\kappa^4}+6q^2\sin^2\theta\right]. \quad (52)$$

Finally, if we wish to apply these expressions to the calculation of the spectrum of mesons produced by a photon beam which is the result of the bremsstrahlung of high energy electrons, we can represent the distribution of energies in the photon beam by

$$\phi(K)dK/K, \quad (53)$$

where $\phi(K)$ is a factor, which is nearly unity over the part of the spectrum of interest, and which indicates the degree of departure from the simple dK/K distribution.[8] At a given meson energy, the distribution in photon energies leads to a distribution in meson angles, with the energies and angles related by the conservation laws of energy and momentum

$$K=(q_0-\mu^2/2)/(1-q_0+q\cos\theta). \quad (54)$$

If

$$d\sigma/dq_0=f(\theta, q_0) \quad (55)$$

then

$$\frac{d\sigma}{dq_0 d\Omega}=f(\theta, q_0)\frac{1}{K}\frac{dK}{d\Omega}\phi(K)=\frac{Kq}{q_0-\kappa^2/2}\frac{\phi(K)}{2\pi}f(\theta, q_0).$$

This spectrum is that shown in Figs. 2–5, with $\phi(K)$ set equal to unity.

[8] W. Heitler, *The Quantum Theory of Radiation*, (Oxford University Press, London, 1944), p. 170.

VII. HIGHER ORDER CORRECTIONS

The perturbation calculations carried out in Section II are for the lowest non-vanishing order in the coupling constants g and e. The corrections of order e^3 and higher are considered negligible, which is probably justified for non-relativistic energies because of the smallness of the expansion parameter $e^2/4\pi=1/137$. Therefore, only terms of order eg^3 are calculated. The pseudoscalar theory is considered because it gives prediction in qualitative agreement with the experimental results of McMillan *et al.*,[1] and because of the simplicity of the theory. Pseudoscalar coupling is used, which is equivalent to pseudovector coupling in lowest order but not in the higher order processes. The calculations made are for energies near threshold where the momenta of the particles can be ignored relative to the rest energies.

The possible diagrams for the corrections to the lowest order result for the production of positive mesons are given in Fig. 7. The diagrams B_3, C, C_1 are forbidden since the nucleons indicated as interacting with the photon are in the neutron state. Diagrams involving neutral mesons are also omitted. The evaluation of these corrections can be carried out using the straightforward methods outlined by Dyson.[7] We simply quote the results given by these calculations. We find for the fourth-order matrix element for photon energies near threshold

$$M_4(A_1)=g^2/16\pi^2(2/15)\kappa^2M_2(A),$$
$$M_4(A_2)=g^2/16\pi^2(4/3)\kappa^4M_2(A),$$
$$M_4(B_1)=-1.26g^2/16\pi^2M_2(B),$$
$$M_4(B_2)=0.88g^2/16\pi^2M_2(B),$$
$$M_4(C_2)=-1.47g^2/16\pi^2M_2(C),$$
$$M_4(C_3)=0.32g^2/16\pi^2M_2(C),$$

where $M_2(A)$, $M_2(B)$, and $M_2(C)$ are the second-order matrix elements corresponding to diagrams A, B, and C of Fig. 8.

If we examine these matrix elements, it is apparent that the corrections from diagrams B_1, B_2, C_2 and C_3 of Fig. 7 are equivalent to an interaction by the nucleons with an anomalous moment in Bohr magnetons

$$\text{proton } g^2/16\pi^2(0.88-1.26)=-0.38g^2/16\pi^2,$$
$$\text{neutron } -g^2/16\pi^2(1.47-0.32)=-1.15g^2/16\pi^2.$$

These results are to be contrasted with those of Case,[5] who also calculated the anomalous moments for a static field, using pseudoscalar meson theory. He found that for charge symmetric theory, the anomalous moments were

$$\text{proton } 0.65g^2/16\pi^2$$
$$\text{neutron } -1.61g^2/16\pi^2,$$

where the notation has been adjusted to agree with that used here.

We find therefore that the correction of order eg^3 is the sum of the contributions from the graphs A_1, A_2, B_1, B_2, C_2, C_3. The first two give corrections which are

less than 1 percent and can be neglected relative to the others. The remaining correction is

$$M_4 = g^2/16\pi^2[0.88-1.26]M_2(B) + g^2/16\pi^2[-1.47+0.32]M_2(C) = 0.62g^2/16\pi^2 M_2(B).$$

Since $g^2/4\pi$ is about 6, we see that the contribution from the fourth-order terms is about two-thirds as large as that fromthe lowest order. The smallness of the total effect, however, is due to near cancellation of the large contributions from the individual effects. This cancellation is probably for tuitous and cannot be expected to be repeated for the next order processes. We also see that the corrections do not affect the predominance of nucleon moment interactions, characteristic of the pseudoscalar theory, and that this is probably true if effects of even higher order are included.

The author is deeply indebted to Professor Robert Serber for continuous advice and guidance in carrying out this work. He also wishes to acknowledge the advice given by Dr. M. L. Goldberger on the early stages of the calculations and by Dr. K. M. Watson on the calculation of the higher order corrections. The author also wishes to thank the experimental workers, including Professor E. McMillan, Dr. Jack Steinberger, and Mr. Jack Peterson for information on the preliminary results of their work. The computational work was carried out by Mr. Will Hicks and Mr. Richard Huddlestone.

The Fine Structure of the Microwave Absorption Spectrum of Oxygen*

JAMES H. BURKHALTER,** ROY S. ANDERSON, WILLIAM V. SMITH, AND WALTER GORDY
Department of Physics, Duke University, Durham, North Carolina

(Received May 12, 1950)

By means of a Zeeman modulation microwave spectrometer used with a lock-in amplifier, the 5 millimeter wave absorption lines of oxygen have been measured at low pressures, where they are completely resolved. Precise measurements of the frequencies of the lines have been made, and uniform deviations from the frequencies predicted by the theoretical formulas of Schlapp were found. The pressure variation of line-width has been measured for three of the observed lines, and found to be linear. The line-width parameter was found to vary with the rotational state. It is 0.053 cm^{-1}/atmos. for $K=3$, and 0.021 cm^{-1}/atmos. for $K=21$. Its order of magnitude is the same for low pressures ($\sim 10^{-1}$ mm Hg) as for high pressures ($\sim$1 atmos.).

I. INTRODUCTION

As early as 1927, Dieke and Babcock[1] measured the splitting of the rotational levels of oxygen in the optical region. Using the sun as a source, they observed the multiplet structure in the $^3\Pi-{}^3\Delta$ transition of molecular oxygen in the atmosphere. Inasmuch as oxygen is in a Σ-ground state, it should have no multiplet structure of the ordinary type; i.e., one caused by the interaction of the electron spin with the quantitized component of the electronic angular momentum along the figure axis of the molecule. However, Kramers[2] showed that the spin-spin interaction of the uncompensated electrons is equivalent to an interaction between the total spin, **S**, of the molecule (=1 for oxygen), and the figure axis of the molecule, averaged over the end-over-end rotation. The result is a splitting of the rotational levels into three components, corresponding to the three ways of combining **S** and **K** vectorially to form the total angular momentum **J**. These are $J=K$, $J=K\pm1$. The expressions for the energy of the levels obtained by Kramers were later corrected by Schlapp,[3] who made the assumption that **S** does not completely decouple from **K**. That is, he assumed that the coupling was intermediate between Hund's case (a) and (b). The expressions obtained by Schlapp are given in Eq. (2) below.

A completely different interpretation of the fine structure was given by Hebb,[4] based on the following effect. Although on the average, the electronic angular momentum in a Σ-state is zero, this angular momentum has a precessing component perpendicular to the figure axis of the molecule. This component interacts with the spin vector **S**. Curiously, Hebb's formulas were of the same form as Schlapp's although based on entirely different postulates.

With the development of microwave spectroscopy, the measurement of lines corresponding to the transitions between these fine structure terms became possible. Using the predicted energy levels and the constants determined from Dieke and Babcock's data, Van Vleck[5] calculated the form of the absorption *vs.* frequency curve for various values of the unknown parameter $\Delta\nu/c$, the so-called line breadth parameter. Comparing his curves with the measured values of the absorption reported by Beringer,[6] Van Vleck obtained a lower limit of 0.02 cm^{-1}/atmos., and an upper limit of 0.05 cm^{-1}/atmos. for this parameter. Lamont[7] has reported data that support this, using a field method of measuring attenuation as a function of distance in air. Further work at a total pressure of 80 cm Hg, both for pure oxygen, and oxygen-nitrogen mixtures in various concentrations, was carried out by Strandberg, Meng, and Ingersoll.[8] Their results indicate that $\Delta\nu/c$ is closer to 0.02 cm^{-1}/atmos. than to 0.05 cm^{-1}/atmos. Beringer and Castle[9] have measured the transitions between the Zeeman components of the rotational levels using high magnetic fields. They used a constant frequency (9360 Mc/sec.), and "pulled" the absorption lines into the frequency by varying the field. Their measurements were made at pressures ranging from 1.5 cm Hg to an atmosphere.

Because the fine structure lines are very weak, being magnetic dipole transitions, all of the previous direct measurements of them were made at pressures of the order of an atmosphere. At this pressure the lines are so broad that they overlap significantly, completely obscuring the fine structure. The present measurements were made on the individual fine structure lines at low pressures, where they were completely resolved. The line-widths are measured on the individual lines, rather than from the integrated absorption.

* The research reported in this document has been made possible through support and sponsorship extended by the Geophysical Research Directorate of the Air Force Cambridge Research Laboratories under Contract No. W19-122-ac-35. It is published for technical information only and does not represent recommendations or conclusions of the sponsoring agency.

** This article is based on a thesis submitted by Mr. Burkhalter in partial fulfillment of the requirements of Doctor of Philosophy at Duke University (1950).

[1] G. H. Dieke and H. D. Babcock, Proc. Nat. Acad. Sci. **13**, 670 (1927).

[2] H. A. Kramers, Zeits. f. Physik **53**, 422 (1929).

[3] R. Schlapp, Phys. Rev. **51**, 342 (1937).

[4] M. H. Hebb, Phys. Rev. **49**, 610 (1936).

[5] J. H. Van Vleck, Phys. Rev. **71**, 413 (1947).

[6] R. Beringer, Phys. Rev. **70**, 53 (1946).

[7] H. R. L. Lamont, Phys. Rev. **74**, 353 (1948).

[8] Strandberg, Meng, and Ingersoll, Phys. Rev. **75**, 1524 (1949).

[9] R. Beringer and J. G. Castle, Jr., Phys. Rev. **73**, 1963 (1949).

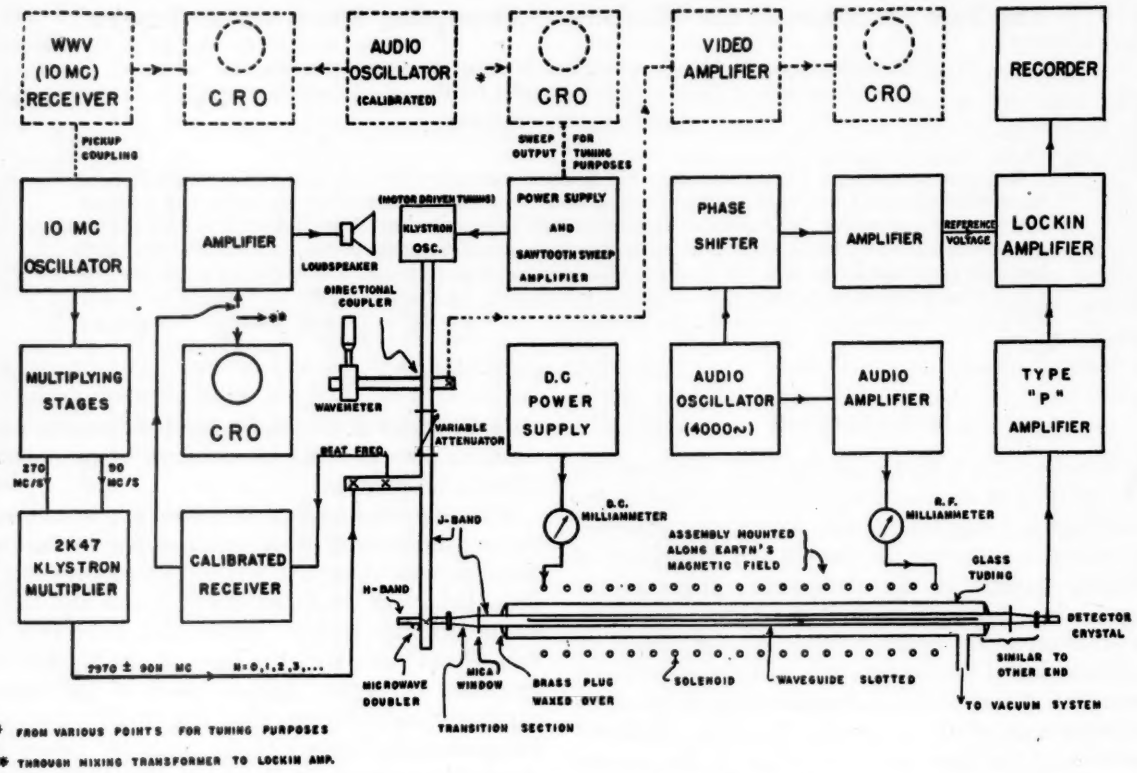

FIG. 1. Block diagram of Zeeman modulation spectroscope.

II. THE ZEEMAN MODULATION SPECTROSCOPE

The block diagram of the apparatus used appears in Fig. 1. Its operation is as follows. A J to H crystal multiplier[10] is used for obtaining energy in the 4 to 5 mm wave region and a K to I doubler in the 5 to 6 mm wave region. The same absorption cell is used for all measurements. It is a 12 foot section of J-band waveguide slotted along the broad side for most of its length to reduce eddy currents, and oriented along the earth's magnetic field so that the latter can be conveniently neutralized. It is surrounded by a glass tube that is part of the vacuum system, and is sealed to the glass tube near the ends. The assembly is surrounded by a solenoid which carries a current modulated at 4000 c.p.s. The modulated current produces a varying magnetic field which modulates the absorption lines of the gas at the same frequency. By using a phase-sensitive lock-in amplifier whose reference voltage is fed from the same audio source, this audio modulation can be detected and amplified with a one c.p.s. band pass. Thus, the noise level is reduced, so that sufficient amplification to detect the lines can be used. Since the Zeeman splitting of the energy levels is independent of the direction of the field, it is necessary that the alternating field be biased to zero at one point in the cycle. Otherwise, the absorption at a given frequency would occur at twice the frequency of the reference voltage. The fields used were of the order of a gauss, so that the effect of the earth's field is not negligible. Thus, the cell is oriented along the earth's field, and a d.c. field superimposed on the a.c. field. This is adjusted to the value that both neutralizes the earth's field and biases the a.c. field.

All frequency measurements are made at the undoubled frequency. A Bethe-hole directional coupler directs a portion of the energy to a wave meter, and a Tee section couples a somewhat larger portion to a mixer crystal, used with a frequency standard. The frequency standard is described elsewhere.[11] It multiples the output of a 10 Mc oscillator, monitored by Station WWV, to the desired region. The mixer crystal detects the beat frequency of these harmonics with the microwave source. Its output is amplified by a calibrated radio receiver.

The J-band klystron is tuned mechanically by a very slow drive motor. As the frequency is driven through an absorption line, the detector crystal detects the audio modulation of the Zeeman components of the line. This signal is amplified by a lock-in amplifier, and fed as a d.c. signal to an Esterline-Angus recorder. A wavemeter reading is made at the time the line appears, to determine the approximate frequency of the line. When the difference between the microwave frequency and

[10] For a definition of the region covered by the designated bands, see W. Gordy, Rev. Mod. Phys. **20**, 668 (1948).

[11] R. R. Unterberger and W. V. Smith, Rev. Sci. Inst. **19**, 580 (1948).

one of the harmonics of the frequency standard is equal to the receiver setting, the receiver detects their beat frequency. This is marked on the recorder tape. The identity of the markers is determined from the wave meter reading. By bracketing the line with several frequency markers, the frequency of the line can be accurately determined. These same markers establish the frequency scale on the recorder tape, from which line widths are determined.

The shape of the recorder trace is that of a center positive maximum (corresponding to the line frequency) with two negative minima, vanishing for frequencies far from resonance (see Fig. 2). If ν_0 is the center maximum, and $\nu_{\min.}$ is either of the symmetrically located minima, it can be shown (see Appendix A) that in the limit of small modulations,

$$\Delta\nu=(\nu_{\min.}-\nu_0), \tag{1}$$

where $\Delta\nu$ is the line-breadth parameter, or half the width at half power. Thus, in making measurements on line widths, runs are made at constant pressure and successively decreasing modulations, with two or more frequency markers on each run. The values of $(\nu_{\min.}-\nu_0)$ are extrapolated to zero modulation. This process is repeated at different pressures, and the value of $\Delta\nu/c$ per atmosphere is inferred.

III. THE FINE STRUCTURE

The theoretical formulas for the energy of the fine structure levels, as given by Schlapp,[3] are

$$\begin{aligned}W_{K+1}&=W_0+(2K+3)B-\lambda+\mu(K+1)\\&\quad-[(2K+3)^2B^2+\lambda^2-2\lambda B]^{\frac{1}{2}}\\W_K&=W_0\\W_{K-1}&=W_0-(2K-1)B-\lambda-\mu K\\&\quad+[(2K-1)^2B^2+\lambda^2-2\lambda B]^{\frac{1}{2}}\end{aligned} \tag{2}$$

where, $B=\hbar^2/8\pi^2Ic$, $W_0=BK(K+1)$, and λ and μ are coupling constants which must be determined empirically; λ is a measure of the energy of coupling proportional to the factor $[3\cos^2(\mathbf{S},\mathbf{K})-1]$, and μ is a measure of the coupling energy proportional to $\cos(\mathbf{S},\mathbf{K})$. The values used by Van Vleck[5] were

$$B=1.43777\ \text{cm}^{-1},\quad \lambda=1.985\ \text{cm}^{-1},\quad \mu=-0.00837\ \text{cm}^{-1}.$$

With the selection rules $\Delta J=\pm1$, $\Delta K=0$, Eqs. (2) give the wave numbers of the lines:

$$\begin{aligned}\nu_+(K)&=-(2K+3)B+\lambda-\mu(K+1)\\&\quad+[(2K+3)^2B^2+\lambda^2-2\lambda B]^{\frac{1}{2}}\\\nu_-(K)&=+(2K-1)B+\lambda+\mu K\\&\quad-[(2K-1)^2B^2+\lambda^2-2\lambda B]^{\frac{1}{2}}\end{aligned} \tag{3}$$

where $\nu_+(K)$ represents the transition $J=K+1\rightarrow K$, and $\nu_-(K)$ represents the transition $J=K-1\rightarrow K$. From (3), the relation

$$\nu_+(K-2)+\nu_-(K)=2\lambda+\mu=\text{constant}, \tag{4}$$

follows immediately. The most populated state at room temperature is the one for $K=13$, although states with K ranging from $K=1$ to $K=25$ have significant populations. Because of symmetry considerations, only states with odd values of K are populated, so that (3) predicts 26 lines, 25 of which are in the region of 2 cm^{-1}. The exception is the $\nu_-(1)$ line, which falls at 4 cm^{-1}. This line was not included in the observations.

The experimental frequencies and wave numbers of the lines are listed in Table I. Table II lists the values of the function $\nu_+(K-2)+\nu_-(K)$. It is seen that this function is not a constant, as predicted by (4). This means that regardless of the values chosen for λ and μ, an empirical fit of the data to (3) cannot be obtained. It was found, however, that the $\nu_+(K)$ series in (3) could be fitted by appropriate choices of λ and μ, but no choice of λ and μ would satisfy the $\nu_-(K)$ series, and that added terms were necessary. Attempts to apply symmetric connections to the $\nu_+(K)$ and $\nu_-(K)$ series have been unsuccessful. The empirical version of the formulas (3) are

$$\begin{aligned}\nu_+(K)&=-(2K+3)B+\lambda-\mu(K+1)\\&\quad+[(2K+3)^2B^2+\lambda^2-2\lambda B]^{\frac{1}{2}}\\\nu_-(K)&=+(2K-1)B+\lambda+\mu K\\&\quad-[(2K-1)^2B^2+\lambda^2-2\lambda B]^{\frac{1}{2}}\\&\quad+\delta K+\alpha/[K(K+1)]^{\frac{1}{2}},\end{aligned} \tag{5}$$

where $\lambda=1.983971$ cm^{-1}, $\mu=-0.0085114$ cm^{-1}, $B=1.437770$ cm^{-1}, $\delta=+0.0015617$ cm^{-1}, $\alpha=+0.0049345$ cm^{-1}. Table III gives the deviations of (5) from experiment. The theoretical significance of the parameters λ and μ is not understood at present. It appears that the δ-term can be explained by assigning the constant $(\mu+\delta)$ the same significance in the $\nu_-(K)$ series that the constant μ has in the $\nu_+(K)$ series. That is, for the states corresponding to $J=K-1$, the $\cos(\mathbf{S},\mathbf{K})$ coupling energy is different from that in the $J=K+1$ states. The α-term, on the other hand, has no immediately apparent significance. It probably represents a higher order effect not taken into account in Schlapp's theory. In view of the fact

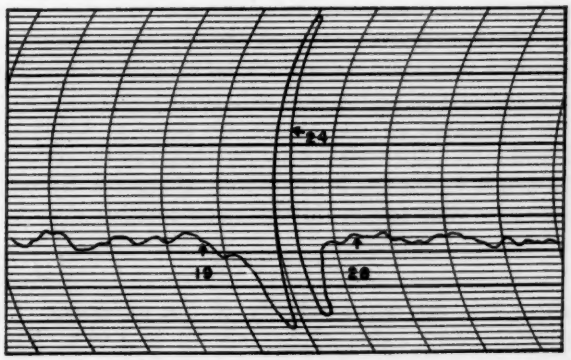

FIG. 2. The $J=14\rightarrow13$ transition at 0.865 mm Hg, and 5 ma a.c. solenoid modulation. The numbers are receiver settings in Mc/sec.

TABLE I. Experimentally determined frequencies.

	K	Series	Frequency (Mc/sec.)	Wave number (cm^{-1})
1	25	−	53,592.2	1.78774
2	23	−	54,130.0	1.805682
3	21	−	54,672.5	1.823779
4	19	−	55,220.8	1.842067
5	17	−	55,784.1	1.860859
6	1	+	56,265.1	1.876905
7	15	−	56,362.8	1.880165
8	13	−	56,968.7	1.900377
9	11	−	57,612.0	1.921836
10	9	−	58,324.0	1.945587
11	3	+	58,446.2	1.949663
12	7	−	59,163.4	1.973586
13	5	+	59,610*	1.9885
14	5	−	60,306.4	2.011715
15	7	+	60,436*	2.0160
16	9	+	61,120*	2.0389
17	11	+	61,800.2	2.061546
18	13	+	62,411.7	2.081944
19	3	−	62,486.1	2.084428
20	15	+	62,970*	2.1006
21	17	+	63,568.3	2.120525
22	19	+	64,127.6	2.139185
23	21	+	64,678.9	2.157575
24	23	+	65,220*	2.1756
25	25	+	65,770*	2.1940

* Measured by wave meter only.

that the added terms appear only in the $\nu_-(K)$ series, it is reasonable to assume that they arise only in the energy levels corresponding to $J=K-1$, and not in those corresponding to $J=K$, or $J=K+1$.

Note added in proof:—It is interesting to compare these microwave frequencies with the most recent infra-red valves (H. Babcock and L. Herzberg, Astrophys. J. **108**, 167 (1948)). The comparison indicates that the infra-red data are accurate to one less significant figure than estimated by the authors. The microwave measurements are at least two significant figures more precise than the infra-red measurements—hence the present observed departures from Schlapp's theory.

IV. LINE WIDTHS

Formula (1) expresses the line-width parameter as a function of frequencies on the recorder tape only in the limit of small modulation fields. However, as the fields are decreased, a decrease in signal to noise ratio occurs, which lowers the sensitivity of the spectroscope. Thus, line-width measurements with the apparatus described require a very good signal to noise ratio. As a result of tube and crystal limitations, only three line widths have been measured to date. These are given in Table IV. The observed line widths may be related to the collision diameters b_K for the interruptions of state K by collisions according to the kinetic theory relation

$$2\Delta\nu=\sqrt{2}n\bar{v}b_K^2 \qquad (6)$$

where $\bar{v}$ is the mean velocity of the molecules. The kinetic theory value of b_K (all K) is 3.61A. Thus, Table IV shows that the microwave collision diameters for low K exceed the kinetic theory value, whereas for high K, they are much less. This implies that, while the larger diameters can be explained by electrostatic interactions, as has been done in the pressure broadening of ammonia[12–14] the smaller diameters may involve other forces, of shorter range. (The magnetic dipole-dipole interactions are too small by orders of magnitude).

Since oxygen has no electric dipole, the only possible electrostatic interactions are quadrupole-quadrupole and polarizability ones. Anderson[15] has shown that polarizability interactions account for slightly more than half of the observed line width, ranging from 0.025 cm^{-1}/atmos. for $K=3$ to 0.014 cm^{-1}/atmos. for

TABLE II. Experimental sum relations.

K	$\nu_+(K-2)+\nu_-(K)$ (Mc/sec.)	(cm^{-1})
3	118,751.2	3.961333
5	118,752.6	3.961378
13	118,768.7	3.961923
15	118,774.5	3.962109
19	118,789.1	3.962592
21	118,800.1	3.962964
23	118,808.9	3.963257

$K=21$. Mizushima[16] has derived a line breadth contribution from quadrupole-quadrupole broadening which for high K is of the form

$$\Delta\nu=2.24\times10^{15}Q\left(\frac{1}{K}-\frac{3}{8K^2}\right)^{\frac{1}{2}}$$

$$cm^{-1}/\text{atmosphere for } K+1\rightarrow K \qquad (7)$$

$$\Delta\nu=2.24\times10^{15}Q\left(\frac{1}{K}+\frac{3}{8K^2}\right)^{\frac{1}{2}}$$

$$cm^{-1}/\text{atmosphere for } K-1\rightarrow K,$$

where Q is the quadrupole moment. The physical assumptions of the theories differ. Nevertheless, the combined polarizability-quadrupole effects calculated from one theory should not differ greatly from those calculated from the other theory,[17] as judged by their similarity when applied to the ammonia self-broadening problem.[12–14]

As Eq. (7) contains the quadrupole moment as an adjustable constant, and gives approximately the correct K dependence, it can be adjusted to fit the data fairly well. Alternatively, the combination of polarizability and quadrupole interactions can be so adjusted. Either procedure, however, requires an assumed oxygen quadrupole moment several times too large. This quantity has not yet been measured, but Smith

[12] H. Margenau, Phys. Rev. **76**, 121 (1949).
[13] P. W. Anderson, Phys. Rev. **76**, 647 (1949).
[14] W. V. Smith and R. Howard, Phys. Rev. **79**, 132 (1949).
[15] P. W. Anderson, Harvard Ph.D. Thesis, (1949).
[16] M. Mizushima, private communication.
[17] For other than dipole-dipole interactions, these two theories give a different dependence of line width on temperature. The difference is not great, however.

and Howard[14] have obtained an upper bound for it of about 0.1×10^{-16} cm². Their observations were made on the pressure broadening of NH_3 lines in NH_3-O_2 mixtures. Thus, it seems probable that still other interactions, important at small collision diameters, contribute to the observed line breadths.[18]

TABLE III. Deviations from experiment.

K	$\nu_-(K)$	$\nu_+(K)$
1		+0.000009
3	+0.000000	+0.000176
5	+0.000089	
7	+0.000063	
9	+0.000081	
11	+0.000036	−0.000036
13	+0.000131	+0.000030
15	−0.000014	
17	−0.000001	−0.000023
19	−0.000037	−0.000009
21	+0.000032	+0.000024
23	−0.000001	
25	−0.00010	

APPENDIX A

If $\delta\nu_i$ is the maximum frequency separation of the ith pair of Zeeman components from the undisplaced line ν_0, $\nu 1_i$, $\nu 2_i$ are the frequencies of these components, and ω is the frequency with which the magnetic field alternates, we have

$$\begin{aligned}\nu 1_i&=\nu_0+(1-\cos\omega t)\delta\nu_i\\ \nu 2_i&=\nu_0-(1-\cos\omega t)\delta\nu_i.\end{aligned}\qquad\text{(a)}$$

The intensity of absorption is proportional to the shape factor,[5]

$$I=\sum_i\left\{\frac{1}{(\nu-\nu 1_i)^2+\Delta\nu^2}+\frac{1}{(\nu-\nu 2_i)^2+\Delta\nu^2}\right\},\qquad\text{(b)}$$

where $\Delta\nu$ is the line breadth parameter. Now, the lock-in amplifier detects only the coefficient of $\cos\omega t$. Substituting (a) into (b), expanding into a Fourier series with arbitrary phase angle γ, this coefficient is found to be

$$a_1=\sum_i 2\delta\nu_i\cos\gamma\left\{\frac{(\nu-\nu_0+\delta\nu_i)}{[(\nu-\nu_0+\delta\nu_i)^2+\Delta\nu^2]^2}-\frac{(\nu-\nu_0-\delta\nu_i)}{[(\nu-\nu_0-\delta\nu_i)^2+\Delta\nu^2]^2}\right\},\qquad\text{(c)}$$

provided $(\delta\nu)^4\ll(\Delta\nu)^4$. Note that γ appears only as an amplitude factor. Differentiating (c) with respect to ν, and equating to zero, one obtains formula (1), provided $\delta\nu_i$ is small. Note that (1) is now independent of $\delta\nu_i$.

TABLE IV. Line breadth parameters.

K	Series	$\frac{\Delta\nu}{c}$ (cm⁻¹/atmos.)	b_K (A)
3	−	0.053	4.4
13	+	0.022	2.8
21	−	0.021	2.8

[18] The purely electrostatic interactions actually contribute more to low K transitions, according to Anderson's general theory, than the values he calculates for O_2. The reason for this is that he calculates specifically for the case $\Delta K=0$, whereas for $K=1$ and $K=3$, there will be an appreciable contribution for $\Delta K\neq0$ collisions. For higher values of K, these contributions vanish much more rapidly than the $\Delta K=0$ contributions.

A Directional and Latitude Survey of Cosmic Rays at High Altitudes*

J. R. WINCKLER,** T. STIX, K. DWIGHT, AND R. SABIN
Palmer Physical Laboratory, Princeton University, Princeton, New Jersey
(Received April 4, 1950)

The directional distribution of cosmic rays at atmospheric depths of 15 to 25 g/cm² has been measured with large counter telescopes carried by constant-level plastic balloons at geomagnetic latitudes of 0°, 20°, 30°, and 40°. From the vertical flux measurements an energy spectrum for primary protons is obtained which has the form $N(E)=0.27/E^{1.9}$, where $N(E)$ is the number of particles in unit energy range at the energy E. The corresponding formula for primaries consisting entirely of alpha-particles is $N(E)=0.32/E^{1.81}$. The power law can be fitted between about 1 and 14 Bev, but there is good evidence that the spectrum flattens out below 1 Bev and becomes steeper at high energies. The total incident energy calculated under the assumption that the measured flux at 15 g/cm² consists of primaries is two times greater than the total incident energy appearing as atmospheric ionization.

The east-west asymmetry values reach a maximum of 0.53 ± 0.05 at the equator and decrease to 0.24 ± 0.09 at 40° geomagnetic latitude. The asymmetry to be expected from the latitude effect if all primaries are positive, reaches 1.20 at the equator, and at all latitudes and zenith angles is considerably higher than the observed asymmetry. It is not possible to decide on the basis of the present experiments whether this discrepancy arises from atmospheric effects or from a sizable fraction of negative primaries.

I. INTRODUCTION

A MEASUREMENT of the azimuthal distribution of the primary cosmic radiation at latitudes near the geomagnetic equator, combined with measurement of the vertical flux over a range of latitudes, in principle enables one to evaluate the energy spectrum and to determine the sign of the charge of the primary radiation over a range of energies from about 1 to at least 14 Bev. The majority of the experiments on which our knowledge of the geomagnetic behavior of cosmic rays is based deal almost entirely with secondary cosmic rays generated in the atmosphere. To compare these data with the extensive theoretical calculations of the motion of primary rays which have reached the earth from infinity one must make assumptions which are difficult to test experimentally.[1] It has become apparent that the magnitude of the various geomagnetic effects increases as the observations are extended to smaller depths in the atmosphere, and for some time it has been considered highly desirable to make observations at very high altitude where there is some hope of separating primary cosmic rays from the atmospheric effects.

Preliminary experiments[2] which studied the zenithal and azimuthal dependence and absorbability in lead of the cosmic radiation at about 20 g/cm² atmospheric depth at 56° N. geomagnetic latitude indicated that although secondary radiation developed particularly at large zenith angles, the bulk of this could be absorbed with lead filters. The primaries and hard secondaries remaining gave an approximately isotropic distribution in zenith and azimuth. One should expect a nearly isotropic distribution of primary flux at this high latitude. Following these preliminary experiments, measurements have been made of the azimuthal asymmetry and latitude effect of the cosmic radiation at various atmospheric depths, but principally between 15 and 25 g/cm², and at geomagnetic latitudes of 0°, 20°, 30°, and 40°. The experiments were conducted from the U.S.S. Norton Sound on a cruise from Port Hueneme, California, to Jarvis Island and return, by arrangement with the ONR and the Chief of Naval Operations. Project "Skyhook" constant-level balloon facilities were provided on the ship by ONR.

II. EXPERIMENTAL METHOD

A. The Counting Telescope

The basic measuring instrument was a threefold Geiger counter coincidence telescope consisting of three 10×10 in. trays of 1 in. diameter counters spaced 50 in. between extremes. This construction represented a considerable improvement in counting rate and angular resolution over the geometry previously employed.[2] The advantage of such a large telescope for high altitude measurements has been demonstrated by H. V. Neher and his collaborators.[3] It is probably relatively less affected by side showers than are small telescopes composed of single counters, and has superior directional properties. The effective or half-angle opening of this telescope was 11° on a side and 16° on a diagonal of the end section. The area-solid angle product was computed from the geometry, and to a sufficiently good approximation is given by the equation

$$B=(a^2b^2/l^2)[1-(a^2+b^2)/3l^2] \quad (1)$$

* This work has been assisted by the joint program of the ONR and AEC.
** Now at the University of Minnesota.
[1] See, for example, D. J. X. Montgomery, *Cosmic Ray Physics* (Princeton University Press, Princeton, New Jersey, 1949), for a survey of the literature and discussion of experiments on this subject up to 1948.
[2] Stroud, Schenck and Winckler, Phys. Rev. **76**, 1005 (1949); J. R. Winckler and W. G. Stroud, Phys. Rev. **76**, 1012 (1949). The interpretation of these experiments was partially based on some calculations of the angular distribution of primary and secondary particles in the atmosphere. These calculations are unsatisfactory in several respects and are being revised.
[3] Biehl, Montgomery, Neher, Pickering and Roesch, Rev. Mod. Phys. **20**, 353 (1948).

assuming an isotropic flux of incident particles at high altitude over the aperture of the telescope, and by

$$B=(a^2b^2/l^2)[1-(a^2+b^2)/2l^2] \qquad (2)$$

assuming a $\cos^2\theta$ dependence of the incident particle flux on zenith angle θ at sea level. Here a and b are the tray dimensions and l is the separation. Equation (2) is the same up to the second degree terms in a/l and b/l in the brackets as that used by Montgomery[4] for a similar telescope. The effective area of the end trays is increased about 2 percent by the circular end sections of the counters. The counter tubes were placed side by side in the trays, and a correction must therefore be made for the dead space introduced by the counter walls. The area-solid angle product was first computed neglecting this dead space, and was then multiplied by the factor $(A'/A)^3$, where A is the tray area and A' is the sensitive area of the counters, thus treating the dead space as a kind of inefficiency. The construction of the counter tubes was as described previously[2] but modified to 10 in. length (9.75 in. effective measured) and with ethylene as a temperature insensitive quenching vapor substituted for ethyl alcohol. The ten counters in each tray were paralleled, with a 10,000 ohm common load resistance and 100 $\mu\mu$f. coupling capacitor to the coincidence circuit. The operating voltage was 1130, about 80 volts above starting. Each tray was provided with an amplifier-clipper stage, a pulse-inverter-sharpener and a Rossi tube. The coincidence output pulse was lengthened into a square wave of 10 msec. suitable for telemetering requirements by an output tube which regenerated back through the screens of the Rossi tubes to form a univibrator circuit. Type 1L4 miniature pentodes were used throughout, and are advantageous because of their high mutual conductance. The resolving time as measured by the accidental rate with a radium source nearby, as well as by observation of the pulse in the circuit was 2 μsec. The corrections to the data due to dead time of the counters and accidentals were negligible. The telescope, complete with high and low voltage dry batteries for 15 hours operation, was an independent unit and was mounted on a horizontal shaft through its center of gravity. In most experiments the bottom counter tray was covered by a 10×10 in.×3 cm thick lead plate very close to the counters. This telescope unit was hung by its shaft in a vertical frame (see Fig. 1) with a motor and gear drive arranged to control the zenith position during flight according to a prescribed schedule.

B. Azimuthal and Zenith Mechanism

During flight the entire gondola was rotated with a period of about 18 min. by a large gear and motor about a ball-bearing vertical shaft. This shaft was effectively anchored to the balloon by a non-twisting, double suspension about 10 feet below the balloon load ring.

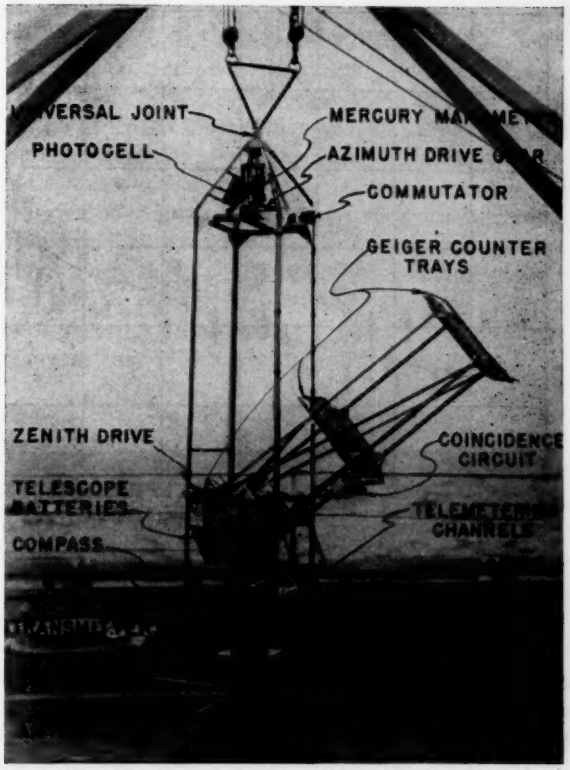

FIG. 1. Complete gondola ready for launching, except for final wrapping.

The azimuthal bearing was determined by a 3 in. nautical compass floating in a 50 percent water-alcohol mixture in a glass cylinder. A light source in the center of the compass housing and four slits in black paper at 90° intervals around the glass housing covered by type 921 photo-tubes constituted the sensing device. A 135° sector secured around the outer edge of the compass float with a height sufficient to block the light beam from the photo-tubes registered a new combination of the four photo-tube signals every 45° of azimuth. The readings were checked in the laboratory by rotating the gondola over an azimuth circle, and during flight the absolute direction of the equipment was determined by a photo-cell recording the sun through a slit. During many of the flights the zenith angle of the telescope was changed periodically from the vertical to 20°, 40° or 60° by a control switch on the azimuth gear and a series of positioning switches which also supplied identification signals for the telemetering system. On some flights the zenith survey was delayed until the balloon reached its ceiling, and during the rising portion the telescope was kept at a fixed zenith position. On a number of flights the zenith mechanism was dispensed with, and the telescope secured at a fixed zenith throughout the flight in the interest of better statistical accuracy.

[4] R. A. Montgomery, Phys. Rev. **75**, 1407 (1949).

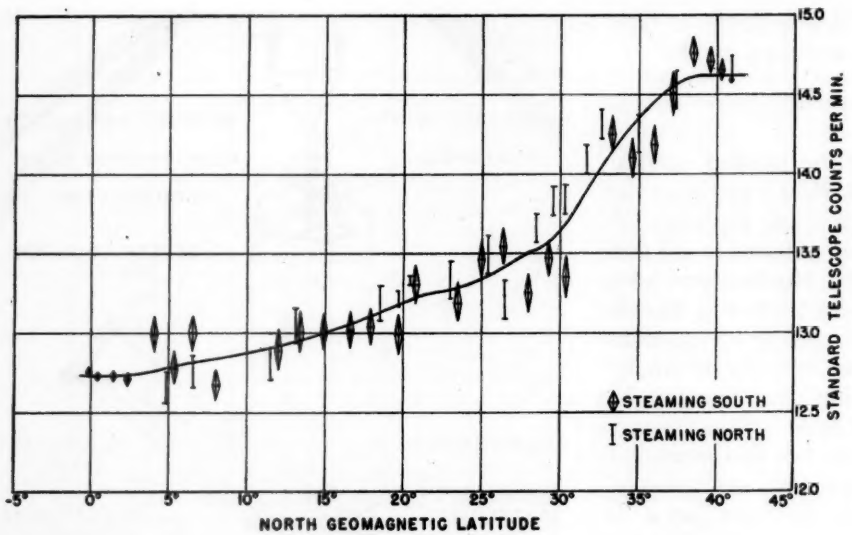

FIG. 2. Latitude effect observed at sea level. Absolute values may be obtained by reference to Table I. Corrected for barometer only.

C. Pressure and Temperature

The pressure was measured during the rising portion of the flight by a "Baroswitch" aneroid element, supplemented by a non-spillable mercury manometer with contacts registering approximately at 8, 10, 12, and 15 mm which spans the pressure range in which the balloon normally levels off. Temperatures were measured by thermistor elements, and remained in a satisfactory range.

D. Telemetering

The telemetering system described previously[2] was incorporated into the present experiment, but with a major improvement brought about by adopting an audio F.M. sub-carrier system of transmission. Two sub-carriers were used, one at 7000 cycles/sec. for transmitting the cosmic-ray coincidences, and one at 5400 cycles/sec. which was multiplexed by a mechanical commutator among all the other instruments in the gondola. This multiplexing system including the recorder was identical with that used in the preliminary experiments but was applied to the sub-carrier instead of to the radiofrequency carrier itself. The use of the sub-carrier method resulted in an improvement in stability, signal-to-noise ratio and over-all performance. The use of a separate sub-carrier for the coincidence circuits made it unnecessary to "store" counts pending survey by the commutator, and much higher counting rates could be accommodated without loss.

Details of the sub-carrier system as applied to cosmic ray research will be found elsewhere.[5] The radiofrequency system was the same as that used previously. All data were recorded on 35 mm film traveling at 6″ per minute, the multiplexed portion exactly as before, but a separate 2″ cathode-ray tube being photographed for the coincidence impulses. These were recorded singly, every sixteenth pulse being increased in size by a scalar. Also, 0.25 sec. timing impulses were recorded in addition to the 0.2 min. marks used formerly. The complete gondolas ready to fly weighed from 105 to 115 pounds.

TABLE I. Coincidence telescope constants and flight notes.

Gondola no.	Sensitivity factor*	Flight no.	Date flown	Geomagnetic latitude	Ceiling pressure (g/cm²)
1	1.013±0.009	2	July 10	0°	15
2	1.008±0.006	5	July 15	0°	31
3	1.038±0.009	6	July 17	0°	19
4	1.012±0.008	7	July 19	0°	24
5	1.023±0.006	3	July 12	0°	13
6	——	4	July 14	0°	—
7	1.031±0.006	8	July 21	0°	20
8	1.000±0.008	9	July 22	0°	—
9	1.028±0.008	10	July 25	20°	16
10	1.003±0.01	13	Aug. 6	20°	15
11	1.012±0.005	12	July 28	20°	13.5
12	1.026±0.006	11	July 27	20°	18
13	1.003±0.004	14	Aug. 10	30°	—
14	1.017±0.005	16	Aug. 14	40°	12
15	1.013±0.005	17	Aug. 15	40°	17
16	0.999±0.01	1	July 3	39°	16
17	0.990±0.0024	15	Aug. 12	31°	13

* Multiply observed counting rate by sensitivity factor to achieve standard telescope rate.

Standard telescope rate at sea level, 40° N. Geo. Lat. = 14.61±0.03 c/min. (Corrected for barometer but not for side showers and absorption in roof and counter walls.) Average of three units. 30 June–3 July and 13 Aug.–15 Aug., 1949.

Standard telescope solid angle = 21.3 steradian − cm², $\cos^2\theta$ distribution.

Standard telescope solid angle = 21.6 steradian − cm², isotropic distribution.

$$\text{Flux} = \text{counts/min.} \times \frac{\text{sensitivity factor}}{\text{standard telescope solid angle}}.$$

E. Standardization Procedures and Sea Level Flux Data

Three telescopes of exactly the same dimension as the gondola units were operated continuously in the vertical position in a light-roofed shelter on the rear deck of the "Norton Sound." In addition to measuring the sea level flux, they were compared with three gondolas at a

[5] T. Coor, Thesis, Princeton (1948).

time to obtain relative response values. As the construction of the telescopes was closely the same, their counting rates differed by only one or two percent, hardly more than the statistical errors. The mechanical registers in the recording circuits were photographed hourly, and in addition, were read twice daily. In Table I are given numerical data which enable one to convert the counting rate of a given telescope into absolute terms of particles/cm²/sec./steradian. All calibration runs were made without the lead filters. The sea level flux obtained at 40° N. geomagnetic latitude, corrected for barometer but not for side showers and absorption in counter walls, etc., is 0.69±0.01 particles/cm²/min./steradian. Montgomery[4] obtains 0.695 particles/cm²/min./steradian under similar conditions. Figure 2 presents all the data taken with the standard telescopes at sea level between 0° and 40° geomagnetic. The total observed effect is 14 percent, which of course includes both the temperature and geomagnetic factors.

The records of the Carnegie Institution cosmic-ray meters at Cheltenham, Maryland, and Huancayo, Peru, were examined[5a] over July and August. The only noticeable disturbance was a 2 percent decrease at both stations on August 4 coinciding with a magnetic disturbance. The intensity steadily increased to normal in about a week. No flights were made on August 3 or 4, and a flight on August 6 failed to show any difference of the vertical intensity at 15 g/cm² from that of a flight on July 29, both being at $\lambda = 20°$.

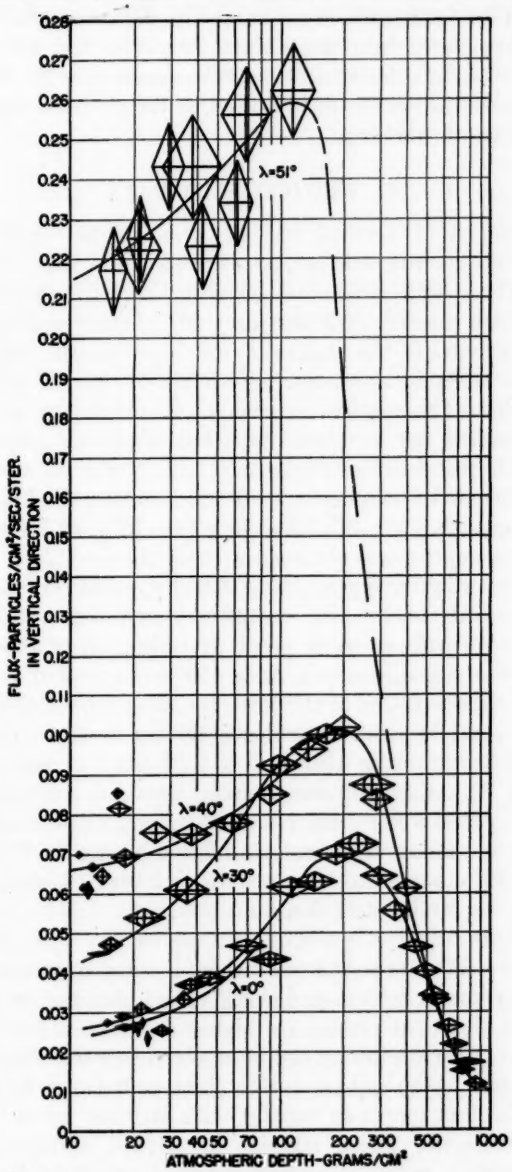

FIG. 3. Vertical flux in the atmosphere at various latitudes, with 3 cm lead filter.

F. Operational Details

Following standardization, gondolas were prepared for flight by following a series of instrument and voltage checks. Geiger tubes were individually checked before and after the standardization runs, and failures were rare. Each section of the telescope and gondola was wrapped with black paper and several layers of cellophane. Launchings followed the standard procedure for "Skyhook" balloons.[6] The construction of the "Norton Sound" was such as to provide a good wind break and sufficient deck launching space. Competent handling of the ship resulted in good wind compensation and smooth launchings with little strain on the equipment. Most of the flights rose at from 700 to 900 ft./min. and leveled off between 90,000 and 100,000 feet altitude. Radio reception was generally good after some initial difficulties had been rectified, and could be relied on to distances of 350 to 400 miles with the balloon at ceiling, which is about the radio horizon. The

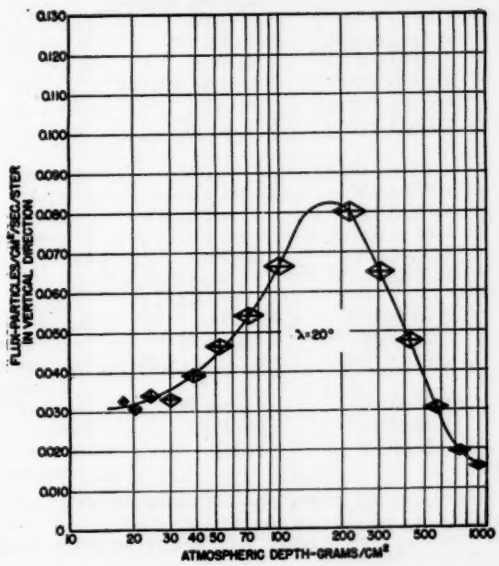

FIG. 4. Vertical flux in the atmosphere at $\lambda = 20°$, with 3 cm lead filter.

[5a] Through the kindness of Dr. S. E. Forbush.
[6] Spilhaus, Schneider, and Moore, J. Meteorology 5, 130 (1948).

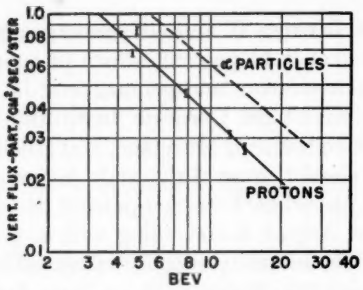

FIG. 5. The integral number-energy spectrum determined from flux measurements at 15 g/cm² from $\lambda=0°$ to $\lambda=40°$.

signal passed through two total null points of about 10 minutes duration before the final fade-out on each flight as the balloon drifted away, due presumably to interference between the direct and reflected signals from the sea. None of the gondolas were recovered, so that post-flight checks were not possible. Radar tracking facilities available on the "Norton Sound" provided time-altitude curves and geographic course charts of the balloons within a 75 mile radius of the ship.

G. Shower Detection Experiment

On one flight at 40°N. an attempt was made to measure the effect of bursts or other multiple events on the telescope coincidence rate. Three out-of-line 10 in. counters with about 2 in. spacing between centers were placed just below the center tray of the telescope, and connected to a threefold coincidence circuit which recorded via the multiplexing circuits. The shower counters were parallel to those in the tray, and two of the three were aligned with the telescope axis. This arrangement was designed to pick up bursts coming up from the lead shield over the botton tray and which might record as a coincidence. Coincidences between the telescope and shower detector could be formed on the film with a resolving time of about 0.2 sec.

TABLE II. Flux values at top of atmosphere.

Geom. lat.	Flux particles/cm²/sec./sterad.	Remarks	
0	0.026±0.001[a]	Separate flights	
0	0.027±0.001	3 cm Pb	15 g/cm² depth
0	0.031±0.001[a]	No Pb	15 g/cm²
0	0.028±0.004[b]	No Pb	Rocket
20	0.031±0.001[a]	Separate flights	15 g/cm²
20	0.031±0.001[a]	3 cm Pb	15 g/cm²
28	0.046±0.001[c]	18 cm Pb	Approx. 15 g/cm²
31	0.046±0.0015[a]	3 cm Pb	15 g/cm²
38.8	0.085±0.003[a]	3 cm Pb	15 g/cm²
39.5	0.068±0.002[a]	3 cm Pb	15 g/cm²
41	0.082±0.002[a]	3 cm Pb	15 g/cm²
41	0.073±0.006[d]	No Pb	Rocket
50	0.15±?[e]	Total radiation estimated	12 g/cm²
50	0.18±0.02[b]	No Pb	Rocket
51	0.22±0.01[f]	1.9 cm Pb	15 g/cm²
52	0.17±0.004[g]	0 to 7.5 cm Pb	"At top of atmosphere"
56	0.23±0.01[h]	1.9 cm Pb	15 g/cm²
58	0.29±0.03[b]	No Pb	Rocket
69	0.25±?[i]	Total	"At top of atmosphere"

[a] Winckler, Stix, Dwight, and Sabin. (W, S, D, S)
[b] J. A. Van Allen and S. F Singer, Phys. Rev. 78, 819 (1950). (U, S)
[c] Schein (unpublished). (S)
[d] See reference b (*G, J, V* on figure).
[e] D. J. X. Montgomery, *Cosmic Ray Physics* (Princeton University Press, Princeton, New Jersey, 1949), p. 131. (M)
[f] J. R. Winckler and W. G. Stroud (unpublished). (W, S)
[g] M. A. Pomerantz, Phys. Rev. 75, 1721 (1949). (P)
[h] Winckler, Stroud, and Shanley, Phys. Rev. 76, 1012 (1949). (W, S)
[i] M. A. Pomerantz and M. S. Vallarta, Phys. Rev. 76, 1889 (1949). (P)

H. Analysis of Records

Film reading was greatly facilitated by a motor-driven projector and phototube pick-ups on the observation screen. The 0.25 sec. timing pulses were detected by one photo-tube and recorded by means of a scaling circuit and mechanical register. A similar system was used for the cosmic-ray counts. The flight records were broken down into ten-minute intervals, and in each interval the counts and time were summed in the eight 45° azimuth sectors as indicated by the compass signals recorded in the film.

III. VERTICAL FLUX DATA

Graphs of vertical flux *vs.* atmospheric depth at various geomagnetic latitudes are shown in Figs. 3 and 4. These data were obtained with the 3 cm Pb filter, and are plotted with pressures on a logarithmic scale to accentuate the region of low atmospheric depths. This scale is approximately linear in height above ground. The vertical extension of the plotted points represents the standard statistical deviation, and the width the pressure range over which the data were averaged. Two flights at $\lambda=0°$ agree quite well (Fig. 3). A vertical flux value at ceiling ($Y=15$ g/cm² atmospheric depth), was obtained without the lead filter, and gives a slightly higher value (0.032 particles/cm²/sec./ster.). At $\lambda=20°$ one complete curve was obtained (Fig. 4) with a check point at ceiling from another flight which agrees well. At $\lambda=30°$ one complete curve was obtained. One of the three standard telescope units was used for this experiment, having been equipped with telemetering gear and a lead filter in the field (Fig. 3). At $\lambda=40°$ one complete curve was measured (Fig. 3) with two check points at ceiling. The full curve does not follow the trend established by the $\lambda=0°$, 20° and 30° curves, and fails to show an increased intensity over the 30° latitude at most atmospheric depths. However, at ceiling it levels off at a higher flux value than the $\lambda=30°$ curve. At $\lambda=40°$ there is some scattering of the points at ceiling, and check values obtained on two other flights at ceiling are higher than the full curve. Most of the scattering can be resolved by correcting for the drift of the balloon during flight, or between flights, as the flux increases rapidly with latitude at 40° N. geomagnetic. There remains at $\lambda=40°$ a difference between a point at ceiling obtained on flight No. 1 (July 3) and values on two other flights (16 and 17,

August 14 and 15) which is outside the statistical error. Fluctuations in primary intensity may account for some of these irregularities. Also given in Fig. 3 are some data obtained in Princeton in November, 1948, at $\lambda=51°$ with a small counter telescope of the type used previously.[2] Between 51° and 56° N. no difference in intensity outside experimental uncertainties at low atmospheric depths was detected with these small telescopes. The $\lambda=51°$ flight carried a 1.9 cm Pb filter. At $\lambda=56°$ various thicknesses between 0 and 17 cm were used, and an appropriate value was chosen for comparison with the $\lambda=51°$ data.

Since all of the flights reached or approached the 15 g/cm² level, the latitude effect can be studied at this depth with little or no extrapolation. In relating the measured values to the flux of primary particles arriving from infinity one is obliged to consider a number of factors, of which the following are important: (*A*) It is believed that most of the primary cosmic rays interact with the atmosphere with a mean free path between 70 and 150 g/cm² of air. According to this, between 10 and 20 percent of the primaries would have interacted above the apparatus. This fraction will depend strongly on the proportion of heavy nuclei, which seem to have a smaller mean free path.[7]

(*B*) Experiments show that at this atmospheric depth the vertical flux is nearly all of penetrating nature,[2,8] at least for $\lambda<51°$. (*C*) If the primary interaction produces mesons by the P–π–μ process, the primaries at 15 g/cm² depth should be accompanied by π and μ mesons. We should expect also knock-on nucleons and "satellite" fragments resulting from the break-up of heavy nuclei present in the primary radiation.[7] These particles together could account for the penetrating flux of (*B*).

(*D*) The flux of particles able to penetrate 3 cm of Pb increases with atmospheric depth at small depths and at latitudes between 0° and 40° geomagnetic. There is evidence that at higher latitudes the average penetrability of secondaries decreases.[2,7] The curves of Figs. 3 and 4 level off with decreasing depth but have obviously not quite reached the plateau above the atmosphere. The single Geiger counter measurements made in rockets exhibit such a plateau[9] but are not directly comparable with the present experiments. The observed increase with depth indicates that the secondary flux able to penetrate 3 cm Pb builds up faster than the primaries disappear. It is possible that the observed flux is 30 to 40 percent above the flux on the plateau outside of the atmosphere which would have been obtained *with the same equipment.* However, the good agreement between the present results and rocket flux values at 0° and 41° indicates that the effect is probably less than the 30 to 40 percent figure, even considering differences in the two kinds of experiments.*

TABLE III. Primary energy flux measured by ionization chambers and counters.

Geom. lat.	(Bev/cm²/sec.) Millikan *et al.* ionization chambers	Flux at the "top of atmosphere"
0°		2.16
3°	0.94	
20°		2.25
38°	1.82	
40°		3.40

(*E*) Various geometrical factors, such as secondary particles arriving within the solid angle of the telescope originating from primaries far outside this angle, and air showers able to register a coincidence and coming from far outside the telescope angle must be considered. The asymmetry measurements give an approximate upper limit to such effects of about 20 percent. Part of the increased flux with depth mentioned in (*D*) may be due to side showers. (*F*) Particles ejected from the atmosphere in a region of bound orbits may travel above the atmosphere for considerable distances before returning. Qualitative considerations show that the effect would not be important in the vertical direction, but that it might be important at large zenith angles.

We make the assumption that the observed vertical flux at 15 g/cm² is a direct measure of the vertical

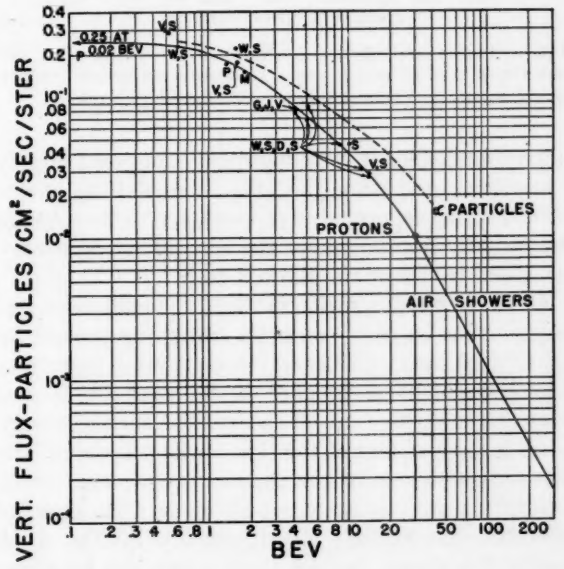

FIG. 6. Integral number-energy spectrum from flux measurements by various investigators at very high altitude. The spectrum given by Hilberry for air showers with $\gamma=2.7$ is joined to form a continuous curve.

[7] Freier, Lofgren, Ney, and Oppenheimer, Phys. Rev. **74**, 1818 (1948); H. L. Bradt and B. Peters, Phys. Rev. **77**, 54 (1950).

[8] M. A. Pomerantz, Phys. Rev. **75**, 69 (1949).

[9] Gangnes, Jenkins, and Van Allen, Phys. Rev. **75**, 57 (1949).

* *Note added in proof:*—Recent rocket measurements (J. A. Van Allen, private communication) with *vertical telescopes* show that the plateau above the atmosphere is reached as low as 30 kml, which is appreciably lower than the beginning of the single counter plateau.

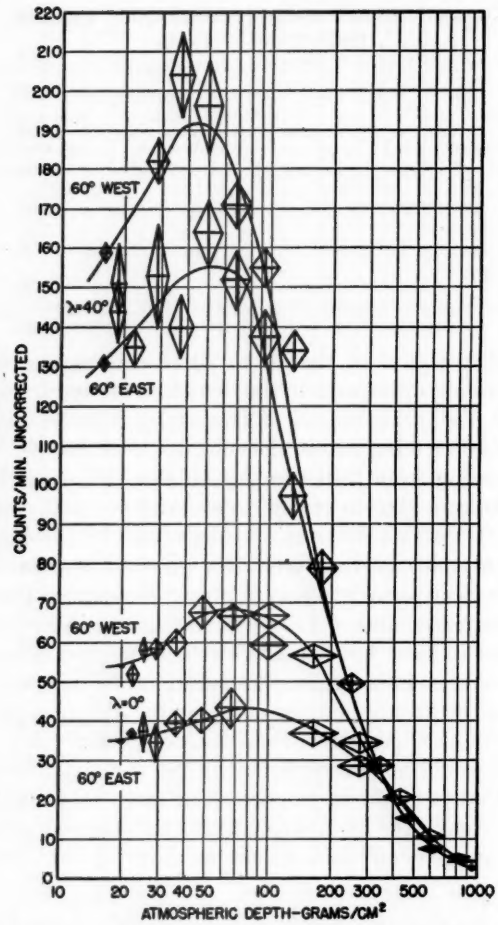

FIG. 7. The eastern and western rates as a function of atmospheric depth at a 60° zenith angle. Data summed in 135° sectors. Upper-gondola 15. Lower-gondola 7. $\lambda=0°$ and 40°.

primary flux, since it is undoubtedly composed largely of primaries, and since the other contributing effects outlined above are probably proportional to the average primary flux. We assume for the vertical cut-off energy that given by the main allowed cone[10] at 0° and 20°. At 30° the penumbra region between the main cone and shadow cone is fairly wide in energy and partially "light," and the cut-off energy is somewhat uncertain. At latitudes of 40° and higher the Störmer cone is used to obtain the vertical cut-off energy. The vertical energy cut-off is independent of the sign of the primaries. The eight measurements of the present experiment, which constitute a self-consistent set all made with identical apparatus, are plotted logarithmically in Fig. 5. A straight line drawn through these points can be represented by the equation $I(E)=0.30E^{-0.90\pm0.05}$ and is the integral number-energy spectrum for primaries, with reservations as discussed above. The differential number-energy spectrum derived from this, i.e., the flux of particles in unit energy interval at E, is $N(E)=0.27E^{-1.90}$. Over this range of energies primaries composed entirely of alpha-particles give for the integral spectrum $I(E)=0.39E^{-0.81}$, and for the differential spectrum $N(E)=0.32E^{-1.81}$.

In Table II are collected all available flux values obtained at the "top" of the atmosphere and with rockets. These are without exception made with Geiger tube telescopes, but with various geometrical arrangements and amounts of filtering. The best fit to these data plotted in logarithmic form (Fig. 6) appears not to be a straight line, but a curve with increasing slope at higher energies. The agreement between the present

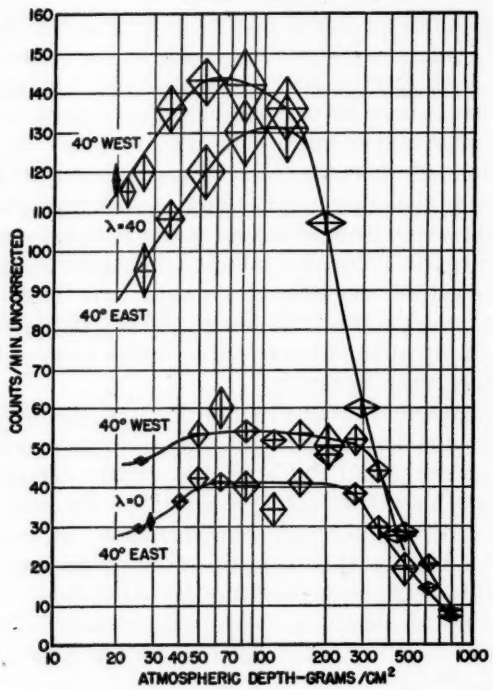

FIG. 8. Eastern and western rates in 135° sectors of azimuth at a 40° zenith angle. Upper-gondola 16. Lower-gondola 4. $\lambda=0°$ and 40°.

experiments and rocket data above the atmosphere at 0°, 41°, and 50°, is noteworthy. The extensive shower spectrum given by Hilberry[11] has been drawn in, principally to demonstrate that there is not necessarily a contradiction between the two spectra although the exponents differ by unity, but that they may be joined smoothly. There appears to be a disagreement in absolute value, for according to Hilberry's spectrum $N(E)=5.45\cdot10^{15}\cdot E^{-2.75}$ particles/cm²/sec./ster. which gives I (10 Bev) = 0.01 particles/cm²/sec./ster. instead of 0.027 as observed here. However, Hilberry's results apply in the region 5.10^{13} to 5.10^{15} ev, and one extends them to 10^{10} ev with considerable uncertainty. The large extrapolation of Hilberry's spectrum to the geomagnetic region of energies below 60 Bev makes the derived flux value in this region very sensitive to the exponent, γ, and the two spectra may be easily brought

[10] M. S. Vallarta, Phys. Rev. **50**, 493 (1936).

[11] N. Hilberry, Phys. Rev. **60**, 7 (1941).

into agreement in absolute value by modifying γ by a few percent, or probably by less than the accuracy of Hilberry's result.

From the curve (Fig. 6) it appears that the spectrum levels off at the low energy end (Pomerantz' measurement at $\lambda=69°$), with a rather broad knee between 50° and 60° N. geomagnetic, or definitely further north than the well-known knee at sea level, which occurs at about 45°. One would expect the sea level knee to be south of the high altitude knee because of energy loss in the atmosphere. It is also possible that the high altitude knee measured at 15 g/cm² depth is partly attributable to atmospheric absorption. It is known that the ionization range for low energy heavy nuclei which may enter at 56° or higher, may be of this order in g/cm², and depending on the relative abundances of heavies and protons, and their spectra, the exact atmospheric depth may be important at high latitudes even at very high altitudes. It would be very desirable to make a self-consistent set of measurements over the knee region to determine its exact shape and location, as the present points scatter too severely.

It is of great importance to compare the present measurements with the ionization-depth measurements of Millikan, Neher and their collaborators on which a major part of our knowledge of the geomagnetic effects

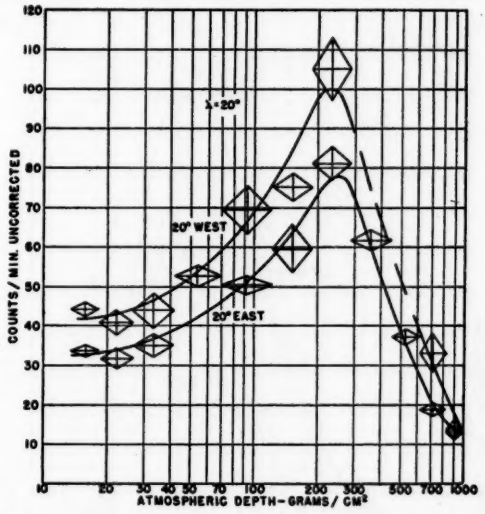

FIG. 9. Eastern and western rates at $\lambda=20°$, zenith angle=20°. Gondola 11.

is based. To make this comparison we calculate the total incident energy assuming that our observed spectrum holds for energies between 3.5 and 60 Bev for protons, which includes all the geomagnetically influenced proton primaries between 0° and 40° latitude. The Hilberry spectrum was assumed above 60 Bev. This energy flux in Bev/cm²/sec. is

$$\Phi(E,\lambda)=\int_{E_{\min}(\lambda)}^{\infty}\Omega(E,\lambda)N(E)EdE. \qquad (3)$$

Here $\Omega(E,\lambda)$ is the solid angle of the allowed cone for energy E at latitude λ, and $N(E)$ is the observed differential number-energy spectrum. We derive Ω graphically from the main cone (Vallarta[10]) at $\lambda=0°$ and $\lambda=20°$, and from the Störmer and the shadow cones[12] at $\lambda=40°$ from the relation

$$\Omega(E,\lambda)=\int_{\theta_{\min}(E,\lambda)}^{\pi/2}\phi\cdot\sin\theta\cos\theta d\theta, \qquad (4)$$

where ϕ is the azimuthal extent of the allowed cone at zenith angle θ. Equation (3) has been integrated graphically and is compared with the Millikan-Neher-Pickering results[13] in Table III.

The flux measurements give about twice the incident energy appearing as ionization at both low and high latitudes. We expect the measured *flux* values to be high due to multiplication, etc. in the atmosphere, as discussed previously. But this may well be compensated by our calculation of the *energy*, which is performed on the basis of protons alone. Since it is very likely that a 20 to 25 percent α-particle component, as well as much smaller but appreciable numbers of heavier nuclei exist throughout the primary spectrum,[13a] the effective energy cut-off and the total energy flux would be *higher* at each latitude than the calculated values. The energy calculations based on particle flux measurements are indirect in the sense that the theory of the allowed cone is utilized with no independent check on its accuracy or applicability, a factor which is not present in the ionization measurements. It presumably would be possible by invoking a sufficient particle flux moving in

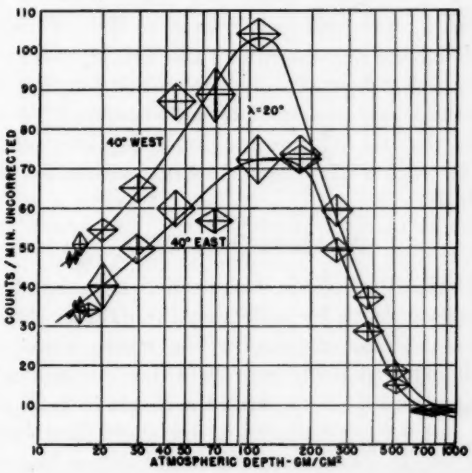

FIG. 10. Eastern and western rates at $\lambda=20°$, zenith angle=40°. Gondola 10.

[12] E. J. Shremp, Phys. Rev. **54**, 153, 158 (1938).

[13] Millikan, Neher and Pickering, Phys. Rev. **61**, 397 (1942). Quoted in L. Jánossy, *Cosmic Rays* (Oxford University Press, London, 1948), p. 298.

[13a] This fact is established over a part of the primary energy spectrum, and the ratio of alpha's to protons seems not to vary rapidly with energy. (Reference 7, and recent unpublished cloud chamber results of E. P. Ney.)

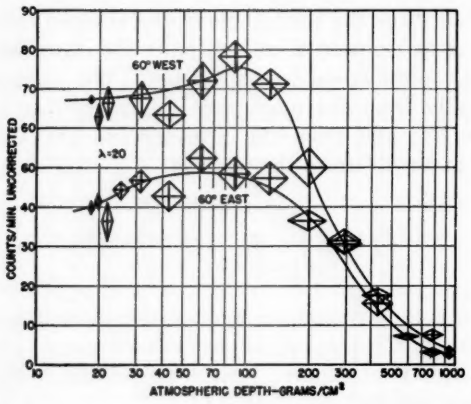

FIG. 11. Eastern and western rates at $\lambda=20°$, zenith angle$=60°$. Gondola 12.

bound orbits, which have not been studied theoretically so far, or by assuming that the equivalent magnetic dipole field of the earth at large distances from the earth is not given by the distribution of magnetic flux on the surface, to explain part of all of the observed differences. However, the large discrepancy shown in Table III can be accounted for most reasonably by primary energy passing into forms not detectable by the ion chambers, such as neutrinos, low energy nuclear fragments and binding energy absorbed during nuclear evaporations of air atoms.

Jánossy (reference 13, pp. 299–300) finds that the Millikan ionization data as well as the vertical energy flow measured with counter telescopes[14] can be accounted for in terms of a differential number-momentum spectrum of the form $c\cdot p^{-\gamma}$ with $\gamma=2.5$. The higher value of γ obtained from such measurements made lower in the atmosphere is related to the difference in absolute energy flux shown in Table III. If, as suggested above, these differences are due to non-ionizing forms of secondary radiation such as neutrinos, then Table III suggests that the relative fraction going into neutrinos must be higher for higher energy primaries (lower latitudes).

IV. AZIMUTHAL DATA

The azimuthal effect was studied as a function of atmospheric depth by collecting the data in three 45° western and eastern sectors. The result of averaging the telescope counting rate over 135° of azimuth in each direction was to decrease the observed E–W asymmetry, but was necessitated by the short time spent by the balloon in each pressure interval during the ascent of the flight. Ten minute intervals were used during most of the ascent, but were increased in length near ceiling as the balloon leveled off, and the lowest pressure points include all of the ceiling data averaged together. In this type of analysis no reference was made to the azimuthal standardization, and the two 135° sectors represent the eastern and western directions only to within 15° or 20°. In one or two of the intervals during ascent the balloon rotated so rapidly that the inertia of the compass produced considerable overshooting and lagging in the azimuthal indications. This effect was discovered by correlating the sun reference photo-cell with the compass, and it was noticed that during such intervals the east-west values fluctuated beyond the statistical error, and usually the east-west asymmetry was reduced. Fortunately, these intervals were not numerous enough to influence the average curve appreciably.

Figures 7 and 8 give the E–W effect as a function of depth for $\lambda=0°$ and $\lambda=40°$, for 40° and 60° zenith angles. Figures 9, 10 and 11 give similar curves at $\lambda=20°$ for 20°, 40°, and 60° zenith angles. These curves show that the E–W effect increases with decreasing depth, and does so with increasing rapidity between 300 and 100 g/cm². The E–W effect is larger at $\lambda=0°$ than at $\lambda=40°$, as would be expected from geomagnetic considerations, and apparently at $\lambda=0°$ persists relatively further into the atmosphere than at $\lambda=40°$. Both the easterly and westerly curves pass through a mild maximum between 50 and 100 g/cm². Above this, at $\lambda=0°$ a leveling off process seems to take place, but at $\lambda=40°$ a sharp downward trend persists to the highest altitudes reached. It was hoped that such data would permit the trend of the asymmetry to be mapped out as

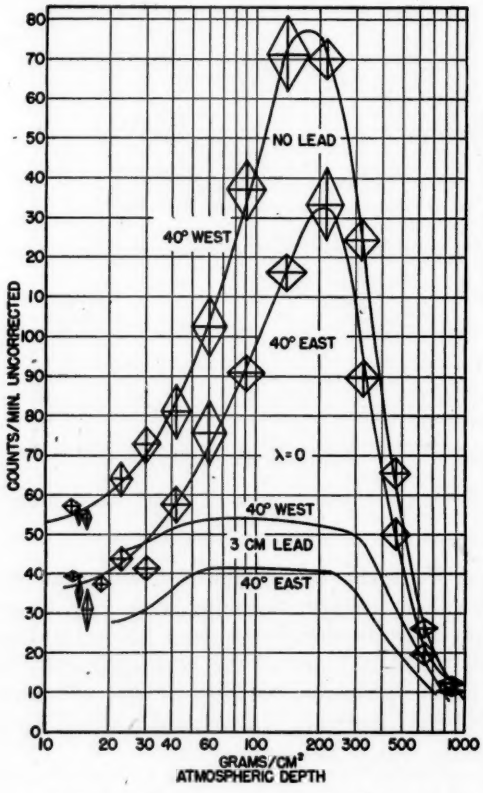

FIG. 12. Eastern and western rates at $\lambda=0°$, zenith angle$=40°$ without the customary 3 cm Pb filter. Lower curves—same measurement with filter.

[14] Millikan, Neher, and Pickering, Phys. Rev. **63**, 234 (1943).

a function of depth near the top of the atmosphere, as an aid in estimating the effect of the atmosphere on the measurements. However, if the asymmetry is plotted as a function of depth in this region no consistent picture emerges. In some cases the asymmetry remains constant, and in others it increases or decreases. It is probable that the statistical accuracy during the ascending portion of the flights is not sufficient to give detailed information of this sort.

Of more interest is the curve if Fig. 12, at $\lambda=0°$, 40° zenith angle *without* the 3 cm Pb filter. Large maxima occur in both the east and west portions, and the asymmetry, or at least the E–W difference, is preserved to a surprising degree. For comparison the corresponding curve with the 3 cm Pb filter is shown. The asymmetry without the filter is only a little smaller at various depths than with it, a result which is in agreement with measurements made by H. V. Neher and collaborators[15] at 250 to 300 g/cm² atmospheric depth. The asymmetry measured from Fig. 12 between 100 and 200 g/cm² is about 27 percent. The asymmetry at the top of the atmosphere, and with the data summed in 45° sectors, increases to 50 percent without lead, and 54 percent with 3 cm (see Table IV). The trend is obviously towards smaller asymmetries with greater depths, wider sectors of azimuth, and less filtering. It seems possible on the basis of this to explain in most part the low asymmetry measured by Johnson and Barry[16] at

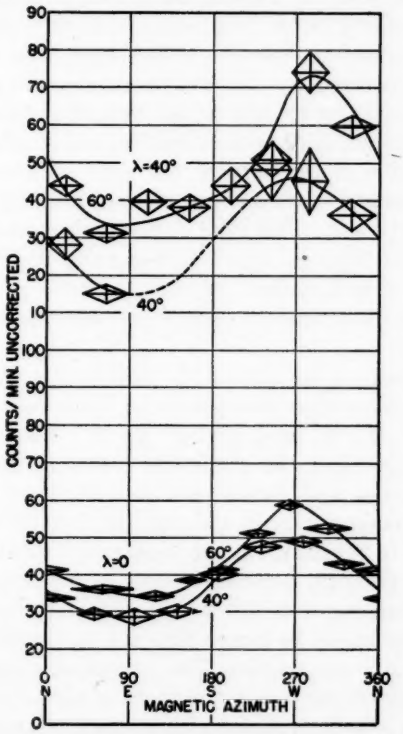

FIG. 13. Azimuthal effect at $\lambda=0°$ and $\lambda=40°$, with zenith angles of 40° and 60°. Gondola numbers top to bottom—15, 15, 7, 4. Atmospheric depth top to bottom—17, 17, 20, 24 g/cm².

[15] Biehl, Neher, and Roesch, Phys. Rev. **76**, 914 (1949).
[16] T. H. Johnson and J. G. Barry, Phys. Rev. **56**, 219 (1939).

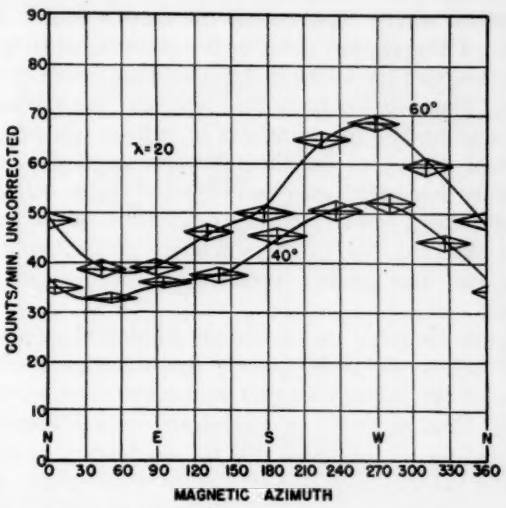

FIG. 14. Azimuthal effect at $\lambda=20°$, zenith angles=40° and 60°. Gondolas 10 and 12. 15 and 18 g/cm², respectively.

$\lambda=20°$, and at about the 100 g/cm² level at a 60° zenith angle. Their telescope was composed of small counters with about a 90° total opening, and data was summed in the 180° E–W sectors. In the present experiments we note that the 50 percent peak asymmetry is reduced to 32 percent if we average over the two 180° sectors, and the atmospheric depth effect further reduces this to about 20 percent. The difference between this and the 7 ± 3 percent measured by Johnson might be accounted for by less obvious features of the two experiments such as the small single counter telescope *vs.* the large tray construction, measurement of azimuth, etc.

Unfortunately, the low statistical accuracy of the present data at the 250 to 300 g/cm² depth, where the balloon spends little time, makes a direct comparison with the Neher data[15] which has high statistical accuracy, inconclusive.

The azimuthal effect measured at the balloon ceiling where a number of hours of data were collected is shown in Figs. 13, 14 and 15. These data were collected at the number of g/cm² indicated under the figure with an uncertainty of a few g/cm² arising from the averaging process over the balloon's time-altitude curve and the finite pressure increments indicated by the manometor contacts. On most flights the balloon remained within an interval of about 5 g/cm² after reaching maximum altitude, which varied between 15 and 25 g/cm². The number of counts and the time were summed in each azimuthal sector in ten-minute intervals as described in Sec. II-H, and totals and rates in each sector were then obtained for the entire constant level portion of the flight. Reference was made to the exact compass calibrations and the sun reference indicator to determine the angular width and magnetic azimuth of each sector. Magnetic north was assumed to lie in the meridian plane through the point of observation of the off-center

equivalent dipole representing the earth's field.[17] The height of the plotted point is the standard statistical deviation, and the width is the azimuthal extent of the sector. These curves as plotted represent the telescope data uncorrected for variations in balloon altitude on different flights, or for the telescope sensitivity, etc. Absolute flux values may be computed easily with the aid of Table I, but all counting rate curves can be compared directly, due to the similarity of the separate telescopes. The gondola numbers are given under the figures.

Figure 13 gives the measured azimuthal effect at $\lambda=0°$ and $\lambda=40°$ at 40° and 60° zenith angles. We find a much larger flux and smaller percentage asymmetry at $\lambda=40°$ than at $\lambda=0°$, in accordance with theoretical expectations. It is notable that the asymmetry at a 60° angle is inappreciably larger than at a 40° angle, and furthermore, the eastern intensity is larger for 60° than for 40° zenith, which is contrary to the predictions of the theory if all the primaries are positively charged. The azimuthal curves at $\lambda=20°$ carry out these same features (Fig. 14), but in qualitative agreement with the main cone diagram for this latitude, the curves are shifted in phase somewhat from the $\lambda=0°$ curves, and have an additional inflection point at approximately 180° magnetic azimuth. The statistical accuracy of the measurements is not good enough to confirm the existence of a north-south effect as predicted theoretically.

In Fig. 16 is shown a comparison of the azimuthal effect at $\lambda=0°$ at zenith angles of 40° and 60° with and without the 3 cm lead shield. The no-lead experiment yields a slightly larger flux, even though its atmospheric depth is less. The asymmetry, however, is very little different with and without the lead shield. This can be interpreted as evidence that the contribution to the counting rate from large energetic star fragments is small, as a large fraction of such star particles would be absorbed in 33 g/cm² of lead. The familiar isotropic distribution of such fragments would certainly conceal the directional properties of the primaries responsible for them. Similar remarks apply to other low energy particles produced at wide angles.

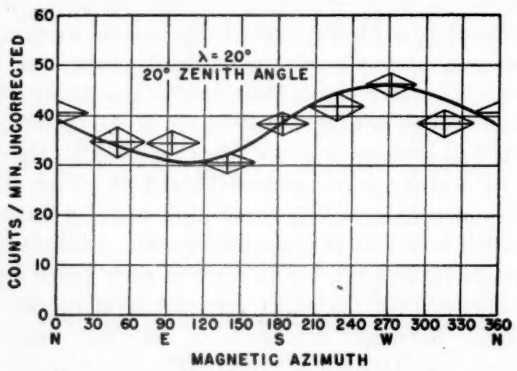

FIG. 15. Azimuthal effect at $\lambda=20°$, zenith angle=20°. Gondola 11, 13.5 g/cm².

[17] J. Bartles, Terr. Mag. 41, 225 (1936).

TABLE IV. Observed and predicted azimuthal asymmetry.*

Geom. lat.	Zenith angle	E. min. (Stormers) E.	E. min. (Stormers) W.	Predicted asymmetry	Observed asymmetry**
0°	40°	0.615	0.430	0.81	0.50±0.08 (No Pb)
	60	0.730	0.420	1.20	0.50±0.09 (No Pb)
	40	0.615	0.430	0.81	0.54±0.10 (3 cm Pb)
	60	0.730	0.420	1.20	0.53±0.05 (3 cm Pb)
20°	20	0.520	0.437	0.41	0.41±0.10 (3 cm Pb)
	40	0.583	0.420	0.71	0.48±0.06 (3 cm Pb)
	60	0.680	0.410	1.08	0.58±0.05 (3 cm Pb)
40°	40	0.317	0.275	0.31	0.24±0.09 (3 cm Pb)
	60	0.500	0.270	1.02	0.26±0.07 (3 cm Pb)

* Asymmetry $=(I_w-I_e)/\frac{1}{2}(I_w+I_e)$.
** Errors determined by calculating the asymmetry with opposite extreme values of I_w and I_e as given by the standard statistical errors in I_w and I_e.

The observed east-west asymmetry values obtained from the curves of Figs. 13, 14, 15 and 16 are collected in Table IV. To test the hypothesis that the primary spectrum consists entirely of positive particles the asymmetry is predicted from the latitude effect of the vertical flux which does not depend on the sign of the charge, but only on the energy spectrum. If all primaries are positive, the azimuthal and latitude effects should be identical as long as the minimum energy of entry expressed in *Störmers* is the same. The range of Störmers covered by the east-west effect is given in column 3 of Table IV. The range covered by the vertical cut-off extends only to 0.500 Störmers, so that some extrapolation of the vertical flux data is necessary to 0.730 Störmers, the eastern minimum energy at 60° zenith and $\lambda=0°$. This type of comparison entirely on the basis of Störmer units and using the observed vertical flux is independent of the e/m ratio of the primaries, and is dependent only on the self-consistency of the theory.

The observed asymmetry is plainly less by a considerable factor than that predicted, with the exception of $\lambda=40°$, $\theta=40°$ and $\lambda=20°$, $\theta=20°$. The factor is much larger than the statistical errors in the asymmetry curves and cannot be accounted for by the various uncertainties in the vertical flux of the type discussed in Sec. III. On the contrary, indications are that the spectrum becomes steeper at higher energies, with γ changing from 1.9 to 2.7, so that the predicted asymmetry might be larger than the calculated value, but certainly not smaller. The azimuthal distribution is probably the most self-consistent of all the measurements, as it is determined with a single instrument repeatedly surveying the complete 360° region, and at quite constant atmospheric depth.

One of the most obvious effects to be studied in explaining the low observed asymmetry is that of the

Figure 4 of reference 2 shows the absence of an azimuthal effect at $\lambda=56°$ greater than five percent.

residual atmospheric path above the equipment, which is longer at zenith angle θ by the factor sec. θ than the vertical path. The zenith angle effect at constant minimum *energy* (and therefore constant primary flux) may be studied by selecting directions intersecting lines of constant Störmer units as given for example in the main cone projections of Vallarta.

In Table V are tabulated the observed counting rates of the telescopes at a number of combinations of the geomagnetic latitude λ, azimuth ϕ and zenith angle θ, which theoretically should correspond to a fixed minimum energy. Two such minimum values, 0.5 and 0.43 Störmers (14 and 10 Bev for protons) are selected, and all positive primaries are assumed. The following points should be noted concerning Table V: (*A*) The $\theta=0°$ and $\theta=40°$ rates for the same minimum energy are in satisfactory agreement. The $\theta=20°$ values at $\lambda=20°$ are somewhat low, but this measurement may reflect the smaller depth obtained on this flight. These zenith angles do not intersect the chosen minimum energies as far north as $\lambda=40°$. (*B*) At $\theta=60°$ the rate at $\lambda=0°$ and $\lambda=20°$ is uniformly higher by 15 to 20 percent for equal minimum energies than the smaller zenith angles. (*C*) At $\lambda=40°$ the $\theta=60°$ rate is higher by a factor of *three* than any of the other rates for equal minimum energy.

From point (*A*) one can conclude that the difference in air path between the vertical and $\theta=40°$ has a small effect on the measurements at about 15 or 20 g/cm² atmospheric depth, as the rates are nearly the same for the same minimum energy. The longer path at $\theta=60°$ produces a noticeable increase in rate, but if we compare with the vertical data on the basis of equal air path in g/cm² as well as equal minimum energy, very reasonable

TABLE V. Observed rates for fixed minimum energy with λ, θ and ϕ variable.

	0.500 Störmers [$E=14$ Bev for protons]							
	$\theta=0$		$\theta=20$		$\theta=40$		$\theta=60$	
λ	ϕ	Rate	ϕ	Rate	ϕ	Rate	ϕ	Rate
0	~	40	88	—	196	41.5	201	45
			351	—	344	39.5	338	46.5
20	—	—	19	37	158	40	170	50
			128	31	352	40	350	51
40	—	—	—	—	—	—	40	137
							115	135
	0.430 Störmers [$E=10$ Bev for protons]							
	$\theta=0$		$\theta=20$		$\theta=40$		$\theta=60$	
λ	ϕ	Rate	ϕ	Rate	ϕ	Rate	ϕ	Rate
0	—	—	—	—	—	—	260	59
							280	58
20	—	—	—	—	209	48	201	58.5
					288	51.5	294	65
25	~	47	—	—	—	—	—	—
40	—	—	—	—	—	—	10	146
							130	136

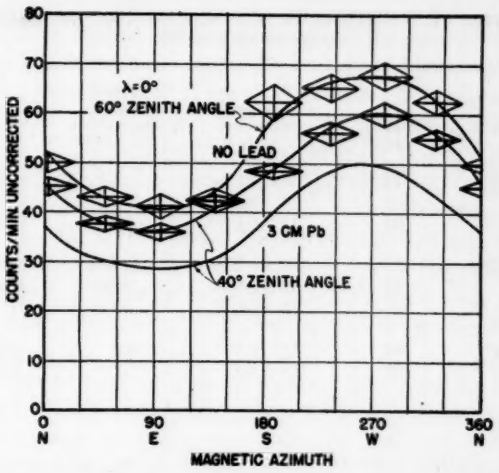

FIG. 16. Azimuthal effect at $\lambda=0°$, zenith angles $=40°$ and $60°$, with and without the 3 cm Pb filter. Top, gondola 5, 13 g/cm². Bottom, gondola 4, 24 g/cm².

agreement between the $\theta=0°$ and $\theta=60°$ data results at latitudes up to 25°. This comparison is made by reading the vertical rate curves at a depth Y sec. θ, where Y is the balloon depth, and ignores meson decay effects.

The large factor which appears at $\lambda=40°$ is far greater than can be explained by simple air path considerations. We note also that the largest discrepancy between the predicted and observed E–W asymmetry (Table IV) occurs at $\lambda=40°$, $\theta=60°$. The fact that with a simple air path correction the intensities at various zeniths and latitudes for the same minimum energy agree seems at first a contradiction to the data given in Table IV, which indicates *disagreement* of a similar comparison assuming all positive primaries. We note, however, that the data in Table V which agree best (mostly for 0.5 Störmers) lie predominantly in the northerly or southerly directions. In these directions, like the vertical, the intensity depends only to a slight degree on the polarity of the particles. The northern or southern intensity is also near the mean value of the east and west intensities.

Another atmospheric effect is the presence of secondary particles produced or scattered upward toward the east, and originating from primaries arriving from the west. Neher and his collaborators[15] find a negligible amount of upward radiation at 300 g/cm² depth, but this is not surprising since the number of primaries which are moving at large zenith angles below this depth, and which therefore are able to produce upward secondaries into the equipment, is very small. This is not true at the top of the atmosphere, however, where even in the horizontal direction an appreciable number of primaries may be present (the ratio of the horizontal air path to the vertical is 27 due to earth curvature, see reference 2). The amount of such upward radiation which would be necessary to reduce the predicted asymmetries to the observed values can be calculated easily

TABLE VI. Estimate of the effect of upward moving particles on asymmetry values.

Geom. lat.	Zenith angle	Observed eastern rate $I(E)$ c/min.	Eastern rate for agreement $I(E_e)$ c/min.	$\frac{I(E)-I(E_e)}{I(W)}$
$\lambda=0°$	40 (no Pb)	36.0±1.5	25.4	0.18
	40	28.5±2.0	21.0	0.15
	60	34.5±1.5	14.8	0.33
$\lambda=20°$	20	30.5±2.0	Agrees	0.00
	40	32.5±1.0	25.0	0.14
	60	38.0±1.5	20.6	0.25
$\lambda=40°$	40	115 ±5	108	0.05
	60	135 ±5	57	0.45

by equating these two values and solving for the easterly counting rate as an unknown. In Table VI is listed at each latitude and zenith angle the observed easterly counting rate, the easterly rate which would produce agreement between the E–W and latitude effects, and the difference expressed as a fraction of the westerly rate at the same zenith angle. The fractions range from 5 to 45 percent, in general being larger for the larger zenith angles. This is of course to be expected since momentum considerations would predict that most energetic secondaries would be projected forward, with few at larger angles to the primary direction. Detailed calculations of the type attempted earlier[2] involving the primary absorption, and the angular distribution and absorption of secondaries may show if this sort of process can satisfactorily produce the amount of upward radiation required by Table VI. That the observed discrepancy can be accounted for by this process seems likely, and one therefore hesitates to invoke any negative primaries until further work is done. However, the necessary flux of primary electrons is a small enough fraction of the total flux to have escaped observation at high latitudes where direct experiments for detecting primary electrons have been carried out.[18,19*] The above discrepancy between the E–W and latitude effects apparently does not exist at 300 g/cm², where Neher and his collaborators[15] find agreement between the east-west effect at $\lambda=25°$, $\theta=45°$ and the vertical latitude effect over the interval $\lambda=0°$ to $\lambda=29°$. A similar result is obtained at greater depths, even at sea level.[20] However, it is notable that the latitude effect of the vertical flux between $\lambda=50°$ and $\lambda=0°$ is 1.1 at sea level, 1.6 at 300 g/cm² and 6.3 at 15 g/cm². The E–W asymmetry is 0.10, 0.30 to 0.35, and 0.54 at the same respective depths at the equator, and does not increase enough with decreasing depth to be consistent with the increase of the latitude effect with depth below 300 g/cm², for positive primaries. Directional measurements, like many other types of cosmic ray phenomena, obviously reflect at each point in the atmosphere those primary particles whose energy is great enough to make their effects felt at that point. The weighting effect of the atmosphere on the number-energy distribution of primaries is very pronounced, and thus the measurements at a depth of $\frac{1}{3}$ atmosphere effectively span a different range of primary energies than the "top of the atmosphere" data, even though the latitude and direction in space may be the same. The agreement in one case and lack of agreement in another between the latitude and E-W effects may therefore not be contradictory if the measurements are made at different depths in the atmosphere.

V. SHOWERS AND BURSTS

One experiment at $\lambda=40°$ (Flight 16) was conducted with counter tubes arranged to detect bursts or air showers (see Sec. II for counter arrangement). The main telescope was vertical during ascent, and the multiple events recorded increased, passed through a mild maximum at a somewhat smaller atmospheric depth than the maximum observed with the telescope, and then decreased near the top of the atmosphere. The multiple events were 15.6(c/min.)/125(c/min.) =13 percent of the telescope rate at maximum, and 13.5(c/min.)/80.5(c/min.)=17 percent at ceiling (12 g/cm²). There was a marked zenith angle dependence, for the rate with the telescope at $\theta=0°$ was 13.5±0.6 c/min., at $\theta=40°$ was 14.8±0.5 c/min. and at $\theta=60°$ was 16.0±0.5 c/min., averaged over several cycles of the telescope. The corresponding telescope rates averaged in azimuth were respectively 80.5, 92.5 and 104.9 c/min., which gives for the ratio of multiple events to telescope events 0.17, 0.16 and 0.15, which is constant within statistical errors. Coincidences between the shower detector and the main telescope could only be formed on the recorder film with rather poor resolving time (0.2 sec.), but an analysis showed that the measured coincidence rate of from 3 to 6 c/min. could be entirely accounted for by accidentals, and the true coincidence rate was therefore a negligible part of either the shower detector or of the telescope rate. The geometry of the shower detector was such as to favor bursts coming up from the lead shield over the bottom counter tray and which would also pass through the telescope. However, the shower detector undoubtedly discriminates against the bursts of fewer particles, as the solid angle subtended by the shower detector at the lead shield is very small. Furthermore, bursts in which only a single particle escaped up through the telescope would in no case be detected as a shower. Considering that the telescope solid angle for bursts is only 1/25 steradian,

[18] R. J. Hulsizer, Phys. Rev. 73, 1252 (1948).
[19] M. Schein, quoted in D. J. X. Montgomery *Cosmic Ray Physics*. See reference 1.
* *Note in proof:*—A recent analysis of 1625 cloud chamber photographs obtained by E. P. Ney at the top of the atmosphere shows that electrons of 1 Bev or over can not constitute more than 0.2 percent of the primary flux at 56° N Geom. Electrons at low latitudes therefore constitute not more than 2 percent of primaries, and can not explain the present discrepancy. (Critchfield, Ney, and Oleksa, Phys. Rev. 79, 402 (1950)).
[20] T. H. Johnson, Rev. Mod. Phys. 10, 193 (1938).

the single particle type might well be most frequently recorded. Better evidence against bursts from the lead shield is the slight increase, rather than decrease in telescope rate with the shield removed at $\lambda=0°$.

Some calculations have been made of the response of the telescope to showers, either of the electron cascade, or multiple-meson type. These calculations predict the probability of registering a shower as a function of the zenith angle and particle density. But since neither the intensity, zenith angle or density distribution of showers is known at the top of the atmosphere, this method of approach is at present unsuccessful.

VI. DISCUSSION AND CONCLUSIONS

The foregoing investigation yields two principal results. The first of these, the number-energy spectrum of primary cosmic rays, is obtained from the vertical flux measurements at various latitudes. The success of this measurement depends on how completely the flux of ionizing particles at about 15 g/cm² matches, in number and direction, the primary flux. The assumption is made that the measured ionizing particles capable of penetrating 3 cm of Pb are largely primaries, and that the remainder of events are proportional to the primary flux. The various measurements can then be satisfactorily represented by the differential number-energy spectrum $N(E)=KE^{-\gamma}$. If the primaries are all assumed to be protons, $K=0.27$ and $\gamma=1.90$. If all α-particles are assumed, $K=0.32$ and $\gamma=1.81$. There is evidence that the true situation is a combination of about 75 $\pm$10 percent of protons and 25$\mp$10 percent of α-particles. If the flux at 15 g/cm² has a constant proportionality to the true primary flux at various energies, then the exponent γ is correct. This condition seems to be not too stringent and the differential number-energy spectrum adopted is $N(E)=0.27E^{-(1.90\pm0.05)}$ over the energy range from 1 to at least 14 Bev. It is evident that the present experiments determine γ much better than they do the constant K. The proton spectrum is adopted because then the various atmospheric effects, which if corrected for would apparently reduce the K-value, may be compensated by the α-particle component, which would increase K. The total incident energy calculated from this spectrum, combined with the high energy spectrum obtained from air showers, is twice that appearing as ionization in an atmospheric column as measured by Millikan, a factor of difference which seems well beyond experimental uncertainties. It is suggested that most of this difference may be due to secondary energy forms which escape the ionization chamber.

The second principal result is obtained by comparing the E–W and latitude effects over the same energy ranges. This can be done independently of the nature of the particles by using Störmer units of energy. In nearly every case the E–W effect is smaller than the latitude effect. It is here suggested that scattering or production of particles upward from below the measuring instrument may account for the differences, and that this effect should be investigated before negative primaries are assumed.

It would be desirable to increase the statistical accuracy of the experiments, but it seems obvious that the possible atmospheric influences are considerably larger than the purely statistical errors. It is regrettable that none of the equipment was recovered for post-flight checks, but a number of other methods of following the behavior of the apparatus indicated that the data presented here have satisfactory reliability. Although the design of the measuring telescope is such as to reduce the effects of air showers and locally produced bursts, the exact influence of these factors is not well-known.

The present investigation appears to contain significant data on the zenith angle effects, and the analysis of these will be given in a later communication.

The authors wish to express their sincere thanks to staff members of the Princeton Naval Ordnance Laboratory and to members of the Princeton faculty, particularly Professors J. A. Wheeler and G. T. Reynolds, for major support of the effort. The successful development of the constant-level plastic balloon by members of the General Mills Aeronautical Research Laboratory made the program feasible. Through the kindness of the ONR and the Chief of Naval Operations arrangements were made for the shipboard operation, and it is a great pleasure to acknowledge the excellent cooperation of the officers and crew of the U.S.S. NORTON SOUND, John Quinn, Captain U.S.N., commanding officer. The construction of special equipment, preparation for flight and modification of the gondolas, and the successful balloon launchings were made possible by the high technical caliber of personnel aboard the NORTON SOUND. The authors were privileged on numerous occasions during the fall of 1949 to discuss the experimental results with Professor M. S. Vallarta of the Institute for Advanced Study, Princeton.

Narrow Air Showers of Cosmic Rays II. Absorption Measurements*

J. P. N. WEI
*Sloane Physics Laboratory, Yale University,** New Haven, Connecticut*
(Received March 6, 1950)

The absorption of narrow air showers in Pb, Fe, and Al has been measured at sea level. Results indicate that there are two components in these narrow air showers, a soft component which consists of electrons and a hard component which consists of μ-mesons. The soft component is practically completely absorbed in four inches of lead, whereas the hard component is not appreciably absorbed in $8\frac{1}{2}$ inches of lead. A wooden roof of only 1 g cm^{-2} produces many local showers, which are nevertheless totally absorbed in a very thin layer of material.

I. INTRODUCTION

IN a previous paper,[1] it was pointed out that the penetrating power of narrow air showers observed at Climax, Colorado, at 3510 meters elevation, was higher than that of extensive air showers. Similar results have been obtained by Alichanian and Shostokovich.[2] A satisfactory interpretation of the nature of the particles in these narrow air showers was not obtained, however, in either investigation. To increase the precision of the measurements, the absorption of narrow air showers has been measured again in the Sloane Physics Laboratory at Yale University, near sea level, with an improved experimental arrangement. The data obtained have much smaller statistical errors than those found previously, and the picture of the nature of particles in narrow air showers is consequently clarified.

II. EXPERIMENTAL ARRANGEMENT

The arrangement of counters and absorbers is shown in Fig. 1. Two groups of counters, A and B, each consisting of five counters in parallel were put at a distance of 30 cm from center to center. Together with another pair of single counters D and E, they were placed above a 2-inch thick pile of lead blocks and were shielded on the sides by 6 inches of lead. The counters were covered with different thicknesses of Al, Fe, or Pb. Two meters from the center of A and B there was a group of ten counters, C, which was not shielded. Cathode followers were built into the counter trays, from which pulses were applied to the coincidence circuits by cables; in trays C, besides the cathode followers, a diode mixer was used to reduce the capacitive load of the counters.

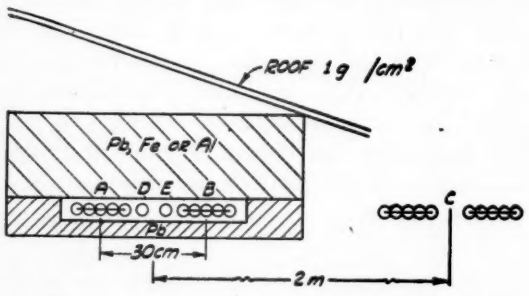

FIG. 1. Arrangement of counters and absorbers.

All counters were of the same dimensions and were filled with an argon-ethyl-ether mixture. They had a starting voltage of about 700 volts and a plateau of about 600 volts. The counters had glass envelopes 0.5 mm thick and an inner diameter of 3.2 cm. The active area of each was 60 cm^2. A thin coating of Aquadag inside the glass wall served as the cathode. The operating voltage used was 1000 volts.

Coincidence circuits were of the conventional Rossi type. The resolving time, τ, of the twofold coincidence circuit AB was measured by equating the rate of accidental coincidences to $2A \cdot B\tau$, from which τ was found to be 1.7 microseconds.

Both counters and circuits were housed in a penthouse built on the roof of the laboratory, at 42 meters above sea level. The penthouse had a thin wooden roof of $\frac{3}{4}$ inch, or about 1 g cm^{-2}.

III. DATA

The experiment consisted in the measurement of the absorption of both narrow and extensive air showers and the effect of the roof in producing local showers.

In the absorption measurement, the coincidence rates AB, ABC, $ABDE$, and $ACDE$ were all recorded simultaneously with different thicknesses of absorbers. A maximum thickness of 9 inches of Al, $8\frac{1}{4}$ inches of Fe, or $8\frac{1}{2}$ inches of Pb was used.

The twofold coincidence AB represented the total shower rate of narrow and extensive showers. Single rates of A and B were measured daily and were used to compute the accidental correction for the AB coincidence rate. No correction for other coincidences was needed, accidentals being negligible.

The difference of the total and the extensive shower rates, AB–ABC, was used as the narrow shower rate, both air showers and local showers. It will be shown that it is easy to eliminate the local showers, leaving only narrow air showers. Note also that this method of taking the difference is essentially an anticoincidence

* Part of a dissertation to be presented to the faculty of the Graduate School of Yale University in candidacy for the degree of Doctor of Philosophy.

** Assisted by the joint program of the ONR and the AEC.

[1] J. Wei and C. G. Montgomery, Phys. Rev. **76**, 1488 (1949).

[2] A. Alichanian and N. Shostokovich, J. Phys. USSR **10**, 518 (1946).

TABLE I. Shower rates under different thicknesses of absorber.

Absorber		Number of coincidences				Total time minutes	Narrow sh. rate, min.$^{-1}$	Ext. sh. rate, min.$^{-1}$	Dense narrow shower rate, min.$^{-1}$
inches	rad. lengths	*AB*	*ABC*	*ABDE*	*ACDE*				
Al 0	0	5350	243	327	58	2750	1.826±0.026	0.088 ±0.006	0.098±0.005
⅜	0.10	4533	308	566	60	4214	0.973±0.015	0.073 ±0.004	0.120±0.005
¾	0.19	39538	2781	5912	596	37492	0.953±0.005	0.074 ±0.001	0.142±0.002
1½	0.39	1594	120	259	31	1392	1.032±0.028	0.086 ±0.008	0.164±0.010
3	0.78	6581	435	1106	102	5316	1.134±0.014	0.082 ±0.004	0.189±0.006
6	1.55	2179	106	392	27	1836	1.101±0.026	0.058 ±0.006	0.199±0.010
9	2.32	12435	588	2519	297	11132	1.042±0.010	0.053 ±0.002	0.200±0.004
Fe ¼	0.35	1733	126	265	20	1440	1.093±0.027	0.088 ±0.008	0.170±0.011
¾	1.04	1450	108	246	33	1134	1.157±0.032	0.095 ±0.009	0.188±0.013
1¼	1.73	5288	304	912	80	4250	1.151±0.017	0.072 ±0.004	0.196±0.007
1¾	2.42	3287	193	628	68	2837	1.070±0.019	0.068 ±0.005	0.197±0.008
2¼	3.11	1720	88	351	30	1605	0.996±0.025	0.055 ±0.006	0.200±0.011
3¼	4.49	2575	117	508	40	2920	0.821±0.017	0.040 ±0.004	0.160±0.007
4¼	5.87	2170	90	483	33	2865	0.706±0.015	0.031 ±0.003	0.157±0.007
5¼	7.25	2780	92	615	34	4330	0.602±0.012	0.021 ±0.002	0.134±0.006
6¼	8.63	6800	217	1640	97	11645	0.547±0.007	0.017 ±0.001	0.133±0.003
8¼	11.4	2894	51	733	20	5363	0.512±0.010	0.010 ±0.001	0.133±0.005
Pb ¼	1.6	2029	119	324	29	1420	1.321±0.031	0.088 ±0.008	0.208±0.012
½	2.8	1775	128	337	44	1455	1.111±0.029	0.088 ±0.008	0.201±0.012
1	5.2	5236	332	1045	116	5305	0.903±0.013	0.063 ±0.004	0.175±0.005
1¼	6.4	7345	415	592		8605	0.780±0.009	0.048 ±0.002	
1½	7.6	5105	291	1177	94	7240	0.685±0.010	0.040 ±0.002	0.150±0.005
2	10.0	2541	95	604	25	4245	0.553±0.012	0.0224±0.002	0.136±0.006
2½	12.5	5308	163	1303		10121	0.487±0.007	0.0163±0.001	
3	14.8	5417	112	1342	42	11170	0.457±0.006	0.0100±0.001	0.116±0.003
4	19.7	5666	63	1502	63	12972	0.415±0.006	0.0040±0.0005	0.111±0.003
5	24.5	2552	11	704	3	5740	0.425±0.009	0.0019±0.0006	0.122±0.004
6½	31.7	2620	11	681	6	6005	0.418±0.008	0.0018±0.0006	0.112±0.004
8½	41.4	4206	10	1092	9	9762	0.412±0.006	0.0010±0.0003	0.111±0.004

method; although it needs more circuits, it gives more information than the conventional method.

All data concerning the rates of narrow air showers under different thicknesses of absorbers are given in Table I. The thickness of lead in radiation lengths given in this table includes also a ¼-inch iron plate on which the weight of the lead blocks was supported. Errors given are standard deviations.

The fourfold coincidences *ABDE* and *ACDE* are also included in the same table. Their difference gives the rate of dense narrow showers which will be of use in later discussions. Note that four rays are needed for either coincidence. In fact, only showers containing many more than four rays were recorded because the areas of both *D* and *E* were much smaller than *A* or *B*.

The absorption of narrow showers under small thicknesses of iron was measured both inside the penthouse and outside, on top of the roof in open air. The data obtained are given in Tables II and III.

IV. RESULTS AND DISCUSSION

The results on the absorption of narrow air showers are plotted in Fig. 2. The abscissa is the thickness of the absorber in radiation lengths. The maximum thickness of lead, iron, and aluminum is about the same in inches, but very different in radiation lengths.

Beyond 20 radiation lengths of lead, the absorption curve is a horizontal line. This indicates the existence of a hard component which is not appreciably absorbed by many inches of lead. This component probably consists of μ-mesons because of this great penetrating power.

For less than 20 radiation lengths of lead, the absorption curve shows the existence of less penetrating particles. The amount of iron used is just about enough to absorb most of this component. If it be assumed that the absorption curve of iron will eventually coincide with the absorption curve of narrow showers in lead when more iron absorbers are used, the same value of the hard component of narrow air showers can be subtracted from both the lead and iron curves in the region of less than 20 radiation lengths and the two absorption curves thus obtained will be the absorption curves for the soft component alone. This procedure implies that the penetrating component of narrow air showers is present in the air and not produced in the absorber. They are plotted in Fig. 3. The amount of aluminum used is not sufficient to allow such a treatment of the observations. However, it does show that the same type of absorption curve may be obtained.

For comparison the absorption curve of extensive air showers in lead is plotted in the same graph. On a semilogarithmic plot, all three are straight lines in the range discussed, and all have the same slope. This indicates that the soft component of narrow air showers must consist of the same kind of particles as in extensive air showers, namely electrons. Furthermore, this

TABLE II. Narrow showers under thin thicknesses of absorber inside penthouse.

Absorber (g/cm^2)	Narrow ($min.^{-1}$)	Extensive ($min.^{-1}$)	Dense narrow ($min.^{-1}$)
0	1.876±0.044	0.088±0.009	0.103±0.010
0.62	1.295±0.033	0.087±0.008	0.133±0.010
1.24	1.152±0.027	0.082±0.008	0.140±0.009
1.86	1.094±0.033	0.095±0.010	0.159±0.012
2.48	1.067±0.017	0.079±0.004	0.154±0.006
3.72	1.122±0.020	0.089±0.006	0.159±0.007
4.96	1.185±0.031	0.096±0.007	0.162±0.009

TABLE III. Narrow showers under thin thicknesses of absorber in open air.

Absorber (g/cm^2)	Narrow ($min.^{-1}$)	Extensive ($min.^{-1}$)
0	1.132±0.029	0.067±0.007
0.7	1.088±0.028	0.078±0.008
1.34	1.099±0.028	0.089±0.008
1.96	1.051±0.026	0.057±0.006
2.58	1.097±0.028	0.082±0.007
5.68	1.324±0.031	0.098±0.008

also shows that this soft component loses energy by radiation, which is a strong evidence of electrons.

In Fig. 2 points from the absorption of narrow air showers taken at Climax are also plotted. Comparison of these two experiments is difficult since both the arrangements of counters and the precision of points obtained are different.

For very small thicknesses of absorbers, a sharp decrease in shower rates is observed. This is attributed to the recording of local showers produced in the roof above. Almost half the showers recorded are locally produced when there is no absorber used. Fortunately these local showers are so soft that they do not penetrate any considerable thickness of the absorbers used. Therefore the result of our experiment is not interfered with because of the existence of such local showers, although the number is large.

This point is clarified by comparing also the absorption of narrow showers inside and outside the penthouse. Data are given in Tables II and III and in Fig. 4. Curve *I* is actually the beginning part of the curves in Fig. 2 with more points and on a different scale. The narrow-shower rate decreases to a minimum at about 2 g cm^{-2} and rises again for larger thicknesses of absorber. In open air (Curve *II*) the shower rate at zero thickness is about the same as that at 2 g cm^{-2}. The higher value at zero absorber thickness inside the penthouse is interpreted as the result of local showers.

Since the values of the shower rate inside and outside are the same at 2 g cm^{-2}, local showers produced in the roof must be practically all absorbed in about that thickness of iron. That corresponds to the penetration of electrons of several Mev of energy. The flat part of the absorption curve from zero to 2 g cm^{-2} in open air shows that there are also some very soft narrow air showers. These might have been produced in the same manner in air as are the local showers in the roof.

Local showers are produced in the roof probably either by the pair production of photons in the roof, or by knock-on electrons. Because there is a minimum in the absorption of photons in air[3] at some tens of Mev, a great number of photons in that energy range must exist at sea level. The roof shifts the minimum towards the lower energy side and thus pairs are produced. Because of the large number of photons in that energy range, there is a considerable number of pairs produced in spite of the low probability of pair production in such a thin roof.

These local showers could also be mesons accompanied by their knock-on electrons. Since the number of knock-ons decreases rapidly with energy[4] most of them are readily absorbed by thin layers of material.

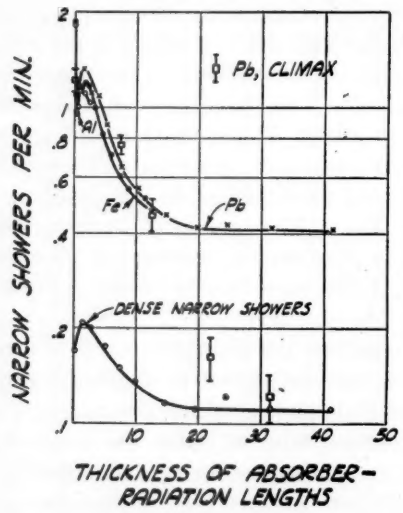

FIG. 2. Absorption of narrow showers at sea level.

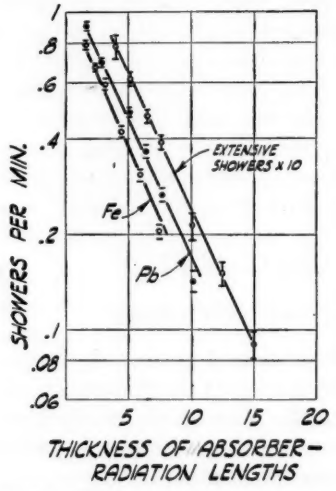

FIG. 3. Absorption of the soft component of narrow air showers.

[3] B. Rossi and K. Greisen, Rev. Mod. Phys. **13**, 263 (1941).
[4] H. J. Bhabha, Proc. Roy. Soc. **A164**, 257 (1938); F. L. Hereford, Phys. Rev. **75**, 923 (1949).

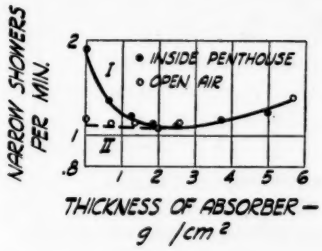

FIG. 4. Absorption of narrow showers under small thicknesses of absorbers.

Data on the number of dense narrow air showers will also support this interpretation. The fact that the absorption curve of showers recorded by *ABDE–ACDE* is parallel to that of the total narrow air showers shows that the former is a part of the narrow air showers recorded by *AB–ABC*. About one-fourth of the total number of narrow air showers are dense ones. At small absorber thicknesses, with the counters inside the penthouse, the dense narrow shower rate decreases continually with the decrease of absorber down to zero thickness. The absence of an increase near zero thickness shows that there is no appreciable number of local showers with four rays or more to produce an *ABDE* coincidence. This agrees with the assumption that they are pairs.

The fact that *ABDE* is much smaller than *AB* proves that the latter is not due to the counting of horizontal single rays, because if it were, *AB* and *ABDE* should be equal. Also, counters are shielded from the sides with 6 inches of lead at all times; the fact that *ABDE* varies with absorbers at top also indicates that the particles do not come through the sides. Furthermore, a test was made by putting one counter directly over *D* just out of line of the rest of the counters. The result obtained indicates that if there were any single rays counted as narrow showers, the number must be smaller than 3 percent of the total shower counts.

The absorption of extensive air showers has been widely studied. The discrepancies among the results of different authors have been pointed out by Auger *et al.*[5]

[5] Auger, Daudin, Freon, and Maze, Comptes Rendus **228**, 178 (1949).

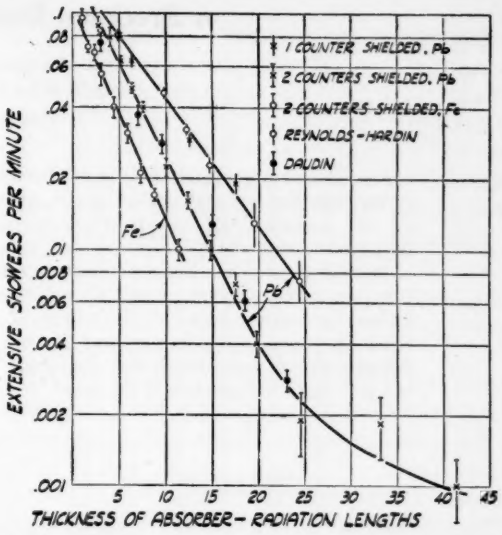

FIG. 5. Absorption of extensive air showers in Pb and Fe.

as being a result of the use of different numbers of counters shielded in lead. They found that results obtained by different authors with the same number of shielded counter trays agreed very well. This is shown also in Fig. 5 by the comparison of data obtained here with those obtained by Reynolds and Hardin[6] for one shielded counter, and that obtained by Daudin[7] for two shielded counters. The absorption curve of extensive air showers in iron is also given in Fig. 5. It is parallel to the lead curve having the same mean free path of 5 radiation lengths. The hard component of extensive air showers is shown by the bend at large thicknesses.

In conclusion the author wishes to express his gratitude to Professor C. G. Montgomery for his continuing interest and guidance throughout the course of these experiments.

[6] G. T. Reynolds and W. D. Hardin, Phys. Rev. **74**, 1549 (1948).

[7] J. Daudin, Cosmic Radiation (Interscience Publishers, Inc., New York, 1949), p. 165.

A Precision Evaluation of h/e by X-Rays

J. A. BEARDEN AND GUENTER SCHWARZ*
Johns Hopkins University, Baltimore, Maryland

(Received March 13, 1950)

Precision x-ray measurements of h/e have been made at potentials from 8000 to 19000 volts. A double crystal spectrometer with perfect calcite crystals was used as the monochromator. The window width was 0.7 volt. A unipotential cathode was developed and the use of this with the narrow monochromator window gave isochromats which broke very sharply at the high frequency limit. Isochromats were recorded with both tungsten and oxide cathodes which experimentally indicated the necessity for making the work function correction to the applied voltage. No evidence was found to support the previously reported effects due to surface films on the target or gas pressure in the x-ray tube. Targets of Au, W, Ta, Mo, Ni, and Cu were used. The pronounced structure near the high frequency limit appears to be much the same for all targets, differing only in some details and magnitude. The value found for h/e is $1.37938 \pm 0.00008 \times 10^{-17}$ erg·sec.·e.s.u.$^{-1}$ and is independent of the target or voltage used.

I. INTRODUCTION

THE excellent studies on the natural constants made by Birge beginning with his review article[1] in 1929 have served not only to supply physicists with a self-consistent set of constants, but of equal importance has been the highlighting of a series of "discrepancies" which his work revealed. Notable among these have been the e and e/m, and more recently the h/e, discrepancies. The latter discrepancy stimulated the present experimental work on a new precision evaluation of h/e from the high frequency limit of the continuous x-ray spectrum.

For a direct measurement of h/e we have several methods available: (1) The measurement of the high frequency limit of the continuous x-ray spectrum; (2) The measurement of the excitation voltages of x-ray lines compared to the corresponding absorption edges; (3) The determination of the ionization and excitation potentials; (4) The photoelectric effect; (5) The measurement of the radiation constant. To date the first method stands out over all the others in attainable precision. However, it is possible that careful experiments and theoretical analysis of the absorption limits might make the second method comparable in precision to the first. In the present work, a few measurements[2] by the second method have been made, but the most conclusive results have been obtained through a series of measurements on the high frequency limit.

In devising a precision experiment on the high frequency limit, the spectral region in the neighborhood of 1.25A to 1.5A has been chosen for most of the present work which corresponds to a potential range of 8000 to 10,000 volts. The advantages of this spectral region are: (1) A double crystal spectrometer of high resolving power and a precisely divided circle can be employed in air; (2) A Geiger counter of high efficiency and low background can be used for measuring the low x-ray intensities observed near the high frequency limit; (3) The potentials can be measured directly with high precision resistance standards; (4) An x-ray tube has been developed for this voltage range with unipotential indirectly heated cathodes; (5) Potentials applied to the x-ray tube and the current through the tube can be highly stabilized (one part in 30,000 to 50,000).

II. EXPERIMENTAL ARRANGEMENTS

(1) The X-ray Tube

The main features of the x-ray tube are shown in Fig. 1. Use has been made of the method whereby gases from the Neoprene gaskets must diffuse a considerable distance between carefully machined surfaces before reaching the high vacuum. The base and body of the tube are made of copper and the flanges which hold the gaskets are of brass. The body and target are water-cooled. The body of the tube can be rotated about a vertical axis so that x-rays can emerge from the small window W at any desired angle with respect to the first crystal of the spectrometer. Two target assemblies have been used: (1) The axis on which the water-cooled target rotates, passes through its surface such that the angle of the emitted x-rays with respect to the target surface can be varied; (2) A four-sided target was designed such that different targets could be employed by rotating the target support by 90°.

The cathode structure was mounted on a glass insulator. In addition to the usual 5-volt, 4-ampere spiral tungsten filament cathode, we developed an indirectly heated oxide cathode. Details of the latter are shown in Fig. 2. Focusing of the electron beam is accomplished by properly locating the oxide surface in the cathode and by adjusting the cathode-target distance. The forming of the oxide cathode surface is a slow process, but once accomplished the life has been found to be 100 or more hours. After the cathode has been properly formed the x-ray tube may be opened to air for short intervals without seriously affecting the cathode emission.

The main difficulty encountered in operating the oxide cathode was in controlling the emission. This was

* Now at Florida State University, Tallahassee, Florida.
[1] R. T. Birge, Rev. Mod. Phys. 1, 1 (1929).
[2] J. A. Bearden and G. Schwarz, Phys. Rev. 59, 934 (1941).

finally accomplished by heating the cathode (back surface) with electron bombardment and controlling the bombarding voltage with a voltage regulator actuated by the current flowing through the x-ray tube. When the regulator was used to control the bombarding current the heating inertia of the filament was too great and "hunting" occurred.

The x-ray tube is exhausted by a three-stage oil fractionating pump backed by a high speed mechanical fore pump. The pressure is measured near the base of the x-ray tube with an ionization gauge. The normal pressure in the x-ray tube when operating at a load of 500 watts was better than 10^{-6} mm and was about 2×10^{-7} mm when the tube was not operating. When tungsten filament cathodes are used the evaporated tungsten gradually forms a visible film over the surface of the target. In the case of the oxide cathode, no visible film was observed.

(2) The X-ray Power Supply

The essential requirement of the high voltage supply is stability and freedom from ripple. In the first measurements[2] a 500-cycle power source was used with a conventional capacity inductance filter. This supply was partially satisfactory but required continuous adjustment by the operator and even then changes of one or two volts frequently occurred during the measurement of the intensity at a selected voltage. A block diagram of the final high voltage power supply is shown in Fig. 3. Two high voltage systems of this type have been constructed. The one used for most of the present work was designed for a maximum of 12,000 volts and 50 ma, the second operates at the same current, but at voltages up to 100,000 volts. Tests on both supplies show excellent regulation. A 10 percent change in input a.c. voltage changes the 12,000-volt d.c. output by less than one volt. The 100,000-volt supply has an equally good percentage performance. The output impedance in each case is approximately 25 ohms.

The ripple voltage was determined by measuring the drop across a 100,000-ohm non-inductive resistance which was connected between ground and a large (0.4 mf) high voltage condenser which was connected to the high voltage. Both an oscilloscope and a peak-reading vacuum tube voltmeter were used to measure the ripple voltage. The measured ripple on the 12,000-volt supply was less than 70 millivolts r.m.s. and on the 100,000-volt supply it was less than 175 millivolts. In both cases the measurements were made at full operating loads.

When a tungsten filament was used as a source of electrons insulated heavy duty storage batteries were used as the source of power. The x-ray tube current was then controlled manually by a resistor which was in series with the batteries and filament. The voltage drop across the filament must be taken into account in determining the high voltage through which the x-ray tube electrons are accelerated. Isochromats were obtained with the high voltage connected in turn to each end of the filament. It was found that the cut-off point of the isochromat in the two cases differed by almost exactly the voltage applied to the filament. This indicates that the IR drop through the filament leads and filament is confined almost entirely to the thermionic emitting region of the filament. The great majority of the electrons emitted do not produce x-rays within a volt of the high frequency limit and hence the isochromat observed does not show a sharp discontinuity at the quantum limit.

In order to eliminate the part of the indefiniteness of the isochromat which is due to the spread in energy of the electrons, a unipotential cathode of the oxide type described above was developed. The cut-off points of the isochromats obtained with this cathode were much more clearly defined and the structures observed above the limit were more pronounced than when the tungsten filament was employed. The oxide cathode operated very satisfactorily for voltages less than 10,000 and while we were able to get a few measurements with it at 20,000 volts, the operation was not comparable to the lower voltages.

(3) Voltage Measurement

The principle used for measuring the high voltage applied to the x-ray tube is shown in Fig. 3. In a number of measurements we used a modification of the above method. The principal advantage of this method over that normally used is that possible errors in the Type K Leeds and Northrup potentiometer are greatly reduced by selecting a value for the high voltage such that the

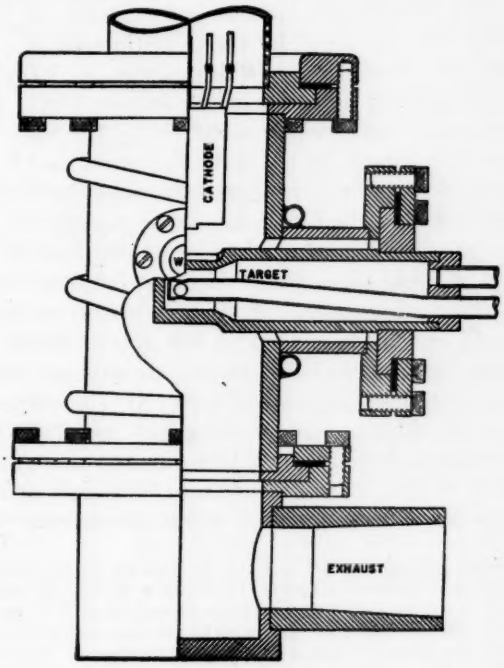

FIG. 1. X-ray tube

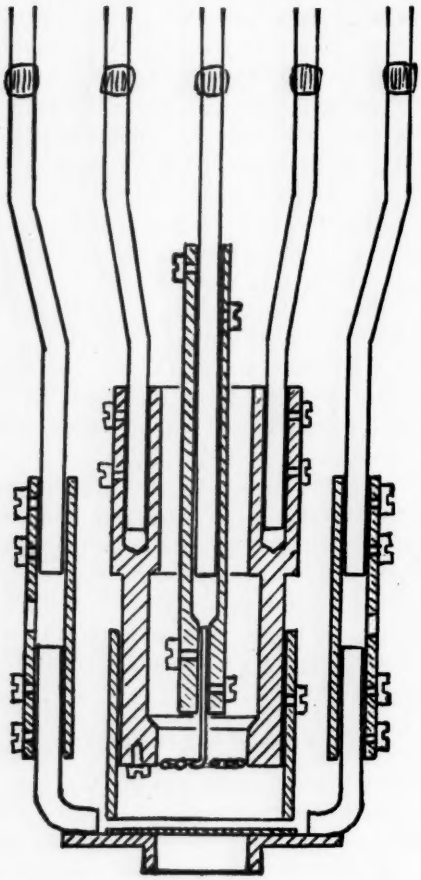

FIG. 2. Indirectly heated oxide cathode.

IR drop across the 100-ohm standard in Fig. 3 is almost balanced by the potential of a second standard cell. The potential then measured by the potentiometer is only the difference between the *IR* drop across the 100-ohm standard and the potential of the standard cell. The potentiometer was carefully calibrated by the National Bureau of Standards for the particular ratios used in all experiments. As a further precaution the potentiometer was rechecked at the conclusion of the experiment.

Two one-megohm manganin wire standards made by Otto Wolf were made available to us for this work.[3] Each standard was made of 40 coils wound on tubes about 15 mm in diameter and 100 mm in length. A constant temperature oil bath was constructed which forced oil through and around each coil. The temperature of the oil was maintained within $\pm 0.01°C$. The two megohm standards have been checked as shown in Table I, by the National Bureau of Standards and no changes have been observed which are greater than normal for high resistance standards. The temperature coefficient of both standards is slightly negative at the temperature used. Three 100-ohm Leeds and Northrup precision resistance standards were periodically intercompared and one was calibrated twice, as shown in Table I.

Through the cooperation of Dr. G. W. Vinal of the National Bureau of Standards we had available three of their standard cells of the saturated type. The calibration is shown in Table I. The cells were kept in the constant temperature oil bath and periodic intercomparisons were made of their voltages. Over a period of eight years no change of more than 10^{-5} volt has been observed in the voltage of any cell.

Each coil of the megohm standard dissipates 2.5 watts when operating at full voltage. Even though rapid circulation of oil was maintained in and around the coils, the insulated manganin wire was at some temperature above that of the oil. Two experiments were undertaken to measure the effect of this heating. In the first experiment the Bureau of Standards used the high powered resistance standards from their high voltage laboratory in order to test the resistance of the Wolf standard under low and high load conditions. The high voltage standards are capable of dissipating large amounts of power without appreciable heating. A bridge circuit was formed using these resistances together with the Wolf standard as the unknown. The latter was operated in the same circulating constant temperature oil bath as was used in the x-ray measurements. A balance was first obtained with 1000 volts on the bridge. Under this condition the coils of the Wolf standard were dissipating only 0.025 watt which should produce a negligible heating of the manganin wire. 10,000 volts were then applied to the bridge and the change in resistance observed was assumed to be due to the heating of the manganin wire. The results were somewhat erratic and the two Wolf standards gave slightly different results. The change in resistance appeared to be about 30 parts in 10^6 for standard 4564 and 15 parts in 10^6 for standard 1427. These values represented just about the limit of accuracy of the measurements.

The second method of measuring the change in resistance with load was made in our own laboratory in which use was made of the 10^5-ohm subdivisions of the Wolf standards. A bridge was formed in which a 10^5-ohm subdivision of one Wolf standard was compared to the entire 10^6-ohm resistance of the other. A balance was first obtained with 100 volts on the bridge and the change in resistance measured when the voltage was increased to 1000 volts. Under the latter condition, a 10^5-ohm section has the same load as in normal use with 10,000 volts on the 10 sections in series. Each 10^5-ohm section was compared in turn and the sum of the corrections amounted to -11 ohms in the total resistances, for standard 4564 and -4 ohms for standard

[3] We are greatly indebted to Dr. J. L. Thomas for his splendid cooperation in loaning us standard resistances and for his special interest in calibrating these standards as well as calibrating the Type K potentiometer. We also wish to express our appreciation of Professor Wheeler Loomis and the Department of Physics of the University of Illinois for the loan of one of the Otto Wolf resistance standards.

1427. The latter measurements are accurate to ±3 ohms. From the two experiments it seems safe to conclude that no change in resistance occurred greater than one part in 10^5 when the standards were used at full load.

The voltage divider measures the x-ray cathode to ground voltage. The x-ray target, however, is grounded through a milliammeter and over current relay and the resistance across which is developed the voltages for the operation of the current and voltage stabilizers. These resistances have been carefully measured and in addition the voltage drop has been measured with a precision vacuum tube voltmeter while isochromats were being recorded. However, in most of the isochromats the voltage correction was obtained by computing the voltage drop from the x-ray tube current and the resistance between cathode and ground.

(4) Monochrometer

The spectrometer used was a high precision double crystal instrument built by the Société Genevoise. The spectrometer was altered such that the first crystal is mounted on a horizontal slide midway between the focal spot of the x-ray tube and the second crystal. The second crystal is accordingly located on the axis of rotation of the high precision divided circle. The diffraction angles of the second crystal are read on the divided circle by four microscopes. The circle has been carefully calibrated by the four microscopes 90° method and the excellence of the circle is indicated by the fact that over the greater part of the circle corrections are less than 0.3 sec. In the wave-length region employed in the present measurements this corresponds to less than 0.1 volt in the position of the isochromats. The measured crystal angles at room temperature were corrected to 18°C by the relation

$$d\theta'' = 2.18(t° - 18°\text{C}) \tan\theta.$$

The sharpness of the isochromat cut-off in the experiments where the oxide cathode was employed is primarily dependent upon the resolving power of the monochrometer. The low x-ray intensity near the quantum limit has forced most previous experimenters to use monochrometers of very low resolving power. Geiger counters have been perfected for recording x-ray intensities to such an extent that theoretically perfect calcites can now be used in the (1+1) position and still give measurable intensities within one volt of the quantum limit. The resolving power may be computed from the relation $\lambda/d\lambda = \lambda D/w$ where D is the dispersion and w is the full width at half-maximum in radians of the (1–1) rocking curve. The calcite crystals used were the same as those used in previous experiments reported many years ago. The crystals have been rechecked at 1.54A and the (1–1) width was 10.0 sec. or 4.85×10^{-5} radian and D is equal to 0.34 which gives 10,800 as the resolving power. The full energy width of the monochrometer "window" at half-maximum intensity is 0.7 volt. The effect of the window on the sharpness of the limit of the isochromats is thus negligible.

The first 4 or 5 volts of an isochromat essentially determines the quantum threshold. Within this range, and under the conditions of the present experiment, the number of quanta diffracted by the calcite crystals is of the order of 10 to 15 quanta per second. In an ionization chamber the radioactive contamination and the cosmic-ray background would make the observation of this number of x-ray photons practically impossible. On the other hand, the background of a properly shielded Geiger counter can be reduced to less than 0.5 count per second. The principal difficulty with Geiger counters is their low absorption of x-rays and this has been overcome by the use of argon and krypton at high pressure. Counters filled with argon to 70 cm pressure and krypton counters filled to 30 cm pressure, plus quenching gases of methylene bromide or halogene mixtures have proved satisfactory. The argon counters absorb about 80 percent of the radiation of the 1.54A range and the krypton counters absorb about 50 percent of the radiation, at 0.6A. The efficiency of these counters makes it possible to record intensities very near the quantum limit. The body of the counters is of stainless steel with a mica window and metal-to-glass insulating seal. Eight inches of lead and iron were placed over the counters to reduce the cosmic-ray background. A scaling circuit arranged to measure the time for a fixed number of counts was used for recording the intensities.

III. CORRECTIONS AND AUXILIARY CONSTANTS

(1) Work Function Correction

DuMond[4] and his co-workers have pointed out the necessity for correcting the measured voltage applied to the x-ray tube by adding the work function of the cathode which supplies the electrons. Ohlin,[5] on the

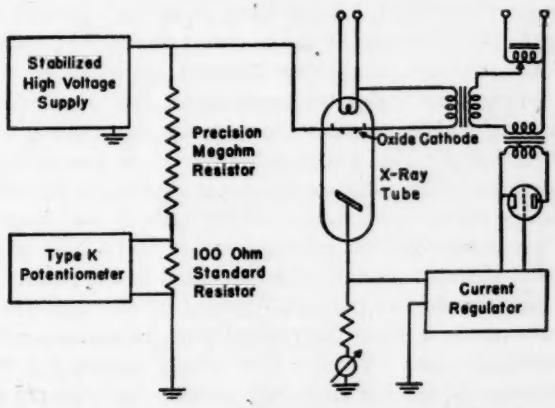

FIG. 3. Source of x-rays and measurement of applied voltage.

[4] J. W. M. DuMond and V. L. Bollman, Phys. Rev. **51**, 412 (1937). Panofsky, Green, and DuMond, Phys. Rev. **62**, 224 (1942).
[5] P. Ohlin, Inaugural Dissertation, Uppsala (1941); Arkiv. f. Mat. Astr. o. Fys. **27B**, No. 10; **29A**, No. 3; **29B**, No. 4; **31A**, No. 9; **33A**, No. 23.

TABLE I. Calibration of resistance and voltage standards by the National Bureau of Standards.

Resistances			
Standard no.	Date	Temp.	Resistance absolute ohms
1427	2/41	22.0°C	1,000,715
1427	2/41	23.8	1,000,726
1427	7/48	23.6	1,000,759
1427	5/49	26.0	1,000,736
4564	2/48	25.0	1,001,110
4564	7/48	24.6	1,001,111
4564	5/49	26.0	1,001,085
649482	5/47	25.0	100.0500
649482	4/49	25.0	100.0507

Standard cells			
Cell no.	Acidity	Ab. volts 20°C	Ab. volts 28°C
968	0.04*N*	1.018614	1.018241
970	0.04*N*	1.018612	1.018239
987	0.04*N*	1.018601	1.018227

other hand, has not corrected his measurements for this effect primarily because his resulting values of h/e at voltages from 2983.3 to 4651.6 volts are more consistent if the work function correction is not made. Furthermore, he has used a BaO-coated platinum cathode in which the work function should be materially different from that of tungsten and the value of h/e observed agrees with his other results if the work function correction is not made. Thus, from two types of measurements he concludes that the energy gained by the electrons in passing through the cathode barrier does not exhibit itself in the position of the high frequency limit of the continuous spectrum. DuMond and Cohen[6] have corrected Ohlin's values for the work function and the resulting values of h/e are spread from 1.3798 to 1.3810×10^{-17} which are much higher than any previous experimental results and also considerably higher than the least squares adjusted value[6] of h/e.

In spite of Ohlin's[5] experimental results (which are not confirmed by the present experiments) the writers are convinced that it is necessary to apply a correction for the energy gained by the electrons due to the heating of the cathode. A slightly different approach to the problem may help to understand the theoretical analysis[4] which indicates the necessity for making the correction. In Fig. 4, the potential, V, of the battery measured by the voltage divider is applied to the conduction levels (dashed lines) of the cathode and target. If we assume the cathode and target to be infinite in extent then the electric field F is equal to the potential V plus the contact potential divided by the separation of the plates, d. Electrons emerge from the cathode with practically zero velocity. The energy gained by the electrons in passing from just outside the cathode to the outside of the target surface is FXd. However, those electrons that reach the conduction band (indicated by dotted line) of the target without a collision gain an additional energy equal to the work function of the target W_t. The maximum energy an electron can attain then is $E_{max}=[(V+\text{contact potential})/d]\times d+W_t$. The contact potential is the difference in work function of the cathode and target or $E_{max}=V+(W_c-W_t)+W_t=V+W_c$ which is exactly the result obtained by the more elaborate argument presented by DuMond.[4] The same result can be arrived at with a thermodynamical cyclic process. If we take as reference point the top of the conduction band of the target, one sees that the maximum energy gained by an electron in a complete cycle is the potential V plus the energy gained by the electron in escaping from a cathode, which again confirms the previous conclusions that the energy added to the electron by cathode heating becomes available for the excitation of the high frequency limit. In addition to the theoretical arguments, it will be shown later that the present experiments with tungsten and with oxide coated cathodes will give inconsistent values of h/e unless proper corrections are made for the work functions.

(2) Isochromats with Target at High Temperature

In many experiments involving electrons and metal surfaces it has been noted that appreciable charges exist even on surfaces newly formed in vacuum. It is conceivable that such surface charges could affect the values of h/e computed from the high frequency limit. These surface effects should disappear at high temperature. A tungsten target with a long heat conduction path to the water-cooled target support was developed such that with normal input power the temperature of the target was raised to about 1600°K. Isochromats, Fig. 5, were taken with the hot target at 10,180 volts and compared to those taken at the same voltage with a water-cooled target. A shift of less than one volt in the location of the isochromat could have been detected and within this experimental error no shift was observed.

(3) Effect of Surface Films on the Target

In the early experiments,[2] where the pumping speed was inferior to the present system, the target accumulated a visible film of carbon and tungsten in a few hours' operation similar to that noted by DuMond[4] and his co-workers. In order to test for the effect of this film, a piece of molybdenum, to which a small piece of iron was spotwelded, was used as a cover over the target during the initial evacuation and early operation of the x-ray tube. The voltage was then adjusted such that a critical point on the initial rise of the isochromat could be observed. The molybdenum cover was removed by a magnet and the intensity of this point quickly observed. Continued measurements were made on the isochromat until an opaque film formed on the target. The structure in the vicinity of the high frequency limit

[6] J. W. M. DuMond and E. R. Cohen, Rev. Mod. Phys. 20, 82 (1948).

changed as the film formed but the position of the high frequency limit remained unchanged.

Panofsky, Green, and DuMond[4] observed a displacement of 90 volts or 0.9 percent between the positions of the isochromats with and without a carbon layer. In view of the fact that DuMond and Cohen[6] suggest that Ohlin's[5] experimental results may have been influenced by target films, it is worth while to examine these observations in more detail.

DuMond[7] has pointed out that an error of 10^3 made in computing the retardation of primary electrons into targets completely invalidated his theory for the fine structure which is observed near the high frequency limit. The same error invalidates the assumed thickness of target films in Ohlin's experiments. Films of only a few molecules in thickness are required to retard the primary electrons and if the primary electron in either Panofsky, Green, and DuMond, or Ohlin's experiments were retarded by carbon layers, then pronounced diffuseness of the foot of the isochromats should have been observed. A large part of the retardation of high velocity electrons in solids is due to very distant electronic encounters. A reasonable value for the loss per encounter is about 10 electron volts. Therefore, it would require about 9 encounters on the average to lose the 90 volts observed by Panofsky, Green, and DuMond.[4] With as many as 9 collisions on the average a few electrons should still reach the underlying target metal with undiminished energy. Therefore the isochromats observed with the carbon layer should have started with a very low intensity at the same point as the isochromats without the carbon deposit and the intensity should have gradually increased in accordance with the distribution losses suffered by the impinging high speed electrons. The fact that no such smearing was observed suggests that the effect observed was due to some other experimental cause.

In the case of Ohlin's[5] experiments the films would need to be only a very few molecules thick and the primary electrons should experience retardations due to probably one encounter. The effect of this would be a displacement of an isochromat of low intensity leaving the main isochromat undisplaced and sharp. The sharpness of Ohlin's isochromats and those of the present experiments indicate that target films normally encountered do not shift the position of the observed isochromats.

(4) h/e as a Function of Gas Pressure in the X-Ray Tube

Ohlin[5] has emphasized that the value of h/e increases as the vacuum in the x-ray tube is improved. In the wave-length range from 2.5A to 4.1A he obtained a value of h/e at pressures of the order of 10^{-4} mm of mercury, which was about 0.1 percent smaller than when the vacuum was maintained at better than 10^{-5} mm of mercury.

In some of our earlier experiments[2] a glass body x-ray tube was used which was evacuated by a moderate speed pumping system. In these experiments a deliberate attempt was made to observe a change in the position of the high frequency limit when the pressure in the tube was such that (estimated to be about 2 to 3×10^{-4} mm) it was barely possible to prevent a gas discharge in the tube. We were unable to observe any shift in the position of the isochromat which could be attributed to the gas pressure in the tube. Instability in operation made it impossible to make precision measurements under these conditions but we believe any changes of the order of magnitude of those reported by Ohlin would have been observed.

It has been suggested that Ohlin's observations may have arisen through scattering by the residual gas in the slit in front of the Geiger counter. An estimate of the expected scattering is so small that the present writers believe this explanation unlikely. The effect is more likely due to a shift in the position of the focal spot of the x-ray tube or some other instrumental difficulty.

(5) Auxiliary Constants Used in Computing h/e

If V represents the total voltage (applied potential plus work function) through which an electron falls, and ν the frequency of the quantum limit, then $Ve=h\nu$. Or, in terms of the wave-length $h/e=\nu\lambda/c$. Details of the proper procedure for precisely relating V and λ will be discussed in the section on computations of h/e. The velocity of light, $c=(2.99776\pm0.00004)\times10^{10}$ cm/sec.

The wave-length λ depends directly on the ruled grating measurement of x-ray wave-lengths. From the excellent agreement in the independent measurements of Becklin, Sodermann, and Bearden[8] the wave-lengths appeared to be known within one or two parts in 10^5. More recent measurements by Tyren[9] however, differ from the average of the above by about 4 parts in 10^5. Crystallographers have decided to give some weight to Tyren's work by lowering the previously accepted ratio of λ_g/λ_s by one part in 10^5. However, Birge,[10] and more recently, DuMond and Cohen[6] have retained $\lambda_g/\lambda_s=1.00203$ and we have used this value in computing our present values of h/e.

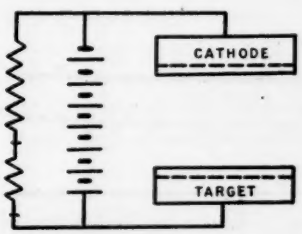

FIG. 4. Work function correction.

[7] J. W. M. DuMond, Phys. Rev. 74, 1883 (1948).

[8] J. A. Bearden, J. App. Phys. 12, 395 (1941).
[9] F. Tyren, Inaugural Dissertation, Uppsala (1940).
[10] R. T. Birge, Am. J. Phys. 13. 63 (1945).

The applied voltage must be corrected by the addition of the work function of the cathode. In the case of tungsten, we have used 4.52 volts. The work function of oxide cathodes[11] depends on the supporting metal and on the process used for activating the cathode. The values of the work function vary from about 0.8 to 1.5 volts. We have assumed an average value of 1.2 volts as applicable to the present measurements. It will be noted in Fig. 6, that if this correction were not made then the resulting isochromats taken with different cathodes would not agree. This correction introduces a greater uncertainty in our final results than all other factors combined. A new experiment is in progress in which we hope to eliminate the major part of this uncertainty.

ISOCHROMATS AND COMPUTATIONS OF h/e

(1) Recording of Isochromats

The x-ray intensity transmitted by the monochrometer was recorded as a function of the voltage applied to the x-ray tube (isochromat method). The number of counts recorded for each point on the isochromat was selected such that a curve could be completed in from one to two hours. The statistical fluctuation of the points on a single curve made it impossible to compute a precise value of h/e from such an isochromat. A large number of isochromats were recorded under identical operating conditions. The intensities for each voltage setting were averaged and the average isochromat plotted as in Figs. 6–8. Most isochromats have been recorded at voltages lower and higher than those plotted. The number of runs averaged varied from 8 to 24. In this method of averaging it is essential that the x-ray tube current, the temperature of the crystals, standard cells, and resistances remain constant. These factors were so well controlled that curves taken many days apart could be averaged without difficulty.

In order to make it possible to compare isochromats taken with different targets and with different voltages, we have computed the voltage in each case which corresponds to a value of h/e equal to 1.3792×10^{-17}. This voltage is plotted as zero in Figs. 6–8, and the observed x-ray intensities of the isochromats have been plotted as functions of the incremental x-ray voltage.

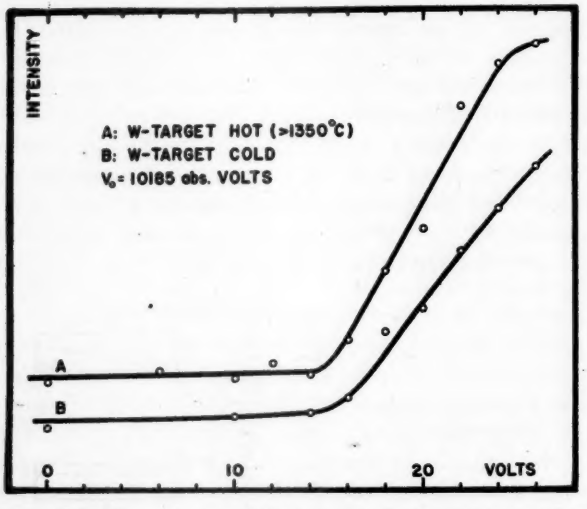

FIG. 5. Isochromats recorded at near room temperature and at 1350°C. The monochromator selected the same wave-length in each case.

[11] Jacobs, Hees, and Crossley, Proc. I.R.E. **36**, 1109 (1948).

(2) Fine Structure in the Isochromats

In our early experiments[2] in 1941–42 structure was observed in the isochromats similar to that shown in Figs. 6–8. Accumulation of surface film on the target usually caused the structure to vanish after a few hours operation, but as emphasized above the location of the high frequency limit was not altered. In the present work where high pumping speeds have been employed deposits and cathode evaporation have been so small that the structure remains pronounced after many hours' operation of the x-ray tube. Furthermore, in every case where we have repeated experiments after replacing cathode and targets, the details of the structure repeat within experimental error.

In all curves in Figs. 6–8, except the one for copper there appears a first peak in the isochromat at from 6 to 9 volts from the high frequency limit. A second peak occurs in the region of 16 to 18 volts and copper shows a peak at this point. Some curves show evidence of additional structure beyond this point, but it is so washed out as to make analysis difficult. Comparing the curves for tungsten at 8045 volts and at 19,600 volts (Fig. 6—curve A) one notes that the first peak occurs at 6 to 8 volts in both cases. Cathode difficulties prevented the curve A from being extended but rough details can be observed in the "washed out" filament cathode curve B. Nilsson and Ohlin[12] have recorded with a curved crystal spectrograph a very similar isochromat for tungsten at 3690 volts. It appears, therefore, that the structure is independent of the applied x-ray voltage. Nilsson and Ohlin[12] recorded similar isochromats for targets of Cr, Fe, Cu, Zn, Au, and Pb. In general, their results are in good agreement with those of Figs. 6–8. Panofsky, Green, and DuMond[4] failed to observe such fine structure in their isochromats both at 10 and 20 kv. They used a gold target and from Fig. 8, one notes that the minimum is not as pronounced in this case as for the other targets. Low resolving power of the monochromator could easily cause the structure in gold to be overlooked.

Considerable speculation on the possible source of the unexpected structure has occurred but no analysis has explained any of the details observed. Nijboer[13] pro-

[12] A. Nilsson and P. Ohlin, Arkiv. f. Mat. Astr. o. Fys. **33A**, No. 23.

[13] B. R. A. Nijboer, Physica **12**, 461 (1946).

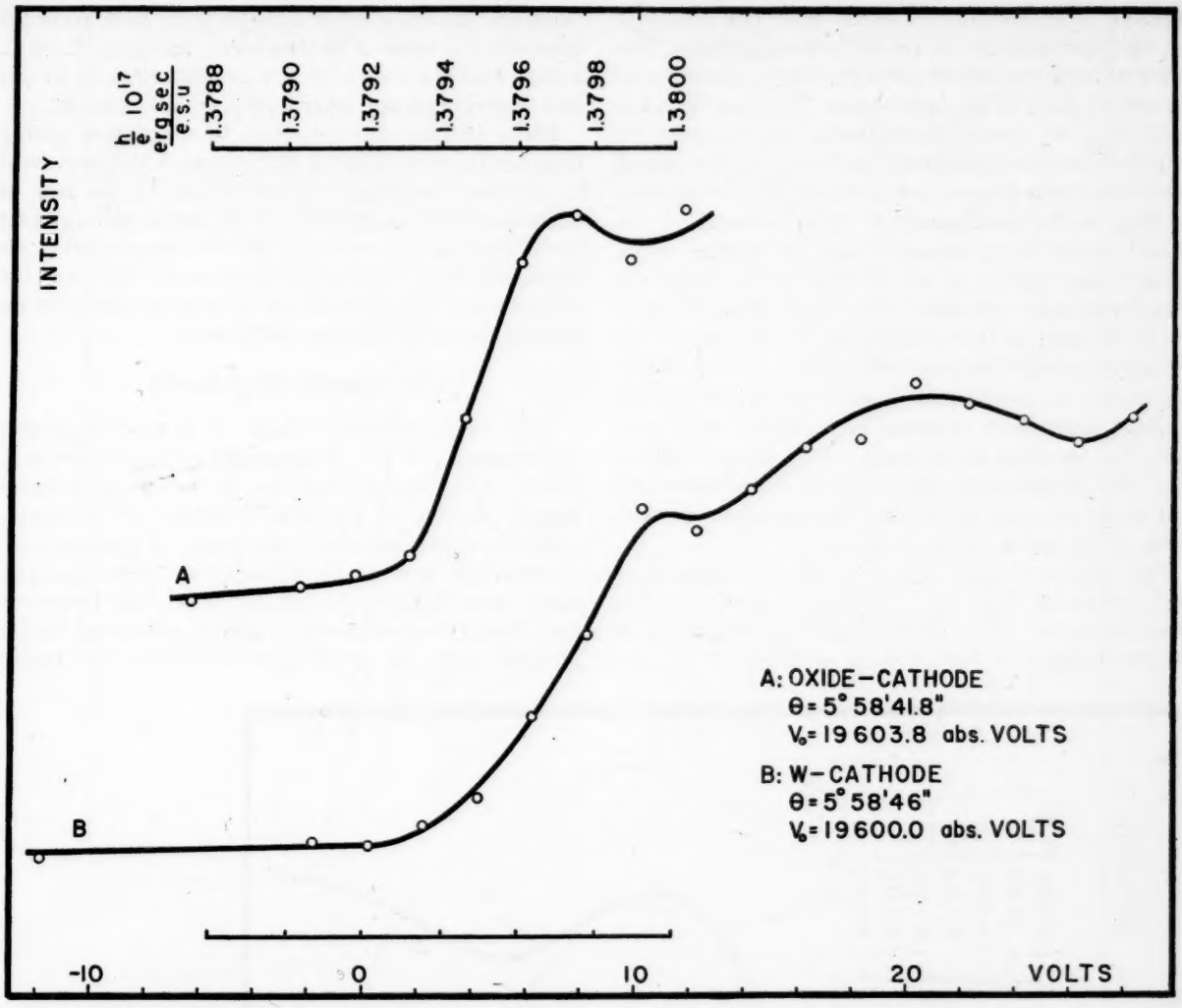

FIG. 6. The increased sharpness of the break in the isochromat due to the unipotential cathode is clearly shown in curve A. The structure at this voltage corresponds to that observed at lower voltages.

poses that the minima could be explained from an analogy with the fine structure observed in x-ray absorption edges. He assumes that in both cases the final state of the electron is one of the lowest unoccupied levels. Further, it is assumed that for small energy losses of the primary electron the energy loss curve for metals shows large fluctuations. Nijboer[13] was unable to make any quantitative calculations of the isochromat to be expected but concluded that it seemed possible to account qualitatively for the first minima in the observed isochromat.

An examination of the isochromats suggests that the curves in general (except copper) are a super-position of isochromats displaced about 10 and 20 volts from the high frequency limit. The energy lost by a high velocity electron in traversing a solid is primarily due to a large number of distant encounters in which the average energy loss is in the range from 7 to 12 volts. The high frequency limit would on this basis correspond to electrons with no energy loss and following this we would have a second high frequency limit corresponding to electrons which had had one collision and hence had lost from 7 to 12 volts, and correspondingly the third high frequency limit would correspond to those electrons which had experienced two encounters and lost approximately 20 volts. The primary difficulty with such an explanation lies in the fact that theoretically the isochromats observed from thin targets should be rectangular in shape and therefore by superposition alone one could not explain the minima observed. Experimental measurements on thin targets with high resolving power have never been made near the high frequency limit. The fine structure observed with thick targets emphasizes the importance of performing such experiments.

(3) Analysis and Computation of h/e from the Isochromats

The "window" of the monochrometor has a sharp peak at a particular wave-length, with the intensity

decaying asymptotically on either side. The energy of the electron beam is not perfectly homogeneous. The result of these two effects is to produce a curvature at the cut-off point of the isochromat. This may be made small as in the present experiments, but it cannot be entirely eliminated. DuMond has shown that the cut-off point is actually represented by the point of maximum bending of the isochromat or the maximum of the second derivative of the isochromat. He further shows theoretically that it is not permissible to locate the cut-off points by extending the straight line portion of the isochromat to the voltage axis. In the present experiments where the resolving power of the monochromator is approximately that given for perfect crystals, and where unipotential cathodes have been used, the resulting isochromats are so sharply defined that the cut-off points estimated by visual inspection and those obtained by the second derivative method agree within 0.2 or 0.3 of a volt.

The voltages at which certain values of h/e occur have been computed from the wave-length setting of the monochromator. These values have been indicated on the isochromats of Figs. 6–8. In addition to the isochromats shown, a large number have been recorded from which a value of h/e has been computed. Table II summarizes the values of h/e as was obtained in our best experiments for several targets and voltages.

Many additional results have been obtained with a tungsten filament cathode which agree with those listed in the table but the error introduced by the lack of sharpness in the isochromat cut-off was so much greater than in the results with unipotential cathodes that we listed only one tungsten filament result. However the accuracy was always sufficient to show the necessity for making the work function correction.

(4) Discussion of Errors

Each value of h/e in Table II is an independent measurement, as far as observational errors are concerned. The possible error due to the use of different targets, change in the work function of differently activated oxide cathodes, adjustment of spectrometer, observational errors in the voltage and current measurement, uncertainty in the location of the high frequency limit from the isochromats, are all contained in the probable error calculated from the independent results

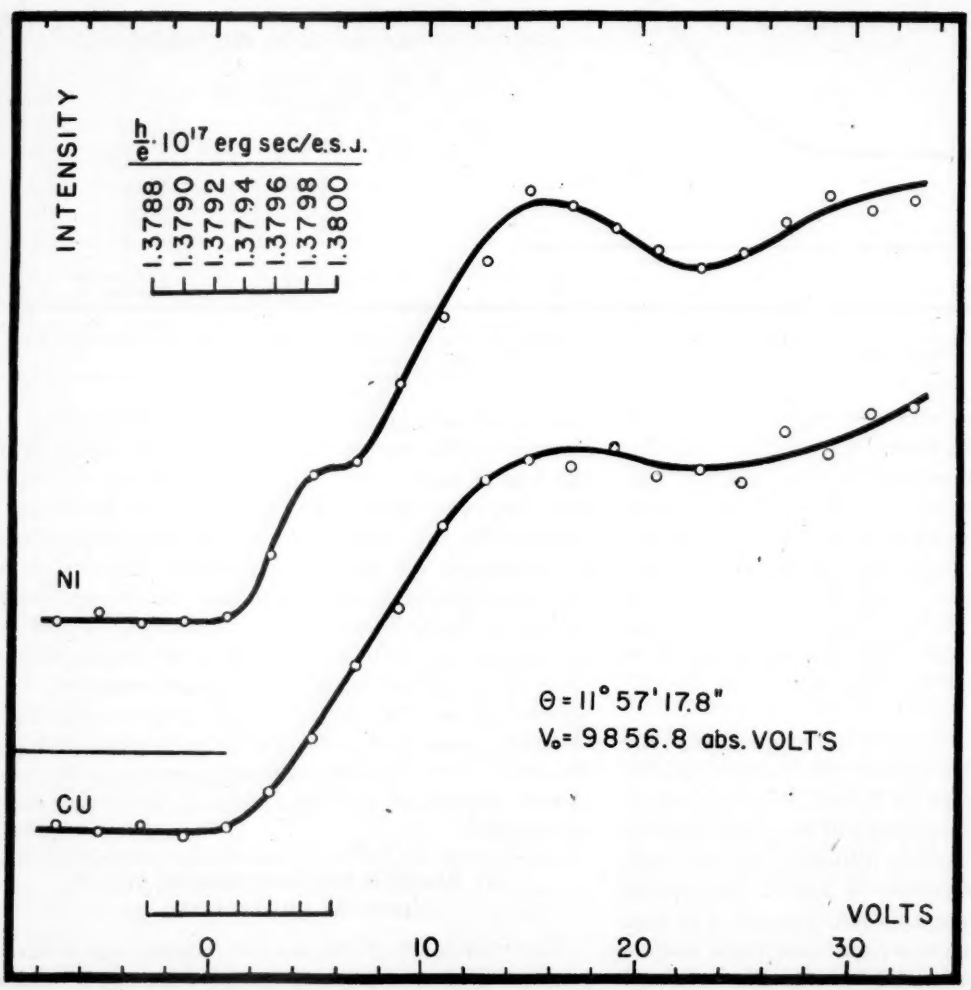

FIG. 7. Isochromats for copper and nickel target at the same voltage.

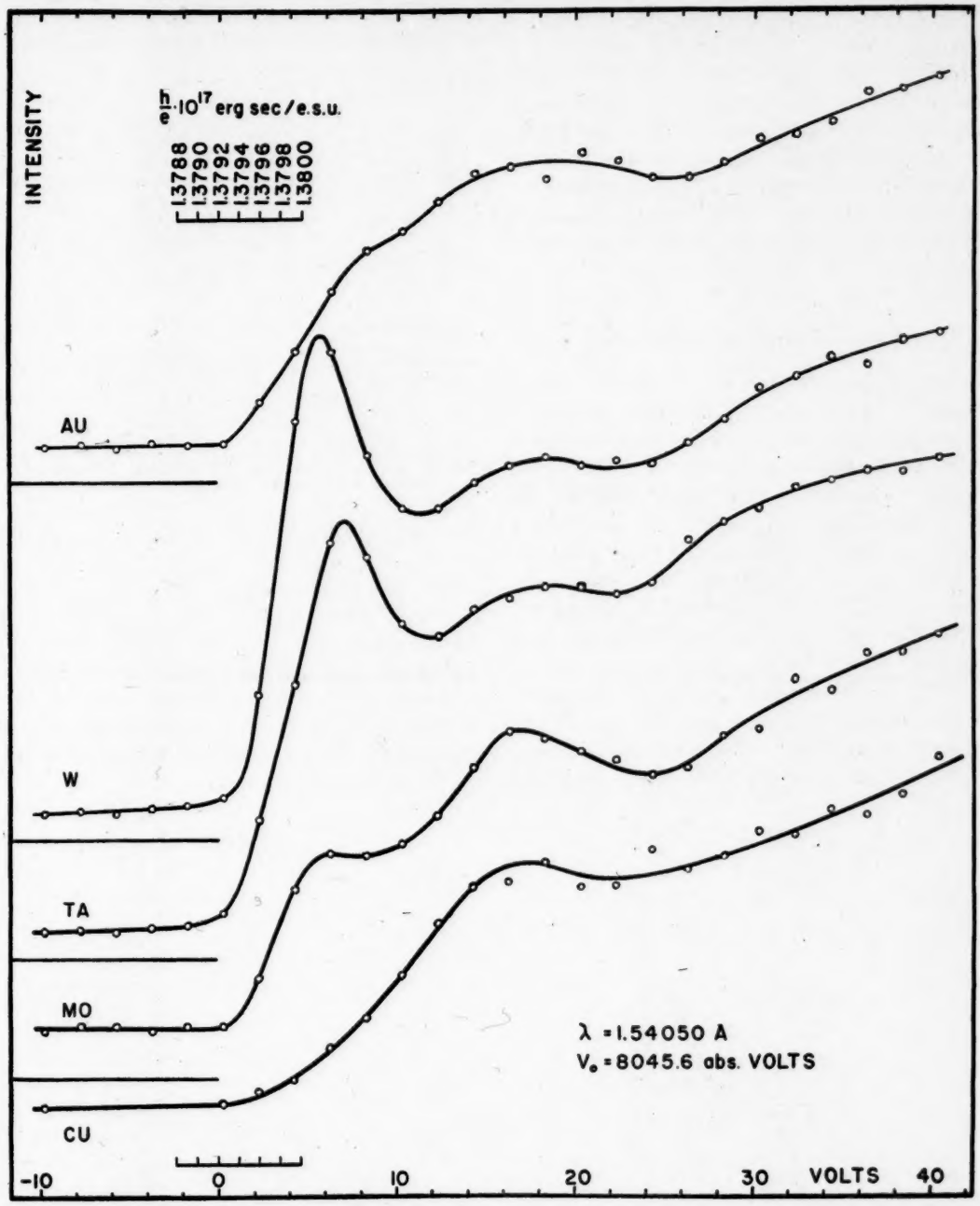

FIG. 8. Isochromats for targets of gold, tungsten, tantalum, molybdenum, and copper at the wave-length of the copper $K\alpha_1$ line.

of Table II. The probable error as calculated from Table II due to all of these factors is hence 3×10^{-5}. The estimated probable errors common to all measurements and their values are as follows:

(1) x-ray monochromator	1×10^{-5},
(2) uncertainty in ruled grating wave-length	2×10^{-5},
(3) resistance of voltage divider	4×10^{-6},
(4) standard cells, including temperature effects	2×10^{-6},
(5) Leeds-Northrup Type K-2 potentiometer	4×10^{-6},
(6) work function of oxide cathodes	5×10^{-6}.

The combination of these probable errors in the usual way gives 6×10^{-5} or

$$h/e=1.3793_8\pm0.00008\times10^{-17}\ \text{erg}\cdot\text{sec.}\cdot\text{e.s.u.}^{-1}.$$

It is well known that the work function of an oxide cathode is quite dependent on the backing metal and on the processing required to activate the surface. In the present use of a cathode in a high potential x-ray tube positive ion bombardment may induce additional uncertainty in the effective value of the work function.

The sharpness of the first peak in the structure for the tungsten target suggests that one could eliminate the cathode correction by making measurements at two voltages and then compute h/e from the difference in the voltages and the frequency separation of the peaks. Such an experiment appears entirely feasible and the precision attainable should be such that the remaining uncertainty in h/e by the x-ray methods would be primarily due to the probable error in the ruled grating x-ray wave-lengths.

(5) Discussion of the Evaluations of h/e

It appears that the values of h/e reported by Ohlin[5] should definitely be corrected for the work function of the cathode used. This correction increases the value of h/e as reported by him from 1.3787 to 1.3803×10^{-17} erg·sec.·e.s.u.$^{-1}$. Panofsky, Green, and DuMond obtained the value $1.3786\pm0.0004\times10^{-17}$ erg·sec.·e.s.u.$^{-1}$ and the present measurements give $1.37938\pm0.00008\times10^{-17}$ erg·sec.·e.s.u.$^{-1}$. DuMond and Cohen[6] computed the value $1.37926\pm0.00009\times10^{-17}$ erg·sec.·e.s.u.$^{-1}$. The last two values agree within the limits of the probable errors and for the first time since the h/e "discrepancy" was highlighted we have agreement between the computed and experimental value. In fact if the present experimental value were used as input data for the least squares adjustment the agreement between computed and experimental would be even closer.

TABLE II. Values of h/e.

Target	Approximate voltage	Cathode	$h/e\times10^{17}$ erg·sec.·e.s.u.$^{-1}$
Cu	8,050	oxide	1.3795
Cu	9,860	oxide	1.3793
Ni	9,860	oxide	1.3793
Mo	8,050	oxide	1.3794
Ta	8,050	oxide	1.3794
W	8,050	oxide	1.3793
W	19,600	oxide	1.3793
W	19,600	W. fil	1.3795
Au	8,050	oxide	1.3794
		Average	1.37938[a]

[a] In computing h/e the absolute volt must be converted to the electrostatic system by the approximate factor of 300. We are tremendously embarrassed by the fact that all of our previous reports on the measurement of h/e have been computed with this approximate factor rather than the correct value 299.776. Thus, we have spent much effort in attempting to find an explanation of the low "experimental results" observed whereas in fact all of our results have been in excellent agreement with the value of h/e computed by least squares analysis. The search for the cause of the "discrepancy" has resulted in the attainment of a precision in the final value that otherwise would not have been the case.

We wish to acknowledge the assistance given by the Bureau of Ordnance USN and our appreciation to Dr. Thomas and Dr. Vinal of the National Bureau of Standards for their cooperation and interest in calibrating the electrical standards, and to Mr. E. H. Byerly for his assistance in developing the electronic equipment which contributed markedly to the success of the present experiments.

Nuclear Electric Quadrupole Interactions in Crystals*

R. V. POUND
Harvard University, Cambridge, Massachusetts
(Received April 3, 1950)

A study is made of the effects of the presence of nuclear electric quadrupole moments on the nuclear magnetic resonance absorption in solids. Necessary theoretical background is followed by descriptions of experiments in which the spectra obtained with an r-f spectrograph, described elsewhere, are found to show marked splitting resulting from the quadrupole interaction with the electric field gradient. Both powder patterns and spectra of single crystals are reported, for Li^7, Na^{23}, and Al^{27}, with splittings varying from about 20 kc to 718 kc, depending on the crystal and the nucleus. Unambiguous indication of the spin values is obtained. The possibility of the detection of a resonance resulting from the electric quadrupole splittings in the absence of a static magnetic field is discussed and an unsuccessful attempt to find such a resonance in ICl is described and the failure tentatively explained. Available signal-to-noise ratios are calculated for such resonances. A method is described of determining the frequency of a large electric quadrupole splitting, by observation of the dependence of the frequency of the magnetic splitting of the levels $m=\pm\frac{1}{2}$, for an odd half-integral spin, on the angle between the direction of a magnetic field and the symmetry axis of the crystalline field. The electric quadrupole moment is shown probably to account for relaxation times of nuclei of spin greater than $\frac{1}{2}$ even in cubic crystals and, as evidence, resonances of Na^{23}, Li^7, I^{127}, and Br^{81} are reported. Assuming partial saturation and electric quadrupolar relaxation, calculations are made to account for a departure of the intensity ratios of the lines, in the Na^{23} spectrum in $NaNO_3$, from the ratios of the transition probabilities for magnetic dipole radiation. The possibility of determining nuclear electric quadrupole moments from splittings or relaxation times in ionic crystals is discussed.

I. INTRODUCTION

NUCLEAR paramagnetic resonance[1] or nuclear induction[2] provides means of observing the interactions between atomic nuclei and their surroundings. Such interactions affect relaxation times,[3,4] line widths,[3,5] and frequencies,[6,7] and in some cases can be the cause of the splittings of otherwise single lines into multiple ones.[8–10] The principal kinds of interactions of which studies have been reported are of magnetic character. The large majority of careful investigations of these aspects of the effect has involved the proton resonance, except in the experiments dealing only with determining nuclear g-factors, and because the proton spin is only $\frac{1}{2}$, no interactions of electric origin could be expected.

Many determinations of g-factors of nuclei of higher spin have been made in aqueous solutions or liquids, and it is common in these to find a resonance line that is considerably broader than a proton line in water and which cannot be saturated easily, indicating a correspondingly short relaxation time.[11,12] This observation has been explained as the effect of the interaction between the nuclear electric quadrupole moment and the gradient of the electric field at the nucleus. Because of the short time, compared with the period of the resonance frequency, in which a local configuration in the liquid changes character, no line structure is contributed by this interaction, the average value of the perturbation over the lifetimes of the nuclear spin orientation being zero. It is a strong mechanism for thermal relaxation, however, and becomes the dominant mechanism for even the deuteron, with the smallest known non-zero quadrupole moment, in D_2O. Unfortunately, the motion in the liquid, especially in concentrated ionic solutions, is so complex that observation of the broadening or of the relaxation effect does not allow a very accurate estimate of the magnitude of the quadrupole interaction. It has been used for rough determinations of the ratios of quadrupole moments of isotopes, however. The two g-factors of the two naturally equally abundant bromine isotopes were assigned by correlating the observed line breadths with the known quadrupole moments.[11]

That the quadrupole interaction can be the dominating relaxation mechanism in the fluctuating liquid system even for the deuteron, indicates that in the solid state one must expect to find line shapes determined predominantly by the electric quadrupole interaction, if it exists. Indeed, it must also be the dominant factor in the thermal relaxation process in the absence of electronically paramagnetic ions or impurities, if one considers a theory along the lines of Waller.[13] Both of these expectations appear to be verified experimentally, in some cases, as will be shown.

II. THEORY

The energy of interaction between a nucleus and a surrounding charge distribution can be written as an expansion in Legendre polynomials as

$$V=\sum_{i,j}(e_ie_j)/r_{ij}=\sum_{i,j}(e_ie_j/r_j)\sum_{k=0}^{\infty}(r_i/r_j)^kP_k(\cos\theta_{ij}), \quad (1)$$

* Some of the results presented here have been reported briefly previously. R. V. Pound, Phys. Rev. **73**, 1247 (1948); R. V. Pound, Proc. Phys. Soc. **61**, 576 (1948).

[1] Purcell, Torrey, and Pound, Phys. Rev. **69**, 37 (1946).
[2] Bloch, Hansen, and Packard, Phys. Rev. **70**, 474 (1946).
[3] Bloembergen, Purcell, and Pound, Phys. Rev. **73**, 679 (1948).
[4] N. Bloembergen, Thesis, Leiden (1948).
[5] Purcell, Bloembergen, and Pound, Phys. Rev. **70**, 988 (1946).
[6] W. D. Knight, Phys. Rev. **76**, 1259 (1949).
[7] W. G. Proctor and F. C. Yu, Phys. Rev. **77**, 717 (1950); W. C. Dickinson, Phys. Rev. **77**, 736 (1950).
[8] G. E. Pake, J. Chem. Phys. **16**, 327 (1948).
[9] N. Bloembergen, Physica (to be published); private communication.
[10] Gutowsky, Kistiakowsky, Pake, and Purcell, J. Chem. Phys. **77**, 972 (1949).
[11] R. V. Pound, Phys. Rev. **72**, 1273 (1948).
[12] R. V. Pound, Phys. Rev. **73**, 1112 (1948).
[13] I. Waller, Zeits. f. Physik **79**, 370 (1932).

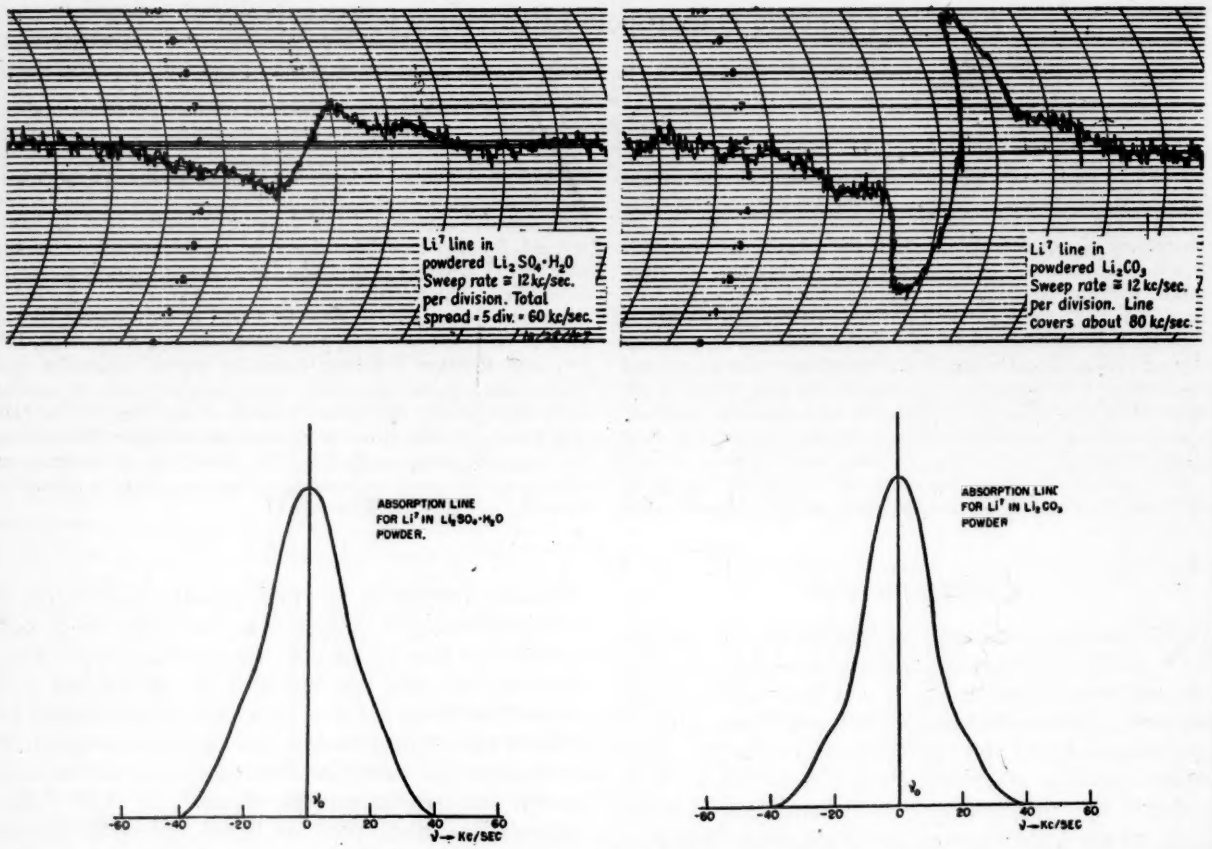
Li⁷ line in powdered Li₂SO₄·H₂O Sweep rate = 12 kc/sec. per division. Total spread = 5 div. = 60 kc/sec.
Li⁷ line in powdered Li₂CO₃ Sweep rate = 12 kc/sec. per division. Line covers about 80 kc/sec.
ABSORPTION LINE FOR Li⁷ IN Li₂SO₄·H₂O POWDER.
ABSORPTION LINE FOR Li⁷ IN Li₂CO₃ POWDER
-60 -40 -20 0 20 40 60
ν − Kc/SEC

FIG. 1. Records of Li^7 resonance near 3 Mc in powdered $Li_2SO_4 \cdot H_2O$, at left, and Li_2CO_3, at right. Below are absorption curves obtained from assuming records are derivatives.

where e_i refers to an element of the nuclear charge, e_j to an external charge, r_i and r_j the distances from the origin, taken at the center of the nucleus, to the charges e_i and e_j, respectively, and θ_{ij} is the angle between these radius vectors. By the addition theorem of spherical harmonics, we can express the interaction in terms of θ_i, ϕ_i, θ_j, and ϕ_j the polar and azimuthal angles between the z axis, the xz plane, and r_i and r_j. Thus (1) becomes

$$V=\sum(e_ie_j/r_j)\sum_{k=0}^{\infty}(r_i/r_j)^k\sum_{q=-k}^{k}(-)^q(4\pi/2k+1)\times Y_k^{-q}(\cos\theta_i,\phi_i)Y_k^q(\cos\theta_j,\phi_j), \quad (2)$$

where $Y_k^q(\cos\theta,\phi)$ is the normalized tesseral harmonic

$$Y_k^q(\cos\theta,\phi)=\Theta_k^q(\cos\theta)\epsilon^{iq\phi}/(2\pi)^{\frac{1}{2}} \quad (3)$$

and the functions $\Theta_k^q(\cos\theta)$ are defined[14] as

$$\Theta_k^q(\cos\theta)=(-)^q[(2k+1)(k-q)!/2(k+q)!]^{\frac{1}{2}}\times\sin^q\theta\frac{d^q}{(d\cos\theta)^q}P_k(\cos\theta) \quad (4)$$

for $q>0$, with

$$\Theta_k^q(\cos\theta)=(1)^q\Theta_k^{-q}. \quad (5)$$

In this manner the interaction can be written as

$$V=\sum_{i,j}(e_ie_j/r_j)\sum_{k=0}^{\infty}(r_i/r_j)^k[C^{(k)}(i)\cdot C^{(k)}(j)], \quad (6)$$

where $C^{(k)}(i)\cdot C^{(k)}(j)$ is the tensor scalar product defined as

$$\sum_{q=-k}^{k}(-)^qC_q^{(k)}(i)C_{-q}^{(k)}(j) \quad (7)$$

and[15]

$$C_q^k=[4\pi/(2k+1)]^{\frac{1}{2}}Y_k^q(\cos\theta,\phi). \quad (8)$$

We are concerned with the electric quadrupole term in the interaction which involves the tesseral harmonics of order $k=2$, the lowest order to be non-zero. Thus the interaction can be written as the dyadic product

$$F=\mathbf{Q}\cdot\nabla\mathbf{E},$$

where

$$\mathbf{Q}=\sum_i e_ir_i^2C^{(2)}(i) \quad (9)$$

[14] E. U. Condon and G. H. Shortley, *The Theory of Atomic Spectra* (Cambridge University Press, London, 1935).

[15] G. Racah, Phys. Rev. 62, 438 (1942).

and

$$\nabla\mathbf{E}=\sum_j (e_j/r_j^3)C^{(2)}(j). \tag{10}$$

From the symmetry properties of the nucleus, the interaction will vanish unless the spin $I\geqslant k/2$ and k is even, which, for the quadrupole interaction $k=2$, requires $I\geqslant 1$.

This formulation of the interaction expresses both the tensors of the nuclear charge and of the external charge as irreducible representations of the three-dimensional rotation group.[16] That at most five independent components are required to determine the tensor can be understood through the consideration of the tensor expressed in rectangular coordinates, which has nine components. However, the requirement that it be symmetric and that it be traceless, since $\nabla\cdot\mathbf{E}=0$, reduces these to five independent components. The definition of $(\nabla E)_0$, above, can be used to express the irreducible tensor components from the components of the rectangular coordinate system, since

$$(\nabla E)_0=\tfrac{1}{2}(\partial E_z/\partial z)=\tfrac{1}{3}[\tfrac{3}{2}(\partial E_z/\partial z)-\tfrac{1}{2}\nabla\cdot\mathbf{E}]. \tag{11}$$

The other components may be derived from this by the same method as that employed to derive the tesseral harmonics from the Legendre polynomials, and one obtains

$$\left.\begin{aligned}(\nabla E)_0&=-\tfrac{1}{2}(\partial E_z/\partial z),\\ (\nabla E)_{\pm1}&=\pm(6^{\frac{1}{2}}/6)[(\partial E_x/\partial z)\pm i(\partial E_y/\partial z)],\\ (\nabla E)_{\pm2}&=-(6^{\frac{1}{2}}/6)[(\partial E_x/\partial x)-(\partial E_y/\partial y)\\ &\qquad\pm 2i(\partial E_x/\partial y)].\end{aligned}\right\} \tag{12}$$

These are analogous to the five components of the nuclear electric quadrupole moment operator derived in a similar manner

$$\left.\begin{aligned}Q_0&=[eQ/2I(2I-1)][3I_z^2-I(I+1)],\\ Q_{\pm1}&=\mp(6^{\frac{1}{2}}/2)[eQ/2I(2I-1)][(I_x+iI_y)I_z\\ &\qquad+I_z(I_x+iI_y)],\\ Q_{\pm2}&=(6^{\frac{1}{2}}/2)[eQ/2I(2I-1)][(I_x+iI_y)^2],\end{aligned}\right\} \tag{13}$$

where the scalar nuclear quadrupole moment Q is defined in the conventional manner[17,18]

$$eQ=(II|\sum_i e r_i^2(3\cos^2\theta_{iI}-1)|II). \tag{14}$$

The non-vanishing matrix elements of the electric quadrupole tensor

$$F=\mathbf{Q}\cdot\nabla\mathbf{E}=\sum_{q=-2}^{2}(-1)^q Q_q(\nabla E)_{-q}, \tag{15}$$

in an I, m representation involve only the well-known matrix elements of the angular momentum and can be written down at once.

$$\left.\begin{aligned}(m|F|m)&=A[(3m^2-I(I+1)](\nabla E)_0,\\ (m|F|m\pm1)&=\mp(6^{\frac{1}{2}}/2)A(2m\pm1)\\ &\qquad\times[(I\pm m+1)(I\mp m)]^{\frac{1}{2}}(\nabla E)_{\pm1},\\ (m|F|m\pm2)&=(6^{\frac{1}{2}}/2)A[(I\mp m)(I\mp m-1)\\ &\qquad\times(I\pm m+1)(I\pm m+2)]^{\frac{1}{2}}(\nabla E)_{\pm2},\end{aligned}\right\} \tag{16}$$

where $A=eQ/2I(2I-1)$. Comparison of these matrix elements with those calculated for the interaction in diatomic molecules[18,19] reveals that the present problem could be treated as the limiting case of that system, regarding J as tending toward infinity, in which case $m_J/J\to\cos\theta$, $[1-(m_J/J)^2]^{\frac{1}{2}}\to\sin\theta$ and the ϕ dependence averages out because of the precession of J about the z-direction. The present treatment has greater utility in that it allows the evaluation of the matrix elements for cases of other than axial symmetry. For axial symmetry, as in diatomic molecules, the five components $(\nabla E)_q$ can be expressed in terms of a single scalar,

$$eq=\sum_j e_j(3\cos^2\theta_j-1)r_j^{-3}, \tag{17}$$

where θ_j is the angle between $\mathbf{r}_j$ and the symmetry axis. For axial symmetry the components of the tensor $\nabla\mathbf{E}$ are

$$\left.\begin{aligned}(\nabla E)_0&=\tfrac{1}{4}eq(3\cos^2\theta-1),\\ (\nabla E)_{\pm1}&=\pm\tfrac{1}{4}6^{\frac{1}{2}}eq\sin\theta\cos\theta\epsilon^{\pm i\phi},\\ (\nabla E)_{\pm2}&=\tfrac{1}{8}6^{\frac{1}{2}}eq\sin^2\theta\epsilon^{\pm 2i\phi},\end{aligned}\right\} \tag{18}$$

where θ is the angle between the axis of symmetry and the z direction and ϕ is the angle between the projection of the axis of symmetry on the x, y plane and the positive x-direction. For lower than axial symmetry one needs to know the three mutually perpendicular principal axes of the tensor in which the 3×3 matrix of the rectangular components of $\nabla\mathbf{E}$ is diagonalized. If the z-axis is chosen along the principal axis having largest component, then $(\nabla E)_0=eq/2$ where q is defined as before, $(\nabla E)_{\pm1}=0$ and $(\nabla E)_{\pm2}=(3^{\frac{1}{2}}/6)\eta eq$ where $\eta=(\partial E_x/\partial x-\partial E_y/\partial y)/(\partial E_z/\partial z)$ and by definition

$$0\leqslant|\eta|\leqslant 1.$$

III. EXPERIMENTAL TECHNIQUE

The foregoing theory will be developed as it applies to the experiments, carried out and contemplated, con-

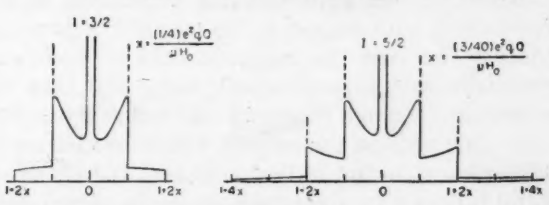

FIG. 2. Calculated absorption curves for $I=3/2$ and $I=5/2$ in powdered samples, ignoring broadening from magnetic dipole interactions.

[16] E. Wigner, *Gruppentheorie, etc.* (Friedr. Vieweg, Braunschweig, 1931), reprinted by J. W. Edwards, Ann Arbor.

[17] H. B. G. Casimir, *On The Interaction Between Atomic Nuclei and Electrons* (De Erven F. Bohn N.V., Haarlem, 1936).

[18] B. Feld and W. E. Lamb, Phys. Rev. **67**, 15 (1945).

[19] Kellogg, Rabi, Ramsey, and Zacharias, Phys. Rev. **57**, 677 (1940).

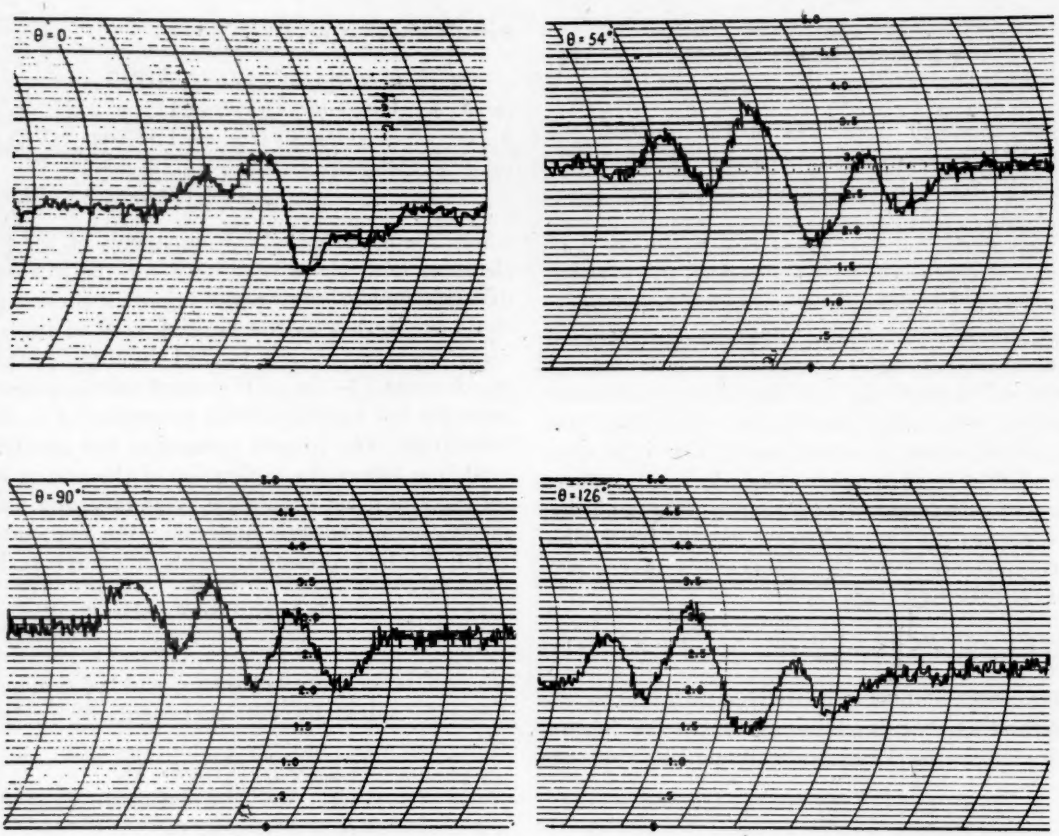

FIG. 3. Recorded resonances of Li^7 in single crystal of $Li_2SO_4 \cdot H_2O$, for various values of θ, the angle between the c axis and H_0, with H_0 in the bc plane. The frequency scale is about 12 kc per division.

currently with the description of the experiments. The apparatus used for most of the experiments was the recording r-f spectrograph described elsewhere[20,21] which has several properties recommending it for investigations of this type. It responds almost uniquely to the absorption part of the nuclear resonance effect. In contrast, bridge circuits[1-3] respond either to the absorption or the dispersion or a mixture of the two, depending on the phase of the residual unbalance signal, which is difficult to maintain constant over long periods of time. The frequency is easily slowly swept continuously over a range as large as 2.5 to 1, at any radiofrequency in the range from 45 Mc downward. The lowest frequency so far tried is 350 kc. The recording milliammeter gives permanent records approximating derivatives of absorption lines with respect to the magnetic field or the frequency, because the magnetic field is modulated sinusoidally with a peak-to-peak swing less than the line-breadth. A rough frequency calibration is provided by the time scale on the records, which correlates with the frequency control of the oscillator. The frequency control is driven by a synchronous motor geared down to a rate ranging from one revolution (two sweeps) in ten hours down to one revolution in ten days.

The earlier experiments were performed with an electromagnet with poles $3\frac{1}{2}$ in. in diameter and a $1\frac{1}{2}$ in. gap, a modulation frequency near 1300 c.p.s., and samples $\frac{1}{2}$ in. diameter by $\frac{1}{2}$ in. long. The magnet was supplied from large storage batteries and was operated continuously, day and night. Many line strengths were such that the 20-sec. time constant, or 0.05 c.p.s. band width had to be used in the recording system and this set an upper limit on the sweep rate that could be used to get full detail in line shapes. Usually a sweep from 4 to 2 Mc in 3 days was used with a straight-line-capacity condenser determining the frequency. Therefore the rate of change of frequency was highest at the high frequency end of the sweep. The magnetic field required for such nuclei as Na^{23}, Br^{79}, Br^{81}, Li^7, and Al^{27} for this range was between 1200 and 2500 gauss and the inhomogeneity of the field of less than 2 gauss over the sample was not a serious handicap because the line-breadth caused by dipole-dipole broadening was usually of this order or larger.

A slow drift of the field made precision measurements of frequency differences difficult, however, and, rather than attempt to control the field for the continuous operation, a permanent magnet was constructed with which the later experiments were performed. This has a gap of 6 in. diameter, $1\frac{3}{8}$ in. spacing, supplied with a

[20] R. V. Pound, Phys. Rev. 72, 527 (1947).
[21] R. V. Pound and W. D. Knight, Rev. Sci. Inst. 21, 219 (1950).

field of 6379 gauss from about 350 lb of Alnico V. The field appears to be homogeneous to better than 0.1 gauss over the same $\frac{1}{2}$ in. diameter samples, and is considerably more homogeneous over $\frac{1}{4}$ in. diameter samples. No long time drift of the field has so far been observed (about six months since first used, one year since originally magnetized to saturation without the conventional small demagnetization for stabilization). There did appear to be a decrease by about 4 gauss during the summer months when the laboratory was excessively hot. This loss of field was regained when the laboratory temperature returned to normal, and could have been caused by a differential thermal expansion effect.

Modulation of the field is achieved in the magnet by a pair of small coils in the gap itself. A modulation frequency of about 280 c.p.s. is used. When frequency differences and ratios were measured, a Navy type LM-18 frequency meter was used and the current in the electromagnet was monitored with a potentiometer and drift corrected as required. Since many hours were consumed in a single set of measurements in some cases, this became very tedious and the permanent magnet has helped greatly in simplifying the procedure and improving the precision obtainable.

IV. RESULTS AND THEORY

Several different kinds of spectra have been found so far and these will be discussed below, classified according to the nucleus of which the magnetic resonance was observed.

Lithium

The resonance of only the Li^7 isotope has so far been detected in the crystalline state. The first samples used were pellets of $Li_2SO_4 \cdot H_2O$ and of Li_2CO_3 compressed from a powder. The resulting records are shown in Fig. 1 together with absorption curves derived from these by numerical integration. That these lines show some evidence of structure is clearer from the recorded derivatives than from the integrals. The width of the Li_2CO_3 line is about 60 kc between the outer ends of the initial and final flats in the record, and this is an order of magnitude greater than would be possible from dipole-dipole broadening, being equivalent to a local field of about ± 18 gauss.

To interpret this line as due to the quadrupole interaction, the first-order perturbation on the energies of the levels m in the magnetic field may be calculated. This is simply

$$E_m = (m\mu H/I) + [eQ/2I(2I-1)][3m^2 - I(I+1)](\nabla E)_0. \tag{19}$$

In this case, since the sample is really a powder, a uniform distribution of the direction of the crystalline axes with respect to the magnetic field direction exists and therefore a corresponding distribution of the magnitude of $(\nabla E)_0$. To solve this problem properly one should know the field symmetry at the nucleus but the lines are not well enough resolved to be significantly affected by such symmetry, and an assumption of axial symmetry may be made. With this assumption, $(\nabla E)_0 = \frac{1}{4}eq(3\cos^2\theta - 1)$ and with a uniform distribution in space of the orientations of the crystalline axes one would expect the line corresponding to $E_{\frac{1}{2}} - E_{-\frac{1}{2}}$ to be at the frequency corresponding to the normal gyromagnetic ratio for Li^7, but the transitions corresponding to $E_{\frac{1}{2}} - E_{\frac{1}{2}}$ and to $E_{-\frac{1}{2}} - E_{-\frac{1}{2}}$ to produce absorption over the ranges, relative to the normal frequency, from $\pm e^2Qq/2h$ to $\mp e^2Qq/4h$, respectively. The resulting shape function for the line is identical to that computed for heteronuclear diatomic molecules of a large J value

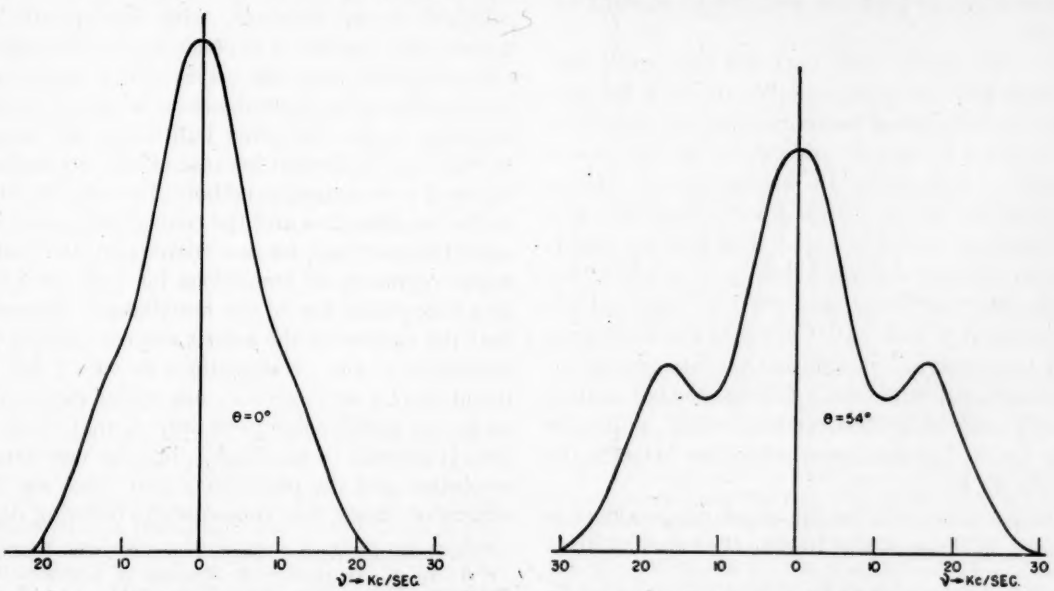

FIG. 4. Absorption curves for the Li^7 line from Fig. 3 for $\theta = 0°$, at left, and $\theta = 54°$, at right.

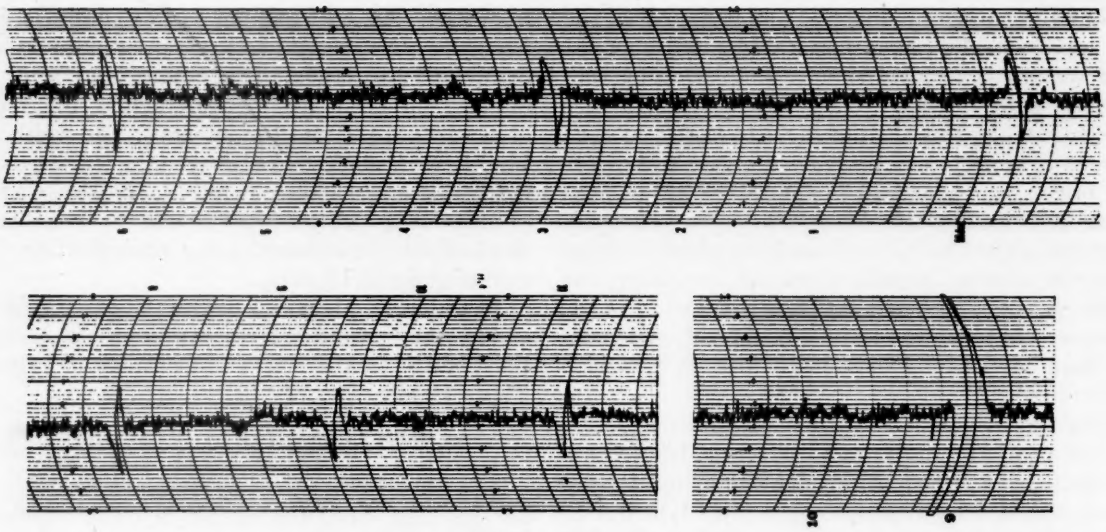

FIG. 5. The Na^{23} resonance in $NaNO_3$ for crystal axis near 0°, 90°, and 54° with respect to H_0. The frequency scale is about 14 kc per division, which corresponds to 15 minutes of time. The frequency of the center line is 7.18 Mc. A small effect explainable through higher order terms in the perturbation can be seen to cause an asymmetry in the line at $\theta=54°$.

by Feld and Lamb,[18] and the arguments given there will not be repeated here. Resulting curves of line intensity for the above case of $I=\frac{3}{2}$ and for the similar situation with $I=5/2$ are reproduced in Fig. 2.

The magnetic dipole interaction has been ignored in the computation of these shapes and if the broadening from this cause is not negligible compared to e^2qQ, the irregular shape would be considerably smoothed out. In addition, there is the possibility that all Li^7 nuclei are not similarly situated, and in that event several such lines with several values of q might be superimposed. Thus very little information is obtained from a spectrum of this type beyond the evidence that a quadrupole interaction seems to be required to account for the breadth.

A single crystal of $Li_2SO_4\cdot H_2O$ was obtained[21a] and the required $\frac{1}{2}$-in. diameter sample cut with its axis normal to the b, c plane of the monoclinic structure. The spectra obtained for several orientations of this crystal in the magnetic field, where the indicated angle θ is the angle between the magnetic field direction and the c axis of the crystal, are shown in Fig. 3. The splitting here is much more distinct and shows a definite triplet structure with a maximum splitting near $\theta=\pm54°$ and $\pm126°$, and minimum at 0° and 180°. Curves at the absorption obtained by numerical integration of the spectra for the maximum and minimum splitting, plotted against a frequency scale in kc/sec. relative to the center are shown in Fig. 4. The maximum separation between the satellites is 45 kc.

An attempt to account for the angular dependence of the splitting in terms of the $Li_2SO_4\cdot H_2O$ crystal structure determined from x-ray diffraction studies[22,23] met with little success. The structure puts two molecules, including two H_2O groups and four Li^+ ions in a unit cell with two of the four Li^+ ions surrounded by a tetrahedron of oxygens belonging to sulfate groups. The other two Li ions were supposed to be surrounded by a tetrahedron of oxygens, three of which belonged to sulfate groups, the fourth being the oxygen of the H_2O group. In this manner, since the Li—O line, for the H_2O oxygen, was supposed to have two different orientations in the unit cell, but symmetrically disposed with respect to the c-axis, it might be supposed that a large part of the gradient of the electric field responsible for the splitting arises from the field of the strongly polarized water molecule, with one quarter of the lithium ions showing a dependence on the angle measured clockwise from the c-axis, and a second quarter showing the same dependence in terms of the counter clockwise angle. The other half of the Li^+ ions would be relatively little split because of the tetrahedral symmetry of their nearest neighbors. The relative intensities of the satellite lines and the central line would be very small because then, for one orientation, the central line might represent all transitions for $\frac{3}{4}$ of the Li^7 nuclei plus the central line of the remaining $\frac{1}{4}$. Remembering that the squares of the matrix elements giving the line intensities of the $2I$ transitions $m\leftrightarrow m-1$ are proportional to $(I+m)(I-m+1)$, one might expect the area under the satellite line to be only $\frac{1}{10}$ that of the central line. It appears to be about $\frac{1}{5}$, but the very incomplete resolution and the probability that there are different relaxation times, and consequently differing degrees of

[21a] The author wishes to thank Dr. G. C. Kennedy for making available this single crystal.

[22] G. E. Ziegler, Zeits. f. Krist. Physik **89**, 459 (1934).

[23] R. W. C. Wyckoff, *The Structure of Crystals* (Rheinhold Publishing Corporation, New York, 1935); *Crystal Structures* (Interscience Publishers, Inc., New York, 1948).

saturation in the two kinds of Li^7 nuclei, makes this aspect of small significance.

The proposed crystal structure would have placed the two protons of a water molecule on a line normal to the c-axis. To check this the splitting, due to the dipole-dipole interaction of the protons, in the proton resonance was observed and found to disagree with such a direction for the proton-proton line. A careful study of this was made by Pake[24] in the same sample, who found that there were two distinctly different directions for the proton-proton line, making the angles of $\pm 50°$ with respect to the c-axis. Thus the suggested structure is incorrect in this respect and it seems difficult to fit this new information into the suggested structure for the rest of the elements of the unit cell. The coincidence in the direction of the proton-proton line and that of maximum splitting of the lithium line might suggest a very near proton with resultant splitting of the lithium line by magnetic dipole interaction. This is ruled out because such an interaction would require, to give the observed splitting equivalent to about ± 14 gauss, a $H-Li^7$ distance of only about 1.3A. The reciprocal interaction of the Li^7 on the H line would be stronger, because of the large value of μ for Li^7, and would completely destroy the $H-H$ coupling effect. The incomplete resolution makes further study of this crystal somewhat unrewarding and it has not been investigated further.

The powder pattern of Li_2CO_3 indicates a more hopeful case, because the crystal structure may be simple, being anhydrous, and yet a good splitting is also indicated. Unfortunately, single crystals of this substance have not yet been obtained.

Because of success with $NaNO_3$ (see below) an attempt was made to observe the Li^7 resonance in an imperfect and rather small crystal of $LiNO_3$, which has the same hexagonal structure as $NaNO_3$. The $LiNO_3$ crystal was grown from aqueous solution at 65°C, to obtain the anhydrous form. The Li^7 resonance was not found and a search for the resonance in a compressed powder pellet, giving a better filling factor than the crystal, revealed only a transient response of one-sided character on the recorder, the sense depending on the direction of approach to resonance. This is interpreted as indicating that the Li^7 relaxation time is very long in this crystal and that it saturates after about two minutes of observation at the level of the oscillator. Therefore the substance could not be used in the pure form for line shape studies. The relaxation effect will be discussed in a later section.

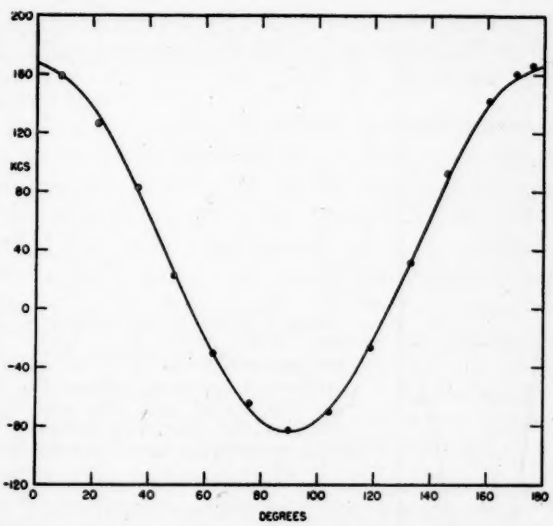

FIG. 6. The frequency interval, in kc, between the central line and the symmetrically placed satellites in $NaNO_3$ as a function of θ, the angle between H_0 and the crystal axis. The smooth curve is $83.5\ (3\cos^2\theta - 1)$.

[24] G. E. Pake, Thesis, Harvard University (1947).

Sodium

The Na^{23} resonance in a single crystal of $NaNO_3$ shows the anticipated quadrupolar interaction characteristic of an axially symmetric field. The structure[22] is hexagonal with the NO_3^- ions and Na^+ ions lying in planes and with the Na^+ ions on a threefold axis. The crystal was cut with the axis perpendicular to the axis of the cylinder and the spectra obtained for an angle of 0, 54° and 90° between the direction of the magnetic

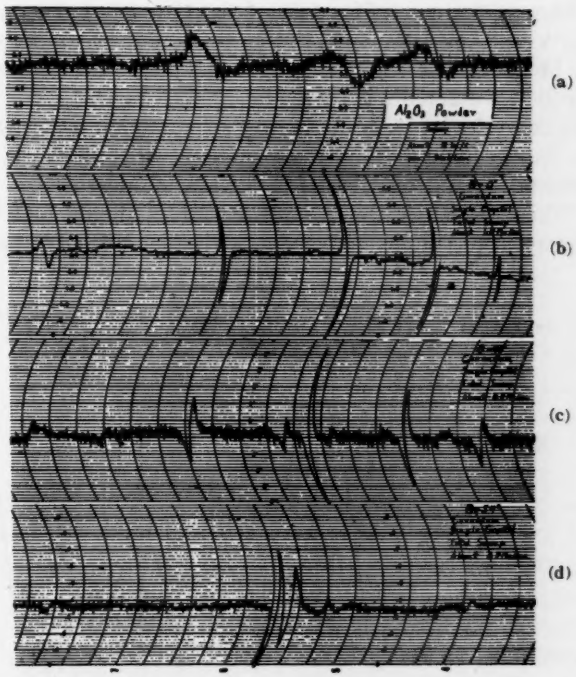

FIG. 7. Spectra of Al^{27} in Al_2O_3. (a) A powder pattern near 3 Mc with total sweep about 900 kc. (b) A single crystal with hexagonal axis parallel to H_0. The total sweep is about 1.6 Mc centered at 3 Mc. The 20-sec. time constant is used here. (c) With the crystal axis perpendicular to H_0, the sweep rate about doubled and the 1-sec. time constant used. (d) With crystal axis at 54° to H_0, same sweep rate and time constant as in (c).

field and that of the threefold axis of the crystal are reproduced in Fig. 5. The frequency of the central line is about 7.17 Mc and the scale corresponds to about 13 kc per division (equals 15 minutes of time). The 0.05-c.p.s. band width was required to obtain adequate signal-to-noise ratio and several weeks of operating time were required to make about thirty observations of the spectrum at various angles. The breadth of the individual lines is about 2 kc (equivalent to 2 gauss) between points of maximum slope which roughly corresponds to the expected dipole-dipole broadening. The recorded spectrum does not give exactly the derivative of the absorption line since, for sufficient sensitivity, it was found necessary to use a modulation amplitude of the magnetic field of about 2 gauss peak-to-peak, which is not small compared to the line breadth and therefore has an effect on the line shape and width.

For this case the first order perturbation calculation using Eqs. (16) and (18) shows that the satellite lines should fall at frequencies, with spin $\frac{3}{2}$,

$$\nu_{m\leftrightarrow(m-1)}=\nu_0+(e^2qQ/4h)(2m-1)[\tfrac{3}{2}\cos^2\theta-\tfrac{1}{2})], \quad (20)$$

where ν_0 is the normal pure Zeeman frequency, $\mu H/Ih$. Measurements of the spacings were made only in the $\theta=0$ region, and relative values for other angles were made from the records by averaging the distances between the central line and each of the two satellites. These records were all made in the permanent magnet. The resulting points for 180° of data are plotted on a curve of 83.5 $(3\cos^2\theta-1)$ in Fig. 6 where the fit is seen to be good. The corresponding value of the maximum frequency difference is 167 ± 1 kc, or e^2qQ/h is 334 ± 2 kc. Higher order terms in the perturbation are not required to fit the data within the precision with which the orientation and relative frequencies were measured.

The area under the absorption curves should be in the ratio 3:4:3, in agreement with the ratios of the squares of the matrix elements of the three transitions, if the r-f signal were small enough to cause a negligible disturbance in the equilibrium populations of the four levels. The records show a nearly equal response of the spectrograph to all three lines at orientations in which they are definitely separated. Not very much weight should be attached to this result because of the high level of the modulation and the lack of data on the thermal relaxation times. One possible cause may be found, however, in the fact that the line breadths of the three lines may be different, through the operation of term B of Eq. (22) of reference 3 (in which, however, the simultaneous flipping of two spins can only occur adiabatically when the two make the identical transition in opposite senses, with, consequently, a reduction in the contribution of term B compared to the purely magnetic case). A second possibility is the thermal relaxation process if it depends on the electric quadrupole interaction. This will be discussed in a later section.

A comparison of the frequency of the central line, with θ at zero, to that for Na^{23} in a solution of NaBr revealed no difference within the accuracy of measurement of about 200 c.p.s. in 7 Mc.

Aluminum

The record reproduced in Fig. 7(a) resulted with a sample of Al_2O_3, in the form of a compressed powder, where distinct evidence of a quadrupole splitting is found. The frequency scale was about 900 kc centered near 3 Mc and a field of 2400 gauss was maintained in the small electromagnet. The peculiarly assymmetric and indistinct character of the resonance is best understood in terms of the results with a single crystal.

A natural corundum crystal having distinctly hexagonal external form was cut to form a cylinder with the

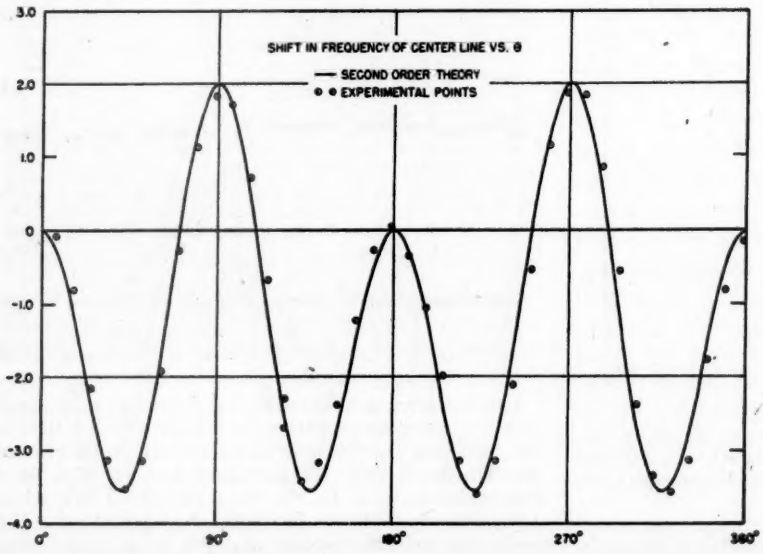

FIG. 8. A plot of the frequency shift of the central line of Al_2O_3 spectrum multiplied by $\nu_0/\Delta\nu^2$, as function of the angle between H and the crystal axis. The solid curve is the theoretical second-order perturbation term, $2(1-9z^2)\cdot(1-z^2)$.

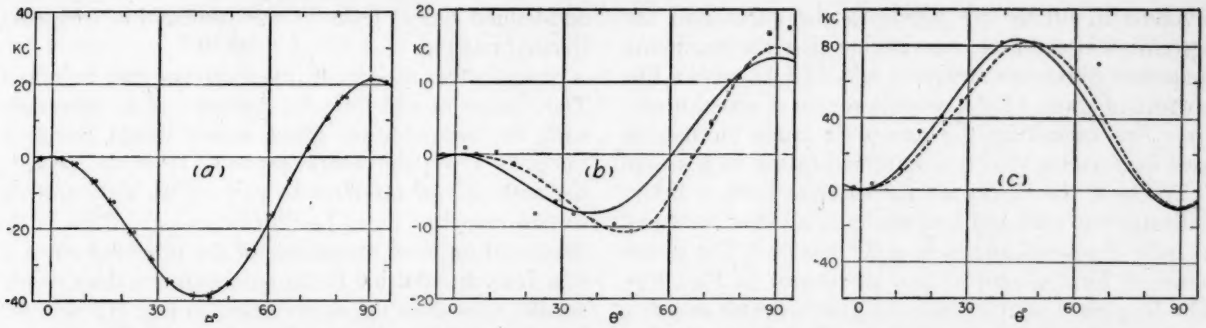

FIG. 9. Higher order perturbation effects in the Al_2O_3 spectrum. (a) The shift in frequency of the central line as a function of the angle θ. The frequency shift is taken as determining the angle from the theoretical second-order curve and this angle is used to evaluate the first-order shifts in the first and second satellite lines. (b) The departure of the first satellite from ν_0 after subtracting $\Delta\nu(3\cos^2\theta-1)$. The solid curve is the theoretical second-order term and the broken one is the sum of the second- and third-order terms. (c) The departure of the second satellite line from ν_0 after subtracting $2\Delta\nu(3\cos^2\theta-1)$. The value of $\Delta\nu$ is determined independently to be 179.5 kc, from measurements of the spectrum of Fig. 7(b).

axis of the cylinder perpendicular to the hexagonal axis of the crystal. The structure[23] of Al_2O_3 is such that the electric field at the Al^{27} nuclei should be axially symmetric with the same symmetry axis as the crystal. The crystal had a strong coloration, indicative of paramagnetic impurities, and this was expected to give a short spin-lattice relaxation time.[3,25,26] Figure 7(b) shows the spectrum found with the angle θ, between the magnetic field direction and the crystal axis, at zero. The total sweep here is 1.8 Mc with center again near 3 Mc and the five-line spectrum is confirmation of the spin value of 5/2. The lines should fall at the frequencies

$$\nu_{m\leftrightarrow(m-1)}=\nu_0+(3e^2qQ/40h)(2m-1)[\tfrac{3}{2}\cos^2\theta-\tfrac{1}{2}], \quad (21)$$

from first-order perturbation theory, using Eqs. (16) and (18), and where $\nu_0=\mu H/Ih$. Measurement for $\theta=0$ showed the frequency spacings to be equal, as accurately as could be determined (±1 kc), and to be each equal to 359.0 ± 1 kc. Thus the total spectrum covers 1436 kc and is a reasonable fraction of the frequency of the central line.

Figures 7(c) and (d) are records taken for $\theta=90°$ and for $\theta=54°$. Here the noise amplitude is greater because the response time of the recorder has been decreased and the sweep rate doubled, to permit a more rapid collection of data. The relaxation time in the crystal was short enough to allow use of a signal level resulting in very adequate response even with the noise pass band in the 1-sec. time constant. In these two records, discrepancies from the first-order perturbation theory show up, the most striking of these being the failure of five lines to converge to a single line at any angle, as they should for the first-order calculation at $(3\cos^2\theta-1)=0$. One can understand this in terms of the effects of the perturbation carried to higher orders where, for instance, one finds that the central line is displaced from the Zeeman frequency ν_0. The energy differences for the five transitions, carried to terms in the cube of $e^2qQ/\mu H$ are found to be

$$W\left(\pm\tfrac{5}{2}\leftrightarrow\pm\tfrac{3}{2}\right)=h\nu_0\left\{1\pm2(3z^2-1)\frac{\Delta\nu}{\nu_0}+(33z^2-1)(1-z^2)\left(\frac{\Delta\nu}{\nu_0}\right)^2\pm\left[60z^2(1-z^2)-\left(\frac{279z^2+6}{4}\right)(3z^2-1)\right](1-z^2)\left(\frac{\Delta\nu}{\nu_0}\right)^3+\cdots\right\}, \quad (22)$$

$$W\left(\pm\tfrac{3}{2}\leftrightarrow\pm\tfrac{1}{2}\right)=h\nu_0\left\{1\pm(3z^2-1)\frac{\Delta\nu}{\nu_0}+\left(\frac{5-21z^2}{4}\right)(1-z^2)\left(\frac{\Delta\nu}{\nu_0}\right)^2\pm\left[\left(\frac{197z^2-17}{8}\right)\times(3z^2-1)-60z^2(1-z^2)\right](1-z^2)\left(\frac{\Delta\nu}{\nu_0}\right)^3+\cdots\right\}, \quad (23)$$

$$W\left(\tfrac{1}{2}\leftrightarrow-\tfrac{1}{2}\right)=h\nu_0\left\{1+2(1-9z^2)(1-z^2)\left(\frac{\Delta\nu}{\nu_0}\right)^2+0\left(\frac{\Delta\nu}{\nu_0}\right)^4+\cdots\right\}, \quad (24)$$

where $\Delta\nu=3e^2qQ/40h$, or one-half the frequency interval between lines when $\theta=0$. Here z is written for $\cos\theta$. The term in these formulas simplest to check experimentally is the term in $(\Delta\nu/\nu_0)^2$ in the central line, $W(\frac{1}{2}\leftrightarrow-\frac{1}{2})$. To measure the frequency at fixed field it was necessary to maintain the magnet current constant by continuous monitoring with a potentiometer across a series resistance. The results are shown in Fig. 8 for a full rotation of the crystal. The circled points represent the data, the shifts in frequency relative to the frequency at $\theta=0$, multiplied by $(\nu_0/\Delta\nu^2)$, where the $\Delta\nu$ is 179.5 kc as determined above. The smooth curve is the function $2(1-9z^2)(1-z^2)$. Thus there is no arbitrary amplitude

[25] R. V. Pound, Phys. Rev. **73**, 523 (1948).
[26] N. Bloembergen, Physica **XV**, 386 (1949).

involved in fitting the points to the curve and the agreement is excellent, considering that the maximum frequency difference measured was 37.5 kc with a line breadth of about 4 kc. The main source of experimental error was caused by the somewhat crude mechanism used for rotating the crystal and indicating its position.

To check the theory on the satellite lines, a better indicator was used and frequencies of all lines measured at each of several angles in a 90° interval. The points obtained for the central line are shown in Fig. 9(a). The frequency shift appears to give a better measure of the angle of the crystal than does the mechanical indicator. Therefore the value of θ obtained from assuming the measured frequency to fall on the curve was used to evaluate the term in $\Delta\nu/\nu_0$ in the expressions for the first and second satellite lines. Thus the remaining frequency difference between the satellite line and the central line, at $\theta=0$, after subtracting the values for the term in $\Delta\nu/\nu_0$, is obtained, and plotted in Fig. 9(b) and (c). Here the solid curve is the amplitude of $(\Delta\nu/\nu_0)^2$ and the broken curve is the sum of this and the function in $(\Delta\nu/\nu_0)^3$. The agreement is seen to be as good as could be expected considering the large effect which a small error in angle could introduce through the first-order term. The absence of a third-order, or any odd-valued order, term in the central-line frequency should be noted.

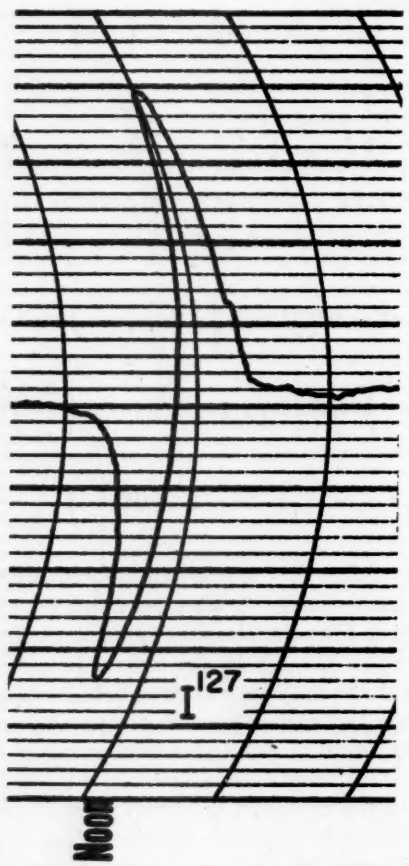

FIG. 10. A record of the line from I^{127} in a single crystal of KI. The frequency is 5.5 Mc and the line is about 600 c.p.s. between the extremes of the derivative.

Several other aspects of this spectrum may be noted. The failure of the lines to converge is in agreement with the second-order effect which would bring, at $(3\cos^2\theta-1)=0$, the central line to $\nu_0[1-(8/3)(\Delta\nu/\nu_0)^2]$, the first pair of satellites to $\nu_0[1-\frac{1}{3}(\Delta\nu/\nu_0)^2]$ and the second satellites to $\nu_0[1+(20/3)(\Delta\nu/\nu_0)^2]$. This is the sense and order of magnitude of the observed effect in Fig. 7(d). In addition to the principal five lines several smaller ones show up, as is evident in Fig. 7(c) and (d). These are explained by the fact that the crystal showed a small amount of striation at an oblique angle, which is believed to correspond to layers of the crystal in a twinned orientation. Thus, in reality, a small part of the sample has a different angle with respect to the magnetic field from that of the main bulk. The records for many angles confirm this explanation.

Something must be said about the relative intensities of the lines. Unfortunately, a constant sensitivity was not obtained with this original spectrograph over such a wide fractional range of frequencies as is covered by this spectrum, but later records taken with the improved spectrograph in the permanent magnet at a 7.2-Mc center frequency indicate that the relative intensities are in the ratio of approximately 25:70:90:70:25. One of these records is reproduced in reference 21. As in the case of Na^{23}, the relative intensities for a sufficiently small signal (avoiding saturation) should be, if the line breadths are equal, that of the squares of the matrix elements, or for spin 5:8:9:8:5. The actual ratio observed is more nearly the square of this and this disagreement is in the opposite sense to that observed for the Na^{23} resonance. The only difference that might be a clue to the opposite sense of the discrepancy seems to be that thermal relaxation in the Al_2O_3 probably results from magnetic interaction with the paramagnetic impurity whereas, in the $NaNO_3$, which was optically pure, it probably results through the quadrupole interaction with the lattice. This possibility will be discussed later.

Finally, it may be of interest that the signal-to-noise ratio of the central line of Fig. 7(b) appears to be about what one calculates by methods analogous to those in the appendix of reference 3, assuming the spin system to be unsaturated by the r-f signal of 0.5 volt across the coil. Taking into account the diminution of a single line compared with the unsplit case (see section on the pure quadrupole spectra) and assuming for $T_2\approx 3\times 10^{-4}$ sec., one finds a possible amplitude signal-to-noise ratio of about 50 to 1. Thus the noise figure of the spectrograph is not seriously greater than unity.

Iodine

As an example of a nuclear resonance in a single crystal, where the nucleus is known to have a large electric quadrupole moment but where the symmetry

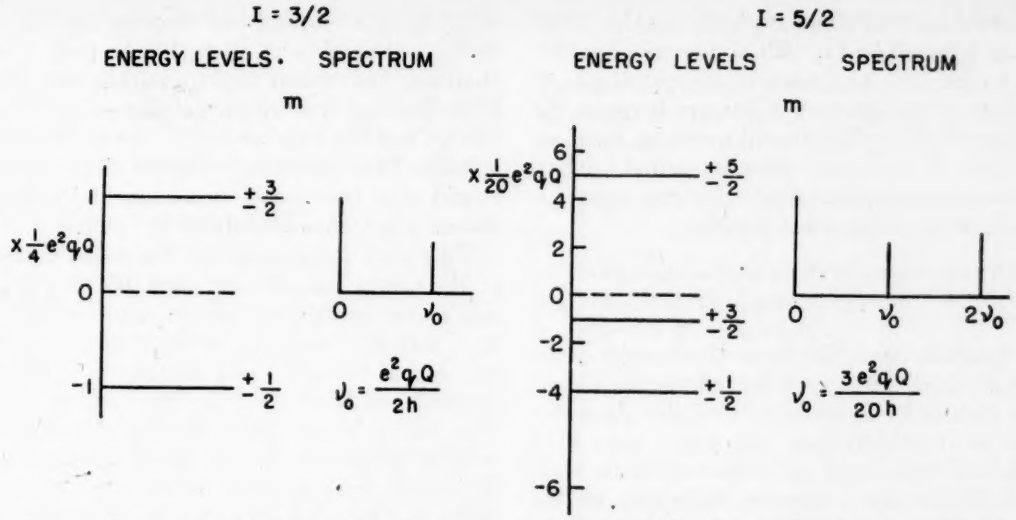

FIG. 11. The energy levels, in zero magnetic field and an axial electric field, for $I=3/2$ and $5/2$, together with the magnetic absorption spectra expected.

of the crystalline field is such that the tensor $\nabla\mathbf{E}$ must be zero, the resonance of I^{127} in a potassium iodide crystal was observed. The line intensity was indicative of the high spin and lack of saturation in the spectrograph indicative of a short relaxation time, although the crystal was probably very free of paramagnetic impurities. In spite of its low g-factor (just $\frac{1}{5}$ that of the proton) an almost noise-free record could be obtained as shown in Fig. 10. This line was found to have a width of only about 600 c.p.s., centered at 5.45 Mc, between points of maximum slope. This is in approximate agreement with the line breadth expected from magnetic dipole-dipole interactions, with the large lattice spacing of the face centered cubic lattice of the I^{127} nuclei. It should be possible, with spin 5/2, for the nucleus to have an electric sixteen-pole moment, corresponding to the terms with $q=4$ in Eq. (2) and an interaction with the cubic potential would give rise to a splitting. Knowledge of the strength of $\partial^4V/\partial z^4$ at the position of the nuclei in the crystal would allow an upper limit to be set on the magnitude of the sixteen-pole moment of I^{127} through the evidence that any splitting must be less than about 200 c.p.s.

An attempt was made to produce an electric quadrupole coupling by applying a strong electric field to polarize the crystal. A thin plate-shaped sample was used and an electric field of about 50,000 volts/cm was applied across it, with no detectable change in the line shape or breadth. A perturbation theory calculation leads to an expected effect less than 1 c.p.s., and proportional to the square of the field. Only in ions with very low lying excited levels would such an effect be large enough to be detectable at fields that could be maintained in a crystal.

V. THE PURE ELECTRIC QUADRUPOLE SPECTRUM

One would expect to be able to find nuclear magnetic resonance, through the transition caused by a rotating magnetic r-f field, without any applied magnetic field, if an electric quadrupole coupling exists. For an axially symmetric potential, the energy levels are then specified by the component of angular momentum, m, taken along the symmetry axis and the levels are given by the formula

$$E_m=\tfrac{1}{4}[e^2qQ/I(2I-1)][3m^2-I(I+1)]. \quad (25)$$

The resulting energy level schemes for $I=5/2$, and $I=3/2$ are shown in Fig. 11, together with the spectra one would expect to find. For spin 5/2 the area of the absorption line at higher frequency to that of the lower line for small signal amplitude would be in the ratio 8:5, corresponding to the 4:5 ratio of the squares of the matrix elements, weighted by the factor of 2 ratio of the Boltzman factors $\exp(-h\nu/kT)$. A single crystal would not be needed for detection of this resonance, but, if the line breadth is only that caused by the magnetic dipole interactions, some information about the magnitude of the interaction to be expected in a given crystal would be almost prerequisite to the discovery of the line. The frequencies for the crystals in which the quadrupole coupling has been found are low (718 and 359 kc in Al_2O_3, for example) and direct observation of these resonances would require special techniques. The available signal-to-noise ratio may be computed by an approach analogous to that in the appendix of reference 3. If a single crystal can be used, with its axis normal to the direction of the oscillating r-f magnetic field, and a small magnetic field along the crystal axis turned on and off, in a square wave fashion, the resonance line may be alternately split into a pair of lines at $\nu_0\pm(\mu/Ih)H$, where ν_0 is the unperturbed zero-field resonance frequency and h is the paraxial magnetic field. Then a spectrometer such as that used in the experiments described above would record a resonance at ν_0 and two oppositely phased resonances of half the amplitude of the first, one at each side of the main one by the fre-

quency interval $(\mu/Ih)H$. The available signal-to-noise amplitude ratio would be Eq. (62) of reference 3 multiplied by a factor $3(I+m)(I-m+1)/I(I+1)(2I+1)$, if the transitions giving rise to the line are between the states characterized by the paraxial quantum numbers $\pm m$ and $\pm(m-1)$. The factor takes account of the fact that only these levels are involved. Thus the signal-to-noise amplitude ratio expression becomes

$$A_s/A_n = V_c^{\frac{1}{2}}Q_0^{\frac{1}{2}}A\zeta h^2\gamma N_0\nu_0^{\frac{1}{2}}T_2^{\frac{1}{2}}(I+m)(I-m+1)/(2I+1)16kT(kTBF)^{\frac{1}{2}}T_1^{\frac{1}{2}}, \quad (26)$$

where all symbols have the same significance as in reference 3. It should also be observed that this same expression, divided by 2, gives the available signal-to-noise ratio for the individual component lines in a strong magnetic field. Thus the line at 719 kc in Al_2O_3 in zero field should have a signal-to-noise ratio for the same sample only about 1/20 as great as that of the central line in the spectrum of Fig. 7(b).

Advantage can be taken, however, of the absence of the magnetic field in that there is then no restriction, from field inhomogeneity requirements, on the size of the sample, and thus on V_c. The gain available here can only be utilized, however, if a spectrometer of as small a noise figure can be made to operate at a correspondingly higher r-f power level, so that the same energy density is obtained in the sample volume.

If a powder is used instead of a single crystal, the same modulation scheme would work except that the line would be smeared out in the half-period that the modulation field was on because of the random orientation of microcrystals with respect to the field. The absorption at ν_0 in the half-period when the modulated field is absent would be smaller than that for a properly oriented crystal by a factor $\frac{2}{3}$ resulting from averaging the square of the component of the r-f magnetic field in the plane normal to a crystal axis over the uniform distribution of orientations of the crystals.

A much higher frequency, and correspondingly stronger resonance, resulting from the electric quadrupole splitting, would be expected in certain molecular crystals composed of molecules such as ICl, CH_3I, and others, where values of e^2qQ are known for the gaseous state from microwave spectroscopy. In ICl, for example, the iodine interaction[27] is 2930 Mc and lines near 879 and 439 Mc would be expected.

An unsuccessful attempt to detect the pure electric quadrupole spectrum of I^{127} in ICl has been made with a c-w oscillator fed into a capacitatively loaded coaxial-line resonator, with tuning provided by variation of the capacity. In this way, a frequency range from about 600 to 1200 Mc was covered. The cavity had a loaded Q of about 600 when operated as a transmission filter feeding a crystal detector. The ICl was contained in a glass doughnut-shaped liner filling the inductive part of the cavity. The r-f oscillator was frequency modulated at 60 c.p.s. by a rotating wire inserted into the oscillator cavity and a swing of about 100 kc peak-to-peak was obtained. The crystal detector output was observed on an oscilloscope synchronized at 60 c.p.s. and r.m.s. noise voltage was less than about 0.1 percent of the detected voltage. Thus resonances sharper than the f-m swing should have been found as a bump in the trace as the system was scanned manually in frequency.

That such a resonance was not found indicated that at the lowest temperature used (90°K) the resonance was either outside the search range or too broad to have sufficient intensity to result in a 0.1 percent absorption. If the latter were assumed to be the cause, an approximate lower limit on the breadth may be set, since the fractional power absorption should be $\Delta P/P_0 = 2Q_L\delta$, where δ is the reciprocal Q of the resonance. The quantity δ is given by Eq. (56) of reference 3, multiplied by $3(I+m)(I-m+1)/I(I+1)(2I+1)$, with $I=m=5/2$, as discussed above, and multiplied by $\frac{2}{3}$ because the sample is a polycrystalline material. Another factor of $\frac{1}{2}$ may be included as an estimate of the filling factor for the sample in the cavity. In this manner, a line breadth of greater than about 100 kc may be estimated to be compatible with the resonance being present in the interval of frequency covered but being undetected.

A possible explanation for the failure to find a resonance in the range is that the line is broader than 100 kc. The broadening to be expected from magnetic dipole interactions is only of the order of magnitude of 1 kc but there exists the possibility that the presence of thermally excited states of torsional oscillation of the diatomic molecules[28] would produce, through the then time dependent electric quadrupole interaction, a very strong relaxation mechanism, with consequent broadening. Such excited states would not necessarily be frozen out at the temperature of liquid nitrogen. A similar broadening would be expected if the diatomic molecules made end for end flips in times less than say 10^{-4} sec. Evidence of such transitions can be obtained from observation of the dielectric dispersion because the ICl molecule has an electric dipole moment.

Evidence of the existence of this dispersion was obtained by placing the doughnut in the center of a short-circuited coaxial line resonator of about seven inches length. From the decrease in Q and the change in the resonant frequency with and without the doughnut containing the ICl, a rough estimate could be made of both the real and imaginary parts of the dielectric constant of the ICl at various temperatures. Because of the presence of the glass container and uncertainty about the density of the ICl in it, the experiment served only to show orders of magnitude. The real part of the dielectric constant appeared to be about 6, and did not change appreciably with temperature. Strong electric absorption was found at 0°C and, as expected, it

[27] Townes, Wright, and Merritt, Phys. Rev. 73, 1334 (1948).

[28] L. Pauling, Phys. Rev. 36, 430 (1930).

decreased rapidly with temperature, becoming indistinguishable from the losses of the resonator itself at −75°C. If the frequency of end-over-end flipping of the molecules is assumed to follow a law of the form $\nu=\nu_0\exp(E/kT)$, one is led to conclude that this cause of broadening should not be severe at liquid nitrogen temperatures.

Recently Dehmelt and Krueger[29] have found the two absorption lines caused by the electric quadrupole splitting for the chlorine isotopes Cl^{35} and Cl^{37} in *trans*$_{1,2}$-dichloroethylene in the region of 35 Mc. They found the lines to be about 10 kc in breadth at 90°K and to broaden as the temperature was raised.[29a] If this breadth is caused by an electric quadrupolar relaxation mechanism, the effect might be about 1000 times larger in the I^{127} resonance in ICl, because of the 30 times larger electric quadrupole coupling. Therefore, the experiment with ICl is about to be tried at liquid helium temperatures. If the existence of such a large electric quadrupole coupling in the crystalline state can be proven, it may be useful for the alignment of nuclei in space at very low temperatures.[30] The fact that the chlorine resonances are near to the frequencies one would expect from the coupling observed in molecules[31] like CH_3Cl is evidence in support of the existence of the larger couplings for nuclei of large electric quadrupole moment.

With a single crystal one would expect to be able to demonstrate the existence of a large electric quadrupole interaction by observation of the resonance in a magnetic field at the normal frequency determined by the g-factor of the nucleus for an odd half-integral spin. The levels $m=\pm\frac{1}{2}$ are degenerate in the absence of a magnetic field with an electric field of axial symmetry. With a magnetic field applied along the symmetry axis, the Hamiltonian is diagonal and the energy difference between the levels $m=\pm\frac{1}{2}$ is simply $\mu H_0/I$ for all relative magnitudes of μH and e^2qQ. If the crystal were rotated, however, so that the field and the axis make an angle θ with respect to one another, one has a much more difficult problem. It is clear that the resulting frequency shift must depend on the relative magnitudes of e^2qQ and μH.

For an axial field and a spin of $\frac{3}{2}$, the problem can be solved in closed form for $\theta=90°$. The non-vanishing matrix elements of the combined electric quadrupole and magnetic interaction, in a scheme with the z direction as the crystal axis are

$$\begin{aligned}
&(\pm\tfrac{3}{2}|\mathcal{H}|\pm\tfrac{3}{2})=-a\pm\tfrac{3}{2}b\cos\theta,\\
&(\pm\tfrac{1}{2}|\mathcal{H}|\pm\tfrac{1}{2})=a\pm\tfrac{1}{2}b\cos\theta,\\
&(\pm\tfrac{1}{2}|\mathcal{H}|\pm\tfrac{3}{2})=(\pm\tfrac{3}{2}|\mathcal{H}|\pm\tfrac{1}{2})=\tfrac{1}{2}3^{\frac{1}{2}}b\sin\theta,\\
&(\pm\tfrac{1}{2}|\mathcal{H}|\mp\tfrac{1}{2})=b\sin\theta,
\end{aligned}\qquad(27)$$

where

$$a=e^2qQ/4,\quad b=\mu H/I.$$

The resulting quartic secular equation has been solved[32] for $\theta=90°$ and the energies of the middle two of the four levels become

$$E_{\pm\frac{1}{2}}=\pm\frac{b}{2}-(b^2\mp ab+a^2)^{\frac{1}{2}}.\qquad(28)$$

Since we are interested in the case $a\gg b$, the radical may be expanded by the binomial theorem and one finds for the energy difference

$$\Delta W_{\frac{1}{2}\leftrightarrow-\frac{1}{2}}\approx 2b\left[1-\frac{3}{16}\left(\frac{b}{a}\right)^2+\cdots\right].\qquad(29)$$

Note that for $a\to\infty$, the line moves to just twice its normal frequency, which is a result previously noted by Ramsey.[33] For a finite value of e^2qQ, the frequency will not be quite doubled. If one denotes by ν_m the frequency for $\theta=0$, $R\nu_m$ the frequency for $\theta=90°$ where $1\leqslant R<2$, and ν_e the electric quadrupole splitting in zero magnetic field, one finds

$$\nu_e=(\tfrac{3}{2})^{\frac{1}{2}}\nu_m/(2-R).\qquad(30)$$

For transitions to be induced by the r-f signal field, it is apparent that the crystal axis should be made normal to both the applied static magnetic field and the r-f magnetic field. A similar effect should result for higher odd-valued half-integral spins but the secular equations may have to be solved by numerical methods. Detection of this resonance would probably also require low temperatures to reduce broadening by thermally excited motions of the molecules.

VI. RELAXATION EFFECTS

It is well recognized that the coupling between the nuclear spin system and lattice vibrations, in a rigid crystal lattice, through the magnetic dipolar interactions of the nuclei, fails to account for the relaxation times commonly found in crystals at room temperature. Instead, most solids in which relaxation times have been studied have been found to contain either some kind of paramagnetic impurity which greatly shortens the relaxation time,[26] or a rotating or jumping constituent nucleus or complex group, also resulting in shortened relaxation time.[34–36]

Several of the crystals used in the experiments described above were probably of very high purity, notably the $NaNO_3$ and the KI crystals, both of which were obtained from the Harshaw Chemical Company. Although relaxation times were not measured, the strength of the iodine resonance in KI was such as to

[29] Dehmelt and Kruger, Naturwiss. [to be published; reported in the European Scientific Notes of ONR, London, 3, 379 (1949)].

[29a] The author wishes to thank Professor H. Kopferman for communicating some details of these results prior to publication.

[30] R. V. Pound, Phys. Rev. 76, 1410 (1949).

[31] Gordy, Simmons, and Smith, Phys. Rev. 72, 344 (1947).

[32] Whitmer, Weidner, Hsiang, and Weiss, Phys. Rev. 74, 1478 (1948).

[33] N. F. Ramsey, Phys. Rev. 74, 286 (1948).

[34] A. M. Sachs, Thesis, Harvard University (1950).

[35] E. H. Turner, Thesis, Harvard University (1950).

[36] R. Newman, J. Chem. Phys. (to be published).

indicate negligible saturation at the level of the spectrograph, whereas the sodium lines in $NaNO_3$ indicated partial saturation. This would indicate that the relaxation time of I^{127} in KI was less than about 0.02 sec. and that of Na^{23} in $NaNO_3$ less than about 0.5 sec. On the other hand, a relaxation time of about two hours was indicated in the Li^7 resonance in $LiNO_3$ from a study of the transient response, previously described, as a function of the time the system was allowed to stand in the magnetic field between observations of the resonance. Although the electric quadrupole moment of Na^{23} is not known, it is probably larger than that of Li^7 and smaller than that of I^{127}. This is substantiated by the fact that no evidence of a large splitting was observed in the transient $LiNO_3$ resonance in contrast with the triple Na^{23} resonance in the isomorphous $NaNO_3$ crystal. Thus one is led to suggest that the thermal relaxation can result from the electric quadrupolar interaction.

Consider a situation in which any quadrupolar splitting of the nuclear resonance in a magnetic field is small compared to the magnetic resonance frequency itself. In Eqs. (16) we see that the electric quadrupole interaction operator has elements corresponding to changes of m by ± 1 and ± 2, as well as the diagonal elements. Vibrations of the lattice result in time dependence of the quantities $(\nabla E)_{\pm 1}$ and $(\nabla E)_{\pm 2}$ and, in analogy to the magnetic dipole interaction discussed in reference 3, one can make a Fourier transformation of these time dependent quantities into their equivalent spectral densities as functions of frequency. In this manner, one finds that the energy in the region of $\pm\nu_0$, where ν_0 is the nuclear resonance frequency in the strong magnetic field, causes non-adiabatic transitions corresponding to $\Delta m = \pm 1$ and that of $(\nabla E)_{\pm 2}$ at $\pm 2\nu_0$ causes transitions corresponding to $\Delta m = \pm 2$. Because a thermal mechanism is involved, downward transitions are weighted more heavily than upward ones by the Boltzmann factor $\exp(h\nu_0/kT)$ and $\exp(2h\nu_0/kT)$ for the changes in $|m|$ of 1 and 2 respectively. Even though there may be no static electric quadrupole interaction, and so no splitting observed, in a field of cubic symmetry in the time average, the field departs from this symmetry during the periods of the lattice vibrations, and a relaxation mechanism is provided. To compute the relaxation times expected, the magnitudes and spectral densities of the functions $(\nabla E)_{\pm 1}$ and $(\nabla E)_{\pm 2}$ must be known. Involved in them are the knowledge of the amplitudes of the lattice vibrations and the shielding effect of the electrons surrounding the nucleus. These will not be dealt with here. Most of the vibrational frequencies are large compared to ν_0. As in the case of the magnetic interaction, because both involve the time dependence of the same functions of θ, ϕ, and r^{-3}, it will be true that a "second-order" effect involving absorption at ν and re-emission at $\nu - \nu_0$ or $\nu - 2\nu_0$, which can operate over the full range of the spectral densities will be the dominant effect.[4]

The relaxation time from this interaction may be estimated by comparison with magnetic case by noting that in its vibration a nucleus varies its distance to a nearby charged ion in the same way as it varies its distance to a nearby nuclear magnetic dipole. Therefore, the magnetic and electric interaction energies for such a pair will be e^2Q/r^3 and μ^2/r^3 respectively. The ratio is simply e^2Q/μ^2 and the ratio of the resulting relaxation times is approximately the square of the interaction energy ratio, $(e^2Q)^2/\mu^4$. For a moderately large value of Q of 10^{-25} cm^2 and a μ of 10^{-23} gauss cm^3, we find the ratio is 6.25×10^4, or the electric quadrupole interaction leads to relaxation times of the order of fractions of seconds if the magnetic one leads to relaxation times of several hours. Because all charged neighbors, and possibly to some extent the electron system of the nucleus itself, can contribute to the quadrupole interaction, instead of only those neighbors having magnetic moments, the ratio should be even larger. Of course, the effects of motions of molecules in molecular crystals considered in the last section might be much larger yet because of the very much larger values of the quadrupole interaction energy.

As further evidence that such an effect is present, consider the spectrum of the cubic alkali-halide crystal NaBr. There are three resonances in a narrow (about 10 percent) region of frequency corresponding to the Na^{23} and the two equally abundant (50 percent each) isotopes Br^{79} and Br^{81}. All three of these nuclei have spins of $\frac{3}{2}$ and electric quadrupole moments. Because of the small differences in their magnetic moments, any relaxation process depending on magnetic interaction should result in nearly equal relaxation times. Such is not the case, as may be seen from Fig. 12, in which the resonances of Na^{23} and Br^{81} are shown at each of three levels of the spectrometer. At 0.12 volt r.m.s. across the coil, the Na^{23} is about double the intensity of the Br resonance, as it should be at a signal level low enough to result is negligible saturation, because this is the abundance ratio. At 0.5 volt r.m.s., however, the Na^{23} line is reduced relatively to the Br^{81} line so that they are nearly equal in amplitude and finally at 1 volt, the Br^{81} line is about twice as intense as the Na^{23} line. Thus an electric quadrupolar relaxation mechanism is indicated and the Na^{23} electric quadrupole interaction is seen to be smaller than that of Br^{81}. It is possible that careful measurement of relative magnitudes of relaxation times of several nuclei in crystals as simple as this could yield valuable information on the relative magnitudes of electric quadrupole moments. Care must be taken to eliminate paramagnetic impurities. This has not been done with the NaBr sample.

The very long relaxation time observed in $LiNO_3$ must be the result of two special situations. First, the smallness of the electric quadrupole moment of Li^7 makes the relaxation from the quadrupole coupling long. Many crystals, such as CaF_2 and LiCl have, however, shorter relaxation times. The F^{19} resonance in

CaF_2 can only be relaxed by magnetic interactions since the spin is $\frac{1}{2}$, and Bloembergen has shown[26] strong correlation between the presence of paramagnetic impurities and the relaxation times in various samples of CaF_2. In crystals such as LiCl, however, there may be present chemically undetectable paramagnetic impurities in the form of F centers, which one might expect to be much less easily produced in $LiNO_3$ and this may be the explanation for the considerably shorter relaxation times commonly observed in LiCl. An investigation of this possibility is being undertaken.

An electric quadrupolar relaxation mechanism seems able to account for the nearly equal intensities of the three Na^{23} lines in $NaNO_3$. This may be understood if one considers the differential equations for the time dependence of the populations of the four levels, for spin $\frac{3}{2}$, in the presence of both a magnetic r-f signal and either a magnetic or electric quadrupolar energy spectrum derived from thermal sources bringing about thermal relaxation.

First consider the case of a magnetic relaxation process. Both the applied signal and the thermal process have matrix elements corresponding to $\Delta m=\pm 1$ and we can write for a signal applied at the $\frac{3}{2}\leftrightarrow\frac{1}{2}$ satellite frequency,

$$\begin{aligned}
\dot{N}_{\frac{3}{2}}&=-(W_{\frac{3}{2}\to\frac{1}{2}}+p_{\frac{3}{2}\to\frac{1}{2}})N_{\frac{3}{2}}+(W_{\frac{1}{2}\to\frac{3}{2}}+p_{\frac{1}{2}\to\frac{3}{2}})N_{\frac{1}{2}},\\
\dot{N}_{\frac{1}{2}}&=(W_{\frac{3}{2}\to\frac{1}{2}}+p_{\frac{3}{2}\to\frac{1}{2}})N_{\frac{3}{2}}-(W_{\frac{1}{2}\to\frac{3}{2}}+W_{\frac{1}{2}\to-\frac{1}{2}}+p_{\frac{1}{2}\to\frac{3}{2}})N_{\frac{1}{2}}\\
&\qquad+W_{-\frac{1}{2}\to\frac{1}{2}}N_{-\frac{1}{2}},\\
\dot{N}_{-\frac{1}{2}}&=W_{\frac{1}{2}\to-\frac{1}{2}}N_{\frac{1}{2}}+W_{-\frac{1}{2}\to-\frac{3}{2}}N_{-\frac{3}{2}}\\
&\qquad-(W_{-\frac{1}{2}\to\frac{1}{2}}+W_{-\frac{1}{2}\to-\frac{3}{2}})N_{-\frac{1}{2}},\\
\dot{N}_{-\frac{3}{2}}&=W_{-\frac{1}{2}\to-\frac{3}{2}}N_{-\frac{1}{2}}-W_{-\frac{3}{2}\to-\frac{1}{2}}N_{-\frac{3}{2}},
\end{aligned}\tag{31}$$

where the W's arise from thermal processes and the p's from the applied signal. These relations can be simplified with the following relationship

$$\begin{aligned}
W_{-\frac{3}{2}\to-\frac{1}{2}}&=W_{\frac{3}{2}\to\frac{1}{2}}=3W,\\
W_{-\frac{1}{2}\to-\frac{3}{2}}&=W_{\frac{1}{2}\to\frac{3}{2}}=3W\exp(h\nu_0/kT)\approx(1+\Delta)3W,
\end{aligned}$$

where $\Delta=h\nu_0/kT$,

$$\begin{aligned}
W_{-\frac{1}{2}\to\frac{1}{2}}&=4W,\quad W_{\frac{1}{2}\to-\frac{1}{2}}\approx(1+\Delta)4W,\\
p_{\frac{1}{2}\to\frac{3}{2}}&=p_{\frac{3}{2}\to\frac{1}{2}}=3p,
\end{aligned}\tag{32}$$

where $p=\frac{1}{4}\gamma^2H_1^2g(\nu)$, and γ, H_1 and $g(\nu)$ have the same significance as in Eq. (4) of reference 3. In this manner one obtains

$$\begin{aligned}
\dot{N}_{\frac{3}{2}}&=W\{-3(1+\Delta+P)N_{\frac{3}{2}}+3(1+P)N_{\frac{1}{2}}\},\\
\dot{N}_{\frac{1}{2}}&=W\{3(1+\Delta+P)N_{\frac{3}{2}}-(7+4\Delta+3P)N_{\frac{1}{2}}+4N_{-\frac{1}{2}}\},\\
\dot{N}_{-\frac{1}{2}}&=W\{4(1+\Delta)N_{\frac{1}{2}}-(7+3\Delta)N_{-\frac{1}{2}}+3N_{-\frac{3}{2}}\},\\
\dot{N}_{-\frac{3}{2}}&=W\{3(1+\Delta)N_{-\frac{1}{2}}-3N_{-\frac{3}{2}}\},
\end{aligned}\tag{33}$$

where $P=p/W$. Assuming a steady state to be maintained as the line is swept through slowly, all terms on the left side may be taken to be zero and one obtains

$$\begin{aligned}
N_{-\frac{3}{2}}&=(1+\Delta)N_{-\frac{1}{2}},\quad N_{-\frac{1}{2}}=(1+\Delta)N_{\frac{1}{2}},\\
N_{\frac{1}{2}}&=[1+\Delta/(1+P)]N_{\frac{3}{2}}.
\end{aligned}\tag{34}$$

With the restriction that $N_{\frac{3}{2}}+N_{\frac{1}{2}}+N_{-\frac{1}{2}}+N_{-\frac{3}{2}}=N$, the total number of the subject nuclei in the sample, we find that the effect of a signal at the line corresponding to the $\frac{3}{2}\to\frac{1}{2}$ transition alters the zero signal population differences only in a second order in Δ for the other two lines but that

$$N_{\frac{1}{2}}-N_{\frac{3}{2}}\approx\frac{N}{4}[1/(1+P)](h\nu/kT)=n_0[1/(1+P)],\tag{35}$$

where n_0 is the equilibrium, zero signal, population difference for all three possible transitions.

A repetition of the above calculation with the signal placed for absorption by the $\frac{1}{2}\to-\frac{1}{2}$ transition gives the same result for the saturation factor of the central line,

$$N_{\frac{1}{2}}-N_{-\frac{1}{2}}\approx n_0[1/(1+P)],\tag{36}$$

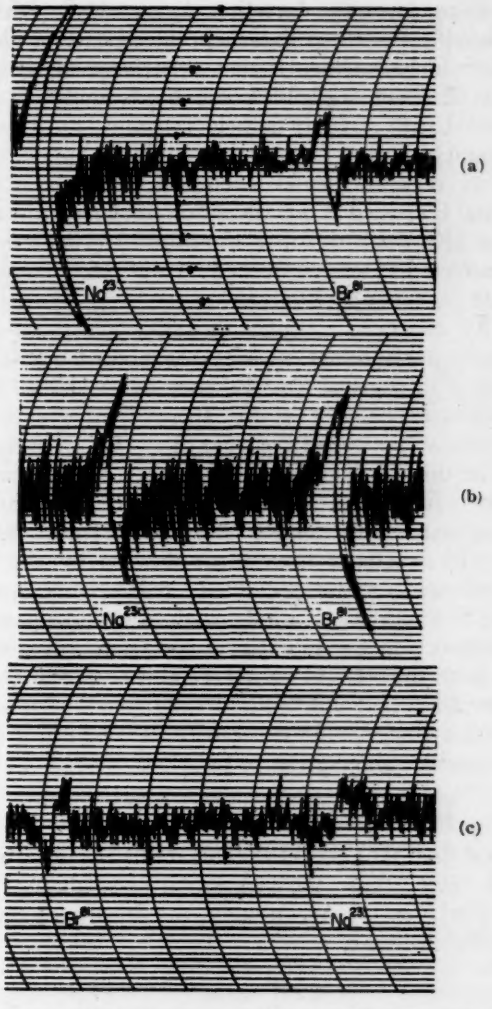

FIG. 12. The Na^{23} and Br^{81} resonances in NaBr show different relaxation times. In (a) and r-f signal level of 0.12 volt is used, in (b) about 0.5 volt, and in (c) about 1 volt across the r-f coil. The tuning capacity was about 150 $\mu\mu$f and with the coil volume of about 5 cc the resulting magnitudes of the rotating magnetic field H_1 are 0.005, 0.02, and 0.04 gauss, respectively.

as a result of the fact that $p_{\frac{1}{2}\leftrightarrow-\frac{1}{2}}=4p$ for this case, assuming the three line shape factors to be identical. The conclusion then is that even for a signal so large that P is not negligible compared to unity, so long as the r-f field strength is held constant, the three lines should be in the same relative amplitudes to one another as at very low signal levels. Furthermore, if a large signal is applied at one transition frequency, the absorption of a small signal at the other two lines would be unaffected so long as $h\nu \ll kT$. A similar argument must hold for other spin values.

By contrast, consider the situation if an electric quadrupole interaction causes the relaxation. The second and third parts of Eq. (16) may be considered as time dependent because of the thermal vibrations of the crystal which cause the quantities $(\nabla E)_{\pm 1}$ and $(\nabla E)_{\pm 2}$ to be time dependent. Non-adiabatic transitions of the spin system can then be produced and transitions downward with $\Delta m=1$ and $\Delta m=2$ must be more heavily weighted than those upward by the factors $\exp(h\nu_0/kT)$ and $\exp(2h\nu_0/kT)$ respectively. Assuming the "second-order" mechanism to be dominant, each frequency in the vibrational spectrum will contribute to both $\Delta m=1$ and to $\Delta m=2$ and one must integrate over the whole spectrum of the crystalline vibrations. In this way, one finds the only non-vanishing upward transition probabilities to be

$$W_{-\frac{1}{2}\to-\frac{3}{2}}=W_{-\frac{3}{2}\to\frac{1}{2}}=W_{\frac{1}{2}\to\frac{3}{2}}=W_{-\frac{3}{2}\to\frac{3}{2}}=W_e \qquad (37)$$

from Eqs. (16) and (18). This result is calculated from the fact that the transition probability $W_{m\to m'} \propto |(m|F|m')|^2$. Accordingly, the downward transition probabilities are

$$\begin{aligned} W_{\frac{3}{2}\to\frac{1}{2}}&=W_{-\frac{1}{2}\to-\frac{3}{2}}\approx(1+\Delta)W_e, \\ W_{\frac{3}{2}\to-\frac{1}{2}}&=W_{\frac{1}{2}\to-\frac{3}{2}}\approx(1+2\Delta)W_e. \end{aligned} \qquad (38)$$

An analysis can be carried out, in a manner analogous to that given above for the magnetic case, to find the steady state populations of the levels in the presence of an applied signal at the frequency of the $\frac{3}{2}\leftrightarrow\frac{1}{2}$ transition, and again at the $\frac{1}{2}\leftrightarrow-\frac{1}{2}$ transition. For the signal applied at the $\frac{3}{2}\leftrightarrow\frac{1}{2}$ transition the results are

$$\begin{aligned} N_{\frac{3}{2}}-N_{\frac{1}{2}}&\approx[1-3P_e/(4+9P_e)][2/(2+3P_e)]n_0, \\ N_{-\frac{1}{2}}-N_{\frac{1}{2}}&\approx[(4+15P_e)/(4+9P_e)]n_0, \\ N_{-\frac{1}{2}}-N_{-\frac{3}{2}}&\approx[1-3P_e/(4+9P_e)]n_0, \end{aligned} \qquad (39)$$

where $P_e=p/W_e$. For the signal applied at the $\frac{1}{2}\leftrightarrow-\frac{1}{2}$ transition, the central line, the steady state populations yield

$$\begin{aligned} N_{\frac{3}{2}}-N_{\frac{1}{2}}&=[1+2P_e/(1+4P_e)]n_0, \\ N_{-\frac{1}{2}}-N_{\frac{1}{2}}&=[1/(1+4P_e)]n_0, \\ N_{-\frac{1}{2}}-N_{-\frac{3}{2}}&=[1+2P_e/(1+4P_e)]n_0. \end{aligned} \qquad (40)$$

Comparison of $N_{\frac{3}{2}}-N_{\frac{1}{2}}$ of Eqs. (39) with $N_{-\frac{1}{2}}-N_{\frac{1}{2}}$ of Eqs. (40) shows that at a given level of signal power, corresponding to a given value of P_e, the satellite line is relatively less saturated than is the central line, and this has the effect of increasing the apparent intensities of the satellite lines relative to that of the central one. Therefore, instead of the 3:4:3 amplitude ratio expected at negligible saturation, the amplitude ratios of the peak absorption itself become 4:3:4 in the limiting case of $P_e \gg 1$. The recorded lines are, of course, not the absorption but a signal derived from it through the modulation of the magnetic field and, for a modulation amplitude approaching the line width, the recorded amplitudes should behave in a manner similar to that of the lines themselves.

Thus the electric quadrupolar relaxation is able to account for the near equality of the three lines in the Na^{23} spectrum in $NaNO_3$. Optimum signal-to-noise ratio results for P_e near unity and, unfortunately, the recorded line strength was not large enough to allow a good test of this theory to be made by observations at lower and higher power levels, because the signal-to-noise ratio became poorer for levels differing in either direction. An interesting test of the theory appears possible by the observation of one line with a low applied signal level while simultaneously heavily saturating another. Thus in Eqs. (39) one sees that saturation of a satellite line should raise the small-signal intensity of the central line to 5/3 its normal intensity. No effect of this kind is present in the purely magnetic case, as is evident from Eqs. (35).

Such an experiment has been carried out. The cylindrical $NaNO_3$ crystal was so filed as to have two parallel flat faces perpendicular to the axis of the crystal and a coil was wound lengthwise around it. Thus, when the crystal was inserted into the r-f coil of the spectrograph, with its axis along the magnetic-field direction, the axis of the new coil was perpendicular to both the magnetic-field direction and the axis of the spectrograph coil. The new coil was resonated with a series condenser of about 15 $\mu\mu$f. This series resonant circuit could be driven with an r-f current in the range of the Na^{23} spectrum from a GR 805-C signal generator. The orthogonality of the two r-f coils was required to minimize their interaction.

The frequency of the auxiliary signal generator was first set exactly at the frequency of the upper satellite line. A record of the central line was made with the spectrograph at a low level (about 0.5 volt r.m.s. across the coil) with the auxiliary signal generator off. The record was then repeated with the auxiliary signal generator supplying 0.2 volt r.m.s. across the series resonant circuit and the central line was found to be approximately doubled in amplitude. On the other hand, when the same experiment was repeated, but at the frequency of the lower satellite line, with the saturating signal still applied at the upper line, the intensity observed with the saturation signal on was only about $\frac{2}{3}$ that found with it off. Finally, the saturation signal was moved over to the frequency of the central line and the effect on the lower satellite observed. This time, to avoid a change in sensitivity of the spectrograph between the two runs from the interaction with the strong applied signal, the auxiliary generator

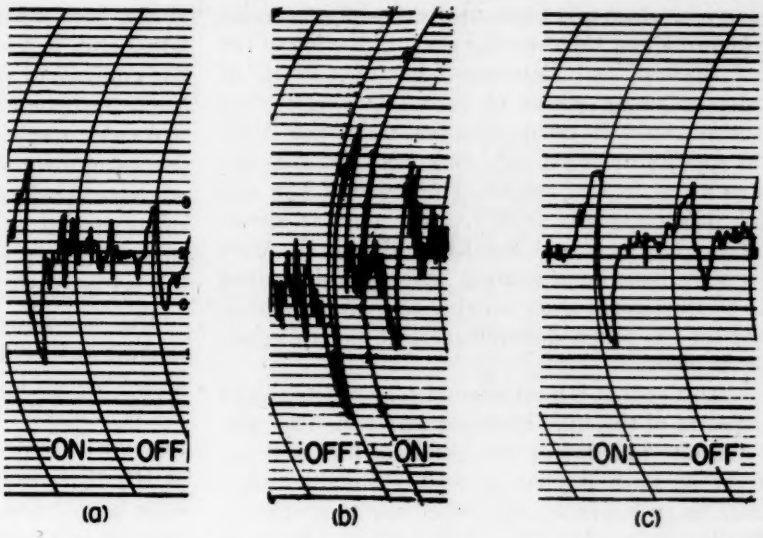

FIG. 13. (a) Record of change in intensity of the central line in the $NaNO_3$ spectrum of Fig. 5 from simultaneously saturating the upper satellite line. The central line with the saturation signal on is about double its normal intensity. (b) The lower satellite line, which is only 2/3 its normal intensity when the saturation signal at the upper satellite is applied. (c) A satellite line is increased to 3/2 times its normal intensity by the application of the saturation signal at the central line.

was kept at a constant level but shifted about 14 kc to be away from the central line on one run. The observed line amplitude with the saturation signal applied was almost exactly $\frac{3}{2}$ times the normal level, in agreement with Eq. (40) for $P_e>1$. The records obtained in these experiments are reproduced in Fig. 13(a), (b), and (c). The agreement of these results with the predictions of Eqs. (39) and (40) must be considered very strong evidence that the thermal equilibrium of the spin system with the lattice is brought about by the electric quadrupole interaction.

VII. CONCLUSIONS

It is seen that the possession of an electric quadrupole moment by a nucleus can strongly affect the nuclear resonance spectrum found. For such nuclei in solids of lower than cubic symmetry a nuclear resonance signal may be expected to be observable in a polycrystalline sample only if the electric quadrupole moment is very small, such as that of Li^7, or in the absence of a static magnetic field. Otherwise the resonance lines are smeared out, as in the Al_2O_3 powder, because of the distribution of directions of crystal axes, and the absorption is very weak. To observe resonances in single crystals, the crystals must be of relatively simple structure to avoid the splitting up of the total absorption into a large number of weak lines. Very large splittings may be expected. This is especially true for molecular crystals in which the splittings may be very large compared to the magnetic energy differences obtainable. It is probable in these cases that relaxation mechanism provided by the thermal oscillations of the molecules about their rest positions are so strong as to greatly broaden the resonance lines and render them detectable only at very low temperatures.

Strong evidence is found for supposing that the principal relaxation mechanism, for nuclei of spin greater than $\frac{1}{2}$, is the electric quadrupole coupling, in ionic as well as molecular crystals of all symmetries, unless considerable paramagnetic impurity is present, as it was in the Al_2O_3 crystal.

Unfortunately, no information concerning the sign of the quadrupole coupling energy is obtained from either the pure electric quadrupole spectrum or that of the combined magnetic and electric interactions, unless temperatures such that $h\nu/kT\sim1$ could be reached. This is in the realm of possibility with such large electric quadrupole interactions as that of I^{127} in ICl, for instance.

As in other cases of observation of electric quadrupole interactions, only a quantity dependent on both the quadrupole moment and its surroundings is determined from these spectra. In the case of fields of axial symmetry the measured quantities can be designated as e^2qQ. The magnitude of Q can be determined only if q can be determined independently. In this connection, ionic crystals, such as the $NaNO_3$ (but preferably simpler ones), may prove useful. Here the ion of the nucleus in question is very often in a singlet-S state and would not be expected to contribute independently to q. The other ions in the crystal, especially if they are monatomic ions, may be treated as point charges and a value of q determined from the relation

$$eq=\sum_j(3\cos^2\theta-1)r_j^{-3}a_je_j,$$

where a_j is the ionic charge. This is not an easy sum to evaluate because it is only slowly convergent. The number of charges in a shell goes as r^2 and their effect as r^{-3}, so that the effect of larger and larger shells falls only as r^{-1}. Convergence results only because the larger shells contain more nearly equal numbers of positive and negative ions more nearly uniformly distributed over the spherical shell. A much more rapidly convergent sum can be obtained if the configuration can be expressed as a small distortion from a cubic or other

symmetry in which q is known to be zero. Little seems to be known about the shielding effect of the ion of the subject nucleus, but determinations of spectra in crystals containing nuclei of known Q would yield information on this point. Unfortunately, the Al_2O_3 crystal appears to be strongly molecular and does not serve as a test in this respect. The value of q in this crystal, using $Q=0.15\pm0.003\times10^{-24}$ cm^2 as determined by Lew[37] is $\pm4.66\pm0.12\times10^{23}$ cm^{-3}. More quantitative data on relaxation times in cubic alkali halide crystals might show whether this effect could be utilized for the rough determination of electric quadrupole moments.

One quantity that is most unambiguously determined from spectra of this kind is the nuclear spin. The principal difficulty in applying this technique for the determination of spins is that of finding suitable single crystals. As an example, some effort has been made to obtain crystals in which the spins of B^{10} and B^{11} could be observed from the structure of their magnetic resonance spectra. Natural crystals containing boron are mostly boro-silicates and are very diluted as samples of boron and, in addition, contain several boron atoms in non-equivalent positions in a unit cell. Borax and similar compounds form crystals containing many water molecules, resulting in dilution of the sample and consequently weak lines. So far a satisfactory crystal has not been obtained. Both the B^{11} and the Na^{23} lines in a single crystal of $Na_2B_4O_7\cdot5H_2O$ have been found to show structure that depends on orientation but it is not yet understood.

The author would like to express gratitude for the interest and encouragement of many of his colleagues in the Lyman Laboratory, especially that of Professor E. M. Purcell. The form of the presentation in the theoretical section has benefited greatly from the work of Dr. R. Bersohn[38] who has treated these and other aspects of the electric quadrupole interaction in solids. Support of a large part of this research by the Society of Fellows at Harvard University is gratefully acknowledged.

[37] H. Lew, Phys. Rev. 76, 1089 (1949).

[38] R. Bersohn, Thesis, Harvard University (1950).

PHYSICAL REVIEW VOLUME 79, NUMBER 4 AUGUST 15, 1950

Quantization of Higher Order Equations

W. THIRRING
Dublin Institute for Advanced Studies, Dublin, Ireland
(Received February 14, 1950)

The prescription for quantization of a field is formulated in a manner such that one gets directly the commutator function, which turns out to be a regularized D function for a field obeying a higher order equation.

I. INTRODUCTION

THE usual prescription for quantization of a field, $\phi_i(x)$, is the following.[1,2] One must write the field equations for $\phi_i(x)$ in Hamiltonian form; that is, one must define a conjugate field, $\pi_i(x)$, in such a way that the equations

$$\begin{aligned}\partial\phi_i(x)/\partial t&=\delta H(x)/\delta\pi_i(x),\\ \partial\pi_i(x)/\partial t&=-\delta H(x)/\delta\phi_i(x),\end{aligned}\tag{1}$$

are equivalent to the field equations. Here δ is the usual variational derivative. $H(x)$ is, as a rule, the energy of the field and is to be expressed in terms of the field $\phi_i(x)$, its spatial derivatives, and the conjugate field $\pi_i(x)$. For quantization one takes for the field non-commutable quantities obeying the commutation relations

$$[\pi_l(\mathbf{x}),\phi_k(\mathbf{x}')]=-i\delta_{lk}\delta(\mathbf{x}-\mathbf{x}').\tag{2}$$

These quantities are now time-independent; the time dependence is associated with the state vector, which varies according to the formula

$$\partial\Psi/\partial t=-i\int H(\mathbf{x})dV\Psi.\tag{3}$$

It is easy to show that the expectation value of the field has then the time dependence which is demanded by the field equation.

If one deals with mutually interacting fields he does not actually use (3) but a much reduced form of this equation. That part of (3) which involves the energy of the non-interacting fields is, as a rule, easily solved and after a canonical transformation in (3) only the interaction energy remains. This transformation makes the field quantities time-dependent according to the vacuum field equation. This representation is then called the interaction representation; it has been applied successfully in the latest developments of quantum electrodynamics.[3-6]

This suggests a reformulation of the quantization prescription in the following manner. One determines the commutator function

$$D_{ik}(x,x')=-i[\phi_i(x),\phi_k(x')]\tag{4}$$

in such a manner that the vacuum field equation, together with the equation,[7]

$$\delta\Psi(\sigma)/\delta\sigma(x)=-iH_{\text{int}}(x)\Psi(\sigma),\tag{5}$$

leads to the correct interaction terms for the field equation in the Heisenberg representation.

This prescription, which is evidently equivalent to the usual one, becomes much simplified if the field equation contains higher derivatives, while the coupling term contains only the field or at most its first derivatives.[8] Quantization of fields with higher derivatives has been performed by several authors,[6,9-12] following the conventional pattern. The formalism thus derived is not only hopelessly complicated but also completely unsuitable for practical calculations, since one does not obtain the explicit space-time dependence of the commutator function (4) and the corresponding associated functions. Recent developments have shown that, using these functions, all calculations become much simpler and more elegant than the conventional methods. In this paper we shall quantize a scalar field following the lines indicated by (4) and (5).

II. QUANTIZATION OF A SCALAR FIELD

We assume the vacuum field equation to be linear, homogeneous, invariant with respect to the Lorentz group, and of finite order. We may then write it in the form

$$\prod_{i=1}^{n}(\Box^2-m_i^2)\phi(x)=0.\tag{6}$$

First we consider the case in which all of the m_i's are different. Equation (6) is derivable from a Lagrangian, L_0, the expression for which is easily available but is not needed here. We assume now, that our field is coupled with another one by the following term in the Lagrangian[13]

$$L=L_0-H_{\text{int}}=L_0-[\phi(x)+\phi^*(x)]\rho(x).\tag{7}$$

[1] W. Heisenberg and W. Pauli, Zeits. f. Physik **56**, 1 (1929).
[2] G. Wentzel, *The Quantum Theory of Wave Fields* (Interscience Publishers, Inc., New York, 1949).
[3] J. Schwinger, Phys. Rev. **74**, 1439 (1948).
[4] J. Schwinger, Phys. Rev. **75**, 651 (1949).
[5] J. Schwinger, Phys. Rev. **76**, 790 (1949).
[6] F. Dyson, Phys. Rev. **75**, 486 (1949).
[7] For a definition of the symbols see reference 3.
[8] We shall avoid the latter possibility since, in order to preserve integrability in Eq. (5), one must add terms to the interaction energy which depend on the direction of the surface, σ.
[9] B. Podolsky and C. Kikuchi, Phys. Rev. **65**, 229 (1944).
[10] T. Chang, Proc. Camb. Phil. Soc. **42**, 133 (1946).
[11] T. Chang, Proc. Camb. Phil. Soc. **44**, 76 (1948).
[12] P. Weiss, Proc. Roy. Soc. **A169**, 102 (1938).
[13] Strictly speaking, our H_{int} is $(-)^{n-1}$ H_{int}, but the sign is irrelevant for our purposes.

If one takes $\phi(x)$ as a meson field, $\rho(x)$ would be the nucleon density. This gives the field equation in the Heisenberg representation. (Heavy print indicates the quantity in Heisenberg representation.)

$$\prod_{i=1}^{n}(\Box^2-m_i^2)\boldsymbol{\phi}(x)=\boldsymbol{\rho}(x). \tag{8}$$

We want now to choose the commutator function

$$D(x,x')=-i[\phi(x),\phi^*(x')] \tag{9}$$

in such a manner that we obtain (8) if we transform $\phi(x)$ from the interaction representation back to the Heisenberg representation. As (9) must be invariant with respect to a displacement of the origin of the coordinate system, D can only depend on the difference of x and x', $D(x,x')=D(x-x')$. It is easy to see that it is not necessary to take a non-vanishing commutator for the field with itself

$$[\phi(x),\phi(x')]=[\phi^*(x),\phi^*(x')]=0.$$

Further, it is evident that $D(x)$ must be an odd invariant solution of the vacuum field equation (6). One can prove that $D(x)$ must be a linear combination of odd invariant solutions of the single operators $(\Box^2-m_i^2)$. The only physically acceptable odd invariant solution of such an operator is the ordinary D function, corresponding to a rest mass m_i. We obtain therefore

$$D(x)=\sum_{i=1}^{n}c_iD_{m_i}(x). \tag{10}$$

The fundamental equation which gives the connection between the derivative of any quantity $F(x)$ in the interaction representation and in the Heisenberg representation is[3]

$$\partial\mathbf{F}(x)/\partial x_\nu=U^{-1}(\sigma)(\partial F(x)/\partial x_\nu)U(\sigma)$$
$$+iU^{-1}(\sigma)\int_\sigma[H(x),F(x')]d\sigma_\nu' U(\sigma). \tag{11}$$

Here U is the unitary operator which performs the transformation between the interaction and the Heisenberg representations. Calculating all successive derivatives of $\boldsymbol{\phi}$ up to the order $2n$ in the Heisenberg representation, we obtain, using (11) and (9), the following conditions for D, in order to make $\boldsymbol{\phi}$ obey (8),

$$\int\partial/\partial x_\mu(\Box^2)^lD(x)d\sigma_\mu=0,\quad l=0,1,2\cdots n-2,$$
$$\int\partial/\partial x_\mu(\Box^2)^{n-1}D(x)d\sigma_\mu=1. \tag{12}$$

The relation $\int(\Box^2)^lD(x)d\sigma_\mu=0$ is automatically fulfilled since D is an odd function vanishing outside the light-cone and σ is a space-like surface. Using (10), and the well-known properties of $D_{m_i}(x)$, Eq. (12) yields

$$\sum c_i=0,\quad \sum c_im_i^2=0\cdots\sum c_im_i^{2(n-2)}=0,$$
$$\sum c_im_i^{2(n-1)}=1. \tag{13}$$

These n equations for the n coefficients c_i are readily solved and give

$$c_i=1/[\prod_{j\neq i}(m_i^2-m_j^2)].$$

Using (12) one deduces further in the usual manner[4] that $\bar{D}(x)=-\frac{1}{2}\epsilon(x)D(x)$ obeys the equation

$$\prod_i(\Box^2-m_i^2)\bar{D}(x)=-\delta(x),\quad \epsilon(x)=x_0/|x_0|. \tag{14}$$

The conditions (13) are Pauli's regularization conditions,[14] which arise here automatically. I have indicated this recently,[15] though in a slightly different form.

If some masses are equal, Eq. (6) can be written as

$$\prod_{i=1}^{n}(\Box^2-m_i^2)^{\alpha_i}\phi(x)=0. \tag{15}$$

There are still

$$k=\sum_{i=1}^{n}\alpha_i$$

independent invariant solutions of (15), namely

$$\frac{\partial^{\rho_i}}{\partial(m_i^2)^{\rho_i}}D_{m_i}(x),\quad \rho_i=0,1,2\cdots\alpha_i. \tag{16}$$

Taking a linear combination of these one can proceed as above and then obtains k equations for the k coefficients. An interesting special case of (15) is the equation obtained with $\alpha_i=2$, $n=1$:

$$(\Box^2-m_1^2)^2\phi(x)=0.$$

Here one gets Feynman's cut-off function[16] as the function

$$D_F(x)=\frac{\partial}{\partial(m^2)}D_{Fm}(x)=\frac{i}{(2\pi)^4}\int\frac{e^{-ipx}}{(p^2-m^2)^2}dp$$

and the exponential potential instead of the Yukawa potential as the time-independent Green function[17]

$$\frac{e^{-mr}}{8\pi m}=\frac{\partial}{\partial(m^2)}\left(-\frac{e^{-mr}}{4\pi r}\right).$$

For a spinor field, $\psi(x)$, one might proceed in a similar manner. We need only take the anticommutator in (4), while the coupling (7) must be bilinear in form, $\bar{\psi}(x)\psi(x)$.

[14] W. Pauli and F. Villars, Rev. Mod. Phys. **21**, 434 (1949).
[15] W. Thirring, Phys. Rev. **77**, 570 (1950).
[16] R. P. Feynman, Phys. Rev. **76**, 749, 769 (1949).
[17] W. Thirring, Phil. Mag. (in the press).

The commutator in (11) is then expressible in terms of the anticommutator

$$[\bar{\psi}(x)\psi(x), \psi(x')] = \bar{\psi}(x)\{\psi(x), \psi(x')\} - \{\bar{\psi}(x), \psi(x')\}\psi(x).$$

This enables one to determine the anticommutator function.

I should like to thank Professor Schrödinger for many valuable discussions in connection with this paper.

Note added in proof:—The squared Klein-Gordon equation was proposed as a meson equation in the meantime by Bhabha (Phys. Rev. **77**, 665 (1950)). For a discussion of the difficulties of field theories with higher order equations see A. Pais and G. E. Uhlenbeck, Phys. Rev. **79**, 145 (1950).

PHYSICAL REVIEW VOLUME 79, NUMBER 4 AUGUST 15, 1950

Generalizations of the Weiss Molecular Field Theory of Antiferromagnetism

P. W. ANDERSON
Bell Telephone Laboratories, Murray Hill, New Jersey

(Received May 8, 1950)

A Weiss field calculation has been carried out for antiferromagnetism in more complicated structures than the usual calculation allows, and has been shown to give results more detailed and more consistent with experimental evidence on the magnetic properties of such structures than does the simpler theory.

I. INTRODUCTION. THE TWO-SUBLATTICE THEORY

A SIMPLE theoretical treatment of antiferromagnetism, the phenomenon of antiparallel ordering of spins in a lattice, has been given by Van Vleck[1] and Néel.[2] This theory is very similar to the Weiss molecular field treatment of ferromagnetism. As Van Vleck points out, it is to a certain extent equivalent in rigor to this treatment; that is, to the first approximation of the Heisenberg theory of ferromagnetism. However, it should be pointed out that the problems encountered in a rigorous quantum theory of antiferromagnetism are greater than those in the ferromagnetic case. For instance, the lowest energy state which one would instinctively write down in this case is not an eigenstate of the Hamiltonian, and indeed even the energy at absolute zero is not correctly given by a molecular field treatment of antiferromagnetism, while the theory of ferromagnetism does not have this difficulty. For further discussion of these problems, the reader is referred to the work of Hulthén;[3] we shall assume here that the molecular field theory is at least adequate in a semiquantitative way, as we shall indeed find it to be.

Van Vleck's theory is quite successful qualitatively; it explains why, above the "Curie temperature," T_c, at which the spins lock in antiparallel, the susceptibility should follow a modified Curie law

$$\chi = C/(T+\theta)$$

with C the usual "free-ion" Curie constant. Below T_c the susceptibility should be slightly field-dependent, but should, for a powder sample, drop to a value two-thirds of the T_c value by $T=0$. The predictions as to C and the susceptibility below the Curie point are roughly correct, but still a third prediction, that $\theta = T_c$, is very poorly satisfied in general. Néel modified the Van Vleck theory by introducing next nearest neighbor spin coupling, which as we shall show can explain some anomalous θ/T_c ratios. However, the main object of the present paper is to show that Néel's procedure is too simple, and that, first, simply from internal consistency Néel cannot explain θ/T_c ratios as large as some of those observed; second, that the simple theory is not applicable to most lattice structures encountered in actual antiferromagnets; and third, that the correct theory, taking into account lattice structure, is more consistent with the experimental results, particularly on θ/T_c. The only difference in principle between the theory here presented and the earlier theories is in the matter of taking into account geometrical lattice structures; the basic approach remains that of the molecular field theory of Weiss.

Van Vleck's theory applies to lattices in which the magnetic ions can be divided into two sublattices, each sublattice having the property that it contains no nearest neighbors of its own members, but all of the nearest neighbors of the members of the other sublattice. Thus if we assume only nearest neighbor interactions, and use an effective field treatment, the effective field on one sublattice is given entirely by the average magnetization of the other sublattice. A typical example of a lattice which can be divided in this manner is the body-centered cubic lattice, in which one can assign the cube corners to one sublattice, the cube centers to the other.

The basic formula of the Weiss field approach is

$$\bar{S} = SB_s(\text{const.} \times H_{\text{eff}}/kT), \quad (1)$$

[1] J. H. Van Vleck, J. Chem. Phys. **9**, 85 (1941). Van Vleck refers to previous papers by Bitter and Néel.
[2] L. Néel, Ann. de Physique **3**, 137 (1948).
[3] L. Hulthén, Arkiv. f. Mat., Astr. o. Fys. **26A**, No. 11 (1938).

where B_s is the Brillouin saturation function for a spin value S. For a simple exposition of the theory we shall need only the expansion of B_s for small values of H:

$$M=\text{const.}\times SB_s(\text{const.}\times H^{\text{eff}}/kT)\cong\gamma H^{\text{eff}}/T, \quad (2)$$

where all the constants are summarized in the symbol γ.

Let us write down the expression for the effective field, under the assumption that the effect of exchange is given by

$$V_{ij}=J\mathbf{S}_i\cdot\mathbf{S}_j, \quad (3)$$

V_{ij} being the interaction energy between spins i and j, J an exchange integral, and $\mathbf{S}_i$ and $\mathbf{S}_j$ the spins of the ith and jth atoms, which are neighbors. The Weiss field method replaces $\mathbf{S}_i$ by $\langle\mathbf{S}_i\rangle_{Av}$, which is proportional to M_i; the interaction then acts as an effective field due to the magnetization of the sublattice containing i. Thus we have two effective fields, one acting on each sublattice.

$$H_1^{\text{eff}}=H_0-\lambda M_2, \quad H_2^{\text{eff}}=H_0-\lambda M_1, \quad (4)$$

or

$$H_i^{\text{eff}}=H_0-\lambda M_j \quad j\neq i.$$

The quantity λ is proportional to the exchange integral J. We may write

$$\mathbf{M}_i=(\mathbf{H}_0-\lambda\mathbf{M}_j)\gamma/T. \quad (5)$$

For the total magnetization we obtain

$$\textstyle\sum_{1,2}\mathbf{M}_i=(2\mathbf{H}_0-\lambda\sum_{1,2}\mathbf{M}_i)\gamma/T \quad (6)$$

and for the susceptibility

$$\chi=\frac{M_{\text{tot}}}{H_0}=\frac{(2\gamma/T)}{1+(\lambda\gamma/T)}=\frac{2\gamma}{T+\theta}\Bigg\}, \quad (7)$$
$$\theta=\lambda\gamma$$

The Curie point can be obtained easily by leaving out $\mathbf{H}_0$ in Eq. (5). The resulting set of homogeneous equations will have a non-zero solution for $\mathbf{M}$ at only one temperature, given by setting the determinant equal to zero.

$$\mathbf{M}_i+(\lambda\gamma/T_c)\mathbf{M}_j=0,$$
$$\begin{vmatrix} 1 & \lambda\gamma/T_c \\ \lambda\gamma/T_c & 1 \end{vmatrix}=0, \quad (8)$$

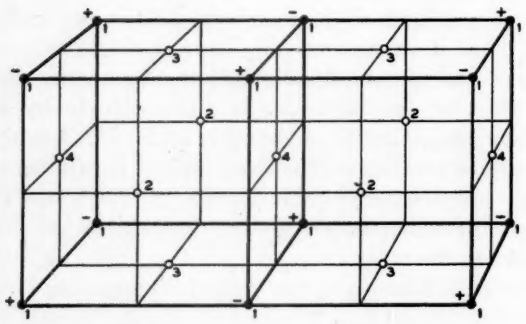

FIG. 1. Division of f.c.c. lattice into four sublattices.

or

$$T_c=\lambda\gamma=\theta. \quad (9)$$

An interesting point which can be made here is that T_c is always proportional to the maximum exchange energy one can obtain by assuming constant magnetization on each of our chosen sublattices. This is true since, in minimizing

$$\mathbf{M}\cdot\mathbf{H}^{\text{eff}} \quad (10)$$
$$=\mathbf{M}\cdot H^{\text{eff}}\cdot(\mathbf{M})$$

(where H^{eff} now can be thought of as a linear operator acting on the quantity $\mathbf{M}$), we solve the eigenvalue problem for the operator H^{eff}, which is essentially the same as solving the secular Eq. (8). The eigenvector $\mathbf{M}$ then gives the best energy arrangement, as well as that holding at T_c. This theorem enables us to check our choice of sublattices in more complicated cases, by trying to find arrangements which will give lower energies than the chosen set can afford.

II. THE FACE-CENTERED CUBIC LATTICE

Many known antiferromagnetics crystallize in structures for which the preceding theory does not hold. The most common of these is the face-centered cubic lattice, which can be divided into no less than four simple cubic sublattices which have the property that the sublattice does not contain nearest neighbors. Figure 1 shows a sublattice division in a face-centered cubic structure; numbers 1, 2, 3, and 4 refer to the various sublattices. It will be seen that each sublattice contains four nearest neighbors in each of the other three. We shall now give a complete treatment of this arrangement.

Refer to the sublattices by the index n, ranging from 1 to 4. The interaction energy is

$$V_{nm}=2ZJ\mathbf{S}_n\cdot\langle\mathbf{S}_m\rangle_{Av} \quad (11)$$

where J is an exchange integral, and Z is the neighbor number, 4 for the f.c.c. lattice. Thus the effective field is

$$\mathbf{H}_n^{\text{eff}}=\mathbf{H}_0-(2JZ/g\beta)\sum_{m\neq n}\langle\mathbf{S}_m\rangle_{Av}, \quad (12)$$

and the magnetization is

$$\mathbf{M}=\tfrac{1}{4}Ng\beta\textstyle\sum\mathbf{S}_n \quad (13)$$

where N is the number of atoms, g the gyromagnetic ratio, and β the Bohr magneton. We have the basic equation of the Weiss theory, corresponding to (2):

$$\bar{S}_n=SB_s(y_n) \quad (14)$$

$$y_n=(Sg\beta/kT)H_n^{\text{eff}}. \quad (15)$$

If we limit ourselves at first to the region above the Curie point, we have small effective fields in general, and we can expand the Brillouin function in (14):

$$SB_s(y)\simeq\tfrac{1}{3}(S+1)y. \quad (16)$$

TABLE I. Constants of antiferromagnetic compounds.

Compound	Crystal structure	Paramagnetic lattice structure	No. of sublattices	θ	T_c	θ/T_c	$\left(\frac{\chi_{T=0}}{\chi_{T=T_c}}\right)$	ϵ/λ (Simple Néel theory)	ϵ/λ (Our theory) Lower	Higher
MnF_2	Rutile	Body-centered rectangular	2	113°	72°	1.57	0.76	0.22		
FeF_2	Rutile	Body-centered rectangular	2	117°	79°	1.48	0.72	0.19		
MnO	NaCl	f.c.c.	4	610°	122°	5.0	$\sim\frac{2}{3}$		0.5	0.5
FeO	NaCl	f.c.c.	4	570°	198°	2.9	0.8		−0.02	+1.07
MnS	NaCl	f.c.c.	4	528°	165°	3.2			0.12	0.91
MnSe[a]	NaCl	f.c.c.	4	~435°	~150°	~3				~1
$FeCl_2$	$CdCl_2$	Hexagonal layer structure	3	48°	23.5°	2.0)?		0.33		
$CoCl_2$	$CdCl_2$	Hexagonal layer structure	3	38.1°	24.9°	1.53)?		0.21		
$NiCl_2$	$CdCl_2$	Hexagonal layer structure	3	68.2°	49.6°	1.37)?		0.16		

[a] The Curie point of MnSe is hard to locate because of a large thermal hysteresis in this crystal, perhaps due to a phase transition (three known crystal structures exist). However, the most reliable data (Shull, private communication) is that given here.

Thus

$$\mathbf{S}_n=\tfrac{1}{3}S(S+1)(g\beta/kT)[\mathbf{H}_0-(2JZ/g\beta)\sum_{m\neq n}\mathbf{S}_m]. \quad (17)$$

Sum from 1 to 4 to get the magnetization:

$$\sum_1^4 \mathbf{S}_n=\tfrac{1}{3}S(S+1)(g\beta/kT)[4\mathbf{H}_0-(6JZ/g\beta)\sum_1^4 \mathbf{S}_n]$$

or,

$$\sum_1^4 \mathbf{S}_n=\frac{\tfrac{1}{3}S(S+1)(4g\beta/kT)H_0}{1+[2JZS(S+1)/kT]}$$

and

$$\left.\begin{aligned}\chi_{T>T_c}&=\frac{M}{H_0}=\frac{\tfrac{1}{3}S(S+1)Ng^2\beta^2/k}{T+S(S+1)2JZ/k}\\&=\text{const.}\times 1/(T+\theta)\end{aligned}\right\} \quad (18)$$

$$\theta=2JZS(S+1)/k. \quad (19)$$

To find the Curie point we use no external field in (17) and find the point at which a non-zero solution of the following equation system is possible:

$$\mathbf{S}_n+\tfrac{1}{3}S(S+1)(2JZ/3kT)\sum_{m\neq n}\mathbf{S}_m=0. \quad (20)$$

The determinant is

$$\begin{vmatrix}1 & x & x & x\\ x & 1 & x & x\\ x & x & 1 & x\\ x & x & x & 1\end{vmatrix}=0,$$

where

$$x=2S(S+1)JZ/3kT.$$

Then

$$(1-x)^3(1+3x)=0$$
$$T_c=2S(S+1)JZ/3k=\theta/3. \quad (21)$$

We can now find the susceptibility at the Curie point, which is

$$\chi_{T_c}=Ng^2\beta^2/8JZ. \quad (22)$$

The behavior of an antiferromagnetic f.c.c. lattice below the Curie point is rather complicated. We can see, by setting $T=T_c$ in (20), that the only restriction on the spins is

$$\sum_n \mathbf{S}_n=0. \quad (23)$$

[It can easily be shown directly that (23) does indeed give the lowest energy for a system of n equally coupled spins.] However, (23) allows, for four spins, an infinite number of possible arrangements of spins, and the actual arrangement will no doubt be determined by next nearest neighbor interactions, anisotropy energy, etc. Since, as we shall see, χ depends on the actual arrangement, it is impossible to find a unique value of χ for $T<T_c$. We can, however, take two simple possible arrangements to show what forms for χ are to be expected.

The first arrangement we choose is that in which two spins are parallel, two antiparallel:

$$\underset{\uparrow}{\mathbf{S}_1}\ \underset{\uparrow}{\mathbf{S}_2}\ \underset{\downarrow}{\mathbf{S}_3}\ \underset{\downarrow}{\mathbf{S}_4}.$$

The spontaneous magnetization can be determined from (14) and (12). Since

$$\sum_{m\neq n}\mathbf{S}_m=-\mathbf{S}_n,$$

$$S_n^0=SB_s[(2SJZ/kT)S_n^0]. \quad (24)$$

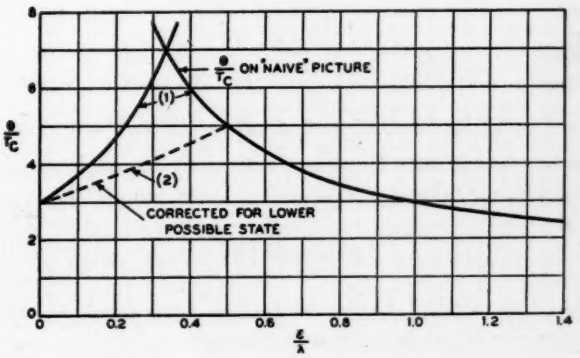

FIG. 2. θ/T_c for f.c.c. lattice with two interactions.

On expansion of all quantities about their values with no external field we have

$$\left.\begin{aligned}\mathbf{H}_n^{\,e}&=\mathbf{H}_n^{\,0}+\delta\mathbf{H}_n\\ \mathbf{S}_n&=\mathbf{S}_n^{\,0}+\delta\mathbf{S}_n\end{aligned}\right\}. \tag{25}$$

Then

$$\delta H_n=H_0-(2JZ/g\beta)\sum_{m\neq n}\delta S_m. \tag{26}$$

We must calculate two cases:

$$\mathbf{H}_0\,\|\,\mathbf{S}_0, \tag{I}$$

$$\mathbf{H}_0\perp\mathbf{S}_0. \tag{II}$$

Case I. Expand the B function in the Taylor's series:

$$S_n^{\,0}+\delta S_n=S[B_s(Sg\beta H_n^{\,0}/kT)+\delta H_n(Sg\beta/kT)B_s']$$

$$\delta S_n=\delta H_n(S^2g\beta/kT)B_s'$$

$$=[H_0-(2JZ/g\beta)\sum_{m\neq n}\delta S_m](S^2g\beta/kT)B_s'$$

add up these equations for $n=1$ to 4:

$$\sum\delta S=\frac{4H_0(S^2g\beta/kT)B_s'}{1+(6JZS^2/kT)B_s'}$$

$$\chi_{II}=\frac{(Ng^2\beta^2S^2/kT)B_s'}{1+(6S^2JZ/kT)B_s'} \tag{27}$$

$$(\chi_{II})_{T=0}=0,\quad \text{since } B_s'(\infty)=0. \tag{28}$$

Case II. Here we simply rotate the spins to be parallel to the effective field which they see. Thus

$$\delta S_n=|S^0|\,\delta H_n/|H_n^{\,0}|=|S_n^{\,0}|\frac{[H_0-(2JZ/g\beta)\sum_{m\neq n}\delta S_m)]}{(2JZ/g\beta)\sum_{m\neq n}S_m^{\,0}}$$

since all δS_n are presumably equal, this leads to

$$\left.\begin{aligned}4\delta S_n&=g\beta H_0/2JZ\\ \chi_\perp&=Ng^2\beta^2/8JZ\end{aligned}\right. \tag{29}$$

so that $\chi_\perp$ is constant, and equal to χ_{T_c} at $T=0$. Since, in averaging over the three directions for an isotropic sample, we take $\chi_\perp$ twice and χ_{II} once, we get

$$(\chi_{tot})_{T=0}=\tfrac{2}{3}\chi_{T_c}. \tag{30}$$

For this particular case we get the same result as that given by Van Vleck's simple theory.

A second case is that in which two pairs of spins are mutually perpendicular.

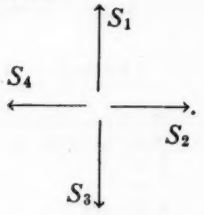

In case $\mathbf{H}_0$ is perpendicular to all four, we obviously get the same result as in the previous case:

$$\chi_\perp=Ng^2\beta^2/8JZ=\chi_{T_c}.$$

In case $\mathbf{H}_0$ is parallel to the plane of the spins, we obtain the following:

$$\delta S_1=\delta S_3,\quad \delta S_2=\delta S_4$$

$$\delta S_1=|S_0|\,\delta H_n/H_n^{\,0}$$

$$=|S_0|[H_0-(2JZ/g\beta)(\delta S_1+2\delta S_2)]/(2JZ/g\beta)|S_0|$$

or

$$2\delta S_1+2\delta S_2=(g\beta/2JZ)H_0.$$

This leads to

$$\chi_{II}=Ng^2\beta^2/8JZ=\chi_\perp=\chi_{T_c}. \tag{31}$$

Thus

$$\chi_{tot}=\chi_{T_c}. \tag{32}$$

Thus there are cases, for the face-centered cubic lattice, for which Van Vleck's relation

$$\chi_{T=0}=\tfrac{2}{3}\chi_{T_c}$$

is not necessarily true.

The comparison of our theory with experiment is shown in Table I. The data on several salts, taken primarily from Bizette's thesis,[4] are presented, together with the crystal structure, the structure of the lattice of paramagnetic ions, and the number of sublattices assuming nearest neighbor interactions. Compounds with the $CdCl_2$ structure are included; here on the simple theory one would assume 3 sublattices and $\theta/T_c=2$, but the data are not clear experimentally, and in addition it is not permissible to apply the Weiss field theory to essentially plane structures.

III. INTRODUCTION OF NEXT NEAREST NEIGHBOR INTERACTION

Néel[2] has explained the large θ/T_c ratios sometimes observed by introduction of a next nearest neighbor interaction ϵ as well as a nearest neighbor interaction λ into the simple two-lattice theory. θ/T_c then becomes $(1+\epsilon/\lambda)/(1-\epsilon/\lambda)$. The ϵ/λ ratios thus computed are given in Table I. We will show later how our theory can be similarly expanded; in most cases quite small ϵ/λ values will suffice.

Some recent results obtained by Shull[5] at Oak Ridge

[4] H. Bizette, thesis (Massonand Company, Paris, 1946). See esp. p. 94.

[5] Private communication.

with neutron diffraction seem at first to contradict the above theory. His measurements are made on MnO. First, a favorable point: he finds, at room temperature ($<\theta$), a pattern corresponding to short-range order, which is physically very reasonable when one examines the mechanism by which θ can become larger than T_c. Namely, the susceptibility (depending on θ) as well as the short-range order should, in first approximation, depend only on the number of neighbors and strength of coupling, whereas T_c is a lattice dependent quantity which measures the lowest energy obtainable with a given lattice. However, the present simple theory cannot give results on short-range order.

The observations of Dr. Shull at low temperatures ($<T_c$) do not confirm our ideas, however. He finds that an unexpected structure is present in which each of the four simple cubic sublattices is arranged antiferromagnetically within itself (as shown by the + and − signs on sublattice 1 in Fig. 1) while the sublattices are either completely uncorrelated, or are correlated in such a way that the spins in one set of (111) planes are all parallel. The neutron diffraction results cannot choose between these structures, nor is it possible to distinguish between them on our theory, as we shall see. We see at once that such a structure does not satisfy our theory, and the primary advantage which our theory has of explaining high θ/T_c ratios without large ϵ/λ ratios has been lost.

Let us see, nonetheless, what our theory does give in case there is a next nearest neighbor interaction. In this case it is necessary to subdivide the lattice still further, dividing each of the 4 sublattices into a + and a − sublattice, as is done in Fig. 1 for sublattice 1. We shall use the simplified notation of the first part of this paper, and work entirely with $T \geq T_c$. Then we can write

$$\mathbf{M}_n^{\pm} = (\gamma/T)H_n^{\pm\text{eff}} \tag{33}$$

and it is easy to see that if we assign an interaction λ to each nearest neighbor contact and ϵ to each next nearest neighbor contact we obtain

$$\mathbf{H}_n^{\pm\text{eff}} = \mathbf{H}_0 - 2\lambda \sum_{m \neq n} (\mathbf{M}_m^{\pm} + \mathbf{M}_m^{\mp}) - 6\epsilon \mathbf{M}_n^{\mp}. \tag{34}$$

We get for the various magnetizations

$$\mathbf{M}_n^{\pm} = (\gamma/T)[\mathbf{H}_0 - 2\lambda \sum_{m \neq n} (\mathbf{M}_m^{\pm} + \mathbf{M}_m^{\mp}) - 6\epsilon \mathbf{M}_n^{\mp}]. \tag{35}$$

To obtain the magnetization we sum over the 8 sublattices:

$$\sum_{n,\pm} \mathbf{M}_n^{\pm} = (\gamma/T)[8\mathbf{H}_0 - 12\lambda \sum \mathbf{M}_n^{\pm} - 6\epsilon \sum \mathbf{M}_n^{\pm}] \tag{36}$$

or,

$$\chi = 8\gamma H_0/[T + 6\gamma(2\lambda + \epsilon)] \tag{37}$$

$$\chi = \text{const.}/(T+\theta), \quad \theta = 6\gamma(2\lambda+\epsilon). \tag{38}$$

To obtain T_c we must solve the secular equation of the following equation system:

$$\mathbf{M}_n^{\pm} + (2\gamma\lambda/T) \sum_{m \neq n} (\mathbf{M}_m^{\pm} + \mathbf{M}_m^{\mp}) + (6\gamma\epsilon/T)\mathbf{M}_n^{\pm} = 0. \tag{39}$$

The secular equation factors as follows:

$$0 = \left(1 - \frac{6\gamma\epsilon}{T}\right)^4 \left(1 + \frac{6\gamma\epsilon}{T} - \frac{4\gamma\lambda}{T}\right)^3 \left(1 + \frac{6\gamma\epsilon}{T} + \frac{12\gamma\lambda}{T}\right).$$

We have two choices for T_c:

$$\left.\begin{aligned} T_{c1} &= 6\gamma\epsilon, \\ T_{c2} &= 4\gamma\lambda - 6\gamma\epsilon. \end{aligned}\right\} \tag{40}$$

Then

$$\left.\begin{aligned} \theta/T_{c1} &= 1 + 2(\lambda/\epsilon), \\ \theta/T_{c2} &= 3(1+\epsilon/2\lambda)/[1 - 3\epsilon/2\lambda]. \end{aligned}\right\} \tag{41}$$

These two values of θ/T_c are plotted as functions of ϵ/λ in Fig. 2 as curve (1). Since we must, of course, always pick the highest value of T_c, or the lowest value of θ/T_c, as the correct one, the solution changes at the point $\epsilon/\lambda = \frac{1}{3}$. We can solve Eq. (36) for the arrangement of M's at the Curie point, and obtain

$$T_{c1}: \mathbf{M}_m^{+} + \mathbf{M}_m^{-} = 0; \text{ no other restriction} \tag{42}$$

$$\left.\begin{aligned} T_{c2}&: \mathbf{M}_m^{+} - \mathbf{M}_m^{-} = 0, \\ &\sum_1^4 \mathbf{M}_m = 0. \end{aligned}\right\} \tag{43}$$

We see that T_{c1} corresponds to Shull's arrangement, which is perfect as far as next nearest neighbors go, but poor for nearest neighbors, while T_{c2} accommodates nearest neighbors but not next nearest neighbors. Thus in the region on the left of Fig. 2, nearest neighbor interaction predominates, while to the right next nearest neighbors are most important.

The case of MnO is not quite so easily accommodated as curve (1) indicates. It is possible to find lower energy configurations than that given by (43). We can see this by observing that if we set (for instance) $\mathbf{S}_1 + \mathbf{S}_2 = 0$ (so that $\mathbf{S}_3 + \mathbf{S}_4 = 0$) the nearest neighbor interaction between 100 planes as a whole vanishes. Thus we may pick a (100) direction, if we like, and change the direction of the spins on each plane at random going along this direction. The next nearest neighbor interaction will actually make it most favorable to change the sign of alternate planes in each sublattice so that the best sublattice structure when nearest neighbors are in control is not that of Fig. 1 but one in which sublattices 1 and 2, 3 and 4 exchange identities every other plane. The energy available now is proportional to $(4\lambda - 2\epsilon)$, rather than to $(4\lambda - 6\epsilon)$ so that, by

our theorem on the relation between T_c and the available energy, we know that the real T_c for the nearest neighbor region is

$$\left.\begin{aligned} T_{c3}&=\lambda(4\lambda-2\epsilon),\\ \text{and}\qquad \theta/T_{c3}&=3(1+\epsilon/2\lambda)/[1-\epsilon/2\lambda].\end{aligned}\right\} \tag{44}$$

This is plotted as the dashed curve (2) of Fig. 2.

It will be seen that $\theta/T_c=5$ is still barely allowed by our theory, but that the ϵ/λ ratio is definitely close to $\frac{1}{2}$ for MnO. The two possible ϵ/λ ratios for all compounds, under our theory, are included in Table I.[6] It is a nice confirmation of our theory that (a) MnO requires a high next nearest neighbor interaction simply because of its θ/T_c value, while Shull's data confirm that next nearest neighbors are furnishing the antiferromagnetic alignment; (b) the theory of superexchange predicts that the next nearest neighbor interaction should increase along the series MnO–MnS–MnSe, as is observed.[7] Shull has shown that MnSe has the "next nearest neighbor" arrangement of MnO, and thus the value $\epsilon/\lambda=1$ is to be preferred.

The reason for the large values of ϵ/λ occurring in the theory must be sought for in a high superexchange[7,8] combined with a large separation of the magnetic ions in the antiferromagnetic crystals, leading to low direct exchange integrals. An examination of Kramers' theory indicates that if the superexchange is due to transitions of p-electrons from the negative to the positive ion (that is, to a partial covalent character of the bonds) the directionality of the superexchange must be that of a p-wave function; i.e., directly through the negative ion to the next nearest neighbor rather than the nearest neighbor. Also, since the other compounds should be expected to be less ionic than MnO, it is probable that their ϵ/λ values are the higher ones, $\cong 1$, rather than the lower ones, as would be more satisfying from a naive picture.

I should like to express my thanks to Drs. C. Kittel, G. H. Wannier, and C. G. Shull for their helpful interest in this work.

[6] It was of interest to carry out the logical extension of the simple Néel two-sublattice theory for high values of the next nearest neighbor interaction: i.e., to divide each sublattice into two sublattices. The result is very like Fig. 2 except that $\theta/T_c>3$ is not allowed in this case. For $\epsilon>\lambda/2$, the sublattices become antiferromagnetic, as in the f.c.c. structure. Thus simply on internal evidence alone the Néel theory cannot explain the θ/T_c ratio in MnO.

[7] P. W. Anderson, Phys. Rev. **79**, 350 (1950).
[8] H. A. Kramers, Physica **1**, 182 (1934).

PHYSICAL REVIEW VOLUME 79, NUMBER 4 AUGUST 15, 1950

μ-Pair Theories and the π-Meson

GREGOR WENTZEL
Institute for Nuclear Studies, University of Chicago, Chicago, Illinois

(Received May 1, 1950)

The μ-pair theory suggests the interpretation of the π-meson as a pair of μ's bound together by a nucleon pair field. Only a non-relativistic description, involving a cut-off in the momentum spaces, is attempted. Various π-meson types, such as are well known from the conventional Yukawa theories, can be constructed, depending on the type of coupling adopted in the interaction Hamiltonian of the pair theory. It appears, however, that only the pseudoscalar coupling, which leads to a pseudoscalar π-meson, is consistent with the experimental data; e.g., on the nuclear scattering of μ's, which indicate that the interaction of μ's with nucleons, at least in such processes, is rather weak. Then, also, the creation of μ-pairs in high energy nuclear collisions is expected to be an infrequent event, compared to the π-creation. Nonetheless, the μ-pair production should furnish a crucial experimental test. Another process predicted is the dissociation of a fast π-meson, passing through matter, into a pair. The existence of heavier mesons, involving more than two μ's, seems likely.

I. INTRODUCTION

As an alternative to Yukawa's theory, the pair theory of nuclear interactions was much discussed some years ago.[1] The great advantage of this kind of theory is that it accounts for the saturation character of the nuclear forces without *ad hoc* assumptions.[2] The present paper is concerned with another implication of the theory. According to μ-pair theories, μ-mesons may be bound together to form composite particles and, in particular, π-mesons may be interpreted as μ-pairs. Thus, a unified picture of both meson specimens seems possible. Heavier mesons may also be foreseen.

It is true that the μ-pair theory has been somewhat discredited lately by the lack of experimental evidence for a strong nuclear interaction of μ-mesons. Even if only pairs of μ's are supposed to interact with nucleons, one expects at least a strong nuclear scattering of

[1] For the literature up to 1944, see W. Pauli and N. Hu, Rev. Mod. Phys. **17**, 267 (1945).
[2] Wigner, Critchfield, and Teller, Phys. Rev. **56**, 530 (1939); G. Wentzel, Helv. Phys. Acta **15**, 111 (1942); A. Houriet, Helv. Phys. Acta **16**, 529 (1943).

μ's,[3] indeed much stronger than has been observed.[4] One way to avoid this difficulty is to assume a particular (pseudoscalar) type of coupling which leads to small matrix-elements for the scattering processes although other matrix-elements are large; for example, those determining the binding energies of compound mesons.

Postponing the further discussion of such questions, we first present the μ-pair theory in a form slightly different from the conventional one. If singly charged "pions"[5] are to be interpreted as μ-pairs, we have to associate a singly charged "muon" with its (hypothetical) neutral counterpart, the "nuon." Consider, then, the four elementary particles, each of spin $\frac{1}{2}$: proton (P), neutron (N), positive muon (μ), and nuon (ν), together with their antiparticles ($\bar{P}$, $\bar{N}$, $\bar{\mu}$, $\bar{\nu}$, to be described according to Dirac's hole theory), coupled by the interaction Hamiltonian

$$\eta \int d^3x (N^* A P)(\mu^* A \nu) + \text{conj.} \tag{1}$$

(the symbols N, P, μ, ν stand for the corresponding spinor field operators, and A is one of the five matrix operators known from β-decay theory). Typical elementary processes described by (1) are:

$$P + \nu \leftrightarrow N + \mu, \tag{1a}$$

i.e., the scattering of nuons or muons by nucleons, with exchange of charge;

$$P \leftrightarrow N + \mu + \bar{\nu}, \tag{1b}$$

i.e., meson pair creation or annihilation by a nucleon;

$$P + \bar{N} \leftrightarrow \mu + \bar{\nu}, \tag{1c}$$

e.g., the annihilation of a nucleon-antinucleon pair into a meson pair. Process (1c) also is the basis for our pion model: A muon and an antinuon combined have a negative self-energy owing to their ability to transform into a proton-antineutron pair and back; this self-energy will be interpreted as the binding energy of the pion. The presence, in our model, of virtual nucleon-antinucleon pairs causing the binding makes for a certain (limited) resemblance to the model proposed by Fermi and Yang.[6]

As to the divergences characteristic of all quantized field theories, since the infinities are even of higher order in pair theories than in Yukawa theories, we shall resort to a primitive cut-off in momentum space because so far no more systematic approach has been worked out. Such a non-relativistic theory will lead necessarily to ambiguities in the interpretation of the theoretical results. For instance, if one calculates the total electric current (space integral of the current density) carried by a pion of momentum $\mathbf{p}$, one finds an expression of the expected form $e\mathbf{p}/m$, but the mass m is not equal to the mass deduced from the energy of the particle at rest, not even in the limit of vanishing $\mathbf{p}$. This kind of difficulty is well known from the Lorentz electron model where the electromagnetic mass calculated from the reaction force differs from the electric rest energy (by a factor 4/3), and is typical for all "extended source" theories. A future theory involving a "universal length" may possibly eliminate such ambiguities. For the time being the least objectionable procedure will be to consider the rest system as a natural frame of reference; in other words, we shall tentatively accept the mass and other quantities, as they are calculated in the rest frame, as the correct ones and shall rely on Lorentz transformations to provide the values for a moving particle.

Even so, there remains the arbitrariness inherent in the cut-off procedure. We shall employ two weight functions $g(p)$ and $G(P)$ for the meson and nucleon momentum, respectively, which may, for instance, be chosen as step-functions:

$$g(p) = \begin{cases} 1 \text{ for } p < k \\ 0 \text{ for } p > k, \end{cases} \qquad G(P) = \begin{cases} 1 \text{ for } P < K \\ 0 \text{ for } P > K. \end{cases} \tag{2}$$

We then have essentially three constants disposable to adapt the theory to the observational data; namely, the coupling constant η in (1), and the two cut-off momenta k, K in (2). Of course, there are several ways to make the theory even more flexible, but it seems that the present experimental knowledge does not require such further complications.

Actually, the parameter k is determined by the range of the nuclear forces, or by the nucleon density in heavy nuclei. Indeed, the two-nucleon potentials, as derived from pair theories, exhibit, for short distances r, a very strong r-dependence (e.g., as r^{-5}) so long as the cut-off is ineffective, and it is the cut-off radius ($\sim 10^{-13}$ cm), or the corresponding cut-off momentum ($\sim 10^{13}$ cm^{-1}), which actually determines the range of the forces.[7] As in this argument the motion of the nucleons is ignored (static approximation), only the cut-off of the mesonic momenta is relevant. We conclude that k, in (2), is to be chosen of the order of magnitude of the mesonic masses. Later we shall see that, similarly, K must be assigned a value close to the nucleonic masses, which seems most adequate in the framework of a non-

[3] J. W. Weinberg, Phys. Rev. **59**, 776 (1941); J. M. Jauch. Helv. Phys. Acta **15**, 221 (1942).

[4] Cf. B. Rossi, Rev. Mod. Phys. **20**, 537 (1948), Section 11.

[5] We adopt the nomenclature introduced by E. Fermi and C. N. Yang, Phys. Rev. **76**, 1739 (1949).

[6] See reference 5. According to the Fermi-Yang theory, a positive pion results from a proton and an antineutron bound together by a strong attractive close distance interaction which is supposed to lead to a binding energy of about 93 percent of the rest energy of the two free nucleons. In our model, because of the smaller masses of the main constituents ($\mu + \bar{\nu}$), the binding energy required is only about 34 percent, which may seem more natural.

[7] A more complete analysis is found in the two last papers quoted in reference 2, where rigorous static solutions (nucleons at rest) are discussed, not only for the two-nucleon problem but also for many nucleons arranged in lattice form. The saturation of the nuclear forces sets in for lattice constants smaller than the cut-off radius.

relativistic theory. Incidentally, it should be noted that the above argument is not invalidated by the fact that, besides the nuclear forces transmitted by the meson-pair field, our theory predicts additional forces of the type familiar from Yukawa theories, transmitted by pions or bound meson pairs.

In pair theories it has been customary to introduce the cut-off in such a way that it amounts to an averaging of every individual field operator in the interaction term over a small region in x-space.[2] Following this procedure we supply the matrix element of the interaction (1) with four form factors of type (2):

$$\eta\delta(\mathbf{P}_0-\mathbf{P}+\mathbf{p}-\mathbf{p}_0)G(P_0)G(P)g(p)g(p_0)\times\sum_\alpha(\mathbf{P}_0\Lambda_0|A_\alpha|\mathbf{P}\Lambda)(\mathbf{p}\lambda|A_\alpha|\mathbf{p}_0\lambda_0). \quad (3)$$

Here, $\mathbf{P}_0\Lambda_0$, $\mathbf{P}\Lambda$, $\mathbf{p}\lambda$, $\mathbf{p}_0\lambda_0$ characterize the momentum and spin states of the neutron, proton, muon, and nuon, respectively. The suffix α has been added to distinguish the components of vectors, tensors, or pseudovectors. Even linear combinations of the five coupling types may be admitted. It should be noted that in application of (3) to antiparticles (holes), $\mathbf{P}_{(0)}$ or $\mathbf{p}_{(0)}$ designate the momentum of the vacant state rather than the particle momentum which is $-\mathbf{P}_{(0)}$ or $-\mathbf{p}_{(0)}$.

II. THE PION MODEL

For the description of the pion at rest we introduce the following probability amplitudes: $f(\mathbf{p}\lambda\lambda_0)$ for the presence of a muon with momentum $\mathbf{p}$ and spin λ and of an antinuon with momentum $-\mathbf{p}$ and spin λ_0 (i.e. the vacant state is to be labeled $+\mathbf{p}\lambda_0$); $F(\mathbf{P}\Lambda\Lambda_0)$ for the presence of a proton with momentum $\mathbf{P}$ and spin Λ and of an antineutron with momentum $-\mathbf{P}$ and spin Λ_0. The interaction (3) couples these probability amplitudes according to the following Schrödinger equation:

$$\begin{aligned}0=&[-\epsilon+(m^2+p^2)^{\frac{1}{2}}+(m_0^2+p^2)^{\frac{1}{2}}]f(\mathbf{p}\lambda\lambda_0)\\&+\eta g^2(p)\sum_\alpha(\mathbf{p}\lambda|A_\alpha|\mathbf{p}\lambda_0)\\&\times\int d^3PG^2(P)\sum_{\Lambda\Lambda_0}(\mathbf{P}\Lambda_0|A_\alpha|\mathbf{P}\Lambda)F(\mathbf{P}\Lambda\Lambda_0),\\0=&[-\epsilon+(M^2+P^2)^{\frac{1}{2}}+(M_0^2+P^2)^{\frac{1}{2}}]F(\mathbf{P}\Lambda\Lambda_0)\\&+\eta G^2(P)\sum_\alpha(\mathbf{P}\Lambda|A_\alpha|\mathbf{P}\Lambda_0)\\&\times\int d^3pg^2(p)\sum_{\lambda\lambda_0}(\mathbf{p}\lambda_0|A_\alpha|\mathbf{p}\lambda)f(\mathbf{p}\lambda\lambda_0).\end{aligned} \quad (4)$$

These equations are not complete because they ignore the existence of virtual intermediate states involving more than one meson and/or nucleon pair. Some of the virtual transitions passing through such states give rise to vacuum and mass renormalization terms only, but there are others which cannot be claimed to be physically meaningless or numerically unimportant. Consider, as an example, the following process involving the virtual creation of both a meson pair and a nucleon pair:

$$(\mu+\bar\nu)\rightarrow(\mu+\bar\nu)+(\bar P+N)+(\mu'+\bar\nu')\rightarrow(\mu'+\bar\nu').$$

Compared with the process treated in (4), *viz.*,

$$(\mu+\bar\nu)\rightarrow(P+\bar N)\rightarrow(\mu'+\bar\nu'),$$

its contribution to the energy is certainly not negligible. However, if one extends the Schrödinger equation accordingly, it turns out that its solutions, for the purposes of our qualitative discussions and rough estimates, are practically equivalent to those of the abbreviated Eq. (4). (The important items are: the structure of the eigenfunction components f, F(5), the general character of the eigenvalue condition (9), and the normalization (11a), neither of which is tangibly altered.) Therefore, studying a more comprehensive Schrödinger equation would mean an unnecessary complication, and the numerical improvement achieved would even remain doubtful at any stage of approximation.

Returning to Eqs. (4), we want to simplify the calculations further by assuming the masses of charged and neutral mesons to be (very nearly) equal:[8]

$$m=m_0, \quad \text{and also} \quad M=M_0.$$

For the free particle energies we write

$$(m^2+p^2)^{\frac{1}{2}}=e(p), \quad (M^2+P^2)^{\frac{1}{2}}=E(P).$$

From the structure of the integral Eqs. (4) it is seen that a solution corresponding to a bound state must have the form:

$$\begin{aligned}f(\mathbf{p}\lambda\lambda_0)&=\frac{g^2(p)}{2e(p)-\epsilon}\sum_\alpha(\mathbf{p}\lambda|A_\alpha|\mathbf{p}\lambda_0)u_\alpha\\F(\mathbf{P}\Lambda\Lambda_0)&=\frac{G^2(P)}{2E(P)-\epsilon}\sum_\alpha(\mathbf{P}\Lambda|A_\alpha|\mathbf{P}\Lambda_0)U_\alpha.\end{aligned} \quad (5)$$

Inserting this into (4), one obtains the following equations for the coefficients u_α, U_α:

$$\mu_\alpha+\eta\sum_\beta C_{\alpha\beta}U_\beta=0, \quad U_\alpha+\eta\sum_\beta c_{\alpha\beta}u_\beta=0, \quad (6)$$

where

$$\begin{aligned}c_{\alpha\beta}&=\int\frac{d^3pg^4(p)}{2e(p)-\epsilon}\sum_{\lambda\lambda_0}(\mathbf{p}\lambda_0|A_\alpha|\mathbf{p}\lambda)(\mathbf{p}\lambda|A_\beta|\mathbf{p}\lambda_0)\\C_{\alpha\beta}&=\int\frac{d^3PG^4(P)}{2E(P)-\epsilon}\sum_{\Lambda\Lambda_0}(\mathbf{P}\Lambda_0|A_\alpha|\mathbf{P}\Lambda)(\mathbf{P}\Lambda|A_\beta|\mathbf{P}\Lambda_0).\end{aligned} \quad (7)$$

[8] Actually, a lower bound for m_0 is set by the requirement that the process $P+\bar\mu\rightarrow N+\bar\nu$, for a negative muon captured in the Coulomb field of any light nucleus, be energetically forbidden. Otherwise this capture process would be much too rapid to permit a β-decay of the negative muon. See V. F. Weisskopf, Phys. Rev. 72, 155 (1947): S. Noma, Prog. Theor. Phys. 2, 159 (1947).

The determinant Δ of Eqs. (6) is a function of the energy parameter ϵ, and the condition

$$\Delta(\epsilon)=0, \quad 0<\epsilon<2m \tag{8}$$

will determine the stationary states (negative eigenvalues of ϵ must be excluded for obvious physical reasons).

As an example let us consider the vector coupling case:

$$A_\alpha=(\alpha, i).$$

The summations in (7) where λ, $\Lambda(\lambda_0, \Lambda_0)$ refer to positive (negative) energy states, can be carried out by the projection operator technique, and, taking spherical symmetry of $g(p)$ and $G(P)$ for granted, one obtains:

$$c_{\alpha\beta}=c_\alpha\delta_{\alpha\beta}; \quad C_{\alpha\beta}=C_\alpha\delta_{\alpha\beta},$$

$$c_1=c_2=c_3=2\int\frac{d^3p g^4(p)}{2e(p)-\epsilon}\left[1-\frac{1}{3}\frac{p^2}{e^2(p)}\right],$$

$$c_4=0,$$

$$C_1=C_2=C_3=2\int\frac{d^3P G^4(P)}{2E(P)-\epsilon}\left[1-\frac{1}{3}\frac{P^2}{E^2(P)}\right],$$

$$C_4=0.$$

Inserting into (6):

$$u_K+\eta C_1 U_K=0, \quad U_K+\eta c_1 u_K=0 \quad (K=1, 2, 3),$$
$$u_4=0, \quad U_4=0.$$

The eigenvalue condition becomes:

$$c_1(\epsilon)C_1(\epsilon)=\eta^{-2}.$$

Since c_1C_1, for $\epsilon<2m$, increases monotonically with increasing ϵ, there is one bound state (of threefold degeneracy) provided that η is chosen such that

$$c_1(0)C_1(0)<\eta^{-2}<c_1(2m)C_1(2m).$$

In particular, one can determine η such that ϵ corresponds to the observed mass of the pion. This composite particle would be a vector meson because u_1, u_2, u_3 transform like vector components under rotations (note that the vectors $\mathbf{u}$ and $\mathbf{U}$ are parallel).

The results for other coupling types are summarized in Table I. The first column lists the five "pure" coupling types (A_α), the second the transformation properties of the u_α or U_α of the resulting bound states. The next two columns refer to the eigenvalue condition which in every case has the general form

$$c(\epsilon)C(\epsilon)=\eta^{-2}, \tag{9}$$

$$\left.\begin{aligned} c(\epsilon)&=2\int\frac{d^3p g^4(p)}{2e(p)-\epsilon}\left[a+b\frac{p^2}{e^2(p)}\right],\\ C(\epsilon)&=2\int\frac{d^3P G^4(P)}{2E(P)-\epsilon}\left[a+b\frac{P^2}{E^2(P)}\right],\end{aligned}\right\} \tag{10}$$

TABLE I. Coupling conditions for composite particles.

Coupling type A	Type of pion	Coefficients in (10) a	b	Pion-nucleon interaction Coupling type	Kemmer[a]
Scalar	Scalar	0	1	Scalar	$H_1{}^a(f_a=0)$
Vector	Vector	1	$-\frac{1}{3}$	Vector	$H_1{}^b(f_b=0)$
Tensor	Vector	1	$-\frac{1}{3}$	Tensor	$H_1{}^b(g_b=0)$
	Axial vector	0	$\frac{1}{3}$	Tensor	$H_1{}^c(f_c=0)$
Pseudovector	Axial vector	0	$\frac{1}{3}$	Pseudovector	$H_1{}^c(g_c=0)$
	Pseudoscalar	1	-1	Pseudovector	$H_1{}^d(f_d=0)$
Pseudoscalar	Pseudoscalar	1	0	Pseudoscalar	$H_1{}^d(g_d=0)$

[a] N. Kemmer, reference 9 (see text for explanation).

with numerical coefficients a and b which are collected in Table I. The last two columns will be explained later.

Both in the tensor and the pseudovector coupling cases, two types of bound states are possible, one of which may, however, be non-existent (if not both). In the tensor case, for instance, the vector pion alone survives if η falls below a certain critical value, whereas the axial vector pion could only exist together with a vector pion of smaller mass ϵ (possibly $\epsilon<0$ which is to be excluded at all events).

If the interaction is a mixture of the pure coupling types, the tensors $c_{\alpha\beta}$, $C_{\alpha\beta}$ (7) may have off-diagonal components, for instance, if A_α and A_β refer to the vector states resulting from the vector and tensor coupling respectively; this coupling gives rise to two modified vector states. The same applies to the two pseudoscalar states listed in the table, whereas the axial vector states happen to remain uncoupled (because of $m=m_0$, $M=M_0$).

For each bound state, once its energy ϵ is known, the Schrödinger-function can be calculated from (6) and (5), except for the normalization constant, which shall be determined by

$$\int d^3p\sum_{\lambda\lambda_0}|f(\mathbf{p}\lambda\lambda_0)|^2+\int d^3P\sum_{\Lambda\Lambda_0}|F(\mathbf{P}\Lambda\Lambda_0)|^2=1. \tag{11}$$

With (5), this reduces to a normalization condition for the "vectors" u and U which has the general form

$$\sum_{\alpha\beta}(d_{\alpha\beta}u_\alpha{}^*u_\beta+D_{\alpha\beta}U_\alpha{}^*U_\beta)=1. \tag{11a}$$

III. PION CREATION

The fundamental process of the Yukawa theory, namely

$$P\leftrightarrow N+\pi, \tag{12}$$

can now be interpreted as a $(\mu+\bar{\nu})$ pair creation, according to (1b), but with the pair particles bound to each other. We can immediately write down the matrix-element for this process in the rest system of the pion for which frame we have above calculated the eigenfunction. Disregarding the F-part which gives only higher order contributions, and supplementing the

f-part with the factor $\delta(\mathbf{p}-\mathbf{p}_0)$ to account for the translational state, we obtain from (3), (5), and (7):

$$H_\pi=\eta G^2(P)\sum_\alpha(\mathbf{P}\Lambda_0|A_\alpha|\mathbf{P}\Lambda)$$

$$\times\int d^3p g^2(p)\sum_{\lambda\lambda_0}f^*(\mathbf{p}\lambda\lambda_0)(\mathbf{p}\lambda|A_\alpha|\mathbf{p}\lambda_0)$$

$$=\eta G^2(P)\sum_\alpha(\mathbf{P}\Lambda_0|A_\alpha|\mathbf{P}\Lambda)(\sum_\beta c_{\alpha\beta}u_\beta)^*,$$

and using (6):

$$H_\pi=-G^2(P)\sum_\alpha(\mathbf{P}\Lambda_0|A_\alpha|\mathbf{P}\Lambda)U_\alpha^*. \tag{13}$$

In H_π, we have omitted the factor $\delta(\mathbf{P}_0-\mathbf{P})$ which only expresses the trivial fact that the nucleon momentum remains unchanged in the rest system of the emitted particle.

Choosing for A one of the pure coupling types, and for U the corresponding scalar, vector, axial vector, or pseudoscalar, according to Table I, one sees immediately that (13) agrees (except for the cut-off factor G^2) with the interaction Hamiltonians currently used in "Yukawa theories." The last two columns of Table I indicate the various interaction types, first in general terms, and then, for the sake of clearer identification, in Kemmer's notation.[9] Of course, the comparison can only be made for the rest system of the pion, while, as explained in the introduction, we assume H_π to transform properly under Lorentz-transformations.

As to the magnitude of the matrix-element (13), the determining factor is the magnitude of U which is given by the normalization condition (11a), combined with (6). Since the coefficients d, D, c, C are strongly dependent on the choice of the cut-off functions g and G, there is no difficulty in adapting the theory to the experimental knowledge; e.g., to the measured cross sections for the production of pions in nucleon-nucleon collisions or by photo-effect.[10] As an example, consider the case of pseudoscalar coupling where the matrix-element for the creation of a pion with momentum $\boldsymbol{\pi}$, in a non-relativistic approximation becomes

$$H_\pi=-(\mathbf{P}_0\Lambda_0|\beta\gamma_5|\mathbf{P}\Lambda)U^*=-((\Lambda_0|\boldsymbol{\sigma}|\Lambda)\cdot\boldsymbol{\pi})U^*/2M.$$

Using the theoretical computations of Feshbach and Lax[11] for the photo-creation cross section, a value $|U|\sim M^{-\frac{1}{2}}$ or slightly larger (in rational units: $\hbar=c=1$) is seen to fit the experimental data,[10] and the same value seems to give the correct order of magnitude for the pion creation by 350-Mev protons.[12] On the other hand, from (11a) and (6), such a $|U|$ value is most naturally obtained by cutting off the nucleon momenta P at $K\sim M$ (certainly $K>M/3$), assuming $k\sim m$ as explained in the introduction.

The pseudoscalar theory is exceptional in that it requires a particularly large $|U|$ value (small K) to compensate the small factor $\pi/2M$ in H_π; in all other theories, $|U|$ should be made a good deal smaller, thus requiring a weaker cut-off ($K>M$). The pseudoscalar theory, however, has been reported to give by far the best agreement with the observed angular and energy distribution of photo-mesons,[13] and emphasis on this theory is also indicated by the analysis of the μ-scattering problem (Section V).

With the known values of the three parameters k, K, and η, or at least their orders of magnitude, further properties of the pion model can be deduced. A comment may be welcome as to the relative weights of the meson-pair and nucleon-pair components (f and F parts) in the pion eigenfunction (see Eq. (11)). Very roughly, one finds for the weight ratio:

$$d|u|^2/D|U|^2=dC/Dc\sim K/k\sim M/m\sim 10.$$

Thus, the pion is predominantly a meson pair, with a comparatively small nucleon pair admixture.

IV. DISINTEGRATION PROCESSES

Since the pion is supposed to be an extended structure, the question will be raised whether it is sufficiently stable against dissociation into two mesons $(\mu+\bar{\nu})$ when passing through matter with high velocity $\mathbf{v}$. In order to examine the effect of the Coulomb field of an atomic nucleus (charge Ze) we transform into the rest frame of the pion where the effective potential is

$$V(\mathbf{r},t)=\frac{Ze}{2\pi^2}(1+\boldsymbol{\alpha}\cdot\mathbf{v})\int d^3g\frac{\exp[i\mathbf{g}\cdot(\mathbf{r}+\mathbf{v}t)]}{g^2-(\mathbf{v}\cdot\mathbf{g})^2}$$

and apply the Born-Dirac approximation. The F-part of the pion eigenfunction is again ignored so that V acts on the charged muon only. Then, the matrix-element for the dissociation of the pion (at rest) into a muon of momentum $\mathbf{p}$ and spin λ, and an antinuon of momentum $-\mathbf{p}_0$ and spin λ_0, becomes

$$\frac{Ze}{2\pi^2}\sum_{\lambda'}\frac{(\mathbf{p}\lambda|1+\boldsymbol{\alpha}\cdot\mathbf{v}|\mathbf{p}_0\lambda')f(\mathbf{p}_0\lambda'\lambda_0)}{|\mathbf{p}-\mathbf{p}_0|^2-(\mathbf{v}\cdot(\mathbf{p}-\mathbf{p}_0))^2}e^{i\omega t}, \tag{14}$$

where

$$\omega=[e(p)+\mathbf{v}\cdot\mathbf{p}]+[e(p_0)-\mathbf{v}\cdot\mathbf{p}_0]-\epsilon.$$

The quantity $\omega(1-v^2)^{-\frac{1}{2}}$ is the energy change in the rest frame of the atomic nucleus. Since $\omega=0$ for the real process, it follows that

$$v|\mathbf{p}-\mathbf{p}_0|\geq\mathbf{v}\cdot(\mathbf{p}_0-\mathbf{p})>2m-\epsilon\quad(\approx 70\text{ Mev})$$

[9] N. Kemmer, Proc. Roy. Soc. **A166**, 127 (1938). See in particular his Eqs. (63a–d), p. 143.

[10] C. Richman, H. Wilcox, Phys. Rev. **78**, 85 (1950); M. Weissbluth, Phys. Rev. **78**, 86 (1950); Peterson, McMillan, and White, Phys. Rev. **78**, 84 (1950).

[11] H. Feshbach and M. Lax, Phys. Rev. **76**, 134 (1949).

[12] T. B. Taylor and G. F. Chew, Phys. Rev. **78**, 86 (1950).

[13] K. A. Brueckner, Phys. Rev. **78**, 84 (1950).

which sets a lower bound to $|\mathbf{p}-\mathbf{p}_0|$, i.e., the total momentum of the two ejected particles, and therefore also to the denominator in (14). Then, remembering that $\int d^3p_0|f(\mathbf{p}_0\lambda'\lambda_0)|^2<1$, according to (11), even if the integration is extended over the entire $\mathbf{p}_0$ space, it is easy to establish an upper limit to the total cross section for dissociation, by comparing it with the cross section for scattering of a muon by the same Coulomb field: Even at energies far above the threshold, the dissociation will be certainly less probable than the wide angle scattering of a 100-Mev muon (cross section $\ll Z^2\times 10^{-29}$ cm^2). The same argument can be used for non-electric (nuclear) interactions. We expect, therefore, that the dissociation $\pi\rightarrow\mu+\bar{\nu}$ will be hard to ascertain experimentally, the more so because of the difficulty of distinguishing it from a scattering process or a $\pi-\mu$-decay.

Another process which might, according to our model, destroy the pion too rapidly is the β-disintegration. Actually, the pion is known to decay after a mean lifetime (at rest) of about 2×10^{-8} sec.,[14] into a muon and a neutral particle, presumably a neutrino, and it is concluded that its mean lifetime against β-decay is at least about 10^{-7} sec. In Fermi's β-theory, the direct transition

$$P\rightarrow N+p+\bar{n} \tag{15a}$$

(p=positron, n=neutrino) is supposed to be an elementary process characterized by the interaction term

$$\eta_\beta\int d^3x(N^*BP)(p^*Bn)+\text{conj.}, \tag{15}$$

similar to (1), where η_β is empirically determined by the lifetimes of β-active nuclei. Then, the matrix-element for the process

$$P+\bar{N}\rightarrow p+\bar{n}$$

is also known, and it is easy to calculate the probability of the decay process

$$\pi\rightarrow p+\bar{n}$$

due to the F-part ($P+\bar{N}$ admixture) of the pion eigenfunction. Indeed, the matrix-element for this process is

$$\eta_\beta\sum_\beta(\mathbf{p}\lambda|B_\beta|\mathbf{p}\lambda_0)\int d^3P\sum_{\Lambda\Lambda_0}(\mathbf{P}\Lambda_0|B_\beta|\mathbf{P}\Lambda)F(\mathbf{P}\Lambda\Lambda_0). \tag{16}$$

One possibility is that the coupling types in (1) and (15) are the same: $B=A$. In this case, (16) can be written, with the help of (5), (6), (7) (and assuming (2)):

$$-(\eta_\beta/\eta)\sum_\beta(\mathbf{p}\lambda|A_\beta|\mathbf{p}\lambda_0)u_\beta.$$

It turns out, however, that this case ($B=A$) must be excluded because the resulting pion lifetime would be too short ($<10^{-9}$ sec.). For the same reason, the following combinations of coupling types are to be excluded:

A, B or B, A=vector, tensor;
A, B or B, A=pseudovector, pseudoscalar.

All other combinations are unobjectionable, giving zero for the matrix element (16). For instance, favoring for A the pseudoscalar, we may consider for B the scalar, vector, or tensor coupling.

An alternative β-theory may be based on the assumption that, instead of (15a),

$$\mu\rightarrow\nu+p+\bar{n} \tag{17a}$$

is the elementary process, so that the nuclear β-decay becomes a two-step process involving (1b):

$$P\rightarrow N+\mu+\bar{\nu}\rightarrow N+p+\bar{n},$$

whereas the pion would disintegrate immediately by $\mu+\bar{\nu}\rightarrow p+\bar{n}$ (f-part). Using B now to denote the coupling type in (17a), the conclusion regarding the objectionable or admissible A, B combinations is the same as above.

The well-known decay of the muon into (at least) three light particles, with a mean lifetime of 2×10^{-6} sec., may also cause a decay of a pion into an antinuon and the three light particles, but this process is, of course, much too slow to compete with the $\pi-\mu$-decay.

As to the latter process which is beyond the scope of this paper, the following comment may be welcome. If the $\bar{\mu}$-capture by light nuclei is interpreted[15] as the transition $P+\bar{\mu}\rightarrow N+\bar{n}$, e.g., described by the interaction term

$$\eta'\int d^3x(N^*A'P)(\mu^*A'n)+\text{conj.}$$

(similar to (1) but with the nuon replaced by the neutrino), this automatically entails the decay of the pion, through its F-part, into a muon and antineutrino ($P+\bar{N}\rightarrow\mu+\bar{n}$). But, again, $A'=A$ and other combinations must be excluded because otherwise the $\pi-\mu$-decay would be too fast, as compared with the measured pion lifetime.[14]

V. NUCLEAR SCATTERING AND PAIR CREATION OF MESONS

Weinberg and Jauch[3] have derived rigorous solutions for the scattering of muons by infinitely heavy nucleons according to the pair theory, assuming scalar or vector coupling. For other coupling types such rigorous solutions are not available because the interaction in the limit of nucleons at rest either involves the nucleon spin (tensor, pseudovector), or vanishes altogether (pseudoscalar). Moreover, the interaction (1) differs from those studied by Weinberg and Jauch in that the elementary process (1a) involves a charge exchange (the proton charge is transferred to the meson) which again prohibits a rigorous (static) solution. We therefore content ourselves with an approximation similar

[14] J. R. Richardson, Phys. Rev. **74**, 1720 (1948); E. A. Martinelli and W. K. H. Panofsky, Phys. Rev. **77**, 465 (1950).

[15] B. Pontecorvo, Phys. Rev. **72**, 246 (1947), see also reference 8.

to the one used in studying the pion (Section II): only states with one nucleon and one meson will be considered, i.e., higher states involving additional pairs will be disregarded. The nucleon velocity need not be small.

Let us consider the process $P+\bar{\mu}\leftrightarrow N+\bar{\nu}$. Introducing the probability amplitude $\varphi(\mathbf{p}\Lambda\lambda)$ for the presence of a proton with momentum $\mathbf{p}$ and spin Λ and of an antimuon with momentum $-\mathbf{p}$ and spin λ, and similarly $\varphi'(\mathbf{p}'\Lambda'\lambda')$ for the presence of a neutron and an antinuon, we obtain a Schrödinger equation of the form

$$0=[-\epsilon^0+E(p)+e(p)]\varphi(\mathbf{p}\Lambda\lambda)+\eta G(p)g(p)\int d^3p'G(p')g(p')\times\sum_{\lambda'\Lambda'}\sum_{\alpha}(\mathbf{p}\Lambda|A_\alpha|\mathbf{p}'\Lambda')(\mathbf{p}'\lambda'|A_\alpha|\mathbf{p}\lambda)\varphi'(\mathbf{p}'\Lambda'\lambda') \quad (18)$$

and a similar equation, with primed and unprimed quantities interchanged. It is convenient to use the relation

$$\sum_{\alpha}(\mathbf{p}\Lambda|A_\alpha|\mathbf{p}'\Lambda')(\mathbf{p}'\lambda'|A_\alpha|\mathbf{p}\lambda)=\sum_{K=1}^{5}g_K\sum_{\alpha}(\mathbf{p}\Lambda|A_\alpha{}^K|\mathbf{p}\lambda)(\mathbf{p}'\lambda'|A_\alpha{}^K|\mathbf{p}'\Lambda')$$

where $A^K(K=1\cdots5)$ stands for any of the pure coupling matrices; the numerical coefficients g_K may be taken from a paper by Fierz.[16] A solution of (18), corresponding to an initial $(P+\bar{\mu})$ state $[\epsilon^0=E(p^0)+e(p^0)]$ may be written as

$$\left.\begin{aligned}\varphi(\mathbf{p}\Lambda\lambda)&=\delta(\mathbf{p}-\mathbf{p}^0)\delta_{\Lambda\Lambda^0}\delta_{\lambda\lambda^0}\\&\quad+\frac{G(p)g(p)}{E(p)+e(p)-\epsilon^0}\sum_{K\alpha}(\mathbf{p}\Lambda|A_\alpha{}^K|\mathbf{p}\lambda)u_\alpha{}^K,\\\varphi'(\mathbf{p}'\Lambda'\lambda')&=\frac{G(p')g(p')}{E(p')+e(p')-\epsilon^0}\\&\quad\times\sum_{K\alpha}(\mathbf{p}'\Lambda'|A_\alpha{}^K|\mathbf{p}'\lambda')v_\alpha{}^K,\end{aligned}\right\}\quad(19)$$

$$\left.\begin{aligned}&u_\alpha{}^K+\eta g_K\sum_{l\beta}c_{\alpha\beta}{}^{Kl}v_\beta{}^l=0,\\&v_\alpha{}^K+\eta g_K\sum_{l\beta}c_{\alpha\beta}{}^{Kl}u_\beta{}^l\\&\qquad=-\eta G(p^0)g(p^0)g_K(\mathbf{p}^0\lambda^0|A_\alpha{}^K|\mathbf{p}^0\Lambda^0),\end{aligned}\right\}\quad(20)$$

$$c_{\alpha\beta}{}^{Kl}=\int\frac{d^3pG^2(p)g^2(p)}{E(p)+e(p)-\epsilon^0}\times\sum_{\lambda\Lambda}(\mathbf{p}\lambda|A_\alpha{}^K|\mathbf{p}\Lambda)(\mathbf{p}\Lambda|A_\beta{}^l|\mathbf{p}\lambda). \quad (21)$$

[16] M. Fierz, Zeits. f. Physik **104**, 553 (1937), Eq. (1.4).

In order that the singularity at $p=p_0$ provide for outgoing waves in ordinary space, ϵ^0 should be given a small, positive imaginary part. φ', of course, represents a scattering with charge exchange, whereas the second term in φ describes the ordinary scattering, the proton and negative muon each retaining their charges.

This method of approximation, when applied to the similar problems treated by Weinberg and Jauch, gives very close agreement with their rigorous results, and there is no reason to doubt its reliability for estimating the cross sections, even in the pseudoscalar coupling case. Agreement with the Born approximation is obtained for $|\eta c_{\alpha\beta}{}^{Kl}|\ll1$. In the first-order Born approximation ($u_\alpha{}^K\to0$) only the scattering with charge exchange remains.

If we wish to retain, for the coupling parameter η and the cut-off momenta k, K, such values as were found compatible with the pion data (Sections II and III), the theory predicts, in general, scattering cross sections roughly a hundred times larger than those observed. As was mentioned in the introduction, this difficulty may be avoided by choosing for A the pseudoscalar $\beta\gamma_5$. To prove this, a Born approximation is sufficient. Indeed, if one expresses the solution of Eqs. (20) as expansions in powers of η, it is easily seen that, owing to certain small matrix elements of $\beta\gamma_5$, the condition

$$\left|\eta\frac{k}{M}\int\frac{d^3pG^2(p)g^2(p)}{E(p)+e(p)-\epsilon^0}\right|\ll1$$

suffices to ensure a rapid convergence of the Born expansion, and this condition is well satisfied for $k\sim m$, $K\sim M$, and η determined by (9), (10). In other words, with respect to the scattering, the coupling (1) may be considered as weak although this is not so for the stationary state problem of the pion (where the coupling strength may be called "intermediate"). The first order approximation leads to the following value for the total scattering cross section:

$$(16\pi^5/3)\eta^2[G(p^0)g(p^0)p^0]^4[E(p^0)+e(p^0)]^{-2}. \quad (22)$$

As mentioned, this value pertains to the scattering with charge exchange, the ordinary scattering having a much smaller probability. Inserting numerical values, one finds that the cross section (22) is quite small except for $p^0\approx k$ where it reaches a peak value of some 10^{-28} cm^2. The experimental data are hardly complete enough to disprove this result.

A phenomenon which should furnish an easier and more decisive observational test is the μ-pair creation in nuclear collisions. Indeed, our theory predicts an immediate correlation between the probabilities for the creation of a $\mu+\bar{\nu}$ pair (free) according to (1b), and for the creation of a pion ($\mu+\bar{\nu}$ bound) according to (12), and this quite independent of the mechanism of excitation. This is a simple consequence of the fact that, in the center of mass system of the mesons, the two

matrix-elements (3) and (13), for $A=\beta\gamma_5$, have the ratio

$$H_{\mu+\nu}/H_\pi=\eta g^2(p)(\mathbf{p}\lambda|\beta\gamma_5|\mathbf{p}\lambda_0)/U^* \qquad (23)$$

which is of the order $|\eta U^{-1}|=|(cC)^{-\frac{1}{2}}U^{-1}|$ (cf. (9), (10)) if $p(=p_0)<k$. The ratio of the cross sections is essentially the square of this constant times the ratio of the meson phase volumina. This latter factor is, of course, strongly energy dependent and makes the pair creation quite insignificant near the threshold. At higher energies the factor $g^2(p)$ in (23) cuts down the momentum space available to the pair particles and causes the μ/π ratio to reach a saturation value of the order $(4\pi/3)k^3|\eta U^{-1}|^2$, i.e., between one and ten percent. The smallness of this numerical value may explain why as yet the experiments have failed to reveal with certainty the creation of muons in high energy nuclear collisions.[17] For 350-Mev protons, the above saturation value should be almost reached, in other words, we expect such protons to produce a few muons per hundred pions. Since most of these muons will be more energetic than those resulting from $\pi-\mu$-decays, it should not be too difficult to test this prediction.

VI. CONCLUDING REMARKS

Of the problems which remain to be examined, those concerning the nuclear forces and the magnetic moments of proton and neutron are the most conspicuous. Here we must consider the contributions of both the pair field and the pion field; they are additive in a first approximation only. A further and more serious complication ensues from the apparent existence of a neutral pion ("neutretto") which one would like to interpret as a bound neutral pair ($\mu+\bar{\mu}$ and/or $\nu+\bar{\nu}$) and which calls for an obvious generalization of the interaction (1). For the problems studied in Sections II to V this is of minor importance (at least the orders of magnitude will be unaffected), but evidently in a problem like the charge dependence of the nuclear forces the effects of neutral pair and pion fields cannot be disregarded.[18] The same complication will encumber the problem of heavier mesons with more than two elementary constituents.[19]

The most objectionable element in our theoretical analysis is the use of the cut-off method which has been taken seriously to the extent that the momentum bounds k and K are postulated to have the same values in all individual applications. Whether this makes sense when viewed in the light of a future more perfect theory is, of course, quite doubtful, and it may be useful to keep some of the possibilities in mind which were discarded above. On the other hand, while no better method is available, it seems encouraging that even when imposing the rather rigid cut-off rules we can obtain a consistent picture of a considerable variety of phenomena which so far is nowhere obviously in conflict with experience.

[17] See for instance, O. Piccioni, Phys. Rev. **77**, 1 (1950); P. H. Fowler, Phil. Mag. **41**, 169 (1950).

[18] See for instance N. Kemmer, Phys. Rev. **52**, 906 (1937), who discusses the charge dependence of forces transmitted by charged and neutral pair fields in terms of isotopic spin operators. In a similar investigations by S. Noma, Prog. Theor. Phys. **3**, 54 (1948), the nuon and the antinuon are assumed to be identical particles, like a Majorana neutrino. The forces due to neutral pions are too well known to call for comments.

[19] To mention one example: Consider the simultaneous creation of 2 pairs: $(\mu+\bar{\nu})+(\nu+\bar{\nu})$; since presumably each two of the four particles attract one another, they may form a particle of "mesonic weight" 4. (The force between μ and ν arises from their ability to exchange a $(P+\bar{N})$ or $(\bar{P}+N)$ pair. Such force might even lead to a bound state $(\mu+\nu)$—different from $\pi=(\mu+\bar{\nu})$ discussed —; but the pair $(\mu+\nu)$ could not be created alone, according to (1).) Most of the compound mesons would be very short-lived due to γ-decay, but metastable states with longer lifetimes may exist.

Letters to the Editor

PUBLICATION of brief reports of important discoveries in physics may be secured by addressing them to this department. The closing date for this department is five weeks prior to the date of issue. No proof will be sent to the authors. The Board of Editors does not hold itself responsible for the opinions expressed by the correspondents. Communications should not exceed 600 words in length.

A Method of Approximation for Cooperative Phenomena

RYOICHI KIKUCHI
Department of Physics, University of Tokyo, Tokyo, Japan
May 4, 1950

A NEW method for approximating the entropy of an order-disorder system having an assigned energy has been developed. By a suitable choice of variables it gives the Bethe-Takagi approximation[1,2] in one case, and the "variation method" introduced by Kramers and Wannier[3] in another. The new method is more intuitive than the latter and is more effective than the quasi-chemical method by Yin-Yuan Li.[4] It can be improved and extended successively.

Two-dimensional square net.—The probability of appearance of a configuration of a cell (a bond, a spin) given on the left column of each part of Fig. 1 is denoted by z_ν, y_ν, or x_ν on the corresponding second column. $\gamma_\nu(\beta_\nu, \alpha_\nu)$ denotes the number of configurations with the same probability z_ν, y_ν, or x_ν. Modifying the method of Takagi[2] for approximating the number of ways of constructing a crystal, the entropy of the system composed of M spins each located at a square net point can be approximated as:

$$S=kM[2\sum_{\nu=1}^{3}\beta_\nu y_\nu \ln y_\nu-\sum_{\nu=1}^{2}\alpha_\nu x_\nu \ln x_\nu-\sum_{\nu=1}^{6}\gamma_\nu z_\nu \ln z_\nu].$$

The energy E is rigorously expressed as

$$E=\tfrac{1}{4}M\sum_{\nu=1}^{3}\epsilon_\nu\beta_\nu y_\nu,$$

where ϵ_ν is the energy of the bond. Minimizing the free energy $F=E-TS$, we get results identical with those obtained by the "variation method" by Kramers and Wannier.[3]

As a by-product it was found that the Kramers-Wannier result[3] for the ordered phase can be simplified as follows: Their Eq. (91.a) can be factorized as

$$\{k^2z^2+(k^4+1)z+k^6\}\{k^4z^2-k^2(k^4-3)z+1\}=0.$$

The true solution is contained in the second factor, which gives

$$\lambda=\{k^6+8k^4-11+(k^4-5)^{\frac{1}{2}}(k^4-1)^{\frac{1}{2}}\}/(2k^6)$$

in place of their Eq. (91.b).

Taking y_ν and x_ν as variables, we can approximate the entropy as

$$S=kM[3\sum_{\nu=1}^{2}\alpha_\nu x_\nu \ln x_\nu-2\sum_{\nu=1}^{3}\beta_\nu y_\nu \ln y_\nu]$$

which gives a result identical with Takagi's[2] and Bethe's.[1]

Simple cubic lattice.—Taking z_ν, y_ν, and x_ν as variables, the entropy of a system with M spins, each located at a simple cubic lattice point, can be approximated as

$$S=kM[9\sum_{\nu=1}^{3}\beta_\nu y_\nu \ln y_\nu-7\sum_{\nu=1}^{2}\alpha_\nu x_\nu \ln x_\nu-3\sum_{\nu=1}^{6}\gamma_\nu z_\nu \ln z_\nu].$$

Minimizing the free energy, we get the following results:

(a). The transition is of the second order and the transition temperature T_t is

$$kT_t/\epsilon=4.6097.$$

(b). The specific heat c_{t+} and c_{t-} on the higher and the lower temperature side respectively at T_t is

$$c_{t+}/k=0.389 \quad \text{and} \quad c_{t-}/k=2.902.$$

(c). Extrapolated, the specific heat for the disordered phase becomes infinite at

$$kT/\epsilon=4.2221.$$

Therefore it might not be in error to infer that the correct transition point T_c would be in the range

$$4.2221<kT_c/\epsilon<4.6097.$$

When we take the probabilities of configurations of a *cubic cell* as variables, we shall have a better approximation, which will be identical with the extension of the "variation method" to the simple cubic case tried by ter Haar and Martin.[5]

Face-centered cubic lattice (Ising model).—Taking as variables the probabilities of configurations of a tetrahedron, we reach the following results:

(a). The transition is of the second order and

$$kT_t/\epsilon=10.0260.$$

(b). $$c_{t+}/\epsilon=0.336 \quad \text{and} \quad c_{t-}/\epsilon=2.789.$$

(c). By the same inference as above we would obtain the following range for the correct transition point, T_c,

$$9.2388<kT_c/\epsilon<10.0260.$$

A more detailed account will be published elsewhere.

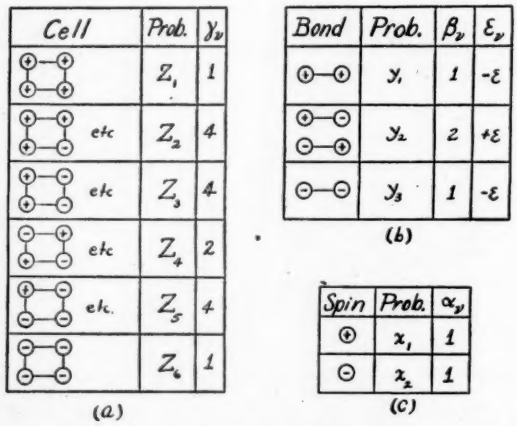

FIG. 1. Configuration scheme.

[1] H. A. Bethe, Proc. Roy. Soc. **A150**, 552 (1935).
[2] Y. Takagi, Proc. Phys. Math. Soc. Japan **23**, 44 (1941).
[3] H. A. Kramers and G. H. Wannier, Phys. Rev. **60**, 252 and 263 (1941).
[4] Yin-Yuan Li, J. Chem. Phys. **17**, 447 (1949); Phys. Rev. **76**, 972 (1949).
[5] D. ter Haar and B. Martin, Phys. Rev. **77**, 721 (1950).

Cosmic Rays Underground

C. M. GARELLI AND G. WATAGHIN
Instituto di Fisica della Università di Torino, Turin, Italy
June 5, 1950

THE variation of cosmic-ray intensity underground has been studied recently by several authors.[1,2] In this note are reported results of calculations of the absorption of π- and μ-mesons underground, performed taking into account the process of creation of π-mesons by direct electromagnetic interaction of charged

incident mesons with nuclei. The cross section for this process was recently calculated by several authors.[3,4] The supplementary energy losses become more important than pair production and bremsstrahlung for energies >100 Bev. Therefore these losses must be taken into account for mesons reaching great depths.

Indeed from the Sneddon and Touschek formulas[3] follows:

$$-dE/dx \cong 3.9\times10^{-7}E(\tfrac{7}{12}\ln 2E-\tfrac{1}{3}) \quad (1)$$

from which, for energies ~100 or 1000 Bev, follows:

$$-dE/dx \cong 3.10^{-6}E \quad (2)$$

where E is the energy, x is the depth in g/cm². We shall assume that, in spite of some approximations made in the deduction of these formulas, (1) gives the right order of magnitude.

For depths $\geqslant$100 m H_2O underground, the cosmic-ray intensity is supposed to be due only to the components deriving from charged mesons of sufficiently high energy. Although slow π-mesons show a strong nuclear interaction and are absorbed with a cross section of the order of the geometrical cross section, there exists no experimental evidence for values of the cross section of π-mesons having energies >100 Bev. Therefore, we shall examine both extreme cases: (1) negligible nuclear absorption for high energy π-mesons; (2) strong nuclear absorption.

Starting from known experimental and theoretical data on the spectrum of π- and μ-mesons at sea level, calculations were performed taking into account the energy losses by ionization, decay, bremsstrahlung, electron pair production and π-meson production. In the first hypothesis (negligible nuclear absorption of energetic π-mesons) the resulting curve is given in Fig. 1 (curve I) and is in satisfactory agreement with the observations (experimental points are marked by ● and ⊙). A similar calculation, assuming a strong nuclear absorption of energetic π-mesons in the matter, gives curve II (Fig. 1), and seems not to be in agreement with the experimental points at great depths (data of Wilson[5] and Nishina and Miyazaki[6,7]).

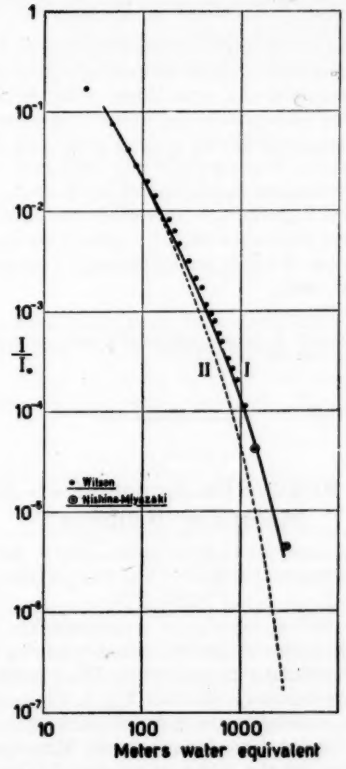

FIG. 1. Curves I and II represent calculated values of relative intensity of cosmic rays as functions of depth. Points ● and ⊙ indicate measured values.

If further experiments confirm this finding one should consider it as an argument showing that the cross section for energetic π-mesons decreases strongly with the energy. This decrease of the cross section signifies a corresponding decrease of the probability of all types of absorption processes for π-mesons. The problem will be discussed elsewhere. Detailed calculations will be published shortly.

[1] K. Greisen, Phys. Rev. **73**, 521 (1948); **76**, 1718 (1949).
[2] S. Hayakawa and S. Tomonaga, Prog. Theor. Phys. **4**, 287 (1949); Phys. Rev. **75**, 1958 (1949).
[3] I. N. Sneddon and B. F. Touschek, Proc. Roy. Soc. (A) **199**, 352 (1949).
[4] E. Strick and D. ter Haar, Phys. Rev. **78**, 68 (1950).
[5] W. C. Wilson, Phys. Rev. **53**, 337 (1938).
[6] Nishina, Sekido, Miyazaki, and Masuda, Phys. Rev. **59**, 401 (1941).
[7] Y. Miyazaki, Phys. Rev. **76**, 1733 (1949).

Energy Levels in C^{12} from $Be^9(\alpha, n)C^{12}$

WILLIAM H. GUIER* AND JAMES H. ROBERTS
Northwestern University, Evanston, Illinois
June 19, 1950

THE neutron energy spectrum from the $Be^9(\alpha, n)C^{12}$ reaction using a thin Po alpha-source and thin Be target was measured by the proton recoil method in Kodak NTA nuclear emulsions. The thin Po source was prepared by the Canadian Radium and Uranium Corporation by plating polonium onto a nickel backing. The beryllium target was prepared by H. Bradner at the Radiation Laboratory of the University of California and was 0.25 mg/cm² thick.

Both the target and source had an effective area of about 4 cm² and were mounted 2.2 cm apart. Photographic plates were mounted about 10 cm from the target in the forward, backward, and 90° positions. To date, 308 acceptable tracks have been measured in the forward direction.

After processing the plates, the tracks were measured with a Leitz Ortholux microscope with an oil immersion objective. Tracks were considered acceptable if they made an angle of 12° or less with the average direction of the incident neutrons. The energies of the recoil protons were determined from their ranges by using the Ilford range energy curves.[1] The neutron energies were found from the proton energies by $E_n = E_p \sec^2\theta$, where θ is the angle between the incident neutron direction and the recoil proton. The intensities must be corrected for the probability of leaving the emulsion[2] and for the $n-p$ scattering cross section. The final distribution is shown in Fig. 1.

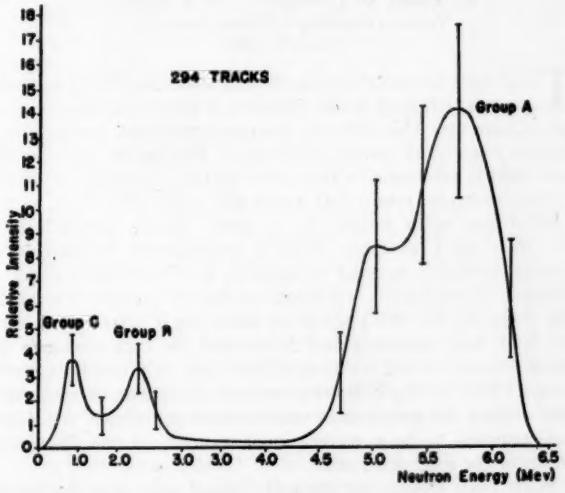

FIG. 1. Neutron spectrum of the reaction $Be^9(\alpha, n)C^{12}$.

Owing to the extended source and target, the energy associated with each neutron group will not be Gaussian in shape. Therefore the usual method of assigning energies could not be used. The method used was to extrapolate the high energy side of each group to the abscissa. Then the probable straggling of the proton in the emulsion was subtracted, giving the neutron energy. For convenience, as is shown in Fig. 1, the groups were labeled. Group A contains 167 tracks while Groups B and C include 127 tracks. The highest energy group corresponding to a transition to the ground state of C^{12} was not analyzed since it contained only 9 tracks. The Q of the reaction for transition to the ground state used was 5.76 Mev. Table I gives the results of the experiment.

TABLE I. Energy levels in C^{12}.

Group	Max. neutron energy (Mev)	Q (Mev)	Energy level in C^{12} (Mev)	Hornyak and Lauritsen[a]
—	—	—	—	—
A	6.30	1.37	4.4±0.2	4.3
B	3.30	−1.34	7.1±0.2	7.1
C	2.35	−2.16	7.9±0.5	—

[a] W. F. Hornyak and T. Lauritsen, Rev. Mod. Phys. **20**, 206 (1948).

Groups A and B agree within the experimental error with those summarized by Hornyak and Lauritsen. The 7.9-Mev level has not been given previously. This level has a large error associated with it since the proton tracks at this energy are short. However, the group appears to be real.

As is shown in Fig. 1, the neutron Group A is very broad, indicating that a level structure may exist here. Using the geometry of the experiment, the width of the group can be calculated and then compared with experiment. If a single level should exist at 4.4 Mev, the calculated width is only about 65 percent of the experimental width.

More tracks are being measured to improve the present poor statistics. Also tracks are being measured in the backward direction, and it is planned to measure tracks in the 90° positions with the hope of obtaining some information on the angular distribution.

* Work done in partial fulfillment of requirements for the Master of Science degree.

[1] Lattes, Fowler, and Cuer, Proc. Phys. Soc. London **59**, 883 (1947).

[2] H. T. Richards, Phys. Rev. **59**, 796 (1941).

Scintillations in Liquids and Solutions

M. AGENO, M. CHIOZZOTTO, AND R. QUERZOLI
Instituto Superiore di Sanita, Rome, Italy
June 23, 1950

THE most severe limitation on the use of scintillation counters in research work is the difficulty of obtaining suitable crystals of large size. This difficulty has much restricted the usefulness of these counters in cosmic-ray research. During the last year we[1] have tried to substitute for the crystal a suitable liquid or solution.[2]

First we made certain that under the action of α-, β- or γ-rays scintillations occur effectively in many liquids and solutions. We then tried to make a rapid quantitative comparison of various specimens in order to establish their usefulness, so far as efficiency is concerned, as a substitute for the crystals of scintillation counters. For this purpose we made use of a string electrometer with leak resistance and determined for each specimen the anode current of the photo-multiplier due to a constant flux of γ-rays (ThC″). The difference between the anode currents with and without the specimen in standardized geometrical conditions was assumed to be a conventional measure of the fluorescing power of the specimen itself.

With pure liquids we generally found very low fluorescing powers, no more than 10^{-1} or 10^{-2} of the fluorescing power of a

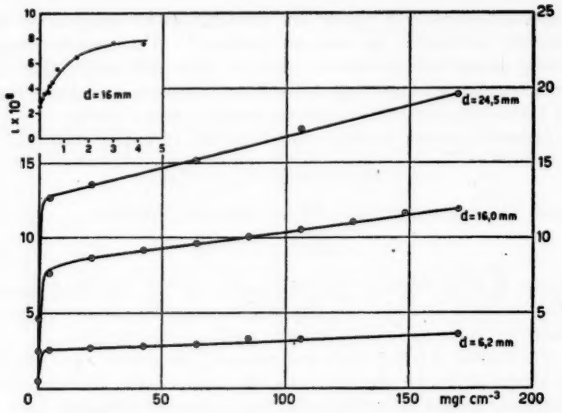

FIG. 1. Fluorescence of naphthalene in xylene.

naphthalene crystal of the same size. However, we obtained more interesting results and higher fluorescing powers with certain solutions. To give an example, the measurements concerning solutions of naphthalene in xylene are plotted in Fig. 1. Concentration values are plotted as abscissa. Different curves refer to different thicknesses of solution.

As one sees, a very low concentration of naphthalene is sufficient to raise the fluorescing power strongly, while an increasing concentration then leaves the fluorescing power almost unvaried. The saturation value increases with the thickness of the solution, which shows that saturation is not due to absorption of light in the solution itself.

We realize that Perrin's law, referring to solutions which show fluorescence excited by ultraviolet light, is not even qualitatively satisfied here. Though we continued our measurements up to the highest concentration obtainable practically, we found no indication of an exponential decrease of the fluorescing power such as is given by Perrin's law.

The trend we found might perhaps be explained by the supposition that some rather stable fluorescing centers are formed in the solution, composed of a naphthalene molecule surrounded by an ordered array of a rather large number of xylene molecules, and that collisions have almost nothing to do with the de-excitation of such centers. This supposition is, supported, moreover, by the fact that liquid naphthalene hardly fluoresces at all, and that in many solvents it produces no increase in the fluorescing power.

Similar results were obtained with other solutions now under examination, some of which have a fluorescing power of the same order as solid crystals.

[1] Ageno, Chiozzotto, and Querzoli, Accad. naz. Lincei **6**, 626 (1949).

[2] Recently Reynolds, Harrison, and Salvini have taken up work on the same idea. (Phys. Rev. **78**, 488 (1950).

On the Relative Production of π^+- and π^--Mesons by Neutrons*

HUGH BRADNER, D. J. O'CONNEL, AND B. RANKIN
Radiation Laboratory, University of California, Berkeley, California
June 20, 1950

WE have made an experiment to determine the relative yields of high energy π^+- and π^--mesons produced by a 270-Mev neutron beam[1] striking a carbon target. The general arrangement used for the investigation is shown in Fig. 1. The target was ½-inch thick graphite, inclined to the neutron beam so that it could be considered as thin for the mesons observed. Mesons with 50 to 65 Mev energy leaving the target at roughly 90° to the incident nuetron beam could be recorded in nuclear emulsions after passing through a ½-inch copper absorber. This energy and angle were

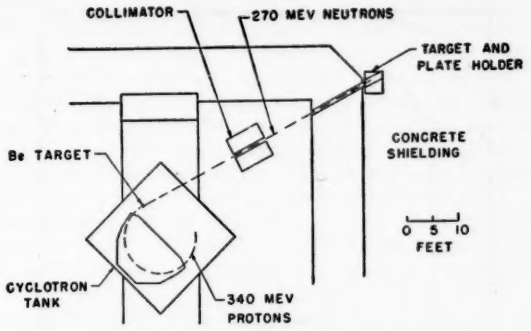

FIG. 1. General arrangement of the apparatus.

chosen to permit comparison with the results from proton beam experiments.[2] A total of 34 π-μ-decays and 307 σ- (star forming) mesons were observed to stop in the emulsions. Assuming that all π^+-mesons undergo π-μ-decay, and that 73 percent of π^--mesons produce stars, this represents a π^+/π^- ratio of $(1/12.6)\pm 12$ percent. Four events classed as π-μ-decays could not be distinguished with certainty from single prong stars with a high energy prong leaving the emulsion. It is not unreasonable that this number of cases should be found in the *307* σ-events observed,[3] and therefore the true π^+/π^- ratio may be approximately 1/14. This is far different from the reciprocal of the 4.8/1 yield found when carbon was bombarded by 345-Mev protons. However, the phase space arguments which Chew[4] employed in discussing the π^+/π^- ratio from protons on carbon can be used to give qualitative agreement with the observed 1/14 ratio. His model would consider the five nucleons which are close together when a neutron enters an α-particle nucleus. If a π^- is created, the remaining particles $(3p, 2n)$ must find room in phase space and at least one proton must be energetic; if a π^+ is created, at least two neutrons of the remaining particles $(1p, 4n)$ must be energetic. The production of π^+ would therefore be inhibited. The magnitude of the effect depends on the energy available to the nucleons, and Chew's arguments would predict a ratio of the order of 1/10 to 1/20 for 50- to 60-Mev mesons.

* This work was done under the auspices of the AEC.
[1] Kelly, Leith, and Wiegand, (to be published).
[2] H. Bradner and S. B. Jones, Phys. Rev. **78**, 90 (1950). C. Richman and H. Wilcox, Phys. Rev. **78**, 85 (1950).
[3] F. Adelman, Phys. Rev. **78**, 86 (1950).
[4] G. Chew and J. L. Steinberger, Phys. Rev. **78**, 497 (1950).

The Excited Nuclear State of Be^7 *

GEORGE D. FREIER AND T. F. STRATTON
University of Minnesota, Minneapolis, Minnesota
AND
L. ROSEN
Los Alamos Scientific Laboratory, Los Alamos, New Mexico
June 16, 1950

RECENT work[1-5] has established the existence of one or more excited levels in Be^7 lying within 1 Mev of the ground state. Neutrons from the $Li^7(p, n)Be^7$ reaction should then occur in energy groups corresponding to reactions leaving Be^7 in the ground state or in an excited level.

200μ Ilford G5 emulsions and 100μ Ilford C2 emulsions were mounted 8 cm from a Li target and at 0° with the incident proton beam. The Li target had 35-kev stopping power at the threshold of the reaction. Protons of 3.49-Mev energy from the Minnesota electrostatic generator then bombarded the target for a period of several hours. Neutrons entering the emulsion produce recoil protons so the $E_p = E_n \cos^2\alpha$, where α is the angle between the direction of the incident neutron and the direction taken by the knock-on proton. In order to obtain the cleanest possible results the coordinates of the track end points were measured, and only those tracks were accepted which made an angle of 10° or less with the direction of the proton beam. Processing of the emulsion causes shrinkage by a factor of 2.5, requiring correction of the dip measurement by this amount.

The G5 plates were read at Minnesota and the C2 plates at Los Alamos. The histogram shown in Fig. 1 is a composite of the results and shows no disagreement between observers. It represents over 600 tracks, with histogram widths of 100 kev. The position of the maximum of a group was estimated by fitting a Gaussian curve to the peak and accepting the center of this curve as the corresponding energy of the neutron group. In this fashion one finds the energy of the neutrons for the reaction leaving Be^7 in the ground state to be 1.80 Mev, and those leaving Be^7 in an excited level to be 1.34 Mev. The computed energy for the neutrons leaving Be^7 in the ground state is 1.80 Mev, in coincidence

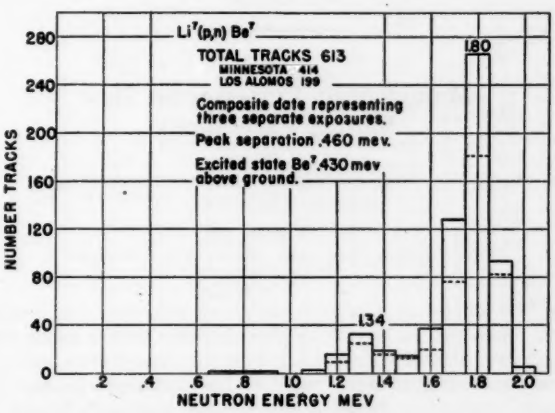

FIG. 1. Histogram showing the number of tracks as a function of the neutron energy in Mev. This histogram was made with 100-kev intervals. The height of the dotted peaks are results from measurements made at Minnesota while the remaining height of the peak shows the results from measurements made at Los Alamos.

with the observed peak, and indicates a good check with the Ilford range energy curve.[6] The best estimates of the middle of the neutron peaks were made from 50-kev width histograms of the Minnesota data.

Only two neutron groups were observed with a peak separation of 460 ± 15 kev. The difference in the Q values for the reactions leading to the ground state and to the excited state of Be^7 is 428 ± 15 kev in agreement with previous experimenters.[2-5] There is no evidence for the existence of the two other states reported by Grosskreutz and Mather,[1] which would correspond to neutron energies of approximately 1.6 Mev for the Be^7 state reported 200 kev above the ground state and 1.0 Mev for an excited level 700 kev above the ground level. With the resolution obtained in this experiment one could not detect a low intensity group of neutrons corresponding to the Be^7 nucleus remaining in an excited state 200 kev above the ground state.

The only correction found to be necessary in order to compare the relative intensities of the groups was for the variation of (n, p) scattering cross section with energy; actually, measuring the coordinates of the track end points places the same requirements on any length track and so puts no emphasis on the shorter tracks. Correction for the different probability of leaving the emulsion for different length tracks was found to be negligible. Applying the correction for (n, p) cross section one finds that the ratio of Be^7 left in the excited state to that left in the ground state is 0.10 ± 0.03.

Plates were also exposed at distances of 4 cm and 18 cm to check the inverse square law from our neutron source. Background runs with no lithium on the tantalum backing were made with

photographic plates, BF_3 counters, and pulse ionization chambers. They all registered an intensity of less than ½ percent of the intensity with the lithium target in place. A survey of competing processes which might produce results such as appear here was made. Available information on the mass of Be^6 eliminates the possibility of the reaction $Li^6(p, n)Be^6$ for protons of 3.5-Mev energy. The (n, p) reaction cross sections of constituents of the emulsions are all quite low compared with the (n, p) scattering cross section. When this consideration is combined with the fact that the relative abundance of hydrogen is 3.0 times that of any other constituent, the contribution of the reaction processes can be eliminated as a source of error.

* This work was supported by the joint program of the ONR and AEC.
[1] J. C. Grosskreutz and K. B. Mather, Phys. Rev. **77**, 580 (1950).
[2] Brown, Chao, Fowler, and Lauritsen, Phys. Rev. **78**, 88 (1950).
[3] T. Lauritsen and R. G. Thomas, Phys. Rev. **78**, 88 (1950).
[4] Johnson, Laubenstein, and Richards, Phys. Rev. **77**, 413 (1950).
[5] B. Hamermesh and V. Hummel, Phys. Rev. **78**, 73 (1950).
[6] Lattes, Fowler, and Cuer, Proc. Phys. Soc. London **59**, 883 (1950).

Multiplication Processes for Slow Moving Dislocations

F. C. FRANK
H. H. Wills Physical Laboratory, University of Bristol, England
AND
W. T. READ, JR.
Bell Telephone Laboratories, Murray Hill, New Jersey
June 19, 1950

THE slip bands observed in the plastic deformation of crystals show that on a typical active slip plane there is about 1000 times more slip than would result from the passage of a single dislocation across the plane. One of us[1] has discussed a possible explanation of this in terms of the reflection and multiplication of dislocations which have acquired velocities approaching that of sound. However, there is as yet no available experimental evidence for fast dislocations and a recent theoretical estimate[2] of the energy dissipated by a moving dislocation indicates that under typical conditions the terminal velocity of a dislocation is less than 1/10 that of sound. Though neither of these arguments is conclusive, they do attach special importance to the recognition of processes whereby a dislocation can produce a large amount of slip and can multiply without first acquiring a large kinetic energy.

We shall first show by purely topological reasoning how an unlimited amount of slip could result from the motion of a single dislocation line *ABC*, Fig. 1. For simplicity we assume that the horizontal planes are the only active slip planes. The segment *AB* is therefore fixed. A small shear stress applied on the slip plane

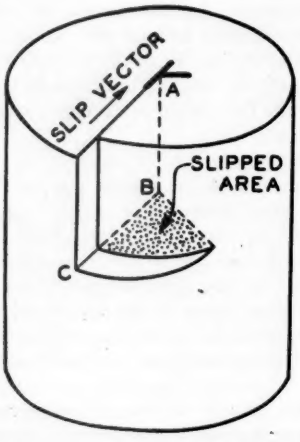

FIG. 1. Slip resulting from the motion of a single dislocation line.

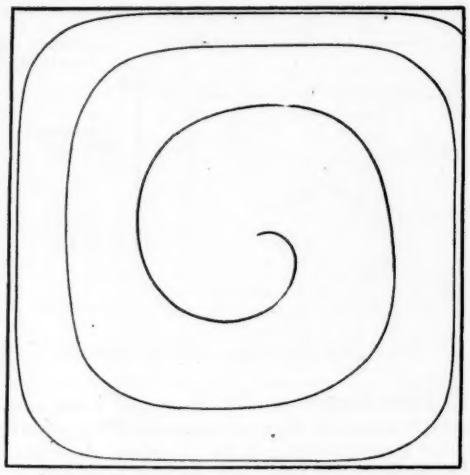

FIG. 2. Spiral form resulting from a square boundary at which slip is prevented.

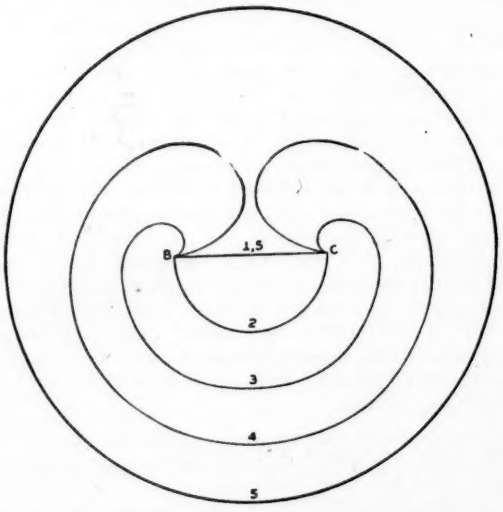

FIG. 3. Generation of successive closed loops of dislocation line.

and in the slip direction will cause the line *BC* to sweep around like the hand of a clock producing slip of one atomic spacing per revolution.

Actually the line *BC* would not remain radial but would develop into a rotating spiral, owing to the higher angular velocity of the innermost portion. The quantitative treatment of the problem is strictly analogous to the theory of crystal growth[3] except that, when the spiral has many turns, a correction must be made for the mutual repulsion between successive turns. If slip is prevented at the boundary (as could occur in a polycrystal), the spiral would reach an equilibrium state, as is illustrated in Fig. 2 for the case of a square boundary.

Another process closely analogous to crystal growth and leading not only to continued slip but also to the generation of successive closed loops of dislocation line is illustrated in Fig. 3. The segment *BC* of a dislocation line lies in the active slip plane, the other parts of the line lying outside of the plane so that the points *B* and *C* are fixed. A suitable applied shear stress will cause *BC* to curve as shown and to generate dislocation loops at essentially the same rate as turns of the spiral were generated in the previous case. The minimum stress at which this will occur is determined by the distance *BC* and is approximately the rigidity modulus divided by the distance *BC* in lattice spacings. At a smaller stress some thermal activation will be required.

It remains to show why dislocations should have portions lying in particular glide planes and pass out of these glide planes at particular points. This is to be expected if dislocation lines have lower energy in particular crystallographic planes. A theory of the reduction in energy can be given for the particular cases of the close packed planes in h.c.p. and f.c.c. metals in terms of dissociation into "extended dislocations."[4] These metals are the ones for which slip on particular planes is most characteristic.

It is necessary for the mechanism we have described that the end points *B* and *C* should be anchored at least in some degree. This anchoring may be provided in various ways in dislocation networks, the simplest example being that in which *BC* is one side of a rectangular dislocation loop *ABCD*, the Burgers vector being normal to the plane of the loop. The stress which causes the motion of *BC* in Fig. 3 produces an opposite motion of *AD*, with no net force on *AB* and *CD*. In many cases (e.g., probably the hexagonal metals) the lower mobility of dislocations in planes of less than closest packing may suffice to anchor the points *B* and *C*.

[1] F. C. Frank, Report of a Conference on the Strength of Solids (Physical Society, London, 1948), p. 46.
[2] G. Liebfried, Zeits. f. Physik **127**, 344 (1950).
[3] F. C. Frank, Discussions of the Faraday Society **5**, 67 (1949).
[4] R. D. Heidenreich and W. Shockley, Report of a Conference on the Strength of Solids (Physical Society, London, 1946), p. 71.

Prismatic Dislocations and Prismatic Punching in Crystals

FREDERICK SEITZ
University of Illinois, Urbana, Illinois
June 27, 1950

SMAKULA and Klein[1] have made indentation studies of the plastic properties of the thallous halides with use of a small conical punch and have found that the strain may be transmitted in a highly concentrated manner through distances large compared to the dimensions of the hole made by the punch. The system behaves as if the punch pushed cylinders or prisms of the material as rigid units in the direction of the axis of the prism, the length of the prism being relatively large compared with the sectional dimensions. The prisms appear to be polygonal in cross section, the planar surfaces being slip planes (110) and the direction of the axis being slip directions (100). A single prism having square cross section is pushed if the indenter is pressed in the (100) direction, but two and three are pushed, respectively, if the load is applied in the (110) and (111) directions. In the latter two cases the axes of the prisms lie in different, symmetrically equivalent, (100) directions. We shall term this *prismatic punching*.

In order to explain these rather dramatic results it is only necessary to discover a mechanism whereby dislocation rings of the type shown in Fig. 1 may be generated in such a way that their contours coincides with the cross section of the prismatical punchings and the Burgers vector is along the axis of the prism. If a dislocation ring of this type moves parallel to the axis of the prism, the inside of the prism will be displaced relative to the outside along the boundary by one unit of slip. Moreover, dislocations of this type are constrained to move on the surface of the cylinder or prism since their projection normal to the axis of the prism must remain unchanged if the temperature is sufficiently low that diffusion cannot occur. For this reason we shall call them *prismatic dislocations*.

It is not difficult to see how the required prismatic dislocations may be generated. The slip planes bounding the surface of the prism, which is displaced by the indenter, intersect the surface of the specimen in the region of maximal shearing stress at the periphery of the area of contact between the indenter and crystal. Thus each such bounding plane becomes the seat of spirals or rings of dislocation which can be generated in a slip plane in the manner suggested by Frank and Read in the accompanying letter. The Burgers vector associated with the rings will be in the direction of the axis of the prism. Two rings (or spirals) which are generated on different planes that intersect on a line parallel to the axis of the prism can meet at the boundary line and interact to form segments of prismatic dislocations. Complete prismatic dislocations can be formed by combining rings from each of the bounding surfaces. An example s ishown schematically in Fig. 1. The rectangular prism *ABCDEFGH* is pushed on the area *ABFE*, which is part of the surface of the specimen, coinciding with the area of contact of the indenter. This prism is bounded by four slip planes: *ABCD*, *ADEH*, *EFGH*- and *BCGF*. The dislocation rings 1, 2, 3, and 4 shown in Fig. 1a are generated on each of these four planes. As a result of the applied shearing stress, they expand within the four planes and may extend beyond the bounding surface of the prism, as shown in Fig. 1b. The rings on different intersecting faces, such as 1 and 2 on *ABCD* and *ADHE*, respectively, may meet at points such as *a* and *b* in Fig. 1b. The cohesion of the lines is weak at junction points such as *a* and *b* and may break under the applied stress to form two prismatic dislocations α and β in Fig. 1c and dislocation rings such as *s*, *t*, *u*, and *v* in the same diagram. The last-named rings are bent so as to lie in two slip planes which meet at the edges of the prism. The prismatic dislocations α and β have opposite signs in the sense that α is the equivalent of an extra layer of atoms equal in thickness to the Burgers vector lying in a cross section of the prism, whereas β is the equivalent of a deficiency of one plane of atoms. The first dislocation may wander down the prism to the opposite face, where it will produce a jutting by one Burgers distance over the area (*CDHG*) representing the intersection of the prism with this surface. (In practice this surface could be much farther from *ABEF*, on a relative scale, than is shown.) On the other hand the prismatic dislocation β will emerge at the surface *ABEF* where the force is applied and produce a depression of one Burgers distance. Bent dislocations of the type *s*, *t*, *u*, and *v* may produce localized plastic flow in the vicinity of the indenter. It may be noted that these dislocations would not be generated if the rings shown in Fig. 1a did not expand beyond the boundary of the prism, as illustrated in Fig. 1b, but met tangentially at the boundary lines.

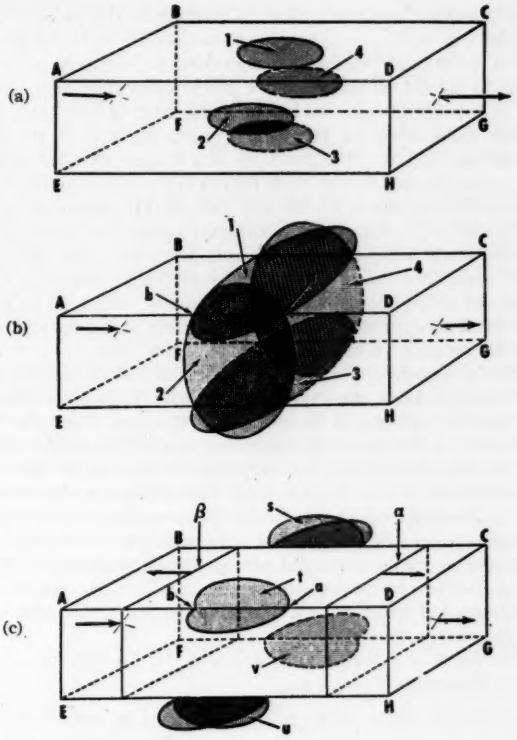

FIG. 1. Possible forms of dislocation rings.

Their presence does not appear to complicate the picture, however, for they will not interfere in any serious way with the generation of additional prismatic dislocations on the surface of the prism. It should be added that a single dislocation ring on one face of the prism may, on reaching the edge of this face, start moving along a second face which meets the first at the edge. For the ring will have the character of a Burgers or screw dislocation at the point of contact with the edge; a screw dislocation may move in any slip plane. In this way a single ring, generated on one face of the prism, may become wrapped around the prism and on meeting itself after complete circumnavigation, form two prismatic dislocations of opposite sign. Similarly a dislocation spiral in one face of the prism, or a pair of oppositely wound spirals which are joined, can produce an unlimited number of prismatic dislocations by wrapping around the surface of the prism.

Once a sequence of prismatic dislocations of the α-type have been started down the cylinder, they may transmit stresses to one another because of their mutual repulsion. Thus the force impressed on the prismatic dislocation nearest the surface $ABDF$ will be transmitted along the entire line to that nearest the opposite end of the prism. The prismatic dislocations α and β shown in Fig. 1c are composed of straight-line segments on each of the four bounding planes. Actually, the segments may be curved. The sequence of events portrayed here evidently could occur on the surfaces of two or more prisms whose axes lie along different slip directions, but which have a common intercept at the area where the indenter is applied.

The writer is indebted to Professor A. H. Cottrell for a stimulating discussion of this topic.

[1] A. Smakula and M. W. Klein, J. Opt. Soc. Am. **39**, 445 (1949).

Special and Magic Numbers as Factors in Nuclear Stability and Abundance*

WILLIAM D. HARKINS
University of Chicago, Chicago, Illinois
June 13, 1950

IN the years 1915 to 1923, the following concept was introduced into nuclear science in about 20 papers.[1] The stability and abundances of nuclear species are determined largely by the relations of special numbers. This concept was received by Rutherford, and later by Goldschmidt, with much approval, but did not meet with so much favor from certain theorists.

It was stated that of all special numbers, 2 is preeminent. The later data of astronomers,[2] and of Goldschmidt,[3] Brown[4] and others indicates that the importance of the number 2 is greater than was supposed initially. In 1920 both Rutherford and the writer indicated that the nucleus consists of protons and neutrons, and Harkins indicated the composition of all nuclei as $(pn)_P n_I$, first expressed by the formula $(pep)_P(pe)_I$ in which it was stated "*pe* represents a neutron." P is the atomic and I the isotopic number.

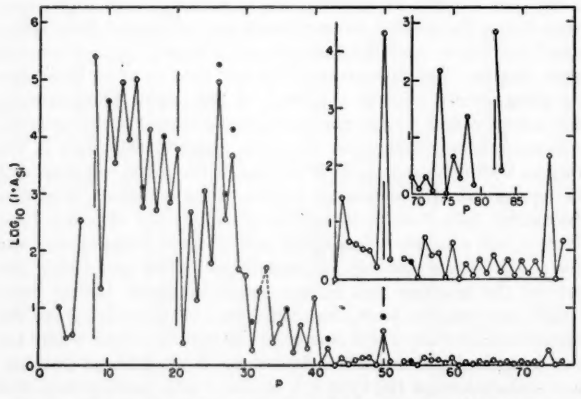

FIG. 1. Abundance of the elements in the meteorites: (A) as compared with that of silicon. The rare gases have been added by a comparison with the composition of the sun and stars. The upper right-hand corner presents values on expanded scales. Values for the ends of nuclear shells are represented by vertical lines. The most striking relative increase in abundance related to a magic number is that for $P=50$, which represents tin.

TABLE I. Atoms per million with even and odd protons.

Element	P even	P odd	P even	P odd	P_e/P_o
Carbon	6		177000		
Nitrogen		7		350000	
Oxygen	8		490000		
Fluorine		9		200	2950
Neon	10		100000		
Sodium		11		1020	60
Magnesium	12		20000		
Aluminum		13		2000	10.5
Silicon	14		22000		
Phosphorus		15		290	52
Sulfur	16		7800		
Chlorine		17		380	13
Argon	18		2200		
Potassium		19		180	11
Calcium	20		1800		
Scandium		21		0.4	2300
Titanium	22		58		
Vanadium		23		5.5	24
Chromium	24		210		
Manganese		25		170	120
Iron	26		40000		
Cobalt		27		220	100
Nickel	28		3000		
Copper		29		10	150
Zinc	30		3.6		
Gallium		31		1.4	3.3
Germanium	32		5.5		
Arsenic		33		10.7	100
Selenium	34		(2200?)		
Bromine		35		0.93	
Krypton	36				
Rubidium		37		0.10	
Strontium	38		0.9		
Yttrium		39		0.22	9.5
Zirconium	40		3.3		
Columbium		41		0.02	9.3
Molybdenum	42		0.42		

Also every multiple of two is a special number. Thus each element which has in its nuclei an even number P_e of protons is in general very much more abundant than either of the adjacent elements with an odd number of protons. Figure 1 shows this but the relation is exhibited much better in Table I. The ratio of P_{even} to P_{odd} varies from *ca.* 3000 to 1.1, the latter for the ratio of Pd+Cd to Ag. (Note: Table I does not go so high as Ag due to lack of space.)

It is apparent that the abundance exhibits waves, in which in general high abundance for even elements are associated with relatively high abundances for odd elements, and peaks occur at oxygen and iron.

Figure 2 shows that in general the abundance of species with any certain even number of neutrons (N_e) is very much greater than that for the adjacent odd number, $N_e \pm 1$. Also the peaks and troughs in abundance lie in relative positions very similar for those for protons, with peaks at 2, 8, 20, 30 and presumably 82 neutrons.

For values of P or of N above 2 the effect on the abundance relations is much more striking in general for *even* numbers than for *magic* numbers. The latter are accompanied by a somewhat greater abundance than the adjacent even numbers.

The value 50 P (tin) exhibits strikingly the increase in abundance related to the end of the 50 P shell. The values 9 P and 21 P show a great lowering in abundance which occurs just after the respective shell (8 P or 20 P) ends. This same type of decrease in abundance occurs just after the closing of the 8, 20, 28 and 50, and 82 N shells, at 9, 21, 29, 51 and 83 N.

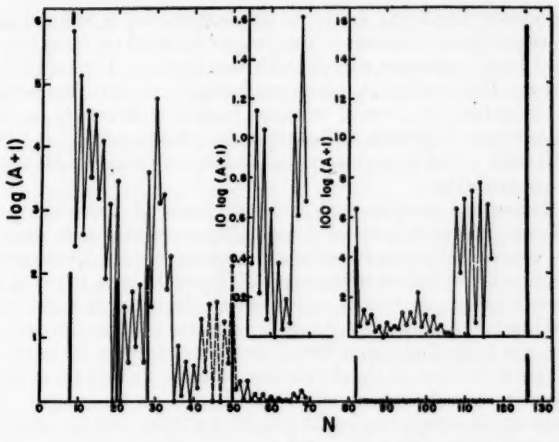

FIG. 2. The same as Fig. 1 except that the abundance is plotted as a function of the number of neutrons (isosteres). In the region of high N where the abundances are low a strikingly high relative abundance is indicated for $N=108$ to $N=116$.

In this communication only relations made more prominent by recent data are considered: many others are discussed in earlier papers.

The earliest suggestion (1915 to 1923) that certain proton and neutron numbers are related to high and low stability and abundance was made by the writer, but the first definite introduction of the concept of nuclear shells appears to be that of Bartlett.[5]

* From a paper on special numbers, presented as an introduction to the symposium on nuclear shells, New York Meeting of the American Physical Society (February 4, 1950).

[1] W. D. Harkins and E. D. Wilson, J. Am. Chem. Soc. **37**, 1367, 1383, 1396 (1915); Proc. Nat. Acad. Sci. **1**, 276 (1915); W. D. Harkins, Phil. Mag. **30**, 723 (1915). See also references 1–14, Phys. Rev. **76**, 989 (1949).

[2] Values collected by J. Greenstein as cited by G. P. Kuiper, *Atmospheres of the Earth and Planets* (University of Chicago Press, Chicago, 1949), p. 309. See also A. Unsöld, Zeits. f. Astrophys. **24**, 323 (1948); **21**, 1 (1941); L. H. Aller and D. H. Menzel, Astrophys. J. **102**, 239 (1945); D. H. Menzel—see Goldberg and Aller, *Atoms, Stars and Nebulae* (The Blakiston Company, Philadelphia, 1943).

[3] D. M. Goldschmidt, *Die Mengenverhältnisse der Elemente und der Atom-Arten* (Oslo, 1938).

[4] H. Brown, Rev. Mod. Phys. **21**, 625 (1949).

[5] J. H. Bartlett, Nature **130**, 165 (1932).

Yields of Photo-Neutrons with Calorimetrically Measured 320-Mev Bremsstrahlung*

D. W. KERST AND G. A. PRICE
Physics Department, University of Illinois, Urbana, Illinois
June 21, 1950

THE numbers of neutrons per erg of 320-Mev bremsstrahlung from samples hung in the beam six meters from the target were detected by a rhodium foil in a large paraffin block. Except for the calorimeter, the equipment and method were the same as those used with the 22-Mev betatron.[1] Corrections generally about 10 percent had to be made because of the distribution of beam intensity over the sample. A correction for the x-ray attenuation in the samples of heavy elements was never greater than 4.5 percent. This correction was not the calculated fractional loss of intensity due to absorption; rather, the correction was found by placing graphite detectors in front of and behind the sample and determining the relative activities. This empirical determination was necessary since degradation of high energy photons passing through the sample largely compensates for absorption of x-rays in the 20-Mev region where $\gamma-n$ processes occur. The rhodium-paraffin detector was calibrated with a known radium-beryllium source of neutrons. An uncertainty in all results described here is due to the unknown variation of efficiency of the detector for the neutron spectra from different elements and from the calibrating source.

For the calorimetric determination of x-ray intensity a collimated beam was absorbed in a lead block whose temperature was compared by thermocouples with that of a similar block not in the beam. The result was that our intermediate standard, a Victoreen 100r ionization chamber behind 0.125 in. of lead, indicated 7.8×10^{-4} joules/cm²/r. Figure 1 shows the yields plotted with the yields[1] determined at 22 Mev for comparison. The numerical ordinates refer only to the 320-Mev yields.

If the bremsstrahlung spectrum is known, and if the effective photon energy for the disintegration is known, then the integral $\Pi=\int\sigma dE$ can be determined from these yields. For the case of deuterium the theoretical cross section can be used to estimate the yield for comparison with observation. Using the energy dependence of the deuterium cross section given by Bethe and Peierls with a maximum cross section of 24×10^{-28} cm², and using the theoretical spectrum used by the Berkeley synchroton group for a platinum target 0.020 in. thick, we calculate 6.3 neutrons/gram atom/erg/cm² averaged over all angles. We observe 6.9 neutrons/gram atom/erg/cm² after correcting the yield in the figure for the angular distribution and for the sensitivity of our apparatus as observed earlier.[1] Thus we observe 10 percent more than theory predicts. Another spectrum calculation for thin targets by Schiff[2] gives a theoretical yield 14 percent lower than is observed. Recent work of Almy and Diven with photo-disintegra-

TABLE I. Integrated cross sections, $\Pi=\int\sigma dE$.

Element	Assumed effective $h\nu$ (Mev)	Our values (Mev-barns)	Other determinations (Mev-barns)
C	30	0.11	0.14[a,b]
Cu	21	1.5	1.4[a,b]
U	16	11.	0.8[c]

[a] J. L. Lawson and M. L. Perlman, Phys. Rev. **74**, 1190 (1948).
[b] G. C. Baldwin and F. R. Elder, Phys. Rev. **78**, 76 (1950).
[c] G. C. Baldwin and G. S. Klaiber, Phys. Rev. **71**, 3 (1947).

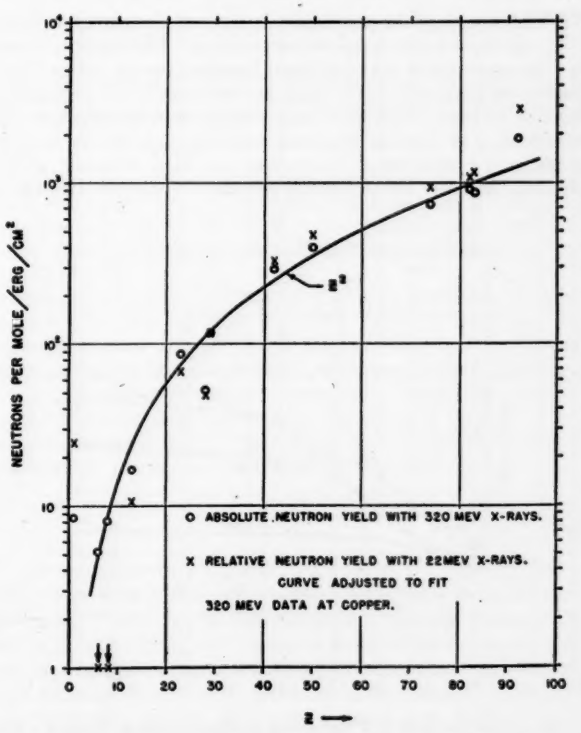
NEUTRONS PER MOLE/ERG/CM²
O ABSOLUTE NEUTRON YIELD WITH 320 MEV X-RAYS.
X RELATIVE NEUTRON YIELD WITH 22MEV X-RAYS.
CURVE ADJUSTED TO FIT
320 MEV DATA AT COPPER.
Z

FIG. 1. Observed neutron yields at 320-Mev bremsstrahlung. The 22-Mev yield curve is adjusted to coincide at copper. The numerical ordinates refer only to the 320-Mev curve.

tions with the 22-Mev betatron has provided an ionization chamber calibration of the beam from that machine. Using their calibration and the previously observed yield at 22 Mev, we find that we observed 26 percent more than the theoretical yield. In this connection it should be noted that theoretically 90 percent of the yield from 320-Mev bremsstrahlung comes from the portion of the spectrum below 22 Mev. Thus the experiments at 320 Mev and at 22 Mev are measuring the photo-effect in the deuteron primarily in the same energy region. The great difference in the spectral shapes for these two energies is the reason for the relatively high yield for deuterium in the 22-Mev graph.

Table I shows some values of Π. Values of Π for the nine other elements can be computed from the yields in the graph, an assumption of $h\nu$, and a spectral shape. These integrals increase much faster than the theoretical Z dependence.[3,4]

Because of uncertain detector efficiency, one should hesitate to say that our type of experiment is good for determining Π in spite of the cases of agreement mentioned above. An unfavorable comparison is with Gaerttner's and Yeater's[5] results for oxygen. For the simple $(\gamma-n)$ disintegration we agree within 7 percent, but we are a factor of 4 below their value of Π which includes $(\gamma-p, n)$ and stars. Since these multiple disintegrations gave neutrons also, we should have detected some of them.

* Supported by the joint program of the ONR and AEC.
[1] G. A. Price and D. W. Kerst, Phys. Rev. **77**, 806 (1950).
[2] G. D. Adams, Phys. Rev. **74**, 1710 (1948).
[3] M. Goldhaber and E. Teller, Phys. Rev. **74**, 1046 (1948).
[4] J. S. Levinger and H. A. Bethe, Phys. Rev. **78**, 115 (1950).
[5] G. R. Gaerttner and M. L. Yeater, Phys. Rev. **77**, 714 (1950).

The Resistivity and Hall Effect of Germanium at Low Temperatures*

C. S. Hung and J. R. Gliessman
Purdue University, Lafayette, Indiana
June 8, 1950

THE theory of the electrical properties of germanium is based on the impurity semiconductor model.[1] The impurity donor and acceptor states are considered localized energy states. Conduction of electricity takes place by electrons in the conduction band or by holes in the filled band. Below room temperature, the contribution of intrinsic electrons and holes can usually be neglected, and conduction is due to only one kind of carrier, either electrons or holes. The activation energies for the impurity states are usually small but finite. As the temperature is reduced the concentration of electrons in the conduction band (or holes in the filled band) decreases rapidly with temperature. The resistivity and the Hall coefficient, which are inversely proportional to the concentration of carriers, therefore increase indefinitely as the temperature is lowered. Measurements of the resistivity and the Hall effect at low temperatures have been carried out to check the above prediction.

Germanium samples with different kinds of impurities and different concentrations were used. Measurements were carried out over a continuous temperature range from room temperature down to liquid helium temperatures. The results were found to be essentially independent of, (a) magnetic field variation between 1000 and 5000 gauss, (b) change by a factor of 10 in the electric field along the direction of flow of the sample current, (c) whether the potential leads to the sample were soldered on with tin or were pressure contacts onto rhodium-plated spots on the sample, (d) whether the sample surface is ground or etched, and (e) whether measurements were taken with increasing temperature or with decreasing temperature. The magnetic field, as measured at room temperature, is not expected to be influenced by the cryostat parts and the solder in the neighborhood of the sample at any temperature.

The resistivity and the Hall curves for some typical samples are shown in Figs. 1 and 2. It is seen that the resistivity and the Hall coefficient do not increase indefinitely as the temperature is reduced, as predicted by the usual theory. Instead, the Hall coefficient for every one of the samples investigated goes through a maximum at low temperatures, while the resistivity approaches a saturation value. This anomaly in the resistivity and the Hall effect calls for a modification of the usual theory of an impurity semiconductor, and will be dealt with separately.[2]

In the temperature region above that at which this anomaly occurs experiment and the usual theory agree satisfactorily. The activation energies for the different samples can be obtained from the slopes of the linear portions of the Hall curves. This activation energy is found to be of the order of 10 millivolts. It is lower for a higher impurity content. Sample SB-5 shows an almost flat Hall curve from room temperature down to 2°K. This may mean a complete overlapping of the impurity states with the conduction band; that is, zero activation energy. Or, it may mean that the mobilities in the conduction and the donor bands are approximately equal.

Owing to this low activation energy the exhaustion range, within which nearly all of the electrons are excited from the impurity states into the conduction band, extends from room temperature

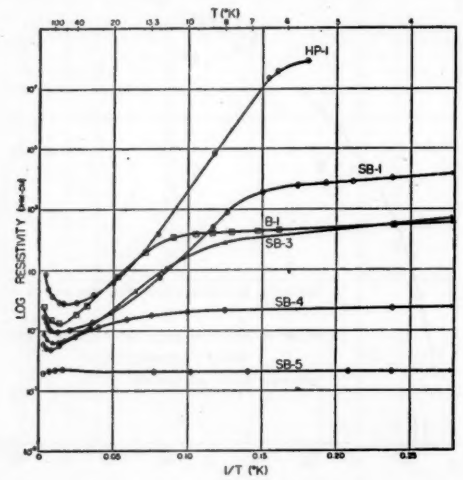

FIG. 1. Resistivity *vs.* $1/T$ for various germanium alloys: HP-1 is a high purity N-type sample; SB-1, SB-3, SB-4, SB-5 are N-type samples with antimony impurities; B-1 is a P-type sample with gallium and arsenic impurities. The impurities in the B-1 sample were introduced by neutron bombardment.

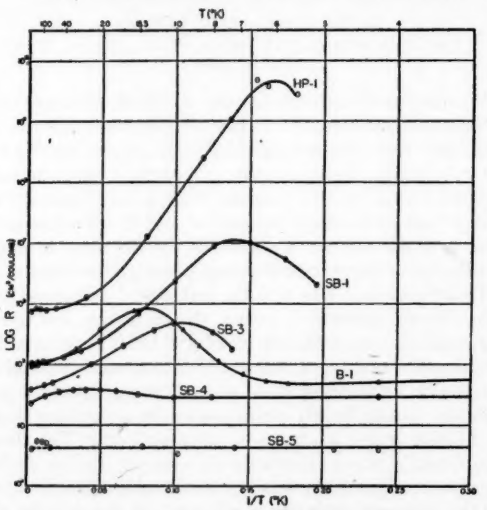

FIG. 2. Hall coefficient *vs.* $1/T$ for various germanium alloys. (See caption of Fig. 1 for description of samples.) For the higher resistance samples, the Hall coefficient at low temperatures became too small to be measured.

down to beyond liquid nitrogen temperature, to 30°K in case of high resistivity samples. The deviation of the Hall curves from flat curves in this region is believed to be due to the fact that the Hall coefficient is not accurately the inverse of the concentration of carriers.[3]

The resistivity in the higher temperature region can be accounted for satisfactorily on the consideration of lattice scattering and impurity ion scattering.[4] The mobility of the carriers, as obtained from the measured resistivity and the Hall coefficient, is of the order of 2000 to 3000 cm²/volt-sec. at room temperature and increases up to 10,000 to 100,000 cm²/volt-sec. at low temperatures. As expected, the mobility increases up to a maximum and then decreases slowly with decreasing temperature. For sample SB-5, due to the high concentration of carriers, consideration of resistivity must be based on degenerate gas theory.[5] Theoretical calculation and experiment again agree.

* Work assisted by Signal Corps contract.
[1] K. Lark-Horovitz, Contractor's Final Report, NDRC 14-585 (Nov. 1945), pp. 33-41 (unpublished).
[2] C. S. Hung, Phys. Rev. **79**, 727 (1950).
[3] V. A. Johnson and K. Lark-Horovitz, Phys. Rev. **79**, 176 (1950).
[4] C. S. Hung and V. A. Johnson, Phys. Rev. **79**, 535 (1950).
[5] V. A. Johnson and K. Lark-Horovitz, Phys. Rev. **71**, 374 (1947); **71**, 909 (1947); **72**, 531 (1947).

Theory of Resistivity and Hall Effect at Very Low Temperatures*

C. S. HUNG
Purdue University, Lafayette, Indiana
June 8, 1950

THE anomalies in the resistivity and the Hall curves of germanium observed at low temperatures[1] could not be explained on the model of an impurity semiconductor with localized impurity states. The Hall coefficient, in the case of some samples, decreases from its maximum by a factor of over 100 as the temperature is reduced. The concentration of carriers in the conduction band (or the filled band), on the other hand, cannot be expected to increase with decreasing temperature. This leads to the conclusion that the usual expressions for resistivity and Hall coefficient, as represented in Eqs. (1) and (2) are no longer valid at low temperatures

$$\rho=(n_e e b_e)^{-1}, \tag{1}$$
$$R=F/(n_e e), \tag{2}$$

where n_e and b_e are the concentration and the mobility of electrons in the conduction band, and F is a numerical factor of the order of unity. According to the free electron theory F is not expected to vary by more than an order of magnitude. Non-homogeneity in the sample, either macroscopic or microscopic, may cause R to decrease with lower temperature even though n_e, at various parts of the sample, may remain constant or decrease. However, to account for the large drop in R observed requires too artificial a model of inhomogeneity.

The anomalies can be understood only if a mechanism is found which includes a combination of different kinds of carriers with different mobilities. James and Ginzbarg[2] pointed out that due to the interaction between the impurity states, an impurity band is formed. In such a case an electron has the possibility of moving from one impurity state to another one in its spatial neighborhood, so that the states are no longer localized, and conduction in the impurity band is to be expected.

When simultaneous conduction in the conduction band and the donor band (or the filled band and the acceptor band) is considered, the expressions for ρ and R are given as follows:

$$\rho=(n_e e b_e+n_D e b_D)^{-1}, \tag{3}$$
$$R=F(n_e e b_e^2+n_D e b_D^2)(n_e e b_e+n_D e b_D)^{-2}, \tag{4}$$

where n_D and b_D are the concentration and mobility of electrons in the donor band. The assignment of a definite mobility b_D to the donor band is justified by the observed ohmic behavior of the saturation resistivity at low temperatures. Equation (4) is adapted from the usual expression for R in the intrinsic range; it is assumed here that this equation holds for the case of carriers in the impurity bands also.

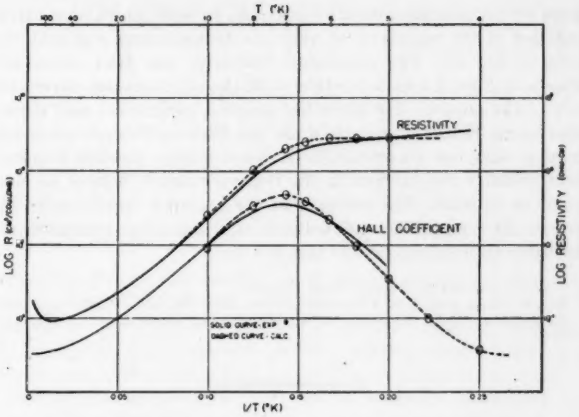

FIG. 1. Resistivity and Hall curves for sample SB-1 (*N*-type, antimony added). The solid curves are experimental and the dashed curves are calculated theoretically. The carriers in the donor band are assumed to be lectrons.

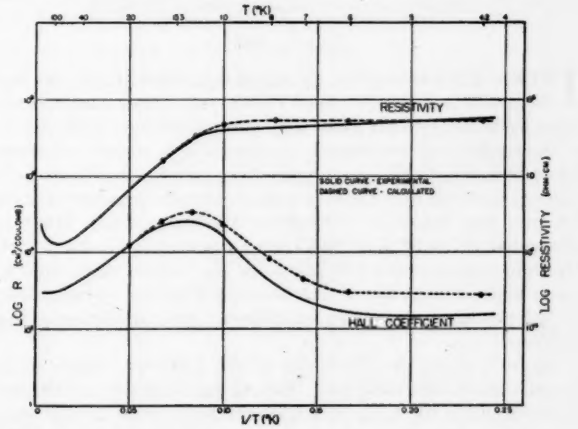

FIG. 2. Resistivity and Hall curves for sample B-1 (*P*-type, neutron bombarded). The solid curves are experimental and the dashed curves are calculated theoretically. The carriers in the acceptor band are assumed to be holes.

Since b_D is usually small compared with b_e, in the limit of high temperatures, the conduction in the impurity band can be neglected and the values of ρ and R are as given by Eqs. (1) and (2) according to the usual theory. However, since n_e decreases indefinitely with decreasing temperature, conduction in the impurity band becomes increasingly important. In the limit of low temperature, conduction in the conduction band can be neglected, and Eqs. (3) and (4) now reduce to the following:

$$\rho=(n_D e b_D)^{-1}, \tag{5}$$
$$R=F/(n_D e). \tag{6}$$

At low temperatures, all the electrons are in the impurity band, and at room temperature, all of them are excited into the conduction band. Therefore, the Hall coefficients at room temperature and at very low temperatures are expected to be the same. This is in approximate agreement with experiment. The deviation may come from the fact that the electrons in the donor band are far from being free, and Eq. (6) is only approximately true.

At the intermediate temperatures, the values of ρ and R can be obtained from the values of n_e, n_D, b_e, and b_D. n_e and b_e can be obtained by extrapolation from high temperatures. n_D is obtained

from the room temperature values of R. b_D is obtained from extrapolation of the resistivity at very low temperatures and with the help of Eq. (5). The calculated resistivity and Hall curves are shown in Figs. 1 and 2 together with the experimental curves for two of the samples. For the other samples, experiment and theory also agree. However, except when the Hall coefficients are measured to very low temperatures, it is not always possible to ascertain whether the carriers in the impurity bands behave as electrons or as holes. The mobility in the impurity bands varies between 10^{-4} and 100 cm²/volt-sec. for impurity concentration between approximately 10^{14} and 10^{17}/cc.

* Work assisted by Signal Corps contract.
[1] C. S. Hung and J. R. Gliessman, Phys. Rev. **79**, 726 (1950).
[2] Ginzbarg, Ph.D. Thesis, Purdue University, Department of Physics, (1949).

Infra-Red Spectra of Condensed Oxygen and Nitrogen*

A. Lee Smith, William E. Keller, and Herrick L. Johnston
Cryogenic Laboratory and Department of Chemistry, Ohio State University, Columbus, Ohio
June 19, 1950

INFRA-RED absorption spectra of condensed O_2 and N_2 have been obtained using a model 12-B Perkin-Elmer spectrometer. The chemically purified gases were purified further by distillation of the liquids, and were finally condensed in a variable thickness low temperature cell[1] fitted with silver chloride windows. Since induced infra-red absorption is weak, a sample thickness of about 7.5 mm was employed throughout the temperature range investigated, 35° to 85°K. A NaCl prism was used in the study of the O_2 fundamental, and a LiF prism for N_2. Careful corrections for water vapor and carbon dioxide absorption gave a reproducibility of ±2 percent transmission on different runs at the same temperature.

Figure 1 shows the absorption in the 1550 cm^{-1} region of the liquid, solid-γ-, and solid-β-O_2. The central frequency at 1559 cm^{-1} in the liquid is the same within experimental error as that given

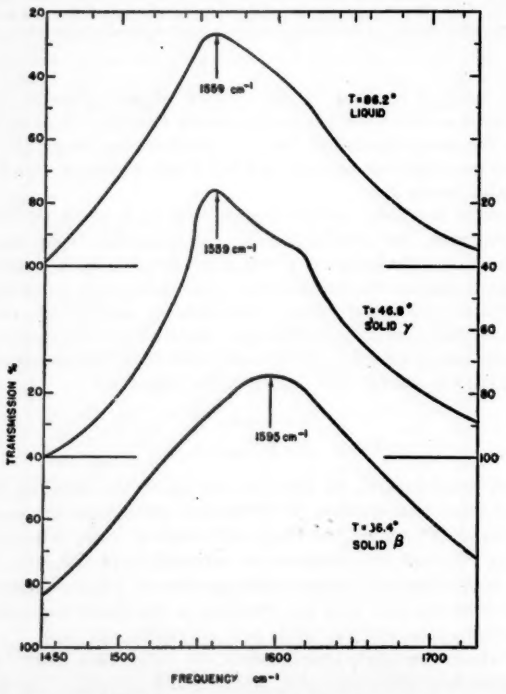

FIG. 1. Infra-red absorption spectra of condensed oxygen.

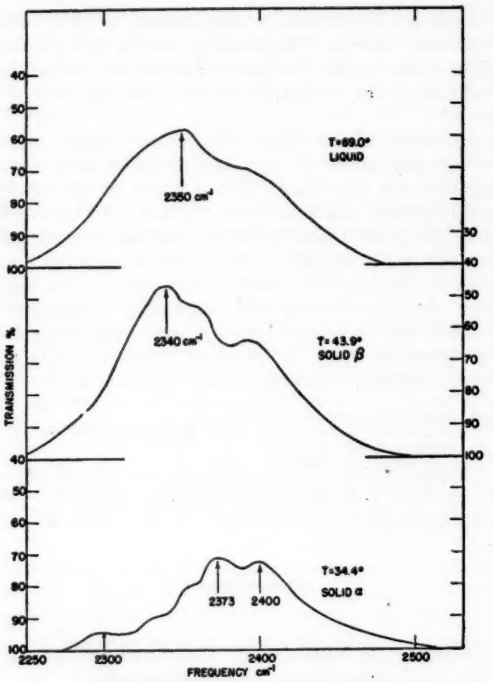

FIG. 2. Infra-red absorption spectra of condensed nitrogen.

for the gas by Crawford and his co-workers.[2] There is no detectable frequency shift as the liquid freezes to solid-γ at 55°K, nor is the transmission reduced. β-O_2, however, is highly scattering, and to register spectra of this phase a slit-width ten times greater than that used for the liquid was necessary.

The analogous results for the three condensed phases of N_2 are shown in Fig. 2. As the liquid freezes at 63°K the character of the absorption remains unchanged, but as the temperature is lowered further there is a gradual shift of the central peak from 2350 to 2336 cm^{-1} at 39°K. On going from solid-β to solid-γ at 36°K, transmission is somewhat reduced and the band center is replaced by two distinct peaks of equal intensity at 2373 and 2400 cm^{-1}.

The fact that the fundamental vibrational band appears in β-N_2 but only weakly in the α-form suggests that in the former phase the molecules are disordered, while in the latter they are ordered.[3] The two strong peaks in the α-N_2 spectrum are probably librational modes having frequencies[3,4] of 40 and 69 cm^{-1} in combination with the comparatively weak fundamental; a weaker subtractive combination is found at 2300 cm^{-1}. An interpretation of the spectrum of β-O_2 cannot be made at this time because of the unusually poor resolution encountered.

A more detailed account of this work and a possible interpretation of the observed envelopes will be presented later.

* This work was supported in part by the ONR under contract with The Ohio State University Research Foundation.
[1] Holden, Taylor, and Johnston (to be published).
[2] Crawford, Welch, and Locke, Phys. Rev. **75**, 1607 (1949).
[3] J. Deitz, Franklin Inst. **219**, 565 (1935).
[4] Vegard, Nature **124**, 267 (1929); **125**, 14 (1930).

Beta-Gamma-Angular Correlation Experiments*

J. R. Beyster and M. L. Wiedenbeck
Department of Physics, University of Michigan, Ann Arbor, Michigan
June 19, 1950

IN recent months several positive examples of beta-gamma-directional correlation have been found. Correlations have been reported for Rb^{86},[1,2] Tm^{170},[2] and Sb^{124}.[3] In many cases, however, no correlation seems to exist.[4]

For these experiments we have used the scintillation counter coincidence apparatus described previously.[3] The sources were mounted on thin zapon film and were at most 1 mg/cm² in thickness. In taking data, the beta-gamma-coincidence rate was observed as a function of angle between counter axes. Runs of 1000 sec. were taken alternately at two angles. The average coincidence rate was based on about 10 runs at each angle. These runs were always consistent statistically.

One of the first substances investigated was K^{42}. Both the individual beta- and gamma-counting rates followed the 12.4-hour half-life. The observed correlation function, listed in Table I, did not appear to depend on whether the experiment was performed in vacuum or at atmospheric pressure, and was not critically sensitive to source thickness. The correlation function was observed with all energies of beta-particles entering the counter. The function does not seem to change perceptibly when electrons with less than 600 kev are not counted. The asymmetry between the 90° and 180° positions has been observed on at least 10 separate occasions with different sources and various experimental arrangements. It might also be pointed out that the apparatus with slight modification was used in performing gamma-gamma-correlations experiments[5] on Co^{60}, Cs^{134}, Na^{24}, and Rh^{106}. The observed functions, in general, agreed with previous work.[6] In addition beta-gamma-correlation experiments have been run with this apparatus on the other activities listed in Table I. The negative results on Na^{24}, Co^{60}, Cs^{134}, and Cd^{115} are consistent with other published work on these activities.[4]

Sources for this work were obtained from the University of Michigan cyclotron and from Oak Ridge. It was necessary to separate sodium from potassium in both the cyclotron and pile produced sources.

The decay scheme of K^{42} has been discussed by Shull and Feenberg.[7] They suggest the angular momenta and parities given in Fig. 1 on the basis of the lifetime and E_{max} for each beta-transition, the shape of the higher energy beta-spectrum, and shell model considerations. Both beta-transitions are thus first forbidden with Gamow-Teller selection rules. According to these selection rules, the lower energy beta-transition may involve four matrix elements. The observed beta-gamma-angular correlation function seems to be compatible with the angular momenta suggested by Shull and Feenberg and with the selection of B_{ij} as a prominent matrix element in the lower energy beta-transition.

The absence of noticeable beta-gamma-angular correlation for Na^{24}, I^{131}, Cs^{134}, and Co^{60} is understandable, since one should not expect to find an asymmetry where the Fermi plot for the beta-spectrum is of the allowed type. Since Cd^{115} has a decay scheme similar to that of K^{42}, it is possible for Gamow-Teller selection rules to again have more than one matrix element present for the lower energy beta-transition. The over-all asymmetry may thus be small if matrix elements occur in the correct proportion. The angular correlation is also Z dependent which may explain in part the lack of a significant effect[8] for Cd^{115}.

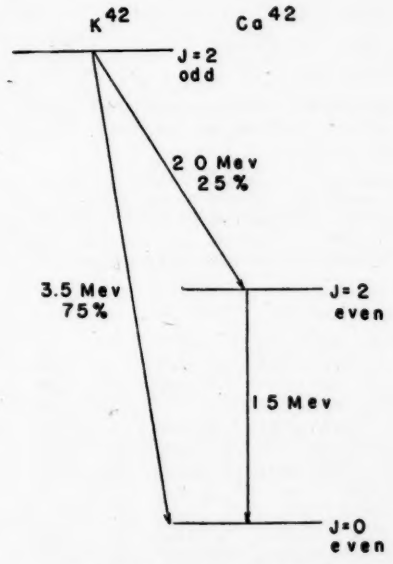

FIG. 1. Decay scheme of K^{42}.

TABLE I. Ratio of the observed beta-gamma-coincidence rate at 180° to that at 90° for various substances.

Isotope	$C(\pi)/C(\pi/2)$
K^{42}	0.938 ±0.015
Na^{24}	1.005 ±0.01
I^{131}	1.00 ±0.029
Cs^{134}	1.00 ±0.018
Co^{60}	0.98 ±0.03
Cd^{115}	0.99 ±0.027
Sb^{124}	0.73 ±0.035

The authors would like to thank Professor G. E. Uhlenbeck and Dr. E. S. Lennox for the many helpful discussions of this problem, and to express their gratitude to the cyclotron staff for sources prepared during the course of this investigation.

* This work was supported in part by AEC.

[1] D. T. Stevenson and M. Deutsch, Phys. Rev. **78**, 640 (1950); R. Stump and S. Frankel, Phys. Rev. **79**, 243 (1950).
[2] T. B. Novey, Phys. Rev. **78**, 66 (1950).
[3] J. R. Beyster and M. L. Wiedenbeck, Phys. Rev. **79**, 169 (1950).
[4] R. L. Garwin, Phys. Rev. **76**, 1876 (1949); Grace, Allen, and Halban, Nature **164**, 538 (1949); S. L. Ridgeway, Phys. Rev. **79**, 243 (1950).
[5] J. R. Beyster and M. L. Wiedenbeck, Phys. Rev. **79**, 411 (1950).
[6] E. L. Brady and M. Deutsch, Phys. Rev. **78**, 558 (1950).
[7] F. B. Shull and E. Feenberg, Phys. Rev. **75**, 1768 (1949).
[8] M. Fuchs and E. S. Lennox, Phys. Rev. **79**, 221 (1950).

Neutron-Deuteron Scattering at 4.5 and 5.5 Mev*

ERNEST WANTUCH**
Brookhaven National Laboratory, Upton, New York
June 16, 1950

THE angular distribution and differential cross section of 4.5- and 5.5-Mev neutrons scattered by deuterons were investigated. The source of neutrons for this investigation was the $D+D \rightarrow n+He^3+3.26$ Mev reaction. Incident deuterons were accelerated by the pressurized van de Graaff Generator at the Department of Terrestrial Magnetism. The target consisted of a thin volume of deuterium gas at atmospheric pressure, separated from the vacuum system by a 0.0001-in. nickel foil. Neutrons emitted in the forward direction within a cone of 3° half-angle, having a calculated energy spread of ±100 kev, were incident on the scatterer. The scattering materials were 7.5 cm³ of deuterium gas at atmospheric pressure or a 0.001-in. layer of heavy paraffin. Recoil deuterons ejected from the scatterer were detected by a twofold coincidence proportional counter telescope. These counters were filled with 25:1 argon-carbon dioxide mixture to a pressure of a few centimeters of mercury. They were operated at a gas amplification of approximately 100. Individual pulses were amplified with amplifiers having a pulse rise time of 0.2 μsec. They were shaped by a univibrator to a duration of approximately 1 μsec. Individual pulses were recorded on scales-of-64. A Rossi coincidence circuit using 6AU6 pentodes was used to determine coincident pulses.

The neutron source was monitored by the accompanying $D+D \rightarrow p+T+3.98$ Mev reaction, the protons being recorded by a small end-window proportional counter opposite a thin mica window in the side of the gas target.

All coincidence counting rates were normalized to a constant number of counts by the monitor. The deuteron current incident on the gas target was integrated as a check on the above-mentioned method of monitoring. The absolute yield of the neutron source was obtained from the results of Hunter and Richards.[1]

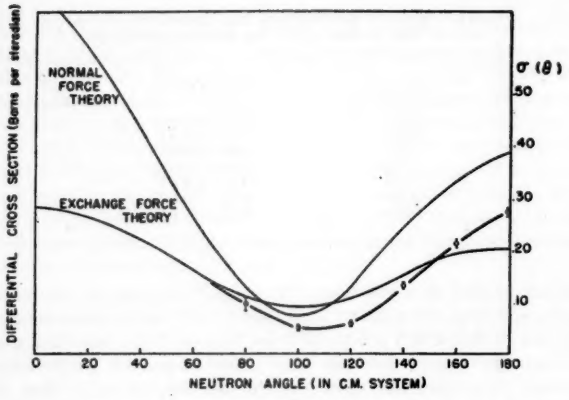

FIG. 1. Neutron-deuteron scattering at 4.5 Mev.

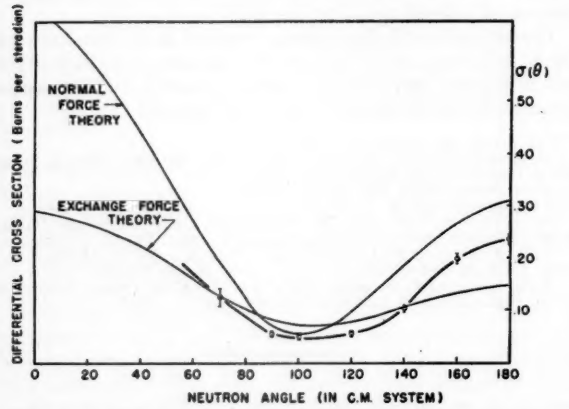

FIG. 2. Neutron-deuteron scattering at 5.5 Mev.

Absolute values of neutron-deuteron differential scattering cross sections were calculated from the known yield of the source, the amount of scattering material, and the geometry of the apparatus.

A measurement of neutron-proton scattering at these energies gave, within five percent statistical errors, the expected isotropic distribution in the center-of-mass system. The total $n-p$ cross section determined from this data agrees with the published values of Bailey and Bennett *et al.*[2]

Neutron-deuteron scattering measurements were compared with the theory of Buckingham and Massey.[3] Their calculations of the scattering phases in the region 0 to 11.5 Mev were interpolated for the energies used here.

Figures 1 and 2 show the results. The total cross sections, if one assumes a reasonable extrapolation to the angles where no experimental data could be obtained, are in acceptable agreement with experimental total cross sections obtained by Nuckolls and Bailey *et al.*[4] The ratio of the differential cross section at 180° to the value at the minimum is approximately 5:1 at both energies which is much larger than the ratio predicted by the exchange force theory (2:1). A full report will be published.

It is a pleasure to acknowledge the aid and the many helpful suggestions of Dr. N. P. Heydenburg at the Department of Terrestrial Magnetism, and to thank Dr. E. O. Salant for suggesting this problem and for critical discussions.

* Research carried out at the Brookhaven National Laboratory under the auspices of the AEC.

** This report is based on a portion of a thesis presented in partial fulfillment of the requirements for the degree of Doctor of Philosophy at New York University.

[1] G. T. Hunter and H. T. Richards, Phys. Rev. **76**, 1445 (1949).
[2] C. L. Bailey *et al.*, Phys. Rev. **70**, 583 (1946).
[3] R. A. Buckingham and H. S. W. Massey, Proc. Roy. Soc. **A179**, 123 (1941).
[4] R. G. Nuckolls *et al.*, Phys. Rev. **70**, 805 (1946).

Intensity and Lateral Distribution of the *N*-Component in the Extensive Showers of the Cosmic Radiation*

G. COCCONI AND V. COCCONI TONGIORGI
Cornell University, Ithaca, New York
June 16, 1950

DURING the summer of 1949 an experiment was performed (Echo Lake, Colorado, 3260 m elevation) to study the intensity and the lateral distribution of the *N*-component[1] present in the extensive air showers.

The general layout of the experiment is sketched in Fig. 1A. C_1, C_2, C_3, C_4 and C_5 (core selectors) are the same as used in a previous experiment on the lateral structure of the extensive showers.[2] The cross section of one of them is drawn in Fig. 1B. As shown in reference 1, the fivefold coincidences (*abcde*) are mostly produced by showers whose cores hit within a distance of 10 to 20 meters from the selectors. Such coincidences generated master pulses, C, which were sent to the other parts of the apparatus; namely, to the density detector and to the *N*-component detector. Both these detectors were located at the center of a circle (of radius d) on which the core selectors were arranged, five meters from one another.

The density detector (i.e., the apparatus for measuring the density of the ionizing particles in the showers) consisted of three groups of three counters each: $L_1L_2L_3$ (effective area 0.15 m²), $M_1M_2M_3$ (effective area 0.02 m²) and $S_1S_2S_3$ (effective area 0.003 m²) (see Fig. 1C). Coincidences $(L_1L_2L_3C)=(LC)$, $(M_1M_2M_3C)=(MC)$ and $(S_1S_2S_3C)=(SC)$ were recorded.

The *N*-component detector (see Fig. 1C) consisted of a Pb-absorber Σ (4 in.×25 in.×45 in.), surrounded by paraffin in which 16 BF_3 proportional counters were embedded. On the basis of the results obtained in previous experiments,[3] the detection of the *N*-component was accomplished by recording the neutrons of moderate energies released in nuclear interactions of the *N*-component with nuclei of the lead. The detector recorded neutrons in the energy range between 1 and 20 Mev, with an over-all efficiency $E=0.04\pm0.01$. The pulses of the neutron counters, n, were put in coincidence with the coincidences (LC), (MC) and (SC) delayed 7 μsec. and shaped in a 200 μsec. square pulse. Coincidences (nLC), (nMC) and (nSC) were recorded. Chance coincidences were negligible.

Four series of measurements were made, with the distance d between the core selectors and the other detectors equal to 10, 18, 50, and 95 meters.[4] The results are given in Table I.

For the interpretation of the results we considered the ratios:

$$P_{LM}=\frac{(nLC)-(nMC)}{(LC)-(MC)} \quad \text{and} \quad P_{MS}=\frac{(nMC)-(nSC)}{(MC)-(SC)},$$

namely, the probability that a shower, which produced a master pulse C in one of the core selectors and struck the density detector

TABLE I. Experimental results with their standard errors. Δ_{LM} (and Δ_{MS}) are the average densities of the showers which struck a core selector and counters L, but not counters M (or M but not S). R_{LM} and R_{MS} are the intensities of the *N*-component, relative to the intensity of all the ionizing particles, in the showers whose average densities are $\bar{\Delta}_{LM}$ and $\bar{\Delta}_{MS}$.

		$d=10$m	$d=18$m	$d=50$m	$d=95$m
C	(h^{-1})	6.25 ±0.15	6.32 ±0.15	6.25 ±0.14	6.10 ±0.14
(LC)	(h^{-1})	4.38 ±0.13	4.67 ±0.13	1.80 ±0.08	0.507 ±0.04
(MC)	(h^{-1})	2.07 ±0.09	1.62 ±0.08	0.29 ±0.03	0.048 ±0.012
(SC)	(h^{-1})	0.37 ±0.04	0.28 ±0.03	0.029 ±0.01	0
(nLC)	(h^{-1})	1.40 ±0.08	0.96 ±0.06	0.15 ±0.02	0.025 ±0.009
(nMC)	(h^{-1})	1.02 ±0.06	0.58 ±0.05	0.061 ±0.013	0.006
(nSC)	(h^{-1})	0.25 ±0.03	0.21 ±0.03	0.016 ±0.007	0
$\bar{\Delta}_{LM}$	(m^{-2})	42	38	24	19
$\bar{\Delta}_{MS}$	(m^{-2})	195	168	115	115
$R_{LM}\times100$		1.42 ±0.17	1.15 ±0.15	0.79 ±0.15	0.66 ±0.30
$R_{MS}\times100$		1.06 ±0.2	0.64 ±0.15	0.46 ±0.20	~0.35

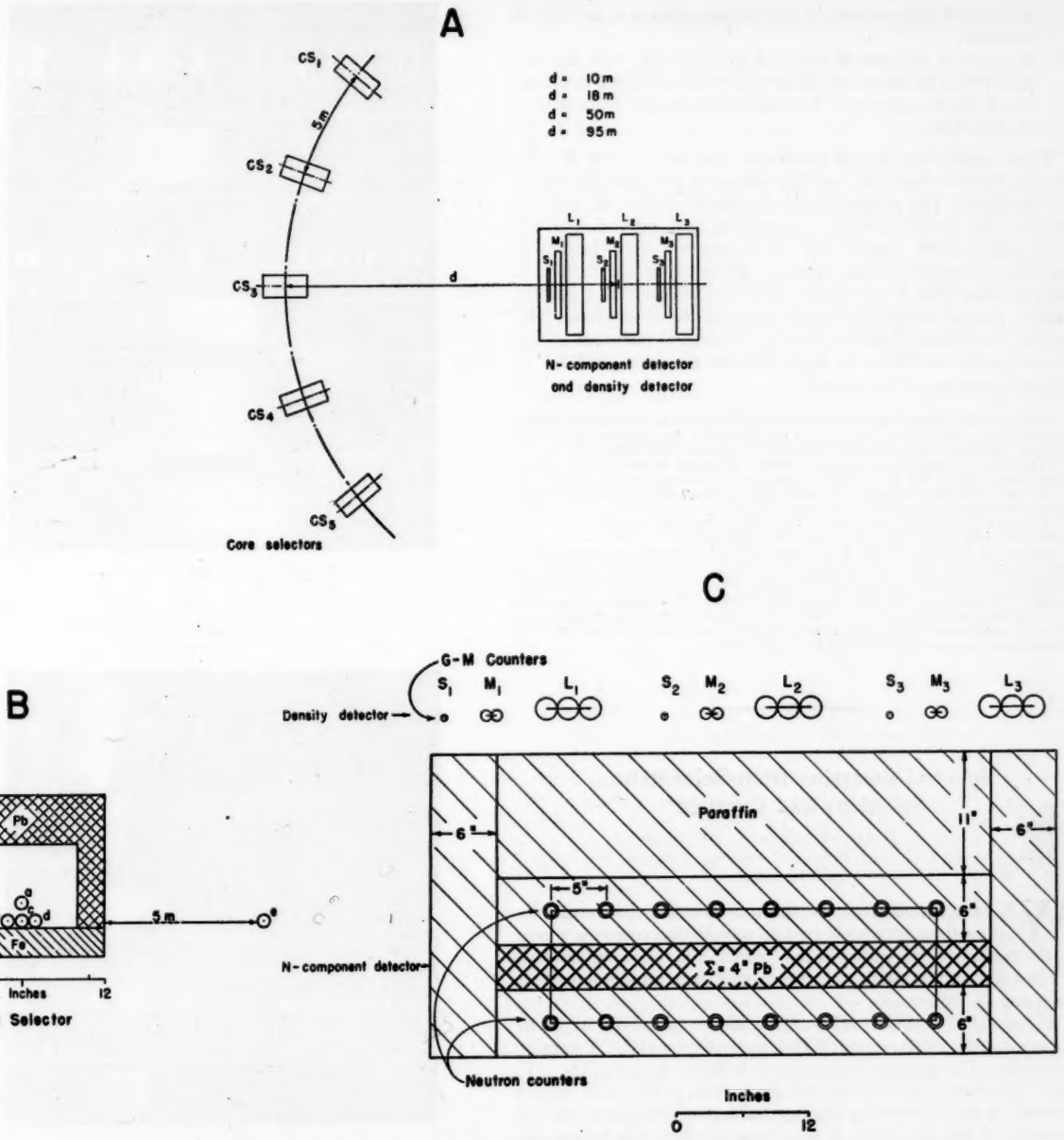

FIG. 1. General layout of the experiment (Fig. 1A). In Fig. 1B is given the cross section of one of the core selectors and in Fig. 1C the cross section of the detectors of the density of the showers and of the N-component.

with a density such as to trigger counters, L, but not M (or M but not S), contained a particle of the N-component which interacted in the absorber Σ and produced at least one neutron recorded by our apparatus. One can write:

$$P_{LM}=1-\exp\{\bar{\Delta}_{LM}\cdot\sigma\cdot(1-e^{-x/\lambda})\cdot[1-(1-E)^{\nu}]\cdot R_{LM}\}$$

(and a similar expression for P_{MS}), where $\bar{\Delta}_{LM}$ is the average density of the ionizing particles in the showers which triggered both one or more of the core selectors and counters L, but not counters M; σ is the surface of the lead Σ and x its thickness; λ the interaction mean free path in lead of the N-component; ν the average multiplicity of the neutrons produced in lead in a nuclear disintegration; and R_{LM} the density of the N-component relative to the total density of ionizing particles in the showers considered.

$\bar{\Delta}_{LM}$ (and $\bar{\Delta}_{MS}$) were deduced from the density spectra obtained in the experiment quoted in reference 1, and from the probabilities of showers of different densities striking counters L, M, and S. The values used for $\bar{\Delta}_{LM}$ and $\bar{\Delta}_{MS}$ are given in Table I.

The mean free path λ was assumed to be equal to 160 g cm^{-2}.

The multiplicity ν has been measured[2] for 2 in. Pb at the average distance of about 10 meters from the core of the showers, and found to be about 60, which gives $1-(1-E)^{\nu}=0.92$. The approximation $1-(1-E)^{\nu}=1$ was used, which implies the assumption that ν does not vary strongly with the distance from the core of the showers.

The results obtained for R_{LM} and R_{MS} are given in Table I. Owing to the large statistical errors in the results and to the uncertainty of the assumptions introduced, particularly for ν, we do not attribute much quantitative significance to the variations of R with the distance from the core and with the average density of the shower. However, the following conclusions can be drawn:

(1) the intensity of the N-component capable of producing nuclear disintegrations is of the order of one percent of all the

ionizing particles present in the extensive showers, at 3260 m elevation;

(2) the value of the ratio R does not vary strongly with the distance from the core of the showers. Hence the lateral distribution of the N-component does not differ strongly from that of the electrons.

These results rule out the possibility that most of the N-component observed near the core of a shower is produced far above the apparatus. The peaked lateral distribution observed, and the fact that the particles of the N-component in a single shower can be as many as 10^6, suggest that the mechanism of production of the N-component inside an extensive shower is similar to that of the electrons. The N-component must be the result of a nuclear cascade process which develops throughout the atmosphere. The core of the shower contains the most energetic particles of the N-component and keeps on supplying less energetic particles to the outer regions of the shower.

* The authors are grateful to the Research Corporation for a grant which covered the expense of performing this experiment. The funds for constructing the apparatus were provided through a contract with the ONR.

[1] The term *N-component* is used here in the sense defined by B. Rossi [Rev. Mod. Phys. 20, 537 (1948)]; namely, the N-component consists of all of the particles capable of producing nuclear disintegrations (high energy neutrons and protons, π-mesons, etc.).

[2] Cocconi, Tongiorgi and Greisen, Phys. Rev. 76, 1020 (1949).

[3] V. Cocconi Tongiorgi, Phys. Rev. 75, 1532 (1949).

[4] We want to point out that the geometrical distances, d, between the core selectors and the N-component detector are to be taken only as an indication of the order of magnitude of the average distances of the particle of the N-component from the core of the showers. As a matter of fact, the true average distances are somewhat smaller than d, since the requirement of the N-component hitting the detector favors the showers whose core lies in between the core selectors and the N-detector.

Spectral Emission from Scintillation Solutions and Crystals*

F. B. HARRISON AND G. T. REYNOLDS
Palmer Physical Laboratory, Princeton University, Princeton, New Jersey
June 19, 1950

WE have investigated the spectral emission of several solutions that have been used as scintillation counters.[1] Some of the results are presented in the figures. The following emission spectra are shown, with a mercury spectrum superimposed on each one for calibration.

Figures (1A) and (1B): Crystalline terphenyl excited by 50 kv x-rays and the mercury line 2537A, respectively. (1C): A solution of terphenyl in benzene irradiated with 50 kv x-rays. (1D), (1E) and (1F): Solutions of terphenyl in benzene, xylene, and toluene excited by the 2537A line, the light falling on the side of the cell opposite to the slit. (1G): A solution of terphenyl in benzene excited by the 2537A line, the light falling on the side of the cell nearest the slit.

Figure (2A): An anthracene crystal excited by 50 kv x-rays. (2B) and (2C): Anthracene crystals excited by 2537A light shining on the side farthest from and nearest to the slit respectively. (2D): A solution of anthracene in xylene irradiated with 50 kv x-rays. This was taken with the spectroscope slit wide open, so that the spectrum is displaced about 100A toward shorter wavelengths. (2E): The same solution excited by 2537A light.

The spectra obtained with particle bombardment (Compton electrons from the x-rays) appear to be the same as the fluorescent spectra caused by ultraviolet light. From Figs. (1D), (1E) and (1F) we see that the light emitted is characteristic of the terphenyl molecule and is the same with different solvents.

There is evidence that some of the light emitted is reabsorbed, both in the solutions and in the crystals. Since the ultraviolet light used to excite the fluorescence is very strongly absorbed by the solutions, the emitted light must travel about 5 mm through the solution if we irradiate the side away from the slit, and only a very short distance if we irradiate the part nearest the slit. In

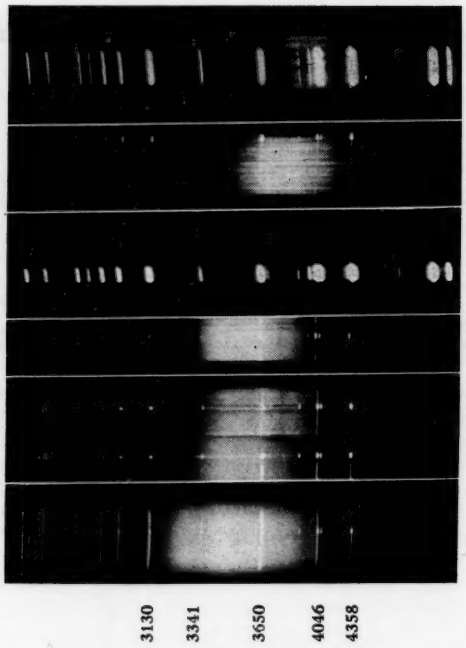

FIG. 1. Emission spectra of terphenyl.

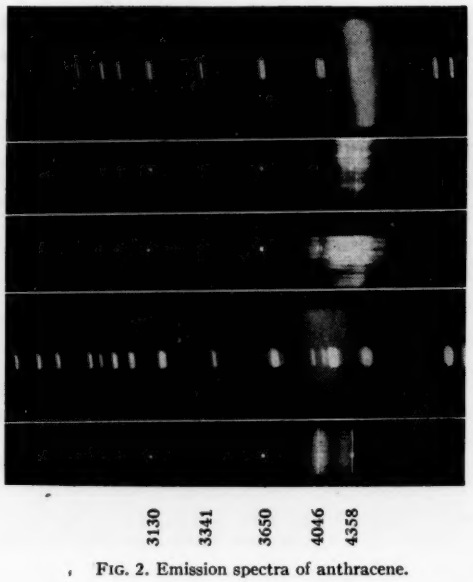

FIG. 2. Emission spectra of anthracene.

Fig. 1 the solution reabsorbs the band at 3280A, and the crystal, which has a much higher density of terphenyl molecules, reabsorbs the 3450A band. The 3720A band is weaker in (1A) than in (1B) because the crystal was thicker. In the same way, as we go from (2A) to (2E) the bands at about 4740A and 4460A disappear and one appears at 4050A.

The 5819 end-window photo-multiplier tube will favor anthracene crystals over terphenyl solutions because of its spectral sensitivity. Observations with this tube show that the pulse height from the terphenyl solutions due to the Cs^{137} 630-kev electron is about 35 percent of the pulse height from an anthracene crystal. When a 1P21 photo-multiplier is used this ratio is about 50 percent; and with a 1P28, which favors the solutions, the ratio of pulse heights is approximately 65 percent.

* Assisted by the joint program of the ONR and AEC.

[1] Reynolds, Harrison, and Salvini, Phys. Rev. 78, 488 (1950).

Temperature Characteristics of Naphthalene-Anthracene Mixtures

S. H. Liebson and R. T. Farrar
Electricity Division, Naval Research Laboratory, Washington, D. C.
June 21, 1950

VARIATION of the light output of organic scintillators under gamma-excitation as a function of temperature have recently been reported.[1,2] In order to clarify the energy transfer mechanism, a series of phosphors was prepared containing known amounts of anthracene in naphthalene. It is believed that, for these mixtures, energy is absorbed by the naphthalene and transferred by a process akin to sensitized fluorescence[3] to the anthracene molecules which, in turn, emit. Accordingly, measurements were made to a higher degree of accuracy than previously reported,[2] and are shown in Fig. 1. A Wratten Type IIA filter was

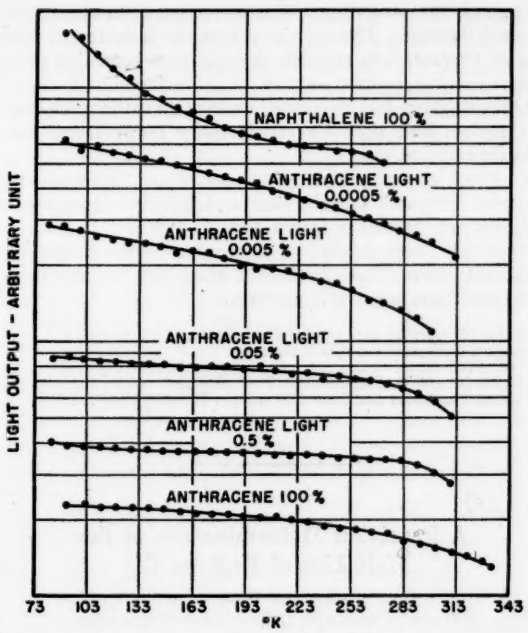
NAPHTHALENE 100 %
ANTHRACENE LIGHT 0.0005 %
ANTHRACENE LIGHT 0.005 %
ANTHRACENE LIGHT 0.05 %
ANTHRACENE LIGHT 0.5 %
ANTHRACENE 100 %
LIGHT OUTPUT - ARBITRARY UNIT
73 103 133 163 193 223 253 283 313 343
°K

FIG. 1. Temperature characteristics of naphthalene-anthracene mixtures.

used to obtain readings of the light output corresponding to the anthracene emission spectra, designated as anthracene light in Fig. 1, and no filter was used when measuring the total emitted light output. The percentage of anthracene light output for the mixtures was in agreement with Bowen,[4] the relative placement of curves in the figure being arbitrary, to provide a ready comparison. For all measurements with the filter, the naphthalene light through the filter was negligible compared with the anthracene light. The melting point of the mixtures was approximately the same, about 353°C. It may be seen that as the percentage of anthracene is reduced, the temperature characteristics assume a greater slope, similar to the characteristics of pure naphthalene. On the other hand, as the percentage of anthracene is increased the characteristics become less temperature dependent and, as can be seen, have a smaller slope at the lower temperatures than does anthracene itself. This was further verified with mixtures containing greater percentages of anthracene. The measurements suggest that the temperature characteristics for these materials are determined by the matrix (naphthalene) crystal, the larger percentages of anthracene corresponding to shorter paths for energy transfer and less thermal quenching.

[1] G. G. Kelley and M. Goodrich, Phys. Rev. **77**, 138 (1950).
[2] S. H. Liebson and J. W. Keller, Phys. Rev. **78**, 385 (1950).
[3] J. Franck and R. Livingston, Rev. Mod. Phys. **21**, 505 (1949).
[4] Bowen, Mikiewicz, and Smith, Proc. Phys. Soc. London **A62**, 26 (1949).

Ambipolar Diffusion in Neon

Manfred A. Biondi
Westinghouse Research Laboratories, East Pittsburgh, Pennsylvania
June 22, 1950

THE results of measurements of the removal of electrons from ionized gases have been presented in two previous papers.[1,2] In particular, studies of ambipolar diffusion in helium and of electron-ion recombination in helium, neon, and several other gases were described. In neon the recombination loss of electrons exceeded the diffusion loss over the range of gas pressures and electron densities which the apparatus was capable of studying. Thus, no reliable measurements of ambipolar diffusion in neon were obtained. In the present experiment an improved, more sensitive, version of the apparatus has been used to study ambipolar diffusion in neon in a region where recombination losses are small.

The method involves the use of microwave techniques to observe the decay of electron density from an initially ionized gas. Free electrons in a microwave cavity will, under the proper conditions, perturb the cavity's resonant frequency in proportion to their concentration. By measuring the change of resonant frequency of a cavity containing a discharge as a function of the time after the maintaining field is removed, the decay of electron density is determined. For the case in which electrons are removed by diffusion to the walls and, to a lesser extent, by recombination with positive ions, the electron density decreases according to the following equation

$$n/(1+\alpha\tau n)=[n_0/(1+\alpha\tau n_0)]\exp(-t/\tau)$$

[see Eqs. (16) and (17) of reference 1], where n is the average electron density, α is the recombination coefficient, and τ is the mean decay time due to diffusion. The recombination correction is minimized by making $(\alpha\tau n)\ll 1$, which requires measurements at low electron densities and at low pressures, since τ decreases with decreasing pressure. The present apparatus achieves an increased frequency stability and higher breakdown fields which permit measurements to be made at electron densities ten times smaller and gas pressures three times lower than those attained by the previous apparatus.

To assure the purity of the gas samples under study, a vacuum system which could be pumped to 4×10^{-9} mm Hg was used. After bake-out at 450°C, the system had a rate of rise of gas pressure of less than 10^{-8} mm/min., when isolated from both the pumps and the pumping action of the ion gauge. The gas samples used were Air Reduction Company's spectroscopically pure neon.

Figure 1 shows a typical experimental curve. The upper curve shows the decay of electron density while the lower curve is ob-

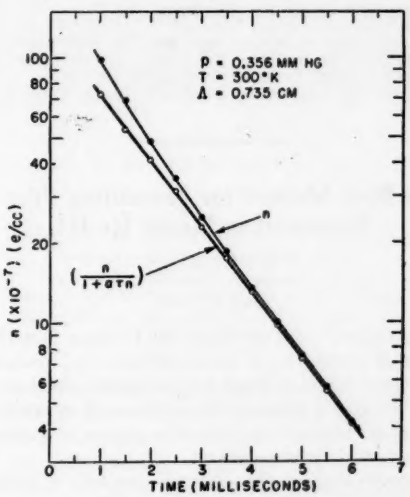

FIG. 1. Loss of electrons in neon by ambipolar diffusion and recombination.

tained using the value $\alpha=2.0\times10^{-7}$ cc/ion-sec. for neon given in reference 2. The slope of the curve yields a value, $\tau=1.75$ milliseconds for the diffusion decay time. The diffusion of the electrons takes place in a quartz cylinder with an inside radius, $R=2.22$ cm and inside height, $H=3.82$ cm. For this geometry, the characteristic diffusion length, Λ, as determined by the equation in Fig. 6 of reference 1 is equal to 0.735 cm.

The ambipolar diffusion coefficient, D_a, is given by Eq. (9) of reference 1.

$$D_a=\Lambda^2/\tau=309 \text{ cm}^2/\text{sec.} \quad (p=0.356 \text{ mm Hg}).$$

Data of the type shown in Fig. 1 were taken over the pressure range 0.27 to 1.10 mm Hg. According to kinetic theory, the product $D_a p$, where p is the gas pressure, should be constant at constant temperature. The experimental results are shown in Fig. 2. The value $D_a p=115\pm10$ (cm²/sec.) − (mm Hg) is obtained

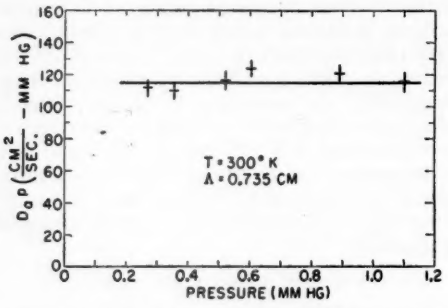

FIG. 2. Pressure dependence of the ambipolar diffusion coefficient for neon.

at $T=300$°K, which agrees with unpublished estimates obtained with the previous apparatus. With the knowledge of $D_a p$, one may calculate the positive ion mobility from Eqs. (18) and (19) of reference 1. The extrapolated value for 760 mm Hg and 20°C is 2.9 cm/sec. per volt/cm as compared to Munson and Tyndall's value[3] of 6.23. As in the analogous case of helium,[4] a possible explanation of the discrepancy is that the ions observed by Munson and Tyndall were molecular; i.e., Ne_2^+. Rough estimates of the rate of conversion of atomic to molecular ions by three-body collisions with normal atoms indicate that, at the pressures used in our experiment, the ions are predominantly atomic. Unfortunately, the lack of pressure data in reference 4 prevents the drawing of conclusions as to the nature of the ions observed.

The author is indebted to Dr. D. Alpert for making available the metal valves and other vacuum devices which made the improved vacuum conditions possible, and to A. O. McCoubrey for his assistance with electronic problems.

[1] M. A. Biondi and S. C. Brown, Phys. Rev. **75**, 1700 (1949).
[2] M. A. Biondi and S. C. Brown, Phys. Rev. **76**, 1697 (1949).
[3] Munson and Tyndall, Proc. Roy. Soc. **A177**, 187 (1941).
[4] M. A. Biondi and S. C. Brown, Phys. Rev. **76**, 302 (1949).

A New Method for Measuring Film Transport in Liquid He II*

H. A. BOORSE† AND J. G. DASH**
Columbia University, New York, New York
June 19, 1950

FILM transport rates of liquid He II have heretofore been measured mainly by a visual method; i.e., by observation of the changes in height of liquid helium columns in glass vessels.[1,2] The optical technique requires the incidence of external radiation upon the helium film, and is limited to studies of transport rates over transparent dielectric surfaces.

In the present method the dielectric property of liquid helium is employed to indicate the total amount of liquid helium between the walls of a cylindrical capacitor. Variations in height of the liquid helium contained within the annular space are observed as changes in capacitance. The capacitor, serving in this way as a depth gauge, is placed within a container of the material over whose surface the transport rate is to be measured. The container and capacitor assembly is enclosed within a copper radiation shield provided with small holes to allow the passage of liquid and vapor. Electrical connections are brought down through the liquid helium bath to minimize thermal conduction to the container.

The capacitor is connected in parallel with the tuned circuit of a radiofrequency oscillator, and changes in capacitance are observed by means of frequency changes of the oscillator. The oscillator frequency has been measured by beating the signal against the output of a heterodyne frequency meter, and reading the frequency of the meter in the condition of zero beat note. An automatic frequency recording circuit has also been used. In this case, the frequency meter is not tuned during the course of a transport rate measurement. The audio beat signal is amplified and fed to a voltage divider consisting of a large resistance in series with an air core inductance. The voltage across the inductance, proportional to frequency, is rectified and fed to a recording potentiometer.

The depth gauge has been calibrated with a cathetometer in the He II region, and shows a satisfactorily linear frequency *vs.* height dependence.

As a check on the method, transport rates in glass containers have been measured in this way, and found to compare very closely with the results of Daunt and Mendelssohn.

Preliminary measurements of creep over copper indicate rates significantly higher than those over glass. Further studies over various materials are now in progress.

* Assisted in part by the ONR and the Research Corporation.
† Barnard College, Columbia University.
** AEC Predoctoral Fellow.
[1] J. G. Daunt and K. Mendelssohn, Proc. Roy. Soc. **A170**, 423, 439 (1939).
[2] Webber, Fairbank, and Lane Phys. Rev. **76**, 609 (1949).

A Precision Determination of the Half-Life of Radium C′

GUY VON DARDEL
Research Institute for Defense, Stockholm, Sweden
June 19, 1950

THE widespread use of RaC′ to check the proper functioning of delayed coincidence and variable resolution coincidence equipment made a redetermination of the half-life with high accuracy desirable.

The apparatus used was a 20-channel time analyzer, originally intended for neutron time-of-flight measurements, and similar in principle to other time-of-flight spectrometers already described.[1,2] For the measurement, a gated amplifier was inserted between the time analyzer proper and the crystal oscillator which produced pulses to switch the analyzer. A β-ray pulse from a set of 6 G-M tubes in parallel will open the amplifier, which stays open for a sequence of 20 pulses. In this way each β-pulse renders all the channels in turn operative once. The six β-ray tubes surround a thin-walled proportional counter, in whose sensitive volume a small thin-walled glass capillary containing radon is mounted. A β-pulse from RaC will be registered by the G-M tubes and is followed by an α-particle from RaC′, which is registered by the proportional counter. The time-distribution of the α-pulses relative to the β-pulses is analyzed by the time analyzer. The α-pulses are first fed to a special prearranging circuit where they are replaced by standard pulses derived from the oscillator. The position of these pulses has been chosen such that they always fall definitely in one channel and not on the border between two channels. These standard pulses are then fed to the time analyzer proper. With this arrangement the channels will be entirely equivalent and will not depend on varying tube characteristics

and stray capacities which would otherwise influence the wave forms of the respective grating pulses and the effective width of the channels.

The number of counts in the channels will fit an exponential curve with the half-life of RaC′, superimposed on a constant background. As all channels are in operation during the entire measurement, all varying factors such as sample decay, and changes in G-M tube characteristics, will influence them in the same way, and would not affect the half-life determination. A close analysis of possible sources of error failed to reveal any important source besides the statistical fluctuations of the number of counts. A treatment of the influence of the statistical fluctuations on the standard error in the half-life determination has been given by Peierls[3] and his procedure has been followed in the treatment of the data.

The measurements included a number of runs with a total measuring time of about 700 hours. For each run the half-life was calculated according to Peierls' procedure. The weighted average of these values was found, and the scattering of the individual values around this mean was checked, and found to agree with what could be expected if the only source of error were the statistical fluctuations of the number of counts. It was considered reasonable, however, to assume the possible existence of unknown systematic errors of the same order of magnitude as those caused by the statistical fluctuations. The final value for the half-life with its standard error under this assumption is 163.7 ± 0.2 μsec. This value is in fair agreement with previous values obtained by the method of delayed coincidences[4] (155 ± 5 μsec.), but seems to be outside the expected accidental errors of the values obtained by the coincidence method of variable resolution, which has yielded values[5–7] of about 145 ± 5 μsec. It is suggested that the possible presence of systematic errors in this method as previously applied should be investigated.

A multichannel system of the present sort seems to be capable of considerably higher precision than are previous methods. It is particularly suited for measurements on rapidly decaying substances where point by point measurements are difficult and inaccurate.

A detailed account of the experiment will be published in *Arkiv för fysik*.

[1] Bacher, Baker, and McDaniel, Phys. Rev. **69**, 443 (1946).
[2] J. Rainwater and W. W. Havens, Jr., Phys. Rev. **70**, 136 (1946).
[3] R. Peierls, Proc. Roy. Soc. **A149**, 467 (1935).
[4] J. C. Jacobsen and T. Sigurgeirsson, Kgl. D. Vid. Selsk. Medd. **20**, No. 11 (1943).
[5] J. Rotblat, Proc. Roy. Soc. **A177**, 260 (1941).
[6] A. G. Ward, Proc. Roy. Soc. **A181**, 183 (1942).
[7] Bunyan, Lundby, Ward, and Walker, Proc. Phys. Soc. London **61**, 300 (1948).

Decay Time and Efficiency of a Liquid Scintillator*

R. F. Post
Stanford University, Stanford, California
June 16, 1950

THE fluorescence decay time and efficiency for fast counting of a liquid scintillator[1,2] has been investigated, using a pulsed counter technique previously described.[3] The liquid studied was a saturated solution of terphenyl (*p*-diphenylbenzene) in toluene. Toluene was chosen as the solvent in preference to xylene because of its simple structure. By contrast, commercial c.p. xylene, which was the only grade available, contains all of the three components, meta, para and ortho. The relative effects of these components on the fluorescence was not known. Thus, although similar results were found using xylene as a solvent, toluene was chosen for the investigation here reported.

To obtain the decay time several photographs of count pulses from a Ag^{110} source immersed in the liquid were analyzed. The pulses were smoothed by tracing and an average decay time was determined, neglecting corrections due to the pulse rise times. The value and r.m.s. deviation found for the decay time (for decay $1/e$) at room temperature was: $1/\lambda=2.2\pm0.3\times10^{-9}$ second. The observed rise times (10 to 90 percent) ranged between 6 and 10×10^{-10} second, so that the error made in neglecting the finite rise time in the measurements is probably small.

For fast counting applications the maximum absolute rate of emission of photons from the scintillator is more important than is the integrated photon output. If observed by a system with a time resolution small compared with the decay time, the scintillation pulse heights are proportional to the rate of emission of photons. Thus, under these circumstances relative pulse heights per unit energy of excitation can be used as a criterion of excellence in comparing scintillators to be used for fast counting. Using an oscilloscope method described below, a measurement was made of maximum pulse heights obtained from the liquid scintillator, and also those obtained from a stilbene crystal of comparable size and shape. In the setup employed it was found that the maximum pulse heights obtainable from the liquid were up to 30 percent greater than those from stilbene. These results are of course peculiar to the particular optical geometry employed. Since no attempt was made to optimize the optical coupling between liquid and photo-multiplier, this performance of the liquid scintillator indicated that it should be superior to stilbene for use in fast counting. Although it can be inferred from the relative decay times of stilbene[4] and the toluene-terphenyl solution that the total number of photons per unit energy of excitation may be smaller in the case of the liquid, the maximum absolute rate of photon emission appears to be higher for the liquid.

In the experiments a small sample of the saturated solution was used, contained in a piece of fused quart tubing, core diameter about 1 cm and length about 3 cm. This tube was held close to the 931A photo-multiplier, and the assembly was then wrapped with aluminum foil to improve the optical coupling. The Bakelite base was removed from the photo-multiplier to reduce lead inductance and capacitance effects. A short length of RG7U 100 ohm coaxial cable was connected to the anode and first dynode of the photo-multiplier. This transmission line was terminated by a 100 ohm resistor at the photo-multiplier. Its other end was connected directly to one deflection plate of a DuMont K1017 high speed cathode-ray tube. A horizontal sweep of about 0.07-μsec. duration was used in obtaining the photographs of the count pulses. To obtain pulse height distributions the sweep connections were removed and a mask was placed across part of the oscilloscope screen. A photo-multiplier viewing the screen and operating into a conventional scaler was used to count pulses which appeared above the mask. Pulse height discrimination was introduced by applying a variable d.c. bias to the lower oscilloscope deflection plate, thus moving the spot away from the edge of the mask.

* This work is associated with the Linear Accelerator program at Stanford, supported by ONR Contract.
[1] Reynolds, Harrison, and Salvini, Phys. Rev. **78**, 488 (1950).
[2] H. Kallmann, Phys. Rev. **78**, 621 (1950).
[3] R. F. Post and N. S. Shiren, Phys. Rev. **78**, 81 (1950).
[4] R. F. Post and N. S. Shiren, Phys. Rev. **78**, 80 (1950).

The Velocity of Second Sound in Mixtures of He^3 and He^4

Ernest A. Lynton and Henry A. Fairbank
Sloane Physics Laboratory, Yale University, New Haven, Connecticut*
June 12, 1950

IT is now well established that small amounts of He^3 dissolved in liquid He II are associated with the normal component of the liquid. Since the normal component density is greatly decreased at low temperatures, many properties of the liquid are substantially affected by even a very small concentration of He^3. In particular, Pomeranchuk[1] has treated theoretically the effect of small amounts of He^3 on the velocity of second sound, and pre-

TABLE I. Velocity of second sound.

T(°K)[a]	Velocity He^3-He^4 (m/sec.)	Velocity He^4 (m/sec.)	Ratio of velocities
1.60	21.1	20.4	1.03
1.40	20.8	19.8	1.05
1.26	20.8	18.9	1.10

[a] H. van Dijk and D. Shoenberg, Nature **164**, 151 (1949).

dicts appreciable changes for concentrations as low as 0.1 percent He^3 in the temperature region below 1.6°K. This letter is a preliminary report on our measurements, which in general support Pomeranchuk's predictions.

Because of the very small amount of He^3 available the velocity measurements were carried out in a Lucite cavity only 1.0 cm in length, and 0.3 cm in diameter. At each end of the cavity was a carbon strip resistor. The whole was enclosed in a helium-tight metal container with Kovar-glass seals at either end through which the coaxial leads to the resistors passed. A 0.015-inch diameter tube was used to fill the cavity with the He^3-He^4 mixture. The measurements were taken by the pulse method,[2,3] in which the time of flight of a heat pulse between two resistors is measured by standard radar techniques. By feeding into the transmitter single pulses of heat and simultaneously pulsing the receiver resistance current, it was possible to minimize the separation of isotopes by heat flux.[4]

The results of preliminary experiments with a 0.09 ± 0.02 percent concentration of He^3 in He^4 are given in Table I, together with values for pure He^4 measured with the same apparatus. The values for He^4 agree with those found by previous observers,[3,5,6] and are about 10 percent lower than the theoretical values given by Pomeranchuk. Hence it is not surprising that the values for He^3-He^4 mixtures found by us are also lower than Pomeranchuk's by about 10 percent; however, the theoretical and experimental values of the ratio of the velocities agree to within the experimental error.

It must be pointed out that, since the liquid was not stirred, complete isotope equilibrium may not have been established in the liquid, so that the quantitative agreement may be fortuitous. However, all velocity measurements taken at the same temperature were consistent to within the experimental error of 1 percent. The correction which must be applied to the total concentration because of unequal vapor and liquid concentrations can be ignored because of the negligibly small vapor space in the filling tube.

The effect of heat flush was demonstrated strikingly by a special set of readings taken at 1.26°K. Instead of pulsing the direct current through the receiver element, as had been done for all other measurements, this current, generating a power of 0.24 milliwatt, was allowed to flow continuously for about 40 sec. During this time 5 measurements were taken, and the second sound velocity was found to decrease from 20.8 m/sec. to 19.6 m/sec., approaching the value for pure He^4 and showing that some of the He^3 initially in the cavity was flushed along the heat path into parts of the liquid volume outside the cavity. Such an effect was not observed when the current was pulsed; indeed, one can calculate that then the heat flush is quite negligible.

The He^3 used in this experiment was part of 1 cm^3, NTP, of 88 percent He^3 obtained from the Atomic Energy Commission. The concentration of He^3 in the mixture used was measured in a mass spectrometer by Dr. A. Zucker and Mr. J. Donaldson, to whom we are very grateful. We further wish to thank Professor H. L. Schultz for his assistance in designing the electronic parts of the apparatus.

Further details of this work will be published in a later article.

* Assisted by the ONR.

[1] I. Pomeranchuk, J. Exp. Theor. Phys. USSR **19**, 42 (1949).
[2] D. V. Osborne, Nature **162**, 213 (1948).
[3] J. R. Pellam, Phys. Rev. **75**, 1183 (1949).
[4] Lane, Fairbank, Aldrich, and Nier, Phys. Rev. **73**, 256 (1948).
[5] V. Peshkov, J. Phys. USSR **10**, 389 (1946).
[6] Lane, Fairbank, and Fairbank, Phys. Rev. **71**, 600 (1947).

The Ionization of Hydrogen in Metals

IRVIN ISENBERG
Institute for the Study of Metals, University of Chicago, Chicago, Illinois
April 26, 1950

THERE exists evidence that hydrogen dissolves in a metal as a proton plus an electron rather than as an atom. The electron contributed by the hydrogen is then indistinguishable from the ordinary valence electrons. Perhaps the most striking example of this occurs in the measurement of the paramagnetic susceptibility of palladium as a function of dissolved hydrogen.[1] The paramagnetic susceptibility drops linearly with increasing hydrogen content becoming zero at a concentration of approximately 0.63 hydrogen atom per palladium atom. For higher hydrogen concentrations the susceptibility is diamagnetic and is independent of the hydrogen concentration.

The interpretation of these facts, given by Mott and Jones,[2] is that the d-band of palladium is filled by the electrons which are stripped from the hydrogen atoms.

The purpose of this note is to demonstrate why hydrogen ionizes when dissolved in a metal. It is proposed that the field of the proton is screened by the conduction electrons to such an extent that in the resulting field there will be no bound state. The model used here will be a semiclassical one. With this model the conclusion is reached that hydrogen should ionize in all metals.

As a model of a metal containing a proton we consider all of the positive charge except that of the proton to be smeared out throughout the volume of the metal. We consider the bottom of the Fermi distribution to follow the potential so that we think of the conduction electrons as being in a box with a hole located in the neighborhood of the proton. Let E be the bottom of the Fermi distribution and ζ the top. Then

$$\zeta=E-\nu e^2k+\hbar^2k^2/2m, \tag{1}$$

where k is the wave number at the top of the Fermi distribution. The exchange energy of an electron at the uppermost level is $-2e^2k$. Although the correlation energy between electrons of the same spin does not have the form $-\nu e^2k$ we may consider this correlation to effectively increase ν to a value somewhat greater than 2.

The electron density is given by

$$n=8\pi k^3/3$$
$$=(8\pi/3h^3)\{(\nu me^2/h)+[(\nu^2m^2e^4/h^2)+2m(\zeta-E)]^{\frac{1}{2}}\}^3. \tag{2}$$

Let

$$\begin{aligned}\gamma&=\nu me^2/h,\\ \xi&=\gamma^2+2m(\zeta-E),\\ n&=(8\pi/3h^3)\{\gamma+\xi^{\frac{1}{2}}\}^3.\end{aligned} \tag{3}$$

Let V = potential energy of an electron.

Then Poisson's equation gives

$$\nabla^2V=-4\pi e^2[n(r)-n(\infty)]. \tag{4}$$

The term $n(\infty)$ takes into account the smeared out positive charge.

Then, since we assume that the bottom of the Fermi level follows the potential

$$\nabla^2V=\nabla^2E=-\nabla^2\xi/2m$$

and

$$\nabla^2\xi=(64\pi^2me^2/3h^3)\{[\gamma+\xi^{\frac{1}{2}}]^3-[\gamma+\xi_\infty^{\frac{1}{2}}]^3\}. \tag{5}$$

We now assume it to be legitimate to solve (5) by a perturbation method

$$\xi=\xi_\infty+\xi_1$$

where in (5) we will neglect all but the first power terms in ξ_1. Upon doing this the equation for ξ_1 is

$$\frac{1}{r^2}\frac{d}{dr}\left(r^2\frac{d\xi_1}{dr}\right)=\frac{64\pi^2me^2}{h^3}\left(\frac{1}{2}\frac{\gamma^2}{\xi_\infty^{\frac{1}{2}}}+\gamma+\tfrac{1}{2}\xi_\infty^{\frac{1}{2}}\right)\xi_1$$

$$\therefore\quad \xi_1=\text{const}\,\exp(+r/r_0)/r \tag{6}$$

where

$$r_0^{-2}=\frac{64\pi^3me^2}{h^3}\left(\frac{1}{2}\frac{\gamma^2}{\xi_\infty^{\frac{1}{2}}}+\gamma+\tfrac{1}{2}\xi_\infty^{\frac{1}{2}}\right)$$

$$=\frac{4(3n_\infty/\pi)^{\frac{1}{3}}}{a_0(3n_\infty/\pi)^{\frac{1}{3}}-(\nu/2\pi^2)}, \tag{7}$$

a_0 is the Bohr radius.

For $\nu=0$ this expression agrees with that obtained by Mott[3] who considered the screened Coulomb field in a metal ignoring exchange terms.

The potential is given by

$$V=-e^2\exp(-r/r_0)/r \tag{8}$$

and the charge distribution is

$$n(r)-n(\infty)=(1/4\pi r_0^2)\exp(-r/r_0)/r. \tag{9}$$

Sachs and Mayer[4] found that for a potential of the form (8) to have no bound state we must have

$$r_0<0.842a_0.$$

This criterion for our case leads to

$$4(0.842)^2(3n_\infty a_0^3/\pi)^{\frac{1}{3}}>(3n_\infty a_0^3/\pi)^{\frac{1}{3}}-(\nu/2\pi^2). \tag{10}$$

The inequality (10) is always satisfied if

$$\nu>1.7. \tag{11}$$

Equation (11) appears to be generally valid so that our model yields the result that a proton in a metal will have no bound state.

An analysis identical to that given above shows that a hydrogen-like atom with charge greater than unity will become singly ionized but not doubly ionized.

[1] J. Aharoni and F. Simon, Zeits. f. physik Chemie **B4**, 175 (1929). B. Svensson, Ann. d. Physik **18**, 229 (1933).
[2] N. F. Mott and H. Jones, *Theory of the Properties of Metals and Alloys* (Oxford University Press, London, 1936), p. 200.
[3] N. F. Mott, Proc. Camb. Phil. Soc. **32**, 281 (1936).
[4] R. G. Sachs and M. Goeppert-Mayer, Phys. Rev. **53**, 991 (1938).

The Virial Theorem and the Variation Principle

IRVIN ISENBERG
Institute for the Study of Metals, University of Chicago, Chicago, Illinois
June 12, 1950

IF, instead of using the correct wave function the best wave function of a certain form is used, the question arises as to whether or not the virial theorem is satisfied. The purpose of this note is to point out that the virial theorem is valid when the wave function is obtained by a variation of the expectation value of the Hamiltonian with respect to a change in scale and also under a slight but important generalization of this variation. Thus, suppose that

$$\psi'(x_i)\equiv\psi'(x_1, y_1, z_1; x_2, y_2, z_2; \cdots x_n, y_n, z_n) \tag{1}$$

is an arbitrary wave function for n particles. If, using the wave function

$$A(\lambda)\psi'(\lambda x_i)\equiv A(\lambda)\psi'(\lambda x_1, \lambda y_1, \lambda z_1; \cdots \lambda x_n, \lambda y_n, \lambda z_n) \tag{2}$$

the expectation value of the Hamiltonian is formed, then λ is determined from

$$\frac{\partial}{\partial\lambda}A^2\int\psi'^*H\psi'd^{3n}x=0; \tag{3}$$

A is a normalization factor.

Let

$$A(\lambda_m)\psi'(\lambda_m x_i)=\psi(x_i), \tag{4}$$

where λ_m satisfies (3).

Then we know that

$$\left[\frac{\partial}{\partial\lambda}\int N^2\psi^*(\lambda x_i)H\psi(\lambda x_i)d^{3n}x\right]_{\lambda=1}=0, \tag{5}$$

where N is determined from

$$N^2\int|\psi(\lambda x_i)|^2d^{3n}x=1$$

or

$$N^2=\lambda^{3n}, \tag{6}$$

since $\psi(x_i)$ is normalized.

If

$$H=-\Sigma_i\frac{\hbar^2}{2m_i}\frac{\partial^2}{\partial x_i^2}+V(x_i).$$

Equation (5) now reads

$$\left[\frac{\partial}{\partial\lambda}\left(\lambda^2\bar{T}+\int\psi^*(\xi_i)V(\xi_i/\lambda)\psi(\xi_i)d^{3n}\xi\right)\right]_{\lambda=1}=0,$$

$$\bar{T}\equiv-\int\psi^*(x_i)\Sigma_i\frac{\hbar^2}{2m_i}\frac{\partial^2}{\partial x_i^2}\psi(x_i)d^{3n}x.$$

But

$$\left[\frac{\partial}{\partial\lambda}V(\xi_i/\lambda)\right]_{\lambda=1}=-\Sigma_i\xi_i\frac{\partial V(\xi_i)}{\partial\xi_i}. \tag{7}$$

Therefore

$$2\bar{T}-\Sigma_i\left\langle x_i\frac{\partial V(x_i)}{\partial x_i}\right\rangle_{Av}, \tag{8}$$

which is the virial theorem.

The above class of trial functions for which the virial theorem holds can be extended to include functions of the form $q(x_i)$, $f(x_i)$ where $q(x_i)$ is a homogeneous function of the x_i and only the scale of the argument of f need be varied. This includes cases like $r^l\exp(-\alpha\lambda r)$.

Now ψ may be a very poor trial function. Consequently the virial theorem cannot be used as a test of the "goodness" of the function chosen. On the other hand, since the above demonstration includes a great many cases which one meets in practice, it can be concluded that the virial theorem is applicable in most of the approximations commonly used.

The existence of a virial theorem depends only on the existence of an energy variation principle. Thus the above argument is applicable in the case of the statistical models, e.g., Thomas-Fermi, Thomas-Fermi-Dirac, the equations of which can be derived from a variation principle[1] in which the charge density is varied. Any trial charge density which has been fitted by a variation in scale will again satisfy a virial theorem.

The author would like to thank Professor C. Zener for very helpful discussions of this subject. This work arose through a conversation with Professor J. C. Slater.

[1] P. Gombas, *Die Statistische Theorie des Atoms* (Springer-Verlag, Berlin, 1949).

Superconductivity of Vanadium

AARON WEXLER AND W. S. CORAK
Westinghouse Research Laboratories, East Pittsburgh, Pennsylvania
June 19, 1950

IT is well known that the superconductive properties of most samples of transition metals of the fourth and fifth groups of the periodic table are characterized by inordinately large values of the magnetic field required for the destruction of superconductivity. These values do not correspond to systems exhibiting a reversible "Meissner effect" and hence are of no value for thermodynamic calculations of the differences in specific heat of the normal and superconductive phases and of the heats of transition. Illustrations of this situation are to be found in the recent work on niobium[1] and uranium.[2] On the other hand, some samples of niobium and tantalum have been found to exhibit at least partial reversibility,[3] and the thermodynamic calculations have led to most interesting consequences.

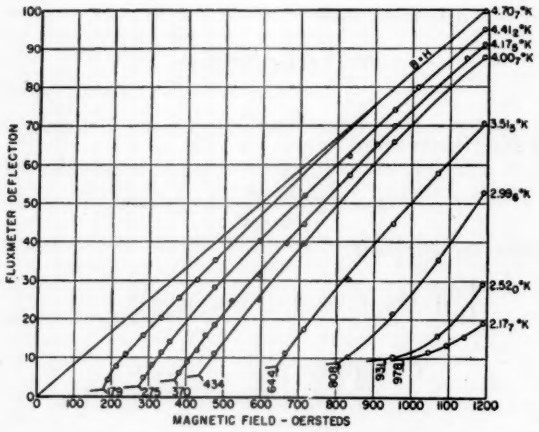

FIG. 1. Magnetic induction of superconductive vanadium.

It appeared to us that for the clarification of the nature of the properties of the hard superconductors the study of the superconductivity of vanadium would be most fruitful. In the first place, the temperature range in which this metal exhibits superconductivity is very convenient from an experimental viewpoint. Secondly, vanadium has a relatively low melting point, a factor which facilitates metallurgical treatment of the metal.

The superconductivity of vanadium, as determined by resistance measurements, was first reported by Meissner and Westerhoff.[4] The recent data of Webber *et al.*[5] gave an initial slope of 4100 oersteds per degree for a particular sample of vanadium.

Through the kindness of Dr. B. W. Gonser of the Battelle Memorial Institute a sample of pure vanadium was made available to us. The magnetic properties of the superconductive material were determined by a method which, in principle, was the same as that used by Keeley and Mendelssohn.[6] A coil of No. 40 copper wire was wrapped around the specimen which was a cylinder 0.070 in. in diameter and 1 in. long. The residual resistivity relative to the ice-point resistivity of a strip rolled from this cylinder was 0.051.

Isothermal measurements were made at each of eight temperatures. These consisted in the determination of a quantity proportional to the integral of the voltage induced in the coil when the field was reduced from a given value to zero. The data are indicated in Fig. 1. For each temperature, the fluxmeter deflection is a linear function of the field until a critical value is reached. These critical values have been assumed to represent the threshold fields at the various temperatures, and have been plotted in Fig. 2. The initial slope of this curve is 400 oersteds per degree; in general the curve is quite similar to that for tantalum on the basis of which Daunt and Mendelssohn have made thermodynamic calculations. From Fig. 1 it is seen that the "Meissner effect" is most pronounced near the critical temperature and that the reversibility becomes much poorer at lower temperatures.

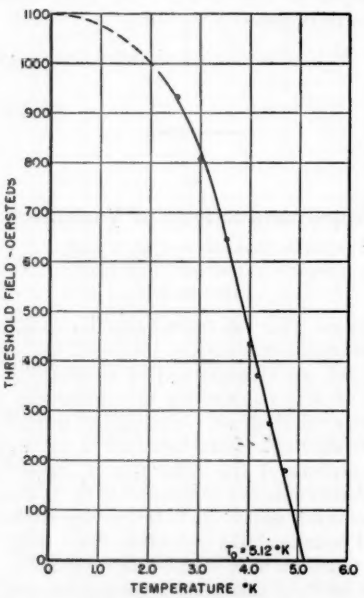

FIG. 2. Threshold fields for superconductive vanadium.

Work is in progress on the factors responsible for the irreversibility associated with the transition and hence the data herein reported are given provisionally.

A detailed account of the experimental methods used and of the effect of metallurgical factors upon the electrical and magnetic properties of superconductive vanadium will be reported in the near future.

[1] Cook, Zemansky, and Boorse, Phys. Rev. **79**, 212 (1950).
[2] B. B. Goodman and D. Shoenberg, Nature **165**, 441 (1950).
[3] J. G. Daunt and K. Mendelssohn, Proc. Roy. Soc. (A) **160**, 127–36 (1937).
[4] W. Meissner and H. Westerhoff, Zeits. f. Physik **87**, 206 (1934).
[5] Webber, Reynolds, and McGuire, Phys. Rev. **76**, 293 (1949).
[6] T. C. Keeley and K. Mendelssohn, Proc. Roy. Soc. (A) **154**, 378 (1936).

Cosmic Rays as the Source of General Galactic Radio Emission

K. O. KIEPENHEUER
Yerkes Observatory, University of Chicago, Williams Bay, Wisconsin
June 20, 1950

THE galactic radio emission is not a thermal free-free radiation of interstellar gas, as was first believed. The electronic temperature would have to be of the order of 100,000° in contradiction to all spectroscopic evidence which gives values around 10,000°. Stars could be considered as sources only under very artificial assumptions. The observed intensities, which must come from the outermost layers of stellar atmospheres, could not be blackbody radiation[1] and might be understood only in terms of coherent plasma oscillations of extended regions. The formation and maintenance of these oscillations is hardly possible in stellar atmospheres.[2]

It will now be shown that the general cosmic radiation of our star system is a high frequency source of sufficient power. In interstellar space, at least inside the interstellar clouds which occupy about 5 percent of space, the mean density of kinetic energy ought to be of the same order as the magnetic-field energy; therefore, fields of around 10^{-6} gauss are to be expected. An energetic electron with energy $W \gg m_0c^2$, which is circulating in this field, is radiating electromagnetic energy into a very narrow cone whose angular aperture is m_0c^2/W in the direction of motion. Therefore, an observer at rest receives very short pulses corresponding to a frequency which is very much higher than the classical Larmor frequency, ν_0. The mean spectral intensity distribution of this radiation will then be[3]

$$P(\nu) \approx (e^2/\pi R)(\nu/\nu_0)^{\frac{1}{3}}$$

for $\nu_0 \ll \nu < \nu_c$, where R is the radius of the electron's circular orbit and $\nu_c = \frac{3}{2}\nu_0(W/m_0c^2)^3$. If n_e is the number of electrons per cm^3 with energy W, the emissivity of high frequency radiation will be

$$\epsilon_\nu \Delta\nu = n_e P(\nu)\Delta\nu = (e^3 H/\pi W) n_e (\nu/\nu_0)^{\frac{1}{3}} \Delta\nu \text{ ergs/cm}^3\text{/sec.}$$

This increases steadily with frequency until $\nu = \nu_c$ and then decreases rapidly. The observed distribution[1,4] within the frequency range of 10 to 3000 Mc seems rather to be $\propto \nu^{-0.3}$. We therefore expect to be already in a region with $\nu \geq \nu_c$. Also the

involved interstellar magnetic field strengths might vary through space and so influence sensibly the spectral intensity distribution. If the thickness of the emitting layer is D, the intensity of the radiation becomes $I=\epsilon_\nu \Delta\nu D$. Let us suppose that there is one electron per 100 cosmic-ray particles,[5] that is, $n_e \approx 3\times 10^{-11}$ cm^{-3}. If we tentatively put $W=10^8$ ev and $D=1000$ light years (1/100 of the diameter of the galaxy), assuming $\nu=100$ Mc, and $\Delta\nu=10$ Mc, we get a radiation intensity of $I\approx 10^{-11}$ erg/cm^2/sec. This agrees in order of magnitude with the observations of Hey, Parsons, and Philips.[4]

The total radiation loss of an electron moving in a homogeneous magnetic field, H, is

$$-dW/dt=(4\pi/3)\nu_0(e^2/R)(W/m_0c^2)^4\sim W^2H^2.$$

Since this radiation loss increases so rapidly with energy, electrons with energies greater than about 10^9 ev are not expected. It seems also possible that electrons are eliminated from cosmic rays in the vicinity of stars by collisions with thermal photons.[6] The composition of cosmic rays we observe at the outer boundary of the earth's atmosphere (being close to the sun) is therefore not an average sample of interstellar space.

The general radio emission shows some relation to the visible structure of the galaxy,[4] but does not seem to be directly correlated with stars or other galactic objects. It follows, therefore, that the sources of radio emission are more closely related to the general shape of the galaxy than to its visible components. This conclusion favors Fermi's hypothesis that the distribution of cosmic rays and of galactic matter is more or less the same, cosmic rays being created in interstellar space and not by the stars.

A relation between radio emission and cosmic rays has previously been suggested by Alfvén[7] for the special case of so-called radio stars (discrete centers of strong radio emission). This interesting suggestion, which has stimulated the above analysis, appears to the writer to be in need of re-examination.

I wish to thank Mr. Grote Reber for helpful discussions.

[1] A. Unsöld, Zeits. f. Astrophysik **26**, 176 (1949).
[2] M. Ryle, Proc. Phys. Soc. London **A62**, 483 (1949).
[3] J. Schwinger, Phys. Rev. **75**, 1912 (1949).
[4] Hey, Parsons, and Philips, Proc. Roy. Soc. **A192**, 425 (1947).
[5] There must be a certain number of electrons in cosmic rays as a direct consequence of their ionization losses in interstellar space and of electron pair production by encounters of protons and thermal starlight photons. Also there is some indication of the existence of electrons in the primary radiation given by direct measurements (B. Rossi, Rev. Mod. Phys. **21**, 104 (1949)) and by the east–west asymmetry (L. Jánossy, *Cosmic Rays* (Oxford University Press, London, 1948)).
[6] E. Feenberg and H. Primakoff, Phys. Rev. **73**, 449 (1948).
[7] H. Alfvén and N. Herlofson, Phys. Rev. **78**, 616 (1950).

Ferromagnetic Block

L. W. McKeehan
Sloane Physics Laboratory, Yale University, New Haven, Connecticut
February 3, 1950

THE theory of ferromagnetic domains has recently been ably discussed,[1] and it is now commonly accepted that a region in which the electron magnetic moments responsible for ferromagnetism are collectively constrained to be nearly parallel is not, in general, homogeneous in all other respects.

Depending upon conditions during crystallization and upon mechanical, thermal, and magnetic treatments thereafter, a single domain in a technically unsaturated specimen may contain many crystals, may be part of one crystal, or may be a temporary coalition of whole crystals and parts of crystals. A single domain boundary may therefore be a crystal boundary in part and may elsewhere be determined by defects in homogeneity within what is ordinarily called a crystal.

The tendency of real crystals[2] to be inhomogeneous, and to constitute so-called mosaics,[3] or lineages[4] of more nearly homogeneous structure, is now very well known, and explains how a domain boundary, in its progress through a crystal after a change in applied field or stress, may be temporarily stopped before a whole crystal has been added to the expanding domain.

The stepwise motion of a domain boundary, the Barkhausen phenomenon, can thus proceed by steps that are individually less than the linear dimensions of whole domains, and this is easier the larger the domains. In a stretched or bent polycrystalline wire, for example, the stable domains may be large fractions of the whole volume, and still the analysis of a jump in their average magnetization will disclose the transfer of very small regions from one domain to another.

These facts have led to some confusion in describing the processes occurring along technical magnetization curves. Thus, authors have estimated "domain" size from data on changes in domain size rather than by more direct means, such as powder patterns, which locate domain boundaries at rest positions. Such confusion would be less likely if a separate term could be used for a region which can be transferred continuously, quickly, and spontaneously, from one domain to another, when the potential barrier to the initiation of the transfer has been surmounted or penetrated. As already suggested, such a region may not, in many cases, be capable of existence as a stable isolated domain, so that it should not be so labeled.

The name suggested for this structural unit of the ferromagnetic domain is "ferromagnetic block." The boundaries of a ferromagnetic block are the surfaces at which local inhomogeneities can stop the migration of a domain boundary under appropriate conditions. This confines a block to a single crystal and usually to a part of a single crystal, whereas a domain is not so limited. It is also clear that domain boundaries are predominantly also block boundaries, but that the converse statement is not valid. In actual changes in magnetization, the transfer of a block is sudden only for particular directions of motion of domain boundaries across it, those directions in which the block has its stable directions of magnetization. In microcrystalline powders, of course, there are still blocks, even when no volume large enough to form a domain can be found.

[1] C. Kittel, Rev. Mod. Phys. **21**, 541 (1949). See also L. W. McKeehan, Phys. Rev. **79**, 745 (1950).
[2] A. Smekal, Ann. d. Physik (4) **83**, 1202 (1927).
[3] F. Zwicky, Proc. Nat. Acad. Sci. **15**, 816 (1929).
[4] M. J. Buerger, Zeits. f. Krist. **89**, 195 (1934).

Debye Modes and Superconductivity

William Band
Department of Physics, State College of Washington, Pullman, Washington
June 20, 1950

RANDOMNESS is an essential characteristic of thermal motion that is omitted from conventional discussions of the modes of vibration of a crystalline solid. Randomness can be taken care of if we include a proper statement concerning the phases of the Debye modes. A complete analysis of the state of motion of the lattice is possible only in terms of boundary conditions at the surface of the crystal. Under thermal bath conditions the boundary of the crystal is subject to random changes due to thermal fluctuations in the bath. An ideal single crystal of finite size is not subject to definable stationary boundary conditions and therefore the phases of the normal modes are not determinable, being necessarily subject to random changes in the course of time.

If we resolve any stationary mode into two progressive waves, there will exist an effective free path during which no phase change will occur. This free path defines a domain magnitude within which the modes are coherent in phase, while between neighboring domains their phases are incoherent. A positive sur-

face energy exists between neighboring domains because the incoherence in phase obliges the lattice points to depart anomalously from their relative equilibrium configurations.

A crystal may conceivably be at so low a temperature that each domain contains nothing but the zero-point energy of its Debye modes. The crystal as a whole will still have non-zero entropy due to the randomness of phase incoherence between the domains. These phase discontinuities will be responsible for residual resistance of the lattice to electric current.

Because of the surface energy in the domains it can be shown that there exists a transition temperature below which the disorder due to phase incoherence gives way to order and phase coherence throughout the crystal. It is suggested that such an order-disorder transition among the phases of the zero-point Debye modes might be at least in part responsible for superconductivity, and could conceivably account for the isotope effect recently reported.[1]

[1] E. Maxwell, Phys. Rev. **78**, 477 (1950); Reynolds, Serin, Wright, and Nesbitt, Phys. Rev. **78**, 487 (1950).

On the Lower Levels of He^5

HERBERT GOLDSTEIN
Massachusetts Institute of Technology, Cambridge, Massachusetts
June 12, 1950

THE backscattering of neutrons in helium has been investigated by Staub and Tatel,[1] who observed a barely resolved double peak at incident neutron energies of 1.0 and 1.3 Mev. These results have generally been taken as evidence of a P doublet of levels in He^5 each about 0.4 Mev wide,[2] with a roughly comparable separation. It has not been possible, however, to reconcile subsequent experiments[3,4] with such a level scheme.[5] Thus, Wheeler and Barschall[6] have shown that the scattering data at a neutron energy[4] of 2.5 Mev require a $|P_{\frac{3}{2}}-P_{\frac{1}{2}}|$ phase shift difference much larger than could be obtained on the basis of the Staub and Tatel level assignment. It is the purpose of this note to suggest an alternative level scheme which is in more general agreement with all of the pertinent published data.

The recently verified similarity in the level structure of the pair of mirror nuclei Li^7, Be^7, suggests using the mirror nucleus Li^5 as a model for the levels of He^5. Unfortunately the data[7] for proton scattering in He up to 3.58 Mev, while much more accurate than those for neutron scattering, have been shown to be consistent with two possible level schemes.[8] It can be seen readily that one of the alternatives, a normal P doublet with a separation of 1.1 Mev, is incompatible with the He^5 data. The other scheme is an inverted P doublet in which the $P_{\frac{1}{2}}$ level lies above the observed energy range. From the measured $P_{\frac{1}{2}}$ phase shift it can be estimated, however, that the separation of the doublet must be between 2 and 5 Mev. It is this level scheme which is consistent, on the whole, with the neutron scattering measurements, and which therefore is probably also the correct one for Li^5.

Although the levels of the doublet are quite wide, the separation is so large that the upper $P_{\frac{1}{2}}$ level can have little influence on phenomena occurring in the neighborhood of the $P_{\frac{3}{2}}$ resonance. On this model it should therefore be possible to explain the observations below 1.6 Mev in terms of a single $P_{\frac{3}{2}}$ level, plus, of course, an S potential scattering. The somewhat crude total cross-section data of Hall and Koontz between 0.6 and 1.6 Mev can indeed be fitted by a $P_{\frac{3}{2}}$ level at 1.20 Mev with a half-width of 1.4 Mev, along with the S potential scattering caused by an impenetrable sphere of radius 2.5×10^{-13} cm. [It is necessary to correct the experimental cross sections above 1.0 Mev for the presence of the second group of neutrons produced in the Li(p, n) reaction.] A single level cannot, of course, reproduce the double peak observed in the backscattering (which in any case depends on only one or two points) but there is otherwise general agreement with the absolute magnitude and width of the curve measured by Staub and Tatel. Destructive interference takes place between the S potential scattering and the $P_{\frac{3}{2}}$ resonance above the position of the level. As a result the back-scattering resonance appears much narrower than the total cross-section curve, which explains the very small backscattering observed by Staub and Tatel above 1.5 Mev. This same phenomenon of interference between resonant and potential scattering accounts for the appearance of the angular distributions measured between 0.6 and 1.6 Mev by Hall and Koontz.[4] In forward scattering the interference is constructive above the resonance and destructive below the resonance. Hence one should expect a progressive shift from predominantly backward scattering at low energies to very pronounced forward scattering above the $P_{\frac{3}{2}}$ level, and this is exactly what is observed. Hall has recently pointed out[9] that the angular distributions must be corrected for the presence of the second group of neutrons in the incident beam, and once this is done quantitative agreement can be obtained with the Hall and Koontz curves using the same nuclear radius given above.

With the available data it is difficult to fix at all precisely the position of the upper component of the doublet. The only published experiments above 2 Mev which might bear on the question are those of Barschall and Kanner[3] on the angular distribution of neutron scattering at 2.5 and 3.1 Mev. It is no longer possible to interpret these measurements solely in terms of the $P_{\frac{3}{2}}$ level, nor can one exclude the possibility of levels other than the P doublet playing some role. If it is assumed that only the P resonances are involved then the data would seem to indicate that the $P_{\frac{1}{2}}$ level is in the neighborhood of 3.5 Mev. More measurements in the region above 2 Mev, especially angular distributions, would appear to be highly desirable in order to determine accurately the splitting of the P doublet.

[1] H. Staub and H. Tatel, Phys. Rev. **58**, 820 (1940).
[2] All energies refer to the laboratory system.
[3] H. H. Barschall and M. H. Kanner, Phys. Rev. **58**, 590 (1940).
[4] T. A. Hall and P. R. Koontz, Phys. Rev. **72**, 196 (1947).
[5] See, for example, the discussion in L. Rosenfeld, *Nuclear Forces* (New York, 1949), p. 363.
[6] J. A. Wheeler and H. H. Barschall, Phys. Rev. **58**, 682 (1940).
[7] Freier, Lampi, Sleator, and Williams, Phys. Rev. **75**, 1345 (1949).
[8] C. L. Critchfield and D. C. Dodder, Phys. Rev. **76**, 602 (1949).
[9] T. A. Hall, Phys. Rev. **77**, 411 (1950).

A Note on Asymmetric Fission*

T. YASAKI AND O. MIYATAKE
Physics Institute, Mathematics Institute, Yamanashi University, Kofu City, Japan
March 20, 1950

WE wish to report on research into the mechanism of the asymmetric fission of uranium by slow neutrons. Frankel and Metropolis[1] have carried out elaborate calculations and concluded that asymmetric fission is not favored in the liquid-drop model.

We have carried out an investigation on the mechanism of fission on the assumption that the nucleus consists of two concentric spherical parts of different charge densities, with uniform mass density and a constant volume for all distortions. The compound nucleus $_{92}U^{236}$ is assumed to have 27 protons and 50 neutrons in its inner part (core), whose radius is 69 percent of that of the nucleus, and its outer part to consist of 65 protons and 94 neutrons.[2] The charge density is supposed to be uniform in each part. The radius vector is expanded as $R'(\mu)=R_0[1+\Sigma a_i P_i(\mu)]$.

The origin of the coordinates is taken at the center of the core. The core is assumed not to be distorted by slow neutrons. The energy difference is given by

$$\Delta E_{S+E}=4\pi R_0^2\{(0.04931+0.04931y)a_1^2-ya_2^2 +(1.34885-1.15115y)a_3^2+(2.92276-1.57724y)a_4^2 +(0.51581+0.51581y)a_1a_3+(1.33422+1.96668y)a_1^2a_2 +(0.56302+1.80514y)a_1a_2a_3+(7.50784+8.74226y)a_1a_3a_4 +(0.27321+0.42380y)a_2^3-(1.79159+1.36995y)a_2a_3^2 -(16.07229+15.66159y)a_2a_4^2-(3.43959+2.83349y)a_2^2a_4 -(17.85011+17.46441y)a_3^2a_4-(7.19208+7.19208y)a_1^2a_4 -(9.63615+9.52171y)a_4^3-(3.05685+2.40685y)a_1^4 -(4.16925+1.15734y)a_2^4-(14.87031+4.80053y)a_3^4 -(35.98336+9.36639y)a_4^4\},$$

where $y=x/1.014-1$, $x=3Z^2e^2/40\pi R_0^3$. We have used the first four harmonics only. The number 1.014 comes from the difference between our model and that of Bohr and Wheeler.[3] We define the dimensionless function $f(x)$ of the charge-mass ratio as is done in the paper of Bohr and Wheeler. We obtain $f(0)=0.260$, $f(1.014)=0$ and $f'(0)=-0.195$. Then the following conclusions may be drawn from the above formula. If we put a_1 equal to zero, the curve of $f(x)$ is always above that of Bohr and Wheeler, and we obtain the value of r_0 as 1.32×10^{-13} cm, and the threshold energy obtained is somewhat larger than that of the experimental results. If a_1 is unconstrained like the other coefficients, the value of $f(x)$ in the neighborhood of $x=0.8$ is about 1/100 of that of Bohr and Wheeler. Thus in order to get agreement with the experimental results, we must assume that a_1 has some degree of freedom. A more detailed account of this point will be published in the near future.

On the other hand, the extremum of the total kinetic energy of the fragments, separated by twice the radius of the compound nucleus, is given when the ratio of their masses is 3:2.

The existence of the core is effective when the excitation energy is low, but it is less effective for high energy excitation. Thus symmetric fission becomes more favorable when the heavy nuclei are bombarded by fast particles.

We are indebted to Professor I. I. Rabi who called our attention to M. Mayer's paper, when he visited Japan at the end of 1948. The assistance given by Miss M. Kazuno is highly appreciated.

* Presented at the Kyoto meeting of Japanese Physical Society, October 20–24, 1949.

[1] S. Frankel and N. Metropolis, Phys. Rev. **72**, 914 (1947).

[2] These figures are taken from Wigner's model and Mayer's idea on the closed shells in nuclei. E. Wigner, University of Pennsylvania Bicentennial Conference (1941); M. G. Mayer, Phys. Rev. **74**, 235 (1948).

[3] N. Bohr and J. A. Wheeler, Phys. Rev. **56**, 426 (1939).

On the Particles Initiating High Energy Penetrating Showers*

M. B. Gottlieb, A. J. Hartzler,** and Marcel Schein
Department of Physics, University of Chicago, Chicago, Illinois

June 20, 1950

A CLOUD chamber[1] with a sensitive volume measuring 16″×24″×7″ deep containing 300 g/cm² of gold in the form of sixteen 1-cm plates[2] was operated at Climax, Colorado (alt. 11,500 ft.). Counters located below and across the center of the chamber enabled the selection of penetrating showers caused either by ionizing or non-ionizing incident particles. The counter control required that at least three particles emerge from the 10 cm of lead below the cloud chamber.

Out of 7360 pictures there are over 1500 showing penetrating showers. Thus far 73 selected events originating above the counters in the chamber have been examined to determine the relative number of events initiated by ionizing and non-ionizing particles. These were all high energy events, showing clearly the production of both cascade radiation and well-collimated penetrating particles. Events occurring near the top or sides of the chamber were not counted. In order to be termed an ionizing incident particle it was necessary that this particle pass through at least one plate before initiating the shower, and be visible in two spaces. Furthermore the direction of the incident track was checked in at least two of the three cameras to see that it was aligned along the axis of the shower. Sixteen counters located above the chamber provided an additional check. A careful estimate indicated that the energy of these events was above 10^{10} ev.

TABLE I. Results on ionizing and non-ionizing particles.

Initiating particle	No. of cases	Percent of total
Ionizing	59	81
Non-ionizing	3	4
Questionable	11	15
Total	73	100

The results of Table I were obtained for the relative numbers of ionizing and non-ionizing particles.

Questionable cases are mainly those in which information from the counter bank above the chamber did not correspond with the observed incident track, and those where an old track in the vicinity made observation of the incident track uncertain.

Even if one were to consider the very improbable case that all of the questionable events are non-ionizing, these data show that the high energy events are predominantly initiated by ionizing particles. This may disagree with the recent results of Powell's group[3] who found about equal numbers of their high energy events to be initiated by ionizing and non-ionizing particles. However, one should consider the fact that their data include only a small number of events of comparable energies. This high fraction of ionizing incident particles would indicate that most of these nuclear events are not initiated by secondary nucleons.

The vertical (zenith angle less than 15°) flux of particles initiating these high energy mixed showers was found to be $1.1\pm0.8\times10^{-6}$ cm^{-2} sec.$^{-1}$ sterad.$^{-1}$. The large error given is mainly due to the fact that corrections of the solid angle for spread of the showers had to be made. This rate is about one-fifth of that measured by Fretter,[4] but in view of our rigid selection and higher energy this difference does not seem unreasonable.

If it is assumed that the particles initiating these penetrating showers are primary protons with a mean free path of 67 g/cm² which corresponds to the geometric cross section in air, then the vertical flux of primary protons at the top of the atmosphere of energy larger than 10^{10} ev turns out to be 0.029 ± 0.02 cm^{-2} sec.$^{-1}$ sterad.$^{-1}$. Assuming the value of the primary flux at 55°N as given by Winckler[5] of 0.16 cm^{-2} sec.$^{-1}$ sterad.$^{-1}$ and the corresponding power law spectrum, one gets the value for the number of protons with energy above 10^{10} ev equal to 0.02 cm^{-2} sec.$^{-1}$ sterad.$^{-1}$, which is as good agreement as can be expected. The effect of the Gross transformation has been calculated and has been found to be small compared with experimental errors.

The measurements of Tinlot[6] and of Walsh and Piccioni[7] have indicated the absorption mean free path for penetrating showers to be 118 g/cm². Using this figure to extrapolate our measured flux to the top of the atmosphere gives about 1/60 of the observed value of the primary flux. This is entirely outside of our experimental errors.

Our figures do not exclude in any way the possibility that in the last mean free path above the apparatus π-mesons have been produced in multiples which can give an additional contribution to the observed shower rate. Within the errors of this experiment, there could be possibly as many as 50 percent of the nuclear events due to π-mesons. This is true, of course, only if, at these high energies, the cross section for penetrating shower production by

π-mesons is comparable to that for protons. Secondary nuclear events occurring in the chamber are now being analyzed to provide more direct information in this matter.

* Assisted by the joint program of the ONR and AEC.
** AEC Predoctoral fellow.
[1] A complete description of the apparatus will be published.
[2] We are very grateful to the ONR for securing so promptly these machined gold plates.
[3] Brown, Camerini, Fowler, Heiller, King, and Powell, Phil. Mag. **VXL**, 862 (1949).
[4] W. B. Fretter, Phys. Rev. **73**, 41 (1948); **76**, 511 (1949).
[5] J. R. Winckler, private communication to Marcel Schein.
[6] J. Tinlot, Phys. Rev. **73**, 1476 (1948); **74**, 1197 (1948).
[7] T. G. Walsh and O. Piccioni, Echo Lake Conference, (June, 1949).

The Measurement of Proton Energies with Scintillation Counters*

W. FRANZEN, R. W. PEELLE, AND R. SHERR
Princeton University, Princeton, New Jersey
June 19, 1950

EXPERIMENTS with energetic heavy particles frequently require the use of energy indicating detectors of large stopping power. Scintillating crystals, due to their high speed of response, are promising materials for this purpose. The size of the light flash produced can usually be interpreted in terms of the energy of the bombarding particle. However, existing information on this question is not very complete.[1–6] For this reason, the response to protons from the Princeton cyclotron as a function of proton energy for sodium iodide, potassium iodide, and anthracene has been investigated, and the widths of the resulting pulse height distributions have been studied.

The apparatus used in this investigation consisted of a scattering tube holding a 0.1-mil platinum foil which caused protons from the external collimated cyclotron beam to be scattered through 30° into the scintillating crystal which was mounted in optical contact with a RCA 5819 photo-multiplier tube. Pulses from the photomultiplier were amplified by a cathode follower and a Model 501 amplifier (having a "rise time" of 0.15 μsec. and a "decay time" of 5 μsec.) and analyzed by a single-channel differential discriminator. Energy calibration of the beam was accomplished by an air range measurement which yielded a value of 16.9 Mev, estimated to be accurate to ± 0.2 Mev.

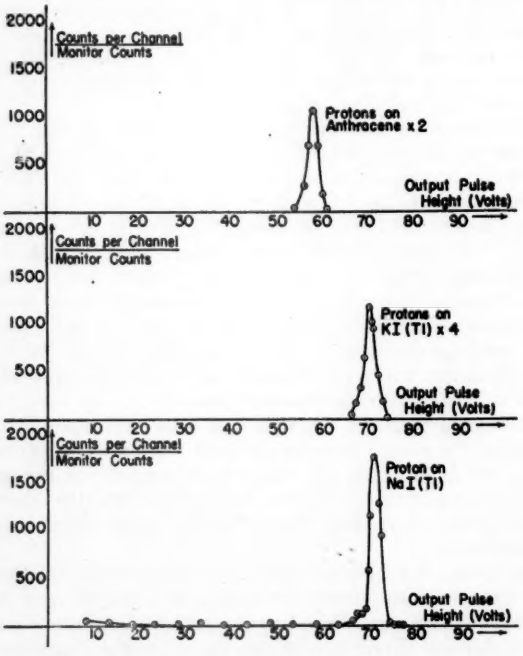

FIG. 1. Pulse height distributions observed with proton bombardment of sodium iodide, potassium iodide and anthracene crystals. The bombarding energy was 16.4 Mev. In the case of sodium iodide, the observed background of small pulses (below the main peak) is shown.

The types of pulse height distributions obtained for the three types of crystals are illustrated by Fig. 1. With sodium iodide and anthracene, nearly Gaussian distributions are observed having a width at half-maximum of three percent of the peak pulse height (bombarding energy 16.4 Mev). The energy spread in the beam does not contribute significantly to this width.

The relationship between the peak pulse height and the energy of the incident protons for the three materials is illustrated by Fig. 2. The energy of the incident protons was varied by interposing aluminum foils. At low energies, the experimental points are less precisely located by this procedure than at high energies. For this reason the intercepts of the straight lines drawn through the experimental points in the cases of sodium iodide and potassium iodide are somewhat indefinite; a shift of $+0.2$ Mev in the energy assumed for the primary proton beam would cause both straight lines to pass through the origin. In anthracene the deviation from proportionality is more marked and cannot be accounted for by the uncertainty of this order in the beam energy.

The noticeable qualitative difference in the behaviors of the ionic crystals and of anthracene indicated by this study is further

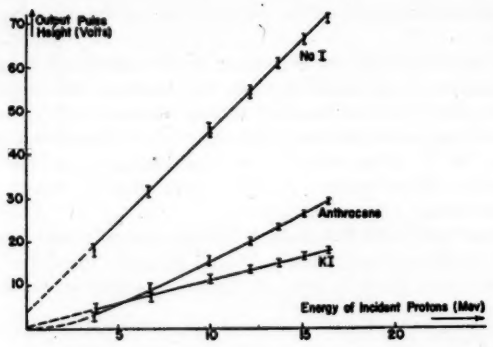

FIG. 2. Relationship between the pulse height deduced from the peak of the pulse height distribution curve and the energy of bombarding protons for the three types of crystals.

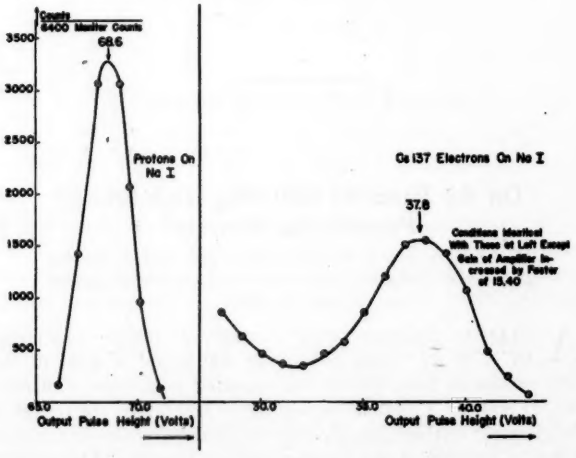

FIG. 3. Comparison between the pulse height distribution observed with 16.4-Mev protons and 0.624-Mev Cs^{137} conversion electrons bombarding sodium iodide. To obtain these curves, a thin Cs^{137} source on a 1.7-mg/cm^2 aluminum foil was mounted in the path of the proton beam at a distance of 4 cm from the surface of the crystal.

borne out by a comparison between the response of these materials to protons, electrons, and alpha-particles. For sodium iodide, a ratio of 26.8 between the proton beam energy and the energy of Cs^{137} conversion electrons corresponded to a pulse height ratio of 28.0. (The manner in which this comparison was carried out is illustrated by Fig. 3.) The corresponding pulse height ratios for potassium iodide and anthracene were 30.1 and 16.4 respectively. Similarly, a ratio of 8.70 between the energy of polonium alpha-particles bombarding the crystal surface and the energy of Cs^{137} conversion electrons corresponded to a pulse height ratio of 6.46 in the case of sodium iodide, 8.18 in the case of potassium iodide, and 0.82 for anthracene. It is believed that these pulse height ratios are affected somewhat by the surface structure of the crystal in the case of alpha-particle bombardment and by backscattering out of the crystal for electron bombardment. Nevertheless, the measurements show that the ionic crystals exhibit a response which is much closer to proportionality with energy (independent of particle type) than is the case for anthracene. Sodium iodide particularly, with suitable calibration, seems to be a very promising material for the observation of monoenergetic groups of high energy heavy particles.

* Supported by the joint program of the ONR and AEC.

[1] T. Broser and H. Kallmann, Nature 163, 20 (1949).
[2] W. H. Jordan and P. R. Bell, Nucleonics 5, No. 4, 30 (1949).
[3] Harding, Flowers, and Epstein, Nature 163, 990 (1949).
[4] G. F. J. Garlick and R. A. Fatehally, Phys. Rev. 75, 1446 (1949).
[5] J. I. Hopkins, Phys. Rev. 77, 406 (1950).
[6] S. A. E. Johannson, Nature 165, 396 (1950).

The Problem of Red Giants and Cepheid Variables

G. GAMOW AND C. LONGMIRE
Los Alamos Scientific Laboratory, Los Alamos, New Mexico
June 19, 1950

ACCORDING to the accepted model of the main sequence stars, these consist of a central convective zone (Cowling's zone) surrounded by an envelope in a state of radiative equilibrium. The energy producing thermonuclear reaction (carbon cycle) takes place near the center of the star, and the convective currents account for the uniform depletion of hydrogen through the entire convection region. The detailed calculations of this model[1] indicate that as the hydrogen in the convective zone gradually changes into helium (assumed change of molecular weight from $\mu=1$, corresponding to original hydrogen content, to $\mu=2$, corresponding to completely dehydrogenized material), the fraction of the stellar mass contained in the convective zone decreases from 15.0 to 8.1 percent. Thus, toward the end of this process, the star will consist of a central core (8 percent) of completely dehydrogenized material, a transitional layer (7 percent) with varying hydrogen content, and the outer envelope (85 percent) of virgin stellar material. Approaching this state of evolution, the star may be expected to pass into the so-called shell source model[2] consisting of an isothermal de-hydrogenized core with the carbon cycle taking place at the boundary between this isothermal region and the hydrogen-rich layers, so that further evolution will consist in a gradual advance of the shell source into the virgin material and the corresponding growth of the central isothermal core. However, more detailed calculation on this model[3] leads to a peculiar difficulty; namely, that no solutions exist which correspond to an equilibrium condition of the star when the amount of material in the isothermal core exceeds 10 percent of the total mass.

Some attempts have been made to remove this difficulty by taking into account the electron degeneracy at the center of the isothermal core. These calculations lead to the interesting result that there exist solutions which make the outer radius of the star increase by a large factor thus bringing it into the region of red giants.[4] Unfortunately, however, all these solutions correspond again to small isothermal cores (less than 10 percent) and can hardly be considered as possible transient stages of normal stellar evolution. In fact, since the shell source cannot be formed within the convective zone, we need such solutions only after the hydrogen in the original Cowling zone is used up and, since that zone contains about 10 percent of the total mass, we find that the solutions disappear just when we can use them!

We want to point out here that although the models with larger cores allow no static solutions, they permit some oscillatory solutions with finite amplitude (as, for example, in the case of an ordinary electric bell). Briefly, the argument in favor of the oscillatory solutions is as follows. Suppose a shell-source star undergoes radial oscillations,

$$r=x[1-\eta(x)f(t)], \tag{1}$$

where x is the average position of an element of mass, $f(t)$ averages to zero over a cycle, and $\eta(x)$ is the relative amplitude of oscillation. P_0, ρ_0 and T_0 are defined to be the pressure, density and temperature at the instants when $r=x$. One now writes down the time-dependent equations for the star; namely, the equation of motion, the equation of state, and the radiation transfer equation. Assuming adiabaticity over a cycle, one averages the time-dependent equations over a cycle, keeping only the zero- and second-order terms in $\eta(x)$. The equation of motion, for example, then has the form

$$A(x)\partial P_0/\partial x=-(GM_x\rho_0/x^2)B(x). \tag{2}$$

Here G is the gravitational constant and M_x is the mass contained within a sphere of radius x. $A(x)$ and $B(x)$ are functions which differ from unity only by terms of the second order in $\eta(x)$. Equation (2) reduces to the static equation when the amplitude of oscillation goes to zero. The equation of state between P_0, ρ_0 and T_0 is of course unchanged by the oscillation, but the radiation flux term also acquires a factor $C(x)$.

One now tries to define new quantities

$$P_1=f(x)P_0, \quad \rho_1=g(x)\rho_0, \quad T_1=h(x)T_0 \tag{3}$$

in such a way that P_1, ρ_1 and T_1 satisfy the ordinary static equations for the shell source model. It has been found possible to do so. It has been found that when P_1, ρ_1, T_1 correspond to a star with, say, 10 percent of the mass in the core, the actual quantities P_0, ρ_0, T_0 correspond to a star with more than 10 percent of the mass in the core, depending on the square of the amplitude of oscillation. The main effect of the oscillation seems to be to let radiation flow more easily into the envelope, raising the temperature and pressure, and consequently pushing some of the mass into a region of weaker gravitational attraction.

Although in calculating the functions A, B and C, we took the pressures, densities, temperatures and relative amplitudes $\eta(x)$ for the normal Cowling star,[5] the result does not seem to depend critically on this fact. We therefore conclude that an oscillating shell-source star can be stable on the average when its depletion of hydrogen exceeds the maximum amount for a static star, although our perturbation method does not allow us to say how far the depletion can be raised over the maximum for the static case.

The above picture may present a possibility for understanding the pulsating properties of cepheid variables. There is also a chance that the above-described oscillations may ultimately become unstable and develop into periodic explosions in which large amounts of nuclear energy are liberated in every cycle. (U-Geminorum stars?)

We hope in the future to carry out some calculations concerning the stability of these oscillations for continuously growing dimensions of the energy producing shell.

In conclusion, we want to express our thanks to R. Landshoff, E. Teller, S. Ulam, and J. Wheeler for valuable discussions.

[1] Marjorie H. Harrison, Astrophys. J. **100**, 343 (1944).
[2] G. Gamow, Astrophys. J. **87**, 206 (1938); C. Critchfield and G. Gamow, Astrophys. J. **89**, 244 (1939).
[3] R. Henrich and S. Chandrasekhar, Astrophys. J. **94**, 525 (1941); M. Schonberg and S. Chandrasekhar, Astrophys. J. **96**, 161 (1942).
[4] G. Gamow, Phys. Rev. **67**, 120 (1945); G. Gamow and G. Keller, Rev. Mod. Phys. **17**, 125 (1945); A. Reiz, Kgl. Danske Vid. Sels. Math.-fys. Medd. **25**, (1948); Arkiv f. Astr. **1**, (1949); Chushrio Hayashi, private communication. Compare also: Marjorie H. Harrison, Astrophys. J. **103**, 193 (1946); **105**, 322 (1947).
[5] See, for example, S. Rosseland, *The Pulsation Theory of Variable Stars* (Oxford University Press, London, 1949), in particular, Figs. 5, 6 and 8.

Pressure Broadening of Spectral Lines

T. HOLSTEIN
Westinghouse Research Laboratories, East Pittsburgh, Pennsylvania
May 1, 1950

THIS note presents a brief summary of some theoretical work on the development of the statistical theory of pressure broadening in terms of the basic "Fourier integral" approach. A more complete report will appear at a later date.

We use here the simplest version of the Fourier integral theory, which assumes the non-degeneracy of both initial and final energy levels. Under this condition, essentially the only effect of interaction between a radiating atom and its neighbors is the modulation of the unperturbed line frequency, ω_0, with a "frequency perturbation" $\omega_p(t)$ equal to $1/\hbar$ times the instantaneous relative shift of the two energy levels. We introduce the "phase perturbation" $\varphi(t)=\int^t\omega_p(t)dt$ and set the zero of our frequency scale at ω_0. The Fourier integral formulation for the spectral intensity, $I(\omega)$, then reads[1]

$$I(\omega)=\langle|A(\omega)|^2\rangle_{Av}, \tag{1}$$

$$A(\omega)=(2\pi T)^{-\frac{1}{2}}\int_{-T/2}^{+T/2}\exp\{i[\varphi(t)-\omega t]\}dt. \tag{2}$$

In these relations, the symbol $\langle\ \rangle_{Av}$ denotes an average over all types of collision, T is an arbitrarily large time interval, and the factor $(2\pi T)^{-\frac{1}{2}}$ takes care of the normalization of $I(\omega)$.

The derivation[2] of the statistical intensity distribution from (1) and (2) proceeds as follows. We take ω large enough so that, on the time scale in which $\omega_p(t)$ and its derivatives undergo appreciable relative variations, $e^{i\omega t}$ is a rapidly oscillating function. In this case the whole integrand of (2) oscillates rapidly except at points t_i such that $d\varphi/dt_i\equiv\omega_p(t_i)=\omega$. Hence, only the neighborhoods of these "coincidence" points contribute significantly to the integral. Developing $\varphi(t)$ in a Taylor series about each t_i and dropping terms of order higher than $(t-t_i)^2$, we have

$$\begin{aligned}A(\omega)\cong(2\pi T)^{-\frac{1}{2}}\Sigma_i\exp\{i[\varphi(t_i)-\omega t_i]\}\\ \times\int_{-\infty}^{+\infty}\exp[(i/2)(d\omega_p/dt_i)(t-t_i)^2]dt\\ =\Sigma_i\exp\{\varphi(t_i)-\omega t_i\pm i\pi/4]\}(T|d\omega_p/dt_i|)^{-\frac{1}{2}},\end{aligned} \tag{3}$$

the plus (minus) sign in the exponent prevailing when $d\omega_p/dt_i$ is positive (negative). Inserting (3) into (1) and ignoring phase correlations between different coincidence points, we obtain

$$I(\omega)=(1/T)\langle\Sigma_i|d\omega_p/dt_i|^{-1}\rangle_{Av} \tag{4}$$

which represents the statistical distribution in its most general form. Namely, the right-hand side of (4) is equal to the *occurrence distribution* of $\omega_p(t)$, i.e., that fraction of the time interval T for which $\omega_p(t)$ is contained in a unit frequency range at ω.

In our detailed calculations, aimed at determining the accuracy and domain of applicability of the above derivation of the statistical distribution, we have treated the case in which the interaction of a radiating atom with its neighbors consists of a succession of binary collisions (low density of perturbing atoms). Each of these encounters is assumed to provide a frequency modulation of the form

$$\omega_p(t)=C/r^n=C/[R_\alpha^2+v^2(t-t_\alpha)^2]^{n/2}, \tag{5}$$

where C and n are interaction constants and v the relative velocity of colliding atoms. The averaging operation of (1) consists in summing over all values of the impact parameter, R_α, and time of closest approach, t_α, for each collision.

On introducing (5) into (2) and evaluating the integrals by the method of steepest descents,[3] we obtain

$$A(\omega)=\Sigma_\alpha\exp\{i[\varphi(t_\alpha)-\omega t_\alpha]\}A_\alpha(\omega) \tag{6}$$

where $A_\alpha(\omega)$, the contribution of the αth collision, is given by an asymptotic series of the form

$$\begin{aligned}A_\alpha(\omega)\cong 2(T|d\omega_p/dt_i|)^{-\frac{1}{2}}\cos[\varphi(t_i)-\varphi(t_\alpha)-\omega(t_i-t_\alpha)-\pi/4]\\ +\text{terms in } d^2\omega_p/dt_i^2,\ \ d^3\omega_p/dt_i^3\cdots.\end{aligned} \tag{7}$$

In this expression, $t_i=t_\alpha+[(C/\omega)^{2/n}-R_\alpha^2]^{\frac{1}{2}}$. It is found that, for large ω—more precisely,[4] $\omega^{1-1/n}C^{1/n}/v\gg1$—Eq. (7) constitutes a satisfactory approximation for all $R_\alpha<(C/\omega)^{1/n}$ exclusive of the immediate neighborhood of the point $R_\alpha=(C/\omega)^{1/n}$ (at which $t_i=t_\alpha$). In this region we use an alternate approach. Expanding (5) binominally in powers of $v^2(t-t_\alpha)^2/R_\alpha^2$, we find it possible to express $A_\alpha(\omega)$ as a series of terms involving Airy's integral[5]

$$\int_{-\infty}^{+\infty}\exp[i(t^3\pm xt)]dt.$$

As $(C/\omega)^{1/n}-R_\alpha$ increases positively, the series in question passes over smoothly into that given by (7); as $(C/\omega)^{1/n}-R_\alpha$ increases negatively (no point of coincidence in the collision), $A_\alpha(\omega)$ drops rapidly to zero.

We now insert (6) into (1) and average over the t_α and R_α. The main effect of the average over t_α is to eliminate any coherence between the contributions of different collisions. In averaging over the R_α, we simply group the collisions according to the values of their impact parameters and integrate. We thus obtain

$$I(\omega)=\int_0^\infty|A_\alpha(\omega)|^2\cdot T\cdot 2\pi NvR_\alpha dR_\alpha, \tag{8}$$

where N is equal to the density of perturbing atoms.

Detailed calculations following the procedure outlined above yield for $I(\omega)$ the expression

$$\begin{aligned}I(\omega)=\frac{4\pi NC^{3/n}}{n\omega^{1+3/n}}\{1-(n/36)(1+1/2n)(1-1/n^2)\\ \times[\omega^{1-1/n}C^{1/n}/v]^{-2}\},\end{aligned} \tag{9}$$

which constitutes the first two terms of an asymptotic series in increasing negative powers of $\omega^{1-1/n}C^{1/n}/v$.

The factor in front of the curly bracket of (9) is the well-known statistical distribution of Kuhn and Margenau[6] for the case of binary collisions. From (9) it is obvious that this distribution is valid when $\omega\gg v^{n/(n-1)}/C^{1/(n-1)}$ (i.e., in the wing of the line). Now, Spitzer[7] has shown that the impact theory of pressure broadening is valid when $\omega\ll v^{n/(n-1)}/C^{1/(n-1)}$ (i.e., in the vicinity of the unperturbed line). Finally, in the case of binary collisions, the ratio of the statistical to the impact distribution[8] turns out to be $\sim(\omega^{1-1/n}C^{1/n}/v)^{(n-3)/(n-1)}$ which is equal to unity for $\omega=v^{n/(n-1)}C^{1/(n-1)}$. These results exhibit the transition between the two theories as well as the domains of applicability of each.

[1] See, for example, H. M. Foley, Phys. Rev. **69**, 616 (1946), p. 619, second column, first equation (where $P(t)$ is equal to our $\omega_p(t)$). This as well as the present formulation requires the additional specification that ω_0 is large compared to ω; such a restriction excludes certain cases of microwave broadening in which one is interested in values of ω comparable to ω_0.
[2] The method was previously employed in a quantum-mechanical treatment of pressure broadening by A. Jablonski, Phys. Rev. **68**, 78 (1945).
[3] G. N. Watson, *Theory of Bessel Functions* (Cambridge University Press, New York, 1945), second edition, pp. 235, 236.
[4] It is instructive to write $\omega^{1-1/n}C^{1/n}/v$ in the form $\omega\tau_c$, where $\tau_c=(C/\omega)^{1/n}/v$ may be considered as the "time of collision."
[5] Reference 3, pp. 188–190.
[6] H. Kuhn, Phil. Mag. **18**, 987 (1934); H. Margenau, Phys. Rev. **48**, 755 (1935).
[7] L. Spitzer, Jr., Phys. Rev. **58**, 348 (1940).
[8] Reference 1, Eqs. (16), (17) and intervening text. For the case of binary collisions the denominator of (16) reduces to ω^2; the quantity γ in (17) is our C multiplied by an unimportant numerical factor.

On the Evaluation of the Fermi β-Distribution Function

HARVEY HALL
Department of Physics, University of Southern California, Los Angeles, California
June 14, 1950

IT was recently announced[1] that an accurate computation is in progress of the Coulomb correction factor involved in Fermi's theory of β-decay. The need for this computation apparently occurs because the literature does not contain a satisfactory analytic expression for the function,

$$f(Z,\eta)=\eta^{2+2S}e^{\pi\nu}|\Gamma(1+S+i\nu)|^2 \quad (1)$$

in the notation of reference 1.

Evaluation of Eq. (1) is difficult only because it depends upon the magnitude of the complex gamma-function. It is the purpose of this letter to point out that the complex gamma-function can be evaluated by means of the asymptotic formula for $\Gamma(z)$ for z large, *even though the value of* $|z|$ *may only be of order unity*. None of the approximate formulas quoted in reference 1 appear to utilize this property of $\Gamma(z)$.

The asymptotic expansion in question is given by the equation[2]

$$\ln\Gamma(z)=\tfrac{1}{2}\ln 2\pi+(z-\tfrac{1}{2})\ln z-z+1/12z+J_1(z), \quad (2)$$

where, for the conditions of this problem

$$|J_1(z)|<1/360(1-\alpha^2)(1+\alpha^2/\eta^2)^{\frac{1}{2}}<1/200.$$

Calculations based on Eq. (2) with $J_1(z)=0$ will thus provide an accuracy for $f(Z,\eta)$ of better than one percent, and a somewhat better accuracy still for the shape of the curve (about three-tenths percent for the worst case of reference 1 with $Z=90$). On the basis of this procedure the following formula is obtained

$$f(Z,\eta)\sim 2\pi\eta^{2z}\exp(-2x+2y\tan^{-1}x/y)(1+\alpha^2/\eta^2)^{x-\frac{1}{2}} \times\exp\{1+x/6(1+\alpha^2/\eta^2)\}, \quad (3)$$

where $x=(1-\alpha^2)^{\frac{1}{2}}$, $y=\alpha(1+\eta^2)^{\frac{1}{2}}/\eta$, $\alpha=Z/137$.

If greater accuracy is desired another term may be retained in the expansion of $\Gamma(z)$. In this case the neglected remainder, J_2, amounts to less than three-tenths percent in the resulting expression for $f(Z,\eta)$. The accuracy provided by Eq. (3) is probably more than adequate for use with available experimental data.

[1] I. Feister, Phys. Rev. **78**, 375 (1950).
[2] T. M. MacRobert, *Functions of a Complex Variable* (Macmillan Publishing Company, New York, 1917), p. 149.

Physical Theory of Ferromagnetic Domains

L. W. MCKEEHAN
Sloane Physics Laboratory, Yale University, New Haven, Connecticut
February 3, 1950

A GENERALLY excellent review bearing the title of this note has recently been published by Kittel.[1] This review, however, fails to mention at least one rather fundamental contribution to the subject, and, possibly as a result of this oversight, claims priority for the observation by Williams and Shockley[2] that Barkhausen noises may be associated with minor fluctuations of a boundary between two ferromagnetic domains rather than with transfer of a whole domain from one direction of magnetization to another.

Such stepwise advance of a domain boundary, in the case of cobalt, was long ago described in detail by Elmore[3] and the significance of this observation in the calculations of domain size was clearly recognized in the last previous American review of this subject by Brown.[4] This review is one of the most important papers omitted from Kittel's bibliography.

The other gaps in the historical background are much less important and are believed to be due in part to the gradual shift in emphasis, during the early history of domain investigations, from crystal anisotropy to strain anisotropy as the most usual determinant for domain or sub-domain boundary fixation. Some of the pertinent stages in this history are mentioned in an accompanying note entitled "Ferromagnetic Block."

The value of Kittel's Appendix B, on crystal lattice sums of dipole arrays, would have been greater if it had mentioned the conditional convergence of the lattice sums presented, and had given some indication of work before[5] and since[6] the single 1930 paper[7] cited. The relative unimportance of dipole magnetic fields in usual materials is now obvious, as Kittel points out in this appendix, but they may yet amount to something in sensibly strain-free single crystals where local magnetic fields of very small magnitude, in comparison with the molecular field, have such striking effects in locating domain boundaries.

[1] C. Kittel, Rev. Mod. Phys. **21**, 541 (1949).
[2] H. J. Williams and W. Shockley, Phys. Rev. **75**, 178 (1949).
[3] W. C. Elmore, Phys. Rev. **53**, 757 (1938).
[4] W. F. Brown, Jr., J. App. Phys. **11**, 160 (1940).
[5] N. S. Akulov, Zeits. f. Physik **52**, 389 (1928).
[6] T. Hayasi, Zeits. f. Physik **72**, 177 (1931); **91**, 818 (1934); F. C. Powell, Proc. Camb. Phil. Soc. **27**, 561 (1931); L. W. McKeehan, Phys. Rev. **43**, 1022 (1933); J. M. Luttinger and L. Tisza, Phys. Rev. **70**, 954 (1946) corrected in Phys. Rev. **72**, 257 (1947).
[7] R. Becker, Zeits. f. Physik **62**, 253 (1930).

Nuclear Size Resonances

K. W. FORD AND D. BOHM
Princeton University, Princeton, New Jersey
June 19, 1950

RECENT data on slow neutron scattering by nuclei[1] have been examined to look for a possible regular variation of scattering amplitude with nuclear size, or with mass number, A. The bound scattering amplitude (=scattering length) plotted *vs.* mass number in Fig. 1 gives some indication of such a regularity, but is by no means conclusive.

If the neutron wave function is influenced in a regular manner by the nuclear size, the scattering amplitude plotted against the mass number curve should show resonances similar to those which appear when this quantity is plotted against neutron energy for a single element. The data indicate one such resonance in the vicinity of $A=55$. The scattering amplitude of Fe^{56} is high; that of Ni^{58} is very high. Mn^{55} and Ti^{48} have negative amplitudes. (The signs for V^{51} and Cr^{52} are unknown.)

Another resonance is indicated near $A=8$. Li^7 has a negative scattering amplitude; Be^9 has a large and positive amplitude. The scattering amplitudes show a regularly decreasing trend from $A=9$ to $A=50$ with the notable exception of Cl. The hard sphere scattering amplitude, however, would be everywhere increasing with A.

If the neutron-nucleus system is close to resonance, the slope of the wave function at the edge of the nucleus is near zero. Small changes in nuclear parameters, or changes in spin orientation will therefore cause large changes in scattering amplitude. Hence if the nuclear spin is different from zero, or if more than one isotope is present, the possibility of destructive interference exists, so that small coherent cross sections are not unexpected in this region. Thus the extremely small coherent cross section of V^{51} can be explained on the assumption that the system is near resonance for this element. Also Ti^{48} and Co^{59} have unusually small coherent cross sections, and that of Mn^{55} is rather small. (Fe^{56}, Ni^{58}, and Ni^{60}, being single isotopes of zero spin, do not have small coherent

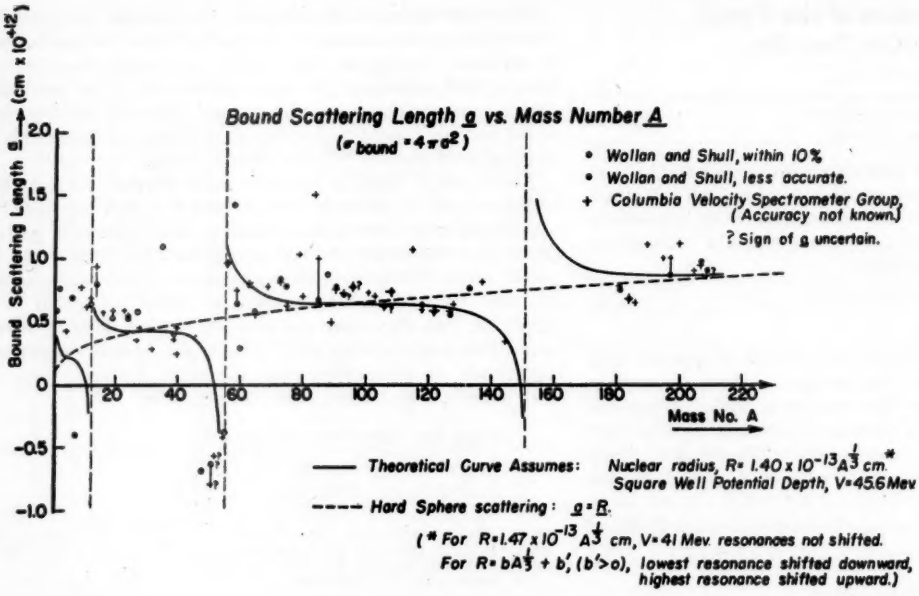
Bound Scattering Length a vs. Mass Number A
(σ bound = 4πa²)
Bound Scattering Length a → (cm x 10⁻¹²)
2.0
1.5
1.0
0.5
0
-0.5
-1.0
20
40
60
80
100
120
140
160
180
200
220
Mass No. A
• Wollan and Shull, within 10%
• Wollan and Shull, less accurate.
+ Columbia Velocity Spectrometer Group, (Accuracy not known)
? Sign of a uncertain.
—— Theoretical Curve Assumes: Nuclear radius, R = 1.40 x 10⁻¹³ A^⅓ cm.*
Square Well Potential Depth, V = 45.6 Mev
---- Hard Sphere scattering: a = R.
(* For R = 1.47 x 10⁻¹³ A^⅓ cm, V = 41 Mev resonances not shifted.
For R = bA^⅓ + b', (b'>0), lowest resonance shifted downward, highest resonance shifted upward.)

FIG. 1. Scattering of slow neutrons by nuclei.

cross sections.) Most other elements show coherent cross sections nearly as large as the bound cross sections.

Several models would predict qualitatively such resonance behavior. (a) A simple square well (without absorption) would give the plotted curve by adjusting the well depth to yield a resonance at $A=55+$, and using $R=1.40\times10^{-13}A^{\frac{1}{3}}$ cm. One obtains in this way a depth V=45 Mev. In this model, one assumes that the neutron moves in the average field of all the other nucleons, and that the collisions with the fluctuating part of the nucleon potential can be neglected to a first approximation. This is just the free particle approximation which underlies the shell structure model.

With this model, two other resonances are predicted, one at $A\cong12$, the other at $A\cong151$. For light nuclei, however, the formula for nuclear radius breaks down. Then $R/A^{\frac{1}{3}}>1.40\times10^{-13}$ cm, which depresses the $A=12$ resonance, so that the observed resonance at $A=8$ is reasonable. Unfortunately, no scattering amplitudes are known near $A=151$ except Nd^{145}, which is small. The most pronounced maximum in thermal neutron absorption cross sections occurs at about $A=155$, however. Otherwise the absorption cross sections do not vary very regularly, since they show arge isotope dependence (large for neutron deficient isotopes) and are more strongly influenced by low lying sharp resonance levels.

(b) The excitation of longitudinal nuclear waves (liquid droplet model) would predict resonances for values of the nuclear radius such that $(\frac{1}{2}n+\frac{1}{4})\lambda=R$, where λ=wave-length of the nuclear compression wave, and n is an integer. This is the same condition as that with the square well model, where the compression wavelength is replaced by the neutron wave-length inside the well, and could give resonances at the same places by adjustment of a single parameter. This demands an "inverse nuclear compressibility" of about 7 Mev$\times A^{\frac{1}{3}}/r_0^2(r_0\equiv R/A^{\frac{1}{3}})$, much smaller than Feenberg's estimate[2] of 50 to 100 Mev$\times A^{\frac{1}{3}}/r_0^2$. Only radially symmetric vibrations would be expected to be excited by thermal neutrons.

(c) An energy level varying in a regular way among the elements (decreasing with increasing A) would predict such a resonance behavior. It would need to be either very broad (~Mev) or very slowly varying with A. Such an energy level has no known theoretical justification.

[1] Wollan and Shull, via K. Way, mostly unpublished; Havens and Taylor Nucleonics 6-2, 74 (1950).
[2] E. Feenberg, Rev. Mod. Phys. 19, 239 (1947).